

Ancient dog genome informs on
domestication pp. 1153 & 1228

Neuroscience gains a foothold
in the West Bank p. 1158

Cool books for hot
summer days p. 1166

Science

\$15
3 JUNE 2016
sciencemag.org

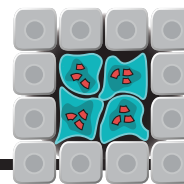
AAAS

METALENS

Metasurfaces make an entry into high-end optics p. 1190

CONTENTS

3 JUNE 2016 • VOLUME 352 • ISSUE 6290



1178

Therapeutically blocking
DNA repair in cancer cells

NEWS

IN BRIEF

1148 News at a glance

IN DEPTH

1152 MOSQUITO HUNTERS SEARCH FOR ZIKA VECTORS

Yellow fever mosquito is confirmed, but others may contribute *By G. Vogel*

1153 DOGS MAY HAVE BEEN DOMESTICATED MORE THAN ONCE

But all living dogs have Asian roots
By D. Grimm

► REPORT P. 1228; VIDEO

1154 'CULINARY FRONTIER' TRACKS MADAGASCAR'S ASIAN SETTLERS

Crop remains record a wave of arrivals from the East *By A. Lawler*

1155 TELESCOPE AND NASA MISSION GET UNDER JUPITER'S SKIN

Ground-based VLA spies giant wave of ammonia, while the Juno spacecraft gears up to go after the water *By E. Hand*

► REPORT P. 1198

1156 CRISPR VIEWS OF EMBRYOS AND CELLS

Genome editor helps record development, cell influences *By K. Kupferschmidt*

FEATURES

1158 PEACE OF MIND

A young Palestinian neuroscientist hopes to create a research oasis in the West Bank that transcends politics
By M. Enserink

..... **1161 Gatherings aim to bridge a wide divide**
By M. Enserink

1162 STRANDING SLEUTH

Gleaning clues from beached marine mammals, Frances Gulland takes the measure of ocean health *By E. Pennisi*



INSIGHTS

BOOKS ET AL.

1166 THE SCIENTIST'S GUIDE TO SUMMER READING

PERSPECTIVES

1172 ECOLOGICALLY RELEVANT DATA ARE POLICY-RELEVANT DATA

Microplastics reduce fish hatching success and survival *By C. M. Rochman*

► REPORT P. 1213

1173 A LIPID ARSENAL TO CONTROL INFLAMMATION

Lipids released from dying cells control immune responses to microbial products *By B. A. Napier and D. M. Monack*

► REPORT P. 1232

1174 BEYOND PREBIOTIC CHEMISTRY

What dynamic network properties allow the emergence of life?
By L. Cronin and S. I. Walker

1176 CONNECTING THE DOTS IN MAGNETIC RECONNECTION

Four formation-flying spacecraft reveal the 3D electron physics of magnetic reconnection *By A. J. Coates*

► RESEARCH ARTICLE P. 1189

1177 PHOTONIC MULTITASKING ENABLED WITH GEOMETRIC PHASE

Metasurface-based phased-array antennas help implement flat optical devices that perform multiple functions
By N. M. Litchinitser

► REPORT P. 1202

1178 DRUGGING DNA REPAIR

Inhibiting DNA repair can have a positive outcome on therapeutic interventions

By S. P. Jackson and T. Helleday

1180 ALIGNING STATISTICAL AND SCIENTIFIC REASONING

Misunderstanding and misuse of statistical significance impede science
By S. N. Goodman

LETTERS

1182 FEDERAL BARRIERS TO CANNABIS RESEARCH

By S. S. Stith and J. M. Vigil

1182 NO SURPRISE THAT COMB JELLIES POOP

By S. L. Tamm

1182 DIGITAL IDENTIFIERS FOR FUNGAL SPECIES

By U. Köljal et al.

1183 RESPONSE

By D. Hibbett

CONTENTS



1177 & 1202

Sculpted beams from metasurfaces

3 JUNE 2016 • VOLUME 352 • ISSUE 6290

RESEARCH

IN BRIEF

1185 From *Science* and other journals

REVIEW

1188 EPIGENETICS

Epigenetic balance of gene expression by Polycomb and COMPASS families
A. Piunti and A. Shilatifard

REVIEW SUMMARY; FOR FULL TEXT:

dx.doi.org/10.1126/science.aad9780

RESEARCH ARTICLES

1189 PLASMA ASTROPHYSICS

Electron-scale measurements of magnetic reconnection in space
J. L. Burch et al.

RESEARCH ARTICLE SUMMARY; FOR FULL TEXT:

dx.doi.org/10.1126/science.aaf2939

► PERSPECTIVE P. 1176

1190 APPLIED OPTICS

Metalenses at visible wavelengths: Diffraction-limited focusing and subwavelength resolution imaging
M. Khorasaninejad et al.

► VIDEO

REPORTS

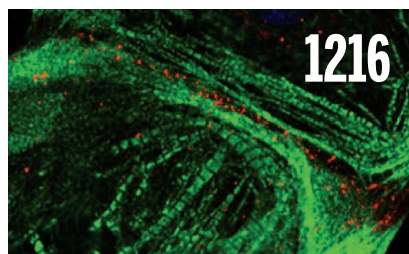
1194 WATER CHEMISTRY

Structure and torsional dynamics of the water octamer from THz laser spectroscopy near 215 μm
W. T. S. Cole et al.

1198 GAS GIANT PLANETS

Peering through Jupiter's clouds with radio spectral imaging
I. de Pater et al.

► NEWS STORY P. 1155



1202 APPLIED OPTICS

Photonic spin-controlled multifunctional shared-aperture antenna array
E. Maguid et al.

► PERSPECTIVE P. 1177

1206 MAGNETISM

Orbital-exchange and fractional quantum number excitations in an f-electron metal, $\text{Yb}_2\text{Pt}_2\text{Pb}$
L. S. Wu et al.

1210 BIOENERGY

Water splitting–biosynthetic system with CO_2 reduction efficiencies exceeding photosynthesis
C. Liu et al.

► PODCAST

1213 ECOTOXICOLOGY

Environmentally relevant concentrations of microplastic particles influence larval fish ecology
O. M. Lönnstedt and P. Eklöv

► PERSPECTIVE P. 1172

1216 CELL REPROGRAMMING

Conversion of human fibroblasts into functional cardiomyocytes by small molecules
N. Cao et al.

1221 BIOCHEMISTRY

ADP-ribose–derived nuclear ATP synthesis by NUDIX5 is required for chromatin remodeling
R. H. G. Wright et al.

1225 RNA TRANSCRIPTION

TT-seq maps the human transient transcriptome
B. Schwalb et al.

1228 NONHUMAN GENETICS

Genomic and archaeological evidence suggests a dual origin of domestic dogs

L. A. F. Frantz et al.

► NEWS STORY P. 1153

1232 INNATE IMMUNITY

An endogenous caspase-11 ligand elicits interleukin-1 release from living dendritic cells

I. Zanoni et al.

► PERSPECTIVE P. 1173

DEPARTMENTS

1147 EDITORIAL

Taking up TOP

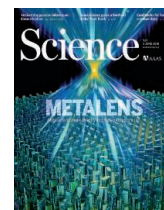
By Marcia McNutt

1246 WORKING LIFE

Flying free before building my nest

By Antoni Margalida

ON THE COVER



Nanoscale titanium dioxide fins in an ultrathin planar lens (a metalens) focus visible light (entering from the bottom and propagating upward) with high efficiency down to a subwavelength spot

(yellow area). Due to their ultracompact geometry and high-resolution imaging capabilities, metalenses have potential to replace conventional lenses in a wide range of applications, such as cameras, wearable displays, and microscopes. See page 1190.

Image: Second Bay Studios

Science Staff	1146
New Products	1238
Science Careers	1239

1190

SCIENCE (ISSN 0036-8075) is published weekly on Friday, except the last week in December, by the American Association for the Advancement of Science, 1200 New York Avenue, NW, Washington, DC 20005. Periodicals mail postage (publication No. 484460) paid at Washington, DC, and additional mailing offices. Copyright © 2016 by the American Association for the Advancement of Science. The title SCIENCE is a registered trademark of the AAAS. Domestic individual membership and subscription (\$1 issues): \$165 (\$74 allocated to subscription). Domestic institutional subscription (\$1 issues): \$1522. Foreign postage extra: Mexico, Caribbean (surface mail) \$55; other countries (air assist delivery) \$89. First class, airmail, student, and emeritus rates on request. Canadian rates with GST available upon request, GST #1254 88122. Publications Mail Agreement Number 1069624. Printed in the U.S.A. Change of address: Allow 4 weeks, giving old and new addresses and 8-digit account number. Postmaster: Send change of address to AAAS, P.O. Box 96178, Washington, DC 20090-6178. Single-copy sales: \$15.00 current issue, \$20.00 back issue prepaid includes surface postage; bulk rates on request. Authorization to photocopy material for internal or personal use under circumstances not falling within the fair use provisions of the Copyright Act is granted by AAAS to libraries and other users registered with the Copyright Clearance Center (CCC) Transactional Reporting Service, provided that \$35.00 per article is paid directly to CCC, 222 Rosewood Drive, Danvers, MA 01923. The identification code for Science is 0036-8075. Science is indexed in the Reader's Guide to Periodical Literature and in several specialized indexes.

Editor-in-Chief Marcia McNutt

Executive Editor Monica M. Bradford **News Editor** Tim Appenzeller

Managing Editor, Research Journals Katrina L. Kelner

Deputy Editors Lisa D. Chong, Andrew M. Sugden(UK), Valda J. Vinson, Jake S. Yeston

Research and Insights

DEPUTY EDITOR, EMERITUS Barbara R. Jasny **SR. EDITORS** Caroline Ash(UK), Gilbert J. Chin, Julia Fahrenkamp-Uppenbrink(UK), Pamela J. Hines, Stella M. Hurlley(UK), Paula A. Kiberstis, Marc S. Lavine(Canada), Kristen L. Mueller, Ian S. Osborne(UK), Beverly A. Purnell, L. Bryan Ray, Guy Riddihough, H. Jesse Smith, Jelena Stajic, Peter Stern(UK), Phillip D. Szurromi, Sacha Vignieri, Brad Noble, Nicholas S. Wigginton, Laura M. Zahn **ASSOCIATE EDITORS** Brent Grocholski, Keith T. Smith **ASSOCIATE BOOK REVIEW EDITOR** Valerie B. Thompson **LETTERS EDITOR** Jennifer Sills **CHIEF CONTENT PRODUCTION EDITOR** Cara Tate **SR. CONTENT PRODUCTION EDITORS** Harry Jach, Lauren Kmec **CONTENT PRODUCTION EDITORS** Jeffrey E. Cook, Chris Filiatreau, Cynthia Howe, Barbara P. Ordway, Catherine Wolner **SR. EDITORIAL COORDINATORS** Carolyn Kyle, Beverly Shields **EDITORIAL COORDINATORS** Aneera Dobbins, Joi S. Granger, Lisa Johnson, Anita Wynn **PUBLICATIONS ASSISTANTS** Jeffrey Hearn, Dona Mathieu, Le-Toya Mayne Flood, Shannon McMahon, Scott Miller, Caitlyn Phillips, Jerry Richardson, Alice Whaley(UK), Brian White **EXECUTIVE ASSISTANT** Anna Bashkirova **ADMINISTRATIVE SUPPORT** Janet Clements(UK), Lizzanne Newton(UK), Maryrose Madrid

News

NEWS MANAGING EDITOR John Travis **INTERNATIONAL EDITOR** Richard Stone **DEPUTY NEWS EDITORS** Robert Coontz, Elizabeth Culotta, David Grimm, David Malakoff, Leslie Roberts **CONTRIBUTING EDITOR** Martin Enserink(Europe) **SR. CORRESPONDENTS** Daniel Clery(UK), Jeffrey Mervis, Elizabeth Pennisi **NEWS WRITERS** Adrian Cho, Jon Cohen, Jennifer Couzin-Frankel, Carolyn Gramling, Eric Hand, Jocelyn Kaiser, Catherine Maticic, Kelly Servick, Robert F. Service, Erik Stokstad(Cambridge, UK), Emily Underwood **INTERNS** Patrick Monahan **CONTRIBUTING CORRESPONDENTS** John Bohannon, Warren Cornwall, Ann Gibbons, Mara Hvistendahl, Sam Kerns, Eli Kintisch, Kai Kupferschmidt(Berlin), Andrew Lawler, Christina Larson(Beijing), Mitch Leslie, Charles C. Mann, Eliot Marshall, Virginia Morell, Dennis Normile(Shanghai), Heather Pringle, Tania Rabesandratana(London), Gretchen Vogel(Berlin), Lizzie Wade(Mexico City) **CAREERS** Donisha Adams, Rachel Bernstein(Editor) **COPY EDITORS** Julia Cole, Dorie Cheven, Jennifer Levin (Chief) **ADMINISTRATIVE SUPPORT** Jessica Adams

Executive Publisher Rush D. Holt

Interim Publisher Bill Moran **Chief Digital Media Officer** Rob Covey

BUSINESS OPERATIONS AND PORTFOLIO MANAGEMENT DIRECTOR Sarah Whalen **PRODUCT DEVELOPMENT DIRECTOR** Will Schweitzer **PRODUCT DEVELOPMENT ASSOCIATE** Hal Moore **BUSINESS SYSTEMS AND FINANCIAL ANALYSIS DIRECTOR** Randy Yi **MANAGER OF FULFILLMENT SYSTEMS** Neal Hawkins **SYSTEMS ANALYST** Nicole Mehmedovich **ASSISTANT DIRECTOR, BUSINESS OPERATIONS** Eric Knott **MANAGER, BUSINESS OPERATIONS** Jessica Tierney **SENIOR BUSINESS ANALYST** Cory Lipman **BUSINESS ANALYSTS** David Garrison, Meron Kebede, Sandy Kim **FINANCIAL ANALYST** Drew Sher **DIRECTOR, COPYRIGHTS LICENSING SPECIAL PROJECTS** Emilie David **PERMISSIONS ASSOCIATE** Elizabeth Sandler **RIGHTS, CONTRACTS, AND LICENSING ASSOCIATE** Lili Kiser

MARKETING DIRECTOR Elise Swinehart **ASSOCIATE MARKETING DIRECTOR** Christina Schlecht **MARKETING MANAGER** Elizabeth Sattler **MARKETING ASSOCIATE** Steven Goodman **CREATIVE DIRECTOR** Scott Rodgerson **SENIOR ART ASSOCIATES** Seil Lee, Paula Fry **ART ASSOCIATE** Kim Huynh **PROGRAM DIRECTOR, AAAS MEMBER CENTRAL** Peggy Mihelich **FULFILLMENT SYSTEMS AND OPERATIONS** membership@aaas.org **MANAGER, MEMBER SERVICES** Pat Butler **SPECIALISTS** Terrance Morrison, Latasha Russell **MANAGER, DATA ENTRY** Mickie Napoleoni **DATA ENTRY SPECIALISTS** Brenden Aquilino, Fiona Giblin

PUBLISHER RELATIONS MANAGER Catherine Holland **PUBLISHER RELATIONS, EASTERN REGION** Keith Layson **PUBLISHER RELATIONS, WESTERN REGION** Ryan Rexroth **SALES RESEARCH COORDINATOR** Aiesha Marshall **MANAGER, SITE LICENSE OPERATIONS** Iquo Edim **SENIOR OPERATIONS ANALYST** Lana Guz **FULFILLMENT ANALYST** Judy Lillibridge **ASSOCIATE DIRECTOR, MARKETING** Christina Schlecht **MARKETING ASSOCIATE** Isa Sesay-Bah

WEB TECHNOLOGIES **PORTFOLIO MANAGER** Trista Smith **TECHNICAL MANAGER** Chris Coleman **PROJECT MANAGER** Nick Fletcher **DEVELOPERS** Ryan Jensen, Jimmy Marks, Brandon Morrison

DIGITAL MEDIA DIRECTOR OF ANALYTICS Enrique Gonzales **DIGITAL REPORTING ANALYST** Eric Hossinger **SR. WEB PRODUCER** Sarah Crespi **WEB PRODUCER** Alison Crawford **VIDEO PRODUCER** Nguyen Nguyen **SOCIAL MEDIA PRODUCER** Brice Russ

DIRECTOR OF OPERATIONS PRINT AND ONLINE Lizabeth Harman **DIGITAL/PRINT STRATEGY MANAGER** Jason Hillman **QUALITY TECHNICAL MANAGER** Marcus Spiegler **PROJECT ACCOUNT MANAGER** Tara Kelly **DIGITAL PRODUCTION MANAGER** Lisa Stanford **ASSISTANT MANAGER** DIGITAL/PRINT Rebecca Doshi **SENIOR CONTENT SPECIALISTS** Steve Forrester, Antoinette Hodal, Lori Murphy, Anthony Rosen **CONTENT SPECIALISTS** Jacob Hedrick, Kimberley Oster

DESIGN DIRECTOR Beth Rakouskas **DESIGN EDITOR** Marcy Atarod **SENIOR DESIGNERS** Garvin Grullón, Chrystal Smith **GRAPHICS MANAGING EDITOR** Alberto Cuadra **SENIOR SCIENTIFIC ILLUSTRATORS** Chris Bickel, Katharine Suttiff **SCIENTIFIC ILLUSTRATOR** Valerie Altounian **INTERACTIVE GRAPHICS EDITOR** Jia You **SENIOR ART ASSOCIATES** Holly Bishop, Nathalie Cary **PHOTOGRAPHY MANAGING EDITOR** William Douthitt **PHOTO EDITOR** Christy Steele

DIRECTOR, GLOBAL COLLABORATION, CUSTOM PUBLICATIONS, ADVERTISING Bill Moran **EDITOR, CUSTOM PUBLISHING** Sean Sanders: 202-326-6430 **ADVERTISING MARKETING MANAGER** Justin Sawyers: 202-326-7061 science_advertising@aaas.org **ADVERTISING SUPPORT MANAGER** Karen Foote: 202-326-6740 **ADVERTISING PRODUCTION OPERATIONS MANAGER** Deborah Tompkins **SR. PRODUCTION SPECIALIST/GRAPHIC DESIGNER** Amy Hardcastle **SR. TRAFFIC ASSOCIATE** Christine Hall **SALES COORDINATOR** Shirley Young **ASSOCIATE DIRECTOR, COLLABORATION, CUSTOM PUBLICATIONS/CHINA/TAIWAN/KOREA/SINGAPORE** Ruolei Wu: +86-186 0082 9345, rnu@aaas.org **COLLABORATION/CUSTOM PUBLICATIONS/JAPAN** Adarsh Sandhu + 81532-81-5142 asandhu@aaas.org **EAST COAST/E. CANADA** Laurie Faraday: 508-747-9395, FAX 617-507-8189 west coast/W. CANADA Lynne Stickrod: 415-931-9782, FAX 415-520-6940 **MIDWEST** Jeffrey Dembski: 847-498-4520 x3005, Steven Loerch: 847-498-4520 x3006 **UK EUROPE/ASIA** Roger Gonçalves: TEL/FAX +41 43 235 1458 **JAPAN** Katsuyoshi Fukumizu(Tokyo): +81-3-3219-5777 kfukumizu@aaas.org **CHINA/TAIWAN** Ruolei Wu: +86-186 0082 9345, rnu@aaas.org

WORLDWIDE ASSOCIATE DIRECTOR OF SCIENCE CAREERS Tracy Holmes: +44 (0) 1223 326525, FAX +44 (0) 1223 326532 tholmes@science-int.co.uk **CLASSIFIED** advertise@sciencecareers.org **U.S. SALES** Tina Burks: 202-326-6577 Nancy Toema: 202-326-6578 **EUROPE/ROW SALES** Sarah Lelarge **SALES ASSISTANT** Kelly Grace **JAPAN** Hiroyuki Masshiki(Kyoto): +81-75-823-1109 hmasshiki@aaas.org **CHINA/TAIWAN** Ruolei Wu: +86-186 0082 9345 rnu@aaas.org **MARKETING MANAGER** Allison Pritchard **MARKETING ASSOCIATE** Aimee Aponte

AAAS BOARD OF DIRECTORS, CHAIR Geraldine L. Richmond **PRESIDENT** Barbara A. Schaaf **PRESIDENT-ELECT** Susan Hockfield **TREASURER** David Evans Shaw **CHIEF EXECUTIVE OFFICER** Rush D. Holt **BOARD** Cynthia M. Beall, May R. Berenbaum, Carlos J. Bustamante, Stephen P.A. Fodor, Claire M. Fraser, Michael S. Gazzaniga, Laura H. Greene, Elizabeth Loftus, Mercedes Pascual

SUBSCRIPTION SERVICES For change of address, missing issues, new orders and renewals, and payment questions: 866-434-AAAS (2227) or 202-326-6417, FAX 202-842-1065. Mailing addresses: AAAS, P.O. Box 96178, Washington, DC 20090-6178 or AAAS Member Services, 1200 New York Avenue, NW, Washington, DC 20005

INSTITUTIONAL SITE LICENSES 202-326-6730 **REPRINTS:** Author Inquiries 800-635-7181 **COMMERCIAL INQUIRIES** 803-359-4578 **PERMISSIONS** 202-326-6765, permissions@aaas.org **AAAS Member Services** 202-326-6417 or http://membercentral.aaas.org/discourts

Science serves as a forum for discussion of important issues related to the advancement of science by publishing material on which a consensus has been reached as well as including the presentation of minority of conflicting points of view. Accordingly, all articles published in Science—including editorials, news and comment, and book reviews—are signed and reflect the individual views of the authors and not official points of view adopted by AAAS or the institutions with which the authors are affiliated.

INFORMATION FOR AUTHORS See pages 624 and 625 of the 5 February 2016 issue or access www.sciencemag.org/authors/science-information-authors

SENIOR EDITORIAL BOARD

Gary King, Harvard University, Susan M. Rosenberg, Baylor College of Medicine, Ali Shilatifard, Northwestern University Feinberg School of Medicine

BOARD OF REVIEWING EDITORS (Statistics board members indicated with \$)

Adriano Aguzzi, U. Hospital Zürich
Takuzo Aida, U. of Tokyo
Leslie Aiello, Wenner-Gren Foundation
Judith Allen, U. of Edinburgh
Sonia Altizer, U. of Georgia
Sebastian Amigorena, Institut Curie
Kathryn Anderson, Memorial Sloan-Kettering Cancer Center
Meinrat O. Andreae, Max-Planck Inst. Mainz
Paola Ariotti, Harvard U.
Johan Auwerx, EPFL
David Awechsel, U. of Chicago
Clare Baker, University of Cambridge
Nenad Ban, ETH Zurich
Jordi Bascompte, University of Zurich
Franz Bauer, Instituto de Astrofísica
Ray H. Baughman, U. of Texas, Dallas
David Baum, U. of Wisconsin
Carlo Beenakker, Leiden U.
Kamran Behnia, ESPCI-ParisTech
Yasmine Belkaid, NIAID, NIH
Philip Benfey, Duke U.
May Berenbaum, U. of Illinois
Gabriele Bergers, U. of California, San Francisco
Bradley Bernstein, Massachusetts General Hospital
Peer Bork, EMBL
Bernard Bourdon, Ecole Normale Supérieure de Lyon
Chris Bowler, Ecole Normale Supérieure
Ian Boyd, U. of St. Andrews
Emily Brodsky, U. of California, Santa Cruz
Ron Brookmeyer, U. of California Los Angeles (\$) **Christian Büchel**, U. Hamburg-Eppendorf
Joseph A. Burns, Cornell U.
Carter Tribble Butts, U. of California, Irvine
Gyorgy Buzsaki, New York U. School of Medicine
Blanche Capel, Duke U.
Mats Carlsson, U. of Oslo
Ib Chorkendorff, U. of Denmark
David Clapham, Children's Hospital Boston
Joel Cohen, Rockefeller U., Columbia U.
James J. Collins, MIT
Robert Cook-Deegan, Duke U.
Lisa Coussens, Oregon Health & Science U.
Alan Cowman, Walter & Eliza Hall Inst.
Robert H. Crabtree, Yale U.
Roberta Croce, Vrije Universiteit
Janet Currie, Princeton U.
Jeff L. Dangel, U. of North Carolina
Tom Daniel, U. of Washington
Frans de Waal, Emory U.
Stanislas Dehaene, Collège de France
Robert Desimone, MIT
Claude Desplan, New York U.
Dennis Discher, U. of Pennsylvania
Gerald W. Dorn II, Washington U. School of Medicine
Jennifer A. Doudna, U. of California, Berkeley
Bruce Dunn, U. of California, Los Angeles
William Dunphy, Caltech
Christopher Dye, WHO
Todd Ehlers, U. of Tuebingen
David Ehrhardt, Carnegie Inst. of Washington
Tim Elston, U. of North Carolina at Chapel Hill
Gerhard Ertl, Fritz-Haber-Institut, Berlin
Barry Everitt, U. of Cambridge
Ernst Fehr, U. of Zurich
Anne C. Ferguson-Smith, U. of Cambridge
Michael Feuer, The George Washington U.
Toren Finkel, NHLBI, NIH
Kate Fitzgerald, U. of Massachusetts
Peter Fratzl, Max-Planck Inst.
Elaine Fuchs, Rockefeller U.
Daniel Geschwind, UCLA
Karl-Heinz Glassmeier, TU Braunschweig
Ramon Gonzalez, Rice U.
Julia R. Greer, Caltech
Elizabeth Grove, U. of Chicago
Nicolas Gruber, ETH Zurich
Kip Guy, St. Jude's Children's Research Hospital
Taekjip Ha, U. of Illinois at Urbana-Champaign
Wolf-Dietrich Hardt, ETH Zurich
Christian Haass, Ludwig Maximilians U.
Sharon Hammes-Schiffer, U. of Illinois at Urbana-Champaign
Michael Hasselmo, Boston U.
Martin Heimann, Max-Planck Inst. Jena
Yka Helariutta, U. of Cambridge
James A. Hendler, Rensselaer Polytechnic Inst.
Janet G. Hering, Swiss Fed. Inst. of Aquatic Science & Technology
Kai-Uwe Hinrichs, U. of Bremen
David Hodell, U. of Cambridge
Lora Hooper, UT Southwestern Medical Ctr. at Dallas
Tamas Horvath, Yale University
Raymond Huey, U. of Washington
Fred Hughson, Princeton U.
Auke Ijspeert, EPFL Lausanne
Stephen Jackson, USGS and U. of Arizona
Steven Jacobsen, U. of California, Los Angeles
Kai Johnsson, EPFL Lausanne
Peter Jonas, Inst. of Science & Technology (IST) Austria
Matt Kaeblerlein, U. of Washington
William Kaelin Jr., Dana-Farber Cancer Inst.
Daniel Kahne, Harvard U.
Daniel Kammen, U. of California, Berkeley
Abby Kavner, U. of California, Los Angeles
Masashi Kawasaki, U. of Tokyo
V. Narry Kim, Seoul National U.
Joel Kingsolver, U. of North Carolina at Chapel Hill
Robert Kingston, Harvard Medical School
Etienne Koechlin, Ecole Normale Supérieure
Alexander Kolodkin, Johns Hopkins U.
Thomas Langer, U. of Cologne
Mitchell A. Lazar, U. of Pennsylvania
David Lazer, Harvard U.
Thomas Lecuit, IBDM
Virginia Lee, U. of Pennsylvania
Stanley Lemon, U. of North Carolina at Chapel Hill
Ottoline Leyser, Cambridge U.
Wendell Lim, U.C. San Francisco
Marcia C. Linn, U. of California, Berkeley
Jianguo Liu, Michigan State U.
Luis Liz-Marzan, CIC biomaGUNE
Jonathan Losos, Harvard U.
Ke Lu, Chinese Acad. of Sciences
Christian Lüscher, U. of Geneva
Laura Machesky, CRUK Beaton Inst. for Cancer Research
Anne Magurran, U. of St. Andrews
Oscar Marin, CSIC & U. Miguel Hernández
Charles Marshall, U. of California, Berkeley
C. Robertson McClung, Dartmouth College
Graham Medley, U. of Warwick
Tom Misteli, NCI
Yasushi Miyashita, U. of Tokyo
Mary Ann Moran, U. of Georgia
Richard Morris, U. of Edinburgh
Alison Murray-Reif, NC State U. (\$) **Thomas Moutrey**, The Hastings Center
Daniel Neumarck, U. of California, Berkeley
Kitty Nijmeijer, U. of Twente
Heiga Novotny, European Research Advisory Board
Ben Olken, MIT
Joe Orenstein, U. of California
Berkeley & Lawrence Berkeley National Lab
Harry Orr, U. of Minnesota
Pilar Ossorio, U. of Wisconsin
Andrew Oswald, U. of Warwick
Margaret Palmer, U. of Maryland
Steve Palumbi, Stanford U.
Jane Parker, Max-Planck Inst. of Plant Breeding Research
Giovanni Parmigiani, Dana-Farber Cancer Inst. (\$) **John H. J. Petrini**, Memorial Sloan-Kettering Cancer Center
Samuel Pfaff, Salk Institute for Biological Studies
Joshua Plotkin, U. of Pennsylvania
Albert Polman, FOM Institute AMOLF
Philippe Poulin, CNRS
Jonathan Pritchard, Stanford U.
David Randall, Colorado State U.
Felix Rey, Institut Pasteur
Trevor Robbins, U. of Cambridge
Jim Roberts, Fred Hutchinson Cancer Research Ctr.
Barbara A. Romanowicz, U. of California, Berkeley
Amy Rosenzweig, Northwestern University
Mike Ryan, U. of Texas, Austin
Shimori Saitou, Kyoto U.
Mitsonori Saitou, Kyoto U.
Miguel Salmeron, Lawrence Berkeley National Lab
Jürgen Sandkühler, Medical U. of Vienna
Alexander Schier, Harvard U.
Vladimir Shalaev, Purdue U.
Robert Silliciano, Johns Hopkins School of Medicine
Denis Simion, Arizona State U.
Uri Simonsohn, U. of Pennsylvania
Lionel Smith, John Innes Centre
Richard Smith, U. of North Carolina (\$) **John Speakman**, U. of Aberdeen
Allan C. Spradling, Carnegie Institution of Washington
Jonathan Sprent, Garvan Inst. of Medical Research
Eric Steig, U. of Washington
Paula Stephan, Georgia State U. and National Bureau of Economic Research
Molly Stevens, Imperial College London
V. S. Subrahmanian, U. of Maryland
Ira Tabas, Columbia U.
Sarah Teichmann, Cambridge U.
John Thomas, North Carolina State U.
Shubha Tole, Tata Institute of Fundamental Research
Christopher Tyler-Smith, The Wellcome Trust
Sanger Inst.
Herbert Virgin, Washington U.
BERT Vogelstein, Johns Hopkins U.
Cynthia Volkert, U. of Göttingen
David Wallach, Weizmann Inst. of Science
Ian Walmsey, U. of Oxford
Jane-Ling Wang, U. of California, Davis (\$) **David A. Wardle**, Swedish U. of Agric. Sciences
David Waxman, Fudan U.
Jonathan Weissman, U. of California, San Francisco
Chris Wikle, U. of Missouri (\$) **Ian A. Wilson**, The Scripps Res. Inst. (\$) **Timothy D. Wilson**, U. of Virginia
Rosemary Wyse, Johns Hopkins U.
Jan Zaenen, Leiden U.
Kenneth Zaret, U. of Pennsylvania School of Medicine
Jonathan Zehr, U. of California, Santa Cruz
Len Zon, Children's Hospital Boston
Maria Zuber, MIT

BOOK REVIEW BOARD

David Bloom, Harvard U. Samuel Bowring, MIT, Angela Creager, Princeton U., Richard Sweder, U. of Chicago, Ed Wasserman, DuPont

Taking up TOP

Nearly 1 year ago, a group of researchers boldly suggested that the standards for research quality, transparency, and trustworthiness could be improved if journals banded together to adopt eight standards called TOP (Transparency and Openness Promotion).^{*} Since that time, more than 500 journals have been working toward their implementation of TOP. The editors at *Science* have held additional retreats and workshops to determine how best to adapt TOP to a general science journal and are now ready to announce our new standards, effective 1 January 2017.[†]

In implementing TOP, *Science* strives to find the right balance between encouraging better transparency about the evidence behind the authors' conclusions and respecting the broad array of norms and cultures across the many disciplines published in the journal. For example, we recognize that pre-registration of studies and analysis plans is becoming commonplace in a few fields, such as clinical trials, and that many more studies would benefit from such practices. Pre-registration of studies can help to avoid the "file drawer effect," in which investigations with null or inconclusive results are not disseminated, leading to a bias in the published literature toward positive, conclusive, and possibly spurious effects. Pre-registration of analysis plans reduces author bias in the interpretation of data. However, until more disciplines are ready to accept these approaches for hypothesis-testing research, it is premature for *Science* to insist that they be submitted. In terms of replications, *Science* will continue to publish such studies, holding them to the same standards as other content submitted to the journal.

On the other hand, we believe the benefits of requiring the availability of data, code, and samples on which the authors' interpretations rest are worth the effort in compliance (and in some cases in adjusting data ownership expectations), while acknowledging that some special circumstances will require exemptions. This

practice increases transparency, enables reproducibility, promotes data reuse, and is increasingly in line with funder mandates. We are also requiring the citation of all data, program code, and other methods not contained in the paper, using DOIs (digital object identifiers), journal citations, or other persistent identifiers, for the same reason. Citations reward those who originated the data, samples, or code and deposited them for reuse. Such a policy also allows accurate accounting for exactly which specific data, samples, or code were used in a given study.

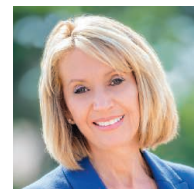
These guidelines also apply to our open-access journal *Science Advances*. The specialized journals that we publish—*Science Translational Medicine*, *Science Signaling*, *Science Immunology*, and *Science Robotics*—may have more specific expectations for design and analysis standards for those disciplines. Our editors are currently working out the fine print before posting detailed standards online.

I have heard that some boards are struggling with how to implement TOP for

their journals. They fear getting too far ahead of their communities in aspects such as requiring data availability from their authors. As part of the team that originally drafted the TOP guidelines, I encourage all journals to consider the flexibility of the TOP guidelines. For example, a journal need not require that all data be publicly available, but simply ask authors to declare whether the data are available. This information is very helpful for reviewers in terms of determining whether the study is likely to be replicable by a third party. Transparency, even without mandates, is a powerful tool.

The benefits of implementing TOP extend well beyond the original goal of facilitating the replicability of published research. TOP creates a framework for sharing not just the findings of a study, but also the data, samples, code, and methods, which in many cases can outlive the findings in making durable contributions to science.

— Marcia McNutt



Marcia McNutt
Editor-in-Chief
Science Journals



*"The editors at Science...
are now ready to announce
our new standards..."*

^{*}B. Nosek et al., *Science* **348**, 1422 (2015). [†]See the supplementary materials for "Implementation of TOP Guidelines for Science."

“It is the end of the road for antibiotics unless we act urgently.”

Thomas Frieden, director of the U.S. Centers for Disease Control and Prevention, in a speech 26 May at the National Press Club on the first U.S. case of an *Escherichia coli* infection resistant to colistin, a drug of last resort for many patients.

IN BRIEF

Study revives cellphone-cancer fears



The new study focuses on the effects of exposure on rats; implications for humans are unclear.

A new study that examines the effects of cellphone radiation on male rats is adding weight to concerns that the ubiquitous devices can pose a health risk to people. A preliminary analysis of the data showed that the exposed rats were more likely to develop rare brain and heart cancers. The findings, posted on the bioRxiv preprint server by the multiagency National Toxicology Program on 26 May, are already triggering calls for more research—and warnings. But although the elaborate \$25 million study (which isn't scheduled to be finished until 2017) is the most comprehensive yet of lab animals exposed to cellphone radiation, researchers say it's far from conclusive. Scientists couldn't say why cancer rates rose in male but not female rats, or why rats exposed to cellphone radiation lived longer on average than radiation-free rats. The study also does not pinpoint a biological mechanism for the findings—and the usual caveats about the findings' applicability to humans apply. The U.S. Food and Drug Administration, which requested the study and has a hand in overseeing health risks posed by cellphones, stated that its own panel of experts is reviewing the data. http://bit.ly/_cellcancer

AROUND THE WORLD

DOE urges U.S. to stay in ITER

WASHINGTON, D.C. | A Department of Energy (DOE) report last week recommended that the United States continue its participation in ITER, the gigantic—and massively overbudget—international fusion experiment under construction in southern France. The report, ordered by congressional budgetmakers last December and delivered last week, urged the United States to remain in the project at least through 2018. But there's a catch: To keep going, DOE says, the U.S. ITER effort will need significantly more money—at least \$230 million in 2018, or \$105 million more than DOE has requested for it in fiscal year 2017, which begins 1 October. And the report doesn't say whether the United States should continue in ITER if, as seems likely, Congress doesn't agree to provide that extra money. <http://bit.ly/USITER>

Science fair gets new sponsor

NEW YORK CITY | Last week, in a ceremony held at the American Museum of Natural History here, the biotechnology giant Regeneron Pharmaceuticals Inc. was named the latest sponsor of the Society for Science and the Public's (SSP's) 75-year-old Science Talent Search (STS). The STS competition will receive \$100 million over 10 years from Regeneron, a sum that SSP says will allow it to nearly double its monetary awards to winners, finalists, and their high schools, and to increase the scale of its outreach and equity programs. Prior to Regeneron, the competition was funded by Westinghouse Electric Corporation from 1942 to 1997, and by Intel from 1998 to September of last year, when Intel suddenly announced it was ending its sponsorship. <http://bit.ly/STSSponsor>

Chemical safety overhaul near

WASHINGTON, D.C. | The U.S. Senate is expected to approve a major overhaul of the nation's primary chemical safety law—marking one of the last steps in a decades-long reform effort. The House of Representatives on 24 May overwhelmingly approved H.R. 2576, a rewrite of the Toxic

Substances Control Act, which governs how industrial chemicals are tested and regulated. A Senate vote is expected next month; the legislation would then move to President Barack Obama for signing. The White House has indicated Obama will sign the bill into law. The measure, perhaps the most far-reaching and influential environmental statute passed by Congress since the body updated the Clean Air Act in 1990, aims to make chemical safety reviews more science-based, and includes provisions designed to reduce the use of animals in chemical testing and promote the study of so-called cancer clusters. <http://bit.ly/newTSCA>

E.U. calls for open access by 2020

BRUSSELS | In what European science chief Carlos Moedas calls a “life-changing” move, E.U. member states have agreed on an ambitious new open-access (OA) target. All publicly funded papers should be freely available by 2020, the Competitiveness Council—a gathering of ministers of science, innovation, trade, and industry—concluded 27 May after a 2-day meeting. But some observers are warning that the goal will be difficult to achieve. The council’s statement is also slightly ambiguous on what exactly should be accomplished by 2020. It calls for “immediate” OA, “without embargoes or with as short as possible embargoes.” Many non-OA journals currently allow authors to make their papers available—for instance in an institutional repository—6 or 12 months after publication. The OA goal is part of a broader set of recommendations in support of open science, a concept that also includes better storage of research data and easier access to it. <http://bit.ly/EUOAcall>

Great Barrier Reef coral deaths

TOWNSVILLE, AUSTRALIA | Mass bleaching has killed 35% of corals on the northern and central sections of the 2300-kilometer-long Great Barrier Reef—the grim toll of an unusually hot summer, researchers at the Australian Research Council Centre of Excellence for Coral Reef Studies announced this week. On 24 of 84 reefs surveyed, 50% of the corals have perished, including specimens that were 50 to 100 years old. Global warming and the ongoing El Niño, a periodic phenomenon that brings unusually warm water to the equatorial Pacific, combined to produce the worst of three major bleaching events in the last 18 years, the researchers said. The finding was announced on the heels of a decision to remove references to the



Ranchers wrangle about 2000 snakes for the annual Sweetwater Rattlesnake Roundup, begun in 1958 to control snake populations.

Battle over the rattles: Lawmakers may ban snake gassing

In Texas, a long-simmering tussle over “gassing”—the use of gasoline to drive snakes from their dens—may be coming to a head as the Texas Parks & Wildlife Commission takes steps toward banning or limiting the practice. Rattlesnake enthusiasts have sought to continue gassing, which involves injecting gasoline into cracks or caves to collect the snakes for rattlesnake roundups or other events—a decades-long tradition in some parts of Texas. Scientists, meanwhile, have documented how the technique harms insects, snails, and other species that live underground within the crag-filled karst ecosystem that underlies much of Texas. “26 species of federally listed karst invertebrates exist in Texas, and spraying petrochemicals will expose [these species] to fumes that are fatal,” says wildlife biologist John Davis of the Texas Parks & Wildlife Department in Austin. Some 29 states already ban the gassing of snake burrows, but Texas has held out for years. At last week’s meeting, the commission asked Davis and his staff to prepare potential language for a rule by November, when commissioners will debate whether to release the rule for public comment. Regulatory options could include an outright ban or seasonal limits on gassing, Davis told commissioners. The Center for Biological Diversity in Tucson, Arizona, hopes the commission will enact a ban, calling it “long overdue.”

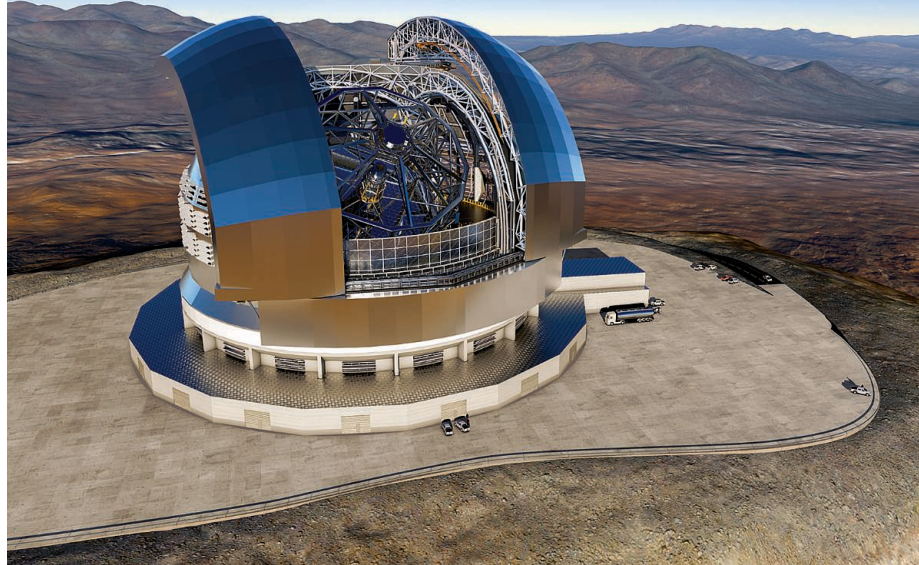
Great Barrier Reef within the “Destinations at risk” chapter in a United Nations climate change report released last week. The Australian Department of the Environment had objected that the references could harm tourism. <http://bit.ly/GBRcorals>

France reduces budget cuts

PARIS | After imposing an unexpected €256 million budget cut on research and higher education on 18 May, the French government scrapped more than half of

the cut less than 2 weeks later in response to an outcry from France’s scientific community. In an op-ed in *Le Monde* last week, seven Nobel Prize winners and a Fields Medal winner slammed the cuts as “scientific and industrial suicide.” After meeting with six of the scientists on 30 May, President François Hollande agreed to cancel €134 million in cuts that would affect four large national research agencies. Another €122 million in cuts that mostly affect higher education were not withdrawn. The French government needed

An artist's rendition of the E-ELT telescope to be built in Chile.



Deal inked for massive telescope

Astronomers have signed an unprecedented contract to build the world's largest ground-based optical and infrared telescope. In a 25 May ceremony at the headquarters of the European Southern Observatory (ESO) in Garching, Germany, ESO Director General Tim de Zeeuw inked a €400 million deal with three Italian engineering firms. They will build the structure that will hold the 39-meter mirror of the European Extremely Large Telescope (E-ELT), as well as the nearly 80-meter-tall domed building that will enclose it, on the mountain Cerro Armazones in Chile. The light-collecting area of the €1.1 billion E-ELT project is greater than that of all ground-based optical research telescopes currently in operation, and it will produce images 15 times as sharp as the Hubble Space Telescope. Roberto Tamai, E-ELT program manager, said the telescope will provide "a transformational step in our understanding of the universe." <http://bit.ly/EELTdeal>

to save a total of €1.1 billion to offset unforeseen expenses. Physicist and Nobel laureate Serge Haroche says Hollande has promised to try to raise science budgets in the future. "He understands the importance of research for the country," Haroche says. "He told us it's part of the culture and the intellectual appeal of France abroad, and he does not want to jeopardize that." <http://bit.ly/Frenchcuts>

NEWSMAKERS

Three Qs

Maria Zuber, a 57-year-old planetary geophysicist and vice president for research at the Massachusetts Institute of Technology (MIT) in Cambridge, has set a number of "first woman to ..." milestones, including

principal investigator on a NASA planetary mission and head of an MIT science department. Last month, she became part of the first all-female leadership team at the National Science Foundation (NSF) when she was named chair of its oversight body, the National Science Board.

Q: Do you ever get angry about having to break those glass ceilings?

A: I've never realized I was first until after the fact. I long for the day when I'm not the first anymore.

Q: Some lawmakers say NSF is wasting money on frivolous grants and that its awards should be "in the national interest."

A: My definition of research in the national interest is great science, as determined by merit review. We've been

BY THE NUMBERS

11.9%

Fraction of drug candidates that made it through development from 2012 to 2015—a sharp uptick from a 15-year low of 7.5% from 2008 to 2011 (*Nature Reviews Drug Discovery*).

74

Number of experiments faked by heart researcher Ricky Malhotra over 6 years, while he was first at the University of Michigan, Ann Arbor, and then the University of Chicago in Illinois, according to an Office of Research Integrity report released 24 May.

meeting with legislators about their concerns, and hopefully they will express an appreciation for what NSF has done. But we realize there's room for NSF to improve transparency.

Q: Is it reasonable to expect research spending to grow in this political climate?

A: Everything is under scrutiny when budgets are tight. But U.S. research and education are what has kept this country at the forefront. Even when flat [funding] is the new up, I think that research spending ought to be up.

Berg new *Science* editor-in-chief

Biochemist **Jeremy Berg** of the University of Pittsburgh (Pitt) in Pennsylvania will become the next editor-in-chief of *Science* magazine and its sister journals on 1 July. Berg will succeed Marcia McNutt, who is stepping down to become president of the National Academy of Sciences. Berg, 58, began his career at Johns Hopkins University School of Medicine in Baltimore, Maryland, studying zinc-containing proteins. From 2003 to 2011 he directed the \$2 billion National Institute of General Medical Sciences. There, he broke new ground by using a blog to share data on grant funding decisions. He has remained involved in biomedical research policy issues while serving as a science strategy adviser and director of the Institute for Personalized Medicine at Pitt.



INFECTIOUS DISEASE

Mosquito hunters search for Zika vectors

Yellow fever mosquito is confirmed, but others may contribute

By Gretchen Vogel

Zika virus, the once obscure pathogen now widely feared for causing birth defects and other problems, has spread very far very quickly since an outbreak was first noticed in northeast Brazil in early 2015. It has reached more than 40 countries across the Americas, even making it to the Cape Verde islands, off the western coast of Africa. More than a million people have become infected.

As public health officials try to contain the epidemic, researchers are racing to answer a key question with important implications for which areas are at risk, and what methods might work to slow its spread: Which mosquitoes are transmitting the virus? Answering the question is no small challenge. Scientists need evidence from both lab-raised and wild-caught mosquitoes to make the case that a given species is guilty.

Just last week, a team in Rio de Janeiro announced that it had nabbed several *Aedes aegypti* infected with Zika—the first infected mosquitoes found in Brazil. The species, the yellow fever mosquito, has long been the prime suspect, but some scientists believe the Zika virus must have other carriers to have spread so quickly—and they have field and lab studies underway to resolve the issue. Until that evidence is in, “we shouldn’t

jump to conclusions,” says Duane Gubler, a virologist at Duke-NUS Medical School in Singapore.

A. aegypti has earned suspicion because it spreads dengue and chikungunya as well as yellow fever and is common in urban areas of Brazil where major outbreaks have occurred and throughout Latin America. But evidence of wild mosquitoes infected with Zika has

“You have to look at a lot of mosquitoes to find [infected ones].”

Duane Gubler, Duke-NUS Medical School

been lacking. It is harder than one might expect to find them. In dengue outbreaks, says Sander Koenraadt, an entomologist at Wageningen University in the Netherlands, researchers typically find that fewer than 1% of sampled mosquitoes are infected with the dengue virus, even where people are falling sick. “You have to look at a lot of mosquitoes to find [infected ones],” Gubler says. The mosquitoes “infect people and die before anyone shows up at the hospital” with disease symptoms, says Oliver Brady, an entomologist at the University of Oxford in the United Kingdom.

For the insects to transmit a virus, they must take up infected blood from a human or animal and become infected themselves. The virus then has to travel from their gut to their saliva. Only some species are susceptible to particular viruses.

To test whether a given species is able to transmit a virus, researchers feed insects on infected blood in the lab and a week or so later collect saliva from them. If the saliva contains infective virus, the species is considered a “competent” vector. Not all lab-competent vectors spread disease, however. That depends on several factors, such as how often the species bites, whether it feeds primarily on humans or other animals, and how long it lives. To confirm that a species is transmitting disease, researchers also need to find virus-infected mosquitoes in the wild.

The team that reported the first Zika-infected mosquitoes in Brazil, led by Ricardo Lourenço-de-Oliveira, an entomologist at the Oswaldo Cruz Foundation (Fiocruz) in Rio de Janeiro, vacuumed up mosquitoes from homes and streets in Rio de Janeiro neighborhoods that were home to people complaining of Zika symptoms. Over 10 months they collected more than 1500 mosquitoes, identified them, and tested pooled samples of the same sex and species for the presence of Zika and other viruses. Nearly half were *A. aegypti*, and most of the rest were *Culex*

Researchers in Brazil have captured thousands of mosquitoes to test them for Zika and other viruses.

quinquefasciatus, another common mosquito in urban Brazil. Roughly 5% were other species. A species called *A. albopictus*, widely known as the Asian tiger mosquito, which can also transmit Zika in the lab and has been found infected with the virus in Mexico and Gabon, made up only about 2% of the catch, Lourenço-de-Oliveira says. They found Zika virus in three sets of female *A. aegypti* mosquitoes, but none of the other species.

The lack of virus in *C. quinquefasciatus* is somewhat reassuring, Lourenço-de-Oliveira says, but the case is not closed. Constância Ayres, an entomologist at Fiocruz in Recife, Brazil, says that her lab has evidence that the species is a possible vector; they have found Zika virus in the saliva of *C. quinquefasciatus* that had fed on infected blood. (Her team has submitted its work for publication.)

Lab tests can be misleading, however. “There is a classic discordance between what you see in the lab and what happens in the wild,” Brady says. “*Albopictus* and *aegypti* are both highly competent in the lab” as vectors for dengue. “But in Europe, where we have widespread *albopictus* and almost no *aegypti*, you don’t have huge dengue outbreaks.”

Ayres and others are still searching for Zika in the wild. She and her colleagues have collected and identified more than 5000 mosquitoes in the Recife area since March, from homes where confirmed Zika patients lived and from urgent care centers. She is waiting for promised grant money before she can run the polymerase chain reaction tests to find which viruses the mosquitoes are carrying, she says.

Culex mosquitoes transmit several viruses related to Zika, and it would not be particularly surprising if both *Culex* and *Aedes* species could spread Zika, Ayres says. Gubler agrees that *Culex* is a plausible carrier. He notes that several Zika relatives spread by *Culex* mosquitoes, including the West Nile virus, target the nervous system, which Zika also seems to do.

If *Culex* mosquitoes can transmit Zika virus, that will make slowing its spread even more difficult. *C. quinquefasciatus* is found as far north as Iowa and Indiana in the United States, although people there are protected by window screens and other factors. In Latin America, most vector control methods are targeted at *A. aegypti*. Those efforts have made barely a dent in curtailing spread of the Zika virus so far, notes Paul Reiter, an entomologist at the Pasteur Institute in Paris. Targeting multiple vectors at once will only make the job harder. “If [*C. quinquefasciatus* is a vector],” he says, “we can forget anything about mosquito control.” ■

EVOLUTION

Dogs may have been domesticated more than once

But all living dogs have Asian roots

By David Grimm

For years, scientists have debated where dogs came from. Did wolves first forge their special relationship with humans in Europe, or in Asia? The answer, according to a new study, is yes. On p. 1228, researchers report that genetic analysis of hundreds of canines reveals that dogs may have been domesticated twice, once in Asia and once in Europe or the Near East, although European ancestry has mostly vanished from today’s dogs. The findings could resolve a rift that has roiled the canine origins community—but the case isn’t closed yet.

“These are fantastic data that are going to be extremely valuable for the field,” says Peter Savolainen, a geneticist at the Royal Institute of Technology in Stockholm and the leading proponent of Asian dog origins. But Robert Wayne, an evolutionary biologist at the University of California, Los Angeles, whose work has shown that dogs arose in Europe, says the results—although plausible—are too preliminary to settle the question. “The story is still a bit of a muddle.”

The study includes a unique specimen: the inner ear bone of a nearly 5000-year-old dog unearthed from Newgrange, a football field-sized mound of dirt and stone on the

east coast of Ireland, built around the time of Stonehenge. Researchers led by Laurent Frantz, an evolutionary geneticist at the University of Oxford in the United Kingdom, sequenced this specimen’s entire nuclear genome—the first complete genome from an ancient dog to be published—and compared it to the nuclear DNA of 605 modern dogs from around the world. The team then created a family tree for the animals, which revealed a deep divide between European dogs (like the Newgrange canine and the golden retriever) and Asian dogs (like the shar pei and free-ranging village dogs from Tibet and Vietnam). “I was like, ‘Holy shit!’” says project leader Greger Larson, an evolutionary biologist at Oxford. “We never saw this split before because we didn’t have enough samples.”

To figure out when this divide occurred, the Newgrange specimen was critical. Researchers used it, in conjunction with the complete genomes of several modern dogs and wolves, to calculate a genetic mutation rate for canines. This rate suggests that the East-West split happened sometime between 6400 and 14,000 years ago. The analysis also revealed a “genetic bottleneck” in Western dogs—a reduction in genetic diversity typically tied to a sharp decline in a population’s numbers, as can occur when a small band of individuals splits off from the main group. (A

Asian dogs like this Tibetan mastiff have been separated from European breeds such as Labradors for more than 6000 years.



similar pattern is seen with the original human migration out of Africa.)

Taken together, the data suggest that humans domesticated dogs in Asia more than 14,000 years ago, and that a small subset of these animals eventually migrated west through Eurasia, probably with people. This implies that all modern dogs, as well as the Newgrange canine, can trace their ancestry back to Asia.

But here's the twist: Archaeologists previously had found the remains of dogs in Germany that may be more than 16,000 years old, suggesting that dogs had *already* been domesticated in Europe by the time the Asian canines got there. Some of today's dogs may carry genetic traces of that early domestication—but it's hard to find, in part because scientists are still trying to recover DNA from those ancient German dogs. "We don't know if the dogs that evolved [early] in Europe were an evolutionary dead end," Frantz says, "but we can safely say that their genetic legacy has mostly been erased from today's dogs."

To Savolainen, the story makes sense. "If people in one place got these fantastic dogs, of course everyone wanted to have them," he says. "Over the course of a few hundred or a thousand years, you could have dogs spread throughout all of Eurasia." Still, he's not completely sold on the idea of two domestications, arguing that if the team's mutation rate is just a bit off, it could allow for all dogs, even those ancient European ones, to have Asian roots. Wayne adds that interbreeding between dogs and wolves could have muddled the picture. Both say that many more samples, especially of ancient dogs and wolves, are needed.

That could happen soon. Although neither Wayne nor Savolainen were involved in the current study, both joined Larson in 2013 as part of an international collaboration to solve the mystery of dog domestication once and for all (*Science*, 17 April 2015, p. 274). Dozens of scientists have been pooling resources and gathering thousands of new samples from around the globe. "The new model is provocative and exciting, but the full collaboration is going to be essential to untangling this complicated story," says John Novembre, a population geneticist at the University of Chicago in Illinois who is not involved with the collaboration or the new work.

For now, a dual origin for dogs remains an intriguing possibility, especially because research has also suggested multiple domestications for cats and pigs. Does that mean these animals were bound to be domesticated? "If it only happened in one place, it was probably a very hard thing to do," Savolainen says. "But if it happened twice, maybe it wasn't as hard as we thought." ■

ARCHAEOLOGY

'Culinary frontier' tracks Madagascar's Asian settlers

Crop remains record wave of arrivals from the East

By **Andrew Lawler**, in Orlando, Florida

The settlement of the Indian Ocean's largest island is one of the great mysteries in humanity's colonization of the globe. Madagascar lies just 400 kilometers off the East African coast. Yet the Malagasy people's cuisine, rituals, and religious beliefs resemble those of Borneo, some 9000 kilometers to the east. Their language is more closely related to Hawaiian than to Bantu, and about half their genes can be traced to Austronesia—that is, Indonesia and the islands of the Pacific. Archaeological evidence of this distant connection was lacking, however.

Now, new studies—recent or soon-to-be-published—trace a wave of Austronesian colonization between 700 C.E. and 1200 C.E. The telltale evidence is, in effect, breadcrumbs: crops distinctive to Austronesia, sprinkled across Madagascar and neighboring islands. "We finally have a signal of this Austronesian expansion," said Nicole Boivin, an archaeologist and director of the Max Planck Institute for the Science of Human History in Jena, Germany, who discussed the findings at the recent Society for American Archaeology (SAA) meeting here.

The study by Boivin and her colleagues, published this week in the *Proceedings of the National Academy of Sciences*, found that these voyagers did not stop at Madagascar. Some also settled the Comoro Islands, scattered between Madagascar and the African coast. "The discovery of an Austronesian connection for the Comoros is surprising," says David Burney, a paleobiologist at the National Tropical Botanical Garden in Koloa, Hawaii, who has studied the region. Yet the Austronesians stopped short of the African coast. "There was a culinary frontier," says Alison Crowther, an archaeologist at the University of Queensland, St. Lucia, in

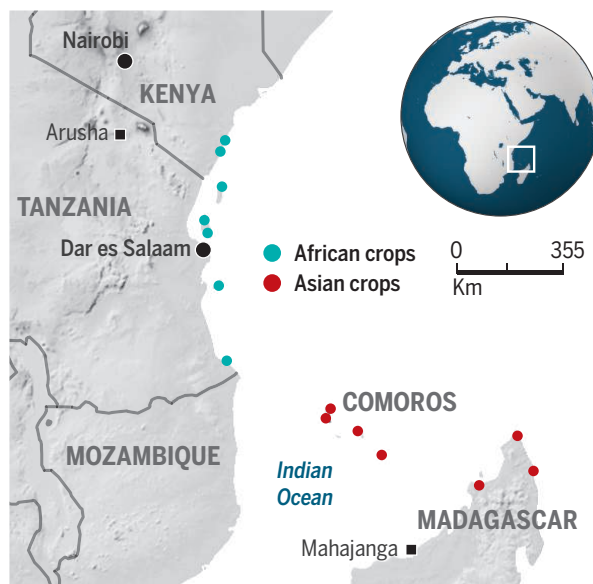
Brisbane, Australia, who led the study.

Her team collected more than 2400 samples of botanical remains at 20 sites on the African mainland, on offshore islands, and on Madagascar and obtained 43 radiocarbon dates from crop seeds. Between 700 C.E. and 1200 C.E., the researchers found a clear boundary between sites dominated by African crops like pearl millet, cowpea, and sorghum, and those with Asian rice, mung bean, and cotton. The Asian crops were common on the Comoros and on Madagascar, but rare on the East African coast.

The line traced by the study shows that the two regions, although close geographically, were worlds apart in their way of life, suggesting a wholesale colonization of Madagascar and the Comoros. A thousand years ago and more, Arab and Indian sailors conducted a bustling trade between East Africa and India (*Science*, 27 June 2014, p. 1440). But the crops indicate that the settlers came from even farther east. Although Asian rice and mung bean are common on the Indian subcontinent, other common Indian crops like horse gram and urd (two legume vari-

Cultural dividing line

Archaeological remains of crops such as Asian rice and mung beans suggest that Austronesian sailors colonized Madagascar and the Comoro Islands. But the ancient Asian culinary influence stops at mainland Africa.



eties) are absent from the Madagascar and Comoros samples.

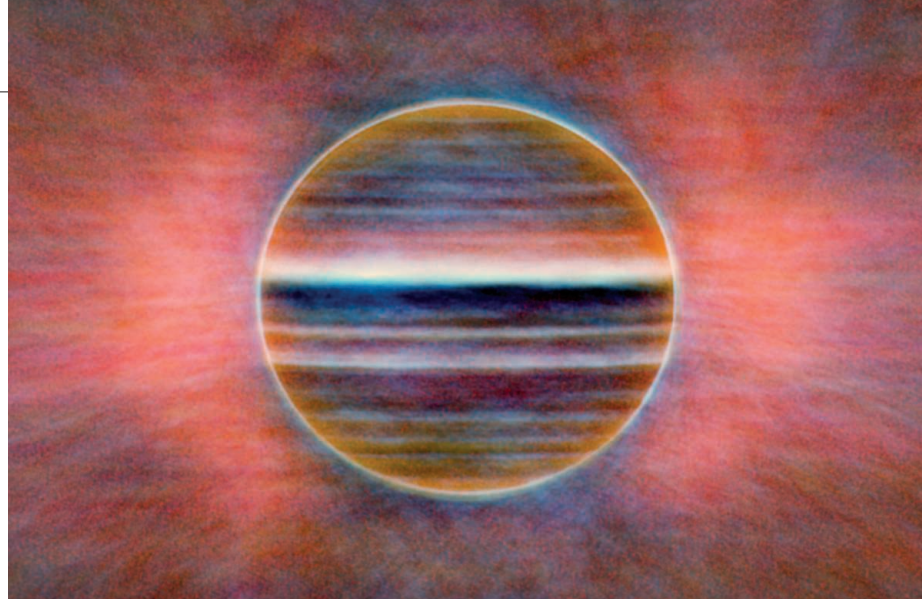
The genetic studies that support the group's conclusion about an Asian colonization also link roughly half the genome in modern Malagasy to Africans. When the Africans arrived is a further mystery. "People have speculated that there might well have been a number of transitory arrivals—most likely from Africa—before settlement on the island really took off" with the arrival of Austronesians, says Peter Forster, an archaeologist at the University of Cambridge in the United Kingdom.

The late Yale University archaeologist Robert Dewar claimed in 2013 that people reached the island around 2000 B.C.E., millennia earlier than had been thought, based on radiocarbon dates of organic matter found with stone artifacts in a rock shelter on the north coast. But even members of Dewar's team were not ready to rewrite Madagascar's history. Burney, meanwhile, says that environmental data, such as signs of widespread burning, suggest the first humans more likely arrived around 400 B.C.E.

Based on studies of the unique megafauna Madagascar once hosted, including giant flightless birds and huge lemurs, paleoecologist Simon Haberle of the Australian National University in Canberra argues that the arrival was likely more recent. He reported at the SAA meeting that radiocarbon dating of fungi from the dung of megafauna at five sites in southwest Madagascar suggests that larger animals, like a 150-kilogram lemur, began to decline about 500 C.E. The decline presumably signals the arrival of human hunters. Megafauna extinctions gathered speed between 700 C.E. and 1000 C.E., coinciding with the wave of Austronesians.

The identity of the earlier settlers, whenever they made landfall, remains obscure. Madagascar still has hunter-gatherers such as the Mikea, who have an oral tradition asserting that they were the island's original inhabitants, driven by later migrants into the dense forests of the island's southwest. A 2013 study, however, found that the group is genetically similar to the Malagasy: a mixture of African Bantu and Austronesian stock. The team suggested that the Mikea were originally farmers who later became hunter-gatherers, rather than a remnant of a pre-Austronesian wave of African colonists.

The latest evidence leaves little doubt about Austronesian settlement, but their predecessors remain in the shadows. "What is clear is that the island has a complex settlement history involving multiple colonizations by different populations at different times," Crowther says. Her new study, she adds, contributes "a small piece to the puzzle." ■



VLA image shows radio emissions from Jupiter's radiation belts (pink) and from bands below ammonia clouds.

PLANETARY SCIENCE

Telescope and NASA mission get under Jupiter's skin

Ground-based VLA spies giant wave of ammonia, while the Juno spacecraft gears up to go after the water

By Eric Hand

Jupiter's seething visage—a psychedelic carousel of haze and ammonia clouds—is a veil. It obscures a vast atmospheric underworld that astronomers can probe only with difficulty, using wavelengths outside the spectrum of visible light. This week, a ground-based radio telescope has pulled back the veil, revealing a giant wave of ammonia that circles the planet and that will guide modelers' attempts to understand the atmosphere's deep roilings. And next month, a NASA spacecraft called Juno will arrive at Jupiter and start to peer even deeper, into a suspected water layer, for clues to where and how the planet formed.

The radio telescope data help resolve a mystery that dates to 1995, when NASA's Galileo spacecraft dropped a probe into the planet's atmosphere. It fell into a "hot spot": a dried-out region with few ammonia clouds and none of the water clouds that astronomers have sometimes seen deep in the atmosphere. As the probe parachuted 100 kilometers below the topmost haze layer, it detected high levels of ammonia before succumbing to the crushing pressures and searing heat. That was surprising, because a decade before, radio telescopes such as the Very Large Array (VLA) in New Mexico had found little ammonia at those

depths. Theorists surmised that Jupiter's upper atmosphere might be ammonia-free except for occasional clouds lofted upward from the depths by thunderstorms.

Not so, the new study on p. 1198 shows. In fact, the atmosphere is rife with ammonia; the Galileo probe just caught the wrong part of a wave. In a region a few thousand kilometers north of Jupiter's equator, the VLA's earlier maps showed a broad, featureless band. Thanks to a recent upgrade, the VLA has now revealed that the band is actually striped with zones of different composition: ammonia-poor regions tens of thousands of kilometers across, alternating with ammonia-rich regions rising in plumes from below. "We finally put it all together that these hot spots and these ammonia-rich regions were really part of the same pattern," says Imke de Pater, a planetary scientist at the University of California, Berkeley, who led the study.

Atmospheric waves reflect how heat is transported up from the depths. So the wavelength and amplitude of this wave offer clues to what's happening below, says Mark Hofstadter, a planetary scientist at the Jet Propulsion Laboratory in Pasadena, California.

The VLA might have probed deeper in the atmosphere by using longer wavelengths, but its view was blocked by radiation from belts of whipped-up electrons that circle the planet. The Juno mission, set to go into a

daring, swooping polar orbit around Jupiter on 4 July, was designed to avoid that problem. It will thread the gap between the radiation belts and the top of the atmosphere.

The special orbit will protect the spacecraft's electronics from frying—allowing for 32 14-day mapping orbits beginning in November—while giving the spacecraft's microwave detector an unobstructed view inside the atmosphere. “They’re looking through a fog,” says Juno principal investigator Scott Bolton of the Southwest Research Institute in San Antonio, Texas, of the VLA team’s results. “We’ll have a clean view.”

Observing in microwave wavelengths, Juno should be able to see several hundred kilometers down, deep enough to spot a water layer that the Galileo probe didn’t reach, Bolton says. Mapping that layer should reveal the roots of many structures high in the atmosphere, including the ammonia wave, along with Jupiter’s zones, bands, and the famed Great Red Spot. Measuring the overall abundance of water in the atmosphere is also important for understanding the planet’s formation. The water originally came from bits of ice that froze out of the protoplanetary disk of gas and dust. If Jupiter has roughly equal amounts of water and elements such as nitrogen and carbon, the planet must have formed farther out in a colder part of the solar system and later migrated inward. In such cold, nitrogen- and carbon-containing ices could freeze out alongside water ice and become part

of the planet. But if water abundances are very high relative to nitrogen and carbon, Jupiter probably formed roughly where it is now: in a neighborhood too warm for the nitrogen and carbon to freeze out and stick to the growing planet.

There is another, long-shot possibility: Jupiter might really be as dry as Galileo said it was. If the probe’s hot spot measurement holds for the rest of the atmosphere, “then we have a lot of explaining to do,” says Amy Simon, a planetary scientist at Goddard Space Flight Center in Greenbelt, Maryland.

Juno will perform much more science. Some of its instruments will map the planet’s radiation belts and magnetic fields. And by measuring the way Jupiter tugs on the spacecraft, scientists will make the most precise map ever of the planet’s gravitational field—information that can be used to study Jupiter’s deepest interior structure and perhaps answer the key question of whether it has a core. Many planet formation models suggest that Jupiter needed a rock-and-ice core of about 10 Earth masses for its gravity to capture hydrogen and helium in the protoplanetary disk before the sun dispersed the gases into space.

To supplement Juno’s close-up view of its host planet, NASA has asked amateur astronomers to map Jupiter’s visible surface throughout the mission. That will help scientists connect what lies beneath to what sits on top. ■

DEVELOPMENT

CRISPR views of embryos and cells

Genome editor helps record development, cell influences

By Kai Kupferschmidt

Alexander Schier simply wanted to make sure he destroyed a gene in zebrafish embryos. So, like many biologists these days, he turned to the genome-editing system called CRISPR. But Schier, a developmental biologist at Harvard University, ended up doing much more than knocking out a gene. He and colleagues devised a new way to trace cells in a developing animal. In its first test, described online last week in *Science*, they used CRISPR-induced mutations to reveal a surprise: Many tissues and organs in adult zebrafish form from just a few embryonic cells.

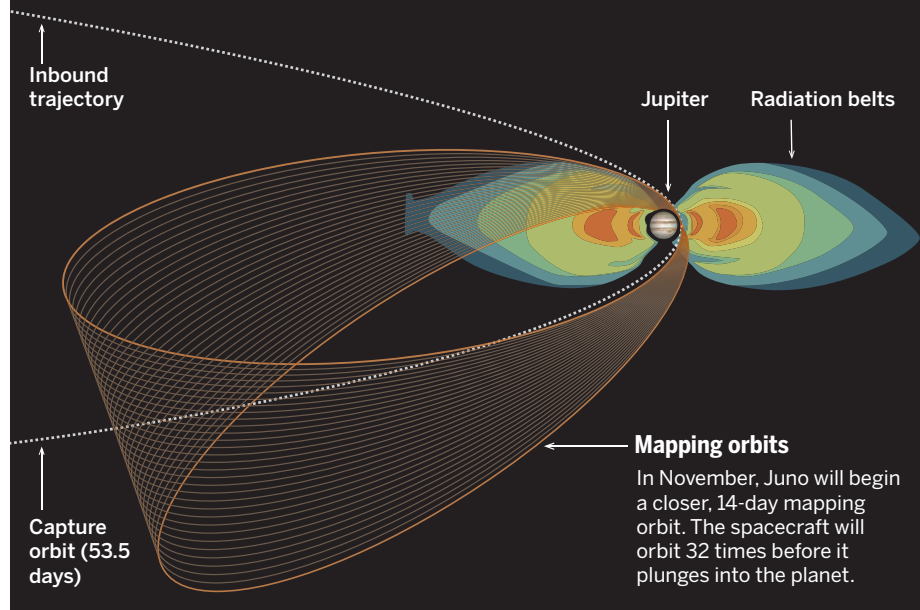
Other researchers are already looking to adapt the method to probe development. “The technique promises to allow the reconstruction of the ‘family tree’ of the cells that compose an animal’s body,” says James Briscoe, a developmental biologist at the Francis Crick Institute in London, who calls it “a creative and innovative use of [the] CRISPR technique.” Some also intend to exploit the method to trace the evolution of tumors. And several groups are racing to develop similar ways of using CRISPR to record a cell’s history—for example, its responses to environmental signals.

Schier and his colleagues took advantage of what Harvard geneticist George Church calls CRISPR’s “genome vandalism.” In its normal editing, a so-called guide RNA precisely targets the enzyme Cas9 to a particular site in the genome so that it can break the double-stranded DNA there. In one of CRISPR’s original uses, a template DNA then tells the cell’s machinery how to repair the double-stranded break, allowing edits as precise as the changing of a single nucleotide. But if scientists supply no template, the gene usually ends up with a “scar,” where some nucleotides go missing or some are added that don’t belong, that knocks out its function.

To make sure the zebrafish gene in his sights was truly obliterated, Schier targeted multiple sites within the gene by introducing several different guide RNAs without any re-

Mind the gap

On 4 July, NASA’s Juno spacecraft will enter a polar orbit that threads a narrow gap between Jupiter’s stormy cloud tops and a deadly radiation belt. Dodging the radiation belt extends the life of the spacecraft’s electronics and allows a microwave instrument to see inside the atmosphere.



pair templates. But repeating the experiment led to very different outcomes: The size of the deletions varied, and the scars included both small and large insertions. That destructive diversity could be put to use, Schier and geneticist Jay Shendure of the University of Washington, Seattle, realized.

In the genomes of zebrafish embryos, Schier and Shendure inserted a cassette of extra DNA, consisting of 10 different target sequences for CRISPR. Then they injected the single-celled embryos with the Cas9 enzyme and 10 guide RNAs that matched the target sequences. As the embryo developed, the CRISPR system repeatedly disrupted the target DNA in each cell, marking it with a pattern of deletions and insertions—a distinctive barcode. Whenever a cell divided, the daughter cells would start out with the same barcode and then diverge when Cas9 cleaved it at different places. The first changes in the barcode seem to happen in the two-cell stage, and then the editing machinery runs out of steam after about 4 hours, when the embryo consists of thousands of cells—after that point, the barcodes that remain will populate the adult animal as cells continue to multiply.

Four months later, the scientists collected organs from the adult fish and isolated more than 1000 different barcodes from about 200,000 cells. Cells with more similar barcodes are likely to have diverged later in development, so the scientists were able to use a computer program to calculate a family tree for the 200,000 cells—essentially a lineage map revealing which cells spawned others. “When you sacrifice the zebrafish at the end of the experiment you’ve actually got a full time read-out of all the cells and where they came from,” Church says.

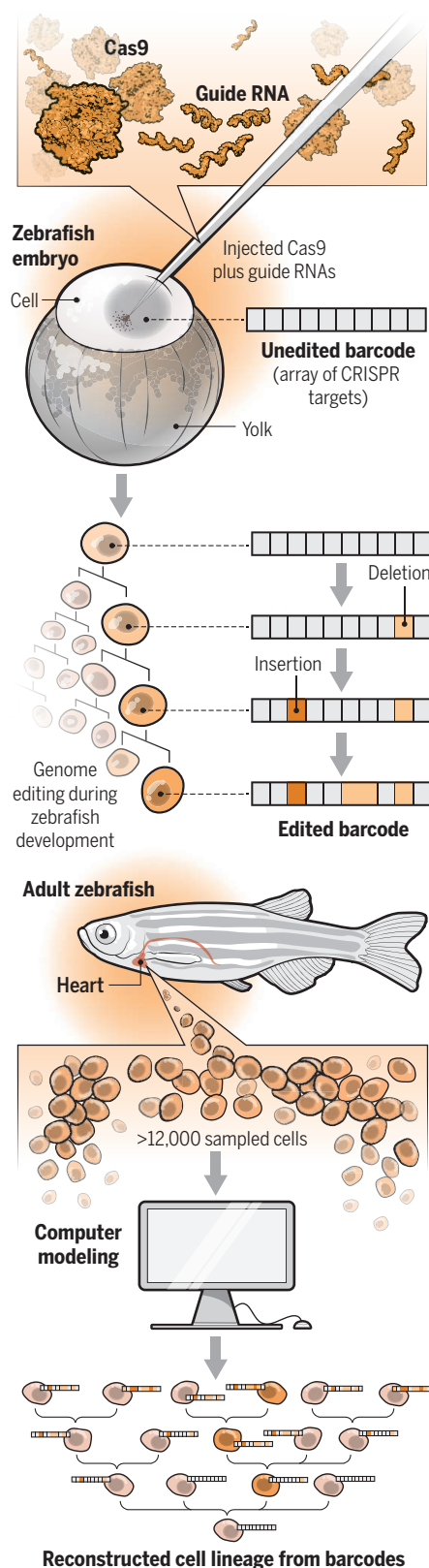
One of the most striking findings was how few cells give rise to the bulk of the tissue in any given organ. More than half of the cells in most organs shared fewer than seven barcodes. In every organ except the brain, more than 90% of the cells had one of just 25 different barcodes. “Tissues may be founded by a much smaller group of cells than I would have anticipated,” Briscoe says.

For developmental biologists, the new technique could help clarify how animals take shape from a single cell. It could also shed light on important questions in cancer research, such as how many precursor cells give rise to a tumor and how cancer cells that have spread are related to the initial tumor.

The technique has shortcomings, Schier says—for example, it does not reliably mark each new generation of cells. But compared with other ways of tracing cells and their progeny, like dyeing them or relying on natural mutations, a CRISPR-generated barcode is potentially more powerful and easier to use. “I think cancer biologists will start

Tracking cell lineages

By repeatedly editing a genetic “barcode” in an embryo’s cells, the CRISPR system can label tissue in a developing organ with a record of its ancestry.



thinking about this because it is a more elegant way of marking cells than we currently use,” says Leonard Zon, who directs the stem cell program at Boston Children’s Hospital. “We definitely want to try it.”

Researchers are already proposing other ways to turn CRISPR into a kind of cellular memory. “I think conceptually that is the most exciting thing, that you can basically record history in the DNA,” Schier says. In a preprint posted online last week, a team from the Massachusetts Institute of Technology in Cambridge may already have demonstrated that. Instead of adding a barcode consisting of 10 CRISPR targets, Timothy Lu and colleagues inserted into cells a single CRISPR target and engineered the site so that it also encodes the guide RNA. As a result, the system targets itself: The guide RNA leads Cas9 to its own source DNA. Cas9 breaks the DNA, leading to a mutation in the sequence, which in turn leads to the production of a mutated guide RNA. That altered guide RNA then leads Cas9 back to the altered target sequence, and the cycle continues, with the DNA sequence and the guide RNA changing in tandem.

By observing how the CRISPR target sequence changed in thousands of single cells endowed with this complicated setup, the researchers estimated how many rounds of Cas9 activity it took to produce certain sequences. (A rough analogy would be estimating how many rounds of the so-called telephone game it takes to scramble the phrase “lobster boil” into “losing team.”) In a follow-up experiment, they coupled the activity of Cas9’s gene with the activity of an inflammatory pathway.

In cells exposed to more of the inflammatory factor TNF, the target sequence was subjected to more rounds of Cas9 alterations. Then they tested the CRISPR recorder by implanting mice with the engineered cells and injecting some with an inflammation-provoking molecule. In those mice, the CRISPR target sequences had more changes than ones from mice not receiving the molecule. This method can “record physiologically relevant biological signals in an analog fashion,” the authors write.

It could also record stimuli that cancer cells are exposed to in the micro-environment of a tumor or track the activity of specific pathways in cells during disease development, Lu and colleagues suggest. Church notes that such methods may also prove valuable in brain studies, for example by recording the activity of pathways involved in memory foundation. “You can take a transient process like the learning of a new task and turn it into a permanent record that’s present in the cell body of every neuron in the brain,” he says. ■



PEACE OF MIND

A young Palestinian neuroscientist hopes to create a research oasis in the West Bank that transcends politics

By **Martin Enserink**, in the West Bank; Photography by **Mahmoud Illean/AP Images**

On a sunny winter afternoon, Mohammad Herzallah is driving his father's Hyundai north on highway 60 to see his family near the town of Jenin. The road weaves through rugged terrain and olive groves in the heart of the West Bank, passing the occasional Palestinian village. Some hilltops

are crowned with the modern contours of Israeli settlements, a major obstacle in the quest for peace. "They're called facts on the ground. ... It's an interesting term," Herzallah says, coolly.

The Israeli military checkpoints dotting the area can paralyze traffic at a moment's notice, but today they aren't causing delays. Herzallah, a Palestinian neuroscientist

now at Rutgers University, Newark, in New Jersey, recalls how hard the roadblocks made life early in his career, when he crisscrossed the West Bank visiting Parkinson's patients. "I learned to live with the checkpoints," Herzallah says. He passes them very slowly. "You don't want to get shot at," he says.

But Herzallah isn't interested in discussing the Israeli occupation. His prime concern

Founder Mohammad Herzallah has sought to keep politics out of the Palestinian Neuroscience Initiative, housed at Al-Quds University in the West Bank.

is the Palestinian Neuroscience Initiative (PNI), which he founded in 2009 as a medical student at the tender age of 24. What he has built is remarkable, colleagues say: a research and training program in the impoverished, conflict-riven West Bank, where neuroscience, until recently, was nonexistent. Based at Al-Quds University in Abu Dis, on Jerusalem's outskirts, PNI has already trained dozens of students, bagged a \$300,000 grant with Rutgers from the U.S. National Institutes of Health (NIH), and started publishing papers. A key focus is clinical depression, which is rampant in the Palestinian territories.

Even without the tools found in neuroscience labs elsewhere—brain imaging equipment, animal facilities, or DNA sequencers—Herzallah has accomplished a lot, says neuroscientist Edvard Moser of the Norwegian University of Science and Technology in Trondheim, who visited PNI in January 2014, 8 months before he and his wife May-Britt Moser won a Nobel Prize in Physiology or Medicine. “He is very determined, balanced, thoughtful, and pragmatic,” Moser says. “I admire him.”

“Mohammad is really a person you don't meet every day,” adds computational neuroscientist Alessandro Treves of the International School for Advanced Studies in Trieste, Italy, a strong PNI supporter and a personal mentor to Herzallah. “Science is a form of personal emancipation for him.”

Herzallah, who visits the West Bank twice a year, sees his project as a recipe for “capacity building”—the elusive goal of strengthening research in developing countries. In his case, sticking to the science is a key ingredient. “If this becomes a political story, it could put everything I've built at risk,” he had warned before my visit. He feels the enervating and seemingly endless Israeli-Palestinian conflict is distracting too many young Palestinians from contributing to society. “We shouldn't produce another generation that can talk only about politics,” he says. “We need people who can speak another language, who can do something else. We need the peace of mind.”

THE MAIN CAMPUS of Al-Quds University abuts the eastern side of the 8-meter-high concrete barrier separating Israel and the West Bank. From some vantage points, you can see Jerusalem, including the glimmering golden dome of Al-Aqsa mosque, which adorns the university's logo. A few Al-Quds departments and training hospitals are in East Jerusalem, on the other side of the wall, greatly complicating life for faculty

and some of the 12,500 students. When Herzallah arrived here as a medical student in 2003, the wall was lower; you could jump it and walk to the old city in less than half an hour, he says. Now, the trip takes twice as long by public transport, via a checkpoint to the north. (West Bank Palestinians are not allowed to drive to Jerusalem.)

The neuroscience program here grew out of a long-time friendship between Mark Gluck, who leads a group at Rutgers focused on memory and learning, and Adel

work, but their proposal was rejected because there was nothing special about Parkinson's in the West Bank, Gluck says. The project “didn't cater to a specific need in the area.”

Clinical depression fits that bill much better. Studies have found that about a quarter of West Bank Palestinians suffer from major depression disorder, a severe, disabling condition. That's about three times the percentage in the United States. (Based on his own unpublished work, Herzallah says the West



Herzallah and his wife, Joman Natsheh, at his parents' home near Jenin. Natsheh is also involved in PNI and has started a project focused on Palestinian women's mental health.

Misk, a neurology professor at Al-Quds. In 2008, Misk and Gluck set out to recruit and train three Palestinian medical students for a study on cognitive function in Parkinson's patients. One, Gluck says, was “a superstar” who overcame all manner of hurdles and collected most of the data. That was Herzallah.

In 2009, Herzallah spent 6 weeks at Gluck's lab, where he finished a paper on the Parkinson's study. (Its main finding: anticholinergic drugs for treating Parkinson's impair generalization, the application of previously learned rules to a new situation.) Together, Gluck and Herzallah raised money from private donors in the United States for what was initially called the Rutgers/Al-Quds Brain Exchange Program. Herzallah later founded PNI at Al-Quds; he moved permanently to Rutgers in 2010 to begin his Ph.D. with Gluck.

As an initial project, the duo applied for NIH funding to expand the Parkinson's

Bank rate may be as high as 36%.) Many blame the Israeli occupation, economic stagnation, and a general sense of hopelessness that pervades the West Bank. Herzallah says he's not sure of the causes: “We're brain scientists, not epidemiologists,” he says.

Few patients here seek treatment because there's a strong stigma attached to mental illness. “It's related to the Arab mindset,” says PNI's Hamza Mousa, a collaborator on the depression project. “Being depressed is seen as shameful and weak. People will think you are crazy. Your daughters may be unlikely to get married.” Even those who want treatment are hard-pressed to get it: Herzallah says there are fewer than 25 psychiatrists in the West Bank, which is home to some 2.8 million Palestinians.

That makes it possible to do studies that would be difficult in the United States, where untreated severe depression is hard to find. “Anybody who has a hint of depression is put on medication,” Gluck says. “If



Mohammad Herzallah discusses results with postdoc Osama Abu-hadid after a lab meeting at Al-Quds University. Back at Rutgers, Herzallah conducts meetings by Skype.

you want to study cognition in clinical depression, you never know if you're looking at the underlying depression or the side effects of the drugs." Gluck and Herzallah convinced NIH that studying depression in the West Bank had local as well as global significance, and they set up several studies that required little more than laptop-based tests.

One paper in 2013 showed that untreated depression patients were slower than healthy controls to guide an animated character named Kilroy out of a maze—a task known to rely on a brain structure called the striatum. Once on treatment with selective serotonin reuptake inhibitors (SSRIs), patients mastered the maze as deftly as controls, but now they had trouble with a generalization task, in which Kilroy suddenly appears in a new environment. That confirms previous evidence that SSRIs have a beneficial effect on the striatum but may dull the hippocampus, the brain region that fires most actively during generalization, Herzallah says.

The paper is one of only five to emerge from data collected in the West Bank, but several more are in the works, Herzallah says. One—which he calls “the Inshallah paper”—could make a splash, he believes. A well-known problem with SSRIs is that half of all patients or more don't respond to treatment. A new study in Palestinian patients suggests that before they are medicated, these nonresponders respond poorly to punishment in a learning task. (In the study, patients had to make predictions about the weather based on clues presented

on a computer screen; the “punishment” for a wrong answer was losing points.)

If the finding holds up, Herzallah thinks it could lead to software or a device that identifies depressed people unlikely to respond to treatment. The correlation may also yield insights into the roots of clinical depression and suggest drug targets, Gluck says.

HERZALLAH GREW UP in Ya'bad, a town 12 kilometers west of Jenin where his family owns a compound with several homes. He calls himself a “half-refugee”: His mother's family was expelled from their home in Haifa, in present-day Israel, in 1948 and she grew up near Ya'bad. For our visit, she has laid out a lavish lunch of grilled turkey, red peppers, and kobbrit-laban, a local specialty made of ground veal cooked in yogurt and herbs. Two sisters and an aunt join the feast.

Herzallah says his family was enormously influential in instilling his scientific curiosity and work ethic. His father is a biochemist who obtained a master's degree in the United Kingdom and a Ph.D. in Germany; he is now a lecturer at An-Najah National University in Nablus. His aunt, a linguist who did her Ph.D. at Cornell University, recalls that Mohammad was a precocious kid who would read English books in her home library. As a fifth-grader, he studied German as well, which later helped him read Albert Einstein's original papers. Physics entranced him, but his father convinced him that the field had a dark future in the West Bank. So he chose medicine.

Herzallah still comes across as older than

his age. That helps him run a tight ship at PNI, where most staff and students are just a few years his junior. At a lab meeting, he smiles rarely, and sternly reminds students of obligations. “He knows how to be strict and firm, but also when to be more like a brother and a friend,” Mousa says. But Mohamad Taha, a PNI alumnus who's now a postdoc at Harvard University, says Herzallah can be a bit overbearing. “He's a very good leader and he keeps people on track, but sometimes they need a little space,” Taha says.

Herzallah mostly wields his influence in the West Bank from across the Atlantic. He spends a few months a year at Al-Quds and the rest of the time at Rutgers, where he teaches, holds lab meetings, mentors students, and discusses papers over Skype and email. He's now a postdoc in Denis Paré's lab at Rutgers, where he's studying the role of the amygdala in rat behavior.

“He really has two parallel jobs,” Gluck says. To keep it up, Herzallah says he starts at 4 a.m. every day and works 7 days a week—a pace that he says has caused friction with his wife, Joman Natsheh, who's doing a Ph.D. in neuroscience at Rutgers. She is involved in PNI and also set up the Palestinian Women Mental Health Initiative, which aims to train female doctors, support research, and reduce the stigma associated with mental health disorders.

Although 18 people are affiliated with PNI one way or another, only three are full-time; most are medical students learning how to do research. Such opportunities are rare in the West Bank, which helps explain

why roughly 50 of the 70 students who enter the medical faculty annually apply to PNI, says Herzallah, who only accepts a few.

Finances are still tight. Herzallah says he has raised some \$150,000 from sponsors in the Arab world, including several Palestinian business executives in Jordan. But now that the NIH grant has run out, it's not enough to sustain the initiative long term, especially with PNI branching out into other neuroscience areas.

Other forms of support have been plentiful. Herzallah has set up student exchanges with scientists at Rutgers, Harvard, and the Swiss Federal Institute of Technology in Lausanne. And Edvard Moser invited Herzallah and four students to a Nordic Neuroscience meeting in Trondheim in 2015. "Palestine is now a Nordic country," quips Herzallah, who hopes one of his students will find a training opportunity in Moser's lab.

Few are willing to discuss any political dimension to their support. "I'll be blunt and say that I'm not going to talk about politics and religion," Gluck says. "I'm not going to analyze the Middle East conflict in *Science* magazine," Moser says.

PNI has no links with Israel and its vibrant neuroscience scene. Few Palestinian scientists do. After the Oslo Accords in the 1990s, when a peaceful solution seemed in sight, ties between Israeli and Palestinian academics flourished. But as violence on both sides flared, virtually all partnerships disintegrated. Al-Quds's policy since 2009 has been to not collaborate with Israel, says the university's president, Imad Abu-Kishk. Any collaboration could lead to political problems—or worse, others say. "You would immediately be labeled a traitor," Treves says. "Your life would be in danger."

The cold shoulder frustrates scientists like Yonatan Loewenstein at Hebrew University in Jerusalem, who co-organizes meetings that bring together Israeli and Arab scientists (see sidebar, right) and is eager to work with Palestinian counterparts. "It doesn't make any sense that I work with researchers in the U.S. and Europe, but I can't meet colleagues who are less than 10 miles away," Loewenstein says.

Herzallah has avoided any collaboration with Israel out of what he calls "a mix of pragmatism and principle." He prefers to stay focused on building up his creation. As the sun sets and he looks out from the roof of his parents' home in Ya'bad over a West Bank valley dotted with scrubby vegetation, Herzallah is clear about his ambitions. "A full-blown institute here in Palestine, where I can pursue my scientific interests. ... That's what I want. I want to show that in spite of all of the suffering and the obstacles, we can move forward." ■

Gatherings aim to bridge a wide divide

By **Martin Enserink**, in Paris

When 20 neuroscientists from Israel and the Arab world gathered for dinner at a Left Bank bistro here in September 2015, it didn't take long for the conversation to turn from duck breast to the Middle East—and for the temperature to rise. The researchers, including two Palestinians, bickered over the Iran nuclear deal, the war in Syria, and, of course, the Israeli-Palestinian conflict. "The two-state solution is dead!" one Arab scientist argued. "We need to think about a one-state model." "That will never work!" an Israeli colleague shot back. As the evening wore on, the debates got more animated and louder.

The scientists didn't solve any problems that night, but at least they were talking—and that was the point.

They had assembled at Paris Descartes University for a 3-day meeting that sought to foster relationships across the political and religious fault lines dividing the Middle East. NeuroBridges, as it's called, is one of several science diplomacy efforts focused on the region; the most ambitious is SESAME, a synchrotron light source in Jordan expected to come online in 2017 that involves nine unlikely bedfellows, including Turkey, Israel, the Palestinian National Authority, Iran, and Pakistan.

NeuroBridges grew from the friendship between Ahmed El Hady, an Egyptian neuroscientist at Princeton University, and his Israeli colleague Yonatan

Loewenstein of the Edmond & Lily Safra Center for Brain Sciences (ELSC) at the Hebrew University of Jerusalem. After they met in Germany, Loewenstein invited El Hady to an ELSC retreat in Ein Gedi, an oasis near the Dead Sea in Israel. During a hike, the duo agreed that science could bring more researchers together, both professionally and personally. The first NeuroBridges, later that year at the University of Göttingen in Germany, came at an awkward time: 3 weeks into the 2014 Gaza war.

"We really need opportunities for dialogue."

Mehdi Khamassi,
Pierre and Marie Curie
University in Paris

Science sat in on the 2015 successor, in a monumental Parisian university hall adorned with tapestries woven for King Louis XIV. After an unusual preamble describing their own geographical, religious, or political background, attendees presented their work, which spanned a range of neuroscience areas. The mood was friendly.

"We really need opportunities for dialogue like this," says Mehdi Khamassi, a French-Tunisian researcher at the Pierre and Marie Curie University in Paris, who noted that relations between Arabs and Jews in France have deteriorated rapidly: "We seem to have imported the conflict from the Middle East." (The meeting took place 2 months before the 13 November 2015 terrorist attacks here.)

Like El Hady, almost all of the Arab participants live and work in Western countries. The mood in most Arab countries is fervently anti-Israel, and scientists there could face a political price for attending NeuroBridges, El Hady says. Mohammad Herzallah, who heads the Palestinian Neuroscience Initiative, has declined an invitation twice (see main story, p. 1158).

Critics of Israel's occupation of the Palestinian Territories say that meetings like NeuroBridges fail to address the root issue. A mostly scientific meeting that doesn't focus on problems faced by Palestinian academics contributes to the "normalization" of the occupation, says Jonathan Rosenhead, chair of the British Committee for the Universities of Palestine in London and an advocate of an academic boycott of Israel. El Hady disagrees. "Academics are the most reasonable people," he says. "If we cut off contact with them, we lose the last resort."

This year's NeuroBridges will be at a chateau in Burgundy, France, in September. To reach a wider and younger audience, it will be a 10-day summer school in computational neuroscience. Can such meetings bring peace in the Middle East any closer? "To be honest, this is not a question that concerns me very much," Loewenstein says after a very long pause. "The question I ask myself is what I can personally do to improve the situation." ■



STRANDING SLEUTH

Gleaning clues from beached marine mammals, Frances Gulland takes the measure of ocean health

By Elizabeth Pennisi

Frances Gulland wants to save whales, though sometimes that can mean killing one. In 1998, she got a call about a whale stranded on a rocky shelf in northern California. Gulland arrived to find that nearby residents had scrambled down a cliff to comfort the gray whale calf. They were waiting for Gulland, a veterinarian at The Marine Mammal Center in Sausalito, California, to rescue it.

That wouldn't be possible, she concluded after examining the distressed calf. But Gulland saw opportunity where others saw

tragedy. The whale was small enough, she realized, that she could decapitate it and transport the head to San Diego, California, where researchers were trying to learn how whales make and hear sounds. "They would really find a fresh head useful," she thought.

Gently, Gulland explained the calf's hopeless situation to the would-be rescuers. They lit candles and said a prayer as she euthanized it. Then she cut off its head, and onlookers helped Gulland haul the 80-kilogram, 1.5-meter-long body part up the cliff. The next day she wrapped the head in newspaper and plastic, checked it as over-

sized luggage on an airliner, and delivered it to the researchers using a rental car. (The package didn't fit in the trunk, so she drove with the lid open.) Ultimately, the head yielded insights into how whales communicate and sense the world.

Gulland's tireless efforts to glean tissue and knowledge from hundreds of whale, dolphin, and seal strandings around the world have made her a prominent figure among marine mammal scientists. But her influence stretches far beyond pure research. She has helped transform a once sleepy rehabilitation facility into a vibrant,



globally recognized science and conservation center, and become a presidentially appointed adviser to policymakers, weighing in on thorny issues such as endangered species management.

Gulland has “fundamentally reshaped our field,” says Charles Littnan, a marine mammal scientist with the National Oceanic and Atmospheric Administration (NOAA) in Honolulu. She and her center “have done unbelievable things,” adds James Harvey, director of the Moss Landing Marine Laboratories in California. “The world considers her to be its marine mammal veterinarian.”

ON A CLOUDY JANUARY DAY, Gulland, 56, dons an old sweatshirt, rubber boots, and a full-body rubberized apron in the necropsy theater at the center, a \$32 million facility located in the Marin Headlands overlooking San Francisco and the Golden Gate Bridge. The theater is a two-story-high room with a garage door that lets in fresh air, as well as the carcasses of sea lions and dolphins to be dissected. It smells slightly like saltwater and a fish market. Above the dissection table, an observation window allows visitors—on this day a group from Asia—to follow the action. A sign warns them that

Frances Gulland prepares to dissect sea lions at her center, which has grown into a marine science hub.

there will be blood and guts.

As she slides on her gloves, Gulland's colleagues maneuver a small porpoise onto the table. It was found dead the day before, its eyes already pecked out by birds, a few kilometers away. Before beginning the dissection, Gulland asks a veterinary intern—one of many that train at the center each year—to practice collecting the animal's spinal fluid with a syringe. Then the team gets down to business: figuring out what killed this porpoise.

Gulland slices open the head, starting from the blowhole. Pádraig Duignan, a veterinary pathologist visiting from the University of Calgary in Canada, uses a bigger knife to open the internal cavity, then breaks the porpoise's ribs to expose the heart, lungs, and gut. The researchers record the condition of each organ and collect urine and tissue samples, including swaths of blubber that can reveal the animal's nutritional status. “We get a gold star if we can find the tonsils,” Gulland announces as she probes the head; eventually they find this tiny organ. “Frances knows her way around the insides of marine mammals like no one else,” says Sarah Mesnick, an ecologist at NOAA's Southwest Fisheries Science Center in San Diego.

SUCH PRAISE would likely have pleased Gulland's long-deceased father, John Alan, a statistician who was a foundational figure in modern fisheries and marine mammal science. Gulland's parents were British, but when she was 4 they moved to Italy, where her dad worked for the United Nations Food and Agriculture Organization (FAO) in Rome. That move helped shape her personality: “I'm British when I hide away with my husband,” she says. “In public, I'm more Italian and open.”

At FAO, her dad helped develop the first models of maximum sustainable yields for fisheries, and in the 1960s was part of the so-called “gang of four” scientists who demonstrated that commercial whaling had put many of these great creatures on a path to extinction—a finding that helped catalyze conservation efforts. Whale experts often came to dinner, Gulland recalls, and the house “was full of whaling type stuff.”

She was instead attracted to horses, riding daily. And she wanted to be a veterinarian—a dream her parents said she'd grow out of. She didn't. A self-described “disaster in the lab,” Gulland in 1984 earned a doctorate in veterinary science from the University of Cambridge in the United Kingdom, where she became interested in studying wildlife, rather than in clinical practice.

“She was a force to be reckoned with,” recalls Michael Moore, who was a year ahead of Gulland in vet school and is now a veterinary scientist at the Woods Hole Oceanographic Institution in Massachusetts. After graduating, Gulland teamed with behavioral ecologist Timothy Clutton-Brock to study flocks of semiwild Bronze Age sheep on the island of Hirta, some 300 kilometers off Scotland. One question was why the population crashed periodically. At the time, researchers were just beginning to appreciate the role of disease in population dynamics. In the case of the sheep, Gulland's work implicated parasites. She showed that periodic food shortages were exacerbated by a nematode infection—and that particular sheep genes influenced its severity.

The Hirta project also highlighted Gulland's playful sense of humor. At first, the U.K. military—which uses Hirta as an outpost—resisted allowing her to be the only woman on the island for months at a time. But once approved, Gulland impressed the soldiers with her athleticism, running down newborn lambs on steep, rocky slopes. And an April Fools' joke she pulled—involving the faked death of a favorite sheep—made her a legend at the Hirta base for decades. “She's as productive a person as you will ever meet,” Harvey says, “but she does it with a little bit of flair and a lot of fun.”

These days, fun for Gulland means other arduous adventures. For her 40th birthday, she ran her first 40-kilometer race, and 5 years later upped the ante with 45 rock climbs in Australia with her husband, Andrew Draper. Her 50th birthday was mellower: She lined up 50 bottles of wine and drank away an evening with friends.

GULLAND'S FOCUS turned to marine mammals in 1994, when Draper noticed an ad for a yearlong fellowship at The Marine Mammal Center. He and Gulland are avid rock climbers; enticed by California's famous climbs, he suggested she apply. At the year's end, they would journey to Alaska.

When Gulland arrived in Sausalito, the center was a mostly volunteer-run effort by animal-lovers to save whales, seals, and sea lions. Sick animals were rehabilitated in a few backyard swimming pools; necropsies were performed in a jury-rigged shipping container. But “there was very little science,” Harvey recalls.

Gulland soon recognized that the steady stream of stranded mammals held a potentially rich trove of data that could be used for tracking ocean health trends. They offered “a fantastic way to see the problems these animals were facing,” she says. Soon, the planned trip to Alaska faded, and Gulland became a permanent employee.



Frances Gulland (left) examines a fin whale on the California coast. Such studies have helped identify threats.

The position enabled Gulland to tackle a wide range of research questions. She and colleagues discovered, for instance, that elephant seals—which breed on the California coast—can be killed by a nematode they share with harbor seals, which are not as severely affected. They also worked out the cyclical nature of a deadly kidney infection, called leptospirosis, in sea lions. And they’ve found that genetics, a herpes virus, and exposure to chemical pollutants may explain why California sea lions—but not sea lions elsewhere—can develop a urogenital cancer that causes massive lymph node tumors and turns the spine into mush.

Dying sea lions also tipped Gulland off to another ocean health issue, one that directly affects humans. In 1998, the center took in hundreds of stranded sea lions that were having epileptic seizures, but otherwise seemed in good condition. The cause turned out to be poisoning by domoic acid, a toxin produced by the algae that create so-called red tides. Sea lions are poisoned when they consume crabs and fish that eat the algae. Although many sea lions survive, recent research at the center has shown that even survivors can suffer from memory problems that make it challenging to navigate and take care of young (*Science*, 18 December 2015, p. 1545). The sea lion epilepsy is akin to symptoms documented in humans who ate contaminated shellfish in 1987, and the threat of domoic acid is rising as red tides become more common along the Pacific Coast.

Such research—which has netted Gulland and the center more than 200 publications—helped put her on the short list of researchers who get a call when large whales and other marine mammals wash ashore. Sometimes, the responders can help save the animals. But more often the animals are

doomed or dead, and offer a rare opportunity to collect tissues and data.

“If there’s a dead whale, [Gulland] wants to be there,” says Shawn Johnson, director of veterinary science at the center. But stranding responses, which have taken Gulland to Mexico and even Australia, can be exhausting. Sometimes, it is a race to dissect a locomotive-sized animal before it decays. To get samples, Gulland has climbed the mountainous backs of sperm whales, wielding a knife in each hand to create handholds, just as a climber ascends an ice face. She’s lassoed carcasses in freezing water and waded directly into stinking flesh, wielding a huge flensing blade. The smell can be so bad that Gulland throws out not only her working clothes, but the next set, too.

The data collected at strandings have had more than academic value. A necropsy that Gulland helped perform in Alaska showed that the victim—a humpback whale—had been killed by a local cruise ship, leading to new speed limits for the vessels. After Gulland’s group showed that ship strikes cause most whale deaths off California, officials pushed for the voluntary rerouting of shipping lanes around key habitat.

Research did not occupy all of Gulland’s time. Her gregarious personality became a fundraising asset; she gave talks and attended dinners to help raise money to expand the center. “A lot of scientists would cringe at having to do that, but she did it,” Duignan says. “If Frances were not here, [the center] would still be a mom-and-pop operation.”

THE NECROPSY ROOM, built in 2009, exemplifies the center’s transformation. As the researchers investigate the porpoise’s demise, they set aside specific tissues that other scientists have requested. The fluke and skin

will go to Frank Fish, a biomechanist at West Chester University in Pennsylvania. Another researcher wants the lower teeth. The brain will become a teaching tool at a local junior college. Extra blubber will go to a shark researcher to help attract sharks.

When they open the porpoise’s esophagus, they find a fish stuck in the tube. Could it have choked? Perhaps, but there is also froth in its airways, suggesting it might have gotten entangled in something and drowned. But the skin shows no obvious signs of fishing lines or nets. The lungs appear healthy, and the team finds a partially digested fish in its stomach—so starvation isn’t likely. The spleen, however, is swollen; that could mean the porpoise died of an infection. And the lymph nodes at the base of the lung are firmer and bigger than expected, so they take a sample to look for morbilliviruses, which have caused deadly outbreaks among seals elsewhere, but not yet in the Pacific. The brain shows signs of concussion—could it have been clubbed? Ultimately, they reach no conclusions. “Sometimes, you never know” why an animal died, Gulland says.

NOW, Gulland has turned to policy. In 2011, President Barack Obama named her to the three-member U.S. Marine Mammal Commission, which weighs in on a wide range of domestic and international issues. She’s added a spark to the typically staid body. “She’s equally adept at wowing you with science, or bringing you to a tiki bar,” NOAA’s Littnan says.

The commission also gives Gulland a platform for pursuing a longstanding interest: saving endangered species. Two years ago, she celebrated the opening of an animal hospital in Hawaii that is dedicated to caring for Hawaiian monk seals. Just 1500 of the animals remain, and Gulland had used her fundraising and organizing skills to help make the hospital a reality. To date, it has helped save 15 monk seal pups—1% of the population.

Now, she’s trying to help accomplish an even more difficult task: saving Mexico’s vaquita, a tiny porpoise threatened by illegal gillnetting. Just 60 vaquitas remain, and earlier this year Gulland traveled to Mexico to meet with colleagues and examine two vaquitas that had been killed by nets. Even though there are efforts to remove sunken gillnets and establish fisheries that would not harm vaquitas, the animal’s plight keeps Gulland up at night, Draper says.

Gulland admits she gets discouraged at times by the complex political, economic, and environmental factors that threaten creatures like the vaquita. But she’s not giving up. “It may be a losing battle,” she says, “but I’m going to go down fighting.” ■

INSIGHTS



BOOKS *et al.*

SUMMER BOOKS

The scientist's guide to summer reading

Convinced that the secret to a sniper's success is all in his aim? You may be underestimating the role of Velcro. Think that artisanal cheesemakers represent the ultimate rejection of mainstream science? Think again. From an upbeat meditation on death to a snarky critique of economics, this year's picks offer delightfully unconventional perspectives on a range of scientific topics. Join a birdsong expert as he ditches academia for a cross-country bicycle tour, embrace the unknown in an exploration of the cosmos, and get lost (pun intended) in a quest to uncover the implications of modern mapping technologies.

Groovy Science

Reviewed by **Monique Dufour**

Long-haired surfers catching waves on hand-crafted shortboards at Laguna Beach. Women practicing home births as a form of "spiritual midwifery" on the famous Tennessee commune, The Farm. Psychologist Timothy Leary, "the most dangerous man in America," imploring us to "turn on, tune in, and drop out." These are quintessential images of American counterculture. But *Groovy Science* will make the reader see them in a surprising new way: as significant scenes of encounter between counterculture and science.

By yoking together the words "groovy" and "science," editors David Kaiser and W. Patrick McCray refute three durable notions about science in the 1970s: that the counterculture was antisience, that science was languishing in a rather moribund phase during this period, and that mainstream researchers lived and worked apart from the counterculture that seemed to spurn them. Instead, the 12 essays that make up *Groovy Science* demonstrate that people and groups strongly ensconced in the counterculture also embraced science, albeit in untraditional and creative ways.

Groovy science was hardly a singular, coherent movement, but the book's four sections create some conceptual order around the ways that people connected science and

counterculture. In "Conversion," neurophysiologists, chemists, and physicists recast Cold War science by simultaneously rejecting "the megamachine" and adapting its "resources and forms of knowledge ... toward new ends." Those engaged in "Seeking"—the book's second section—pursued science as a path to countercultural virtues such as authenticity, cooperation, and environmentalism. The "Personae" in part three—Immanuel Velikovsky, Timothy Leary, and Hugh Hefner—seized mass media to fashion themselves as science-minded iconoclasts. And in "Legacies," we discover the un-

The reviewer is at the Department of History, Virginia Polytechnic Institute and State University, Blacksburg, VA 24061, USA. Email: msdufour@vt.edu



Groovy Science

Knowledge, Innovation, and American Counterculture
David Kaiser and W. Patrick McCray, Eds.

University of Chicago Press,
2016. 432 pp.



acknowledged influence of groovy science on contemporary commonplaces such as sustainability, innovation, and organic food.

In “Blowing Foam and Blowing Minds: Better Surfing through Chemistry,” Peter Neushul and Peter Westwick dramatize the period’s “shortboard revolution,” when surfers resisted mass-produced surfboards and extolled hand-made, customized boards. The movement may have been fueled in part by psychedelic drugs, but as Neushul and Westwick show, it also wouldn’t have been possible without polyurethane foam, polyester resin, and fiberglass: cheap products of industrial-scale chemistry.

Despite its rejection of mainstream values, the counterculture was intertwined with the seemingly antithetical force of consumerism. In “When Chèvre Was Weird: Hippie Taste, Technoscience, and the Revival of American Artisanal Food Making,” Heather Paxson shows that although the rise of artisanal chèvre may have been inspired by a desire for natural products, even hippie cheesemak-

ers were creating a product to sell. Moreover, their handcrafted goods relied on scientific resources, including acidimeters, pH probes, bacterial cultures, and coagulants.

Scientists were also shaped by countercultural concerns, including environmentalism, antimilitarism, and nonconformity. In “Santa Barbara Physicists in the Vietnam Era,” Cyrus C. M. Mody tells the story of three public-spirited physicists—Philip Wyatt, David Phillips, and Virgil Elings—who founded start-ups to explore new interdisciplinary collaborations and lines of research in areas that had been neglected during the focus on defense research during the Cold War.

Chèvre isn’t weird anymore. Start-ups are conventional. And rallying for environmental causes through science seems all but natural. Even in this age of technoscience, perhaps we’re still groovy after all.

Who Cooked Adam Smith’s Dinner?

Reviewed by **Jacqueline Strenio**

If I asked you to close your eyes and picture an economist, “pale, male, and stale” might come to mind. The “dismal science” is not only overwhelmingly composed of men (*I*) but also built around a hypothetical eco-

Who Cooked Adam Smith’s Dinner?
A Story About Women and Economics

Katrine Marçal
Pegasus, 2016. 240 pp.



nomie man, known as *homo economicus*. *H. economicus* was never cared for by others, nor does he care for others, engaging in his pleasure-maximization calculations without being influenced by those around him. In *Who Cooked Adam Smith’s Dinner?*, Katrine Marçal recounts how economics came to rely on this calculating and self-interested man as the prototype of human behavior. Luckily, this is not your standard economics text and Marçal, a Swedish journalist who writes in snappy (and often spirited) prose, focuses on what an alternative, and more inclusive, economics should look like.

Marçal weaves the history of mainstream economic doctrines with pop culture references to tell the story of economic man’s construction and his rise to dominance. By focusing on a selfish and market-oriented man, she argues, the discipline has created a self-

The reviewer is at the Department of Economics,
University of Utah, Salt Lake City, UT 84112, USA.
E-mail jacquelineastrenio@gmail.com

fulfilling prophecy, limiting itself to market analysis of self-interested individuals.

Marçal begins her story in the 18th century with Adam Smith, the father of modern economics. Smith famously pointed out that we owe our dinner not to the kindness of “the butcher, the brewer, or the baker” but rather to their self-interest. When everyone acts selfishly, he maintained, the market is so elegantly coordinated that it’s as if it were led by an “invisible hand.”

However, Marçal argues that Smith omits an important actor in this framework: the person who transforms the meat, beer, and bread into an actual meal. As a well-off, never-married man, Smith likely did rely on the market to secure cooking services on occasion, but Marçal’s point is well taken: A slab of meat doesn’t magically become dinner. That process requires significant labor and expertise.

This nonmarket work, and the disproportionately female population that does such work, is unaccounted for in Smith’s reckoning of the economy. Even today, it’s not captured by gross domestic product (GDP), our standard measure of economic well-being.

Marçal concludes with a plan for dismantling economic man by redefining economics as a discipline dedicated to the study of well-being: one that considers not only the butcher but also the butcher’s wife; not only the cost of meat but also the time costs of cooking dinner. Although feminist economists have been making this argument for decades, Marçal’s book serves as an accessible and lively primer on the topic.

Marçal, and the feminist economists she cites, would likely argue that the feminist lens

can’t focus solely on remedying the exclusion of unpaid provisioning activities but must be applied to all aspects of mainstream economics. *Who Cooked Adam Smith’s Dinner?* is a well-written and thoroughly researched call to change economics into a discipline that makes “room for the entire human existence” that all economists would do well to heed.

REFERENCES

1. Less than 12% of all full professors in economics are women (2).
2. M. B. McElroy, 2014 Annual Report, *CSWEP News*, 2015, Issue I (2015), p. 13.

Grunt

Reviewed by **Joshua Marino**

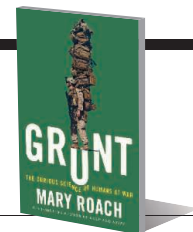
Early on in my military career, a high-ranking officer made the decision to introduce black berets to the entire U.S. Army. Up until that point, those who wore the black berets were members of the elite Army Rangers. By having every soldier wear the headgear of the Rangers, the officer reasoned that morale and professionalism would increase exponentially. Unfortunately, that wasn’t exactly how things panned out; the berets were woolen and hot, required an extensive fitting and shaping process, lacked the sun-blocking ability of the traditional patrol cap’s bill, and were rarely worn properly.

Enter Mary Roach and her brilliant exploration of military science, *Grunt: The Curious Science of Humans at War*. Roach is quick to explain that she will not be investigating the science of killing; there are already countless

Grunt
The Curious Science of Humans at War

Mary Roach

Norton, 2016. 285 pp.



volumes dedicated to that subject. Rather, she is “interested in the parts no one makes movies about—not the killing but the keeping alive.”

In researching this book, Roach traveled around the globe, attending briefings and exercises with both researchers and military operators. She visits the U.S. Army Natick Soldier Research, Development, and Engineering Center, where everything from the melting point of fabrics to the design and placement of zippers is explored with an eye to functionality and comfort. She travels to Camp Lemonnier in the African nation of Djibouti to learn about the alarming frequency with which diarrhea affects deployed troops and learns what types of education and research are being performed to reduce and mitigate this debilitating condition. In a somewhat cringe-inducing pair of chapters, Roach visits the Urology Department at Walter Reed National Military Medical Center in Bethesda, Maryland, recounting every painful detail of phalloplasty and reconstructive surgery of the reproductive organs.

Throughout *Grunt*, Roach employs a quick wit, at times bordering on cynicism. Her humor does not detract from but rather adds to the message by introducing a human (read: civilian) element to what could easily be a dry and daunting topic of discussion.

Where a casual reader would be turned off by the technical jargon, acronyms, and minutiae of military research and development, Roach is able to retain the attention of the audience by connecting with them on a personal, relatable level. In each chapter, her ability to weave her experiences with researchers into the nature and necessity of their studies drives the topic and allows for an easily understood narrative.

From my own military experience and from what I learned in *Grunt*, I know that there will always be decision-makers within the Army who disregard the science. But with every decade there are advancements made in military technology, and the capabilities and effectiveness of the force are strengthened. Our ability to wage war or maintain peace requires countless machinations behind the curtains of bureaucracy. It is not only the senior echelons but also the researchers working behind the scenes who ultimately move us forward.

The reviewer is in the Human Engineering Research Laboratories, University of Pittsburgh, Pittsburgh, PA 15206, USA. Email: callico7997@gmail.com



Crews aboard the Polynesian voyaging canoes Hōkūleʻa (shown above) and Hikianalia are in the midst of circumnavigating the Earth without the aid of GPS or other modern navigational instruments.



"Heat exhaustion is embarrassing but not particularly dangerous," writes Mary Roach in *Grunt*.

Pinpoint

Reviewed by **Renée M. Blackburn**

Today, the Global Positioning System (GPS) is so precise, it can home in on a single beet in a field. And that, according to Greg Milner, is just the beginning. In his book *Pinpoint: How GPS Is Changing Technology, Culture, and Our Minds*, Milner lays out the history of GPS, examining its emergence as a military project that eventually became a crucial part of the technological infrastructure of the world. Through a multitude of examples—from Polynesian navigation to precision agriculture to the U.S. military—the world according to GPS emerges, and with it a new way to understand our own sense of place and time.

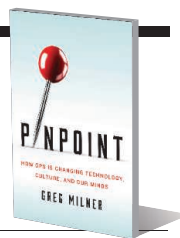
Our navigational story begins aboard the *Endeavour*, a research vessel in service of the British Royal Navy in the 18th century. Here, we meet Tupaia, a Polynesian navigator aboard the ship. While on board, Tupaia generated a map of the Pacific that included his home island of Tahiti, as well as 130 other islands spanning a distance of more than 2500 miles. Milner uses the stories of Tupaia and Tevake, a 20th-century Polynesian navigator with a similar gift for orientation, to examine traditional forms of navigation and to explore the subjective experience of geolocation. Milner draws on these stories as the basis for his assumptions regarding navigation, space, and time that emerge throughout the book.

Pinpoint is broken into two parts. Much of part one is dedicated to the story of how GPS grew out of military navigational projects in

Pinpoint
How GPS Is Changing
Technology, Culture,
and Our Minds

Greg Milner

Norton, 2016. 336 pp.



the late 20th century. In telling the stories of the various military projects that contributed to the development and dissemination of today's technology, we come to understand its complex nature as an infrastructure system, as well as the political, economic, and social stakes that rest upon accurate and timely data gathering. In one example, Milner describes how GPS was used to keep American soldiers safe and reduce civilian casualties in the Gulf War, as compared to Vietnam, when it was not yet available.

But Milner's more interesting provocations appear in part two. Here, he explores cognitive mapping and the effects of GPS on our relationship to space, privacy, and security. Cognitive maps, first introduced by Edward Tolman in 1948, are mental representations of our spatial environments. Milner cites evidence that widespread use of GPS has altered our cognitive mapping abilities, creating greater reliance on the technology. This can prove deadly, as he shows, when people follow GPS directions into a lake or off a main road, hoping to find a shorter route.

The reviewer is in the Program in History, Anthropology, and Science, Technology, and Society (HASTS), Massachusetts Institute of Technology, Cambridge, MA 02139, USA. Email: rblack@mit.edu

Whether it is used in tracking potential criminals, aiding commercial planes in difficult landings, or monitoring for earthquakes, GPS produces a sense of security and safety against the unknown and the dangerous. But civilian GPS has created scenarios that exist outside of black-and-white legal definitions of privacy and security and mostly hinge upon safety concerns of individuals and societies as a whole. Milner's detailed examples will leave you questioning the ways in which GPS has infiltrated our lives.

Milner concludes by chronicling a trans-Pacific voyage that combined etak, a traditional system used by navigators from Micronesia, with a Western process known as dead reckoning. In doing so, he reminds us that our understandings of place and space, though now mostly defined through GPS, remain subjective. Like Tupaia and his map of the Pacific, our location is defined both by objective data and by our own assumptions about the world in which we live.

Death on Earth

Reviewed by **Collin McCabe**

Death. It happens to all living things, from the tiniest of cyanobacteria to the most enormous of elephants and everything in between. In a universe spiraling toward chaos (see the second law of thermodynamics), life is a rare bastion of order, but we living things can't stave off the inevitable forever. From the moment we are born, the chaos starts to build: Telomeres shorten, free radicals accumulate, and we encounter things that want to eat

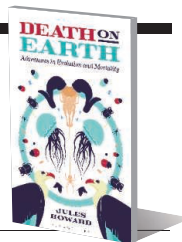
or maim us from inside and out. Sooner or later, the chaos wins, and we die—bleak, I know, but hear me out.

I'm ashamed to admit that, as an evolutionary biologist, I'd never thought too deeply or thoroughly about death as a scientific phenomenon. I just sort of took it for granted, much as I presume most other biologists do. But Jules Howard's *Death on Earth* made me see death from many new angles, introducing such topics as the physics and thermodynamics governing the maintenance of life, human and animal perceptions of dying, and the evolutionary pressures that act on senescence and death itself. Howard spends each chapter digging into (sometimes quite literally) different aspects of death, from longevity to suicide, mourning, and decomposition, just to name a few. What results is an altogether eye-opening, engaging, and enjoyably humorous (but never distasteful) guided tour through the world of death.

Howard's curiosity and keen eye for the unusual within the natural world take this book to places that few other writers would willingly go. In one scene, he leads the reader through a farm full of decaying pigs in northern England in order to provide a fuller appreciation for the successional living communities that benefit from death: from the bluebottle blowflies that lay their eggs in decaying flesh to the beetles and wasps that feed and parasitize on the flies' offspring. In another, he plants a magpie

Death on Earth
Adventures in Evolution
and Mortality
Jules Howard

Bloomsbury Sigma, 2016.
296 pp.



corpse in the woods and patiently waits to see whether local crows and jays will host a “funeral” (a cacophonous gathering observed after a death in some corvid populations). The mourners never show.

Humor runs throughout the book (often as parenthetical asides), adding depth to what is already a wonderfully written piece of nonfiction. Unusually absurd imagery is peppered throughout the book, including a scene in which Howard must smuggle a dead magpie across England (for the aforementioned funeral experiment) and another in which he engages in a shouting match with his 3-year-old daughter in an ultimately vain attempt to get her to grasp the concept of death.

Howard's self-aware commentary makes the book feel less like a rigid science text and more like a fast-paced conversation with an eccentric, death-obsessed friend. Readers who enjoy the quirky narrative

The reviewer is at the Department of Human Evolutionary Biology, Harvard University, Cambridge, MA 02138, USA. Email: mccabe@g.harvard.edu

writing styles of Mary Roach or Bill Bryson will be happy to have picked up this book.

Overall, *Death on Earth* provides a multifaceted treatment of the many aspects of the science surrounding mortality (and immortality). It's an incredibly approachable and oddly enjoyable exposition of a topic about which many of us would rather not think (probably because it scares us to death).

Listening to a Continent Sing

Reviewed by **Helena J. Barr**

Two bicycles, camping gear, and a shotgun microphone—this is what Donald Kroodsma, the illustrious ethologist, used to tune into nature's soundscape in 2003. Accompanied by his son, Kroodsma embarked on a trans-American cycling adventure, carefully documenting and decoding an incredibly diverse voice calling out across the country—bird-song—along the way. Blurring the lines between travelogue and casual scientific observation, *Listening to a Continent Sing* recounts their journey and transports the reader into the mind of a scientist renewing his awe of nature through an endearing portrayal of avian vocal communication and behavior.

Research using songbirds has undergone tremendous growth since its beginnings in ornithology, becoming a preeminent model for studying the neural, genetic, and behavioral underpinnings of vocal learning, development, and communication. Songbirds learn their vocalizations from conspecifics, vary them depending on who is listening, and use fine acoustic differences in song to recognize other individuals and make social decisions. Although this book does not go into scientific depth on these topics, the author's anthropomorphic portrayal of bird behavior renders avian ethology accessible to a larger audience.

Over the course of their 71 days of travel, Kroodsma acts as a cross-species translator. He tells us what changes in tone, pitch, vibrato, and song repetition mean in bird-song: from barred owls serenading each other in Virginia to a western tanager signaling dawn in the Grand Tetons. He draws connections between geographical changes in human accents and within-species dialects demonstrated by birds like the dickcissel. He also performs a number of spon-

The reviewer is in the Integrated Program in Neuroscience, McGill University, Montreal, QC H3A 0G4, Canada. Email: helena.barr@mail.mcgill.ca

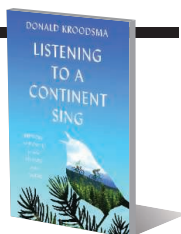


Donald Kroodsma reflects on the beauty and purpose of birdsong in *Listening to a Continent Sing*.



A laser beam is fired into the night sky from NASA's Goddard Space Flight Center in Greenbelt, Maryland.

Listening to a Continent Sing
Birdsong by Bicycle from the Atlantic to the Pacific
Donald Kroodsmas
Princeton University Press,
2016. 327 pp.



taneous scientific observations: counting which songs a mockingbird imitates to deduce its favorites or wondering why female blackbirds risk giving away their nest location just to vocalize.

Raising the topic of animal intelligence, Kroodsmas contrasts his own navigational troubles on the road with the remarkable sense of direction demonstrated by purple martins that migrate from Brazil to the United States and back each year. Scattered with illustrations of bird species and QR codes that link to sound samples, the book offers both a visual and auditory exploration of the fascinating avian world.

During his journey across the United States, the author also finds himself on a metaphorical road of self-reflection. His tranquil admiration of fauna, flora, and human characters met along the way (many just as colorful as the birds) conveys a mindful appreciation for life in all its forms. He leaps from descriptions of Civil War battlefields and the Louisiana Purchase to daydreams of Pangea to the Pleistocene ice age, all the while contemplating the immense evolutionary tree that links all living species back to common ancestors.

In its refreshing mix of history, linguistics, biology, and ethology, *Listening to a Continent Sing* brings back the joy and enthusiasm for scientific pursuits that can sometimes wane with time. Kroodsmas reminds the reader that science goes beyond the pressure to produce significant results and publications. It is a lifestyle filled with curiosity, fascination, and appreciation for the world we live in. And for anyone hoping to do the same, he provides concise advice: “[T]he more I listened the more I heard.”

The Unknown Universe

Reviewed by **Megan Engel**

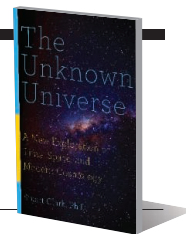
Every clear night, 300 quadrillion particles of light are fired by an enormous laser at mirrors less than half a meter wide on the Moon, allowing scientists to measure the Moon's orbital motion with extreme accuracy and precision. The handful of particles that make it back to Earth deliver vital information: whether or not Einstein's theory of gravity continues to correctly describe nature. So far, it does. But as Stuart Clark suggests in *The Unknown Universe*, breakthroughs happen when a “brave scientist [throws] away a cherished assumption,” rather like Einstein himself did in overturning Newton's understanding of gravity.

As the current gravitational framework has been verified to one part in 10^{13} , the scientists conducting the lunar laser ranging experiment are certainly brave for maintaining confidence that there's “a deeper theory of gravity to be found.” According to Clark, they exemplify “the true gold standard for science: constant self-questioning.”

The book's scope is admirably broad: Instead of delving directly into modern cosmology, Clark journeys outward through concentric circles of human discovery of the cosmos, highlighting unknowns at every scale: from the Moon, whose origins are still uncertain, to the Sun, whose magnetic cycles remain baffling. He proceeds from our solar system—which, according to some astronomers, likely contains undiscovered giant planets—to galaxies and the universe at large, whose dynamics are so perplexing that scientists have invoked “dark matter” and “dark energy”—so named because of their wholly mysterious nature—as explanations. Clark's narration is accessible to any reader with basic mathematical understanding, but it is also enriching

The reviewer is at the Rudolf Peierls Centre for Theoretical Physics, University of Oxford, Oxford OX1 3NP, UK. Email: megan.engel@physics.ox.ac.uk

The Unknown Universe
A New Exploration of Time, Space, and Modern Cosmology
Stuart Clark
Pegasus, 2016. 303 pp.



for specialists, providing ample references to technical papers for further reading.

Multiple eras of human history inform Clark's description, connected by common threads: continual subversion of established scientific dogma and deep, lingering questions. A central theme of the book is the incompleteness and necessary dynamism of science: that ever-shifting landscape where the only constant is the “unknown.” By emphasizing the “hole[s] in our understanding of the Universe,” Clark provides an incisive critique of scientific entrenchment: the tendency of some modern scientists to describe our theories as “almost perfect” even when mysteries remain.

Eschewing the simplistic “lone genius” narrative, Clark details a broad cast of players, emphasizing their interconnectedness. For example, he discusses how Isaac Newton's foundational theory of gravity rested upon a serendipitous visit from Edmond Halley (of Halley's Comet fame).

Female scientists could have been treated more prominently, however. For instance, while Clark lauds William Herschel for contributing to our understanding of the universe's structure through his observations of galaxies, which he called “nebulae,” Herschel's sister Caroline, who actually made the first observations of “nebulae” with William's telescope, is described merely as her brother's “amanuensis.” Jocelyn Bell, discoverer of pulsars—small, rapidly rotating remnants of exploded stars—is also conspicuously absent.

While the strength of the book is its comprehensive treatment of the history and nature of the astrophysical sciences, readers hungry for exotic theories will be sated. The book discusses other universes, 11-dimensional worlds, and the notion of a “timescape,” a universe where time runs differently in each location, such that some parts may be 5 billion years older than others.

Physics and cosmology are often triumphantly presented as staid things. Clark recounts their charged history and cites instances of scientific “hubris run aground,” instead painting a portrait of a universe that continues to surprise, defy understanding, and derail popular belief. *The Unknown Universe* reminds us that the quest for knowledge demands uncompromising skepticism and abundant humility alongside the insatiable curiosity that has always characterized the human heart.

10.1126/science.aaf6929

ECOLOGY

Ecologically relevant data are policy-relevant data

Microplastics reduce fish hatching success and survival

By Chelsea M. Rochman^{1,2}

History tells us that the motivation for new environmental policy is much stronger when there is demonstrated ecological impact. Multinational agreements to stop the use of DDT followed the precipitous decline of predatory bird populations. Similarly, decisions to regulate emissions to prevent acid rain followed widespread degradation of aquatic habitats. Ideally, environmental policy should be catalyzed by scientific evidence rather than environmental catastrophe. As scientists, we can do our part by providing evidence that is relevant to the natural environment. On page 1213 of this issue, Lönnstedt and Eklöv (1) take an important step forward in this regard by reporting ecologically relevant evidence on a growing environmental issue: microplastic pollution.

Plastic can remain in the environment for hundreds to thousands of years. Moreover, its production and global consumption outpace waste management (2). The mismanagement of plastic waste is now coming back to haunt us as marine and freshwater debris. Much of this debris is microplastics: plastic frag-

ments <5 mm in all dimensions that are either manufactured that way (plastic microbeads in many personal care products) or are broken-down bits of larger pieces of debris (see the photo). Microplastic fragments float on the surface of every major ocean (3); microbeads are found in freshwater lakes (4); plastic fibers shed from clothing are coming down with rain (5); and a medley of plastic particles have been found in commercial sea salt (6), fish (7), and oysters (8).

Hundreds of studies have demonstrated global microplastic contamination, but few have investigated its impacts on animal populations, communities, and ecosystems. This pattern is not unique. For many chemical contaminants in the environment, widespread contamination is documented, yet little is known about their ecological impacts (9). A recent systematic review found that evidence of ecological impacts of microplastic debris is not lacking because there are none, but because scientists are not asking questions about impacts at biological levels above the individual organism (10). Most studies investigate suborganismal effects such as cell death, organ damage, or changes in gene expression in animals exposed to quick and unrealistically large doses of microplastics (10). These studies are critical for understanding physiological mechanisms but tell us little about ecological impacts that may be occurring in nature now (11).

Microplastic pollution. Microplastics like these from the Patapsco River, Chesapeake Bay, are found in watersheds and oceans worldwide, but few have studied their ecological effects under environmentally relevant conditions.

To increase understanding of ecological impacts, Lönnstedt and Eklöv exposed fish to concentrations of polystyrene microplastics comparable to those found in nature. They studied European perch (*Perca fluviatilis*) at the sensitive embryonic and larval stages and exposed them to microplastics similar in size to those found in ocean samples. Most importantly, they asked ecologically relevant questions about survival and recruitment in their laboratory populations.

The results show that exposure of embryos to microplastics decreases hatching success. Moreover, exposed 2-week-old larvae were much less able to escape predation, leading to reduced survival. In another recent study, Sussarellu *et al.* exposed reproductively active oysters to an environmentally relevant concentration of polystyrene microplastics and found similar results: decreases in egg production and motile sperm, leading to reduced larval yield (12). Such ecologically relevant impacts, including compromised reproduction, reduced survival, and changes in predator-prey interactions, may translate to population- or community-level impacts.

Lönnstedt and Eklöv's study marks an important step toward understanding ecological impacts of microplastics. Future work should ask questions about multigenerational impacts, changes in biodiversity indices, community structure, and ecosystem function. Ideally, such studies will guide mitigation efforts—for example, by determining the types of microplastics that may be most hazardous and by identifying the most sensitive populations, species, and/or ecosystems. With such data in hand, practitioners can shift their energy toward prevention and avoid the need for costly recovery and restoration. ■

REFERENCES AND NOTES

1. O. M. Lönnstedt, P. Eklöv, *Science* **352**, 1213 (2016).
2. J. Jambeck *et al.*, *Science* **347**, 768 (2015).
3. E. van Sebille *et al.*, *Environ. Res. Lett.* **10**, 124006 (2015).
4. M. Eriksen *et al.*, *Mar. Pollut. Bull.* **77**, 177 (2013).
5. R. Dris *et al.*, *Mar. Pollut. Bull.* **104**, 290 (2016).
6. D. Yang *et al.*, *Environ. Sci. Technol.* **49**, 13622 (2015).
7. C. Rochman *et al.*, *Sci. Rep.* **5**, 14340 (2015).
8. L. Van Cauwenbergh, C. Janssen, *Environ. Pollut.* **193**, 65 (2014).
9. E. Johnston, M. Mayer-Pinto, T. Crowe, *J. Appl. Ecol.* **52**, 140 (2015).
10. C. Rochman *et al.*, *Ecology* **97**, 302 (2016).
11. P. Sussarellu *et al.*, *Environ. Int.* **33**, 492 (2007).
12. R. Sussarellu *et al.*, *Proc. Natl. Acad. Sci. U.S.A.* **113**, 2430 (2016).

ACKNOWLEDGMENTS

I thank K. L. Law, D. L. Mahler, and A. J. Underwood for comments and the David H. Smith Conservation Research Fellowship Program for support.

¹Department of Earth Sciences, University of Toronto, Toronto, Ontario M5S 3B1, Canada. ²Department of Anatomy, Physiology and Cell Biology, University of California Davis, Davis, CA 95616, USA. Email: cmrochman@ucdavis.edu

IMMUNOLOGY

A lipid arsenal to control inflammation

Lipids released from dying cells control immune responses to microbial products

By **Brooke A. Napier** and **Denise M. Monack**

Innate immune cells act as a surveillance system, detecting and responding to pathogens and endogenous danger signals. The complex patterns of signals they receive are detected by a variety of pattern recognition receptors (PRRs). On page 1232 of this issue, Zandoni *et al.* (1) find that innate immune responses to microbial products do not occur in a vacuum; rather, there is a complex array of danger signals in surrounding damaged tissue that can determine an immune cell type-specific response to pathogens. They describe a host-derived lipid that binds to a PRR to induce a hyperactive innate immune response that enhances long-lived protective immunity against invading microbes.

Caspase-11 is a unique cytosolic PRR that binds to, and is activated by, lipopolysaccharide (LPS), a microbial-derived lipid found in the outer leaflet of Gram-negative bacteria (2). In macrophages, an innate immune cell type, LPS binds to and activates caspase-11, inducing caspase-11- and caspase-1-dependent pyroptosis, or inflammatory cell death. Activation of caspase-11 by LPS also induces the cleavage of gasdermin-D (Gsdmd), a protein whose physiological role is still unknown, and may act as an executioner protein during pyroptosis (2, 3). Pyroptosis is associated with the release of proinflammatory cytokines interleukin (IL)-1 α/β , IL-18, and high-mobility group box 1 (HMGB1) from multiple cell types, which correlates with protection and clearance of bacterial pathogens and contributes to exacerbation of sepsis (3, 4). Although caspase-11 plays an important role in responding to microbial lipids, it was unknown whether it can bind and respond to additional ligands.

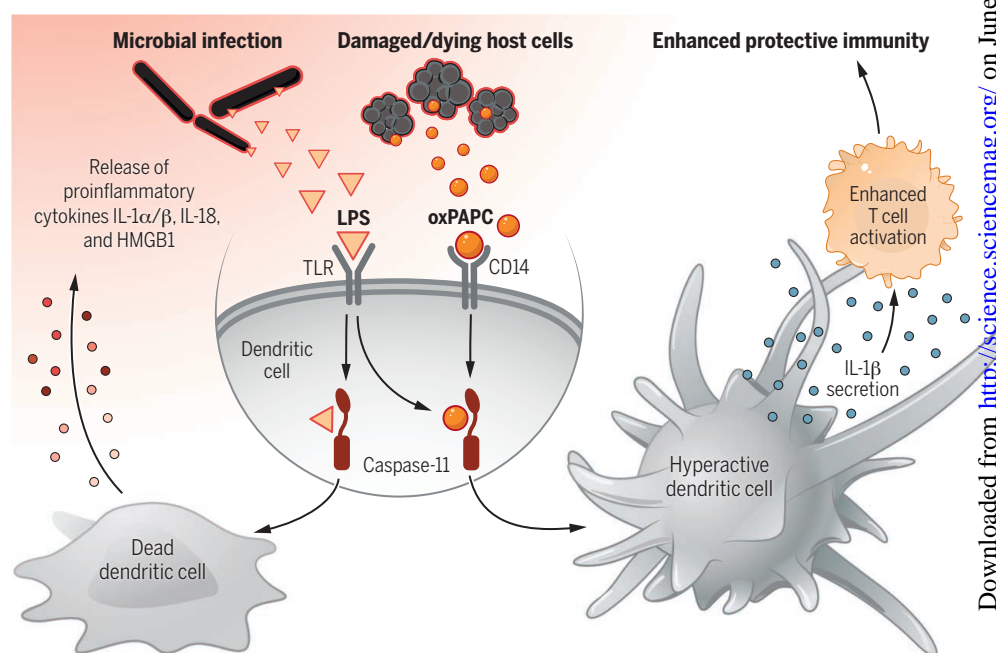
Zandoni *et al.* describe a newly discovered host-derived caspase-11 ligand: oxidized phospholipids, a group of lipids released from dying cells in damaged tissue. The combination of microbial products and the oxidized phospholipid oxPAPC (oxidized 1-palmitoyl-2-arachidonoyl-*sn*-glycero-3-phosphocholine) triggers the release of the potent proinflammatory cytokine IL-1 β from dendritic cells without inducing pyroptosis. The

authors describe this enhanced dendritic cell activation state as “hyperactive” (see the figure). Interestingly, this hyperactive state was not found in macrophages, which suggests that oxPAPC inhibition of caspase-11-dependent cell death is cell type-specific. The specificity of this regulatory effect will likely prove to be important in the complex innate immune response and subsequent adaptive immune responses during microbial infection in a whole organism.

These results demonstrate that within dendritic cells, oxPAPC is inducing release

channel subunit transient receptor potential channel 1 (TRPC1) by caspase-11 enhances IL-1 β secretion and not cell death (7). Thus, it will be interesting to elucidate a potential role for this receptor, and other potential proteins, in IL-1 β secretion by dendritic cells.

IL-1 β also modulates the adaptive immune response to microbial pathogens. Zandoni *et al.* show that the oxPAPC-dependent hyperactive dendritic cell state promotes a potent adaptive immune response that depends on caspase-11. These findings not only highlight a link between caspase-11 and T cell activa-



Hyperactivating lipids. During infection, dendritic cells detect the presence of microbial lipopolysaccharide (LPS) and host-derived oxidized phospholipids (oxPAPC) that are released from damaged and dying cells. oxPAPC binds to CD14, enters the host cell through an unknown mechanism, and then binds to caspase-11, inducing secretion of proinflammatory IL-1 β and inhibiting cell death. These hyperactive dendritic cells also activate T cells, enhancing protective adaptive immunity from the infecting microbe.

of IL-1 β , which is the focus of much interest due to its importance in inflammation during tissue injury, autoinflammatory disease, and microbial infection. IL-1 β lacks the proper signal to traffic through the classical protein secretory pathway, and recent single-cell analyses have found that IL-1 β release is associated with cell death (5, 6). Zandoni *et al.* show an uncoupling of IL-1 β release and cell death in dendritic cells, suggesting the existence of a secretory pathway for IL-1 β . In macrophages, degradation of the cationic

tion, but also indicate that oxPAPC can act as an adjuvant in the presence of microbial products in a caspase-11-dependent manner.

Zandoni *et al.* use a myriad of biochemical techniques to show that oxPAPC binds directly to the catalytic domain of caspase-11 to induce IL-1 β secretion and inhibit caspase-11- and caspase-1-dependent cell death in hyperactive dendritic cells, independent of caspase-11's catalytic function. Intriguingly, another inflammatory caspase, caspase-12, requires its catalytic domain, but not

Department of Microbiology and Immunology, Stanford School of Medicine, Stanford University, Stanford, CA 94306, USA. Email: dmonack@stanford.edu

enzymatic activity, to block caspase-1 activation in the presence of microbial products (8). This suggests the existence of multiple layers of regulation for these inflammatory caspases during infection.

In contrast to oxPAPC binding, the function of the caspase-11 catalytic domain is required for cleavage of Gsdmd, which is potentially the executioner protein in caspase-11- and caspase-1-dependent cell death. Zanoni *et al.* show that there is no cell death correlated with activation of caspase-11; thus, perhaps oxPAPC binding to the caspase-11 catalytic domain blocks cell death by inhibiting Gsdmd cleavage in dendritic cells. Future studies should reveal the physiological importance of oxPAPC and Gsdmd, and their interactions, in caspase-11 activation and cell death.

Zanoni *et al.* uncover a role for host lipids in controlling caspase-11 activation and cell death. Such knowledge is important for understanding the involvement of caspase-11 in disease models where LPS is scarce. For example, caspase-11-dependent cell death plays an important role in neuronal necrosis in models of stroke, multiple sclerosis, Parkinson's disease, and methamphetamine-induced inflammation (9–12). Additionally, it is currently unknown whether caspase-11 plays a role during viral infection. Thus, studies to identify the role of endogenous ligands, such as oxPAPC, and their regulation of caspase-11-induced inflammation during neuronal injury and viral infection will be of great importance.

Many gaps remain in our knowledge of caspase-11—specifically, how activation and its resolution are regulated, and how this regulation differs by cell type and can affect the adaptive immune response. Zanoni *et al.* reveal previously unsuspected functions of host lipids in regulating caspase-11 activation and cell death. In addition, their findings demonstrate how the innate immune system has evolved to decode the complexity of microbial- and host-derived signals to harness an appropriate adaptive immune response to infection. ■

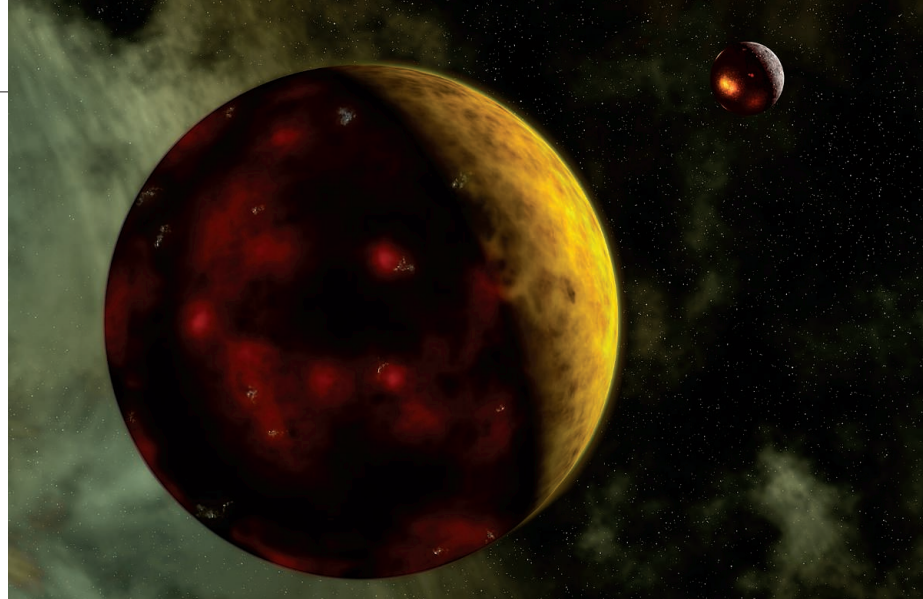
REFERENCES AND NOTES

1. I. Zanoni *et al.*, *Science* **352**, 1232 (2016).
2. J. Shi *et al.*, *Nature* **514**, 187 (2014).
3. N. Kayagaki *et al.*, *Nature* **479**, 117 (2011).
4. N. Kayagaki *et al.*, *Nature* **526**, 666 (2015).
5. Y. Shirasaki *et al.*, *Sci. Rep.* **4**, 4736 (2014).
6. T. Liu *et al.*, *Cell Rep.* **8**, 974 (2014).
7. F. Py *et al.*, *Cell Rep.* **6**, 1122 (2014).
8. M. Saleh *et al.*, *Nature* **440**, 1064 (2006).
9. S. J. Kang *et al.*, *J. Cell Biol.* **149**, 613 (2000).
10. S. Hisahara *et al.*, *J. Exp. Med.* **193**, 111 (2001).
11. T. Furuya *et al.*, *J. Neurosci.* **24**, 1865 (2004).
12. W. Huang *et al.*, *Toxicol. Sci.* **145**, 68 (2015).

ACKNOWLEDGMENTS

Funding from the National Institute of Allergy and Infectious Diseases, National Institutes of Health Award AI095396-05 (D.M.M.) and 1F32AI115950-01 (B.A.N.).

10.1126/science.aag0366



ORIGIN OF LIFE

Beyond prebiotic chemistry

What dynamic network properties allow the emergence of life?

By Leroy Cronin¹ and Sara Imari Walker^{2,3}

How can matter transition from the nonliving to the living state? The answer is essential for understanding the origin of life on Earth and for identifying promising targets in the search for life on other planets. Most studies have focused on the likely chemistry of RNA (1), protein (2), lipid, or metabolic “worlds” (3) and autocatalytic sets (4), including attempts to make life in the lab. But these efforts may be too narrowly focused on the biochemistry of life as we know it today. A radical rethink is necessary, one that explores not just plausible chemical scenarios but also new physical processes and driving forces. Such investigations could lead to a physical understanding not only of the origin of life but also of life itself, as well as to new tools for designing artificial biology.

A transition from the limited function and memory possible in a soup of weakly interacting molecules to more strongly interacting networks was essential for the emergence of life on Earth (see the figure). Left unattended, sophisticated chemistry becomes more dilute and disordered. A quick route to complexity and enrichment that could lead to the development of evolvable units seems to be required to avoid this serious issue. Yet, most

research efforts have focused on detailing precise chemical mechanisms for producing high yields of individual bio-inspired products, without addressing the processes necessary to form increasingly complex molecules and networks.

What happens to our traditional perspectives if we do not restrict attention to the chemical substrates of known life? The development of networks over time may be more important than the specific chemical nature of their molecular components: Even RNA can form cooperative networks, diversifying its potential role in the earliest evolving chemistries (5); autocatalytic networks can evolve in the absence of genes (4). The first networks would have had to be simple, challenging the notion that highly complex and improbable molecules are needed to jump-start life. The molecular constituents of simple networks are more likely to arise by chance than the highly evolved molecules of extant life. Starting from networks composed of simple molecules could therefore dramatically reduce the time necessary for the emergence of life and potentially increase the probability of an origins event.

A concept of information relevant to biological organization may be essential to identifying these networked processes. Adami and LaBar have described life at a basic level as “information that copies itself” (6). Given that life not only copies information but also uses information to construct itself, we might instead describe the start of life as “simple machines that can construct slightly more complicated machines.” Focusing on information in this way moves the narrative

¹WestCHEM, School of Chemistry, University of Glasgow, Glasgow G12 8QQ, UK. ²School of Earth and Space Exploration, Beyond Center for Fundamental Concepts in Science, Arizona State University, Tempe, AZ 85287, USA. ³Blue Marble Space Institute for Science, Seattle, WA 98154, USA. Email: lee.cronin@glasgow.ac.uk; sara.i.walker@asu.edu

Artist's impression of the young Earth. Life evolved shortly after Earth's surface cooled enough for a solid crust to form.

even further from a chemistry-specific mode than focusing on networks alone but may perhaps provide our best shot at uncovering universal laws of life that work not just for biological systems with known chemistry but also for putative artificial and alien life. For example, Walker *et al.* have recently shown that information-theoretic measures distinguish biological networks from random ones, even in cases where the biological networks share important network properties (such as topological features) with random networks (7). Life requires chemistry, but the properties of the living state emerge from the dynamical properties of that chemistry, including the temporal and spatial organization of molecular networks and their information management.

Another way to reconceptualize the problem is to consider life's emergence as a phase transition that manifests as a sudden change in how chemistry can process and use information and free energy. Understanding this phase transition requires new approaches to nonequilibrium physics that hold promise for explaining the origin of structure at multiple hierarchical scales (8). Heterogeneity in the early Earth environment played a central role in facilitating the emergence of life by helping to sustain, select, and drive the emergence of organized systems that could persist over time. For example, pores in rocks may have influenced chemical selection, leading to increasingly lifelike chemistries over time (9).

One important order parameter in characterizing life's origin as a phase transition is the homochirality. Jafarpour *et al.* have shown that homochirality emerges spontaneously as a symmetry-breaking process in models of noisy autocatalytic systems, a result that could be experimentally tested (10). Insights may also come from studying other transitions in the biosphere where organization has emerged from messy dy-

namical systems, including the origins of social systems (11). Such comparisons could yield insights into universal properties of dynamic networks.

However, speculation should be restricted to the development of experimentally testable hypotheses that address key questions and provide a focus for progress. First, how did evolution begin if the complex machinery for evolution was not in place? Experimental studies addressing this question could evaluate the evolvability and robustness of molecular networks or systems with a lower molecular complexity than a full-blown ribosome. Second, can the emergence of life be substrate-independent? Answers may come from investigation of evolvable chemical

"Focusing on information... may perhaps provide our best shot at uncovering universal laws of life that work not just for biological systems with known chemistry but also for putative artificial and alien life."

pathways in the laboratory that are based on alternative polymers. This includes demonstrating how function can be transferred between molecules with different chemical make-up while preserving the overall network structure. Third, at what point in the historical origins of life did the current chemistry of life get selected? Could more than one version of biology exist on the planet today or in the past? This could in principle be tested in one-pot experiments and simulations that include in vitro competition between alternative chemical scenarios for early life.

In more abstract terms, it remains unclear whether the problems of life's origin, evolution, and understanding the living state

will be understood within a single unified theory or will be shown to involve different processes (12, 13). In connecting these areas, understanding common features such as the emergence of complexity becomes important. For example, how complex must a chemical signature need to be before it can be considered a biosignature? Looking for complex objects that could not form randomly in an environment, but arise only as a result of lifelike machinery, might help in classifying potential biosignatures and the processes that generate them. Earth's complex inorganic and organic worlds are certainly highly connected in this respect, with even Earth's mineral diversity in part dictated by life (14).

Progress will be made by challenging all historical prerequisites assumed to be important in the origin of life. We should aim to develop measurable and collaborative routes to explore the physics and chemistry of life's origins and the living state. Not only is a comprehensive understanding of what it means for a physical system to be alive required but also a new multidisciplinary, multinational project to generate new life in the lab or in silico, to search for life on Earth that uses an alternative chemistry to that found in biology (15), and to explore the potential for life on other worlds. For this to be possible, researchers must challenge the current models and historical approach and be willing to work together across disciplinary boundaries to see if a process-based model can be used to understand and control the transition from inorganic matter to biology. ■

REFERENCES AND NOTES

1. S. A. Benner, H. J. Kim, M. A. Carrigan, *Acc. Chem. Res.* **45**, 2025 (2012).
2. M. Rodríguez-García *et al.*, *Nat. Commun.* **6**, 8385 (2015).
3. J. C. Blain, J. W. Szostak, *Ann. Rev. Biochem.* **83**, 615 (2014).
4. V. Vasas, C. Fernando, M. Santos, S. A. Kauffman, E. Szathmáry, *Biology Direct* **7**, 1 (2012).
5. N. Vaidya *et al.*, *Nature* **491**, 72 (2012).
6. C. Adami, T. LaBar, From entropy to information: Biased typewriters and the origin of life, <http://arxiv.org/abs/1506.06988> (2015).
7. S. I. Walker, H. Kim, P. C. W. Davies, *Philos. Trans. R. Soc. A* **374**, 20150057 (2016).
8. H. Morowitz, E. Smith, *Complexity* **13**, 51 (2007).
9. W. Martin, M. J. Russell, *Philos. Trans. R. Soc. Lond. B Biol. Sci.* **358**, 59 (2003).
10. F. Jafarpour, T. Biancalani, N. Goldenfeld, *Phys. Rev. Lett.* **115**, 158101 (2015).
11. S. DeDeo, Major transitions in political order, <http://arxiv.org/abs/1512.03419> (2015).
12. D. H. Erwin, *Curr. Biol.* **25**, R930 (2015).
13. E. Baptiste, *Trends Genet.* **29**, 439 (2013).
14. E. G. Grosch, R. M. Hazen, *Astrobiology* **15**, 922 (2015); 10.1089/ast.2015.1302.
15. P. C. W. Davies, *Philos. Trans. R. Soc. A* **369**, 624 (2011).

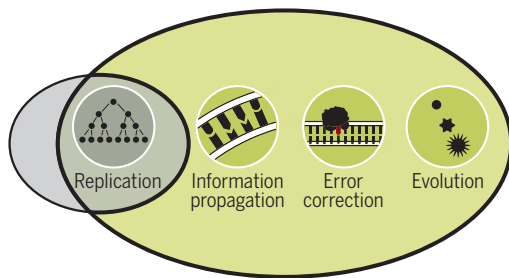
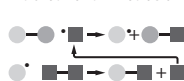
ACKNOWLEDGMENTS

This Perspective was inspired in part by a workshop held at the Carnegie Institution for Science in Washington, D.C., from 9 to 15 November 2015, and we thank the contributors to this conference.

10.1126/science.aaf6310

Nonliving network

Radical chain reaction



Living network

DNA polymerase chain reaction



Comparison of nonliving and living networks. Nonliving and living systems both replicate or copy, but the DNA-based living network allows information propagation, evolution, and error correction. Progress in understanding the origin of life may come from studying how simple chemical networks can transform into living networks.

ASTRONOMY

Connecting the dots in magnetic reconnection

Four formation-flying spacecraft reveal the 3D electron physics of magnetic reconnection

By **Andrew J. Coates**

That plasmas don't mix well is a key aspect of this magnetized, highly conducting fourth state of matter. Magnetized plasmas are ubiquitous in our solar system, in astrophysics, and in the lab. The same fundamental process is common to solar flares, coronal mass ejections, the solar wind, the magnetospheres of Earth and other planets, comet tails, magnetars, and tokamaks. We know that plasma regions with embedded magnetic fields actually do spontaneously mix via the process of magnetic reconnection, with explosive results—we see the effects of particle acceleration in the aurora and solar energetic particles. On page 1189 of this issue, Burch *et al.* (1) present results that help shed light on the process of magnetic reconnection. They have probed a magnetic reconnection site in Earth's magnetosphere using a constellation of four spacecraft in close proximity, with unprecedentedly fast electron measurements to reveal what triggers reconnection and the vital role that electrons play on the small scale.

Plasma is not just a superheated gas with fluid-like properties; additional interest and complexity come from its constituents: charged particles, electrons, and ions. On large length scales, the gas can be approximated as a fluid but with additional collective effects associated with the charges. This is the realm of magnetohydrodynamics (MHD). For a plasma of infinite conductivity (ideal MHD), the magnetic field becomes “frozen in” to the plasma flow. In this approximation the plasma behaves like a magnetized gas, leading to

separate regions of the plasma with different characteristics (2).

On smaller length scales, the motions of individual particles become important. The mass dependence of particle gyration in a magnetic field means that ions have a much larger gyration radius than electrons. To understand all the physics, in particular the

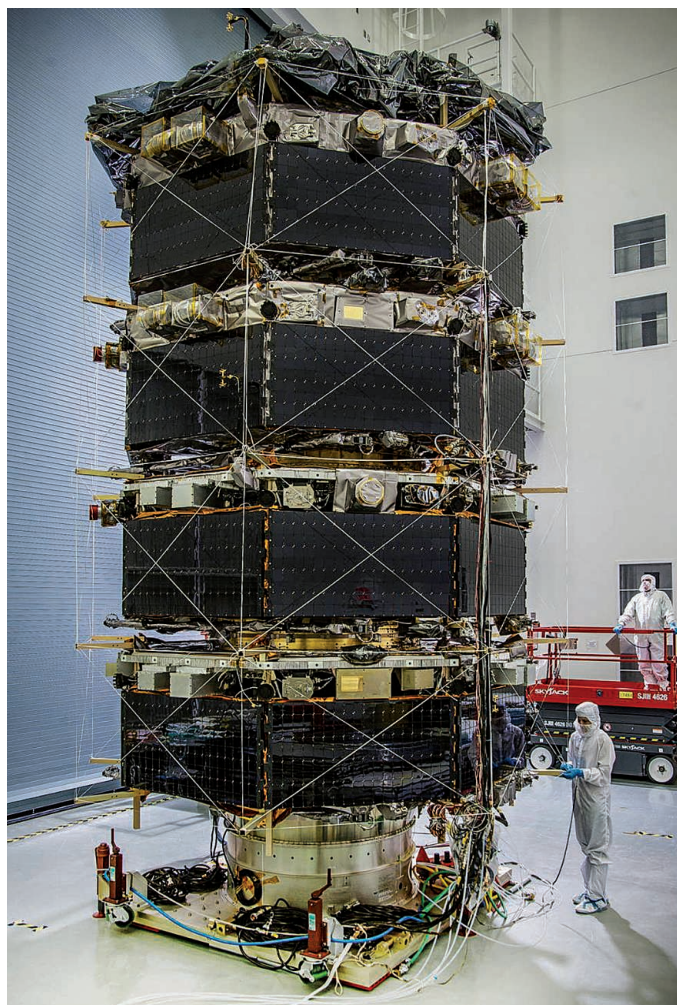
oppositely directed magnetic fields spontaneously connect, accelerating particles as part of the process. Reconnection occurs between solar wind and terrestrial magnetic fields at the magnetopause, and between oppositely directed magnetic fields in Earth's magnetotail. A major focus of solar-terrestrial physics concerns the structure of the reconnection region, the details of how it is triggered, and how it leads to magnetic storms (4). But the fundamental question of how the reconnection process works has remained unresolved.

Early models for reconnection included resistive diffusion occurring over small distance scales (5, 6), but this cannot explain some of the fast reconnection rates observed in solar flares. Slow-mode shocks were then proposed (7) to play a role in separating the inflow and outflow regions, providing faster rates, although some approximations such as anomalous resistivity were not appropriate. A fully kinetic description, involving both ion and electron diffusion regions, was found to be important in theory and simulations. At progressively smaller scales, the ions and electrons become demagnetized as diffusion becomes important and dissipation results.

Earth's magnetopause and tail provide excellent laboratories for studying reconnection. Space-based missions are able to measure not only magnetic and electron fields, but also particle flows, directions, and velocities (the velocity distribution function) for electrons and ions, and they can measure plasma waves, which are important in understanding the physics. In

general, a charged-particle flow is a current that shapes the magnetic field, and particle distribution functions may be unstable and drive instabilities that can shape and disrupt the flow (4).

With advances in computing power, we are now getting to the stage where enough particles can be followed for a full kinetic simu-



MMS stacked. The four Magnetospheric Multiscale spacecraft showing the multiple particle detectors and other instruments above the solar panels.

ability to mix plasma across fluid boundaries, we must zoom in from the large, fluid-like scale to the kinetic scale with ions and, ultimately, electrons.

Since reconnection was first proposed as the mechanism that allows the solar wind to pass Earth (3), it has been seen as a key process. Reconnection may happen when

Mullard Space Science Laboratory, Department of Space and Climate Physics, University College London, London WC1E 6BT, UK. Email: a.coates@ucl.ac.uk

lation of reconnection, and space missions are keeping pace. In the 1970s and 1980s, dual, widely spaced space missions made some progress, but starting with Cluster in 2000, more closely spaced multi-spacecraft missions have been able to probe reconnection regions near to Earth (8). Together with the increasing capability of plasma particle instruments, this has led to good advances in our understanding of reconnection at Earth, Mercury (9), and Saturn (10). But the Cluster particle measurements relied on spacecraft spin to view the whole sky, and the time resolution was limited to half a spin.

The key aspect of the Magnetospheric Multiscale (MMS) mission (see the photo) is to look at the physics of reconnection in detail, in the electron diffusion/dissipation region. This requires kilometer-scale separation, 30-ms resolution on 3D measurements of electrons, and measurements of the 3D electric field, as well as good magnetic field measurements. This required a leap in technology from using one or two particle sensors on earlier missions, to remove the dependence on spacecraft spin. Onboard each MMS spacecraft are four dual-electron sensors, making a total of eight sensors measuring electrons simultaneously.

Burch *et al.* report the first detailed kinetic electron physics associated with magnetic reconnection at Earth's magnetopause and compare the findings with state-of-the-art simulations. The results include a precise measurement of the electric field associated with reconnection and the identification of current-carrying electrons that shape the structure and result in particle acceleration. Some of the results obtained from the data are beyond those available from simulations at present and will inspire new simulation analysis (for example, the formation of a nonpredicted crescent electron distribution along the parallel velocity direction, indicative of field line opening). The results should prove an important data set for researchers to better understand space, laboratory, and astrophysical plasmas. ■

REFERENCES

1. J. L. Burch *et al.*, *Science* **352**, 1189 (2016).
2. H. O. G. Alfven, *IEEE Trans. Plasma Sci.* **18**, 5 (1990).
3. J. W. Dungey, *Phys. Rev. Lett.* **6**, 47 (1961).
4. S. A. Fuselier, W. S. Lewis, *Space Sci. Rev.* **160**, 95 (2011).
5. P. A. Sweet, in *IAU Symposium 6, Electromagnetic Phenomena in Cosmical Physics*, B. Lehnert, Ed. (Kluwer, Dordrecht, Netherlands, 1958), p. 123.
6. E. N. Parker, *J. Geophys. Res.* **62**, 509 (1957).
7. H. E. Petschek, in *The Physics of Solar Flares*, proceedings of the AAS-NASA Symposium, 28 to 30 October 1963 (Goddard Space Flight Center, Greenbelt, MD, 1964), p. 425.
8. G. Paschmann, M. Øieroset, T. Phan, *Space Sci. Rev.* **178**, 385 (2013).
9. J. A. Slavin *et al.*, *Science* **324**, 606 (2009).
10. C. S. Arridge *et al.*, *Nat. Phys.* **12**, 268 (2016).

10.1126/science.aaf7269

APPLIED OPTICS

Photonic multitasking enabled with geometric phase

Metasurface-based phased-array antennas help implement flat optical devices that perform multiple functions

By Natalia M. Litchinitser

The constructive and destructive interference of waves is often exploited in optics and signal transmission. The interference pattern is a direct measure of the phase difference between two or more beams. Such a phase difference may result from the difference between the optical paths traversed by the light beams. However, phase can change for a single beam if it propagates through an “anisotropic parameter space,” a medium that curves the light; this property is called geometric or topological phase (1–4). On page 1202 of this issue, Maguid *et al.* (5) use

“Modern photonics applications, however, call for ultracompact, multifunctional, integrated optical devices...”

metasurfaces—ultrathin, planar engineered structures (6–9)—to form shared-aperture antenna arrays that impart geometric phase to optical signals. These devices can control photonic spin and enable multiple optical functions.

Geometric phase shift arises when rotations are caused by moving through an anisotropic parameter space, so the phase will depend on the path traveled. Consider moving an arrow over a sphere, with the requirement that it always stays in the plane tangent to the surface of the sphere; the arrow can be thought of as the top of a wavefront (see the figure, panel A). If we move the arrow without rotating it around the axis normal to the surface, after completion of the closed path, it rotates by an angle α . Had we traveled twice as far along the bottom arc, the angle would have been 2α . Thus, the angle depends on the paths taken to return to the top. On a flat surface, the

arrow would have remained parallel to its original orientation throughout the circuit.

This difference in so-called parallel transport on a curved or flat surface is a direct result of the geometric phase. One of the manifestations of the geometric phase in optics is the Pancharatnam-Berry phase that appears when the polarization of a light beam evolves along a similar geodesic triangle, but on the Poincaré sphere commonly used to describe these phase relations (10), the phases of the final and initial states differ by an amount equal to half of the solid angle enclosed by the triangle.

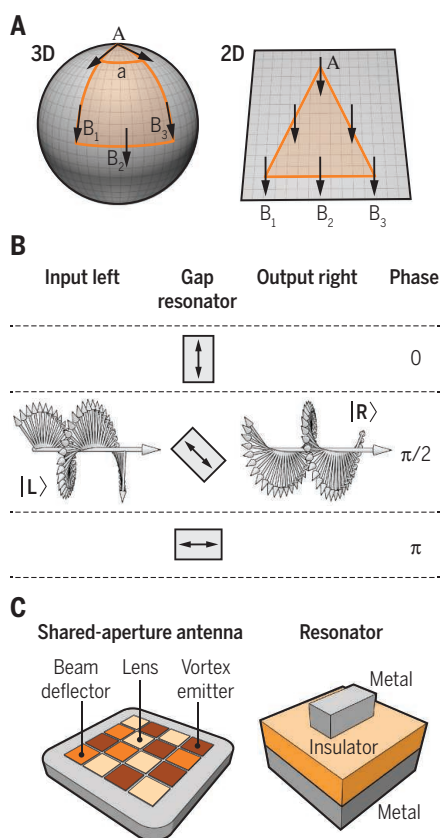
Unlike conventional optical components such as lenses or prisms that introduce phase changes through optical path differences, metasurfaces facilitate strong light-matter interaction on a subwavelength scale through the careful arrangement of resonant optical antennas. Phase accumulation in gradient metasurfaces results from space-variant polarization manipulations, as opposed to requiring propagation through a certain thickness of a material to accumulate sufficient phase. A variety of gradient metasurfaces, where antennas with subwavelength separation and spatially varying shape, size, and orientation enable optical wavefront shaping, have been demonstrated. These types of structure have enabled a plethora of potential functionalities, including beam steering, lensing, holography, and structured light generation (11).

Building further on this approach, Maguid *et al.* created complex geometric-phase metasurfaces from subwavelength half-wave-plate elements. These wave plates are the metal-insulator-metal structures, with the top metal layer consisting of a periodic arrangement of nanoantennas forming from gap-plasmon resonators (see the figure, panel B) (12). Like the birefringent mineral calcite, these structures introduce different phase shift in different directions. The main difference, however, is that in conventional macroscopic wave plates, such differential phase shifts are introduced by the direction-dependent difference in refractive indices, whereas in metasurfaces, they rely on the two electric dipole scat-

Electrical Engineering Department, State University of New York, Buffalo, NY 14260, USA. Email: natashal@buffalo.edu

ters whose resonances are oppositely detuned from a design frequency. The wave plates are oriented so that one of these directions, the fast axis, depends on the spatial position. By manipulating the local orientations of the nanoantennas, multiple wave fronts with different functionalities are generated. The resulting polarization is space-varying because it depends on the local orientation of the wave plate. Thus, at different points, the beam navigates different paths on the Poincaré sphere, resulting in a space-variant phase-front modification originating from the geometric phase.

A majority of the metasurfaces that have been reported were designed to enable a single functionality. Modern photonics applications, however, call for ultracom-



Geometric phase meets phased-array antennas. (A)

Geometric phase is illustrated by parallel transport on a curved surface (sphere), which results in a change of phase angle α , but no change on a flat surface. (B) Maguid *et al.* used subwavelength metal-insulator-metal gap-plasmon resonators as half-wave plates to create metasurfaces. Depending on orientation, these resonators convert input left circularly polarized waves into right circularly polarized waves, with an additional phase accumulation that depends on the position of the double-headed arrow, which shows the position of the fast axis of the half-wave plate. (C) A schematic of the shared-aperture antenna concept, in which different sets of nanoantennas (different colors) implement different functionalities.

compact, multifunctional, integrated optical devices that enable independent control of the phase, amplitude, and polarization. Building on the concept of shared-aperture antennas (13), which are a class of phased-array antennas originally introduced to steer radar beams, Maguid *et al.* address this critical need and demonstrate multifunctional, geometric-phase metasurfaces. The antennas use a single common aperture to perform multiple functions simultaneously (see the figure, panel C).

Several individual functionalities can be combined on the same platform in three different ways: segmentation, interleaving, and harmonic response. Geometric-phase metasurfaces with interleaved and asymmetric harmonic response are excellent candidates for realizing on-demand, multifunctional on-chip photonics. As an example, Maguid *et al.* converted a conventional linearly polarized beam into azimuthally and radially polarized beams that carry orbital angular momentum. Moreover, space-variant polarization manipulation enables the realization of multiple vectorial optical vortices by the coherent superposition of wavefronts with opposite helicities. Such complex beams are of interest for the next generation of optical communication systems, as they offer the opportunity to facilitate an entirely new technology for increasing future optical network capacity.

Finally, Maguid *et al.* used interleaved geometric-phase metasurfaces to build a simple and ultracompact spectropolarimeter. This device simultaneously measures the polarization state and spectrum of a wave transmitted through a semitransparent object. Potential applications include drug development, cancer diagnostics, remote sensing, and astrophysics. The alliance between the geometric phase and the shared-aperture antenna arrays technology enables multifunctional wavefront shaping using a single, achromatic, and ultrathin nanoscale broadband photonic device. ■

REFERENCES

1. M. V. Berry, *Sci. Am.* **259**, 46 (June 1988).
2. S. Pancharatnam, *Proc. Ind. Acad. Sci.* **44**, 247 (1956).
3. M. V. Berry, *J. Mod. Opt.* **34**, 1401 (1987).
4. N. Herbert, *New Scientist* **1564**, 37 (1987).
5. E. Maguid *et al.*, *Science* **352**, 1202 (2016).
6. D. Lin, P. Fan, E. Hasman, M. L. Brongersma, *Science* **345**, 298 (2014).
7. N. Yu *et al.*, *Science* **334**, 333 (2011).
8. X. Yin, Z. Ye, J. Rho, Y. Wang, X. Zhang, *Science* **339**, 1405 (2013).
9. M. I. Shalaev *et al.*, *Nano Lett.* **15**, 6261 (2015).
10. Z. Bomzon, V. Kleiner, E. Hasman, *Opt. Lett.* **26**, 1424 (2001).
11. N. Yu, F. Capasso, *J. Lightwave Technol.* **33**, 2344 (2015).
12. A. Pors, M. G. Nielsen, S. I. Bozhevolnyi, *Opt. Lett.* **38**, 513 (2013).
13. R. L. Haupt, *IEEE Trans. Antennas Propag.* **53**, 2858 (2005).

10.1126/science.aaf8391

DNA REPAIR

Drugging DNA repair

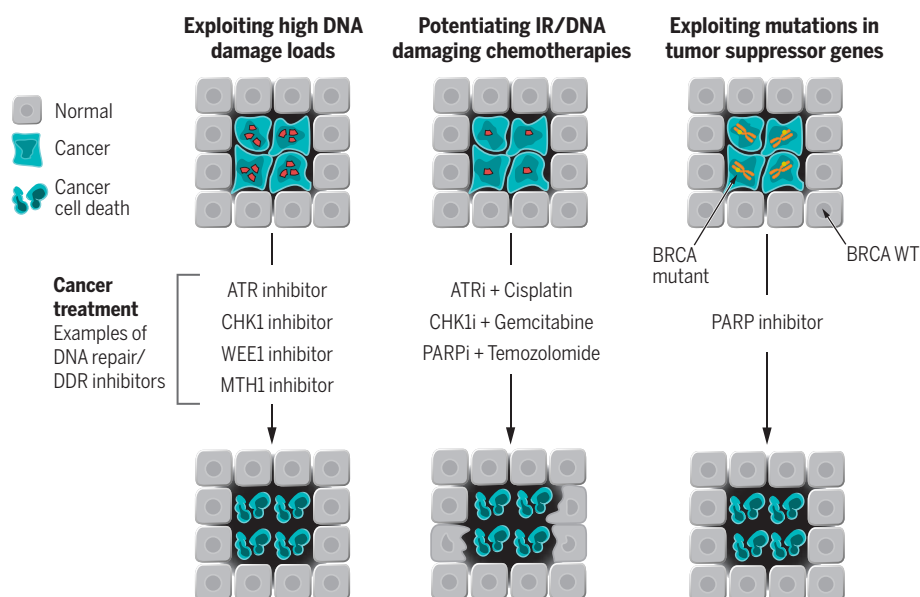
Inhibiting DNA repair can have a positive outcome on therapeutic interventions

By Stephen P. Jackson^{1,2} and Thomas Helleday³

All the cells in our bodies suffer many thousands of DNA lesions every day (1). The vast majority of these lesions are safely dealt with by cellular DNA repair and associated DNA damage response (DDR) activities that are, as a consequence, vital for life. Defects in or deregulation of our DNA repair/DDR systems are linked to many human pathologies (2). Yet, perhaps counterintuitively, pharmacological inhibitors of DNA repair/DDR have considerable potential in treating various human diseases, particularly cancer.

Many human proteins function in or affect DNA repair/DDR. These include factors that sense various types of damaged DNA, those that mediate the enzymatic stages of DNA repair, and yet others that control interactions between various DNA repair/DDR components and modulate other cellular processes such as DNA replication, transcription, control of chromatin structure, and apoptosis. Because many DNA repair/DDR proteins are enzymes, it has proven possible to develop druglike compounds that selectively modulate their activity and, therefore, to explore these DNA repair/DDR proteins as potential therapeutic targets.

DNA damage and defective DNA repair can cause cancer through the accrual of mutations in genomic DNA. Many cancers are also particularly susceptible to DNA damage, and this is exploited by radiotherapy and chemotherapy treatments. Tumor cells' susceptibilities to such treatments may be explained by their high underlying levels of DNA damage—for example, caused by oncogene-induced replication stress, shortened telomeres, or DNA repair/DDR defects (2). Because cancer cells suffering from replication stress depend more on DNA repair/DDR than do normal cells for survival, inhibitors of the DDR kinases ataxia telangiectasia mutated (ATM) and Rad3-related (ATR) and checkpoint kinase 1 (CHK1) or the cell-cycle-related kinase WEE1 are currently being tested in the clinic for their



DNA repair/DDR inhibitors in cancer treatment. (Left) Deregulated cellular metabolism can result in cancer cells having high DNA damage loads (red dots), making them particularly dependent on DNA repair/DDR for survival. (Middle) DNA repair/DDR inhibitors can be used to potentiate radio- (IR, ionizing radiation) or chemotherapy. (Right) Mutations (yellow dots on orange chromosomes) can make cancer cells more susceptible to DNA repair/DDR inhibitors—the synthetic-lethal paradigm for selectively killing cancer cells with particular mutations.

ability to selectively kill tumor cells (3) (see the figure, left).

Cancer cells also often exhibit abnormal redox homeostasis, resulting in high levels of oxidative stress that cause damage to DNA or its nucleotide precursors. Enzymes such as MutT homolog 1 (MTH1) (4, 5) are involved in preventing oxidized nucleotides from becoming incorporated into, and therefore damaging, DNA. Targeting such enzymes or exploiting other aspects of altered nucleotide metabolism in cancer cells (6) thus offers ways to selectively introduce toxic DNA damage into cancer cells. DNA repair/DDR inhibitors are also being explored in combination with widely used radio- and chemotherapy regimens (see the figure, middle).

Another strategy for the therapeutic targeting of DNA repair/DDR has been to exploit the cancer-specific loss of tumor suppressors, such as P53, breast cancer 1 and 2 (BRCA1/2), or ATM, that control or are otherwise linked to DNA repair/DDR. In some cases, these losses lead to cancer cells becoming much more reliant than normal cells on the DNA repair/DDR pathways that they still possess. This reliance can manifest itself as a total dependency on a particular pathway that is otherwise nonessential in

normal cells. This phenomenon is termed synthetic lethality. It has been leveraged as a pharmacological strategy by the demonstration that cancer cells with hereditary or somatically acquired mutations in *BRCA1* or *BRCA2*, resulting in defective DNA repair by homologous recombination, are hypersensitive to inhibition of the DNA-repair enzyme poly(ADP-ribose) polymerase (PARP) (7, 8) (see the figure, right). Thus, the PARP inhibitor olaparib has become the first DNA repair enzyme inhibitor marketed as a drug, gaining regulatory approval in 2014 for treating BRCA-mutated ovarian cancers. In a recent trial, 33% of patients with metastatic castration-resistant prostate cancers responded to olaparib (9). It seems likely that PARP inhibitors will be approved for other neoplasms, either as stand-alone agents or combined with other therapies. Given the success of the BRCA-PARP paradigm, further synthetic-lethal cancer therapies are actively being pursued.

In certain instances, human disease appears to arise through DNA repair/DDR pathway hyperactivation, so drugs that dampen down these pathways could be used in disease suppression (2). For instance, PARP hyperactivity has been linked to ischemia-reperfusion injury, inflammatory diseases, and some cardiovascular diseases, with studies in model organisms suggesting how PARP inhibition might lead to disease suppression (10). Furthermore, as viruses and microbial infectious agents use their own or host-cell DNA repair/DDR

mechanisms, specific inhibition of such mechanisms might offer protection from infections (11). Pathologies associated with certain genetic diseases, such as Huntington's disease, are caused by the expansion of DNA-repeat sequences in both germline and somatic tissues. Drugs that inhibit the DNA repair enzyme OGG1 or other factors involved in such expansions therefore have the potential to slow disease progression, as do inhibitors of the DDR protein ATM, whose activity has been linked to Huntington's disease pathologies (12, 13).

Although individuals can reduce their load of DNA lesions through changes in diet or environmental exposures, it is clear that DNA-damage induction is an inevitable outcome of the biochemical processes that sustain life (1). However, strategies to lower DNA damage loads by bolstering DNA repair/DDR processes could reduce the incidence or severity of cancer and other age-related diseases. Bolstering DNA repair/DDR could be accomplished by gene therapy, pharmacological activators of DNA repair/DDR components, or by developing drugs to trigger homeostatic mechanisms that up-regulate the expression or activity of these components. Such “compensation” strategies could be particularly efficacious in individuals with genetic diseases such as Hutchinson-Gilford progeria, whose cells experience abnormally high DNA damage levels (14), or diseases where hyperactivated DDR pathways mediate pathogenesis.

Therapeutically exploiting DNA repair is still in its infancy, and DNA repair/DDR mechanisms are under intense investigation. With the growing realization that these mechanisms affect many areas of human health and disease, it seems likely that we will soon witness the development of important new DNA repair/DDR inhibitors for the treatment of various human diseases. ■

REFERENCES AND NOTES

1. T. Lindahl, *Nature* **362**, 709 (1993).
2. S. P. Jackson, J. Bartek, *Nature* **461**, 1071 (2009).
3. M. Dobbelsstein, C. S. Sorensen, *Nat. Rev. Drug Discov.* **14**, 405 (2015).
4. K. V. Huber et al., *Nature* **508**, 222 (2014).
5. H. Gad et al., *Nature* **508**, 215 (2014).
6. M. Zauri et al., *Nature* **524**, 114 (2015).
7. H. Farmer et al., *Nature* **434**, 917 (2005).
8. H. E. Bryant et al., *Nature* **434**, 913 (2005).
9. J. Mateo et al., *N. Engl. J. Med.* **373**, 1697 (2015).
10. P. Pachter, C. Szabo, *Drug Rev.* **25**, 235 (2007).
11. A. Lau et al., *Nat. Cell Biol.* **7**, 493 (2005).
12. X. H. Lu et al., *Sci. Transl. Med.* **6**, 268ra178 (2014).
13. I. V. Kovtun et al., *Nature* **447**, 447 (2007).
14. D. Larrieu, S. Britton, M. Demir, R. Rodriguez, S. P. Jackson, *Science* **344**, 527 (2014).

ACKNOWLEDGMENTS

S.P.J. founded and scientifically led KuDOS Pharmaceuticals, which developed the drug Lynparza (olaparib). T.H. is named inventor on patents for the use of PARP and MTH1 inhibitors in treatments of cancer.

10.1126/science.aab0958

STATISTICS

Aligning statistical and scientific reasoning

Misunderstanding and misuse of statistical significance impede science

By Steven N. Goodman

Imagine the American Physical Society convening a panel of experts to issue a missive to the scientific community on the difference between weight and mass. And imagine that the impetus for such a message was a recognition that engineers and builders had been confusing these concepts for decades, making bridges, buildings, and other components of our physical infrastructure much weaker than previously suspected.

That, in a sense, is what happened with the recent release of a statement from the American Statistical Association (ASA), with the deceptively innocuous title, “ASA statement on statistical significance and p-values” (1). The scientific measure in need of clarification was the *P* value—perhaps the most ubiquitous statistical index used in scientific research to help decide what is true and what is not. The ASA saw misunderstanding and misuse of statistical significance as a factor in the rise in concern about the credibility of many scientific claims (sometimes called the “reproducibility crisis”) and is hoping that its official statement on the matter will help set scientists on the right course.

The formal definition of *P* value is the probability of an observed data summary (e.g., an average) and its more extreme values, given a specified mathematical model and hypothesis (usually the “null”). The problem is that this index by itself is not of particular interest. What scientists want is a measure of the credibility of their conclusions, based on observed data. The *P* value neither measures that nor is it part of a formula that provides it.

This confusion between the index we have and the measure we want produces misconceptions that the *P* value is the probability that the null hypothesis is true or that the observed data occurred by chance—different ways of saying the same thing (2, 3). This pernicious error creates the illusion that the *P* value alone measures the credibility of a conclusion, which opens the door to the mistaken notion that the dividing line between scientifically justified and unjustified claims is set by whether the *P* value has crossed the

“bright line” of significance, to the exclusion of external considerations like prior evidence, understanding of mechanism, or experimental design and conduct.

Bright-line thinking, coupled with attendant publication and promotion incentives, is a driver behind selective reporting: cherry-picking which analyses or experiments to report on the basis of their *P* values. This in turn corrupts science and fills the literature with claims likely to be overstated or false. We cannot solve these problems without understanding how we got to this point.

R. A. Fisher revolutionized statistical inference and experimental design in the 1920s and ’30s by establishing a comprehensive framework for statistical reasoning and writing the first statistical best-seller for experimenters. He formalized an approach to inference involving *P* values and assessment

of significance, based on the frequentist notion of probability, defined in terms of verifiable frequencies of repeatable events. He wanted to avoid the subjectivity of the Bayesian approach, in which the probability of a hypothesis (“inverse probability”), neither repeatable nor observable, was central.

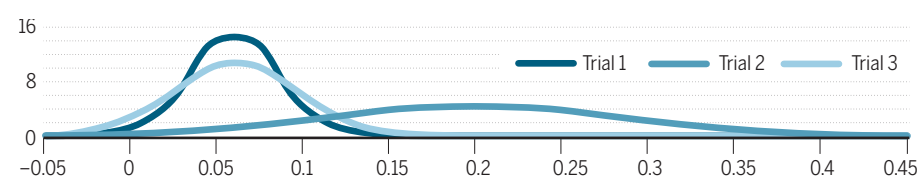
Fisher was a champion of *P* values as one of several tools to aid the fluid, inductive process of scientific reasoning—not to substitute for it. Fisher used “significance” merely to indicate that an observation was worth following up, with refutation of the null hypothesis justified only if further experiments “rarely failed” to achieve significance (4). This is in stark contrast to the modern practice of making claims based on a single demonstration of statistical significance.

In their development of “hypothesis testing” in the 1930s, Jerzy Neyman and Egon

A. How can these data be interpreted?

APPROACH	QUESTION	STATISTICAL ANALYSIS	INTERPRETATION
Hypothesis test (“bright line”)	Should we act as though the observed effect is nonzero (given prespecified error rates)?	1. $P \leq 0.05$ 2. $P \leq 0.05$ 3. NS	Studies 1 and 2 indicate action based on a nonzero true effect is justified. Study 3 indicates it is not.
Fisherian <i>P</i> value	How much evidence is there that the true effect is different from zero?	1. $P = 0.03$ 2. $P = 0.05$ 3. $P = 0.11$	Studies 1 and 2 provide moderate, statistically significant evidence that the new treatment is better. Study 3 supplies weak but insufficient evidence to say the treatment is effective.
Estimation	What range of true effects is statistically consistent with the observed effects?	Effect, 95% confidence interval (%) 1. 6, 0.5 to 12 2. 20, 2.5 to 38 3. 6, -1.4 to 13	Studies 1 and 3 indicate the new treatment had a small to moderate effect. Study 2 is consistent with either small or large effects.
Bayes factor	How strongly do the data support a large, clinically important effect (10 to 25%) versus a small, unimportant one (0 to 10%)?	Bayes factor, large:small effect 1. 1:14 2. 3:1 3. 1:7	Studies 1 and 3 together decrease odds of an important effect 98 fold ($1/7 \times 1/14 = 1/98$). Study 2 increases odds 3 fold, for net 33 fold decrease ($3 \times 1/98 = 1/33$).

B. Likelihood functions



Changing questions, changing answers. Three randomized trials show response rates of 20% in the control arm and rates in the treatment arms of (1) 26% ($n = 900$), (2) 40% ($n = 100$), and (3) 26% ($n = 500$). The effect deemed clinically important is 10%. (A) Each statistical approach asks a different question, hence interpretations are different. Scientists must decide which statistical question best matches their scientific question. (B) Likelihood functions, proportional to the probability of the observed data (vertical axis) under each possible true effect (horizontal axis), measure how strongly the observed effects support different true effects (which cannot be directly observed).

Departments of Medicine and of Health Research and Policy, Stanford University School of Medicine, Division of Epidemiology, Meta-research Innovation Center at Stanford (METRICS), Stanford, CA 94305, USA. Email: steve.goodman@stanford.edu

Pearson went where Fisher was unwilling to go (5). In a hypothesis test, one specifies a null statistical hypothesis and an alternative, and is to “reject” the null and “accept” the alternative—or vice versa—on the basis of whether an estimate falls into a prespecified region defined by two error rates: type I (alpha, false positive) and type II (beta, false negative). Once these error rates are set, scientific reasoning is effectively out of the picture (see the figure). Judgment ideally enters through customization of the alternative hypothesis and the error rates, contingent on the seriousness of each kind of error.

The Neyman-Pearson method did not use *P* values, but was combined with the Fisherian *P*-value approach in textbooks and research articles (6, 7). Without foundational justification, this created the illusion that quantitative inference could be automated, with hypothesis rejection determined by whether the *P* value is less than the type I error, set at 5% in most sciences today. This combination did violence to both approaches, particularly to Fisher's. He vehemently opposed using *P* values for automatic inference, referring to hypothesis tests disparagingly as “decision functions” or “acceptance procedures.” His dismay was pointed and prescient:

[N]o scientific worker has a fixed level of significance at which from year to year, and in all circumstances, he rejects hypotheses; he [examines] each particular case in the light of...evidence and...ideas [p. 42 of (8)].

The concept that the scientific worker can regard himself as an inert item in a vast co-operative concern working according to accepted rules, is encouraged by directing attention away from his duty to form correct scientific conclusions,...and by stressing his supposed duty to mechanically make a succession of automatic “decisions”.... The idea that this responsibility can be delegated to a giant computer programmed with Decision Functions belongs to a phantasy of circles, rather remote from scientific research [pp. 104–105 (8)].

Sixty years later, we have the ASA expressing the same sentiment:

Researchers should bring many contextual factors into play to derive scientific inferences, including the design of a study, the quality of the measurements, the external evidence for the phenomenon under study, and the validity of assumptions that underlie the data analysis.... The widespread use of “statistical significance” (generally interpreted as “ $p \leq 0.05$ ”) as a license for making a claim of a scientific finding (or implied truth) leads to considerable distortion of the scientific process (1).

The concordance of these statements, separated by over half a century, underscores lack of progress in approaches to statistical inference in the applied literature, despite advances in statistical methodology. This is due in part to the way statistical inference is taught to scientists; not as a variety of named, competing approaches, each with strengths and weaknesses, but as anonymized procedures, universally applicable, seemingly without controversy or alternatives (6, 7).

Contrast this situation with other sciences. In any high-school physics textbook, one will find theories and models by Copernicus, Galileo, Newton, Einstein, and so on. Students are trained to understand the incomplete explanatory power of each theory, the controversies, why new theories were accepted (or not), and what questions they raised.

Theories of statistical inference are no less nuanced or contested, as evidenced by the 23 commentaries that followed the ASA statement (1). But such controversy, rarely taught in applied courses or texts, is unappreciated by most who use statistical tools. This seeming absence of controversy about the foundations of these methods has fostered growth of social-scientific structures reifying those

“Theories of statistical inference are...nuanced [and] contested....”

values—enshrined in journal practices, promotion, and funding criteria, as well as in the standard discourse of science—which makes them extraordinarily difficult to change.

Another reason these practices persist is that, until the recent rise of concern about research reproducibility (9), the scientific community has perceived few adverse consequences from their use. Many papers over the past century have issued cautions similar to those of the ASA, but have largely been ignored by the general scientific community. Benefits of having seemingly objective rules have outweighed theoretical cavils (6, 10).

The ASA suggested several ways to improve statistical interpretation, including more complete reporting of all analyses performed, and a number of alternative inferential approaches. One of these, Bayes factors (11, 12), is a measure derived from Bayes theorem indicating how strongly the data should shift belief toward one hypothesis versus another. If we were told that the experimental results lowered the prestudy odds of the null hypothesis by a factor of 4, this would lead to a far different reasoning process than does “ $P = 0.03$,” which is difficult to combine with external knowledge (11) (see the chart).

Bayes factors and fully Bayesian analyses are not without their own complications (10, 12–15), as are all other recommended approaches. But, if they were more widely used, rules would evolve. That said, no *P*-value alternatives will solve the problems noted by the ASA if they are used in bright-line fashion, such as applying a confidence interval only to see if it includes the null value.

P values are unlikely to disappear, and the ASA did not recommend their elimination—rather, a change in how they are interpreted and used. But how can scientists follow the ASA (and Fisher's) dictates to combine them with contextual factors? There are few examples in the scientific literature. How many papers explain why, in one context, a finding with $P = 0.006$ is insufficient to make a claim, whereas, in another, $P = 0.08$ might be all that is needed (11)? Any attempt to do that in an individual research paper would likely meet resistance from reviewers or editors.

The field of genomics has shown us that evidential thresholds are changeable within disciplines, with $P \leq 10^{-8}$ now sought for claiming relations derived from genome-wide scanning. Thresholds in physics are far lower than the $P \leq 0.05$ level used in biomedicine and the social sciences. Whether such thresholds can or should be modified by design, by discipline, or by individual study are rich areas for future exploration (16).

Science has progressed dramatically over the past 90 years, despite these issues. How much faster and more efficiently can it proceed if new statistical approaches to inference are adopted, and if optimal statistical and scientific practices are aligned with incentive structures? The ASA has posed a challenge to all who use statistical measures to justify their claims. Let us hope the next century will see as much progress in the inferential methods of science as in its substance. ■

REFERENCES

1. R. L. Wasserstein, N. A. Lazar, *Am. Stat.* 10.1080/00031305.2016.1154108 (2016).
2. S. Goodman, *Semin. Hematol.* **45**, 135 (2008).
3. D. R. Cox, *Br. J. Clin. Pharmacol.* **14**, 325 (1982).
4. R. A. Fisher, *J. Min. Agric. Great Britain* **33**, 503 (1926).
5. J. Neyman, E. S. Pearson, *Philos. Trans. R. Soc. Lond. A* **231**, 289 (1933).
6. G. Gigerenzer et al., *The Empire of Chance* (Cambridge Univ. Press, Cambridge, 1989).
7. G. Gigerenzer, J. N. Marewski, *J. Manage.* **41**, 421 (2015).
8. R. A. Fisher, *Statistical Methods and Scientific Inference* (Hafner, New York, ed. 1, 1956).
9. F. S. Collins, L. A. Tabak, *Nature* **505**, 612 (2014).
10. B. Efron, *Am. Stat.* **40**, 1 (1986).
11. S. N. Goodman, *Ann. Intern. Med.* **130**, 1005 (1999).
12. R. E. Kass, A. E. Raftery, *J. Am. Stat. Assoc.* **90**, 773 (1995).
13. S. Greenland, C. Poole, *Epidemiology* **24**, 62 (2013).
14. H. Hoijtink, P. van Kooten, K. Hulscher, *Multivariate Behav. Res.* **51**, 2 (2016).
15. R. D. Morey, E. J. Wagenmakers, J. N. Rouder, *Multivariate Behav. Res.* **51**, 11 (2016).
16. V. E. Johnson, *Proc. Natl. Acad. Sci. U.S.A.* **110**, 19313 (2013).

10.1126/science.aaf5406

LETTERS

Edited by Jennifer Sills

Federal barriers to Cannabis research

ALTHOUGH THE MAJORITY of the general public (1) and the professional medical community (2) in the United States support the therapeutic use of *Cannabis sativa* as a pharmacological agent, the U.S. federal government's *Cannabis* research policies have blocked externally valid, randomized clinical trials on the effects of *Cannabis*. To conduct research on *Cannabis*, scientists must submit to a lengthy and arduous application process, often lasting for years. The research requires permission from multiple governmental agencies, including some with expressly stated opposition to any therapeutic uses, such as the Drug Enforcement Agency (3).

However, the application process is a mere nuisance compared with the biggest obstacle presented by the federal government: All *Cannabis* used for research purposes must be purchased through the National Institute on Drug Abuse (NIDA) (4). The tetrahydrocannabinol (THC) potency levels in the *Cannabis* available through NIDA are much lower than those in *Cannabis* products used by medical patients. The highest THC level available to researchers is 12.4% (5). The only two clinical studies funded by NIH in 2015 used products with potency levels between 3.5 and 7.0% THC (6, 7). In contrast, the *Cannabis* sold in Colorado now averages 18.7% THC, with some strains registering as high as 35% THC (8), and no potency limits exist for the concentrates and ingestible products sold in most states where medical *Cannabis* is legal at the state level.

The scarce research the U.S. government has approved thus offers little insight into the effects actually experienced by patients and recreational users. As long as clinical research on *Cannabis* is controlled by regulators expressly opposed to any increase in its consumption, health care cost reductions may be missed, and intoxication and long-term effects will remain unknown. Most important, many severely ill patients may suffer unnecessarily because no one knows the true risks and benefits of consuming *Cannabis sativa*.

Sarah See Stith¹ and Jacob Miguel Vigil^{2*}

¹Department of Economics, University of New Mexico, Albuquerque, NM 87131, USA. ²Department



Cannabis sativa.

of Psychology, University of New Mexico, Albuquerque, NM 87131, USA.

*Corresponding author. Email: vigilJ@unm.edu

REFERENCES

1. J. M. Jones, "In the U.S., 58% back legal marijuana use" (2015); www.gallup.com/poll/186260/back-legal-marijuana.aspx.
2. J. N. Adler, J. A. Colbert, *N. Engl. J. Med.* **368**, e30 (2013).
3. M. H. Andreae et al., *Am. J. Bioeth.* **16**, 36 (2016).
4. U.S. Food and Drug Administration, Marijuana Research with Human Subjects (www.fda.gov/newsevents/publichealthfocus/ucm421173.htm).
5. National Institute on Drug Abuse, Marijuana Plant Material Available from the NIDA Drug Supply Program (www.drugabuse.gov/researchers/research-resources/nida-drug-supply-program-dsp/marijuana-plant-material-available-nida-drug-supply-program).
6. B. L. Wilsey, "A randomized, cross-over controlled trial of Dronabinol and vaporized cannabis in neuropathic low back pain" (https://projectreporter.nih.gov/project_info_description.cfm?aid=8964406&icde=29620573&ddparam=&ddvalue=&ddsub=&cr=1&csb=default&cs=ASC).
7. H. Zhao, "The effect of vaporized cannabis on neuropathic pain in spinal cord injury" (https://projectreporter.nih.gov/project_info_description.cfm?aid=8494032&icde=29620604&ddparam=&ddvalue=&ddsub=&cr=1&csb=default&cs=ASC).
8. B. Briggs, "Colorado marijuana study finds legal weed contains potent THC levels" *NBC News* (2015); www.nbcnews.com/storyline/legal-pot/legal-weed-surprisingly-strong-dirty-tests-find-n327811.

10.1126/science.aaf7450

No surprise that comb jellies poop

AS ONE OF the organizers of the recent meeting on comb jellies (ctenophores), I feel obliged to comment on the News In Depth story "Comb jelly 'anus' guts ideas on origin of through-gut" (A. Maxmen, 25 March, p. 1378), published online on

23 March with the title, "Why watching comb jellies poop has stunned evolutionary biologists." I was stunned that videos showing defecation of waste through the anal pores of ctenophores astonished anyone. Those who have looked closely at comb jellies have seen and reported this process for well over a century.

In 1850, Louis Agassiz found that waste products were expelled from comb jellies through sphincter-like anal pores, which open and close during bouts of defecation (1). Thirty years later, the German zoologist Carl Chun used injected dyes and tracking of waste particles to expand on Agassiz's results in great detail (2). Since then, scientists have amply confirmed Agassiz's and Chun's findings and studied how the process of defecation works (3). Nearly every invertebrate textbook in the 20th century shows the anal pores of ctenophores. This literature was omitted or grossly misrepresented in the News story to erroneously claim a novel discovery of a through-gut in comb jellies.

It is now recognized that ctenophores expel waste from both ends. They eject bulky indigestible food fragments, which do not enter the stomach or food canal system, through the mouth. Meanwhile, unused or small waste particles in the food canals are periodically shunted into the stomach and anal canals, where they are expelled through the anal pores (3). In contrast to the implication of the News story, the two exit methods of waste products are not contradictory or mutually exclusive. It should not surprise anyone that comb jellies poop and have a through-gut.

Sidney L. Tamm

Eugene Bell Center for Regenerative Biology and Tissue Engineering, Marine Biological Laboratory, Woods Hole, MA 02543, USA. Email: tamm@bu.edu

REFERENCES

1. L. Agassiz, *Am. Acad. Arts Sci.* **III**, 221 (1850).
2. C. Chun, *Flora Fauna Golfes Neapel* **1**, 1 (1880).
3. S. L. Tamm, *Invert. Biol.* **133**, 1 (2014).

10.1126/science.aaf8170

Digital identifiers for fungal species

SPECIES-LEVEL CLASSIFICATION OF life has been a cornerstone of biology for centuries. Most macro-organisms are described soon after discovery, but species of prokaryotes, micro-eukaryotes, and fungi often lag far behind in formal description because they are small, extremely diverse, and difficult to cultivate and often lack discriminatory morphological characteristics.

D. Hibbett ("The invisible dimension of

fungal diversity,” Perspectives, 11 March, p. 1150) recently argued that missing species names (Latin binomials) in the kingdom Fungi hamper communication about formally undescribed species derived from molecular surveys of the environment. He pleaded for changes in the International Code of Nomenclature for Algae, Fungi, and Plants (1). We argue that Latin binomials are not urgently needed for precise communication and delimitation of environmental species known only from DNA barcode sequences.

In the UNITE database for molecular identification of fungi, we have adopted the species hypotheses concept to provide unique digital object identifiers (DOIs) for all fungal species known from sequence data (2, 3). We have, for example, used this concept to analyze the Archaeorhizomycetes species (4) examined by Hibbett. The species hypotheses concept accounts for taxonomic uncertainty through multiple alternative cut-off levels for species delimitation. As in the Linnaean tradition, it relies on molecular keys, reference sequences, and voucher material specified by taxonomists.

Several major microbial identification pipelines, notably QIIME (5), use the species hypotheses identifiers as a community standardization measure. The Barcode of Life Data System similarly assigns barcode index numbers to animal taxa (6). Both systems enable straightforward communication of machine-readable but formally undescribed species across scientific studies. Both serve to facilitate future descriptions of those taxa by aggregating data on, for example, geographical distribution and substrate of collection. When voucher material or cultures become available, a formal species description can draw on the molecular and other data amalgamated in the above databases.

**U. Kõljalg,^{1*} L. Tedersoo,² R. H. Nilsson,³
K. Abarenkov²**

¹Institute of Ecology and Earth Sciences, University of Tartu, Tartu 51005, Estonia. ²Natural History Museum, University of Tartu, Tartu 51014, Estonia.

³Department of Biological and Environmental Sciences, University of Gothenburg, Göteborg SE-40530, Sweden.

*Corresponding author. Email: urmas.koljalg@ut.ee

REFERENCES

1. J. McNeil *et al.*, Eds., *International Code of Nomenclature for Algae, Fungi, and Plants* (Melbourne Code) (Koeltz Scientific Books, 2012).
2. U. Kõljalg *et al.*, *Mol. Ecol.* **22**, 5271 (2013).
3. R. H. Nilsson *et al.*, *Mycoskeys* **12**, 29 (2016).
4. K. Abarenkov *et al.*, *PlutoF* 10.15156/BIO/587447 (2016); <https://plutof.ut.ee/#/datacite/10.15156/BIO/587447>.
5. J. G. Caporaso *et al.*, *Nat. Meth.* **7**, 335 (2010).
6. S. Ratnasingham, P. D. N. Hebert, *PLOS One* **8**, e66213 (2013).

10.1126/science.aaf7115

Response

SPECIES CLASSIFICATION PLATFORMS based on DNA sequences, including the UNITE system, allow ecologists and evolutionary biologists to conduct sophisticated research programs without reference to Latin binomials. However, the entities that they catalog—such as species hypotheses (described by Kõljalg *et al.*), virtual taxa (1), or barcode index numbers (2)—are obscure concepts. Although useful to specialists, these concepts are unfamiliar to the general public. In contrast, the notion of species is deeply ingrained in human culture, even if evolutionary biologists understand that there is no universal, objective criterion for defining a species (3). Species names in the form of Latin binomials are useful for communicating knowledge of biodiversity not only to nontechnical audiences such as legislators, educators, and members of the media, but also to the vast majority of biologists, who are not microbial ecologists.

Kõljalg *et al.* assert that species classification is a cornerstone of biology and lament the lag between discovery and description of fungal species and other microorganisms. This lag time would be greatly diminished if species could be formally defined based on molecular sequences. However, this is not possible under the International Code of Nomenclature for Algae, Fungi and Plants (4), which requires physical type specimens regardless of their quality or scientific utility. The Code can only be modified once every 7 years by a vote of the Nomenclature Section of the International Botanical Congress. The next opportunity to change the Code will be in 2017. Adoption of sequence-based species description would promote the integration of molecular ecology and traditional taxonomy, which would be facilitated by resources such as UNITE.

David Hibbett

Biology Department, Clark
University, Worcester, MA 01610, USA.
Email: dhibbett@clarku.edu

REFERENCES

1. M. Öpik *et al.*, *Botany* **92**, 135 (2014).
2. S. Ratnasingham, P. D. N. Hebert, *PLOS One* **8**, e66213 (2013).
3. D. Baum, *System. Biol.* **58**, 74 (2009).
4. J. McNeil *et al.*, Eds., *International Code of Nomenclature for Algae, Fungi, and Plants* (Melbourne Code) (Koeltz Scientific Books, 2012).

10.1126/science.aaf7370

REVIEW SUMMARY

EPIGENETICS

Epigenetic balance of gene expression by Polycomb and COMPASS families

Andrea Piunti and Ali Shilatifard*

BACKGROUND: Multicellular organisms depend on the precise orchestration of gene expression to direct embryonic development and to maintain tissue homeostasis through their life spans. Exactly how such cell type-specific patterns of gene expression are established, maintained, and passed on to the next generation is one of the most fundamental questions of biology. Eukaryotes package their DNA into nucleosomes to form chromatin fibers. Chromatin plays a central role in regulating accessibility to DNA in many different DNA templated processes, including machineries that transcribe DNA into RNA, i.e., transcription. Transcriptional control through sequence-specific DNA binding factors (transcription factors) is well established; however, proteins that change chro-

matin structure (chromatin modifiers and remodelers) provide an additional layer of regulation and are considered major epigenetic determinants of cell identity and function. Among the numerous chromatin modifiers, the members of the Polycomb group (PcG) and the Trithorax group (TrxG) of proteins, in particular, have been scrutinized genetically and biochemically for decades. However, new and unexpected functions for these complexes are constantly emerging because of the intense interest in the critical role these proteins play in maintaining a balanced state of gene expression.

ADVANCES: In the classical view, PcG and TrxG proteins regulate the repressed and activated states of gene expression, respectively. Both PcG

and TrxG are organized in multiprotein complexes, which include the Polycomb repressive complex 1 and 2 (PRC1 and PRC2, respectively), and the complex of proteins associated with Set1 (COMPASS) family. Polycomb and COMPASS families are well known for their opposing roles in balancing gene expression, a phenomenon initially characterized using classical *Drosophila melanogaster* genetic approaches at a time when their biochemical functions

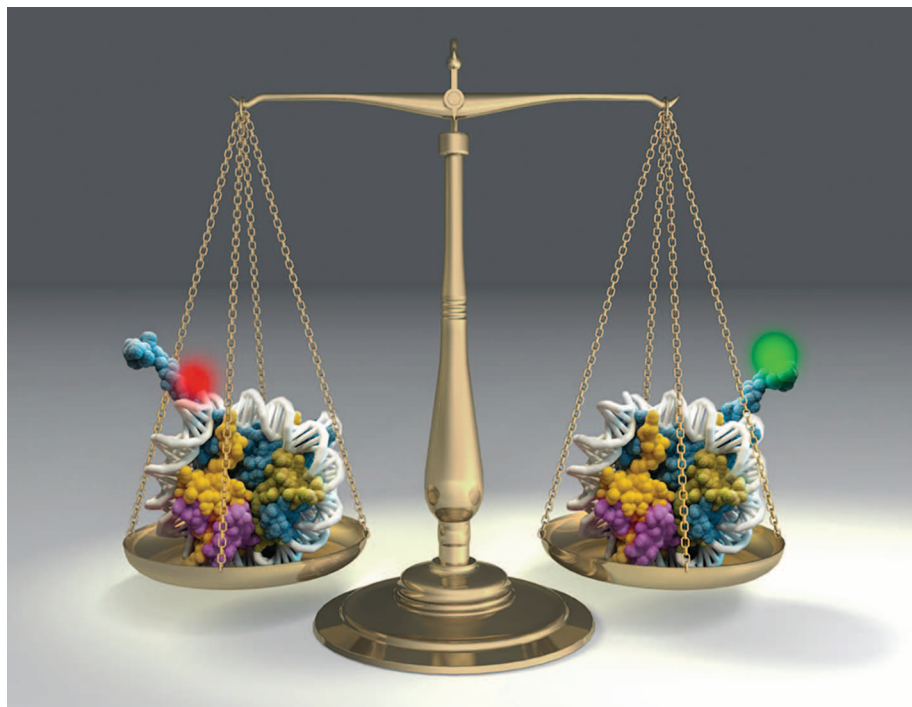
were still unknown. Later studies demonstrated that Polycomb and COMPASS complexes have enzymatic activities modifying different sites on a common target,

ON OUR WEBSITE

Read the full article at <http://dx.doi.org/10.1126/science.aad9780>

nucleosome. Nucleosomes can be posttranslationally modified in a variety of ways, many of which strongly correlate with different states of gene expression. Through their ability to regulate gene expression, several components of both the Polycomb and COMPASS complexes are involved in a plethora of crucial biological processes ranging from the regulation of embryonic development to widespread involvement in neoplastic pathogenesis.

OUTLOOK: Recent genome-wide studies have demonstrated that a large number of the components of the Polycomb and COMPASS families are often mutated in different forms of cancer. Some mutations result in gene deletion or early termination, such as loss-of-function (LOF) mutations, whereas gain-of-function (GOF) mutations increase or change their normal activities. Although it cannot be excluded that some of those are passenger rather than driver mutations, they suggest a relevant function of these proteins in tumorigenesis. Moreover, animal models have provided convincing evidence supporting a role for these complexes in tumor progression. However, even after decades of study, how Polycomb and COMPASS control normal or aberrant gene regulatory networks is not fully understood yet. From the perspective of their catalytic activities, the degree to which catalytic versus noncatalytic functions contribute to their roles in development and cancer has just begun to emerge. Concurrently, the possibility that PcG and TrxG enzymatic activities modify non-nucleosome substrates remains a fascinating, although largely unexplored, hypothesis. Ongoing efforts to decipher how mutations affecting members of these complexes disturb transcriptional balances and promote oncogenesis could provide critically needed new strategies for cancer therapeutics. ■



The balanced state of gene expression. The scale symbolizes the transcriptional status of a gene. Each dish contains a nucleosome that is either lysine 4 trimethylated (green light) or lysine 27 trimethylated (red light) on histone H3 (one tail is depicted for simplicity). These two histone marks strongly correlate, respectively, with transcriptional activation induced by COMPASS and transcriptional repression induced by PcG.

The list of author affiliations is available in the full article online.

*Corresponding author. Email: ash@northwestern.edu
Cite this article as A. Piunti, A. Shilatifard, *Science* 352, aad9780 (2016). DOI: 10.1126/science.aad9780

REVIEW

EPIGENETICS

Epigenetic balance of gene expression by Polycomb and COMPASS families

Andrea Piunti and Ali Shilatifard*

Epigenetic regulation of gene expression in metazoans is central for establishing cellular diversity, and its deregulation can result in pathological conditions. Although transcription factors are essential for implementing gene expression programs, they do not function in isolation and require the recruitment of various chromatin-modifying and -remodeling machineries. A classic example of developmental chromatin regulation is the balanced activities of the Polycomb group (PcG) proteins within the PRC1 and PRC2 complexes, and the Trithorax group (TrxG) proteins within the COMPASS family, which are highly mutated in a large number of human diseases. In this review, we will discuss the latest findings regarding the properties of the PcG and COMPASS families and the insight they provide into the epigenetic control of transcription under physiological and pathological settings.

Any given cell is constantly challenged by different endogenous or exogenous perturbations or signals. The ability of cells to integrate these stimuli and respond to them largely involves precise and complex changes in the cellular transcriptome that can either be transient (e.g., stress response) or permanent (e.g., cellular differentiation). Although transcription factors are essential for driving the transcriptional response as one of the immediate steps of gene expression, chromatin modifiers and remodelers collectively referred to as “epigenetic factors” are indispensable for shaping and maintaining the transcriptional response during biological processes, such as development (1). Indeed, once transcription factors instruct the transcriptional output, in some cases, the resulting change is meant to be maintained and inherited during cell divisions by epigenetic factors. These factors generally function as part of a multiprotein complex to modify nucleosomes, the main subunit of chromatin. Nucleosomes are mainly composed of DNA and histones, both of which can be extensively modified. DNA changes—such as methylation, hydroxymethylation, and further oxidations—play important roles in gene expression. Histones can undergo a plethora of different posttranslational modifications including methylation, acetylation, phosphorylation, and ubiquitination, and these modifications strongly correlate with different transcriptional outcome, depending on the context of the modified residues (2, 3). Some histone modifications are associated with a specific transcriptional status independent of the specific modified residue. Indeed, lysine acetylation on histones is generally regarded as a positive regulator of transcription. However, other

modifications, such as histone methylation, correlate with different transcriptional contexts depending on the specific residue modified. A classic example is given by the opposite activity of histone methylation implemented by the Polycomb group (PcG) and Trithorax group (TrxG) of proteins. These groups of proteins include additional chromatin modifiers and, during the past three decades, have been among the most extensively studied epigenetic factors. Proteins belonging to the PcG and TrxG families were originally described in *Drosophila melanogaster* to respectively repress or activate the same developmental target genes (4, 5). Thus, the antagonistic activities of the PcG and TrxG proteins establish a balanced and regulated state of gene expression. This review provides an overview of the biochemical composition and enzymatic properties of the Polycomb and Trithorax groups of protein complexes and examines recent findings on the role of these factors in regulation of gene expression in the embryonic stem cells and throughout development. Further, we discuss how the misregulation of the Trithorax and Polycomb group enzymatic activities results in the pathogenesis of human disease, including cancer.

Trithorax and Polycomb groups of proteins

Trithorax group proteins (TrxGs) are a heterogeneous group of factors with varied activities mainly related to chromatin modification and remodeling to activate transcription (5). As genetically defined in *D. melanogaster*, genes classified to the TrxG family are involved in the activation of developmental genes, such as homeotic genes, and in counteracting the silencing activity of the Polycomb group proteins (PcGs) (6). The *Trithorax* (*Trx*) gene was serendipitously discovered in *D. melanogaster* because of the homeotic phenotype of the partial transformation of a haltere to a wing as the result of a spontaneous mutation

(7). Evidence of its activity as a transcriptional activator goes back >30 years, when it was demonstrated that mutations in *Trx* prevented the derepression of the bithorax complex (Hox genes) in a PcG mutant background (8). Other *Drosophila* TrxG proteins include the adenosine triphosphate-dependent nucleosome remodeler Brahma (Brm), related to mammalian SWI2 (9), and the *Drosophila* protein female sterile homeotic (Fsh), related to mammalian BRD4. These factors were initially discovered as homeotic modulators in *D. melanogaster*, and both contain bromodomains that bind acetylated lysine localized at active chromatin (10).

Like TrxGs, Polycomb group proteins (PcGs) were initially identified genetically in *Drosophila* as a heterogeneous group of factors whose mutations resulted in homeotic defects during fly development (11). The first Polycomb phenotype was described in 1947 by Pamela Lewis as an x-ray-induced *Drosophila* mutant displaying an abnormal number of sex combs and an *Antennapedia*-like phenotype of antenna-to-leg transformation (12). Thirty years later, the first *Polycomb* gene (*Pc*) locus was mapped (13), and the connection between *Pc* and repressive activity on the Bithorax complex (BX-C) locus was realized (14). The antagonistic roles of PcG in transcriptional repression and TrxG in transcriptional activation of homeotic genes in *Drosophila* led to the paradigm of the tight regulation of transcription by PcG and TrxG for the spatiotemporal control of developmental genes (8, 15).

After the identification of *Pc*, many other Polycomb group genes were identified in *Drosophila* on the basis of their similarity to the *Pc* homeotic phenotype (16). Subsequent work demonstrated that many PcG and TrxG proteins are organized in multiprotein complexes that have chromatin-modifying activities (17). In contrast to the TrxG, no PcG proteins exist in *Saccharomyces cerevisiae*, although homologs are present in the filamentous fungus *Neurospora crassa* and in the budding yeast *Cryptococcus neoformans* (18, 19). This difference in conservation suggests that TrxG-independent functions, beyond the classical counteraction of PcG activity, are likely to exist. Here, we provide a current analysis of the balanced state of gene expression orchestrated by the interaction of Trx and related proteins within the COMPASS family and PcG family proteins of the PRC1 and PRC2 complexes. We will also discuss how the misregulation of their activities tips the balanced state of gene expression, which results in disease pathogenesis, including cancer (Tables 1 to 3).

TrxG family members and COMPASS-like complexes are histone H3K4 methylases

The cloning of the *mixed-lineage leukemia* (*MLL*) gene revealed that this proto-oncogene shares extensive homology with *Drosophila Trx* (5, 17, 20). In addition, the yeast protein Set1 has strong sequence similarity to the C terminus of Trx and MLL (21). Endeavoring to understand the function of MLL in leukemia, yeast Set1 was purified biochemically to homogeneity and found within a

Department of Biochemistry and Molecular Genetics, Northwestern University Feinberg School of Medicine, 320 East Superior Street, Chicago, IL 60611, USA.

*Corresponding author. Email: ash@northwestern.edu

Table 1. The COMPASS family in development and cancer. The COMPASS family components in *S. cerevisiae*, *D. melanogaster*, and *Homo sapiens* are listed. Developmental role of each component is reported as a phenotypical outcome arising from knockout mice for each of them as described in the literature. Representative examples of each component's role in cancer are indicated. Additional abbreviations: E#, embryonic day; ND, not determined; AML, acute myeloid leukemia; LOF, loss of function; NPCs, neural precursor cells; HR, homologous recombination.

COMPASS family			Role in mammalian development <i>Mus musculus</i> (homozygous gene deletion)	Example of roles in tumorigenesis <i>M. musculus</i> and <i>H. sapiens</i>
Yeasts <i>S. cerevisiae</i>	Flies <i>D. melanogaster</i>	Mammals <i>H. sapiens</i>		
Set1	Set1 (SET domain-containing 1)	SET1A (Su[var]3-9, Enhancer of Zeste, Trithorax 1A)	Fail to pass the epiblast stage, no embryos after E7.5 (117)	- Promotes liver cancer growth (184)
		SET1B (Su[var]3-9, Enhancer of Zeste, Trithorax 1B)	Fail to develop properly, no embryos after E11.5 (117)	ND
	Trx (Trithorax)	MLL1 (KMT2A) (Mixed-lineage leukemia 1)	Fail to develop properly, no embryos after E10.5 (185)	- Forms fusion proteins with different SEC components in AML (129) - Required for MLL fusion protein-driven oncogenesis in AML (132)
		MLL2 (KMT2B) (Mixed-lineage leukemia 2)	Fail to develop properly, no embryos after E11.5 (186)	ND
	Trr (Trithorax-related)	MLL3 (KMT2C) (Mixed-lineage leukemia 3)	Mice die perinatally (187)	- LOF mutations and putative recessive tumor suppressive activity in different tumors (142–144) - Homozygous <i>MLL3ΔSET</i> mice show hyperproliferation of urothelial cells (145)
		MLL4 (KMT2D) (Mixed-lineage leukemia 4)	Fail to develop, no embryos after E11.5 (187)	- LOF mutations in NHL and MB (137, 138, 141) - Homozygous deletion in B lymphocytes accelerates lymphomagenesis (139, 140)
Cps30 (Swd3)	wds (Will die slowly)	WDR5 (WD repeat domain5)	ND	- Small molecules targeting WDR5-MLL1 interaction inhibit leukemic growth (133, 134)
Cps60 (Bre2)	Ash2 (Absent, small or homeotic disc 2)	ASH2L (Absent, small or homeotic disc-like)	Fail to develop properly, no embryos after E8.5 (188)	- Amplified in breast cancer cell lines, expression correlates with ERα levels (189)
Cps50 (Swd1)	Rbbp5 (Retinoblastoma-binding protein 5)	RBBP5 (Retinoblastoma-binding protein 5)	ND	ND
Cps25 (Sdc1)	Dpy-30L1 (Dumpy-30-like 1)	DPY30 (Dumpy-30)	Fail to develop properly, no embryos after E8.5 (190)	ND
Cps35 (Swd2)	Wdr82 (WD repeat domain 82)	WDR82 (WD repeat domain 82)	ND	ND
Not reported	Mnn1 (Menin 1)	MEN1 (multiple endocrine neoplasia 1)	Fail to develop properly, no embryos after E12.5 (191)	- Numerous different LOF mutations in multiple endocrine neoplasia-type 1 (192) - Menin-MLL interaction inhibitors impair leukemia growth (193, 194) - Menin-MLL interaction inhibitors impair H3K27M-transformed NPCs (176)

Continued on next page

Continued from previous page

COMPASS family			Role in mammalian development <i>Mus musculus</i> (homozygous gene deletion)	Example of roles in tumorigenesis <i>M. musculus</i> and <i>H. sapiens</i>
Yeasts <i>S. cerevisiae</i>	Flies <i>D. melanogaster</i>	Mammals <i>H. sapiens</i>		
Not reported	<i>Hcf</i> (Host cell factor)	<i>HCF1</i> (Host cell factor 1)	Fail to develop properly, no embryos after E8.5 (195)	ND
Not reported	<i>Ptip</i> (PAX transcription activation domain-interacting protein)	<i>PTIP</i> (PAX transcription activation domain-interacting protein)	Fail to develop properly, no embryos after E9.5 (196)	- Indispensable for 53BP1-mediated HR inhibition in <i>Brca1</i> null cells (197)
Not reported	<i>Pa1</i> (PTIP-associated 1)	<i>PA1</i> (PTIP-associated 1)	ND	ND
Not reported	<i>Utx</i> (Ubiquitously transcribed X chromosome tetratricopeptide repeat protein)	<i>UTX</i> (Ubiquitously transcribed X chromosome tetratricopeptide repeat protein)	Female embryos fail to develop properly, no embryos after E11.5 (198)	- LOF mutations frequently found in cancer cells (146) - Tumor suppressive function in T-ALL (163) - Enhance invasiveness of breast cancer cells (199)
Not reported	<i>NcoA6</i> (Nuclear receptor coactivator 6)	<i>NCOA6</i> (Nuclear receptor coactivator 6)	Fail to develop properly, no embryos after E12.5 (200)	ND

multiprotein complex named COMPASS (complex of proteins associated with Set1) (21). Set1 within COMPASS was the first histone H3 lysine 4 (H3K4) methylase purified and biochemically characterized (5, 21, 22).

After its discovery in *S. cerevisiae* (21), COMPASS homologs that methylate histone H3K4 were readily identified in fruit flies, mice, and humans, which suggests the fundamental importance of these multiprotein complexes during evolution (23). Although yeast COMPASS (yCOMPASS) is present as a single H3K4 methyltransferase complex in *S. cerevisiae*, there are three different COMPASS-like complexes in *D. melanogaster*; and six in mammals that represent duplications of each of the three *Drosophila* complexes (24, 25) (Table 1 and Fig. 1). These three types of complexes can be divided into Set1-like, Trx-like, and trithorax-related (Trr)-like (Fig. 1). Set1 and/or COMPASS is responsible for global di- or trimethylated histone H3 at lysine 4 (H3K4me2/3) deposition in *Drosophila* (24, 26). Although *Trx* mutations result in homeotic and other developmental defects and *Trx*'s role in the positive regulation of the *Ubx* gene is well known (27), the overall requirement for *Trx*'s histone methyltransferase (HMT) activity in vivo is not yet completely defined. *Trx*'s down-regulation in imaginal discs or in *Drosophila* S2 cells' effect on the global reduction of histone H3K4 methylation levels is not dramatic (24, 26). This suggests that *Trx* may control histone H3K4 methylation deposition at a specific subset of genes. Indeed, Trx binds to and is required for the transcription of genes containing promoter-associated TrxG- and PcG-responsive elements (TRE and PRE) (28). TRE and PRE are specifically found in *Drosophila* and are defined as the minimal genomic region capable of recruit-

ing PcG proteins to chromatin (6). These sequences create a highly dynamic platform for PcG and TrxG proteins that, from different stimuli, can maintain, respectively, the repressive or active transcriptional status of genes that were initially induced by specific transcription factors and thus generate what is called "epigenetic memory" (4, 29).

Drosophila Trr/COMPASS and MLL3/4 COMPASS in enhancer function

The specific spatiotemporal transcriptional regulation of developmental genes is controlled by cis-regulatory elements known as enhancers (30–33). Given that only 2% of the human genome encodes for protein-coding genes, vast expanses of noncoding DNA may serve as regulatory elements and enhancers. Enhancers communicate with promoters through DNA looping (Figs. 1 and 2) and can be classified as poised or active, depending on their potential or active support to transcription. Typically, poised enhancers can be found close to developmental genes ready to be activated by environmental stimuli, whereas active enhancers support the transcription network characteristic of the specific cell type, which ensures proper cell identity. Epigenetic and chromatin studies have demonstrated that the enhancer regions can be characterized by containing high levels of histone H3K4me1 and histone H3K27me3 for poised enhancers or H3K27 acetylation for active enhancers (25). In *Drosophila*, H3K4me1 is largely dependent on the COMPASS family member *Trr* (*Trithorax-related*), a specific histone H3K4 monomethyltransferase that acts in a dCOMPASS-related multiprotein complex (25) (Fig. 1). On active enhancers, the implementation of histone H3K27 acetylation (H3K27ac) is thought to be accomplished by cAMP response element-binding pro-

tein (CREB)-binding protein (CBP) or p300 (34). Histone H3K27ac is also deposited at active promoters and positively correlates with histone H3K4me3 (35). Together, these studies demonstrate functional specification among the COMPASS family in *Drosophila* development.

Mammalian COMPASS family

In mammals, all of the genes encoding the central HMT proteins that form the different COMPASS and COMPASS-related complexes are duplicated (5, 36) (Table 1). The central core of all of the complexes is called WARD (or WRAD), because it is composed of WDR5, ASH2, RBBP5, and DPY30 factors, and it is shared and functionally required by all of the COMPASS and COMPASS-related complexes (37, 38) (Fig. 1). Set1A/B are the central H3K4 trimethylases for the mammalian COMPASS (mCOMPASS), which have been shown to play a default global histone H3K4me3 activity in mammalian cells (5, 39). However, the extent to which the overall biological function of mCOMPASS is related to its HMT activity still remains poorly characterized and understood in mammals.

MLL1 and *MLL2* are the two mammalian HMT homologs of *Drosophila Trx*, and like Trx, their proteins are found within similar macromolecular complexes called COMPASS-related complexes (36) (Fig. 1). Although they share the same domain architecture, *MLL* (*KMT2A* or *MLL1*) and *MLL2* (*KMT2B*) have nonredundant functions, as demonstrated by the frequent leukemogenic chromosomal translocations that involve *MLL1*, but never the *MLL2* gene (40). Both *MLL1* and *MLL2* can be part of a highly similar COMPASS-related complex, although they are mutually exclusive, with no *MLL2* being found in *MLL1*/COMPASS and vice versa (41, 42). Consistent with their

PRC2		Role in mammalian development	Example of roles in tumorigenesis
Flies	Mammals	<i>M. musculus</i>	<i>M. musculus</i> and <i>H. sapiens</i>
<i>D. melanogaster</i>	<i>H. sapiens</i>	(homozygous gene deletion)	
PRC2 catalytic subunits			
			Pro-oncogenic
			- Overexpressed and required in a variety of tumors (202)
			- Trx-G-deficient cancer cells are sensitized to EZH2 catalytic inhibitors (203–205)
			- Frequent GOF mutations involved in the development of DLBCL (155, 161)
			Pro-tumor suppressive
			- LOF mutations promote T-ALL (162, 163)
			- LOF mutations correlate with poor prognosis in MDS (206)
<i>E(z)</i> (Enhancer of zeste)	<i>EZH2</i> (Enhancer of zeste 2)	Fail to develop, no embryos after E7.5 (201)	
		<i>EZH1</i> (Enhancer of zeste 1)	
		Viable and fertile (207)	ND
PRC2 core subunits			
<i>Su(z)12</i> (Suppressor of zeste 12)	<i>SUZ12</i> (Suppressor of zeste 12)	Fail to develop, no embryos after E8.5 (50)	- Frequently fused to JAZF1 in ESS (208)
			- LOF mutations promote MPNTS tumorigenesis (165, 166)
			- Required for MLL/AF9 leukemia (210, 211)
			- LOF mutations promote MPNTS tumorigenesis (165, 166)
			- LOF cooperates with KRAS in NSCLC pathogenesis (212)
<i>Esc</i> (Extra sexcombs)	<i>EED</i> (Embryonic ectoderm development)	Fail to develop, no embryos after E8.5 (209)	
		<i>RBAP46</i> (Retinoblastoma-associated protein 46)	
		Males have low T cell number (http://www.informatics.jax.org/allele/MGI:4455962)	- Required for tumorigenesis of bladder cancer cells (213)
<i>Caf1-55/Nurf55</i> (Chromatin assembly factor 1, p55 subunit)	<i>RBAP48</i> (Retinoblastoma-associated protein 48)	ND	ND
<i>Jarid2</i> (Jumonji, AT-rich interactive domain 2)	<i>JARID2</i> (Jumonji, AT-rich interactive domain 2)	Fail to develop, no embryos after E11.5 (214)	- Inhibition of myogenic differentiation of rhabdomyosarcoma cells (215)

nonredundant functions, MLL2 has been demonstrated to be mainly responsible for the histone H3K4me3 deposition at bivalent clusters in mouse embryonic stem cells (mESCs), with MLL1 having little or no major role in histone H3K4me3 deposition in these cells despite its being expressed (36, 43). Histone H3K4me3 at bivalent promoters was proposed to be essential for rapid transcriptional induction from prodifferentiation stimuli; however, despite the almost complete absence of this histone mark at bivalent promoters upon MLL2 depletion or deletion, rapid transcription induced by retinoic acid in mESCs is not altered (36, 43).

Another major source of histone H3K4 methylation comes from the COMPASS-related complexes containing MLL3 (KMT2C) or MLL4 (KMT2D) (36) (Fig. 1 and Table 1). These two HMTs are the mammalian homologs of the *Drosophila* HMT Trr (25). Like Trr in *Drosophila*, MLL3 and MLL4 COMPASS-related complexes control the H3K4me1 deposition at enhancer elements in mammalian cells (44) (Fig. 1). However, MLL3/4-dependent H3K4me1 deposition can also be found at the promoters of myoblast genes when they are repressed; depletion of MLL3/4 induces the transcription of these genes, which coincides with the

recruitment of both mCOMPASS and MLL1/mCOMPASS (45). These findings suggest that multiple mCOMPASS family members can coregulate a subset of genes during development, albeit at different regulatory steps (Fig. 1).

PcG proteins: Transcriptional repressive complexes

The PcG proteins have been extensively studied in mammals in relation to development and cancer (Tables 2 and 3); however, a unifying theory on PcG's role in mammals is still not clear (46). The PcG proteins are organized into

Table 3. PRC1 in development and cancer. PRC1 components in *D. melanogaster* and *H. sapiens* are listed. Developmental role of each component is reported as a phenotypical outcome arising from knockout mice for each of them as described in the literature. Representative examples of each component's role in cancer are mentioned.

PRC1		Role in mammalian development	Example of roles in tumorigenesis
Flies	Mammals	<i>M. musculus</i>	<i>M. musculus</i> and <i>H. sapiens</i>
<i>D. melanogaster</i>	<i>H. sapiens</i>	(homozygous gene deletion)	
PRC1 catalytic subunits			
Sce (sex combs extra)	RING1B (Real interesting new gene 1B)	- Fail to develop, no embryos after E10 (216)	- Required for melanoma progression (217) - Required for MLL/AF9 leukemogenesis (218)
	RING1A (Real interesting new gene 1A)	- Anterior axial transformation (219)	- Required for MLL/AF9 leukemogenesis (218)
Canonical PRC1 core subunits			
Psc (Posterior sex combs)	BMI1/PCGF4 (B cell-specific Mo-MLV integration site 1)	- Perinatal lethality - Ataxia - Severe hematopoietic defects - Posterior transformation of the axial skeleton (220)	- Cooperates with MYC to induce lymphomagenesis (221, 222) - Required for leukemogenesis (223) - Required for a glioma mouse model (224) - Deficient hematopoietic cells induce myelofibrosis (225)
	MEL18/PCGF2 (Melanoma nuclear protein 18)	- Perinatal lethality - Posterior transformation of the axial skeleton (226)	- Tumor suppressor in breast cancer (227, 228)
Su(z)2 (Suppressor of zeste 2)	CBX2/M33 (Chromobox 2)	- Growth retarded and high rate of postnatal lethality - Antero-posterior axis malformation - Male-to-female gonadal sex reversal (229, 230)	ND
	CBX4 (Chromobox 4)	- Perinatal lethality - Thymic hypoplasia (231)	- Supports angiogenesis in hepatoma xenografts in mice (232)
Pc (Polycomb)	CBX6 (Chromobox 6)	- Decreased total body fat amount - Decreased circulating glucose and cholesterol levels - Increased circulating sodium and chloride levels (www.informatics.jax.org/allele/MGI:4441849)	ND
	CBX7 (Chromobox 7)	- Increased body length - High-fat tissue mass (233, 234)	- Cooperates with MYC to induce leukemogenesis (235) - Homozygous null mice are prone to solid tumors (233) - Overexpression in HSC leads to leukemia (236)
Ph-p and Ph-d (Polyhomeotic proximal and polyhomeotic distal)	CBX8 (Chromobox 8)	ND	- Required for MLL/AF9 leukemia (237)
	PHC1/RAE28 (Polyhomeotic 1)	- Perinatal lethality - Posterior skeletal transformation - Defects in neural crest-related tissues (238)	ND
	PHC2 (Polyhomeotic 2)	- Posterior transformation of the axial skeleton (239)	ND
	PHC3 (Polyhomeotic 3)	ND	ND

Continued on next page

Continued from previous page

PRC1		Role in mammalian development <i>M. musculus</i> (homozygous gene deletion)	Example of roles in tumorigenesis <i>M. musculus</i> and <i>H. sapiens</i>
Flies <i>D. melanogaster</i>	Mammals <i>H. sapiens</i>		
Noncanonical PRC1 core subunits			
Rybp (Ring and YY1 binding protein)	RYBP (Ring and YY1 binding protein)	Fail to develop properly, no embryos after E6.5 (240)	- Transient overexpression leads to apoptosis of different cancer cell lines but not nontransformed cells (241) - Required for MLL-AF9 leukemogenesis (218)
Kdm2 [Lysine (K)-specific demethylase 2]	KDM2B/FBXL10 [Lysine (K)-specific demethylase 2b]	Fail to develop properly, no embryos after E13.5 (242)	- Required for lymphoblastic leukemia (242) - Homozygous deletion accelerates a mouse model of myeloid leukemia (242) - Promotes pancreatic cancer (243)
Not reported	PCGF1/NSPC1 (Nervous system polycomb 1)	ND	- Required for MLL-AF9 leukemogenesis (218)

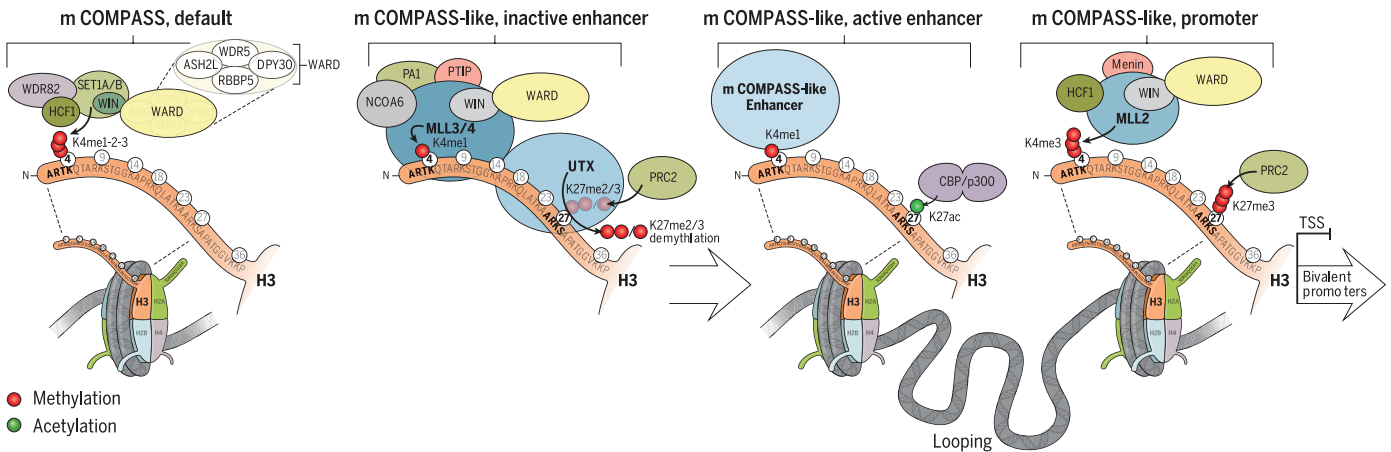


Fig. 1. The COMPASS family of histone H3K4 methylases. (Left) mCOMPASS and its activity exerted by SET1A/B on mono-, di-, and trimethylation of lysine 4 on histone H3. (Center) mCOMPASS-like activity at enhancers exerted by the monomethyltransferase activity of MLL3/4 COMPASS on lysine 4 of histone H3. Highlighted is the putative demethylase function of UTX (member of MLL3/4 COMPASS-like) that can counteract H3K27me2/3 repressive marks deposited by PRC2 and thus possibly favor H3K27ac deposition by the histone acetyltransferases (HATs) CBP/p300. (Right) mCOMPASS-like activity at bivalent

promoters exerted by MLL2/COMPASS as a trimethyltransferase toward lysine 4 on histone H3. This is suggested to positively regulate, when stimulated, the expression of genes transcriptionally poised because of the restrictive presence of PRC2 activity. MLL1/COMPASS is also a trimethylase that functions in the regulation of developmental gene expression. In the figure, only one N-terminal tail of one histone H3 is depicted. For a detailed description on the composition of the COMPASS families and the regulation of their enzymatic and catalytic properties, see (5). TSS, transcription start site.

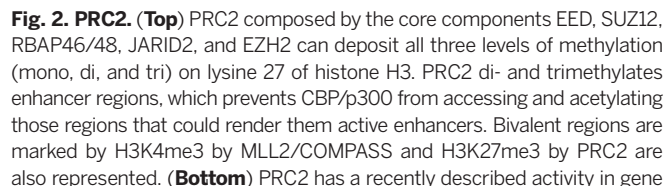
two types of macromolecular complexes: Polycomb repressive complex 1 (PRC1) and Polycomb repressive complex 2 (PRC2). As their names suggest, these complexes are generally regarded as transcriptional repressors; however, a growing body of evidence suggests that they may also play a role in transcriptional activation in a context-specific manner (46, 47).

PRC2 is the smaller of the two complexes and has a well-defined core composition. This complex is characterized by the presence of EZH2 (or its homolog EZH1), a SET domain-containing protein that has HMT-specific activity toward histone H3 lysine 27 (H3K27) (48). The other three core PRC2 components are EED, SUZ12, and RBAP46/48. EED and SUZ12 are essential for

PRC2 complex integrity and for EZH2/1 catalytic activity, whereas RBAP46/48 are most likely involved in nucleosome recognition, but dispensable for PRC2 catalytic activity (49–53).

Along with its core components, PRC2 is also characterized by several other components, which have been reported to regulate its molecular and biological functions (Fig. 2). JARID2 has been demonstrated to globally regulate PRC2 binding to chromatin in ESCs (54–56). Recently, it was also shown that Jarid2 is a nonhistone substrate of PRC2, and methylated JARID2 is a binding partner for the EED component of PRC2 (57). Another component of PRC2, the zinc finger protein AEBP2, can function with JARID2 to potentiate PRC2 catalytic activity toward unmodified

nucleosome substrates in vitro, but their precise roles in modulating PRC2 enzymatic activity in vivo are still debated (58). Other interesting non-core PRC2 components are the Polycomb-like proteins (PCL1-3), also known respectively as PHF1, MTF2, and PHF19 (47). All the PCL proteins have been shown to regulate PRC2 catalytic function and recruitment (53, 59, 60). Of particular interest, PCL3/PHF19 was initially suggested to inhibit PRC2 catalytic activity by the recognition of and binding to H3K36me3 through its Tudor domain (61). This was consistent with the inhibitory activity exerted on PRC2 by activating histone marks in vitro (62). However, other studies have shown that PHF19 is crucial for PRC2 recruitment and functions at several promoters in mESCs



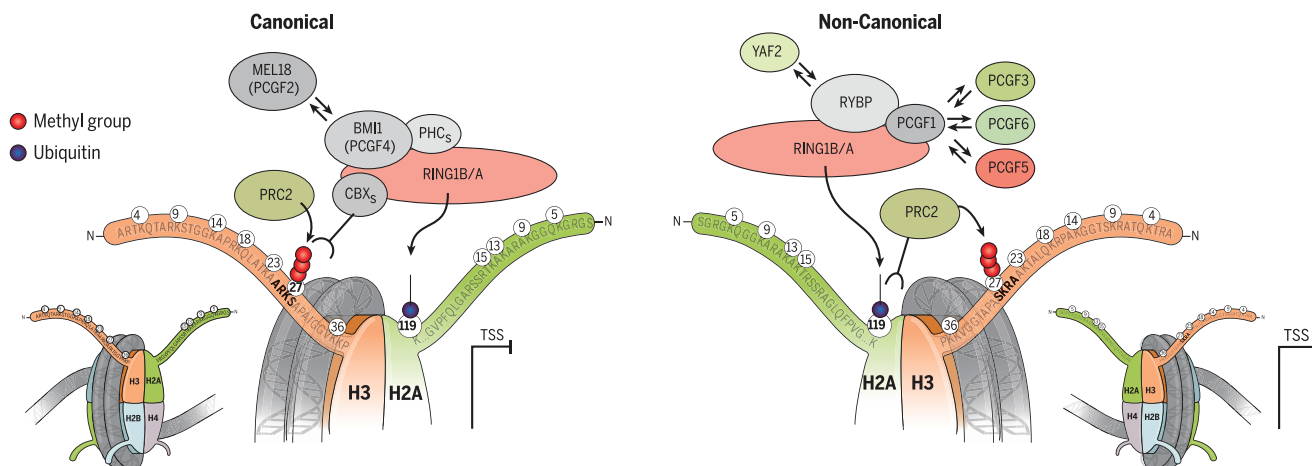


Fig. 3. PRC1. (Left) The canonical PRC1-containing CBXs, which mediate the recognition of the H3K27me3 mark deposited by PRC2. PCGF2/4 proteins assist the E3 ubiquitin ligases RING1B/A in mediating the monoubiquitination of H2AK119. (Right) The noncanonical PRC1 contains RYBP, which is a common component of all of the noncanonical PRC1, which can also contain any of the different PCGF proteins (PCGF1/3/5/6). The binding of noncanonical PRC1 to chromatin is PRC2-independent but has been implicated in the recruitment of PRC2 through the deposition of monoubiquitinated H2AK119. In the figure, only one N-terminal tail of one histone H2A or H3 is depicted.

to facilitate chromatin compaction and transcriptional silencing, although RING1B ubiquitin ligase activity is dispensable for the repression of Hox loci in mESCs (80). Very recently, however, it was demonstrated that the E3 enzymatic activity of RING1B is dispensable for early mouse development and for global target gene repression in mESCs and in *Drosophila* embryos, which raises the question of the precise function of this posttranslational modification (81, 82).

PRC1 complexes can be classified as being canonical or noncanonical (Fig. 3), with canonical PRC1-containing one of the Polycomb-like chromobox homolog (CBX) proteins that recognizes the H3K27me3 mark implemented by PRC2 (78). Canonical PRC1 complexes also contain BMI1 (PCGF4), which is required for the correct formation of canonical PRC1 and which is also required for RING1A/B E3 ligase activity (83). BMI1's closest homolog, MEL18 (PCGF2), can substitute for BMI1 to form a stable PRC1 complex but fails to enhance RING1A/B enzymatic activity in vitro (83). This could allow PRC1 recruitment, subsequent H2AK119ub deposition, chromatin compaction, and transcriptional silencing (84). This is generally regarded as the canonical sequential PRC2-dependent PRC1 recruitment model (Fig. 3).

The existence of noncanonical PRC1 was first suggested when it was demonstrated that PRC2 depletion does not cause a dramatic effect on the global H2AK119ub deposition in mESCs, which, in turn, suggests alternative mechanisms of PRC1 recruitment on chromatin (85) (Fig. 3). Indeed, recruitment of RYBP containing PRC1 was demonstrated to be PRC2-independent (85) (Fig. 3). Although canonical (PRC2-dependent and CBX-containing PRC1 subcomplexes) and noncanonical (PRC2-independent and RYBP/YAF2-containing PRC1 subcomplexes) are two distinct biochemical entities, they can both colocalize in mESCs on several developmental loci characterized by full repression and high PRC2 occupancy (78, 86).

The coexistence of canonical and noncanonical PRC1 can be explained by the recent finding that noncanonical PRC1 can recruit PRC2 on chromatin through the H2AK119ub mark (87) (Fig. 3). This is consistent with the findings demonstrating that PRC2 binds H2AK119ub-modified nucleosomes, which enhances PRC2's H3K27me3 catalytic activity through AEBP2 and JARID2 in vitro (88). Although canonical and noncanonical PRC1 biochemical compositions have been clarified, their diverse biological and molecular activities remain to be fully investigated, along with a possible cooperation at specific genomic loci (86).

Landscape of PRC1 and PRC2 in mESCs and cellular differentiation

Both TrxG and PcG have been implicated as central factors required in development and cellular differentiation from *Drosophila* to human (89) (Tables 1 and 2). Initial studies in *Drosophila* highlighted the importance of these two classes of genes in regulating the spatiotemporal transcriptional outcome at important homeotic loci, for example, *Bithorax*, through the integration of external stimuli and a dynamic competition at the regulatory elements (PRE/TRE) (90). In mammalian systems, several TrxG and PcG loss-of-function mouse models show severe developmental abnormalities, which further asserts the importance of these factors during mammalian development (91). One of the most important cellular models used to characterize the molecular functions of both of the TrxG and PcG proteins during cellular differentiation are mESCs. Several conditional or straight PcG and TrxG knockout mESCs have been generated and studied both at the transcriptional and phenotypical levels, which has uncovered the fundamental role of the epigenetic control of cellular differentiation and mouse development (92) (Tables 1 and 2). The importance of these proteins in ensuring a correct lineage commitment was also highlighted by the strict

requirement for them during cell reprogramming (93).

The PcG has been extensively studied in mESCs; however, many aspects of their function in these cells still remain to be elucidated (46). Strong molecular evidence that PcG directly contributes to the transcriptional program of mouse embryonic development comes from studies that mapped PcG target genes using chromatin immunoprecipitation coupled to promoter array (ChIP-chip) in mESCs (94). Both PRC1 and PRC2 proteins were demonstrated to be bound to key genes implicated in cellular differentiation and embryonic development in mESCs (94). As expected by their very early requirement during embryonic development, the PRC1 catalytic components RING1A/B are indispensable to maintaining mESCs' pluripotency. Indeed, mESCs acutely deprived of *Ring1b/a* reveal an acute proliferation defect accompanied by a loss of pluripotency and the up-regulation of a set of PRC1 target genes involved in cellular differentiation programs or tissue development (95). RING1B and OCT3/4 co-occupancy was demonstrated at some loci that are essential for mESCs differentiation, with RING1B recruitment depending on OCT3/4 occupancy, and its loss correlating with gene derepression upon differentiation (95). However, a more thorough genome-wide analysis of co-occupied sites could better reveal an overall interaction between PRC1 and the core pluripotency network.

It is not surprising, given the reciprocal recruitment of PRC2 and PRC1 on common genomic loci in mESCs (Fig. 3), that the vast majority of PRC1-binding sites are also bound by PRC2, and this is especially evident at bivalent genes important for cellular differentiation and development (96). Even though PRC2 overlaps with PRC1 at many loci, PRC2 seems to have a less crucial role in mESCs. Indeed, mESCs without the core components of PRC2, maintain pluripotency and demonstrate minimal transcriptional alterations compared with

wild-type mESCs (71). In contrast, the general differentiation potential of PRC2 null mESCs, as measured by the embryoid body formation assay, is severely altered (73). This potentially reiterates PRC2's role during embryogenesis, that is, dispensable at very early stages (i.e., inner cell mass formation) but required when massive tissue specification and cellular differentiation occurs (i.e., gastrulation). An intriguing and emerging area of PcG control of mESCs' pluripotency is their ability to shape the spatial organization of the genome (97). This important activity was initially observed in *Drosophila*, mainly by using chromosome conformation-capturing techniques that revealed how PRE and, in general, PcG targets are organized in higher chromatin structures that are important for PcG-mediated gene silencing (98, 99). This regulation is conserved in mammals. Indeed, EED is indispensable for maintaining the interaction between PRC2-occupied promoters in mESCs without altering the overall chromatin structure organization (100). Only recently, RINGIA and B were reported to control genome organization in mESCs (101). These main components of PRC1 spatially constrain four *Hox* gene clusters by maintaining enhancer-promoter interactions. The acute genetic deletion of both of the main components of PRC1 induces the release of these interactions, without altering enhancer-promoter interactions, which leads to the subsequent transcriptional activation of *Hox* genes present in the clusters (101). An interesting and still open question in this area remains whether or not the catalytic activity of both PRC1 and PRC2 are required for their activity in regulating higher chromatin architecture.

PcG recruitment to chromatin: A complex issue

An important issue, still not completely understood, concerns both PRC1 and PRC2 recruitment to chromatin in mESCs. Recent studies show that, although transcriptional silencing is sufficient to recruit PRC2 and trigger H3K27me3 deposition (70, 71), GC-rich DNA, including an exogenous bacterial-derived region, can recruit PRC2 in mESCs (69). Despite these observations, global transcriptional silencing is not sufficient to recruit PRC2 to all CpG islands present in the mouse genome (71, 102), which suggests alternative pathways for PRC2 recruitment other than silent CpG islands. Global genome-wide PRC2 binding to chromatin in mESCs is dependent on its component JARID2 (54–56). However, although a positive role of JARID2 in modulating PRC2 catalytic activity in vitro has been clearly demonstrated (58), this role in vivo is still unclear. JARID2 is proposed to be the DNA binding protein that mediated PRC2 recruitment on chromatin; however, the ARID domain (AT-rich interacting domain) of JARID2 has no preference toward a CG-rich-containing sequence in vitro (103), and in *Drosophila*, Jarid2 demonstrates both PcG-dependent and -independent functions (104). Considering that PRC2 binding on chromatin in mESCs is highly overlapping with CpG islands, (71) this opens up the possibility that other DNA binding proteins besides JARID2 could be responsible for targeting PRC2 to CpG islands.

It has been suggested that PRC1-dependent H2AK119ub contributes to PRC2 recruitment in mESCs (87). One of the noncanonical PRC1 complexes contains the histone demethylase KDM2B/FBXL10, which contains a ZF-CxxC domain that specifically recognizes unmethylated CpG islands (105). Indeed, KDM2B depletion (knockdown) in mESCs impairs RING1B recruitment to chromatin, implementation of H2AK119ub, and proper transcriptional repression in mESCs (106–108). Furthermore, deletion of *Kdm2b*'s ZF-CxxC domain in mESCs leads to a reduction of SUZ12, RING1B, H3K27me3, and H2AK119ub, which results in transcriptional derepression. Consistently, *Kdm2b* Δ ZF-CxxC heterozygous mice show an axial posterior transformation, a common PcG-depletion homeotic phenotype (87). This noncanonical PRC1-dependent recruitment of PRC2 opens up the possibility that the canonical PRC1 (CBX-containing PRC1) (Fig. 3) is indirectly recruited by the non-canonical (RYBP-containing PRC1) (Fig. 3), which explains the overlapping profiles of CBX7 and RYBP at developmental gene promoters (86). CBX7 is the main CBX component of the canonical PRC1 in mESCs, and although its relevance in the maintenance of mESCs pluripotency is debated, it plays an essential role in regulating differentiation during embryoid body formation. For example, CBX7 loss of function in this regard can lead to the deregulation of lineage marker expression, derepression of *Hox* genes, with some defects already evident at the pluripotent state (109, 110). Although all of the currently published evidence clearly supports an overall role for PRC1 in the maintenance of mESC pluripotency, further studies are needed to investigate what the specific determinants for both canonical and non-canonical PRC1 are that play a role in mESCs' pluripotency maintenance.

Chromatin bivalency: A functional balance between PcG and COMPASS?

Although histone H3K4me3 marks actively transcribed genes and histone H3K27me3 marks the repressed state of gene expression, subsets of H3K4me3-marked gene promoters are co-occupied by the repressive histone mark H3K27me3. These dually active/repressed marked promoters are referred to as "bivalent domains" (111). It has been suggested that these bivalent domains are enriched at the developmental genes in pluripotent cells that are kept in a poised transcriptional state, ready to be activated or repressed upon stimulation by prodifferentiation signals (111). The presence of both the H3K4me3 and H3K27me3 marks on poised genes suggests that they were under the control of the TrxG and PcG complexes similar to what is seen at the *Hox* genes in *Drosophila* (111). Although intriguing, this model has been challenged by several studies. From such a model, bivalency should be rapidly resolved to an activated or repressed state upon differentiation stimuli. However, nonpluripotent stem cells, such as hematopoietic stem cells (HSCs), retain thousands of bivalent marks, and some of them resolve upon erythrocyte differentiation (112). This suggests that bivalent marks can play a general

role in poising genes required for differentiation. However, cells with limited or absent differentiation potential, such as mouse embryonic fibroblasts (MEFs) and T cells, contain a large number of bivalent genes, which indicates that the presence of these opposing marks on gene promoters is not restricted to pluripotent or multipotent cells (113–115). Although the H3K27me3 at bivalent and not bivalent promoters is deposited by PRC2 (73), the H3K4me3 at bivalent genes is specifically deposited by MLL2/COMPASS (36, 43). Even though bivalency was suggested to be important during rapid transcriptional induction, MLL2/COMPASS depletion, and the consequent specific loss of H3K4me3 at bivalent genes, none of these affects pluripotency or the rapid transcriptional induction of those genes upon retinoic acid stimulation (36, 43).

Although dispensable for rapid transcriptional activation of bivalent genes, the loss of *MLL2* affects mESCs embryoid body formation with delayed ectodermal and mesodermal differentiation (116). Single deletion of *MLL1*, *MLL2*'s closest homolog, has little impact on H3K4me3 deposition and gene transcription in mESCs (43). Double *MLL1* and *MLL2* acute deletion shows that MLL1/COMPASS can potentially substitute for MLL2-dependent H3K4me3 deposition at some bivalent genes during mESCs differentiation induced by retinoic acid treatment (43). However, whether double *MLL1/2* knockout affects mESCs pluripotency has not yet been clarified. Both *MLL2*^{−/−} and *Setd1a*^{−/−} mESCs were reported to have a reduced cell proliferation and an increased apoptotic rate (116, 117). However, only *Setd1a*^{−/−} mESCs show a global decrease of all three methylation states of H3K4 (H3K4me1/2/3) (117). This demonstrates SET1A/COMPASS's default activity toward that of H3K4 trimethylation (Fig. 1).

Balance of Polycomb and COMPASS in cancer

Various components of the PcG and COMPASS family of complexes are involved in tumor progression and cancer (84, 118), including the well-known and highly frequent rearrangements of the methyltransferase MLL1 that generate oncogenic fusion, as well as the BMI1 deregulation that is crucial for leukemia pathogenesis and maintenance (119, 120) (Tables 1 to 3). Note that a growing body of evidence suggests that chromatin modifiers are major targets for mutations in cancer (118, 121). Members of the COMPASS family and several PRC2 components are indeed found frequently mutated in different types of cancer (118, 122). Whether all of the translocation and mutations reported so far are driving, cooperating, or passenger mutations remains unknown. Several such examples are described in detail below.

MLL/COMPASS translocations and transcriptional elongation checkpoint defects in leukemogenesis

MLL1 was the first TrxG protein reported to be directly involved in tumor formation, as it was cloned from a genomic region frequently translocated in

leukemia (5, 20, 123). In all of the MLL translocations, MLL1's SET domain is lost; however, the chimeric proteins still have the MLL1-CxxC domain (124). This domain is essential for MLL fusion proteins to bind unmethylated DNA, and it is strictly required to maintain their oncogenic activity; indeed, point mutations that disrupt the CxxC domain abolish the tumorigenic potential of MLL chimeras (124, 125). The central role for this domain in recruitment of the MLL chimeric protein to chromatin independently of the fusion partner suggests a possible common mechanism for the leukemogenic potential based on the CxxC-dependent recruitment. The ELL protein was the first MLL fusion partner for which a biochemical function was assigned and biochemically well characterized (126). ELL was demonstrated to play a positive role in transcriptional elongation control by increasing the catalytic properties of elongating RNA polymerase II (126). On the basis of these very early observations, we proposed more than 20 years ago that transcriptional elongation control could play a central role in leukemic pathogenesis through MLL translocations. Similar to ELL, other MLL translocation partners have been shown to have positive roles in transcriptional control, such as ENL (127), AFF1 (AF4), and AF9 (128).

Detailed biochemical purifications of several of the MLL chimeras found in childhood leukemia led to the identification of AFF4 (a known rare MLL partner in leukemia) as a common factor found in many of the purified chimeras (129). When AFF4 was purified to homogeneity from nonleukemic cells, it was demonstrated that AFF4 is a central component of a transcriptional elongation complex containing many of the known MLL partners found in childhood leukemia including AFF1, AFF4, ENL, and AF9, as well as well-known elongation factors, such as ELL, ELL2, ELL3, and P-TEFb (129). This complex, named the super elongation complex (SEC), demonstrates that it is the translocation of MLL1 into SEC that is involved in the misrecruitment of SEC to MLL target genes, which perturbs transcription elongation checkpoints at MLL1 target loci and results in leukemic pathogenesis (129). Accordingly, deletion of the AFF4-binding domain from MLL-AFF4 strongly impairs its oncogenic activity and the transactivation of the canonical MLL1 downstream target *HOXA9* (129, 130). It is now known that not only is SEC involved in the regulation of transcription of the MLL1 target genes in leukemia but also that this elongation complex is the central factor regulating transcription elongation control and rapid transcriptional response in many of the cellular models tested (118). This observation, and subsequent published studies, confirms our model proposed more than 20 years ago that misregulation of transcriptional elongation control is central to leukemic pathogenesis through MLL translocations.

MLL fusions and the mammalian COMPASS

Some other members of the mammalian COMPASS family have been shown to be essential for

MLL fusion protein oncogenic activity. MEN1 (Menin) depletion causes proliferation arrest of MLL-AF9-driven leukemia, and this is partially driven by the positive direct transcriptional control of *HOXA9* (131). It has been suggested that MEN1 is capable of recruiting MLL1 to *HOXA9* and mediating its expression; however, in global studies, MLL1 recruitment in the absence of MEN1 has not been demonstrated. Furthermore, the endogenous MLL1 is essential for MLL-AF9 driven leukemogenesis, likely through maintaining the active transcription of essential oncogenes, such as *HOXA9* (132). Notably, a small-molecule-inhibiting WDR5 binding to MLL1 has been recently reported to reduce the leukemogenic potential of MLL fusion proteins (133); however, the molecular mechanism for this process and its specificity through WDR5, which is a shared component of all of the COMPASS family is missing. Another small-molecule targeting the MLL1-WDR5 interaction was also reported to specifically affect the leukemogenic potential of p30/CEBP α driven leukemia (134). However, its efficacy in MLL fusion protein-driven leukemia was not tested nor was the specificity for MLL1/COMPASS versus other family members determined. Nonetheless, these findings suggest the possibility that targeting the mammalian COMPASS family protein interactions in different types of leukemia could be a successful strategy for the treatment of these cancers.

Mutations in enhancer-associated COMPASS-like MLL3/4 in cancer

Mutations in epigenetic factors, both loss and gain of function, are becoming more evident as hallmarks of cancer (118, 135). Genes encoding for the mammalian COMPASS family are among the most mutated chromatin modifiers in several types of cancer (118). *MLL4* (KMT2D) mutations were initially found in patients affected by the Kabuki syndrome, a rare genetic disease that causes multiple malformations (136). Two comprehensive analyses of genetic lesions in the two most common non-Hodgkin's lymphomas (NHLs), diffuse large B cell lymphomas (DLBCLs) and follicular lymphomas (FLs), identified *MLL4* as a highly frequently mutated gene (around 23 to 32% of primary DLBCL and 89% of primary FL) (137, 138). However, almost all of the mutations found were monoallelic, which suggests that *MLL4* haploinsufficiency might play a role in DLBCL and FL pathogenesis (137, 138). Notably, two independent groups demonstrated that *MLL4* deficiency in mice accelerates lymphomagenesis, which confirms the crucial role of *MLL4*/COMPASS activity at enhancers in tumor suppression in the germinal center (139, 140). High rates of missense, nonsense, and frameshift indel mutations in the *MLL4* gene have also been reported in medulloblastomas (MBs) (141). Although with less frequency, this study also identified *MLL3* mutations in MBs. *MLL3* gene mutations are also found in other tumors, such as kidney and bladder tumors (142–144). Almost half of homozygous *MLL3* Δ Set mice are characterized by an unscheduled hyperproliferation of urothelial cells

and urothelial neoplasia. *MLL3* serves as a p53 transcriptional coactivator in these tumors and, accordingly, all *MLL3* Δ Set; p53 $+/+$ compound mice develop urothelial tumors with an earlier incidence compared with *MLL3* Δ Set mice (145).

Mutations of the MLL3/4 COMPASS components and UTX and enhancer malfunction as a common driver of cancer

In addition to the mutations of *MLL3* and *MLL4* in cancer, the methyltransferase components of COMPASS-like complexes, a component common to both complexes, UTX, is frequently mutated in bladder cancer and in a variety of other forms of cancers (Fig. 1) (146). In particular, UTX is frequently mutated in T cell acute lymphoblastic leukemia (T-ALL), and accordingly, murine models of Notch-driven T-ALL are more aggressive when *Utx* is genetically deleted (147, 148). UTX could conceivably demethylate H3K27me2/3 present at enhancers to facilitate the conversion from poised to active enhancers by means of CBP/p300 acetylation at the same residue, which leads to activation of the transcription network regulated by those enhancers (Fig. 2) (25). This suggests a tumor suppressive role of UTX through ensuring the maintenance of proper transcriptional network activation by erasing the putative oncogenic silencing induced by PRC2.

Although an antagonism between UTX-mediated demethylation and PRC2 methylation to regulate acetylation at enhancers represents an interesting hypothesis that could also extend to normal cellular differentiation, it remains largely unexplored (149). Along with mammalian COMPASS-like members, *EP300* and *CREBBP*, which encode two major histone acetyltransferases involved in enhancer specification (150), are also mutated in the same tumors (137, 138, 143). The frequent rate of mutations to these enhancers' regulatory proteins strongly suggests that tumor initiation and/or maintenance needs to evade tissue-specific enhancer transcriptional networks, which leads to the hypothesis that mutations at enhancer regions or at enhancers' chromatin modifiers may be a driving force during oncogenesis, and so enhancer malfunction is identified as a new hallmark of cancer (30, 31, 118, 151).

PRC2: Oncogene or tumor suppressor?

Ezh2 is the most studied component of PRC2 in cancer (46, 84). EZH2 was initially identified as a putative proto-oncogene since it was found up-regulated in a variety of different tumors, and its down-regulation or overexpression was correlated, respectively, with a loss or gain of proliferation and transformation potential (152–154). After these first studies, and with the discovery of the PRC2 methyltransferase activity (51), the role of PRC2 methylation in cancer has garnered much interest and has been widely investigated (84).

Recently, a frequent point mutation in the EZH2 SET domain [Tyr⁶⁴¹ (Y641)] was discovered in NHL (155). Even though it was initially identified as an inactivating mutation, the frequent EZH2 overexpression in lymphomas (156) and

the heterozygous nature of the mutation (155) strongly suggested an alternative explanation. Indeed, it was subsequently demonstrated that Y64I mutations are catalytic gain-of-function mutations that lead to an increased conversion of H3K27me2 to H3K27me3 (157, 158) (Fig. 2). Small molecules that are specifically designed to inhibit EZH2 Y64I mutants selectively impair the oncogenic potential of lymphoma cells both in vitro and in vivo (159, 160). A mouse model that expresses an EZH2 Y64I mutant allele in germinal centers was also generated. This mutant leads to germinal center hyperplasia, with additional genetic alterations, e.g., Bcl2 overexpression resulting in lymphoma (161).

Although several studies strongly indicate that PRC2 components have oncogenic functions, some other studies indicate that PRC2 can serve as a tumor suppressor in specific tumors. *Ezh2* deletion in the hematopoietic system results in the pathogenesis of T-ALL in mice (162). This was further supported by alterations in *EZH2* and *SUZ12* in human T-ALL (163). It has also been demonstrated that, even though *Ezh2* deletion can lead to T-ALL, the genetic deletion of its homolog *Ezh1* in *Ezh2* null T-ALL results in leukemia regression in mice (164). This study suggests that, although *Ezh2* mutations can lead to T-ALL, overall PRC2 function is still oncogenic in these tumors. Nonetheless, highly frequent homozygous PRC2 component mutations were found in malignant peripheral nerve sheath tumors (MPNST) (165, 166). Notably, reexpression of *SUZ12* in MPNST cells characterized by *SUZ12* homozygous deletion restores H3K27me3 and impairs cell proliferation (165). Together, the published data in the literature so far indicate that different components of PRC2 can function as tumor suppressors or oncogenes depending on the chromatin context and tissues of origin of the cancer. Certainly, further molecular characterization of the cancers depending on the PRC2 complex and its components should shed further light on this matter.

Another interesting example of the role of histone H3K27 methylation in cancer concerns the discovery of a recurrent single-nucleotide substitution in diffused intrinsic pontine gliomas (DIPGs). This mutation results in a lysine-to-methionine conversion at position 27 in the histone variant H3.3 (H3.3K27M) (167, 168). Although this mutation only affects a single histone H3.3 allele, a global loss of H3K27me3 and reduced PRC2 catalytic activity was observed (169, 170). This indicates that reduced global PRC2 activity can be required for tumor formation. However, genome-wide analyses also demonstrated that H3K27M positive DIPG cells still have loci marked by H3K27me3 and have PRC2 loaded on chromatin, which raises the possibility that selective inhibition of PRC2 at specific loci can be tumorigenic (170, 171). The mechanism through which H3.3K27M impairs PRC2 function is still debated. Although it was initially shown that H3.3K27M can sequester EZH2 by direct binding (169), a recent study from our laboratory failed to show preferential binding of PRC2 toward H3.3K27M compared with wild-type H3.3 (172). We demonstrated that

cells expressing H3K27M contain higher levels of H3K27 acetylated nucleosomes and also identified BRD4 to preferentially copurify with H3.3K27M-containing nucleosomes compared with wild-type H3.3. BRD4 is a well-known therapeutic target in cancer (173). Moreover, PRC2 mutations sensitize PMNSTs to BRD4 inhibition (174), possibly because of an increase of H3K27ac that occurs in cells deficient in PRC2 activity (172, 175) (Fig. 2). Therefore, H3.3K27M-positive DIPG tumors could be promising candidates for BRD4 inhibition therapy.

Whether the H3.3K27M mutation is an oncogenic driving force in DIPGs is still not completely understood. Histone H3.3K27M can synergize with overexpression of the gene for platelet-derived growth factor receptor α (*PDGFR α*) and p53 loss to enhance proliferation and transformation of human ESC-derived neural stem cells (NSCs) (176). This suggests that H3K27M could participate in tumor formation. Whether H3K27M is required for tumor maintenance and the detailed molecular mechanism of its action remain open for questions. Note that pharmacological inhibition of JMJD3, a known H3K27me3 demethylase, can selectively impair H3.3K27M DIPG cells' tumorigenic potential by restoring normal levels of H3K27me3 (177), which supports restoration of full PRC2 activity as a potential treatment for H3.3K27M-positive DIPGs.

Future direction of studies on Polycomb and COMPASS families in development and during disease pathogenesis

PcG and COMPASS are fundamental, evolutionarily conserved families of enzymes and are central regulators of gene expression. Accordingly, perturbation of their composition and activities can substantially alter normal biological processes in development, including cellular proliferation and differentiation. Although, in *Drosophila*, the interplay between the two groups is well established (6), the interconnection between PcG and TrxG in mammals is less clear, given the fact that there are six COMPASS families in mammals as opposed to three in *Drosophila*. Whether the different phenotypes presented in this review are caused by an overactive role of PcG or TrxG because of the missing or mutated counterparts in mammals is an interesting and largely unexplored area. The COMPASS family of proteins and PRC1/PRC2 each use different enzymatic activities to posttranslationally modify nucleosomes. Although all of these nucleosome posttranslational modifications are frequently associated with differential transcriptional outcomes, the formal proof that they are directly involved in transcriptional regulation is still missing for all marks (178). In *Drosophila*, changing lysine 27 to arginine (K27R) in all of the genes coding for histone H3 leads to derepression of canonical PcG targets and homeotic transformation (179). Furthermore, H3K27M-expressing flies display derepression of homeotic genes and developmental defects similar to those of PRC2-deficient flies (172). This strongly suggests that, at least in *Drosophila*, the PRC2 catalytic activity toward

the H3K27 residue is required for some of its biological functions. In contrast, dRing (Ring1a/b homolog in *Drosophila*) activity toward H2AK119 was shown to be largely dispensable for gene repression and canonical Polycomb-associated phenotypes (82). Similarly, mESCs expressing catalytically dead RING1B still achieve chromatin compaction and transcriptional repression at the Hox clusters (180). These studies, along with the in vitro evidence that PRC1 can compact nucleosome arrays independently of the presence of histone tails (181), support an important catalytic-independent role for PRC1 in transcriptional regulation. Examples of PRC2 catalytic-independent functions were also reported in a prostate cancer model in which PRC2 acts as a coactivator for the androgen receptor (182).

For the COMPASS family of proteins, to date, there is not any convincing evidence for catalytic-dependent versus independent functions in cancer. All the while, the precise role(s) of H3K4 methylations, besides their ability to predict transcription or chromatin states, are still elusive (150). It is not known at this time how different COMPASS-related complexes deposit specific states of methylation (H3K4me1/2/3) and how such intricate small differences in the pattern in histone modifications (H3K4me1/2/3) are deciphered by cells. For examples, *Trx* proteins, such as SNF5, were demonstrated to directly counteract PcG (e.g., complex eviction) at commonly regulated loci, similar to what happens in *Drosophila* (183). These are exciting and still unexplored areas that can help us understand the missing details of the regulation of gene expression exerted by the balance between the PcG and COMPASS family proteins, and the extent to which the balance or imbalance of their activities contributes to development and disease.

REFERENCES AND NOTES

1. R. Jaenisch, A. Bird, Epigenetic regulation of gene expression: How the genome integrates intrinsic and environmental signals. *Nat. Genet.* **33** (Suppl.), 245–254 (2003). doi: 10.1038/ng1089; pmid: 12610534
2. R. D. Kornberg, Y. Lorch, Twenty-five years of the nucleosome, fundamental particle of the eukaryote chromosome. *Cell* **98**, 285–294 (1999). doi: 10.1016/S0092-8674(00)81958-3; pmid: 10458604
3. A. J. Bannister, T. Kouzarides, Regulation of chromatin by histone modifications. *Cell Res.* **21**, 381–395 (2011). doi: 10.1038/cr.2011.22; pmid: 21321607
4. P. A. Steffen, L. Ringrose, What are memories made of? How Polycomb and Trithorax proteins mediate epigenetic memory. *Nat. Rev. Mol. Cell Biol.* **15**, 340–356 (2014). doi: 10.1038/nrm3789; pmid: 24755934
5. A. Shilatifard, The COMPASS family of histone H3K4 methylases: Mechanisms of regulation in development and disease pathogenesis. *Annu. Rev. Biochem.* **81**, 65–95 (2012). doi: 10.1146/annurev-biochem-051710-134100; pmid: 22663077
6. B. Schuettengruber, D. Chourrout, M. Vervoort, B. Leblanc, G. Cavalli, Genome regulation by Polycomb and Trithorax proteins. *Cell* **128**, 735–745 (2007). doi: 10.1016/j.cell.2007.02.009; pmid: 17320510
7. P. W. Ingham, *trithorax* and the regulation of homeotic gene expression in *Drosophila*: A historical perspective. *Int. J. Dev. Biol.* **42**, 423–429 (1998). pmid: 9654027
8. P. W. Ingham, Differential expression of *bithorax* complex genes in the absence of the *extra sex combs* and *trithorax* genes. *Nature* **306**, 591–593 (1983). doi: 10.1038/306591a0; pmid: 24937863

9. J. W. Tamkun *et al.*, *brahma*: A regulator of *Drosophila* homeotic genes structurally related to the yeast transcriptional activator SNF2/SWI2. *Cell* **68**, 561–572 (1992). doi: [10.1016/0092-8674\(92\)90191-E](https://doi.org/10.1016/0092-8674(92)90191-E); pmid: [1346755](https://pubmed.ncbi.nlm.nih.gov/1346755/)
10. P. Filippakopoulos, S. Knapp, Targeting bromodomains: Epigenetic readers of lysine acetylation. *Nat. Rev. Drug Discov.* **13**, 337–356 (2014). doi: [10.1038/nrd4286](https://doi.org/10.1038/nrd4286); pmid: [24751816](https://pubmed.ncbi.nlm.nih.gov/24751816/)
11. J. Simon, Locking in stable states of gene expression: Transcriptional control during *Drosophila* development. *Curr. Opin. Cell Biol.* **7**, 376–385 (1995). doi: [10.1016/0955-0674\(95\)80093-X](https://doi.org/10.1016/0955-0674(95)80093-X); pmid: [7662368](https://pubmed.ncbi.nlm.nih.gov/7662368/)
12. P. H. Lewis, New mutants report. *Drosoph. Inf. Serv.* **21**, 69 (1947).
13. J. Puro, T. Nygrén, Mode of action of a homeotic gene in *Drosophila melanogaster*. Localization and dosage effects of *Polycomb*. *Hereditas* **81**, 237–247 (1975). doi: [10.1111/j.1601-5223.1975.tb01038.x](https://doi.org/10.1111/j.1601-5223.1975.tb01038.x); pmid: [814109](https://pubmed.ncbi.nlm.nih.gov/814109/)
14. E. B. Lewis, A gene complex controlling segmentation in *Drosophila*. *Nature* **276**, 565–570 (1978). doi: [10.1038/276565a0](https://doi.org/10.1038/276565a0); pmid: [103000](https://pubmed.ncbi.nlm.nih.gov/103000/)
15. A. A. Mills, Throwing the cancer switch: Reciprocal roles of polycomb and trithorax proteins. *Nat. Rev. Cancer* **10**, 669–682 (2010). doi: [10.1038/nrc2931](https://doi.org/10.1038/nrc2931); pmid: [20865010](https://pubmed.ncbi.nlm.nih.gov/20865010/)
16. J. A. Kennison, The Polycomb and trithorax group proteins of *Drosophila*: Trans-regulators of homeotic gene function. *Annu. Rev. Genet.* **29**, 289–303 (1995). doi: [10.1146/annurev.ge.29.120195.001445](https://doi.org/10.1146/annurev.ge.29.120195.001445); pmid: [8825476](https://pubmed.ncbi.nlm.nih.gov/8825476/)
17. A. Shilatifard, Chromatin modifications by methylation and ubiquitination: Implications in the regulation of gene expression. *Annu. Rev. Biochem.* **75**, 243–269 (2006). doi: [10.1146/annurev.biochem.75.103004.142422](https://doi.org/10.1146/annurev.biochem.75.103004.142422); pmid: [16756492](https://pubmed.ncbi.nlm.nih.gov/16756492/)
18. K. Jamieson, M. R. Rountree, Z. A. Lewis, J. E. Stajich, E. U. Selker, Regional control of histone H3 lysine 27 methylation in *Neurospora*. *Proc. Natl. Acad. Sci. U.S.A.* **110**, 6027–6032 (2013). doi: [10.1073/pnas.1303750110](https://doi.org/10.1073/pnas.1303750110); pmid: [23530226](https://pubmed.ncbi.nlm.nih.gov/23530226/)
19. P. A. Dumesic *et al.*, Product binding enforces the genomic specificity of a yeast Polycomb repressive complex. *Cell* **160**, 204–218 (2015). doi: [10.1016/j.cell.2014.11.039](https://doi.org/10.1016/j.cell.2014.11.039); pmid: [25533783](https://pubmed.ncbi.nlm.nih.gov/25533783/)
20. S. Ziemien-van der Poel *et al.*, Identification of a gene, *MLL*, that spans the breakpoint in 11q23 translocations associated with human leukemias. *Proc. Natl. Acad. Sci. U.S.A.* **88**, 10735–10739 (1991). doi: [10.1073/pnas.88.23.10735](https://doi.org/10.1073/pnas.88.23.10735); pmid: [1720549](https://pubmed.ncbi.nlm.nih.gov/1720549/)
21. T. Miller *et al.*, COMPASS: A complex of proteins associated with a trithorax-related SET domain protein. *Proc. Natl. Acad. Sci. U.S.A.* **98**, 12902–12907 (2001). doi: [10.1073/pnas.231473398](https://doi.org/10.1073/pnas.231473398); pmid: [11687631](https://pubmed.ncbi.nlm.nih.gov/11687631/)
22. N. J. Krogan *et al.*, COMPASS, a histone H3 (Lysine 4) methyltransferase required for telomeric silencing of gene expression. *J. Biol. Chem.* **277**, 10753–10755 (2002). doi: [10.1074/jbc.C200023200](https://doi.org/10.1074/jbc.C200023200); pmid: [11805083](https://pubmed.ncbi.nlm.nih.gov/11805083/)
23. J. C. Eisenberg, A. Shilatifard, Histone H3 lysine 4 (H3K4) methylation in development and differentiation. *Dev. Biol.* **339**, 240–249 (2010). doi: [10.1016/j.ydbio.2009.08.017](https://doi.org/10.1016/j.ydbio.2009.08.017); pmid: [19703438](https://pubmed.ncbi.nlm.nih.gov/19703438/)
24. M. Mohan *et al.*, The COMPASS family of H3K4 methylases in *Drosophila*. *Mol. Cell. Biol.* **31**, 4310–4318 (2011). doi: [10.1128/MCB.06092-11](https://doi.org/10.1128/MCB.06092-11); pmid: [21875999](https://pubmed.ncbi.nlm.nih.gov/21875999/)
25. H. M. Herz *et al.*, Enhancer-associated H3K4 monomethylation by Trithorax-related, the *Drosophila* homolog of mammalian Mll3/Mll4. *Genes Dev.* **26**, 2604–2620 (2012). doi: [10.1101/gad.201327.112](https://doi.org/10.1101/gad.201327.112); pmid: [23166019](https://pubmed.ncbi.nlm.nih.gov/23166019/)
26. M. B. Ardehali *et al.*, *Drosophila* Set1 is the major histone H3 lysine 4 trimethyltransferase with role in transcription. *EMBO J.* **30**, 2817–2828 (2011). doi: [10.1038/emboj.2011.194](https://doi.org/10.1038/emboj.2011.194); pmid: [21694722](https://pubmed.ncbi.nlm.nih.gov/21694722/)
27. S. Petruk *et al.*, Transcription of *bxd* noncoding RNAs promoted by trithorax represses *Ubx* in cis by transcriptional interference. *Cell* **127**, 1209–1221 (2006). doi: [10.1016/j.cell.2006.10.039](https://doi.org/10.1016/j.cell.2006.10.039); pmid: [17174895](https://pubmed.ncbi.nlm.nih.gov/17174895/)
28. L. Ringrose, R. Paro, Polycomb/Trithorax response elements and epigenetic memory of cell identity. *Development* **134**, 223–232 (2007). doi: [10.1242/dev.02723](https://doi.org/10.1242/dev.02723); pmid: [17185323](https://pubmed.ncbi.nlm.nih.gov/17185323/)
29. M. Gerber, A. Shilatifard, Transcriptional elongation by RNA polymerase II and histone methylation. *J. Biol. Chem.* **278**, 26303–26306 (2003). doi: [10.1074/jbc.R300014200](https://doi.org/10.1074/jbc.R300014200); pmid: [12764140](https://pubmed.ncbi.nlm.nih.gov/12764140/)
30. H. M. Herz, D. Hu, A. Shilatifard, Enhancer malfunction in cancer. *Mol. Cell* **53**, 859–866 (2014). doi: [10.1016/j.molcel.2014.02.033](https://doi.org/10.1016/j.molcel.2014.02.033); pmid: [24656127](https://pubmed.ncbi.nlm.nih.gov/24656127/)
31. E. Smith, A. Shilatifard, Enhancer biology and enhanceropathies. *Nat. Struct. Mol. Biol.* **21**, 210–219 (2014). doi: [10.1038/nsmb.2784](https://doi.org/10.1038/nsmb.2784); pmid: [24599251](https://pubmed.ncbi.nlm.nih.gov/24599251/)
32. C. Benoist, P. Chambon, In vivo sequence requirements of the SV40 early promoter region. *Nature* **290**, 304–310 (1981). doi: [10.1038/290304a0](https://doi.org/10.1038/290304a0); pmid: [6259538](https://pubmed.ncbi.nlm.nih.gov/6259538/)
33. Y. Shen *et al.*, A map of the cis-regulatory sequences in the mouse genome. *Nature* **488**, 116–120 (2012). doi: [10.1038/nature11243](https://doi.org/10.1038/nature11243); pmid: [22763441](https://pubmed.ncbi.nlm.nih.gov/22763441/)
34. M. P. Creighton *et al.*, Histone H3K27ac separates active from poised enhancers and predicts developmental state. *Proc. Natl. Acad. Sci. U.S.A.* **107**, 21931–21936 (2010). doi: [10.1073/pnas.1016071107](https://doi.org/10.1073/pnas.1016071107); pmid: [21106759](https://pubmed.ncbi.nlm.nih.gov/21106759/)
35. D. Shlyueva, G. Stampfel, A. Stark, Transcriptional enhancers: From properties to genome-wide predictions. *Nat. Rev. Genet.* **15**, 272–286 (2014). doi: [10.1038/nrg3682](https://doi.org/10.1038/nrg3682); pmid: [24614317](https://pubmed.ncbi.nlm.nih.gov/24614317/)
36. D. Hu *et al.*, The Mll2 branch of the COMPASS family regulates bivalent promoters in mouse embryonic stem cells. *Nat. Struct. Mol. Biol.* **20**, 1093–1097 (2013). doi: [10.1038/nsmb.2653](https://doi.org/10.1038/nsmb.2653); pmid: [23934151](https://pubmed.ncbi.nlm.nih.gov/23934151/)
37. M. M. Steward *et al.*, Molecular regulation of H3K4 trimethylation by ASH2L, a shared subunit of MLL complexes. *Nat. Struct. Mol. Biol.* **13**, 852–854 (2006). doi: [10.1038/nsmb1131](https://doi.org/10.1038/nsmb1131); pmid: [16892064](https://pubmed.ncbi.nlm.nih.gov/16892064/)
38. Y. Dou *et al.*, Regulation of MLL1 H3K4 methyltransferase activity by its core components. *Nat. Struct. Mol. Biol.* **13**, 713–719 (2006). doi: [10.1038/nsmb1128](https://doi.org/10.1038/nsmb1128); pmid: [16878130](https://pubmed.ncbi.nlm.nih.gov/16878130/)
39. M. Wu *et al.*, Molecular regulation of H3K4 trimethylation by Wdr82, a component of human Set1/COMPASS. *Mol. Cell. Biol.* **28**, 7337–7344 (2008). doi: [10.1128/MCB.00976-08](https://doi.org/10.1128/MCB.00976-08); pmid: [18838538](https://pubmed.ncbi.nlm.nih.gov/18838538/)
40. K. T. FitzGerald, M. O. Diaz, *MLL2*: A new mammalian member of the *trx/MLL* family of genes. *Genomics* **59**, 187–192 (1999). doi: [10.1006/geno.1999.5860](https://doi.org/10.1006/geno.1999.5860); pmid: [10409430](https://pubmed.ncbi.nlm.nih.gov/10409430/)
41. Y. Dou *et al.*, Physical association and coordinate function of the H3 K4 methyltransferase MLL1 and the H4 K16 acetyltransferase MOF. *Cell* **121**, 873–885 (2005). doi: [10.1016/j.cell.2005.04.031](https://doi.org/10.1016/j.cell.2005.04.031); pmid: [15960975](https://pubmed.ncbi.nlm.nih.gov/15960975/)
42. H. Jiang *et al.*, Regulation of transcription by the MLL2 complex and MLL complex-associated AKAP95. *Nat. Struct. Mol. Biol.* **20**, 1156–1163 (2013). doi: [10.1038/nsmb.2656](https://doi.org/10.1038/nsmb.2656); pmid: [23995757](https://pubmed.ncbi.nlm.nih.gov/23995757/)
43. S. Denisov *et al.*, Mll2 is required for H3K4 trimethylation on bivalent promoters in embryonic stem cells, whereas Mll1 is redundant. *Development* **141**, 526–537 (2014). doi: [10.1242/dev.102681](https://doi.org/10.1242/dev.102681); pmid: [24423662](https://pubmed.ncbi.nlm.nih.gov/24423662/)
44. D. Hu *et al.*, The MLL3/MLL4 branches of the COMPASS family function as major histone H3K4 monomethylases at enhancers. *Mol. Cell. Biol.* **33**, 4745–4754 (2013). doi: [10.1128/MCB.0181-13](https://doi.org/10.1128/MCB.0181-13); pmid: [24081332](https://pubmed.ncbi.nlm.nih.gov/24081332/)
45. J. Cheng *et al.*, A role for H3K4 monomethylation in gene repression and partitioning of chromatin readers. *Mol. Cell* **53**, 979–992 (2014). doi: [10.1016/j.molcel.2014.02.032](https://doi.org/10.1016/j.molcel.2014.02.032); pmid: [24656132](https://pubmed.ncbi.nlm.nih.gov/24656132/)
46. A. Scelfo, A. Piunti, D. Pasini, The controversial role of the Polycomb group proteins in transcription and cancer: How much do we not understand Polycomb proteins? *FEBS J.* **282**, 1703–1722 (2015). doi: [10.1111/febs.13112](https://doi.org/10.1111/febs.13112); pmid: [25315766](https://pubmed.ncbi.nlm.nih.gov/25315766/)
47. S. Aranda, G. Mas, L. Di Croce, Regulation of gene transcription by Polycomb proteins. *Sci. Adv.* **1**, e1500737 (2015). doi: [10.1126/sciadv.1500737](https://doi.org/10.1126/sciadv.1500737); pmid: [26665172](https://pubmed.ncbi.nlm.nih.gov/26665172/)
48. R. Margueron, D. Reinberg, The Polycomb complex PRC2 and its mark in life. *Nature* **469**, 343–349 (2011). doi: [10.1038/nature09784](https://doi.org/10.1038/nature09784); pmid: [21248841](https://pubmed.ncbi.nlm.nih.gov/21248841/)
49. R. Cao, Y. Zhang, SUZ12 is required for both the histone methyltransferase activity and the silencing function of the EED-EZH2 complex. *Mol. Cell* **15**, 57–67 (2004). doi: [10.1016/j.molcel.2004.06.020](https://doi.org/10.1016/j.molcel.2004.06.020); pmid: [15225548](https://pubmed.ncbi.nlm.nih.gov/15225548/)
50. D. Pasini, A. P. Bracken, M. R. Jensen, E. L. Denchi, K. Helin, Suz12 is essential for mouse development and for EZH2 histone methyltransferase activity. *EMBO J.* **23**, 4061–4071 (2004). doi: [10.1038/sj.emboj.7600402](https://doi.org/10.1038/sj.emboj.7600402); pmid: [15385962](https://pubmed.ncbi.nlm.nih.gov/15385962/)
51. R. Cao *et al.*, Role of histone H3 lysine 27 methylation in Polycomb-group silencing. *Science* **298**, 1039–1043 (2002). doi: [10.1126/science.1076997](https://doi.org/10.1126/science.1076997); pmid: [12351676](https://pubmed.ncbi.nlm.nih.gov/12351676/)
52. M. Nekrasov, B. Wild, J. Müller, Nucleosome binding and histone methyltransferase activity of *Drosophila* PRC2. *EMBO Rep.* **6**, 348–353 (2005). doi: [10.1038/sj.embor.7400376](https://doi.org/10.1038/sj.embor.7400376); pmid: [15776017](https://pubmed.ncbi.nlm.nih.gov/15776017/)
53. E. Walker *et al.*, Polycomb-like 2 associates with PRC2 and regulates transcriptional networks during mouse embryonic stem cell self-renewal and differentiation. *Cell Stem Cell* **6**, 153–166 (2010). doi: [10.1016/j.stem.2009.12.014](https://doi.org/10.1016/j.stem.2009.12.014); pmid: [20144788](https://pubmed.ncbi.nlm.nih.gov/20144788/)
54. D. Pasini *et al.*, JARID2 regulates binding of the Polycomb repressive complex 2 to target genes in ES cells. *Nature* **464**, 306–310 (2010). doi: [10.1038/nature08788](https://doi.org/10.1038/nature08788); pmid: [20075857](https://pubmed.ncbi.nlm.nih.gov/20075857/)
55. J. C. Peng *et al.*, Jarid2/Jumonji coordinates control of PRC2 enzymatic activity and target gene occupancy in pluripotent cells. *Cell* **139**, 1290–1302 (2009). doi: [10.1016/j.cell.2009.12.002](https://doi.org/10.1016/j.cell.2009.12.002); pmid: [20064375](https://pubmed.ncbi.nlm.nih.gov/20064375/)
56. X. Shen *et al.*, Jumoni modulates polycomb activity and self-renewal versus differentiation of stem cells. *Cell* **139**, 1303–1314 (2009). doi: [10.1016/j.cell.2009.12.003](https://doi.org/10.1016/j.cell.2009.12.003); pmid: [20064376](https://pubmed.ncbi.nlm.nih.gov/20064376/)
57. S. Sanulli *et al.*, Jarid2 Methylation via the PRC2 Complex Regulates H3K27me3 Deposition during Cell Differentiation. *Mol. Cell* **57**, 769–783 (2015). doi: [10.1016/j.molcel.2014.12.020](https://doi.org/10.1016/j.molcel.2014.12.020); pmid: [25620564](https://pubmed.ncbi.nlm.nih.gov/25620564/)
58. J. Son, S. S. Shen, R. Margueron, D. Reinberg, Nucleosome-binding activities within JARID2 and EZH1 regulate the function of PRC2 on chromatin. *Genes Dev.* **27**, 2663–2677 (2013). doi: [10.1101/gad.225888.113](https://doi.org/10.1101/gad.225888.113); pmid: [24352422](https://pubmed.ncbi.nlm.nih.gov/24352422/)
59. R. Cao *et al.*, Role of hPHF1 in H3K27 methylation and Hox gene silencing. *Mol. Cell. Biol.* **28**, 1862–1872 (2008). doi: [10.1128/MCB.01589-07](https://doi.org/10.1128/MCB.01589-07); pmid: [18086877](https://pubmed.ncbi.nlm.nih.gov/18086877/)
60. K. Sarma, R. Margueron, A. Ivanov, V. Pirrotta, D. Reinberg, Ezh2 requires PHF1 to efficiently catalyze H3 lysine 27 trimethylation in vivo. *Mol. Cell. Biol.* **28**, 2718–2731 (2008). doi: [10.1128/MCB.02017-07](https://doi.org/10.1128/MCB.02017-07); pmid: [18285464](https://pubmed.ncbi.nlm.nih.gov/18285464/)
61. C. A. Musselman *et al.*, Molecular basis for H3K36me3 recognition by the Tudor domain of PHF1. *Nat. Struct. Mol. Biol.* **19**, 1266–1272 (2012). doi: [10.1038/nsmb.2435](https://doi.org/10.1038/nsmb.2435); pmid: [23142980](https://pubmed.ncbi.nlm.nih.gov/23142980/)
62. F. W. Schmitges *et al.*, Histone methylation by PRC2 is inhibited by active chromatin marks. *Mol. Cell* **42**, 330–341 (2011). doi: [10.1016/j.molcel.2011.03.025](https://doi.org/10.1016/j.molcel.2011.03.025); pmid: [21549310](https://pubmed.ncbi.nlm.nih.gov/21549310/)
63. G. L. Brien *et al.*, Polycomb PHF19 binds H3K36me3 and recruits PRC2 and demethylase N066 to embryonic stem cell genes during differentiation. *Nat. Struct. Mol. Biol.* **19**, 1273–1281 (2012). doi: [10.1038/nsmb.2449](https://doi.org/10.1038/nsmb.2449); pmid: [23160351](https://pubmed.ncbi.nlm.nih.gov/23160351/)
64. C. Ballaré *et al.*, Phf19 links methylated Lys36 of histone H3 to regulation of Polycomb activity. *Nat. Struct. Mol. Biol.* **19**, 1257–1265 (2012). doi: [10.1038/nsmb.2434](https://doi.org/10.1038/nsmb.2434); pmid: [23104054](https://pubmed.ncbi.nlm.nih.gov/23104054/)
65. L. Cai *et al.*, An H3K36 methylation-engaging Tudor motif of polycomb-like proteins mediates PRC2 complex targeting. *Mol. Cell* **49**, 571–582 (2013). doi: [10.1016/j.molcel.2012.11.026](https://doi.org/10.1016/j.molcel.2012.11.026); pmid: [23273982](https://pubmed.ncbi.nlm.nih.gov/23273982/)
66. J. A. Simon, R. E. Kingston, Mechanisms of polycomb gene silencing: Knowns and unknowns. *Nat. Rev. Mol. Cell Biol.* **10**, 697–708 (2009). pmid: [19738629](https://pubmed.ncbi.nlm.nih.gov/19738629/)
67. P. Vella, I. Barozzi, A. Cuomo, T. Bonaldi, D. Pasini, Yin Yang 1 extends the Myc-related transcription factors network in embryonic stem cells. *Nucleic Acids Res.* **40**, 3403–3418 (2012). doi: [10.1093/nar/gkr1290](https://doi.org/10.1093/nar/gkr1290); pmid: [22210892](https://pubmed.ncbi.nlm.nih.gov/22210892/)
68. M. Bauer, J. Trupke, L. Ringrose, The quest for mammalian Polycomb response elements: Are we there yet? *Chromosoma* (2015). doi: [10.1007/s00412-015-0539-4](https://doi.org/10.1007/s00412-015-0539-4); pmid: [26453572](https://pubmed.ncbi.nlm.nih.gov/26453572/)
69. E. M. Mendenhall *et al.*, GC-rich sequence elements recruit PRC2 in mammalian ES cells. *PLoS Genet.* **6**, e1001244 (2010). doi: [10.1371/journal.pgen.1001244](https://doi.org/10.1371/journal.pgen.1001244); pmid: [21170310](https://pubmed.ncbi.nlm.nih.gov/21170310/)
70. P. Jermann, L. Hoerner, L. Burger, D. Schübeler, Short sequences can efficiently recruit histone H3 lysine 27 trimethylation in the absence of enhancer activity and DNA methylation. *Proc. Natl. Acad. Sci. U.S.A.* **111**, E3415–E3421 (2014). doi: [10.1073/pnas.1400672111](https://doi.org/10.1073/pnas.1400672111); pmid: [25092339](https://pubmed.ncbi.nlm.nih.gov/25092339/)
71. E. M. Rissing *et al.*, Gene silencing triggers polycomb repressive complex 2 recruitment to CpG islands genome wide. *Mol. Cell* **55**, 347–360 (2014). doi: [10.1016/j.molcel.2014.06.005](https://doi.org/10.1016/j.molcel.2014.06.005); pmid: [24999238](https://pubmed.ncbi.nlm.nih.gov/24999238/)
72. K. H. Hansen *et al.*, A model for transmission of the H3K27me3 epigenetic mark. *Nat. Cell Biol.* **10**, 1291–1300 (2008). doi: [10.1038/ncb1787](https://doi.org/10.1038/ncb1787); pmid: [18931660](https://pubmed.ncbi.nlm.nih.gov/18931660/)
73. K. J. Ferrari *et al.*, Polycomb-dependent H3K27me1 and H3K27me2 regulate active transcription and enhancer fidelity. *Mol. Cell* **53**, 49–62 (2014). doi: [10.1016/j.molcel.2013.10.030](https://doi.org/10.1016/j.molcel.2013.10.030); pmid: [24289921](https://pubmed.ncbi.nlm.nih.gov/24289921/)
74. S. S. Levine *et al.*, The core of the polycomb repressive complex is compositionally and functionally conserved in flies and humans. *Mol. Cell. Biol.* **22**, 6070–6078 (2002). doi: [10.1128/MCB.22.17.6070-6078.2002](https://doi.org/10.1128/MCB.22.17.6070-6078.2002); pmid: [12167101](https://pubmed.ncbi.nlm.nih.gov/12167101/)

75. M. D. Gearhart, C. M. Corcoran, J. A. Wamstad, V. J. Bardwell, Polycomb group and SCF ubiquitin ligases are found in a novel BCOF complex that is recruited to BCL6 targets. *Mol. Cell. Biol.* **26**, 6880–6889 (2006). doi: [10.1128/MCB.00630-06](https://doi.org/10.1128/MCB.00630-06); pmid: [16943429](https://pubmed.ncbi.nlm.nih.gov/16943429/)
76. C. Sánchez et al., Proteomics analysis of Ring1B/Rnf2 interactors identifies a novel complex with the Fbxl10/JhdmlB histone demethylase and the Bcl6 interacting corepressor. *Mol. Cell. Proteomics* **6**, 820–834 (2007). doi: [10.1074/mcp.M600275-MCP200](https://doi.org/10.1074/mcp.M600275-MCP200); pmid: [17296600](https://pubmed.ncbi.nlm.nih.gov/17296600/)
77. A. Lagarou et al., dKDM2 couples histone H2A ubiquitylation to histone H3 demethylation during Polycomb group silencing. *Genes Dev.* **22**, 2799–2810 (2008). doi: [10.1101/gad.484208](https://doi.org/10.1101/gad.484208); pmid: [18923078](https://pubmed.ncbi.nlm.nih.gov/18923078/)
78. Z. Gao et al., PCGF homologs, CBX proteins, and RYBP define functionally distinct PRC1 family complexes. *Mol. Cell* **45**, 344–356 (2012). doi: [10.1016/j.molcel.2012.01.002](https://doi.org/10.1016/j.molcel.2012.01.002); pmid: [22325352](https://pubmed.ncbi.nlm.nih.gov/22325352/)
79. H. Wang et al., Role of histone H2A ubiquitination in Polycomb silencing. *Nature* **431**, 873–878 (2004). doi: [10.1038/nature02985](https://doi.org/10.1038/nature02985); pmid: [15386022](https://pubmed.ncbi.nlm.nih.gov/15386022/)
80. M. Endoh et al., Histone H2A mono-ubiquitination is a crucial step to mediate PRC1-dependent repression of developmental genes to maintain ES cell identity. *PLOS Genet.* **8**, e1002774 (2012). doi: [10.1371/journal.pgen.1002774](https://doi.org/10.1371/journal.pgen.1002774); pmid: [22844243](https://pubmed.ncbi.nlm.nih.gov/22844243/)
81. R. S. Illingworth et al., The E3 ubiquitin ligase activity of RING1B is not essential for early mouse development. *Genes Dev.* **29**, 1897–1902 (2015). pmid: [26385961](https://pubmed.ncbi.nlm.nih.gov/26385961/)
82. A. R. Pengelly, R. Kalb, K. Finkl, J. Müller, Transcriptional repression by PRC1 in the absence of H2A monoubiquitylation. *Genes Dev.* **29**, 1487–1492 (2015). doi: [10.1101/gad.265439.115](https://doi.org/10.1101/gad.265439.115); pmid: [26178786](https://pubmed.ncbi.nlm.nih.gov/26178786/)
83. R. Cao, Y. Tsukada, Y. Zhang, Role of Bmi-1 and Ring1A in H2A ubiquitylation and Hox gene silencing. *Mol. Cell* **20**, 845–854 (2005). doi: [10.1016/j.molcel.2005.12.002](https://doi.org/10.1016/j.molcel.2005.12.002); pmid: [16359901](https://pubmed.ncbi.nlm.nih.gov/16359901/)
84. A. Piunti, D. Pasini, Epigenetic factors in cancer development: Polycomb group proteins. *Future Oncol.* **7**, 57–75 (2011). doi: [10.2217/fon.10.157](https://doi.org/10.2217/fon.10.157); pmid: [21174538](https://pubmed.ncbi.nlm.nih.gov/21174538/)
85. L. Tavares et al., RYBP-PRC1 complexes mediate H2A ubiquitylation at polycomb target sites independently of PRC2 and H3K27me3. *Cell* **148**, 664–678 (2012). doi: [10.1016/j.cell.2011.12.029](https://doi.org/10.1016/j.cell.2011.12.029); pmid: [22325148](https://pubmed.ncbi.nlm.nih.gov/22325148/)
86. L. Morey, L. Aloia, L. Cozzuto, S. A. Benitah, L. Di Croce, RYBP and Cbx7 define specific biological functions of polycomb complexes in mouse embryonic stem cells. *Cell Reports* **3**, 60–69 (2013). doi: [10.1016/j.celrep.2012.11.026](https://doi.org/10.1016/j.celrep.2012.11.026); pmid: [23273917](https://pubmed.ncbi.nlm.nih.gov/23273917/)
87. N. P. Blackledge et al., Variant PRC1 complex-dependent H2A ubiquitylation drives PRC2 recruitment and polycomb domain formation. *Cell* **157**, 1445–1459 (2014). doi: [10.1016/j.cell.2014.05.004](https://doi.org/10.1016/j.cell.2014.05.004); pmid: [24856970](https://pubmed.ncbi.nlm.nih.gov/24856970/)
88. R. Kalb et al., Histone H2A monoubiquitination promotes histone H3 methylation in Polycomb repression. *Nat. Struct. Mol. Biol.* **21**, 569–571 (2014). doi: [10.1038/nsmb.2833](https://doi.org/10.1038/nsmb.2833); pmid: [24837194](https://pubmed.ncbi.nlm.nih.gov/24837194/)
89. A. Sparmann, M. van Lohuizen, Polycomb silencers control cell fate, development and cancer. *Nat. Rev. Cancer* **6**, 846–856 (2006). doi: [10.1038/nrc1991](https://doi.org/10.1038/nrc1991); pmid: [17060944](https://pubmed.ncbi.nlm.nih.gov/17060944/)
90. V. Orlando, E. P. Jane, V. Chinwalla, P. J. Harte, R. Paro, Binding of trithorax and Polycomb proteins to the bithorax complex: Dynamic changes during early *Drosophila* embryogenesis. *EMBO J.* **17**, 5141–5150 (1998). doi: [10.1093/emboj/17.17.5141](https://doi.org/10.1093/emboj/17.17.5141); pmid: [9724650](https://pubmed.ncbi.nlm.nih.gov/9724650/)
91. N. Soshnikova, Dynamics of Polycomb and Trithorax activities during development. *Birth Defects Res. A Clin. Mol. Teratol.* **91**, 781–787 (2011). doi: [10.1002/bdra.20774](https://doi.org/10.1002/bdra.20774); pmid: [21290568](https://pubmed.ncbi.nlm.nih.gov/21290568/)
92. L. Morey, A. Santanach, L. Di Croce, Pluripotency and epigenetic factors in mouse embryonic stem cell fate regulation. *Mol. Cell. Biol.* **35**, 2716–2728 (2015). doi: [10.1128/MCB.00266-15](https://doi.org/10.1128/MCB.00266-15); pmid: [26031336](https://pubmed.ncbi.nlm.nih.gov/26031336/)
93. T. T. Onder et al., Chromatin-modifying enzymes as modulators of reprogramming. *Nature* **483**, 598–602 (2012). doi: [10.1038/nature10953](https://doi.org/10.1038/nature10953); pmid: [22388813](https://pubmed.ncbi.nlm.nih.gov/22388813/)
94. L. A. Boyer et al., Polycomb complexes repress developmental regulators in murine embryonic stem cells. *Nature* **441**, 349–353 (2006). doi: [10.1038/nature04733](https://doi.org/10.1038/nature04733); pmid: [16625203](https://pubmed.ncbi.nlm.nih.gov/16625203/)
95. M. Endoh et al., Polycomb group proteins Ring1A/B are functionally linked to the core transcriptional regulatory circuitry to maintain ES cell identity. *Development* **135**, 1513–1524 (2008). doi: [10.1242/dev.014340](https://doi.org/10.1242/dev.014340); pmid: [18339675](https://pubmed.ncbi.nlm.nih.gov/18339675/)
96. M. Ku et al., Genomewide analysis of PRC1 and PRC2 occupancy identifies two classes of bivalent domains. *PLOS Genet.* **4**, e1000242 (2008). doi: [10.1371/journal.pgen.1000242](https://doi.org/10.1371/journal.pgen.1000242); pmid: [18974828](https://pubmed.ncbi.nlm.nih.gov/18974828/)
97. G. Cavalli, PRC1 proteins orchestrate three-dimensional genome architecture. *Nat. Genet.* **47**, 1105–1106 (2015). doi: [10.1038/ng.3411](https://doi.org/10.1038/ng.3411); pmid: [26417860](https://pubmed.ncbi.nlm.nih.gov/26417860/)
98. C. Lanzuolo, V. Roure, J. Dekker, F. Bantignies, V. Orlando, Polycomb response elements mediate the formation of chromosome higher-order structures in the bithorax complex. *Nat. Cell Biol.* **9**, 1167–1174 (2007). doi: [10.1038/ncb1637](https://doi.org/10.1038/ncb1637); pmid: [17828248](https://pubmed.ncbi.nlm.nih.gov/17828248/)
99. F. Bantignies et al., Polycomb-dependent regulatory contacts between distant Hox loci in *Drosophila*. *Cell* **144**, 214–226 (2011). doi: [10.1016/j.cell.2010.12.026](https://doi.org/10.1016/j.cell.2010.12.026); pmid: [21241892](https://pubmed.ncbi.nlm.nih.gov/21241892/)
100. M. Denholtz et al., Long-range chromatin contacts in embryonic stem cells reveal a role for pluripotency factors and polycomb proteins in genome organization. *Cell Stem Cell* **13**, 602–616 (2013). doi: [10.1016/j.stem.2013.08.013](https://doi.org/10.1016/j.stem.2013.08.013); pmid: [24035354](https://pubmed.ncbi.nlm.nih.gov/24035354/)
101. S. Schoenfelder et al., Polycomb repressive complex PRC1 spatially constrains the mouse embryonic stem cell genome. *Nat. Genet.* **47**, 1179–1186 (2015). doi: [10.1038/ng.3393](https://doi.org/10.1038/ng.3393); pmid: [26323060](https://pubmed.ncbi.nlm.nih.gov/26323060/)
102. F. Antequera, A. Bird, Number of CpG islands and genes in human and mouse. *Proc. Natl. Acad. Sci. U.S.A.* **90**, 11995–11999 (1993). doi: [10.1073/pnas.90.24.11995](https://doi.org/10.1073/pnas.90.24.11995); pmid: [7505451](https://pubmed.ncbi.nlm.nih.gov/7505451/)
103. A. Patsialou, D. Wisker, E. Moran, DNA-binding properties of ARID family proteins. *Nucleic Acids Res.* **33**, 66–80 (2005). doi: [10.1093/nar/gki145](https://doi.org/10.1093/nar/gki145); pmid: [15640446](https://pubmed.ncbi.nlm.nih.gov/15640446/)
104. H. M. Herz et al., Polycomb repressive complex 2-dependent and -independent functions of Jarid2 in transcriptional regulation in *Drosophila*. *Mol. Cell. Biol.* **32**, 1683–1693 (2012). doi: [10.1128/MCB.06503-11](https://doi.org/10.1128/MCB.06503-11); pmid: [22354997](https://pubmed.ncbi.nlm.nih.gov/22354997/)
105. H. K. Long, N. P. Blackledge, R. J. Klose, ZF-CxxC domain-containing proteins, CpG islands and the chromatin connection. *Biochem. Soc. Trans.* **41**, 727–740 (2013). doi: [10.1042/BST20130028](https://doi.org/10.1042/BST20130028); pmid: [23697932](https://pubmed.ncbi.nlm.nih.gov/23697932/)
106. A. M. Farcas et al., KDM2B links the Polycomb Repressive Complex 1 (PRC1) to recognition of CpG islands. *eLife* **1**, e00205 (2012). doi: [10.7554/eLife.00205](https://doi.org/10.7554/eLife.00205); pmid: [23256043](https://pubmed.ncbi.nlm.nih.gov/23256043/)
107. J. He et al., Kdm2b maintains murine embryonic stem cell status by recruiting PRC1 complex to CpG islands of developmental genes. *Nat. Cell Biol.* **15**, 373–384 (2013). doi: [10.1038/ncb2702](https://doi.org/10.1038/ncb2702); pmid: [23502314](https://pubmed.ncbi.nlm.nih.gov/23502314/)
108. X. Wu, J. V. Johansen, K. Helin, Fbxl10/Kdm2b recruits polycomb repressive complex 1 to CpG islands and regulates H2A ubiquitylation. *Mol. Cell* **49**, 1134–1146 (2013). doi: [10.1016/j.molcel.2013.01.016](https://doi.org/10.1016/j.molcel.2013.01.016); pmid: [23395003](https://pubmed.ncbi.nlm.nih.gov/23395003/)
109. L. Morey et al., Nonoverlapping functions of the Polycomb group Cbx family of proteins in embryonic stem cells. *Cell Stem Cell* **10**, 47–62 (2012). doi: [10.1016/j.stem.2011.12.006](https://doi.org/10.1016/j.stem.2011.12.006); pmid: [22226355](https://pubmed.ncbi.nlm.nih.gov/22226355/)
110. A. O'Loghlen et al., MicroRNA regulation of Cbx7 mediates a switch of Polycomb orthologs during ESC differentiation. *Cell Stem Cell* **10**, 33–46 (2012). doi: [10.1016/j.stem.2011.12.004](https://doi.org/10.1016/j.stem.2011.12.004); pmid: [22226354](https://pubmed.ncbi.nlm.nih.gov/22226354/)
111. B. E. Bernstein et al., A bivalent chromatin structure marks key developmental genes in embryonic stem cells. *Cell* **125**, 315–326 (2006). doi: [10.1016/j.cell.2006.02.041](https://doi.org/10.1016/j.cell.2006.02.041); pmid: [16638019](https://pubmed.ncbi.nlm.nih.gov/16638019/)
112. K. Cui et al., Chromatin signatures in multipotent human hematopoietic stem cells indicate the fate of bivalent genes during differentiation. *Cell Stem Cell* **4**, 80–93 (2009). doi: [10.1016/j.stem.2008.11.011](https://doi.org/10.1016/j.stem.2008.11.011); pmid: [19128795](https://pubmed.ncbi.nlm.nih.gov/19128795/)
113. T. S. Mikkelsen et al., Genome-wide maps of chromatin state in pluripotent and lineage-committed cells. *Nature* **448**, 553–560 (2007). doi: [10.1038/nature06008](https://doi.org/10.1038/nature06008); pmid: [17603471](https://pubmed.ncbi.nlm.nih.gov/17603471/)
114. N. S. Christophersen, K. Helin, Epigenetic control of embryonic stem cell fate. *J. Exp. Med.* **207**, 2287–2295 (2010). doi: [10.1084/jem.20101438](https://doi.org/10.1084/jem.20101438); pmid: [20975044](https://pubmed.ncbi.nlm.nih.gov/20975044/)
115. P. Voigt, W. W. Tee, D. Reinberg, A double take on bivalent promoters. *Genes Dev.* **27**, 1318–1338 (2013). doi: [10.1101/gad.219626.113](https://doi.org/10.1101/gad.219626.113); pmid: [23788621](https://pubmed.ncbi.nlm.nih.gov/23788621/)
116. S. Lubitz, S. Glaser, J. Schaff, A. F. Stewart, K. Anastasiadis, Increased apoptosis and skewed differentiation in mouse embryonic stem cells lacking the histone methyltransferase Mll2. *Mol. Biol. Cell* **18**, 2356–2366 (2007). doi: [10.1091/mbc.E06-11-1060](https://doi.org/10.1091/mbc.E06-11-1060); pmid: [17429066](https://pubmed.ncbi.nlm.nih.gov/17429066/)
117. A. S. Bledau et al., The H3K4 methyltransferase Setd1a is first required at the epiblast stage, whereas Setd1b becomes essential after gastrulation. *Development* **141**, 1022–1035 (2014). doi: [10.1242/dev.098152](https://doi.org/10.1242/dev.098152); pmid: [24550110](https://pubmed.ncbi.nlm.nih.gov/24550110/)
118. M. A. Morgan, A. Shilatfard, Chromatin signatures of cancer. *Genes Dev.* **29**, 238–249 (2015). doi: [10.1101/gad.255182.114](https://doi.org/10.1101/gad.255182.114); pmid: [25644600](https://pubmed.ncbi.nlm.nih.gov/25644600/)
119. M. Mohan, C. Lin, E. Guest, A. Shilatfard, Licensed to elongate: A molecular mechanism for MLL-based leukaemogenesis. *Nat. Rev. Cancer* **10**, 721–728 (2010). doi: [10.1038/nrc2915](https://doi.org/10.1038/nrc2915); pmid: [20844554](https://pubmed.ncbi.nlm.nih.gov/20844554/)
120. J. J. Schuringa, E. Vellenga, Role of the polycomb group gene Bmi1 in normal and leukemic hematopoietic stem and progenitor cells. *Curr. Opin. Hematol.* **17**, 294–299 (2010). doi: [10.1097/MOH.0b013e328338c439](https://doi.org/10.1097/MOH.0b013e328338c439); pmid: [20308890](https://pubmed.ncbi.nlm.nih.gov/20308890/)
121. K. A. Skulte, L. Phan, S. J. Clark, P. C. Taberlay, Chromatin remodeler mutations in human cancers: Epigenetic implications. *Epigenomics* **6**, 397–414 (2014). doi: [10.2217/epi.14.37](https://doi.org/10.2217/epi.14.37); pmid: [25333849](https://pubmed.ncbi.nlm.nih.gov/25333849/)
122. W. Timp, A. P. Feinberg, Cancer as a dysregulated epigenome allowing cellular growth advantage at the expense of the host. *Nat. Rev. Cancer* **13**, 497–510 (2013). doi: [10.1038/nrc3486](https://doi.org/10.1038/nrc3486); pmid: [23760024](https://pubmed.ncbi.nlm.nih.gov/23760024/)
123. G. Cimino et al., Cloning of ALL-1, the locus involved in leukemias with the t(4;11)(q21;q23), t(9;11)(p22;q23), and t(11;19)(q23;p13) chromosome translocations. *Cancer Res.* **51**, 6712–6714 (1991). pmid: [1835902](https://pubmed.ncbi.nlm.nih.gov/1835902/)
124. T. Cierpicki et al., Structure of the MLL CXXC domain-DNA complex and its functional role in MLL-AF9 leukemia. *Nat. Struct. Mol. Biol.* **17**, 62–68 (2010). doi: [10.1038/nsmb.1714](https://doi.org/10.1038/nsmb.1714); pmid: [20010842](https://pubmed.ncbi.nlm.nih.gov/20010842/)
125. P. M. Ayton, E. H. Chen, M. L. Cleary, Binding to nonmethylated CpG DNA is essential for target recognition, transactivation, and myeloid transformation by an MLL oncoprotein. *Mol. Cell. Biol.* **24**, 10470–10478 (2004). doi: [10.1128/MCB.24.23.10470-10478.2004](https://doi.org/10.1128/MCB.24.23.10470-10478.2004); pmid: [15542854](https://pubmed.ncbi.nlm.nih.gov/15542854/)
126. A. Shilatfard, W. S. Lane, K. W. Jackson, R. C. Conaway, J. W. Conaway, An RNA polymerase II elongation factor encoded by the human ELL gene. *Science* **271**, 1873–1876 (1996). doi: [10.1126/science.271.5257.1873](https://doi.org/10.1126/science.271.5257.1873); pmid: [8596958](https://pubmed.ncbi.nlm.nih.gov/8596958/)
127. J. E. Rubnitz, J. Morrissey, P. A. Savage, M. L. Cleary, ENL, the gene fused with HRX in t(11;19) leukemias, encodes a nuclear protein with transcriptional activation potential in lymphoid and myeloid cells. *Blood* **84**, 1747–1752 (1994). pmid: [8080983](https://pubmed.ncbi.nlm.nih.gov/8080983/)
128. R. Prasad et al., Domains with transcriptional regulatory activity within the ALL1 and AF4 proteins involved in acute leukemia. *Proc. Natl. Acad. Sci. U.S.A.* **92**, 12160–12164 (1995). doi: [10.1073/pnas.92.26.12160](https://doi.org/10.1073/pnas.92.26.12160); pmid: [8618864](https://pubmed.ncbi.nlm.nih.gov/8618864/)
129. C. Lin et al., AFF4, a component of the ELL/P-TEFb elongation complex and a shared subunit of MLL chimeras, can link transcription elongation to leukemia. *Mol. Cell* **37**, 429–437 (2010). doi: [10.1016/j.molcel.2010.01.026](https://doi.org/10.1016/j.molcel.2010.01.026); pmid: [20159561](https://pubmed.ncbi.nlm.nih.gov/20159561/)
130. A. Yokoyama, M. Lin, A. Naresh, I. Kitabayashi, M. L. Cleary, A higher-order complex containing AF4 and ENL family proteins with P-TEFb facilitates oncogenic and physiologic MLL-dependent transcription. *Cancer Cell* **17**, 198–212 (2010). doi: [10.1016/j.ccr.2009.12.040](https://doi.org/10.1016/j.ccr.2009.12.040); pmid: [20153263](https://pubmed.ncbi.nlm.nih.gov/20153263/)
131. Y. X. Chen et al., The tumor suppressor merlin regulates hematopoiesis and myeloid transformation by influencing Hox gene expression. *Proc. Natl. Acad. Sci. U.S.A.* **103**, 1018–1023 (2006). doi: [10.1073/pnas.0510347103](https://doi.org/10.1073/pnas.0510347103); pmid: [16415155](https://pubmed.ncbi.nlm.nih.gov/16415155/)
132. A. T. Thiel et al., MLL-AF9-induced leukemogenesis requires coexpression of the wild-type Mll allele. *Cancer Cell* **17**, 148–159 (2010). doi: [10.1016/j.ccr.2009.12.034](https://doi.org/10.1016/j.ccr.2009.12.034); pmid: [20159607](https://pubmed.ncbi.nlm.nih.gov/20159607/)
133. F. Cao et al., Targeting MLL1 H3K4 methyltransferase activity in mixed-lineage leukemia. *Mol. Cell* **53**, 247–261 (2014). doi: [10.1016/j.molcel.2013.12.001](https://doi.org/10.1016/j.molcel.2013.12.001); pmid: [24389101](https://pubmed.ncbi.nlm.nih.gov/24389101/)
134. F. Grebien et al., Pharmacological targeting of the Wdr5-MLL interaction in C/EBP α N-terminal leukemia. *Nat. Chem. Biol.* **11**, 571–578 (2015). doi: [10.1038/nchembio.1859](https://doi.org/10.1038/nchembio.1859); pmid: [26167872](https://pubmed.ncbi.nlm.nih.gov/26167872/)
135. M. A. Dawson, T. Kouzarides, Cancer epigenetics: From mechanism to therapy. *Cell* **150**, 12–27 (2012). doi: [10.1016/j.cell.2012.06.013](https://doi.org/10.1016/j.cell.2012.06.013); pmid: [22770212](https://pubmed.ncbi.nlm.nih.gov/22770212/)
136. S. B. Ng et al., Exome sequencing identifies MLL2 mutations as a cause of Kabuki syndrome. *Nat. Genet.* **42**, 790–793 (2010). doi: [10.1038/ng.646](https://doi.org/10.1038/ng.646); pmid: [20711175](https://pubmed.ncbi.nlm.nih.gov/20711175/)
137. L. Pasqualucci et al., Analysis of the coding genome of diffuse large B-cell lymphoma. *Nat. Genet.* **43**, 830–837 (2011). doi: [10.1038/ng.892](https://doi.org/10.1038/ng.892); pmid: [21804550](https://pubmed.ncbi.nlm.nih.gov/21804550/)

138. R. D. Morin *et al.*, Frequent mutation of histone-modifying genes in non-Hodgkin lymphoma. *Nature* **476**, 298–303 (2011). doi: [10.1038/nature10351](https://doi.org/10.1038/nature10351); pmid: [21796119](https://pubmed.ncbi.nlm.nih.gov/21796119/)
139. J. Zhang *et al.*, Disruption of KMT2D perturbs germinal center B cell development and promotes lymphomagenesis. *Nat. Med.* **21**, 1190–1198 (2015). doi: [10.1038/nm.3940](https://doi.org/10.1038/nm.3940); pmid: [26366712](https://pubmed.ncbi.nlm.nih.gov/26366712/)
140. A. Ortega-Molina *et al.*, The histone lysine methyltransferase KMT2D sustains a gene expression program that represses B cell lymphoma development. *Nat. Med.* **21**, 1199–1208 (2015). doi: [10.1038/nm.3943](https://doi.org/10.1038/nm.3943); pmid: [26366710](https://pubmed.ncbi.nlm.nih.gov/26366710/)
141. D. W. Parsons *et al.*, The genetic landscape of the childhood cancer medulloblastoma. *Science* **331**, 435–439 (2011). doi: [10.1126/science.1198056](https://doi.org/10.1126/science.1198056); pmid: [21163964](https://pubmed.ncbi.nlm.nih.gov/21163964/)
142. C. Kandath *et al.*, Mutational landscape and significance across 12 major cancer types. *Nature* **502**, 333–339 (2013). doi: [10.1038/nature12634](https://doi.org/10.1038/nature12634); pmid: [24132290](https://pubmed.ncbi.nlm.nih.gov/24132290/)
143. Y. Gui *et al.*, Frequent mutations of chromatin remodeling genes in transitional cell carcinoma of the bladder. *Nat. Genet.* **43**, 875–878 (2011). doi: [10.1038/ng.907](https://doi.org/10.1038/ng.907); pmid: [21822268](https://pubmed.ncbi.nlm.nih.gov/21822268/)
144. G. Guo *et al.*, Whole-genome and whole-exome sequencing of bladder cancer identifies frequent alterations in genes involved in sister chromatid cohesion and segregation. *Nat. Genet.* **45**, 1459–1463 (2013). doi: [10.1038/ng.2798](https://doi.org/10.1038/ng.2798); pmid: [24121792](https://pubmed.ncbi.nlm.nih.gov/24121792/)
145. J. Lee *et al.*, A tumor suppressive coactivator complex of p53 containing ASC-2 and histone H3-lysine-4 methyltransferase MLL3 or its paralogue MLL4. *Proc. Natl. Acad. Sci. U.S.A.* **106**, 8513–8518 (2009). doi: [10.1073/pnas.0902873106](https://doi.org/10.1073/pnas.0902873106); pmid: [19433796](https://pubmed.ncbi.nlm.nih.gov/19433796/)
146. G. van Haften *et al.*, Somatic mutations of the histone H3K27 demethylase gene UTX in human cancer. *Nat. Genet.* **41**, 521–523 (2009). doi: [10.1038/ng.349](https://doi.org/10.1038/ng.349); pmid: [19330029](https://pubmed.ncbi.nlm.nih.gov/19330029/)
147. J. Van der Meulen *et al.*, The H3K27me3 demethylase UTX is a gender-specific tumor suppressor in T-cell acute lymphoblastic leukemia. *Blood* **125**, 13–21 (2015). doi: [10.1182/blood-2014-05-577270](https://doi.org/10.1182/blood-2014-05-577270); pmid: [25320243](https://pubmed.ncbi.nlm.nih.gov/25320243/)
148. P. Ntziachristos *et al.*, Contrasting roles of histone 3 lysine 27 demethylases in acute lymphoblastic leukaemia. *Nature* **514**, 513–517 (2014). doi: [10.1038/nature13605](https://doi.org/10.1038/nature13605); pmid: [25132549](https://pubmed.ncbi.nlm.nih.gov/25132549/)
149. K. Agger *et al.*, UTX and JMJD3 are histone H3K27 demethylases involved in HOX gene regulation and development. *Nature* **449**, 731–734 (2007). doi: [10.1038/nature06145](https://doi.org/10.1038/nature06145); pmid: [17713478](https://pubmed.ncbi.nlm.nih.gov/17713478/)
150. E. Calo, J. Wysocka, Modification of enhancer chromatin: What, how, and why? *Mol. Cell* **49**, 825–837 (2013). doi: [10.1016/j.molcel.2013.01.038](https://doi.org/10.1016/j.molcel.2013.01.038); pmid: [23473601](https://pubmed.ncbi.nlm.nih.gov/23473601/)
151. B. Akhtar-Zaidi *et al.*, Epigenomic enhancer profiling defines a signature of colon cancer. *Science* **336**, 736–739 (2012). doi: [10.1126/science.1217277](https://doi.org/10.1126/science.1217277); pmid: [22499810](https://pubmed.ncbi.nlm.nih.gov/22499810/)
152. S. Varambally *et al.*, The polycomb group protein EZH2 is involved in progression of prostate cancer. *Nature* **419**, 624–629 (2002). doi: [10.1038/nature01075](https://doi.org/10.1038/nature01075); pmid: [12374981](https://pubmed.ncbi.nlm.nih.gov/12374981/)
153. A. P. Bracken *et al.*, EZH2 is downstream of the pRB-E2F pathway, essential for proliferation and amplified in cancer. *EMBO J.* **22**, 5323–5335 (2003). doi: [10.1093/emboj/cdg542](https://doi.org/10.1093/emboj/cdg542); pmid: [14532106](https://pubmed.ncbi.nlm.nih.gov/14532106/)
154. A. Piumi *et al.*, Polycomb proteins control proliferation and transformation independently of cell cycle checkpoints by regulating DNA replication. *Nat. Commun.* **5**, 3649 (2014). doi: [10.1038/ncomms4649](https://doi.org/10.1038/ncomms4649); pmid: [24728135](https://pubmed.ncbi.nlm.nih.gov/24728135/)
155. R. D. Morin *et al.*, Somatic mutations altering EZH2 (Tyr641) in follicular and diffuse large B-cell lymphomas of germinal-center origin. *Nat. Genet.* **42**, 181–185 (2010). doi: [10.1038/ng.518](https://doi.org/10.1038/ng.518); pmid: [20081860](https://pubmed.ncbi.nlm.nih.gov/20081860/)
156. F. J. van Kemenade *et al.*, Coexpression of BMI-1 and EZH2 polycomb-group proteins is associated with cycling cells and degree of malignancy in B-cell non-Hodgkin lymphoma. *Blood* **97**, 3896–3901 (2001). doi: [10.1182/blood.V97.12.3896](https://doi.org/10.1182/blood.V97.12.3896); pmid: [11389032](https://pubmed.ncbi.nlm.nih.gov/11389032/)
157. C. J. Sneeringer *et al.*, Coordinated activities of wild-type plus mutant EZH2 drive tumor-associated hypertrimethylation of lysine 27 on histone H3 (H3K27) in human B-cell lymphomas. *Proc. Natl. Acad. Sci. U.S.A.* **107**, 20980–20985 (2010). doi: [10.1073/pnas.1012525107](https://doi.org/10.1073/pnas.1012525107); pmid: [21078963](https://pubmed.ncbi.nlm.nih.gov/21078963/)
158. D. B. Yap *et al.*, Somatic mutations at EZH2 Y641 act dominantly through a mechanism of selectively altered PRC2 catalytic activity, to increase H3K27 trimethylation. *Blood* **117**, 2451–2459 (2011). doi: [10.1182/blood-2010-11-321208](https://doi.org/10.1182/blood-2010-11-321208); pmid: [21190999](https://pubmed.ncbi.nlm.nih.gov/21190999/)
159. S. K. Knutson *et al.*, A selective inhibitor of EZH2 blocks H3K27 methylation and kills mutant lymphoma cells. *Nat. Chem. Biol.* **8**, 890–896 (2012). pmid: [23023262](https://pubmed.ncbi.nlm.nih.gov/23023262/)
160. M. T. McCabe *et al.*, EZH2 inhibition as a therapeutic strategy for lymphoma with EZH2-activating mutations. *Nature* **492**, 108–112 (2012). doi: [10.1038/nature11606](https://doi.org/10.1038/nature11606); pmid: [23051747](https://pubmed.ncbi.nlm.nih.gov/23051747/)
161. W. Béguelin *et al.*, EZH2 is required for germinal center formation and somatic EZH2 mutations promote lymphoid transformation. *Cancer Cell* **23**, 677–692 (2013). doi: [10.1016/j.ccr.2013.04.011](https://doi.org/10.1016/j.ccr.2013.04.011); pmid: [23680150](https://pubmed.ncbi.nlm.nih.gov/23680150/)
162. C. Simon *et al.*, A key role for EZH2 and associated genes in mouse and human adult T-cell acute leukemia. *Genes Dev.* **26**, 651–656 (2012). doi: [10.1101/gad.186411.111](https://doi.org/10.1101/gad.186411.111); pmid: [22431509](https://pubmed.ncbi.nlm.nih.gov/22431509/)
163. P. Ntziachristos *et al.*, Genetic inactivation of the polycomb repressive complex 2 in T cell acute lymphoblastic leukemia. *Nat. Med.* **18**, 298–303 (2012). doi: [10.1038/nm.2651](https://doi.org/10.1038/nm.2651); pmid: [22237151](https://pubmed.ncbi.nlm.nih.gov/22237151/)
164. M. Mochizuki-Kashio *et al.*, Ezh2 loss in hematopoietic stem cells predisposes mice to develop heterogeneous malignancies in an Ezh1-dependent manner. *Blood* **126**, 1172–1183 (2015). doi: [10.1182/blood-2015-03-634428](https://doi.org/10.1182/blood-2015-03-634428); pmid: [26219303](https://pubmed.ncbi.nlm.nih.gov/26219303/)
165. W. Lee *et al.*, PRC2 is recurrently inactivated through EED or SUZ12 loss in malignant peripheral nerve sheath tumors. *Nat. Genet.* **46**, 1227–1232 (2014). doi: [10.1038/ng.3095](https://doi.org/10.1038/ng.3095); pmid: [25240281](https://pubmed.ncbi.nlm.nih.gov/25240281/)
166. M. Zhang *et al.*, Somatic mutations of SUZ12 in malignant peripheral nerve sheath tumors. *Nat. Genet.* **46**, 1170–1172 (2014). doi: [10.1038/ng.3116](https://doi.org/10.1038/ng.3116); pmid: [25305755](https://pubmed.ncbi.nlm.nih.gov/25305755/)
167. G. Wu *et al.*, St. Jude Children's Research Hospital–Washington University Pediatric Cancer Genome Project, Somatic histone H3 alterations in pediatric diffuse intrinsic pontine gliomas and non-brainstem glioblastomas. *Nat. Genet.* **44**, 251–253 (2012). doi: [10.1038/ng.1102](https://doi.org/10.1038/ng.1102); pmid: [22286216](https://pubmed.ncbi.nlm.nih.gov/22286216/)
168. J. Schwartzentruber *et al.*, Driver mutations in histone H3.3 and chromatin remodelling genes in paediatric glioblastoma. *Nature* **482**, 226–231 (2012). doi: [10.1038/nature10833](https://doi.org/10.1038/nature10833); pmid: [22286061](https://pubmed.ncbi.nlm.nih.gov/22286061/)
169. P. W. Lewis *et al.*, Inhibition of PRC2 activity by a gain-of-function H3 mutation found in pediatric glioblastoma. *Science* **340**, 857–861 (2013). doi: [10.1126/science.1232245](https://doi.org/10.1126/science.1232245); pmid: [23539183](https://pubmed.ncbi.nlm.nih.gov/23539183/)
170. K. M. Chan *et al.*, The histone H3.3K27M mutation in pediatric glioma reprograms H3K27 methylation and gene expression. *Genes Dev.* **27**, 985–990 (2013). doi: [10.1101/gad.217778.113](https://doi.org/10.1101/gad.217778.113); pmid: [23603901](https://pubmed.ncbi.nlm.nih.gov/23603901/)
171. S. Bender *et al.*, Reduced H3K27me3 and DNA hypomethylation are major drivers of gene expression in K27M mutant pediatric high-grade gliomas. *Cancer Cell* **24**, 660–672 (2013). doi: [10.1016/j.ccr.2013.10.006](https://doi.org/10.1016/j.ccr.2013.10.006); pmid: [24183680](https://pubmed.ncbi.nlm.nih.gov/24183680/)
172. H. M. Herz *et al.*, Histone H3 lysine-to-methionine mutants as a paradigm to study chromatin signaling. *Science* **345**, 1065–1070 (2014). doi: [10.1126/science.1255104](https://doi.org/10.1126/science.1255104); pmid: [25170156](https://pubmed.ncbi.nlm.nih.gov/25170156/)
173. M. Jung, K. A. Gelato, A. Fernández-Montalván, S. Siegel, B. Haendler, Targeting BET bromodomains for cancer treatment. *Epigenomics* **7**, 487–501 (2015). doi: [10.2217/epi.14.91](https://doi.org/10.2217/epi.14.91); pmid: [26077433](https://pubmed.ncbi.nlm.nih.gov/26077433/)
174. T. De Raedt *et al.*, PRC2 loss amplifies Ras-driven transcription and confers sensitivity to BRD4-based therapies. *Nature* **514**, 247–251 (2014). pmid: [25119042](https://pubmed.ncbi.nlm.nih.gov/25119042/)
175. D. Pasini *et al.*, Characterization of an antagonistic switch between histone H3 lysine 27 methylation and acetylation in the transcriptional regulation of Polycomb group target genes. *Nucleic Acids Res.* **38**, 4958–4969 (2010). doi: [10.1093/nar/gkq244](https://doi.org/10.1093/nar/gkq244); pmid: [20385584](https://pubmed.ncbi.nlm.nih.gov/20385584/)
176. K. Funato, T. Major, P. W. Lewis, C. D. Allis, V. Tavar, Use of human embryonic stem cells to model pediatric gliomas with H3.3K27M histone mutation. *Science* **346**, 1529–1533 (2014). doi: [10.1126/science.1253799](https://doi.org/10.1126/science.1253799); pmid: [25525250](https://pubmed.ncbi.nlm.nih.gov/25525250/)
177. R. Hashizume *et al.*, Pharmacologic inhibition of histone demethylation as a therapy for pediatric brainstem glioma. *Nat. Med.* **20**, 1394–1396 (2014). pmid: [25401693](https://pubmed.ncbi.nlm.nih.gov/25401693/)
178. S. Henikoff, A. Shilatifard, Histone modification: Cause or cog? *Trends Genet.* **27**, 389–396 (2011). doi: [10.1016/j.tig.2011.06.006](https://doi.org/10.1016/j.tig.2011.06.006); pmid: [21764166](https://pubmed.ncbi.nlm.nih.gov/21764166/)
179. A. R. Pengelly, Ö. Copur, H. Jäckle, A. Herzig, J. Müller, A histone mutant reproduces the phenotype caused by loss of histone-modifying factor Polycomb. *Science* **339**, 698–699 (2013). doi: [10.1126/science.1231382](https://doi.org/10.1126/science.1231382); pmid: [23393264](https://pubmed.ncbi.nlm.nih.gov/23393264/)
180. R. Eskeland *et al.*, Ring1B compacts chromatin structure and represses gene expression independent of histone ubiquitination. *Mol. Cell* **38**, 452–464 (2010). doi: [10.1016/j.molcel.2010.02.032](https://doi.org/10.1016/j.molcel.2010.02.032); pmid: [20471950](https://pubmed.ncbi.nlm.nih.gov/20471950/)
181. N. J. Francis, R. E. Kingston, C. L. Woodcock, Chromatin compaction by a polycomb group protein complex. *Science* **306**, 1574–1577 (2004). doi: [10.1126/science.1100576](https://doi.org/10.1126/science.1100576); pmid: [15567868](https://pubmed.ncbi.nlm.nih.gov/15567868/)
182. K. Xu *et al.*, EZH2 oncogenic activity in castration-resistant prostate cancer cells is Polycomb-independent. *Science* **338**, 1465–1469 (2012). pmid: [23239736](https://pubmed.ncbi.nlm.nih.gov/23239736/)
183. C. Kadoch, G. R. Crabtree, Mammalian SWI/SNF chromatin remodeling complexes and cancer: Mechanistic insights gained from human genomics. *Sci. Adv.* **1**, e1500447 (2015). doi: [10.1126/sciadv.1500447](https://doi.org/10.1126/sciadv.1500447); pmid: [26601204](https://pubmed.ncbi.nlm.nih.gov/26601204/)
184. T. Li *et al.*, SET1A cooperates with CUDR to promote liver cancer growth and hepatocyte-like stem cell malignant transformation epigenetically. *Mol. Ther.* **24**, 261–275 (2016). doi: [10.1038/mt.2015.208](https://doi.org/10.1038/mt.2015.208); pmid: [26581161](https://pubmed.ncbi.nlm.nih.gov/26581161/)
185. B. D. Yu, J. L. Hess, S. E. Horning, G. A. Brown, S. J. Korsmeyer, Altered Hox expression and segmental identity in Mll-mutant mice. *Nature* **378**, 505–508 (1995). doi: [10.1038/378505a0](https://doi.org/10.1038/378505a0); pmid: [7477409](https://pubmed.ncbi.nlm.nih.gov/7477409/)
186. S. Glaser *et al.*, The histone 3 lysine 4 methyltransferase, MLL2, is only required briefly in development and spermatogenesis. *Epigenetics Chromatin* **2**, 5 (2009). doi: [10.1186/1756-8935-2-5](https://doi.org/10.1186/1756-8935-2-5); pmid: [19348672](https://pubmed.ncbi.nlm.nih.gov/19348672/)
187. J. E. Lee *et al.*, H3K4 mono- and di-methyltransferase MLL4 is required for enhancer activation during cell differentiation. *eLife* **2**, e01503 (2013). doi: [10.7554/eLife.01503](https://doi.org/10.7554/eLife.01503); pmid: [24368734](https://pubmed.ncbi.nlm.nih.gov/24368734/)
188. J. Z. Stoller *et al.*, Ash2l interacts with Tbx1 and is required during early embryogenesis. *Exp. Biol. Med. (Maywood)* **235**, 569–576 (2010). doi: [10.1258/ebm.2010.009318](https://doi.org/10.1258/ebm.2010.009318); pmid: [20463296](https://pubmed.ncbi.nlm.nih.gov/20463296/)
189. J. Qi, L. Huo, Y. T. Zhu, Y. J. Zhu, Absent, small or homeotic 2-like protein (ASH2L) enhances the transcription of the estrogen receptor α gene through GATA-binding protein 3 (GATA3). *J. Biol. Chem.* **289**, 31373–31381 (2014). doi: [10.1074/jbc.M114.579839](https://doi.org/10.1074/jbc.M114.579839); pmid: [25258321](https://pubmed.ncbi.nlm.nih.gov/25258321/)
190. A. Bertero *et al.*, Activin/nodal signaling and NANOG orchestrate human embryonic stem cell fate decisions by controlling the H3K4me3 chromatin mark. *Genes Dev.* **29**, 702–717 (2015). doi: [10.1101/gad.255984.114](https://doi.org/10.1101/gad.255984.114); pmid: [25805847](https://pubmed.ncbi.nlm.nih.gov/25805847/)
191. J. S. Crabtree *et al.*, A mouse model of multiple endocrine neoplasia, type 1, develops multiple endocrine tumors. *Proc. Natl. Acad. Sci. U.S.A.* **98**, 1118–1123 (2001). doi: [10.1073/pnas.98.3.1118](https://doi.org/10.1073/pnas.98.3.1118); pmid: [11158604](https://pubmed.ncbi.nlm.nih.gov/11158604/)
192. S. C. Chandrasekharappa *et al.*, Positional cloning of the gene for multiple endocrine neoplasia-type 1. *Science* **276**, 404–407 (1997). doi: [10.1126/science.276.5311.404](https://doi.org/10.1126/science.276.5311.404); pmid: [9103196](https://pubmed.ncbi.nlm.nih.gov/9103196/)
193. J. Grembecka *et al.*, Menin-MLL inhibitors reverse oncogenic activity of MLL fusion proteins in leukemia. *Nat. Chem. Biol.* **8**, 277–284 (2012). doi: [10.1038/nchembio.773](https://doi.org/10.1038/nchembio.773); pmid: [22286128](https://pubmed.ncbi.nlm.nih.gov/22286128/)
194. D. Borkin *et al.*, Pharmacologic inhibition of the Menin-MLL interaction blocks progression of MLL leukemia in vivo. *Cancer Cell* **27**, 589–602 (2015). doi: [10.1016/j.ccr.2015.02.016](https://doi.org/10.1016/j.ccr.2015.02.016); pmid: [25817203](https://pubmed.ncbi.nlm.nih.gov/25817203/)
195. S. Minocha, T.-L. Sung, D. Villeneuve, F. Lammers, W. Herr, Compensatory embryonic response to allele-specific inactivation of the murine X-linked gene Hcfc1. *Dev. Biol.* **412**, 1–17 (2016). doi: [10.1016/j.ydbio.2016.02.019](https://doi.org/10.1016/j.ydbio.2016.02.019); pmid: [26921005](https://pubmed.ncbi.nlm.nih.gov/26921005/)
196. E. A. Cho, M. J. Prindle, G. R. Dressler, BRCT domain-containing protein PTIP is essential for progression through mitosis. *Mol. Cell. Biol.* **23**, 1666–1673 (2003). doi: [10.1128/MCB.23.5.1666-1673.2003](https://doi.org/10.1128/MCB.23.5.1666-1673.2003); pmid: [12588986](https://pubmed.ncbi.nlm.nih.gov/12588986/)
197. E. Callen *et al.*, 53BP1 mediates productive and mutagenic DNA repair through distinct phosphoprotein interactions. *Cell* **153**, 1266–1280 (2013). doi: [10.1016/j.cell.2013.05.023](https://doi.org/10.1016/j.cell.2013.05.023); pmid: [23727112](https://pubmed.ncbi.nlm.nih.gov/23727112/)
198. C. Wang *et al.*, UTX regulates mesoderm differentiation of embryonic stem cells independent of H3K27 demethylase activity. *Proc. Natl. Acad. Sci. U.S.A.* **109**, 15324–15329 (2012). doi: [10.1073/pnas.1204166109](https://doi.org/10.1073/pnas.1204166109); pmid: [22949634](https://pubmed.ncbi.nlm.nih.gov/22949634/)
199. J. H. Kim *et al.*, UTX and MLL4 coordinately regulate transcriptional programs for cell proliferation and invasiveness in breast cancer cells. *Cancer Res.* **74**, 1705–1717 (2014). doi: [10.1158/0008-5472.CAN-13-1896](https://doi.org/10.1158/0008-5472.CAN-13-1896); pmid: [24491801](https://pubmed.ncbi.nlm.nih.gov/24491801/)
200. M. A. Mahajan, H. H. Samuels, Nuclear receptor coactivator/coregulator NCoA6(NRC) is a pleiotropic coregulator involved in transcription, cell survival, growth and development. *Nucl. Recept. Signal.* **6**, e002 (2008). pmid: [18301782](https://pubmed.ncbi.nlm.nih.gov/18301782/)

201. D. O'Carroll *et al.*, The polycomb-group gene Ezh2 is required for early mouse development. *Mol. Cell. Biol.* **21**, 4330–4336 (2001). doi: [10.1128/MCB.21.13.4330-4336.2001](https://doi.org/10.1128/MCB.21.13.4330-4336.2001); pmid: [11390661](https://pubmed.ncbi.nlm.nih.gov/11390661/)
202. K. H. Kim, C. W. Roberts, Targeting EZH2 in cancer. *Nat. Med.* **22**, 128–134 (2016). doi: [10.1038/nm.4036](https://doi.org/10.1038/nm.4036); pmid: [26845405](https://pubmed.ncbi.nlm.nih.gov/26845405/)
203. K. H. Kim *et al.*, SWI/SNF-mutant cancers depend on catalytic and non-catalytic activity of EZH2. *Nat. Med.* **21**, 1491–1496 (2015). doi: [10.1038/nm.3968](https://doi.org/10.1038/nm.3968); pmid: [26552009](https://pubmed.ncbi.nlm.nih.gov/26552009/)
204. B. G. Bitler *et al.*, Synthetic lethality by targeting EZH2 methyltransferase activity in ARID1A-mutated cancers. *Nat. Med.* **21**, 231–238 (2015). pmid: [25686104](https://pubmed.ncbi.nlm.nih.gov/25686104/)
205. L. M. LaFave *et al.*, Loss of BAP1 function leads to EZH2-dependent transformation. *Nat. Med.* **21**, 1344–1349 (2015). doi: [10.1038/nm.3947](https://doi.org/10.1038/nm.3947); pmid: [26437366](https://pubmed.ncbi.nlm.nih.gov/26437366/)
206. R. Bejar *et al.*, Clinical effect of point mutations in myelodysplastic syndromes. *N. Engl. J. Med.* **364**, 2496–2506 (2011). doi: [10.1056/NEJMoa1013343](https://doi.org/10.1056/NEJMoa1013343); pmid: [21714648](https://pubmed.ncbi.nlm.nih.gov/21714648/)
207. E. Ezhkova *et al.*, EZH1 and EZH2 cogovern histone H3K27 trimethylation and are essential for hair follicle homeostasis and wound repair. *Genes Dev.* **25**, 485–498 (2011). doi: [10.1101/gad.201981](https://doi.org/10.1101/gad.201981); pmid: [21317239](https://pubmed.ncbi.nlm.nih.gov/21317239/)
208. J. I. Koontz *et al.*, Frequent fusion of the JAZF1 and JAZ1 genes in endometrial stromal tumors. *Proc. Natl. Acad. Sci. U.S.A.* **98**, 6348–6353 (2001). doi: [10.1073/pnas.101132598](https://doi.org/10.1073/pnas.101132598); pmid: [11371647](https://pubmed.ncbi.nlm.nih.gov/11371647/)
209. A. Schumacher, C. Faust, T. Magnuson, Positional cloning of a global regulator of anterior-posterior patterning in mice. *Nature* **384**, 648 (1996). doi: [10.1038/384648a0](https://doi.org/10.1038/384648a0); pmid: [8984348](https://pubmed.ncbi.nlm.nih.gov/8984348/)
210. T. Neff *et al.*, Polycomb repressive complex 2 is required for MLL-AF9 leukemia. *Proc. Natl. Acad. Sci. U.S.A.* **109**, 5028–5033 (2012). doi: [10.1073/pnas.1202258109](https://doi.org/10.1073/pnas.1202258109); pmid: [22396593](https://pubmed.ncbi.nlm.nih.gov/22396593/)
211. W. Kim *et al.*, Targeted disruption of the EZH2-EED complex inhibits EZH2-dependent cancer. *Nat. Chem. Biol.* **9**, 643–650 (2013). doi: [10.1038/nchembio.1331](https://doi.org/10.1038/nchembio.1331); pmid: [23974116](https://pubmed.ncbi.nlm.nih.gov/23974116/)
212. M. Serresi *et al.*, Polycomb repressive complex 2 is a barrier to KRAS-driven inflammation and epithelial-mesenchymal transition in non-small-cell lung cancer. *Cancer Cell* **29**, 17–31 (2016). doi: [10.1016/j.ccell.2015.12.006](https://doi.org/10.1016/j.ccell.2015.12.006); pmid: [26766588](https://pubmed.ncbi.nlm.nih.gov/26766588/)
213. H. H. Yeh *et al.*, Ras induces experimental lung metastasis through up-regulation of RbAp46 to suppress RECK promoter activity. *BMC Cancer* **15**, 172 (2015). doi: [10.1186/s12885-015-1155-7](https://doi.org/10.1186/s12885-015-1155-7); pmid: [25885317](https://pubmed.ncbi.nlm.nih.gov/25885317/)
214. T. Takeuchi, M. Kojima, K. Nakajima, S. Kondo, jumoni gene is essential for the neurulation and cardiac development of mouse embryos with a C3H/He background. *Mech. Dev.* **86**, 29–38 (1999). doi: [10.1016/S0925-4773\(99\)00100-8](https://doi.org/10.1016/S0925-4773(99)00100-8); pmid: [10446263](https://pubmed.ncbi.nlm.nih.gov/10446263/)
215. Z. S. Walters *et al.*, JARID2 is a direct target of the PAX3-FOXO1 fusion protein and inhibits myogenic differentiation of rhabdomyosarcoma cells. *Oncogene* **33**, 1148–1157 (2014). doi: [10.1038/nc.2013.46](https://doi.org/10.1038/nc.2013.46); pmid: [23435416](https://pubmed.ncbi.nlm.nih.gov/23435416/)
216. J. W. Voncken *et al.*, Rnf2 (Ring1b) deficiency causes gastrulation arrest and cell cycle inhibition. *Proc. Natl. Acad. Sci. U.S.A.* **100**, 2468–2473 (2003). doi: [10.1073/pnas.0434312100](https://doi.org/10.1073/pnas.0434312100); pmid: [12589020](https://pubmed.ncbi.nlm.nih.gov/12589020/)
217. K. Rai *et al.*, Dual Roles of RNF2 in Melanoma Progression. *Cancer Discov.* **5**, 1314–1327 (2015). doi: [10.1158/2159-8290.CD-15-0493](https://doi.org/10.1158/2159-8290.CD-15-0493); pmid: [26450788](https://pubmed.ncbi.nlm.nih.gov/26450788/)
218. V. van den Boom *et al.*, Non-canonical PRC1.1 targets active genes independent of H3K27me3 and is essential for Leukemogenesis. *Cell Reports* **14**, 332–346 (2016). doi: [10.1016/j.celrep.2015.12.034](https://doi.org/10.1016/j.celrep.2015.12.034); pmid: [26748712](https://pubmed.ncbi.nlm.nih.gov/26748712/)
219. M. del Mar Lorente *et al.*, Loss- and gain-of-function mutations show a polycomb group function for Ring1A in mice. *Development* **127**, 5093–5100 (2000). pmid: [11060235](https://pubmed.ncbi.nlm.nih.gov/11060235/)
220. N. M. van der Lugt *et al.*, Posterior transformation, neurological abnormalities, and severe hematopoietic defects in mice with a targeted deletion of the bmi-1 proto-oncogene. *Genes Dev.* **8**, 757–769 (1994). doi: [10.1101/gad.8.7.757](https://doi.org/10.1101/gad.8.7.757); pmid: [7926765](https://pubmed.ncbi.nlm.nih.gov/7926765/)
221. Y. Haupt, M. L. Bath, A. W. Harris, J. M. Adams, bmi-1 transgene induces lymphomas and collaborates with myc in tumorigenesis. *Oncogene* **8**, 3161–3164 (1993). pmid: [8414519](https://pubmed.ncbi.nlm.nih.gov/8414519/)
222. J. J. Jacobs *et al.*, Bmi-1 collaborates with c-Myc in tumorigenesis by inhibiting c-Myc-induced apoptosis via INK4a/ARF. *Genes Dev.* **13**, 2678–2690 (1999). doi: [10.1101/gad.13.20.2678](https://doi.org/10.1101/gad.13.20.2678); pmid: [10541554](https://pubmed.ncbi.nlm.nih.gov/10541554/)
223. J. Lessard, G. Sauvageau, Bmi-1 determines the proliferative capacity of normal and leukaemic stem cells. *Nature* **423**, 255–260 (2003). doi: [10.1038/nature01572](https://doi.org/10.1038/nature01572); pmid: [12714970](https://pubmed.ncbi.nlm.nih.gov/12714970/)
224. S. W. Bruggeman *et al.*, Bmi1 controls tumor development in an Ink4a/Arf-independent manner in a mouse model for glioma. *Cancer Cell* **12**, 328–341 (2007). doi: [10.1016/j.ccr.2007.08.032](https://doi.org/10.1016/j.ccr.2007.08.032); pmid: [17936558](https://pubmed.ncbi.nlm.nih.gov/17936558/)
225. H. Oguro *et al.*, Lethal myelofibrosis induced by Bmi1-deficient hematopoietic cells unveils a tumor suppressor function of the polycomb group genes. *J. Exp. Med.* **209**, 445–454 (2012). doi: [10.1084/jem.20111709](https://doi.org/10.1084/jem.20111709); pmid: [22351929](https://pubmed.ncbi.nlm.nih.gov/22351929/)
226. T. Akasaka *et al.*, A role for mel-18, a Polycomb group-related vertebrate gene, during theanteroposterior specification of the axial skeleton. *Development* **122**, 1513–1522 (1996). pmid: [8625838](https://pubmed.ncbi.nlm.nih.gov/8625838/)
227. W. J. Guo *et al.*, Mel-18 acts as a tumor suppressor by repressing Bmi-1 expression and down-regulating Akt activity in breast cancer cells. *Cancer Res.* **67**, 5083–5089 (2007). doi: [10.1158/0008-5472.CAN-06-4368](https://doi.org/10.1158/0008-5472.CAN-06-4368); pmid: [17545584](https://pubmed.ncbi.nlm.nih.gov/17545584/)
228. J. Y. Lee *et al.*, Mel-18 negatively regulates INK4a/ARF-independent cell cycle progression via Akt inactivation in breast cancer. *Cancer Res.* **68**, 4201–4209 (2008). doi: [10.1158/0008-5472.CAN-07-2570](https://doi.org/10.1158/0008-5472.CAN-07-2570); pmid: [18519679](https://pubmed.ncbi.nlm.nih.gov/18519679/)
229. N. Coré *et al.*, Altered cellular proliferation and mesoderm patterning in Polycomb-M33-deficient mice. *Development* **124**, 721–729 (1997). pmid: [9043087](https://pubmed.ncbi.nlm.nih.gov/9043087/)
230. Y. Katoh-Fukui *et al.*, Male-to-female sex reversal in M33 mutant mice. *Nature* **393**, 688–692 (1998). doi: [10.1038/31482](https://doi.org/10.1038/31482); pmid: [9641679](https://pubmed.ncbi.nlm.nih.gov/9641679/)
231. B. Liu *et al.*, Cbx4 regulates the proliferation of thymic epithelial cells and thymus function. *Development* **140**, 780–788 (2013). doi: [10.1242/dev.085035](https://doi.org/10.1242/dev.085035); pmid: [23362346](https://pubmed.ncbi.nlm.nih.gov/23362346/)
232. J. Li *et al.*, Cbx4 governs HIF-1 α to potentiate angiogenesis of hepatocellular carcinoma by its SUMO E3 ligase activity. *Cancer Cell* **25**, 118–131 (2014). doi: [10.1016/j.ccr.2013.12.008](https://doi.org/10.1016/j.ccr.2013.12.008); pmid: [24434214](https://pubmed.ncbi.nlm.nih.gov/24434214/)
233. F. Forzati *et al.*, CBX7 is a tumor suppressor in mice and humans. *J. Clin. Invest.* **122**, 612–623 (2012). doi: [10.1172/JCI58620](https://doi.org/10.1172/JCI58620); pmid: [22214847](https://pubmed.ncbi.nlm.nih.gov/22214847/)
234. F. Forzati *et al.*, CBX7 gene expression plays a negative role in adipocyte cell growth and differentiation. *Biol. Open* **3**, 871–879 (2014). doi: [10.1242/bio.20147872](https://doi.org/10.1242/bio.20147872); pmid: [25190058](https://pubmed.ncbi.nlm.nih.gov/25190058/)
235. C. L. Scott *et al.*, Role of the chromobox protein CBX7 in lymphomagenesis. *Proc. Natl. Acad. Sci. U.S.A.* **104**, 5389–5394 (2007). doi: [10.1073/pnas.0608721104](https://doi.org/10.1073/pnas.0608721104); pmid: [17374722](https://pubmed.ncbi.nlm.nih.gov/17374722/)
236. K. Klauke *et al.*, Polycomb Cbx family members mediate the balance between haematopoietic stem cell self-renewal and differentiation. *Nat. Cell Biol.* **15**, 353–362 (2013). doi: [10.1038/ncb2701](https://doi.org/10.1038/ncb2701); pmid: [23502315](https://pubmed.ncbi.nlm.nih.gov/23502315/)
237. J. Tan *et al.*, CBX8, a polycomb group protein, is essential for MLL-AF9-induced leukemogenesis. *Cancer Cell* **20**, 563–575 (2011). doi: [10.1016/j.ccr.2011.09.008](https://doi.org/10.1016/j.ccr.2011.09.008); pmid: [22094252](https://pubmed.ncbi.nlm.nih.gov/22094252/)
238. Y. Takihara *et al.*, Targeted disruption of the mouse homologue of the *Drosophila* polyhomeotic gene leads to altered anteroposterior patterning and neural crest defects. *Development* **124**, 3673–3682 (1997). pmid: [9367423](https://pubmed.ncbi.nlm.nih.gov/9367423/)
239. K. Isono *et al.*, Mammalian polyhomeotic homologues Phc2 and Phc1 act in synergy to mediate polycomb repression of Hox genes. *Mol. Cell. Biol.* **25**, 6694–6706 (2005). doi: [10.1128/MCB.25.15.6694-6706.2005](https://doi.org/10.1128/MCB.25.15.6694-6706.2005); pmid: [16024804](https://pubmed.ncbi.nlm.nih.gov/16024804/)
240. M. K. Pirity, J. Locker, N. Schreiber-Agus, Rybp/DEAF is required for early postimplantation and for central nervous system development. *Mol. Cell. Biol.* **25**, 7193–7202 (2005). doi: [10.1128/MCB.25.16.7193-7202.2005](https://doi.org/10.1128/MCB.25.16.7193-7202.2005); pmid: [16055728](https://pubmed.ncbi.nlm.nih.gov/16055728/)
241. A. Danen-van Oorschot *et al.*, Human death effector domain-associated factor interacts with the viral apoptosis agonist Apoptin and exerts tumor-preferential cell killing. *Cell Death Differ.* **11**, 564–573 (2004). doi: [10.1038/sj.cdd.4401391](https://doi.org/10.1038/sj.cdd.4401391); pmid: [14765135](https://pubmed.ncbi.nlm.nih.gov/14765135/)
242. J. Andricovich, Y. Kai, W. Peng, A. Foudi, A. Tzatsos, Histone demethylase KDM2B regulates lineage commitment in normal and malignant hematopoiesis. *J. Clin. Invest.* **126**, 905–920 (2016). doi: [10.1172/JCI84014](https://doi.org/10.1172/JCI84014); pmid: [26808549](https://pubmed.ncbi.nlm.nih.gov/26808549/)
243. A. Tzatsos *et al.*, KDM2B promotes pancreatic cancer via Polycomb-dependent and -independent transcriptional programs. *J. Clin. Invest.* **123**, 727–739 (2013). pmid: [23321669](https://pubmed.ncbi.nlm.nih.gov/23321669/)

ACKNOWLEDGMENTS

We thank all of the members of the Shilatifard laboratory for helpful discussions and in particular E. Smith and M. Morgan for critical suggestions and help with the manuscript, and L. Shilatifard for editorial assistance. We are also grateful to M. Miller for assistance during the preparation of figures for this review. A.P. is an EMBO postdoctoral fellow (ALTF 372-2015), AIRC and Marie Curie Actions – People – COFUND. A.S. is on the scientific advisory boards of Genentech and Cell Signaling Technology. The studies in the Shilatifard laboratory in regard to the Polycomb and COMPASS family are supported by the National Cancer Institute grant R35CA197569.

10.1126/science.aad9780

RESEARCH ARTICLE SUMMARY

PLASMA ASTROPHYSICS

Electron-scale measurements of magnetic reconnection in space

J. L. Burch,* R. B. Torbert, T. D. Phan, L.-J. Chen, T. E. Moore, R. E. Ergun, J. P. Eastwood, D. J. Gershman, P. A. Cassak, M. R. Argall, S. Wang, M. Hesse, C. J. Pollock, B. L. Giles, R. Nakamura, B. H. Mauk, S. A. Fuselier, C. T. Russell, R. J. Strangeway, J. F. Drake, M. A. Shay, Yu. V. Khotyaintsev, P.-A. Lindqvist, G. Marklund, F. D. Wilder, D. T. Young, K. Torkar, J. Goldstein, J. C. Dorelli, L. A. Avanov, M. Oka, D. N. Baker, A. N. Jaynes, K. A. Goodrich, I. J. Cohen, D. L. Turner, J. F. Fennell, J. B. Blake, J. Clemmons, M. Goldman, D. Newman, S. M. Petrinen, K. J. Trattner, B. Lavraud, P. H. Reiff, W. Baumjohann, W. Magnes, M. Steller, W. Lewis, Y. Saito, V. Coffey, M. Chandler

INTRODUCTION: Magnetic reconnection is a physical process occurring in plasmas in which magnetic energy is explosively converted into heat and kinetic energy. The effects of reconnection—such as solar flares, coronal mass ejections, magnetospheric substorms and auroras, and astrophysical plasma jets—have been studied theoretically, modeled with computer simulations, and observed in space. However, the electron-scale kinetic physics, which controls how magnetic field lines break and reconnect, has up to now eluded observation.

RATIONALE: To advance understanding of magnetic reconnection with a definitive exper-

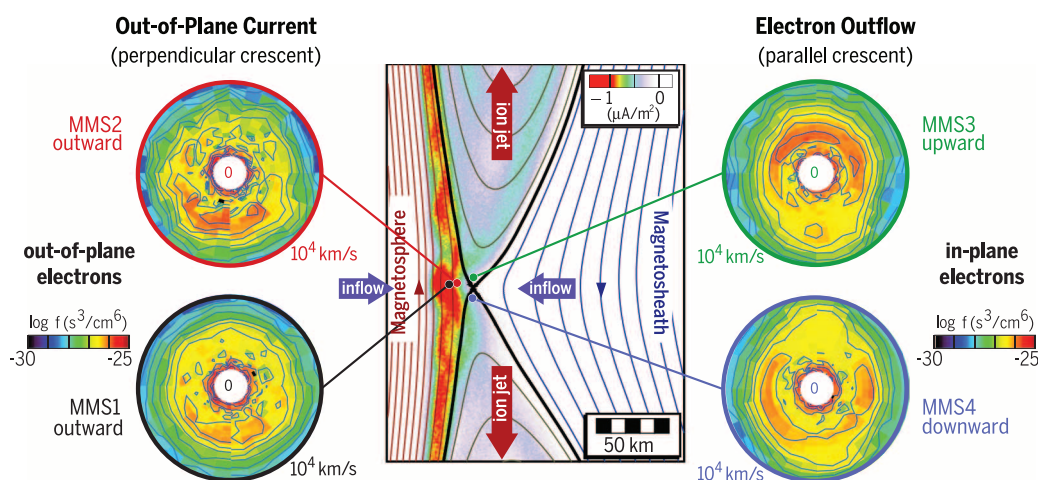
iment in space, NASA developed and launched the Magnetospheric Multiscale (MMS) mission in March 2015. Flying in a tightly controlled tetrahedral formation, the MMS spacecraft can sample the magnetopause, where the interplanetary and geomagnetic fields reconnect, and make detailed measurements of the plasma environment and the electric and magnetic fields in the reconnection region. Because the reconnection dissipation region at the magnetopause is thin (a few kilometers) and moves rapidly back and forth across the spacecraft (10 to 100 km/s), high-resolution measurements are needed to capture the microphysics of reconnection. The most critical measurements are of the three-dimensional electron

distributions, which must be made every 30 ms, or 100 times the fastest rate previously available.

RESULTS: On 16 October 2015, the MMS tetrahedron encountered a reconnection site on the dayside magnetopause and observed (i) the conversion of magnetic energy to particle kinetic energy; (ii) the intense current and electric field that causes the dissipation of magnetic energy; (iii) crescent-shaped electron velocity distributions that carry the current; and (iv) changes in magnetic topology. The crescent-shaped features in the velocity distributions

(left side of the figure) are the result of demagnetization of solar wind electrons as they flow into the reconnection site, and their acceleration and deflection by an outward-pointing electric field that is set up at the magnetopause boundary by plasma density gradients. As they are deflected in these fields, the solar wind electrons mix in with magnetospheric electrons and are accelerated along a meandering path that straddles the boundary, picking up the energy released in annihilating the magnetic field. As evidence of the predicted interconnection of terrestrial and solar wind magnetic fields, the crescent-shaped velocity distributions are diverted along the newly connected magnetic field lines in a narrow layer just at the boundary. This diversion along the field is shown in the right side of the figure.

CONCLUSION: MMS has yielded insights into the microphysics underlying the reconnection between interplanetary and terrestrial magnetic fields. The persistence of the characteristic crescent shape in the electron distributions suggests that the kinetic processes causing magnetic field line reconnection are dominated by electron dynamics, which produces the electric fields and currents that dissipate magnetic energy. The primary evidence for this magnetic dissipation is the appearance of an electric field and a current that are parallel to one another and out of the plane of the figure. MMS has measured this electric field and current, and has identified the important role of electron dynamics in triggering magnetic reconnection. ■



Electron dynamics controls the reconnection between the terrestrial and solar magnetic fields. The process of magnetic reconnection has been a long-standing mystery. With fast particle measurements, NASA's Magnetospheric Multiscale (MMS) mission has measured how electron dynamics controls magnetic reconnection. The data in the circles show electrons with velocities from 0 to 10^4 km/s carrying current out of the page on the left side of the X-line and then flowing upward and downward along the reconnected magnetic field on the right side. The most intense fluxes are red and the least intense are blue. The plot in the center shows magnetic field lines and out-of-plane currents derived from a numerical plasma simulation using the parameters observed by MMS.

The list of author affiliations is available in the full article online.

*Corresponding author. Email: jburch@swri.edu
Cite this article as J. L. Burch et al., *Science* 352, aaf2939 (2016). DOI: 10.1126/science.aaf2939

RESEARCH ARTICLE

PLASMA ASTROPHYSICS

Electron-scale measurements of magnetic reconnection in space

J. L. Burch,^{1*} R. B. Torbert,^{1,2} T. D. Phan,³ L.-J. Chen,⁴ T. E. Moore,⁵ R. E. Ergun,⁶ J. P. Eastwood,⁷ D. J. Gershman,⁵ P. A. Cassak,⁸ M. R. Argall,² S. Wang,⁴ M. Hesse,⁵ C. J. Pollock,⁵ B. L. Giles,⁵ R. Nakamura,⁹ B. H. Mauk,¹⁰ S. A. Fuselier,¹ C. T. Russell,¹¹ R. J. Strangeway,¹¹ J. F. Drake,⁴ M. A. Shay,¹² Yu. V. Khotyaintsev,¹³ P.-A. Lindqvist,¹⁴ G. Marklund,¹⁴ F. D. Wilder,⁶ D. T. Young,¹ K. Torkar,⁹ J. Goldstein,¹ J. C. Dorelli,⁵ L. A. Avanov,⁵ M. Oka,³ D. N. Baker,⁶ A. N. Jaynes,⁶ K. A. Goodrich,⁶ I. J. Cohen,¹⁰ D. L. Turner,¹⁵ J. F. Fennell,¹⁵ J. B. Blake,¹⁵ J. Clemmons,¹⁵ M. Goldman,¹⁶ D. Newman,¹⁶ S. M. Petrinen,¹⁷ K. J. Trattner,⁶ B. Lavraud,¹⁸ P. H. Reiff,¹⁹ W. Baumjohann,⁹ W. Magnes,⁹ M. Steller,⁹ W. Lewis,¹ Y. Saito,²⁰ V. Coffey,²¹ M. Chandler²¹

Magnetic reconnection is a fundamental physical process in plasmas whereby stored magnetic energy is converted into heat and kinetic energy of charged particles. Reconnection occurs in many astrophysical plasma environments and in laboratory plasmas. Using measurements with very high time resolution, NASA's Magnetospheric Multiscale (MMS) mission has found direct evidence for electron demagnetization and acceleration at sites along the sunward boundary of Earth's magnetosphere where the interplanetary magnetic field reconnects with the terrestrial magnetic field. We have (i) observed the conversion of magnetic energy to particle energy; (ii) measured the electric field and current, which together cause the dissipation of magnetic energy; and (iii) identified the electron population that carries the current as a result of demagnetization and acceleration within the reconnection diffusion/dissipation region.

Magnetic reconnection is an energy conversion process that operates in many astrophysical environments, producing energetic phenomena such as geomagnetic storms and aurora, solar flares and coronal mass ejections, x-ray flares in magnetars, and magnetic interactions between neutron stars and their accretion disks. Reconnection is also crucially important in laboratory plasma physics, where it has proved to be an impediment to the achievement of magnetic-confinement fusion

through the sawtooth crashes that it triggers. A better understanding of reconnection is an important goal for plasma physics on Earth and in space, but a complete experiment is impossible to conduct in most environments, which are too distant, too hot, or too small for comprehensive *in situ* measurements (1).

Earth's magnetosphere has been explored by many spacecraft missions, some of which have made multipoint measurements in and around regions containing collisionless magnetic reconnection (2–7). Results from these missions have verified many of the predictions about magnetic reconnection phenomena on the magnetohydrodynamic (MHD) and ion scales. However, to make major progress in the study of collisionless reconnection in space, it is necessary to extend the measurements to the electron scale and make accurate three-dimensional measurements of electric and magnetic fields. Also required are accurate ion composition measurements, which can help to determine the role of ionospheric particles in reconnection, as well as energetic particle measurements, which can help to determine where magnetic fields interconnect and how particles are accelerated to high energies.

NASA's Magnetospheric Multiscale (MMS) mission (8) was designed to perform a definitive experiment in space on magnetic reconnection at the electron scale, at which dissipation of magnetic energy and the resulting interconnection of

magnetic fields occur. Electron-scale kinetic physics in the region around the reconnection site (or the X-line) where field line breaking and reconnection occur has not previously been investigated experimentally in space, owing to insufficiently detailed measurements. Our knowledge of this region at the electron scale has come mainly from computer simulations (9–13) and laboratory experiments (14, 15). The higher resolution of MMS measurements in both time and space relative to previous missions offers an opportunity to investigate the cause of reconnection by resolving the structures and dynamics within the X-line region.

The data set obtained by MMS incorporates the following advances: (i) four spacecraft in a closely controlled tetrahedron formation with adjustable separations down to 10 km; (ii) three-axis electric and magnetic field measurements with accurate cross-calibrations allowing for the measurement of spatial gradients and time variations; and (iii) all-sky plasma electron and ion velocity-space distributions with time resolution of 30 ms for electrons and 150 ms for ions.

The four MMS spacecraft were launched together on 13 March 2015 (UT) into a highly elliptical (inclination 28°) orbit with perigee at 1.2 Earth radii (R_E) and apogee at 12 R_E (both geocentric). The mission is being conducted in two phases, the first phase targeting the dayside outer boundary of Earth's magnetosphere (the magnetopause) and the second phase targeting the geomagnetic tail, for which the apogee is raised to 25 R_E . This article focuses on magnetopause measurements during the first science phase of the mission, which began on 1 September 2015. For this phase, a region of interest was identified as geocentric radial distances of 9 to 12 R_E , during which all instruments are operated at their fastest cadence, producing burst-mode data. Within the region of interest, the four spacecraft are maintained in a tetrahedral formation with separations variable between 160 and 10 km. A quality factor for the tetrahedra, defined by the ratio of their surface area to their volume, is maintained to within 80% of the ratio for a regular tetrahedron.

By 14 December 2015, the spacecraft had crossed the magnetopause more than 2000 times. On the basis of detection of plasma jetting and heating within the magnetopause current sheets, we infer that at least 50% of the crossings encountered magnetic reconnection. Most crossings occurred in the reconnection exhaust downstream of the X-line, but a few of them passed very close to the X-line. The data for one of these events (16 October 2015, 13:07 UT) are presented here as an example of the electron-scale measurements of the reconnection diffusion/dissipation region around an X-line.

MMS measurements

The set of measurements made on each of the four MMS spacecraft are listed in Table 1. The improvement in time resolution for three-dimensional plasma distribution measurements was substantial: 30 ms for electrons and 150 ms for ions, as

¹Southwest Research Institute, San Antonio, TX, USA.

²University of New Hampshire, Durham, NH, USA. ³University of California, Berkeley, CA, USA. ⁴University of Maryland, College Park, MD, USA. ⁵NASA, Goddard Space Flight Center, Greenbelt, MD, USA. ⁶University of Colorado LASP, Boulder, CO, USA. ⁷Blackett Laboratory, Imperial College London, London, UK. ⁸West Virginia University, Morgantown, WV, USA. ⁹Space Research Institute, Austrian Academy of Sciences, Graz, Austria. ¹⁰Johns Hopkins University Applied Physics Laboratory, Laurel, MD, USA. ¹¹University of California, Los Angeles, CA, USA. ¹²University of Delaware, Newark, DE, USA. ¹³Swedish Institute of Space Physics, Uppsala, Sweden. ¹⁴Royal Institute of Technology, Stockholm, Sweden. ¹⁵Aerospace Corporation, El Segundo, CA, USA. ¹⁶University of Colorado, Boulder, CO, USA. ¹⁷Lockheed Martin Advanced Research Center, Palo Alto, CA, USA. ¹⁸Institut de Recherche en Astrophysique et Planétologie, Toulouse, France. ¹⁹Department of Physics and Astronomy, Rice University, Houston, TX, USA. ²⁰Institute for Space and Astronautical Sciences, Sagami-hara, Japan. ²¹NASA, Marshall Space Flight Center, Huntsville, AL, USA.

*Corresponding author. Email: jlburch@swri.edu

compared to previous resolutions in the few-second range. This improvement required the use of multiple analyzers rather than one spinning analyzer, resulting in stringent requirements on their absolute calibration and intercalibration.

Two benefits of this approach are the ability to make accurate measurements of currents and of electron drift velocities. Another advance is the accurate measurement of three-axis electric fields, which are crucially important for the investiga-

tion of reconnection. Data taken at the highest measurement resolution are referred to as burst-mode data, and all instruments operate in burst mode whenever the spacecraft are beyond a geocentric distance of $9 R_E$ on the dayside of Earth.

Table 1. Measurements made on each MMS spacecraft.	
Fields	Three-dimensional electric and magnetic field measurements at time resolution of <1 ms (direct current) and waves to 6 kHz (<i>B</i>) and 100 kHz (<i>E</i>).
Fast plasma	Full-sky viewing of plasma electrons and ions at 32 energies (10 eV to 30 keV): electrons in 30 ms, ions in 150 ms.
Energetic particles	Full-sky viewing of ion and electron energetic particles (20 to 500 keV) with composition.
Plasma composition	Composition-resolved 3D ion distributions (1 eV to 40 keV) for H ⁺ , He ²⁺ , He ⁺ , and O ⁺ . Full sky at 10 s.
Potential control	Maintenance of spacecraft potential to ≤4 V using ion emitter.

A reconnection dissipation region encountered by MMS

Figure 1 shows summary plasma and field data for MMS1 at a time resolution of ~4 s on 16 October 2015. Because of data downlink limitations, only 2 to 4% of the burst-mode data can be transmitted to Earth. Data selection is made with two mechanisms: (i) an onboard system, which evaluates 10-s intervals of burst-mode data and prioritizes them according to expected reconnection signatures; and (ii) a scientist-in-the-loop system by which scientists view summary data (such as shown in Fig. 1) to select boundary crossings, flow jets, and other features that might have been

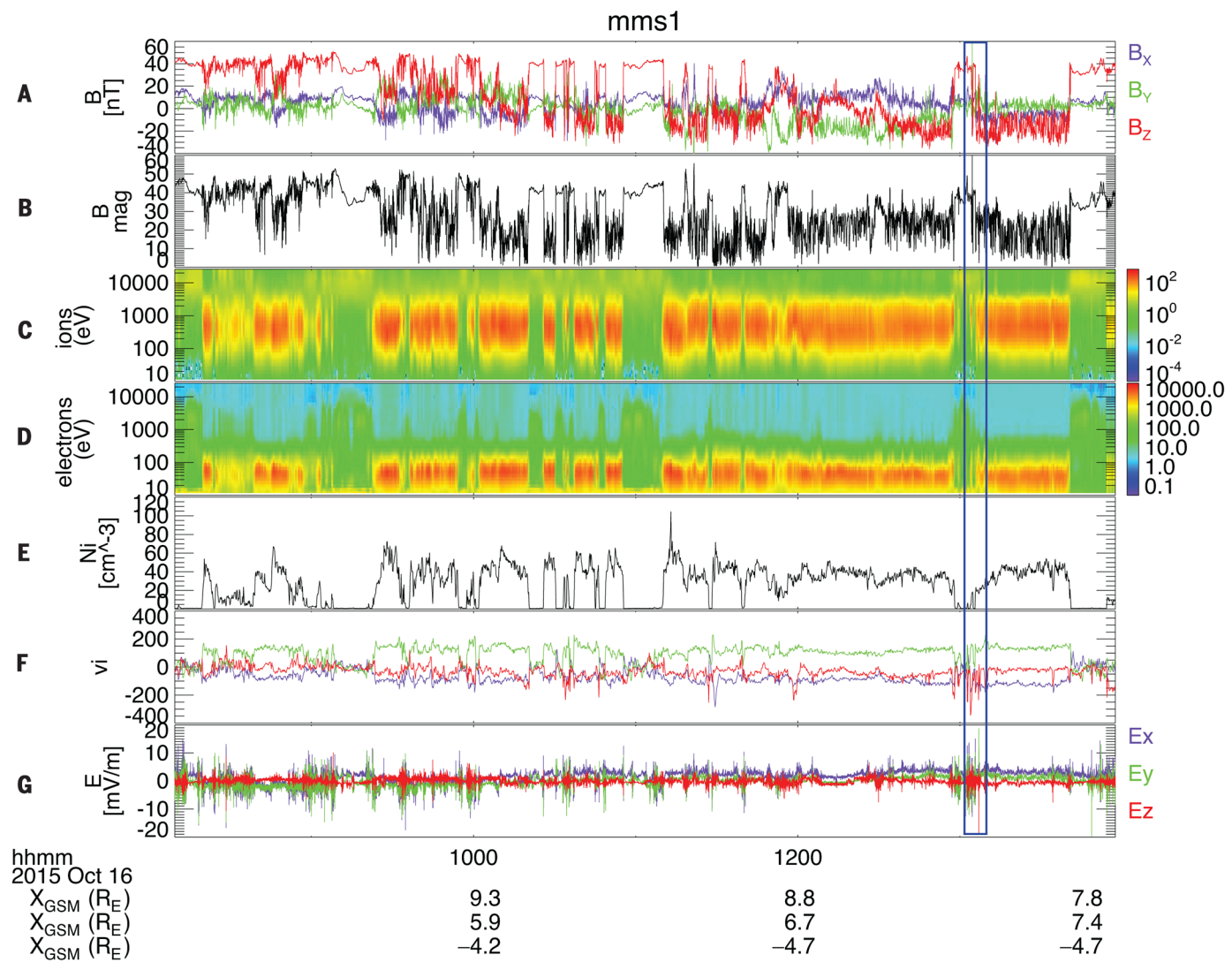


Fig. 1. Summary data in GSM (geocentric solar magnetospheric) coordinates from MMS1 on 16 October 2015. The GSM coordinate system has **X** toward the Sun, **Z** the projection of Earth's magnetic dipole axis (positive = north) onto the plane perpendicular to **X**, and **Y** completing the right-hand system (approximately toward dusk). (A) Magnetic field vector. (B) Magnetic field magnitude. (C) Ion energy-time spectrogram in energy flux (eV cm⁻² sr⁻¹ s⁻¹). (D) Electron energy-time spectrogram in energy flux (eV cm⁻² sr⁻¹ s⁻¹). (E) Ion density. (F) Ion velocity vector. (G) Electric field vector.

Downloaded from <http://science.sciencemag.org/> on June 3, 2016

missed by the onboard system. Both mechanisms have been effective in identifying possible reconnection sites. Several magnetopause crossings were observed on this day. The particular event chosen for further analysis (near 13:07 UT) is noted by the blue box in Fig. 1.

Figure 2A shows the orbit as projected onto the ecliptic plane; Fig. 2B shows the tetrahedron occupied by the four spacecraft at 13:07:00 UT on 16 October 2015. During this time period, the separation among the spacecraft was controlled at 10 km. As shown in Fig. 2, MMS4 was located ~10 km south (toward $-Z$) of MMS2 and MMS3. The detailed electron distribution functions from the four spacecraft show evidence that the reconnection X-line was located to the north of MMS4 and to the south of MMS2 and MMS3. MMS1 was displaced toward negative values of X (toward Earth) so that as the magnetopause moved inward across the four spacecraft, MMS1 detected the dissipation region slightly later than the other three spacecraft (Fig. 2).

The 10-km average separation of the four spacecraft amounted to ~6 electron skin depths (the depth in a plasma to which electromagnetic radiation can penetrate) based on a magnetosheath (shocked solar wind) density of $\sim 12 \text{ cm}^{-3}$. At such small spacecraft separations, the plasma and fields measured by the four spacecraft are nearly identical throughout most of the regions, except in thin electron-scale layers near the reconnection X-line.

Overview of two magnetopause crossings

Figure 3 shows MMS2 data during two encounters with the magnetopause over a period of almost 2 min. The magnetopause crossings are denoted by the two pairs of vertical blue dashed

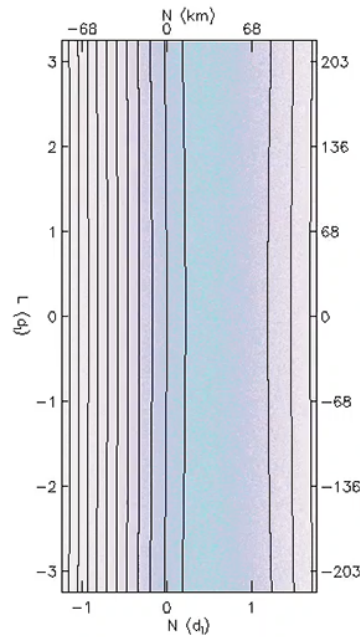


Fig. 2. Locations of the four MMS spacecraft during the magnetopause crossing investigated in this study. (A) Ecliptic-plane projection of MMS orbit in geocentric-solar-ecliptic (GSE) coordinates on 16 October 2015. The beige area is the MMS region of interest where burst-mode data are taken. Hours of the day are noted along the orbit. (B) MMS tetrahedral formation in GSE coordinates (X toward Sun, Z perpendicular to ecliptic plane, Y toward dusk).

Movie 1. An electromagnetic particle-in-cell simulation with parameters corresponding to the event is performed with the P3D code (27). Particles are advanced using a relativistic Boris stepper with electromagnetic fields extrapolated to the particles' positions (28). Electromagnetic fields are evolved using the trapezoidal leapfrog scheme on Maxwell's equations with second-order spatial derivatives. The simulation is two-dimensional with periodic boundary conditions in both directions. Magnetic fields in the simulation are normalized to the magnitude of the L component of the magnetosheath magnetic field, 23 nT. Densities are normalized to the magnetosheath density, 11.3 cm^{-3} . Distances are normalized to 67.8 km (the magnetosheath ion inertial scale $d_{i,sh} = c/\omega_{pi,sh}$), and current densities to $0.270 \mu\text{A}/\text{m}^2$. The initial conditions for the upstream values of the L and M components of the magnetic field, the densities, and the electron and ion temperatures on both sides of the current sheet are taken to match the event to the extent possible: $B_{L,ms} = 39 \text{ nT}$, $B_{L,sh} = 23 \text{ nT}$, $B_{M,ms} = B_{M,sh} = 2.278 \text{ nT}$, $n_{ms} = 0.7 \text{ cm}^{-3}$, and $n_{sh} = 11.3 \text{ cm}^{-3}$, where "ms" denotes the magnetospheric side and "sh" denotes the magnetosheath side. For the temperatures, magnetosheath values are $T_{p,sh} = 320 \text{ eV}$ and $T_{e,sh} = 28 \text{ eV}$ to match the MMS data. For the magnetosphere, the low density

makes measuring temperatures difficult, so for the purposes of the simulation we defined the magnetospheric temperature as that required to balance total pressure in the fluid sense with a proton temperature 6 times the electron temperature: $T_{p,ms} = 1800 \text{ eV}$, $T_{e,ms} = 300 \text{ eV}$. No bulk flow of the upstream plasma is included in the initial conditions. The profiles for the initial conditions had double tanh profiles for the magnetic field and temperature, and the density profile is chosen to enforce pressure balance in the fluid sense. The domain size is 40.96×20.48 in normalized units and the grid scale is 0.01 in both directions. The time step is 0.001 in units of the magnetosheath inverse ion cyclotron frequency $\Omega_{ci,sh}^{-1}$ and is run until $t = 40$. The time step on the electromagnetic fields is half that of the particles to resolve light waves. The simulation is initialized with 500 particles per grid. The ion-to-electron mass ratio is 100 and the ratio of the speed of light to the initial magnetosheath Alfvén speed is 15 ($\omega_{pi,sh}/\Omega_{ci,sh} = 15$); these differ from the realistic values of 1836 and 2000, respectively, but it is common to use smaller values for numerical expediency and is not expected to adversely affect the simulations. <http://bcove.me/o51zgjqt>.

lines. The diagram on the right side of Fig. 3 shows the typical structure of a magnetopause in which asymmetric reconnection is occurring, taken from a numerical plasma simulation shown in Movie 1 for the observed magnetosheath and magnetospheric conditions of the complete MMS magnetopause crossing at 13:05:30 UT. The diagram shows the northward magnetic field on the magnetosphere side of the boundary and the southward magnetic field on the magnetosheath side. The shear angle between the magnetosphere and magnetosheath magnetic fields is very large ($\sim 170^\circ$), implying a crossing with low guide field (the magnetic field component normal to the plane of the diagram). The converging plasma flows carry the two nearly oppositely directed magnetic field domains toward each other. An

X-line directed normal to the plane of the diagram denotes the small region in the reconnection plane where the field lines interconnect, and this X-line is likely to extend by hundreds to thousands of kilometers in the east-west direction (16), which is why a large number of exhaust regions are typically crossed by spacecraft near the magnetopause. Another reason why reconnection events are routinely observed is the presence of the exhaust jets (red arrows) flowing northward and southward from the X-line and the nearby dissipation region (or diffusion region). Although the results of reconnection are readily observed with measurements at the fluid and ion scales, it is the electron-scale phenomena acting within the dissipation region that determine how reconnection occurs.

The color scale in the plasma simulation result in Fig. 3 shows the plasma current normal to the plane of the picture (J_M), which is nearly all due to fast-moving electrons generated by the reconnection process. The strong $-J_M$ values (shown in green) are highly localized at the dissipation region and X-line. The approximate path of the MMS tetrahedron, based on the plasma and field measurements, is shown by a blue dashed curve. Because the velocity of the magnetopause is approximately 100 times the spacecraft velocities, the MMS path shown is produced entirely by the motion of the magnetopause along L and N (directions defined in the Fig. 3 caption). For the magnetopause crossing centered at 13:07 UT, the spacecraft traversed both exhaust jet regions and passed through the dissipation region between them.

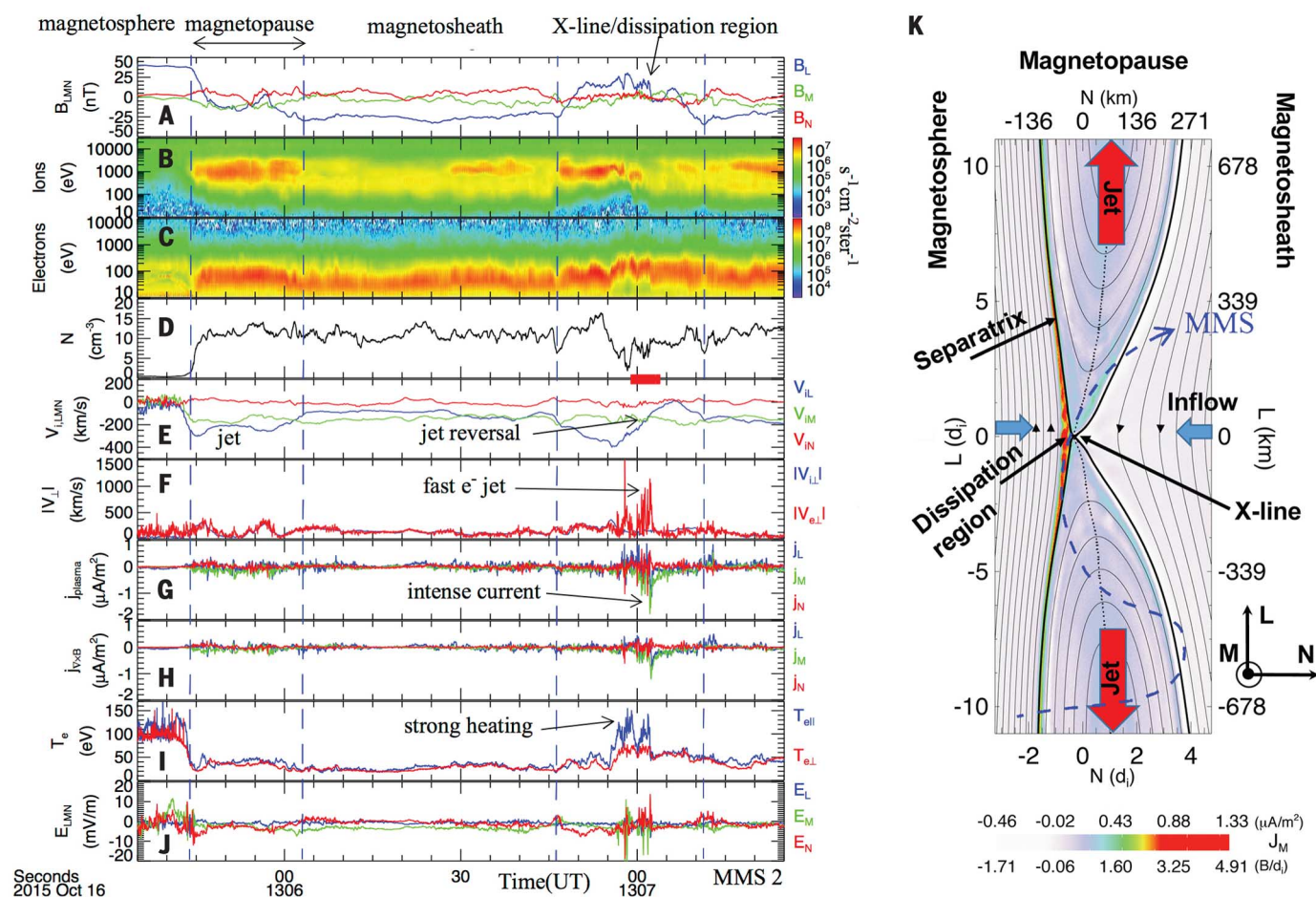


Fig. 3. Summary data for two magnetopause crossings of MMS2 on 16 October 2015. The crossings are shown by the vertical blue dashed lines. Boundary-normal coordinates (L , M , N) are used with N normal to the boundary and away from Earth, L perpendicular to N and in the plane of reconnection (nearly along the magnetospheric magnetic field direction), and M normal to the L , N plane (generally westward). These directions were determined from a minimum variance analysis of the magnetic field data between 13:05:40 and 13:06:09 UT. The (x , y , z) GSE components of the L , M , and N axes are $L = (0.3665, -0.1201, 0.9226)$ GSE, $M = (0.5694, -0.7553, -0.3245)$ GSE, and $N = (0.7358, 0.6443, -0.2084)$ GSE. Panel data include (A) magnetic field vectors, (B) energy-time spectrogram of ion energy flux, (C) energy-time spectrogram

of electron energy flux, (D) total plasma density, (E) ion flow velocity vectors, (F) magnitudes of electron and ion convection velocities, (G) current computed from velocity moments of ions and electrons, (H) current computed from $\nabla \times \mathbf{B}$, (I) parallel and perpendicular (to \mathbf{B}) electron temperatures, and (J) electric field vectors. In the very-low-density region to the left of the first vertical blue dashed line, spacecraft charging effects on plasma moment calculations may affect the data. The diagram to the right is the result of a numerical plasma simulation (Movie 1) using parameters from the magnetopause crossing centered on 13:05:52 UT. Spatial coordinates in the diagram are shown both in kilometers and in ion diffusion lengths, $L(d_i)$. Color scale indicates J_M current density.

In comparison, the magnetopause crossing centered at about 13:05:52 UT occurred completely southward of the X-line in the exhaust, so that although it did include a traversal from well within the magnetosphere to well into the magnetosheath, it did not encounter the dissipation region. This difference is best seen in the ion flow velocities in Fig. 3E, which when high in magnitude denote the exhaust jets. For the first magnetopause crossing, only southward jets ($V_{IL} < 0$) were observed, whereas for the second event (13:07 UT) both southward and northward jets were observed, with no gap between them. During the flow reversal near 13:07 UT, the reconnecting magnetic field (B_L) component was close to zero, suggesting that the spacecraft was in close proximity to the X-line. The red highlight bar at the top of Fig. 3E shows this reversal.

Another strong indicator of the dissipation region is the aforementioned $-J_M$ current, which can be seen in Fig. 3, G and H. The green trace is $-J_M$ (eastward current), which is predicted by the simulation to peak at the dissipation region. With MMS there are two ways to measure the currents: (i) $\nabla \times \mathbf{B}$ calculated from the magnetic field data from the four spacecraft (as in Fig. 3A), or (ii) $qn(\mathbf{V}_i - \mathbf{V}_e)$ using the computed moments of the ion and electron distribution functions, where q is the electronic charge and n is the plasma density. The correspondence between the two methods shown in Fig. 3 required a high level of calibration and cross-calibration of the various plasma instruments. Differences between the two methods at the smallest scales are mostly because even with 10-km separation, the currents are not completely uniform across the MMS tetrahedron, which is assumed in the $\nabla \times \mathbf{B}$ calculation.

The third strong indicator for a dissipation region is the enhancement of $-E_M$ (the reconnection electric field), which is shown by the green trace in Fig. 3J. The size of the E_M bursts of more than 10 mV/m is substantially larger than the correction due to X-line motion, which is on the order of 1 mV/m or less. There are also strong E_N components bracketing 13:07 UT, which are electric fields pointing outward and normal to the magnetopause. This normal component is predicted by simulations (17), and in a simple sense is caused by the deeper penetration into the magnetosphere of the magnetosheath ions because of their larger gyroradius relative to electrons with similar energies. The resulting charge separation produces an ambipolar electric field, E_N .

There are important differences between the reconnection exhaust at 13:05:52 UT and the region surrounding the X-line near 13:07 UT. First, as shown in Fig. 3I, the degree of electron heating (relative to the magnetosheath temperature) near the X-line ($\Delta T_{e||} \sim 120$ eV) is substantially higher than the heating in the exhaust ($\Delta T_{e||} \sim 20$ eV). Second, the electron flow speed perpendicular to the magnetic field, which largely tracks the ion perpendicular speed in the magnetosheath and the exhaust, significantly exceeds the ion flow speed near the X-line (Fig. 3F), resulting in a current that is much larger near the X-line than in the exhaust. These differences further support

the identification of the X-line regions near 13:07 UT.

Details of plasma and field observations from MMS2

Figure 4 shows the 4 s marked with the red bar in Fig. 3E of MMS2 data near the X-line. Figure 4A shows that a deep magnetic field minimum occurred just after 13:07:02.4 UT; Fig. 4B shows a strong plasma current (J_M) starting at 13:07:02.1 UT (on the magnetosphere side of the X-line) and extending through the minimum magnetic field. Figure 4C shows vector electric fields. Inside the $-J_M$ current layer, the E_N component, which points outward from the magnetopause as described above, is the strongest. It is also noteworthy that E_M , the reconnection electric field, is negative, as is the J_M current. Figure 4D shows a comparison between \mathbf{E}_M and $-(\mathbf{V}_e \times \mathbf{B})_M$. There is excellent agreement except near the dissipation region. Figure 4E shows the electric field component parallel to \mathbf{B} , which is strongest in the region of the J_M plasma current. Figure 4F shows $\mathbf{J} \cdot \mathbf{E}'$, where $\mathbf{E}' = \mathbf{E} + \mathbf{V}_e \times \mathbf{B}$, along with its parallel and perpendicular components. $\mathbf{J} \cdot \mathbf{E}'$ has been referred to as the “dissipation quantity” in simulation results (18). The plot in Fig. 4F shows clearly that the reconnection dissipation is caused by the strong $-J_M$ current and $-E_M$ electric field, which are perpendicular to \mathbf{B} in the dissipation region as \mathbf{B} is dominated by B_L in that region. Because reconnection is known to be a dissipative process that converts magnetic energy to heat and particle kinetic energy, the observation that $\mathbf{J} \cdot \mathbf{E} \approx J_M E_M > 0$ provides a form of “smoking gun” for a reconnection dissipation region.

Shown in Fig. 4, G to I, are energy-time spectrograms of electrons moving parallel, perpendicular, and antiparallel to the local magnetic field direction, respectively. In the region of dissipation (13:07:02.15 to 13:07:02.29 UT), the parallel fluxes shift to lower energies, the perpendicular fluxes rise in intensity and shift to lower energies, and the antiparallel fluxes remain at high energies. All of the fluxes drop to lower magnetosheath levels after exiting the dissipation region. The electron velocity-space distribution functions in Fig. 4, J to L, show three cuts through 3D distributions at 30-ms intervals through the dissipation region. Figure 4J shows cuts perpendicular to \mathbf{B} , where $V_{\text{perp1}} = (\mathbf{b} \times \mathbf{v}) \times \mathbf{b}$ and $V_{\text{perp2}} = -\mathbf{v} \times \mathbf{b}$ (\mathbf{b} and \mathbf{v} are unit vectors of the magnetic field and the electron velocity moment, respectively). Shown in Fig. 4, K and L, are two orthogonal cuts containing the magnetic field direction V_{para} .

Before MMS, the best 3D plasma measurement resolution was 3 s; that is, only a single plasma distribution would have been measured in such a brief interval. In comparison, MMS measured 26 ion distributions and 133 electron distributions in this interval. Movie 2 shows all of the MMS2 electron velocity-space distributions in video form for a 3-s interval centered in Fig. 4. The movie demonstrates that the 30-ms time resolution of MMS is necessary for performing this

type of definitive investigation of the reconnection dissipation region.

The first column of distribution functions (on the magnetosphere side of the X-line) shows a crescent-shaped distribution in the perpendicular plane centered along the $+V_{\text{perp1}}$ axis in Fig. 4J, parallel heating in Fig. 4, K and L, along with a vertical cut through the crescent along $+V_{\text{perp1}}$ in Fig. 4K. This type of crescent-shaped distribution has been predicted from a simulation (9) that showed reduced distribution functions (integrated along V_{para}). In that simulation, the electrons in the crescent population were described as “meandering particles” consisting of accelerated magnetosheath electrons. Subsequent distribution functions in Fig. 4J show that as the X-line is approached along the path sketched in Fig. 3, the crescent-shaped distribution wraps around the origin and becomes a ring, which moves to lower energies. This energy shift is shown in the spectrogram in Fig. 4H.

Shown in Fig. 4, K and L, is a result that had not been predicted: the formation of a crescent-shaped distribution along V_{para} , indicating the transition of the perpendicular crescent electrons to field-aligned flow. Such a transition is strong evidence for the opening of magnetic field lines. At the end of the dissipation-region interval, the parallel crescent also begins to wrap around the origin and move to lower energies, as shown by the spectrogram in Fig. 4G. The crescent electrons are moving along \mathbf{B} ($+V_{\text{para}}$) while the electrons along $-V_{\text{para}}$ continue to show the electron-heating feature (the elongation along $-V_{\text{para}}$), which extends to higher energies than the crescent population. The direction of the field-aligned flow of the crescent electrons indicates that MMS2 has moved above the X-line while still within the dissipation region (Fig. 3K). Because the electron spectrograms in Fig. 4, G to I, plot energy flux, they are much more sensitive to the high-energy parts of the distribution, and this fact explains why the antiparallel energy fluxes in Fig. 4I remain level throughout the dissipation region.

In summary, the data in Fig. 4 establish that MMS2 passed through a reconnection dissipation region around an X-line. The flow directions shown in the electron velocity-space distributions (crescent shifting from perpendicular to along \mathbf{B}) suggest that MMS2 moved northward from approximately the same L location as the X-line. Parallel electric fields (Fig. 4E) also occur in the dissipation region. In addition, there is a strong normal electric field, E_N , which may be related to the normal electric field predicted theoretically to result from magnetopause pressure gradients along the entire magnetopause (19). The crescent-shaped distributions are due to finite Larmor radius effects of magnetosheath electrons that have been accelerated toward the magnetosphere by E_N (Fig. 4C) in the weak magnetic field region near the X-line. This Larmor motion, together with acceleration by the reconnection electric field, results in a net out-of-plane electron bulk motion or electron current $-J_M$ that is observed (Fig. 4B). As the high-density magnetosheath electrons penetrate more deeply into the region

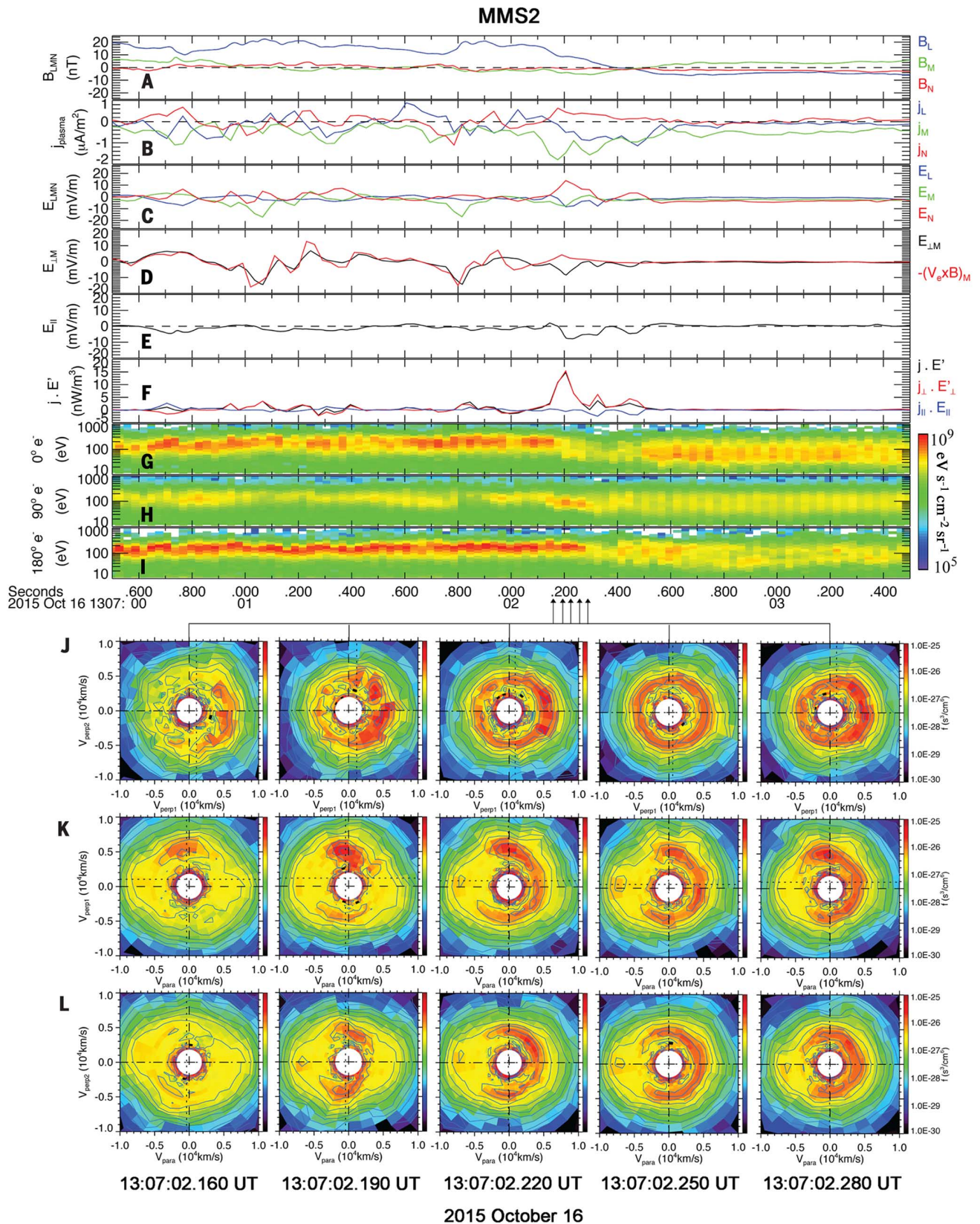


Fig. 4. MMS2 plasma and field data on 16 October 2015. (A) Magnetic field vector. (B) Currents from plasma measurements. (C) Electric field vector. (D) Comparison of M component of \mathbf{E} and $-\mathbf{V}_e \times \mathbf{B}$. (E) $E_{||}$. (F) $\mathbf{J} \cdot \mathbf{E}$. (G) Electron energy-time spectrogram (pitch angle = 0° to 12°). (H) Electron energy-time spectrogram (pitch angle = 84° to 96°). (I) Electron energy-time spectrogram (pitch angle = 168° to 180°). (J) Electron velocity-space distribution ($V_{\text{perp}1}$, $V_{\text{perp}2}$). (K) Electron velocity-space distribution (V_{para} , $V_{\text{perp}1}$). (L) Electron velocity-space distribution (V_{para} , $V_{\text{perp}2}$). $V_{\text{perp}1}$ is in the $(\mathbf{b} \times \mathbf{v}) \times \mathbf{b}$ direction, which is a proxy for $\mathbf{E} \times \mathbf{B}$.

with $B_L > 0$, they gain more energy from E_N , and this effect can be clearly seen by comparing the first and fifth columns of Fig. 4J. Because the X-line moved along the N direction across the spacecraft tetrahedron, the energy of accelerated magnetosheath electrons increases from right to left in Fig. 4. As can be seen in Movie 2, the electron distributions at the magnetic field minimum ($\sim 13:07:02.45$ UT) are isotropic at very low energy, indicating demagnetization, as would be expected. As the electrons move inward (Earthward) toward the dissipation region, they gain successively more energy as they cross the open field lines at the outer part of the dissipation region (parallel crescent) and then develop the highest-energy perpendicular crescent as the parallel crescent disappears at the inner part (the magnetosphere side) of the dissipation region.

Multi-spacecraft observations of the dissipation region

Figure 5 shows multi-spacecraft plasma and field data for the same 4-s time period as in Fig. 4. The vector magnetic field data in Fig. 5A show that MMS 2, 3, and 4 all passed through the magnetopause together, with MMS1 following them by ~ 0.2 s. The spatial scale (along the magnetopause normal direction) of the various electron layers can be estimated as follows: The consecutive detections by the four spacecraft of the B_L gradient at 13:07:02.2 to 13:07:02.4 reveal that this structure moved at a speed of ~ 45 km/s along the normal direction. Thus, the width of the region where seven crescent distributions (each sampled over 30 ms) were observed is ~ 9 km, or 6 electron skin depths. The region of strong dissipation is even narrower, as shown by the electric field measurements in Fig. 5.

All four spacecraft measured somewhat similar electric field and currents with important

differences in their amplitudes and duration, particularly with the trailing MMS1. Shown in Fig. 5, B to D, are E_M , E_N , and $E_{||}$, respectively. Near the dissipation region, MMS2, MMS3, and MMS4 measured the perpendicular and parallel electric fields at various levels and strong J_M current. The strongest $\mathbf{J} \cdot \mathbf{E}'$ peak was detected by MMS2, indicating its deepest penetration into the dissipation region.

The same types of electron velocity-space distributions presented in Fig. 4 for MMS2 were observed by MMS3 and MMS4. In Fig. 5, H to J, MMS4 distributions are shown in the first column, and MMS3 distributions are displayed in the other three columns. The first column of Fig. 5H shows that as MMS4 was entering the dissipation region, it saw the perpendicular crescent nearly wrapped around the origin as a ring. At the same time, Fig. 5J shows the formation of a parallel crescent as in Fig. 3, but in this case, it is centered on the $-V_{para}$ axis. This shift indicates that MMS4 was located below (or southward of) the X-line, which, as noted before, is consistent with its location shown in Fig. 2B. Also consistent with Fig. 2B are the parallel crescents that form in the third and fourth columns of Fig. 5, I and J, which are centered along the $+V_{para}$ axis, as was the case with MMS2. This direction indicates that MMS3, like MMS2, was located above (or northward of) the X-line. Exactly as for MMS2, the MMS3 perpendicular crescent in the second column of Fig. 5H appears first without a corresponding parallel crescent, but then evolves toward a ring in columns 3 and 4 as the parallel crescents develop.

Energetic electron evidence for the opening of magnetic field lines

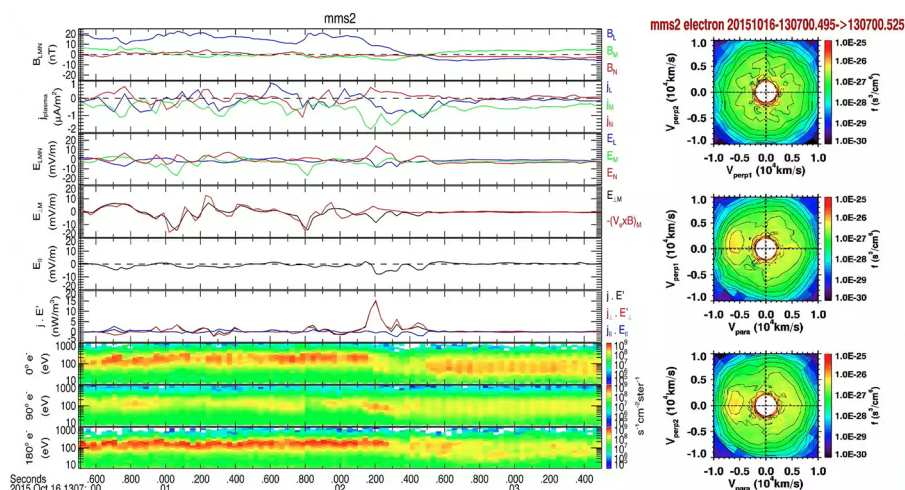
For the analysis of magnetopause reconnection, very-high-energy electron features can be a val-

uable adjunct to analyses of lower-energy particles, because such electrons still have relatively small gyroradii (relative to the large-scale current sheet thickness) and are not expected to be perturbed by the strong electric fields in the vicinity of the electron diffusion region. The complex magnetic geometries of a reconnection site are expected to redirect energetic electrons in a fashion that reflects the magnetic geometry and topology of the small region. Interesting energetic electron signatures were indeed observed in the vicinity of the X-line by the Fly's Eye Energetic Particle Spectrometer (FEEPS), a part of the Energetic Particle Detector (EPD) investigation (20, 21). The bottom panel of Fig. 6 shows the magnetic field data and identifies the location of the electron dissipation region (EDR). The top panel shows a pitch-angle distribution of >50 -keV electrons, in which particles that travel parallel and antiparallel to the magnetic field are respectively located near the bottom and the top of the plot, and particles that gyrate nearly perpendicular to the magnetic field are near the vertical center of the plot. Our expectation has been that near an EDR, electrons might stream outward from the energetic particle populations residing on the Earthward side toward the magnetosheath side along field lines that are reconnected close to the EDR. Electrons are indeed streaming along field lines, and in the context of the spacecraft trajectory relative to the EDR developed elsewhere in this paper (Fig. 3K), the electrons appear to be traveling away from Earth. Specifically, starting around 13:06:55 UT, enhanced fluxes of >50 -keV electrons were streaming primarily in the parallel direction with respect to the magnetic field and away from the Earthward side, based on the inferred location of the EDR. After MMS passed through the EDR around 13:07:02 UT, these electrons exhibited streaming in the magnetically opposite direction, predominantly antiparallel to the magnetic field, but the inferred trajectory of the spacecraft through the EDR (Fig. 3K) indicates that the electrons are again traveling away from Earth. These observations lend support to the idea that field lines connecting the magnetosphere and magnetosheath sides are generated through the reconnection process over small spatial scales dictated by electron processes.

Note that the time resolution of FEEPS (2.5 s) does not allow measurements within the EDR, but rather shows the reversal of the magnetic field-aligned motion of the >50 -keV electrons from southward of the EDR to northward of it as MMS2 made this traversal. In this sense, the FEEPS data provide independent confirmation of the opening of magnetic field lines across the EDR, as deduced from the appearance of the parallel crescent in the low-energy electron data.

Data interpretation

The existence of the crescent-shaped electron distributions in the plane perpendicular to \mathbf{B} , as shown in Figs. 4 and 5, can be explained conceptually as follows. There is typically a large ion pressure gradient across the magnetopause. During magnetic reconnection, this pressure gradient



Movie 2. Three-second segment of burst-mode electron distributions keyed to a plot of plasma and field data covering the same time period as Fig. 4. One hundred electron velocity-space distributions are shown over this period. Previous missions that used the spacecraft spin to cover the full sky could only acquire one or fewer distributions over a time period of this length. This factor of 100 increase in electron time resolution is an important reason why MMS is able to investigate the electron-scale physics of reconnection. <http://bcove.me/9fkcpfn1>.

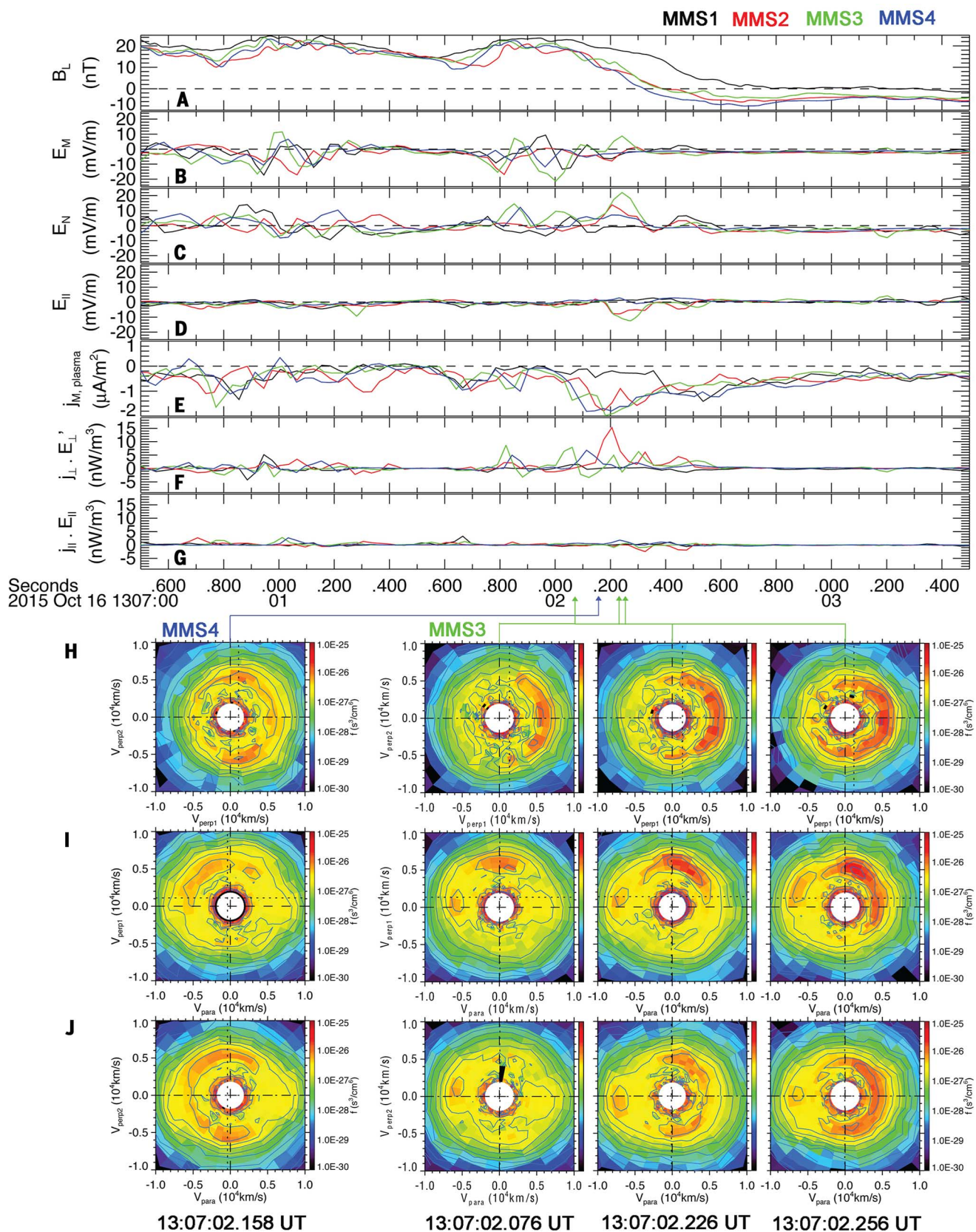


Fig. 5. Line plots of MMS field data from all four spacecraft on 16 October 2015. At the bottom are electron velocity-space distributions for MMS4 and MMS3. Panels are as in Fig. 4, except that the electron energy-time spectrograms are not shown. The parallel crescent in (J) for MMS4 is oriented in the opposite direction to that of MMS3, which is consistent with MMS4 being southward of the X-line and MMS3 being northward of it so that the electron flows are in opposite directions.

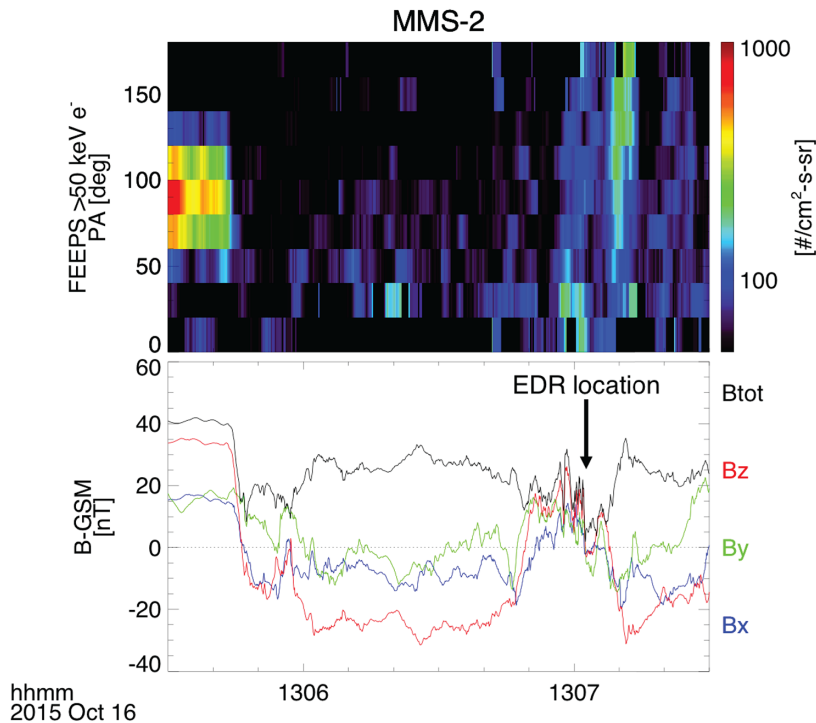


Fig. 6. Energetic electron data measured by FEEPS. Top: Pitch angle versus time spectrogram of energy flux carried by ~50-keV electrons. Bottom: Magnetic vectors in GSM coordinates and magnetic field magnitude.

produces a large normal electric E_N in an LMN coordinate system that points toward the Sun. This electric field balances the ion pressure gradient and keeps ions flowing from the magnetosheath from penetrating the magnetosphere. In the vicinity of the X-line, E_N modestly overlaps the null field region ($B_L = B_N = 0$). The strong out-of-plane current J_M during magnetopause reconnection actually peaks not at the X-line but displaced to the magnetosphere side of the X-line where E_N peaks. The high J_M is carried by high-velocity electrons with a crescent-shaped distribution in the V_M - V_N (perpendicular to B) plane that is symmetric across the V_M axis. This crescent distribution results from cusp-like orbits of electrons associated with the motion in the M - N plane controlled by $E_N(N)$ and $B_L(N)$ (22, 23). The motion is similar to that of pickup ions in the solar wind (24). Electrons around $B_L = 0$ are accelerated toward the magnetosphere by E_N . As they gain energy, B_L causes them to turn in the M direction. Eventually they turn around, reaching a peak velocity along M that is around twice the $\mathbf{E} \times \mathbf{B}$ velocity $V_{EB} = cE_N/B_L$. The electrons return to $B_L = 0$ with zero velocity (ignoring their thermal spread) and repeat their cusp-like motion. The electron distribution function can be calculated analytically. With increasing distance from the null region to the turning point in N , it transitions from a hot thermal distribution to a horseshoe-like distribution (with more particles at higher V_M and a depletion of particles around V_M , $V_N = 0$) and then to a crescent centered at a velocity V_M that increases with distance into the region of high E_N and narrows in the V_M direction.

As the magnetopause moves inward in this event, the crescent-shaped electron population enters a region of very weak magnetic field containing open field lines in the inner part of the electron exhaust. In the exhaust region, newly reconnected field lines move rapidly away from the X-line northward and southward—a phenomenon that has been described as a double slingshot (1) or simply a magnetic slingshot (2). It is likely that these exhaust region dynamics are responsible for redirection of the perpendicular crescents into the observed parallel crescents. Although the perpendicular crescents (averaged over V_{parallel}) were predicted in simulations (9), the parallel crescents have not been. Their direct observation by MMS therefore represents a new target for simulations.

Summary and implications

The MMS mission, which was designed to perform a definitive experiment on magnetic reconnection in space, has investigated electron-scale physics in an encounter with the dissipation region near a reconnection X-line at Earth's magnetopause. The high temporal resolution and accuracy of the MMS plasma and field measurements were both necessary and sufficient for the investigation of the electron physics controlling reconnection.

Using measurements of plasma currents and reconnection electric fields, we have shown that $\mathbf{J} \cdot \mathbf{E}' > 0$ in the vicinity of the X-line, as predicted for the dissipative nature of reconnection. Electron distribution functions were found to contain characteristic crescent-shaped features in velocity

space as evidence for the demagnetization and acceleration of electrons by an intense electric field near the reconnection X-line. MMS has directly determined the current density based on measured ion and electron velocities, which allowed the resolution of currents and associated dissipation on electron scales. These scales are smaller than the spacecraft separation distances and hence smaller than currents that can be determined by $\nabla \times \mathbf{B}$. The X-line region exhibits electron demagnetization and acceleration (by both E_N and E_M), which results in intense J_M current that is carried by the crescent-shaped electron distributions. Kinetic simulations had predicted some elements of the crescent distributions near the X-line, which raises the prospect of active interplay between theory and experiment, because the two techniques are now on a similar footing. The MMS measurements have led to discoveries about the evolution of electron acceleration in the dissipation region, as well as the escape of energized electrons away from the X-line into the downstream exhaust region. The latter was detected by at least two MMS spacecraft located on opposite sides of the X-line. The observed structures of the normal electric field and electron dynamics near the X-line by the four spacecraft are highly variable spatially and/or temporally, even on electron scales.

Among the implications of this initial MMS experiment is the discovery that the X-line region is important not only for the initiation of reconnection (breaking of the electron frozen-in condition), but also for electron acceleration and energization, leading to much stronger electron heating and acceleration than seen in the downstream exhaust. The details of the electron distribution functions, which show the rapid transition (within 30 ms) of the perpendicular crescent distributions to parallel crescents, provide experimental evidence for the opening up of magnetic field lines while also demonstrating that it is the electron dynamics that drives reconnection. Because of the importance of reconnection in many astrophysical and laboratory environments and the improvement achieved by its measurement resolution (25, 26), MMS has opened up a new window on the universal plasma process of magnetic reconnection.

Materials and methods

The science phase of MMS began on 1 September 2015, when the orbit apogee precessed beyond the dusk meridian toward the dayside, after which it skimmed the magnetopause for 6 months. The scientific strategy was to position the four spacecraft in a tetrahedral formation at radial distances from 9 to 12 R_E , first at the ion scale (160 km) and progressing to the smaller electron scale (10 km), so that magnetic reconnection could be investigated as the magnetopause crossed back and forth across the tetrahedron in response to variations in the solar wind dynamic pressure. This strategy bore fruit as several magnetopause crossings were observed on most days, with many of these crossings showing evidence for magnetic reconnection based on the appearance of plasma jetting. A

small subset of these reconnection events was sampled directly when the MMS spacecraft crossed near or through the electron dissipation region within which magnetic energy is converted to particle kinetic energy. Effective sampling at the electron scale requires measurements at the highest instrument data rate, termed a “burst mode.” Whenever the spacecraft are between 9 and 12 R_E (the region of interest), all instruments are run at their maximum data rates.

Because of data downlink volume limitations coupled with the unprecedentedly high internal data rate of the MMS instruments, careful selection of data to be downlinked is necessary. Two methods are used for the downlink data selection, both of which involve the use of a 96-GB onboard memory, which contains all the burst-mode data for two or more orbits of MMS. The first method of data selection involves the reporting of data evaluations by each instrument on a 10-s time scale, resulting in figures of merit for each interval, which are combined to generate a spacecraft figure of merit. These figures of merit are transmitted to the ground along with summary data for entire orbits. The summary data are similar to those shown in Fig. 1. Aggregate figures of merit for the four spacecraft are combined with ground software to generate a mission-level figure of merit. These automatically generated figures of merit then determine the priorities by which burst data are transmitted during the next ground contact.

The second data downlink selection method builds on the first one by using a scientist-in-the-loop to examine the figures of merit and the summary data for each day, with the goal of optimizing the data downlink selection by either adjusting the figures of merit or identifying new high-priority intervals that were not selected by the onboard system. Both systems are effective and both are being used throughout the mission. The data from all the independent sensors on each satellite, and between the four satellites, are intensively intercalibrated (25, 26).

Beginning on 1 March 2016, the entire MMS data set has been available online at <https://lasp.colorado.edu/mms/sdc/public/links/>. Fully calibrated data are placed online at this site within 30 days of their transmission to the MMS Science Operations Center. The data are archived in the NASA Common Data Format (CDF) and so can be plotted using a number of different data display software packages that can use CDF files. A very comprehensive system called the Space Physics Environment Data Analysis System (SPEDAS) is available by downloading http://themis.ssl.berkeley.edu/socware/bleeding_edge/andselectingspsdw_latest.zip.

Training sessions on the use of SPEDAS are held on a regular basis at space physics-related scientific meetings. All of the data plots in this paper were generated with SPEDAS software applied to the publicly available MMS database, so they could readily be duplicated.

REFERENCES AND NOTES

- J. L. Burch, J. F. Drake, Reconnecting magnetic fields. *Am. Sci.* **97**, 392–399 (2009). doi: [10.1511/2009.80.392](https://doi.org/10.1511/2009.80.392)
- G. Paschmann *et al.*, Plasma acceleration at the Earth's magnetopause: Evidence for reconnection. *Nature* **282**, 243–246 (1979). doi: [10.1038/282243a0](https://doi.org/10.1038/282243a0)
- M. Øieroset, T. D. Phan, M. Fujimoto, R. P. Lin, R. P. Lepping, In situ detection of collisionless reconnection in the Earth's magnetotail. *Nature* **412**, 414–417 (2001). doi: [10.1038/35086520](https://doi.org/10.1038/35086520); pmid: [11473310](https://pubmed.ncbi.nlm.nih.gov/11473310/)
- F. S. Mozer, S. D. Bale, T. D. Phan, Evidence of diffusion regions at a subsolar magnetopause crossing. *Phys. Rev. Lett.* **89**, 015002 (2002). doi: [10.1103/PhysRevLett.89.015002](https://doi.org/10.1103/PhysRevLett.89.015002); pmid: [12097047](https://pubmed.ncbi.nlm.nih.gov/12097047/)
- G. Paschmann, S. J. Schwartz, C. P. Escoubet, S. Haaland, Eds., *Outer Magnetospheric Boundaries: Cluster Results* (Springer, 2005).
- A. Vaivads *et al.*, Structure of the magnetic reconnection diffusion region from four-spacecraft observations. *Phys. Rev. Lett.* **93**, 105001 (2004). doi: [10.1103/PhysRevLett.93.105001](https://doi.org/10.1103/PhysRevLett.93.105001); pmid: [15447408](https://pubmed.ncbi.nlm.nih.gov/15447408/)
- T. Nagai *et al.*, Construction of magnetic reconnection in the near-Earth magnetotail with Geotail. *J. Geophys. Res.* **116**, 4222 (2011). doi: [10.1029/2010JA016283](https://doi.org/10.1029/2010JA016283)
- J. L. Burch, T. E. Moore, R. B. Torbert, B. L. Giles, Magnetospheric Multiscale overview and science objectives. *Space Sci. Rev.* **199**, 5–21 (2016). doi: [10.1007/s11214-015-0164-9](https://doi.org/10.1007/s11214-015-0164-9)
- M. Hesse, N. Aunai, D. Sibeck, J. Birn, On the electron diffusion region in planar, asymmetric, systems. *Geophys. Res. Lett.* **41**, 8673–8680 (2014). doi: [10.1002/2014GL061586](https://doi.org/10.1002/2014GL061586)
- L.-J. Chen, M. Hesse, S. Wang, N. Bessho, W. Daughton, Electron energization and structure of the diffusion region during asymmetric reconnection. *Geophys. Res. Lett.* **43**, 2405–2412 (2016). doi: [10.1002/2016GL068243](https://doi.org/10.1002/2016GL068243)
- J. R. Shuster *et al.*, Spatiotemporal evolution of electron characteristics in the electron diffusion region of magnetic reconnection: Implications for acceleration and heating. *Geophys. Res. Lett.* **42**, 2586–2593 (2015). doi: [10.1002/2015GL063601](https://doi.org/10.1002/2015GL063601)
- N. Bessho, L.-J. Chen, J. R. Shuster, S. Wang, Electron distribution functions in the electron diffusion region of magnetic reconnection: Physics behind the fine structures. *Geophys. Res. Lett.* **41**, 8688–8695 (2014). doi: [10.1002/2014GL062034](https://doi.org/10.1002/2014GL062034)
- P. A. Cassak, M. A. Shay, Scaling of asymmetric magnetic reconnection: General theory and collisional simulations. *Phys. Plasmas* **14**, 102114 (2007). doi: [10.1063/1.2795630](https://doi.org/10.1063/1.2795630)
- M. Yamada, J. Yoo, S. Zenitani, Energy conversion and inventory of a prototypical magnetic reconnection layer. In *Magnetic Reconnection*, W. Gonzalez, E. Parker, Eds. (Springer, 2016), pp. 143–179.
- M. Yamada, R. Kulsrud, H. Ji, Magnetic reconnection. *Rev. Mod. Phys.* **82**, 603–664 (2010). doi: [10.1103/RevModPhys.82.603](https://doi.org/10.1103/RevModPhys.82.603)
- T. D. Phan *et al.*, Extended magnetic reconnection at the Earth's magnetopause from detection of bi-directional jets. *Nature* **404**, 848–850 (2000). doi: [10.1038/3509050](https://doi.org/10.1038/3509050); pmid: [10786785](https://pubmed.ncbi.nlm.nih.gov/10786785/)
- P. L. Pritchett, Collisionless magnetic reconnection in an asymmetric current sheet. *J. Geophys. Res.* **113**, A06210 (2008). doi: [10.1029/2007JA012930](https://doi.org/10.1029/2007JA012930)
- S. Zenitani, M. Hesse, A. Klimas, M. Kuznetsova, New measure of the dissipation region in collisionless magnetic reconnection. *Phys. Rev. Lett.* **106**, 195003 (2011). doi: [10.1103/PhysRevLett.106.195003](https://doi.org/10.1103/PhysRevLett.106.195003)
- D. M. Willis, Structure of the magnetopause. *Rev. Geophys.* **9**, 953–985 (1971). doi: [10.1029/RG009i004p00953](https://doi.org/10.1029/RG009i004p00953)
- J. B. Blake *et al.*, The Fly's Eye Energetic Particle Spectrometer (FEEPS) sensors for the Magnetospheric Multiscale (MMS) Mission. *Space Sci. Rev.* **199**, 309–329 (2016). doi: [10.1007/s11214-015-0163-x](https://doi.org/10.1007/s11214-015-0163-x)
- B. H. Mauk *et al.*, The Energetic Particle Detector (EPD) investigation and the Energetic Ion Spectrometer (EIS) for the Magnetospheric Multiscale (MMS) Mission. *Space Sci. Rev.* **199**, 471–514 (2016). doi: [10.1007/s11214-014-0055-5](https://doi.org/10.1007/s11214-014-0055-5)
- M. A. Shay *et al.*, Kinetic signatures of the region surrounding the X-line in asymmetric (magnetopause) reconnection. *Geophys. Res. Lett.* **43**, 1828–1836 (2016). doi: [10.1002/2016GL069034](https://doi.org/10.1002/2016GL069034)
- N. Bessho, L.-J. Chen, M. Hesse, Electron distribution functions in the diffusion region of asymmetric magnetic reconnection. *Geophys. Res. Lett.* **43**, 1828–1836 (2016). doi: [10.1002/2016GL067886](https://doi.org/10.1002/2016GL067886)
- A. J. Coates, A. D. Johnstone, B. Wilken, K. Jockers, K.-H. Glassmeier, Velocity space diffusion of pickup ions from the water group at comet Halley. *J. Geophys. Res.* **94**, 9983–9993 (1989). doi: [10.1029/JA094iA08p09983](https://doi.org/10.1029/JA094iA08p09983)
- C. Pollock *et al.*, Fast Plasma Investigation for Magnetospheric Multiscale. *Space Sci. Rev.* **199**, 331–406 (2016). doi: [10.1007/s11214-016-0245-4](https://doi.org/10.1007/s11214-016-0245-4)
- R. B. Torbert *et al.*, The FIELDS Instrument Suite on MMS: Scientific objectives, measurements, and data products. *Space Sci. Rev.* **199**, 105–135 (2016). doi: [10.1007/s11214-014-0109-8](https://doi.org/10.1007/s11214-014-0109-8)
- A. Zeiler *et al.*, Three-dimensional particle simulations of collisionless magnetic reconnection. *J. Geophys. Res.* **107**, 1230 (2002). doi: [10.1029/2001JA000287](https://doi.org/10.1029/2001JA000287)
- C. K. Birdsall, A. B. Langdon, *Plasma Physics via Computer Simulation* (Taylor & Francis, 2004).

ACKNOWLEDGMENTS

The dedicated efforts of the entire MMS team are greatly appreciated. We are especially grateful to the leadership of C. Tooley, B. Robertson, and R. Black. Special thanks are due to C. Pankratz and K. Larsen of the University of Colorado for their leadership of the MMS Science Operations Center. Supported by NASA contract NNG04EB99C at Southwest Research Institute, which funded work at most of the co-author institutions in the United States. The IRAP contribution to MMS was supported by CNES. The Austrian contributions to the MMS mission are supported by grants from the Austrian Research Promotion Agency FFG. The UK work was supported by the UK Science and Technology Facilities Council through grants ST/K001051/1 and ST/N000692/1. The work by NASA GSFC authors was supported by the NASA Solar Terrestrial Probes program. The work of the GSFC-resident University of Maryland co-authors was supported by NASA Goddard Planetary Heliophysics Institute contract NNG11P02A. Work at U.C. Berkeley was supported by NASA MMS-IDS grant NNX08A083G through the University of California. Work at the University of Colorado by M.G. and D.N. was supported by NASA MMS-IDS Grant NNX08A084G through the University of Colorado. Work at the Swedish Institute for Space Physics and the Royal Institute of Technology was supported by the Swedish National Space Board. Work at West Virginia University was supported by NSF grants AGS-0953463 and AGS-1460037 and by NASA grants NNX16AG76G and NNS16AF75G.

20 January 2016; accepted 3 May 2016

Published online 12 May 2016

10.1126/science.aaf2939

RESEARCH ARTICLE

APPLIED OPTICS

Metalenses at visible wavelengths: Diffraction-limited focusing and subwavelength resolution imaging

Mohammadreza Khorasaninejad,^{1*} Wei Ting Chen,^{1*} Robert C. Devlin,^{1*} Jaewon Oh,^{1,2} Alexander Y. Zhu,¹ Federico Capasso^{1†}

Subwavelength resolution imaging requires high numerical aperture (NA) lenses, which are bulky and expensive. Metasurfaces allow the miniaturization of conventional refractive optics into planar structures. We show that high-aspect-ratio titanium dioxide metasurfaces can be fabricated and designed as metalenses with NA = 0.8. Diffraction-limited focusing is demonstrated at wavelengths of 405, 532, and 660 nm with corresponding efficiencies of 86, 73, and 66%. The metalenses can resolve nanoscale features separated by subwavelength distances and provide magnification as high as 170×, with image qualities comparable to a state-of-the-art commercial objective. Our results firmly establish that metalenses can have widespread applications in laser-based microscopy, imaging, and spectroscopy.

Metasurfaces are composed of subwavelength-spaced phase shifters at an interface, which allows for unprecedented control over the properties of light (1, 2), and have advanced optical technology by enabling versatile functionalities in a planar structure (1–30). Various optical components, ranging from lenses, holograms and gratings to polarization-selective devices, have been demonstrated using silicon-based (7–19) and plasmonic metasurfaces (3, 4, 21–27). However, the high intrinsic losses of silicon and plasmonic materials in the visible range (400 to 700 nm) have prevented the realization of highly efficient metasurfaces in this region. Although this challenge can be partially overcome by using dielectric materials with a transparency window in the visible spectrum (e.g., GaP, SiN, and TiO₂), achieving full control over the phase of light requires precise, high-aspect-ratio nanostructures, which are in turn restricted by available nanofabrication methods. Recently, we have developed an approach based on titanium dioxide (TiO₂) (31) prepared by atomic layer deposition (ALD) (32), which enables fabrication of high-aspect-ratio metasurfaces that are lossless in the visible spectrum. Here, we demonstrate highly efficient metalenses at visible wavelengths ($\lambda = 405, 532,$ and 660 nm) with efficiencies as high as 86%. They have high numerical apertures (NA) of 0.8 and are capable of focusing light into diffraction-limited spots. At their respective design wavelengths, these focal

spots are smaller by a factor of ~1.5 than those from a commercially available, high-NA objective (100× Nikon CFI 60; NA = 0.8). Imaging using these metalenses shows that they can yield subwavelength resolution, with image qualities comparable to that obtained by the commercial objective.

Planar lens design and fabrication

Typical high-NA objectives consist of precision-engineered compound lenses which make them bulky and expensive, limiting their applications and hindering their integration into compact and cost-effective systems. Singlet planar lenses with high NA in the visible range are in particularly high demand due to their potential widespread applications in imaging, microscopy, and spectroscopy. Although visible planar lenses can be realized by diffractive components, high NA and efficiency are not attainable because their constituent structures are of wavelength scale, which precludes an accurate phase profile.

Figure 1A shows a schematic of a transmissive dielectric metalens. The building blocks of the metalens are high-aspect-ratio TiO₂ nanofins (Fig. 1, B to E). To function like a spherical lens, the phase profile $\varphi_{nf}(x, y)$ of the metalens needs to follow (25)

$$\varphi_{nf}(x, y) = \frac{2\pi}{\lambda_d} \left(f - \sqrt{x^2 + y^2 + f^2} \right) \quad (1)$$

where λ_d is the design wavelength, x and y are the coordinates of each nanofin, and f is the focal length. This phase profile is imparted via rotation of each nanofin at a given coordinate (x, y) by an angle $\theta_{nf}(x, y)$ (Fig. 1E). In the case of right-handed circularly polarized incident light, these rotations yield a phase shift, $\varphi_{nf}(x, y) = 2\theta_{nf}(x, y)$,

accompanied by polarization conversion to left-handed circularly polarized light (33, 34). Thus, each nanofin at (x, y) is rotated by an angle

$$\theta_{nf}(x, y) = \frac{\pi}{\lambda_d} \left(f - \sqrt{x^2 + y^2 + f^2} \right) \quad (2)$$

To maximize the polarization conversion efficiency, the nanofins should operate as half-waveplates (11–13, 21). This is achieved due to the birefringence arising from the asymmetric cross section of nanofins with appropriately designed height, width, and length (Fig. 1, C and D). Simulations using a commercial finite difference time domain (FDTD) solver (Lumerical Inc., Vancouver) in Fig. 1F show that conversion efficiencies as high as 95% are achieved and that the metalens can be designed for a desired wavelength via tuning of nanofin parameters. The conversion efficiency is calculated as the ratio of transmitted optical power with opposite helicity to the total incident power.

Three distinct metalenses were fabricated with respective design wavelengths (λ_d) of 660, 532, and 405 nm. All of these metalenses have the same diameter of 240 μm and a focal length of 90 μm , yielding a NA = 0.8. The fabrication process uses electron-beam lithography to create the lens pattern in the resist (ZEP 520A). The thickness of the resist is the same as the designed nanofin height, H , and ALD is subsequently used to deposit amorphous TiO₂ onto the developed resist. Amorphous TiO₂ is chosen because it has low surface roughness, no absorption at visible wavelengths, and a sufficiently high refractive index (~2.4). Due to the ALD process being conformal, a deposition thickness of at least $W/2$ (where W is the nanofin width) is required to produce void-free nanofins (31). However, the deposition also leaves a TiO₂ film of equal thickness on top of the resist, which is then removed by controlled blanket reactive ion etching. Finally, the remaining electron beam resist is stripped, and only high-aspect-ratio nanofins remain. Figure 1, G and H, shows optical and scanning electron microscope (SEM) images of a fabricated metalens, respectively. Additional SEM micrographs of the metalens are shown in fig. S1 (35). Because the geometrical parameters of the nanofins are defined by the resist rather than top-down etching, high-aspect-ratio nanofins with ~90° vertical sidewalls are obtained. It is important to note that achieving these atomically smooth sidewalls is very challenging with a conventional top-down approach (e.g., lithography followed by dry etching), because inevitable lateral etching results in surface roughness and tapered/conical nanostructures.

Characterizing metalens performance

The metalenses' focal spot profiles and efficiencies were measured using the experimental setup shown in fig. S2. Figure 2A shows a highly symmetric focal spot that is obtained for the metalens at its design wavelength $\lambda_d = 660$ nm. The vertical cut of the focal spot is also shown in Fig. 2G with a diffraction-limited ($\frac{\lambda}{2 \times \text{NA}}$) full-width at half-maximum (FWHM) of 450 nm. Figure 2, B and H, show the focal spot of the metalens

¹Harvard John A. Paulson School of Engineering and Applied Sciences, Harvard University, Cambridge, MA 02138, USA.

²University of Waterloo, Waterloo, ON N2L 3G1, Canada.

*These authors contributed equally to this work. †Corresponding author. Email: capasso@seas.harvard.edu

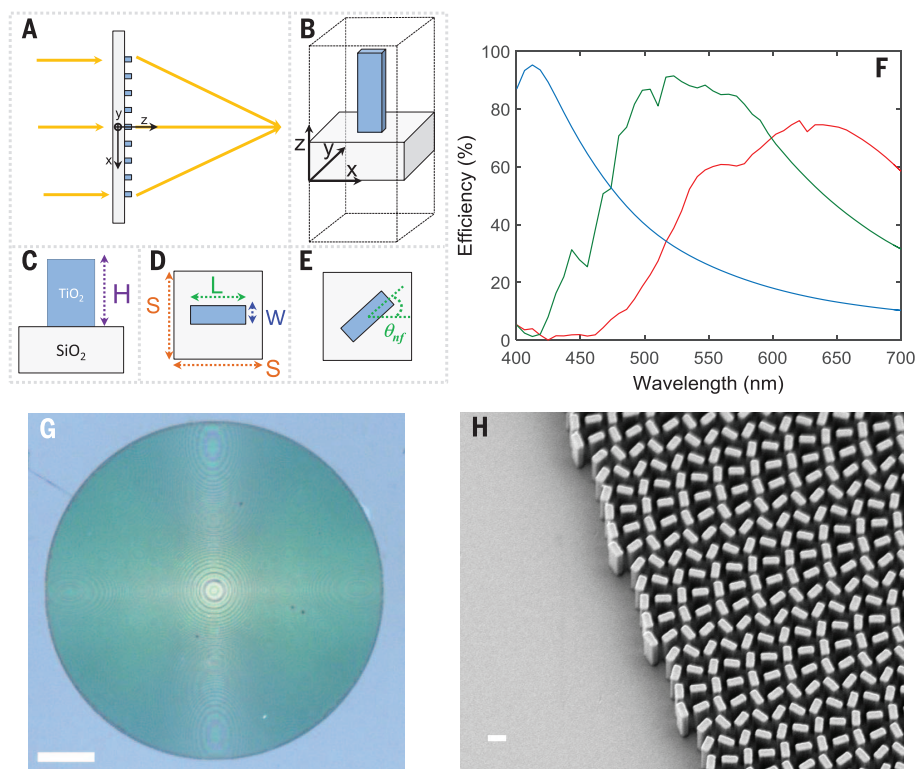


Fig. 1. Design and fabrication of metalenses. (A) Schematic of the metalens and its building block, the TiO_2 nanofin. (B) The metalens consists of TiO_2 nanofins on a glass substrate. (C and D) Side and top views of the unit cell showing height H , width W , and length L of the nanofin, with unit cell dimensions $S \times S$. (E) The required phase is imparted by rotation of the nanofin by an angle θ_{nf} , according to the geometric Pancharatnam-Berry phase. (F) Simulated polarization conversion efficiency as a function of wavelength. This efficiency is defined as the fraction of the incident circularly polarized optical power that is converted to transmitted optical power with opposite helicity. For these simulations, periodic boundary conditions are applied at the x and y boundaries and perfectly matched layers at the z boundaries. For the metalens designed at $\lambda_d = 660$ nm (red curve), nanofins have $W = 85$, $L = 410$, and $H = 600$ nm, with center-to-center spacing $S = 430$ nm. For the metalens designed at $\lambda_d = 532$ nm (green curve), nanofins have $W = 95$, $L = 250$, and $H = 600$ nm, with center-to-center spacing $S = 325$ nm. For the metalens designed at $\lambda_d = 405$ nm (blue curve), nanofins have $W = 40$, $L = 150$, and $H = 600$ nm, with center-to-center spacing $S = 200$ nm. (G) Optical image of the metalens designed at the wavelength of 660 nm. Scale bar, 40 μm . (H) SEM micrograph of the fabricated metalens. Scale bar, 300 nm.

designed at the wavelength of 532 nm and its corresponding vertical cut. Moreover, this metalens design can be extended to the shorter wavelength region of the visible range, which is of great interest in many areas of optics, such as lithography and photoluminescence spectroscopy. Figure 2C depicts the intensity profile of the focal spot from the metalens designed at the wavelength $\lambda_d = 405$ nm with a FWHM of 280 nm (Fig. 2I). Although this wavelength is very close to the band gap of TiO_2 $\lambda_g = 360$ nm, the absorption loss is still negligible (37).

To compare the performance of our metalenses with a commercially available lens, we selected a state-of-the-art Nikon objective. This objective has the same NA as our metalenses (0.8) and is designed for visible light. Focal spot intensity profiles of the objective at wavelengths of 660, 532, and 405 nm were measured using the same setup as in fig. S2 (see Fig. 2, D to F). A comparison of the corresponding focal spot cross sections in Fig. 2, G to I, and Fig. 2, J to L, reveals

that the metalenses provide smaller (~ 1.5 times) and more symmetric focal spots. This can be understood because conventional high-NA objectives are designed to image under broadband illumination. That is, wavefront aberrations need to be corrected for multiple wavelengths over a range of angles of incidence to meet industry standards for the required field of view. This is typically implemented by cascading a series of precisely aligned compound lenses. Fabrication imperfections in each individual optical lens and residual aberration errors, particularly spherical aberration, result in a focal spot size larger than theoretical predictions (36). In contrast, our metalens is designed to have a phase profile free of spherical aberration for normally incident light, which results in a diffraction-limited spot at a specific design wavelength (37). For example, the theoretical root mean squares of the wave aberration function (WAF_{RMS}) for the metalenses designed for 405, 532, and 660 nm are 0.049λ , 0.060λ , and 0.064λ , respectively. These values are

very close to the condition for a perfect spherical wavefront (37). We also calculated the Strehl ratio from the measured beam profiles for the three metalenses at their design wavelengths and found that they are close to 0.8 (see materials and methods and fig. S3), consistent with the observed diffraction-limited focusing. In addition, due to the use of the geometric phase, the phase profile of the metalens is only dependent on the rotation of the nanofins. This is controlled with very high precision, as is characteristic of electron-beam lithography. Alternatively, other high-throughput lithography methods such as deep-ultraviolet (UV) can provide similar fabrication accuracy.

It is important to note that although the metalenses were designed at specific wavelengths, we still observe wavelength-scale focal spots at wavelengths away from the design. For example, for the metalens designed at $\lambda_d = 532$ nm, we measured focal spot sizes of 720 and 590 nm at wavelengths of $\lambda = 660$ and 405 nm, respectively (fig. S4). The broadening of the focal spots with respect to the theoretical diffraction-limited values comes from chromatic aberration because metasurfaces are inherently dispersive. Chromatic aberrations in our metalens are more pronounced than the lenses based on refractive optics, resulting in a wavelength-dependent focal length (fig. S5A). This is generally not an issue for laser-related imaging, microscopy, and spectroscopy because monochromatic sources with narrow linewidths are used. For example, in Raman microscopes/spectrometers, a 532-nm laser with a linewidth of a few picometers is common. In this case, the linewidth-induced broadening of the focal spot size and change in focal length is negligible.

We also measured the focusing efficiency of the metalenses. As shown in Fig. 3A, the metalens designed at $\lambda_d = 660$ nm has a focusing efficiency of 66%, which remains above 50% in most of the visible range. Figure 3A also shows the measured focusing efficiency of the metalens designed at $\lambda_d = 532$ nm. This metalens has a focusing efficiency of 73% at its design wavelength. In addition, we measured the beam intensity profile of this metalens in the x - z cross section within a 40- μm span around the focal point (Fig. 3B). Details of this measurement are discussed in the supplementary materials (35) (see fig. S2 and materials and methods). The negligible background signal not only demonstrates excellent phase realization, where the beam converges to a diffraction-limited spot, but also shows the high conversion efficiency of each nanofin. For the metalens designed at the wavelength of 405 nm, a measured focusing efficiency of 86% is achieved. The latter measurement was done using a diode laser (Ondax Inc., Monrovia, CA) because the shortest wavelength that our tunable laser (SuperK Varia) can provide was ~ 470 nm. All of the efficiency measurements were performed using right circularly polarized incident light. However, the polarization sensitivity of the design can be overcome by implementing the phase profile using circular cross section nanopillars in

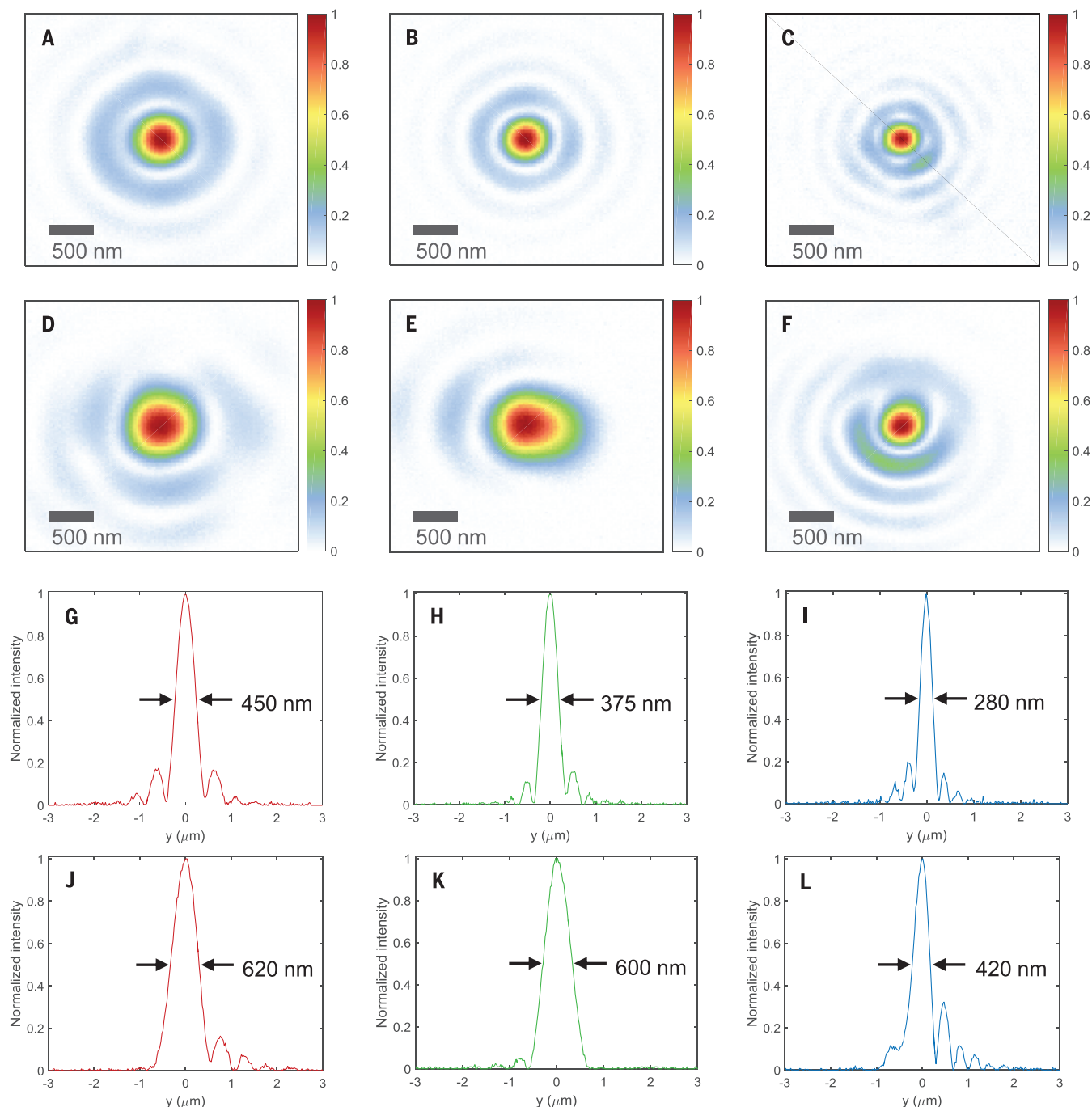


Fig. 2. Diffraction-limited focal spots of three metalenses (NA = 0.8) and comparison with a commercial state-of-the-art objective. (A to C) Measured focal spot intensity profile of the metalens designed at (A) $\lambda_d = 660$, (B) $\lambda_d = 532$, and (C) $\lambda_d = 405$ nm. (D to F) Measured focal spot intensity profiles of the objective (100 \times Nikon CFI 60, NA = 0.8) at wavelengths of (D) 660, (E) 532, and (F) 405 nm. (G to I) Corresponding vertical cuts of the metalenses' focal spots. Metalenses designed at wavelengths of 660,

532, and 405 nm have FWHMs = 450, 375, and 280 nm, respectively. The symmetric beam profiles and diffraction-limited focal spot sizes are related to the quality of the fabricated metalenses and accuracy of the phase realization. (J to L) Corresponding vertical cuts of the focal spots of the objective, at wavelengths of (J) 660, (K) 532, and (L) 405 nm. FWHMs of the focal spots are labeled on the plots. These values are ~ 1.5 times as large as those measured for the metalenses.

which the phase is controlled via changing their diameters.

Imaging demonstration

To demonstrate the use of our metalens for practical imaging, we fabricated a metalens with di-

ameter $D = 2$ mm and focal length $f = 0.725$ mm giving NA = 0.8. First, we characterized the imaging resolution using the 1951 United States Air Force (USAF) resolution test chart (Thorlabs Inc., Jessup, MD) as the target object. The measurement configuration is shown in fig. S6. Figure 4A

shows the image formed by the metalens. The light source was a tunable laser (SuperK Varia) set at 530 nm with a bandwidth of 5 nm. Because the resulting image was larger than our charge-coupled device (CCD) camera, we projected the image onto a translucent screen and took its

photo with a Canon digital single-lens reflex (DSLR) camera. The smallest features in this object are lines with widths of $2.2\ \mu\text{m}$ and center-to-center distances of $4.4\ \mu\text{m}$ (the bottom element in the highlighted region). A similar image quality is achieved at wavelengths covering the visible spectrum (fig. S7). Images of the smallest features were taken with a CCD camera shown in Fig. 4, B to E, at wavelengths of 480, 530, 590, and 620 nm, respectively. It is clear that the metalens can resolve these micrometer-sized lines. We repeated a similar experiment using a Siemens star target and showed that all features can be resolved over the whole visible range (figs. S8 and S9). As mentioned previously, the focal length of the metalens varies as the wavelength changes, resulting in different levels of magnification (fig. S5B). In our experimental setup, we used the metalens together with a tube lens ($f = 100\ \text{mm}$), giving a magnification of $138\times$ ($100/0.725$) at 530 nm. For wavelengths of 480, 590, and 620 nm, magnifications of $124\times$, $152\times$, and $167\times$ are obtained, respectively, by comparing the ratio of the image sizes formed on the camera to the known physical size of the USAF test object.

To characterize the effects of chromatic aberration, we imaged the same object at 530 nm without changing the distance between the metalens and the object, while varying the bandwidth of the source from 10 to 100 nm (the limit of our tunable laser). These results are shown in Fig. 4, F to I. Although the quality of the image slightly degrades from increasing the bandwidth, the smallest features are still resolvable even at the maximum bandwidth of 100 nm. Finally, for comparison of the imaging quality to that of a conventional objective, we fabricated an H-shaped object composed of arrays of holes with gaps of $\sim 800\ \text{nm}$ using a focused ion beam (FIB). An SEM micrograph of the object is shown in Fig. 4J. The image formed by the metalens (Fig. 4K) has comparable quality to the one formed by the $100\times$ Nikon objective (Fig. 4L) with the same NA = 0.8. The change in the image sizes comes from the difference in the magnification of the imaging systems. We also tested the resolution limit of our metalens: Four holes with subwavelength gap sizes of $\sim 450\ \text{nm}$ can be well resolved (Fig. 4M). This value agrees with the measured modulation transfer function of our metalens (supplementary materials and fig. S10).

Concluding remarks

The demonstrated visible-range metalenses, using TiO_2 with NA = 0.8 and efficiencies as high as 86%, show that they are able to provide diffraction-limited focal spots at arbitrary design wavelengths, which make them ideal devices for use in optical lithography, laser-based microscopy, and spectroscopy. Providing a magnification as high as $170\times$ and capable of resolving structures with subwavelength spacing, the compact configuration of our metalenses can enable portable/handheld instruments for many applications. Although our metalenses are subject to chromatic aberrations, the latter can be corrected with approaches such as dispersive phase compensation demonstrated

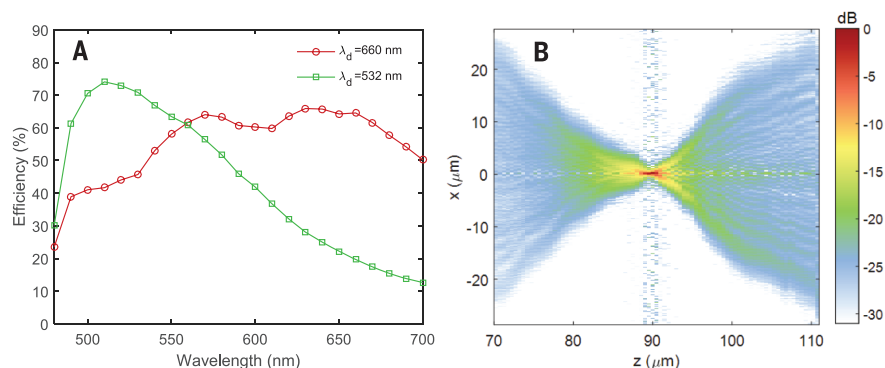


Fig. 3. Characterization of the metalenses. (A) Measured focusing efficiency of the metalenses designed at wavelengths of 660 nm and 532 nm. (B) Intensity distribution in dB of the x-z plane, showing the evolution of the beam from $20\ \mu\text{m}$ before and $20\ \mu\text{m}$ after the focus. This measurement was performed on the metalens designed at $\lambda_d = 532\ \text{nm}$. The wavelength of incident light was 532 nm.

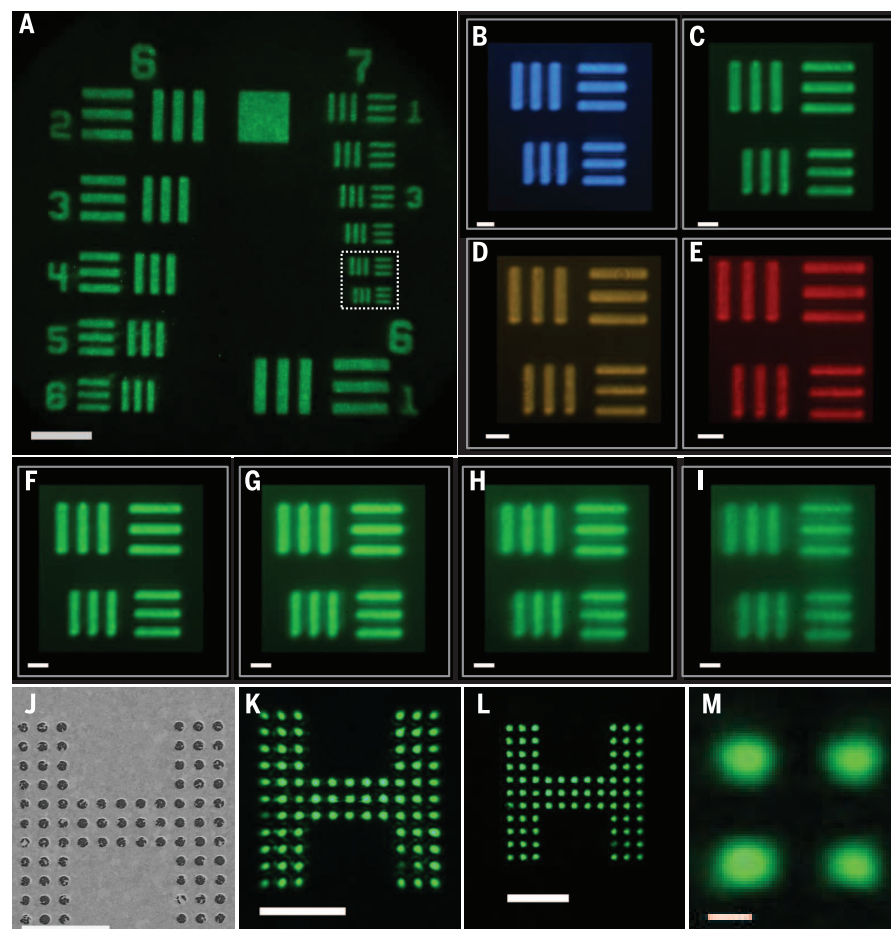


Fig. 4. Imaging with a metalens designed at $\lambda_d = 532\ \text{nm}$ with diameter $D = 2\ \text{mm}$ and focal length $f = 0.725\ \text{mm}$. (A) Image of 1951 USAF resolution test chart formed by the metalens taken with a DSLR camera. Laser wavelength is set at 530 nm. Scale bar, $40\ \mu\text{m}$. (B to E) Images of the highlighted region in Fig. 4A at wavelengths of (B) 480, (C) 530, (D) 590, and (E) 620 nm. Scale bar, $5\ \mu\text{m}$. (F to I) Images of the highlighted region in Fig. 4A at a center wavelength of 530 nm and with different bandwidths: (F) 10, (G) 30, (H) 50, and (I) 100 nm. Scale bar, $5\ \mu\text{m}$. (J) Nanoscale target prepared by FIB. The smallest gap between neighboring holes is $\sim 800\ \text{nm}$. (K) Image of target object (Fig. 4J) formed by the metalens. (L) Image of target object formed by the commercial state-of-the-art objective. Scale bar, $10\ \mu\text{m}$ in Fig. 4, J to L. (M) Image formed by the metalens shows that holes with subwavelength gaps of $\sim 450\ \text{nm}$ can be resolved. Scale bar, $500\ \text{nm}$.

in (9, 10). The single-layer lithographic fabrication of the metalenses can make use of existing foundry technology (deep-UV steppers) used in the manufacturing of integrated circuits, which is crucial for high throughput.

REFERENCES AND NOTES

1. N. Yu, F. Capasso, *Nat. Mater.* **13**, 139–150 (2014).
2. A. V. Kildishev, A. Boltasseva, V. M. Shalae, *Science* **339**, 1232009 (2013).
3. N. Yu *et al.*, *Science* **334**, 333–337 (2011).
4. X. Ni, N. K. Emani, A. V. Kildishev, A. Boltasseva, V. M. Shalae, *Science* **335**, 427–427 (2012).
5. A. Silva *et al.*, *Science* **343**, 160–163 (2014).
6. F. Monticone, N. M. Estakhri, A. Alù, *Phys. Rev. Lett.* **110**, 203903 (2013).
7. S. Jahani, Z. Jacob, *Nat. Nanotechnol.* **11**, 23–36 (2016).
8. D. Fattal, J. Li, Z. Peng, M. Fiorentino, R. G. Beausoleil, *Nat. Photonics* **4**, 466–470 (2010).
9. F. Aieta, M. A. Kats, P. Genevet, F. Capasso, *Science* **347**, 1342–1345 (2015).
10. M. Khorasaninejad *et al.*, *Nano Lett.* **15**, 5358–5362 (2015).
11. D. Lin, P. Fan, E. Hasman, M. L. Brongersma, *Science* **345**, 298–302 (2014).
12. Z. Bomzon, G. Biener, V. Kleiner, E. Hasman, *Opt. Lett.* **27**, 285–287 (2002).
13. M. Khorasaninejad, K. B. Crozier, *Nat. Commun.* **5**, 5386 (2014).
14. K. E. Chong *et al.*, *Nano Lett.* **15**, 5369–5374 (2015).
15. A. Arbabi, Y. Horie, A. J. Ball, M. Bagheri, A. Faraon, *Nat. Commun.* **6**, 7069 (2015).
16. C. J. Chang-Hasnain, *Semicond. Sci. Technol.* **26**, 014043 (2011).
17. Y. Yang *et al.*, *Nano Lett.* **14**, 1394–1399 (2014).
18. M. Khorasaninejad, W. Zhu, K. Crozier, *Optica* **2**, 376–382 (2015).
19. P. Spinelli, M. A. Verschuuren, A. Polman, *Nat. Commun.* **3**, 692 (2012).
20. S. Liu *et al.*, *Optica* **1**, 250–256 (2014).
21. G. Zheng *et al.*, *Nat. Nanotechnol.* **10**, 308–312 (2015).
22. E. T. Rogers *et al.*, *Nat. Mater.* **11**, 432–435 (2012).
23. S. Sun *et al.*, *Nano Lett.* **12**, 6223–6229 (2012).
24. S. Larouche, Y.-J. Tsai, T. Tyler, N. M. Jokerst, D. R. Smith, *Nat. Mater.* **11**, 450–454 (2012).
25. F. Aieta *et al.*, *Nano Lett.* **12**, 4932–4936 (2012).
26. X. Yin, Z. Ye, J. Rho, Y. Wang, X. Zhang, *Science* **339**, 1405–1407 (2013).
27. W. T. Chen *et al.*, *Nano Lett.* **14**, 225–230 (2014).
28. A. Grbic, L. Jiang, R. Merlin, *Science* **320**, 511–513 (2008).
29. M. Khorasaninejad, F. Capasso, *Nano Lett.* **15**, 6709–6715 (2015).
30. R. Merlin, *Science* **317**, 927–929 (2007).
31. R. C. Devlin, M. Khorasaninejad, W.-T. Chen, J. Oh, F. Capasso, *arXiv:1603.02735* (2016).
32. A. A. High *et al.*, *Nature* **522**, 192–196 (2015).
33. M. V. Berry, *J. Mod. Opt.* **34**, 1401–1407 (1987).
34. S. Pancharatnam, *Proceedings of the Indian Academy of Sciences, Section A* (Springer, 1956), vol. 44, pp. 398–417.
35. Supplementary materials are available on Science Online.
36. F. Yoshida, U.S. Patent App. 13/760,681, 2013.
37. F. Aieta, P. Genevet, M. Kats, F. Capasso, *Opt. Express* **21**, 31530–31539 (2013).

ACKNOWLEDGMENTS

This work was supported in part by the Air Force Office of Scientific Research (MURI, grant FA9550-14-1-0389), Charles Stark Draper Laboratory, Inc. (SC001-0000000959), and Thorlabs Inc. W.T.C. acknowledges postdoctoral fellowship support from the Ministry of Science and Technology, Taiwan (104-2917-I-564-058). R.C.D. is supported by a Charles Stark Draper Fellowship. A.Y.Z. thanks Harvard John A. Paulson School of Engineering and Applied Sciences and A*STAR Singapore under the National Science Scholarship scheme. Fabrication work was carried out in the Harvard Center for Nanoscale Systems, which is supported by the NSF. We thank E. Hu for the supercontinuum laser (NKT “SuperK”).

SUPPLEMENTARY MATERIALS

www.sciencemag.org/content/352/6290/1190/suppl/DC1
Materials and Methods
Figs. S1 to S10
Movie S1
References (38, 39)

10 March 2016; accepted 22 April 2016
10.1126/science.aaf6644

REPORTS

WATER CHEMISTRY

Structure and torsional dynamics of the water octamer from THz laser spectroscopy near 215 μm

William T. S. Cole,^{1*} James D. Farrell,^{2*} David J. Wales,^{2†} Richard J. Saykally^{1†}

Clusters of eight water molecules play an important role in theoretical analysis of aqueous structure and dynamics but have proven to be challenging experimental targets. Here we report the high-resolution spectroscopic characterization of the water octamer. Terahertz (THz) vibration-rotation-tunneling (VRT) spectroscopy resolved 99 transitions with 1 part per million precision in a narrow range near 46.5 wave numbers, which were assigned to the h_{16} octamer via detailed isotope dilution experiments. Fitting to a semi-rigid symmetric top model supports predictions of two coexisting cuboidal structures and provides precise values for the changes in their rotational constants. Comparison with theory and previous spectroscopic data provides a characterization of the two structures and the observed torsional vibration and supports the prediction that the D_{2d} symmetry structure is lower in energy than the S_4 isomer.

Spectroscopic study of water clusters provides accurate benchmarks for detailed characterization of the complex pairwise and many-body forces that operate in bulk water phases, which have proven difficult to adequately capture through bulk experiments or theory (1–4). The need to accomplish this goal is underscored by recurring controversies surrounding the fundamental intermolecular structure and dynamics of water (2, 5, 6). Clusters ranging from dimer through heptamer, as well as nonamer and decamer (7), have been studied in detail by high-precision microwave and terahertz spectroscopy, but the octamer has proven elusive (1, 2, 8–10). Whereas the most stable structures of smaller clusters evolve with size from quasiplanar rings to three-dimensional (3D) cages, the octamer represents the transition to cuboidal (8) structures formed by stacking quasiplanar four- and five-membered rings, a dominant motif in larger systems.

Accordingly, the water octamer has become a benchmark for theory, starting with the early work of Stillinger and David (11), Brink and Glasser (12), and Tsai and Jordan (13). Many groups have since investigated the structures, melting transitions, and hydrogen bond (HB) rearrangement dynamics of the octamer cluster (14–30). However, experimental characterization has been very challenging, with only a few successful mid-infrared (IR) spectroscopy (31–34) and crystallographic studies (35–37). The mid-IR results are particularly interesting, revealing two nonpolar low-energy struc-

tures (Fig. 1) formed by stacking of homodromic tetramer rings with the in-plane HBs directed in either the same (S_4 symmetry) or opposite (D_{2d} symmetry) senses. Both structures possess two distinct monomer environments: single HB donor and double HB donor, with the latter responsible for the association between the two tetramer rings. These structures have subsequently been refined by theory, with several groups calculating the ground state energy difference between the S_4 and the D_{2d} structures to be <0.1 kJ/mol (14–17, 37). Given such a small energy difference, both structures should be present even in very low temperature environments, e.g., supersonic beams.

Here we present the results of a study of the water h_{16} -octamer by terahertz vibration-rotation-tunneling (VRT) spectroscopy, involving the measurement of a very low frequency torsional vibration in both low-lying isomers. Nearly 100 individual vibration-rotation transitions have been measured to parts per million (ppm) accuracy and fitted to a standard semi-rigid symmetric rotor model, producing rotational constants, which, when combined with theoretical values, characterize the structures and vibrational distortions of the cluster. The results are in good agreement with recent theoretical predictions of the HB rearrangement tunneling rates (8) and cluster structures.

In an earlier study, Richardson *et al.* presented VRT spectra comprising 99 weak transitions measured near 1.4 THz and assigned to the h_{16} -water octamer cluster on the basis of detailed isotopic dilution studies (8). Spectral assignment was not possible at that time. In the same study, application of the ring polymer perturbative instanton method predicted the HB rearrangement tunneling rates for the h_{16} -octamer. Those results indicated that even for the most energetically accessible rearrangement, the magnitude of the tunneling

¹Department of Chemistry, University of California, Berkeley, CA 94705, USA. ²Department of Chemistry, University of Cambridge, Cambridge CB2 1EW, UK.

*These authors contributed equally to this work. †Corresponding author. Email: saykally@berkeley.edu (R.J.S.); dw34@cam.ac.uk (D.J.W.)

splitting was <42 Hz, well below our experimental resolution (~1 MHz). Subsequently, we have employed a statistical spectral assignment algorithm, which has enabled the detailed assignment of the spectra. A least-squares fit of the transitions yielded precise values for the vibrationally induced changes in the rotational constants of both isomers, which,

in combination with the earlier results of Gruenloh *et al.* (32, 33), provide a good estimate of the excited state rotational constants. Harmonic normal mode analysis predicts a diamond-type vibrational mode, shown in Fig. 1, for both isomer structures.

The measurement of VRT spectra and assignment to the h_{16} -water octamer with the Berkeley

Terahertz spectrometer is described in detail in (1–3) and in the supplementary materials. Because the 99 measured octamer transitions are confined to a very compact region (~350 MHz), it was assumed that the transitions belong to a Q branch. This is consistent with our previous THz VRT results for the similar h_{12} -hexamer, in which the Q branches were observed to have higher intensity than P- or R-branch transitions. To approach assignment of the very dense observed spectrum, we created a pattern recognition program to search the spectrum for transitions that displayed the energy-level pattern characteristic of the D_{2d} and S_4 structures. These patterns are distinct in that the D_{2d} equilibrium structure is an oblate symmetric rotor, whereas the S_4 structure is a prolate symmetric rotor, exhibiting opposite-intensity variations with the same J -quantum numbers. Using the output of this program as a starting point facilitated the assignment of 91 transitions to the D_{2d} (60 transitions) and S_4 (31 transitions) structures. The assignment, along with the eight weak unassigned lines, is shown in Fig. 2A. Figure 2, B and C, shows a comparison between the calculated and observed experimental spectrum for a representative Q-branch progression of each symmetry. As predicted (8), no evidence for tunneling splittings was observed. Figure 3 shows a measured vibration-rotation absorption feature, compared with the predicted tunneling splitting. We ultimately determined that the assigned transitions belong to two distinct parallel ($\Delta K = 0$) bands. The complete collection of assigned transitions is given in tables S1 and S2.

After assignment, the transitions were fitted to a standard, semi-rigid rotor energy-level expression (Eq. 1):

$$E(J, K) = \nu + \Delta B \times J(J+1) + \Delta M \times K^2 - \Delta D_J \times J^2(J+1)^2 - \Delta D_{JK} \times J(J+1)K^2 - \Delta D_K \times K^4 \quad (1)$$

Here ν is the band origin, B is the perpendicular rotational constant, and the D terms are the standard centrifugal distortion constants. The band origins are defined with respect to the absolute ground state of the respective cluster structures. All differences are defined as excited state minus ground state. The term ΔM is

$$\Delta M = (A' - B') - (A'' - B'') \text{ for the } S_4 \text{ octamer}$$

$$\Delta M = (B'' - C'') - (B' - C') \text{ for the } D_{2d} \text{ octamer}$$

Here ν is the band origin, B is the perpendicular rotational constant, and the D terms are the standard centrifugal distortion constants. The band origins are defined with respect to the absolute ground state of the respective cluster structures. All differences are defined as excited state minus ground state. The term ΔM is

$$\Delta M = (A' - B') - (A'' - B'') \text{ for the } S_4 \text{ octamer}$$

$$\Delta M = (B'' - C'') - (B' - C') \text{ for the } D_{2d} \text{ octamer}$$

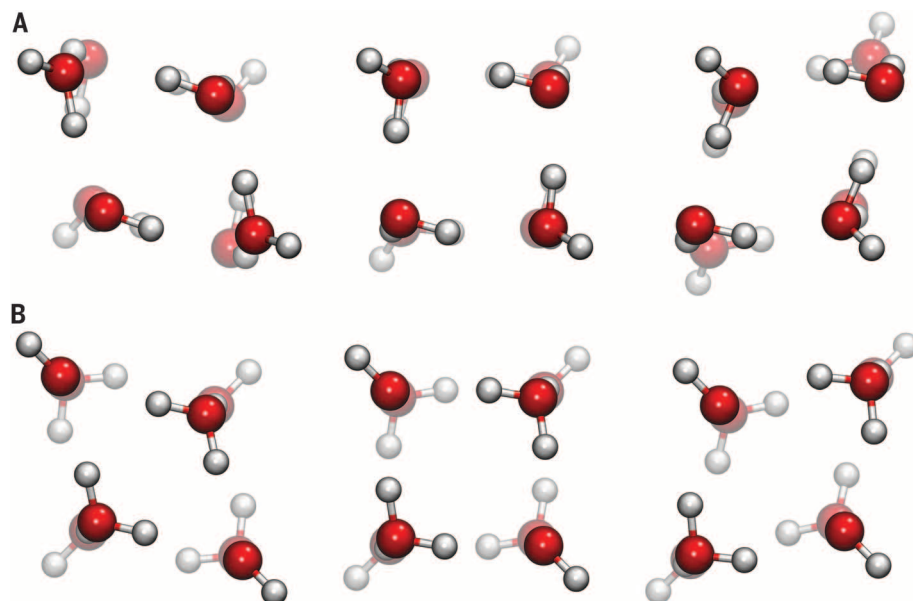


Fig. 1. The two lowest-energy structures predicted for the water octamer, viewed along the principal axes. Tentatively assigned low-frequency vibrational motions are also depicted. (A) The S_4 structure, viewed along the long axis (middle), pictured with displacements along the normal mode on either side. (B) The corresponding D_{2d} structure and displacements, viewed along the short axis. The D_{2d} structure is predicted to be slightly lower in energy, whereas entropy favors the S_4 structure (16).

Table 1. Fitted constants (in MHz) for the D_{2d} structure based on 60 assigned transitions.

Band origin is 46.13503 (cm^{-1}). Root mean square deviation of fit: 2.7 MHz.

Constant	Value	Error
ΔB	4.455	3.0×10^{-2}
ΔM	0.881	8.3×10^{-3}
ΔD_J	1.03×10^{-2}	9.0×10^{-5}
ΔD_{JK}	1.74×10^{-2}	7.9×10^{-4}
ΔD_K	-4.13×10^{-4}	4.5×10^{-5}
Band origin	1383093.60	1.6

Table 2. Fitted constants (in MHz) for the S_4 structure based on 31 assigned transitions.

Band origin is 46.13951 (cm^{-1}). Root mean square deviation of fit: 2.5 MHz.

Constant	Value	Error
ΔB	2.705	1.3×10^{-1}
ΔM	1.960	9.6×10^{-2}
ΔD_J	-1.58×10^{-3}	3.3×10^{-4}
ΔD_{JK}	-1.40×10^{-2}	3.3×10^{-3}
ΔD_K	4.16×10^{-3}	8.6×10^{-4}
Band origin	1383227.90	5.5×10^{-1}

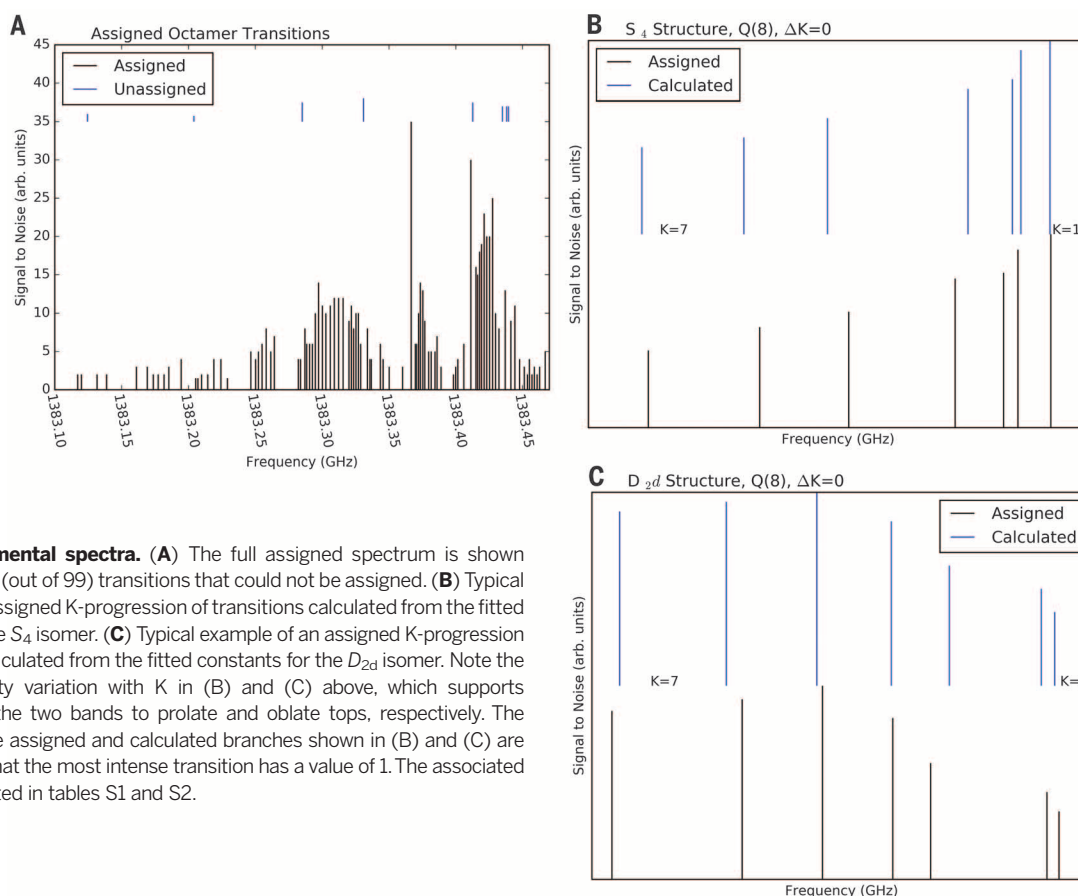


Fig. 2. Experimental spectra. (A) The full assigned spectrum is shown along with the 8 (out of 99) transitions that could not be assigned. (B) Typical example of an assigned K-progression of transitions calculated from the fitted constants for the S₄ isomer. (C) Typical example of an assigned K-progression of transitions calculated from the fitted constants for the D_{2d} isomer. Note the opposite-intensity variation with K in (B) and (C) above, which supports assignment of the two bands to prolate and oblate tops, respectively. The intensities of the assigned and calculated branches shown in (B) and (C) are normalized so that the most intense transition has a value of 1. The associated data are presented in tables S1 and S2.

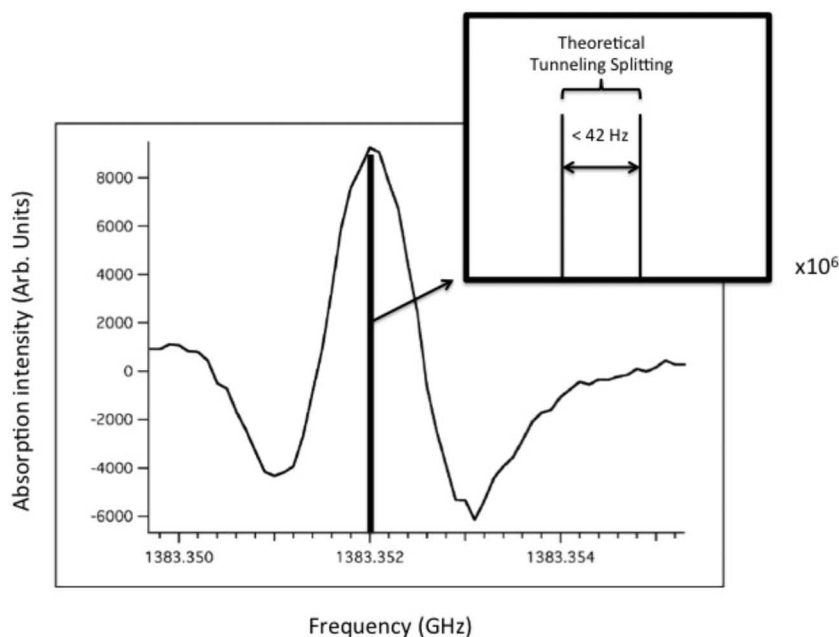


Fig. 3. A measured absorption transition showing the characteristic second derivative line shape observed. The full width at half-maximum linewidths are ~1 MHz. Tunneling splittings predicted in (8) are well below the experimental resolution, which is determined by the residual Doppler width in the planar supersonic expansion.

A and C represent the two remaining rotational constants, and primed values refer to excited state terms, whereas the double-primed values are those of the ground state. The difference in the ΔM terms reflects the two octamer structures being different types of symmetric rotors, as previously noted.

A least-squares fit of the 91 assigned transitions to Eq. 1 yielded root mean square deviations of 2.7 MHz (D_{2d}) and 2.5 MHz (S₄), respectively. Tables 1 and 2 present the fitted constants of both octamer structures for the ground and excited states, along with the 1 σ errors. Correlation matrices for the fits are given in figs. S1 and S2. Although a simple symmetric top rigid rotor energy expression produced a good fit of the assigned data, it is well known that water clusters are actually highly non-rigid complexes and as such may violate simple selection rules because the projection of rotational angular momentum along the symmetry axis (quantum number, K) is not rigorously conserved (2, 38).

Although spectroscopic determination of structural parameters is not possible without R- or P-branch assignments, the detailed isotope dilution results previously presented in (8) and the absence of any asymmetry splittings unambiguously identified the spectral carrier as the h₁₆-water octamer.

The observation of two distinct bands (at 46.13503 and 46.13951 cm^{-1}) can be rationalized in two ways. Either the bands could originate from two different vibrational modes of a single octamer structure, or each could belong to a similar vibration from separate octamer isomers. We argue that the second option is more likely. Two experimental observations support this conclusion. First, the two bands have opposite-intensity patterns, one displaying higher K components with lower intensity and the other higher K components with higher intensity, as evident in Fig. 2, B and C. These observations are consistent with the ground state energy-level diagrams of prolate and oblate symmetric tops, respectively. We have neglected vibrationally induced dipole changes here, as the transitions within a Q branch can reasonably be assumed not to differ appreciably in that regard. Second, the vibrational changes in rotational constants of the two bands are markedly similar, indicating that the corresponding motions are nearly identical. Moreover, even in molecules of this size, it is unlikely that two modes would exist in such extreme proximity (less than 0.005 cm^{-1}) as observed herein. On the basis of these considerations, we are confident in assigning the two bands to different water octamer isomers, one an oblate symmetric top and the other a prolate top.

Because the supersonic expansion cools the clusters to about 4 K, we are confident that the two structures are the D_{2d} and S_4 isomers, because they are consistently predicted to be particularly close in energy (14, 17, 27, 30, 32) and to have prolate (S_4) and oblate (D_{2d}) symmetric rotor eigenstates. On this basis, we assign the two observed bands to the S_4 or D_{2d} water octamer isomers.

The group comprising the energetically accessible permutation-inversion operations for the water octamer (i.e., operations that do not break a covalent bond) contains on the order of $8! \times 2^8 \times 2 = \sim 10^8$ elements. As for previous water clusters (1–3, 25), the water octamer is expected to display a high degree of nonrigidity. Assuming a rigid system enables us to exploit the corresponding point groups; however, this simplification may fail if the system is substantially nonrigid. A symmetric rotor energy-level expression is thus an approximation of the true energy-level structure of the complex. As with other water clusters, nonrigidity could lead to tunneling splittings of the simple symmetric top rigid rotor energy levels. Although we did not observe any tunneling in the spectra reported herein (in agreement with predictions) (8), the system still displays substantial nonrigidity in the form of low-frequency torsional vibrations and relaxed selection rules. A direct consequence of this nonrigidity is encountered in the description of the vibrational mode observed herein.

The observed transitions belong to parallel bands, implying a change in the dipole moment along the principal rotation axis. This result requires the observed vibration to have B symmetry in the case of the S_4 structure and B_2 symmetry for the D_{2d} competitor. A normal-mode analysis with the MB-pol potential (4, 39, 40) reveals that the lowest-frequency B_2 vibration corresponds to the

pattern in Fig. 1B, where the tetramers in the perpendicular plane distort to diamond geometries (see supplementary materials for methodological details and harmonic frequencies). The harmonic frequency of this mode is 74.8 cm^{-1} . The next lowest B_2 mode occurs at 204.1 cm^{-1} , involving the antisymmetric compression and expansion of the perpendicular faces. It is unlikely that these modes would reorder upon inclusion of anharmonic effects.

Given that both octamer structures display similar changes in rotational constants and noting the close proximity of the two bands, it is reasonable to expect that this vibrational motion is similar in the D_{2d} and S_4 isomers. The two lowest B modes of the S_4 structure occur at 69.9 and 76.9 cm^{-1} , the second of which is most similar in frequency to the mode assigned to the D_{2d} vibration and describes an almost identical displacement (Fig. 1A).

We stress that this description of the vibrational motion is but a starting point for future work. Previous studies of water clusters (1–3, 38, 41) have shown that nonrigidity results in vibrational motions that deviate appreciably from simple harmonic or rigid rotor approximations. Detailed quantitative analysis of the intermolecular vibrations in the octamer will clearly require further experiments and calculations.

Given the complexity of the nonrigid octamer structures, spectroscopically accurate calculations for the vibrational modes present a major challenge. Furthermore, a simple analysis of the energy landscape using TIPXP water potentials ($X = 3$ to 5) suggests that the number of minima may increase rapidly in the presence of an electric field (23). Shields and co-workers (17, 27) report the lowest anharmonically corrected ab initio intermolecular vibrational frequencies for the octamer as 57.2 (D_{2d}) and 54.7 (S_4) wave numbers, considerably higher than the experimental values near 46.1 cm^{-1} . Clearly, further theoretical advances are necessary to compute such cluster properties reliably, noting that much progress in this regard has recently been achieved for the water hexamer (41).

Finally, we report evidence in support of calculations showing that the D_{2d} structure is the lowest in energy (14, 23, 27, 29). If we assume that the transition dipole moment is similar for the competing cuboids, we can use the number and intensities of the observed transitions to infer the relative energetics. For the D_{2d} structure, we observe J values from 2 to 17, with some of the higher J subbands lacking some K value components. For the S_4 structure, we observe J values of only 5 to 10, and again, the higher J subbands are missing some K-value transitions. From this evidence, we infer that the D_{2d} structure is the lowest in energy.

REFERENCES AND NOTES

1. K. Liu, J. D. Cruzan, R. J. Saykally, *Science* **271**, 929–933 (1996).
2. F. N. Keutsch, R. J. Saykally, *Proc. Natl. Acad. Sci. U.S.A.* **98**, 10533–10540 (2001).
3. A. Mukhopadhyay, W. T. S. Cole, R. J. Saykally, *Chem. Phys. Lett.* **633**, 13–26 (2015).

4. V. Babin, C. Leforestier, F. Paesani, *J. Chem. Theory Comput.* **9**, 5395–5403 (2013).
5. R. S. Fellers, C. Leforestier, L. B. Braly, M. G. Brown, R. J. Saykally, *Science* **284**, 945–948 (1999).
6. Y. Wang, V. Babin, J. M. Bowman, F. Paesani, *J. Am. Chem. Soc.* **134**, 11116–11119 (2012).
7. C. Pérez et al., *Angew. Chem. Int. Ed. Engl.* **53**, 14368–14372 (2014).
8. J. O. Richardson et al., *J. Phys. Chem. A* **117**, 6960–6966 (2013).
9. C. Pérez et al., *Chem. Phys. Lett.* **571**, 1–15 (2013).
10. C. Pérez et al., *Science* **336**, 897–901 (2012).
11. F. Stillinger, C. W. David, *J. Chem. Phys.* **73**, 3384 (1980).
12. G. Brink, L. Glasser, *J. Phys. Chem.* **88**, 3412–3414 (1984).
13. C. J. Tsai, K. D. Jordan, *J. Chem. Phys.* **95**, 3850 (1991).
14. S. S. Xantheas, E. Aprà, *J. Chem. Phys.* **120**, 823–828 (2004).
15. M. B. Day, K. N. Kirschner, G. C. Shields, *Int. J. Quantum Chem.* **102**, 565–572 (2005).
16. R. M. Shields, B. Temelso, K. A. Archer, T. E. Morrell, G. C. Shields, *J. Phys. Chem. A* **114**, 11725–11737 (2010).
17. B. Temelso, G. C. Shields, *J. Chem. Theory Comput.* **7**, 2804–2817 (2011).
18. E. Asare, A. R. Musah, E. Curotto, D. L. Freeman, J. D. Doll, *J. Chem. Phys.* **131**, 184508 (2009).
19. J. Hernández-Rojas, B. S. González, T. James, D. J. Wales, *J. Chem. Phys.* **125**, 224302 (2006).
20. P. Nigra, M. A. Carignano, S. Kais, *J. Chem. Phys.* **115**, 2621 (2001).
21. Y. Sun, E. Gao, D. Wei, *Inorg. Chem. Commun.* **10**, 467–470 (2007).
22. D. J. Wales, I. Ohmine, *J. Chem. Phys.* **98**, 7245 (1993).
23. T. James, D. J. Wales, J. Hernández Rojas, *J. Chem. Phys.* **126**, 054506 (2007).
24. A. Tharrington, K. D. Jordan, *J. Phys. Chem. A* **107**, 7380–7389 (2003).
25. D. J. Wales, I. Ohmine, *J. Chem. Phys.* **98**, 7257 (1993).
26. T. Miyake, M. Aida, *Chem. Phys. Lett.* **427**, 215–220 (2006).
27. B. Temelso, K. A. Archer, G. C. Shields, *J. Phys. Chem. A* **115**, 12034–12046 (2011).
28. J. Gelman-Constantin, M. A. Carignano, I. Szleifer, E. J. Marceca, H. R. Corti, *J. Chem. Phys.* **133**, 024506 (2010).
29. S. Maeda, K. Ohno, *J. Phys. Chem. A* **111**, 4527–4534 (2007).
30. E. Miliordos, S. S. Xantheas, *J. Chem. Phys.* **142**, 234303 (2015).
31. U. Buck, I. Ettischer, M. Melzer, V. Buch, J. Sadlej, *Phys. Rev. Lett.* **80**, 2578–2581 (1998).
32. C. J. Gruenloh et al., *Science* **276**, 1678–1681 (1997).
33. C. J. Gruenloh et al., *J. Chem. Phys.* **109**, 6601 (1998).
34. B. P. Suiite, S. D. Belair, J. S. Francisco, *Phys. Rev. A* **71**, 043204 (2005).
35. W. B. Blanton et al., *J. Am. Chem. Soc.* **121**, 3551 (1999).
36. H.-J. Hao, D. Sun, F.-J. Liu, R.-B. Huang, L.-S. Zheng, *Cryst. Growth Des.* **11**, 5475–5482 (2011).
37. T. K. Prasad, M. V. Rajasekharan, *Cryst. Growth Des.* **6**, 488–491 (2006).
38. J. D. Cruzan et al., *Science* **271**, 59–62 (1996).
39. V. Babin, G. R. Medders, F. Paesani, *J. Chem. Theory Comput.* **10**, 1599–1607 (2014).
40. G. R. Medders, V. Babin, F. Paesani, *J. Chem. Theory Comput.* **10**, 2906–2910 (2014).
41. J. O. Richardson et al., *Science* **351**, 1310–1313 (2016).

ACKNOWLEDGMENTS

The Berkeley Terahertz project is supported by Chemical Structure, Dynamics, and Mechanisms—A Division of the National Science Foundation under grant no. 1300723. J.D.F. gratefully acknowledges A. Thom and D. Chakraborty for stimulating discussions. We thank the referees for thoughtful discussion during review. For details of the pattern recognition methodology, contact the authors or visit www.cchem.berkeley.edu/rjsgrp/.

SUPPLEMENTARY MATERIALS

www.sciencemag.org/content/352/6290/1194/suppl/DC1
Materials and Methods
Figs. S1 and S2
Tables S1 to S5
References (42–46)

12 November 2015; accepted 2 May 2016
10.1126/science.aad8625

GAS GIANT PLANETS

Peering through Jupiter's clouds with radio spectral imaging

Imke de Pater,^{1,2,3*} R. J. Sault,⁴ Bryan Butler,⁵ David DeBoer,¹ Michael H. Wong¹

Radio wavelengths can probe altitudes in Jupiter's atmosphere below its visible cloud layers. We used the Very Large Array to map this unexplored region down to ~8 bar, ~100 kilometers below the visible clouds. Our maps reveal a dynamically active planet at pressures less than 2 to 3 bar. A radio-hot belt exists, consisting of relatively transparent regions (a low ammonia concentration, NH_3 being the dominant source of opacity) probing depths to over ~8 bar; these regions probably coincide with 5-micrometer hot spots. Just to the south we distinguish an equatorial wave, bringing up ammonia gas from Jupiter's deep atmosphere. This wave has been theorized to produce the 5-micrometer hot spots; we observed the predicted radio counterpart of such hot spots.

Despite the fact that Jupiter has been observed for decades from the ground and in situ by spacecraft, questions remain about its bulk composition and global atmospheric dynamics. Much information on Jupiter's deep atmospheric composition was obtained, however, by the probe on the Galileo spacecraft, even though it descended in a 5- μm hot spot; i.e., a region that is "dry": devoid of clouds and condensable gases. The deep (>8 bar) mole fractions of NH_3 and H_2S were found to be enriched by a factor of 3 to 5 over the solar composition (1). This was several times higher than NH_3 mole fractions derived from radio spectra globally at higher altitudes [pressure (P) < 4 bar] and locally over the North Equatorial Belt (NEB) and Equatorial Zone (EZ) (2). With NH_3 being the dominant source of opacity at radio wavelengths, this difference could not be reconciled. A longitude-resolved global radio map of Jupiter (3), constructed from data at a single frequency of 15 GHz, showed regions similar to 5- μm hot spots with depleted NH_3 down to $P > 5$ bar but no regions with NH_3 mole fractions equal to the Galileo-derived deep abundance. A two-layer model of Jupiter's cloud-layer circulation was developed (4), explaining that NH_3 could be globally depleted (at 0.5 to 4 bar) if upward transport occurred primarily in precipitating thunderstorms. Our observations show that a two-layer circulation pattern is not needed to explain the NH_3 concentrations, at least in the equatorial region.

We used the upgraded Karl G. Jansky Very Large Array (VLA) (Table 1) to observe Jupiter over the full frequency range from 4 to 18 GHz

(1.7 to 7 cm) (5). Our new maps have a sensitivity up to an order of magnitude higher than the previously obtained longitude-resolved 15-GHz map, and achieve a 2 to 5 times higher spatial resolution (~1300 km at disk center in the new 15-GHz map versus ~5000 km in the previous map). These maps probe depths in Jupiter's atmosphere between ~0.5 and ~10 bar, a vertical range of over 100 km (2, 6), covering the altitude range where Jupiter's main cloud layers are formed (Fig. 1) (7).

Figure 2, A to D, shows radio maps averaged over 12 to 18 GHz, 8 to 12 GHz, and 4 to 8 GHz, after subtraction of a best-fit uniform limb-darkened disk (5). Panels E to H show Jupiter's almost-simultaneous appearance at visible wavelengths for comparison (8). A wealth of structure is visible in each radio map, which is easily distinguished from some "ripples" and large-scale dark and light areas that are instrumental artifacts. In panel D, some of these large-scale patterns are caused by Jupiter's synchrotron radiation (2, 5). Brightness temperatures (T_b s) in excess of the best-fit subtracted disk show up as bright (light-colored) regions, and lower temperatures are dark. A higher T_b indicates probing deeper levels in the atmosphere and hence suggests a low atmospheric opacity (i.e., low NH_3 concentration), and dark regions correspond to a high opacity. Our observations thus provide the three-dimensional distribution of NH_3 gas, which we use to trace dynamics, assuming the following: In parcels of rising air, NH_3 is enriched above solar levels, or within and above the NH_3 ice layer, NH_3 is saturated. Descending flows that originate at or above the NH_3 cloud base carry depleted ammonia with respect to the deep abundance.

Historically, the zone-belt structures at visible, 5- μm , and radio wavelengths were thought to be well correlated. Brownish belts were thought to correspond to bands that are bright at 5 μm and in the radio, and whiter zones to bands that were dark at 5 μm and in the radio (9). A detailed comparison of the images in Fig. 2, however,

reveals important refinements to this view. A radio-hot belt is visible right at the interface between the NEB and EZ, on the north side of the 7.8°N eastward jet. The northern and southern edges of the South Equatorial Belt (SEB) are radio-bright, whereas the darkest reddish interior is radio-dark. Several radio-bright bands are seen between 40° and 60°S, which do not necessarily seem to be connected to optical counterparts. The radio-hot belt at ~8°N contains structure at the limits of our resolution, as well as bright regions elongated in longitude. Elongated radio-bright regions coincide with the dark-gray-bluish regions in Fig. 2, E to H, at the same latitude (yellow arrows in Fig. 2, B and F) and are usually interpreted as "holes" in the cloud deck. These radio-bright, dark-gray-bluish regions are most likely related 5- μm hot spots (3, 10, 11).

All of these radio-bright bands are also visible at 4 to 8 GHz, although those at 40° to 60°S just barely. The radio-hot belt at ~8°N shows less detailed structure overall than at 8 to 12 GHz, despite the higher spatial resolution in this band. To determine how deep the low NH_3 concentration in this radio-hot belt extends, we made longitude-smeared and longitude-resolved maps integrated over 1-GHz-wide frequency bands (Table 1), and we modeled these maps with radiative transfer (RT) calculations (5, 6, 12). In our calculations, we assume that the NH_3 concentration (mole fraction) is equal to 5.7×10^{-4} at $P > 8$ bar, the average value detected by the Galileo probe at these depths (1), which is enhanced by a factor of ~4.5 over the solar N/H ratio (13). We assume that all constituents (C, S, N, and O) are enhanced by this same factor. Ammonia vertical profiles in Fig. 3A include an equilibrium case (profile a), where ammonia gas is decreased at higher altitudes due to solution in the water cloud (~7.3 bar), the formation of the NH_4SH cloud (~2.5 bar), and the NH_3 ice cloud (~0.8 bar). NH_3 follows the saturated vapor pressure curve within and above the NH_3 ice cloud. Several other NH_3 profiles used in our calculations (Fig. 3, B to F) are indicated. For simplicity, we adopt step functions at different altitudes, as shown. For some profiles we adopted a relative humidity (RH) of ~1 to 10% above the NH_3 ice cloud. All model atmospheres have a temperature of 165 K at 1 bar to match the Voyager radio occultation profile (14). By changing the NH_3 profile, the contribution functions in an atmosphere may change substantially (Fig. 1), which helps to understand differences in the model spectra.

Figure 3B shows spectra of the NEB, at the location of the longitude-smeared radio-hot belt (peak NEB values from fig. S3), and the EZ (minimum values) (5), with several models based on the profiles in Fig. 3A superimposed. Clearly, the radio-hot belt is well matched by profile e: NH_3 is depleted with respect to the deeper atmosphere by a factor of 5 to 6 down to $P \sim 8$ bar, or likely deeper as shown by profile e'. In contrast, the EZ is consistent with profile a, contradicting prior analyses that the EZ is depleted in

¹Department of Astronomy, 501 Campbell Hall, University of California, Berkeley, CA 94720, USA. ²Faculty of Aerospace Engineering, Delft University of Technology, 2629 HS Delft, Netherlands. ³SRON Netherlands Institute for Space Research, 3584 CA Utrecht, Netherlands. ⁴School of Physics, University of Melbourne, Victoria 3010, Australia. ⁵National Radio Astronomy Observatory, Socorro, NM 87801, USA.

*Corresponding author. Email: imke@berkeley.edu

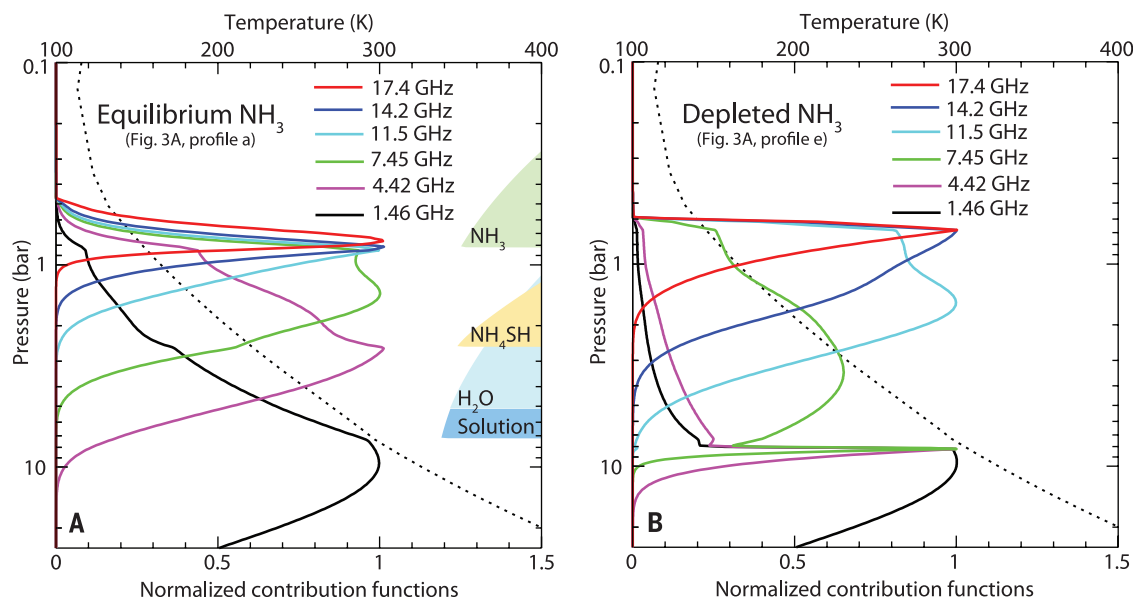


Fig. 1. Contribution functions. (A and B) Normalized contribution functions are shown for two different NH_3 profiles, as marked. The dotted line is the temperature-pressure curve in Jupiter's atmosphere. Cloud layers that are expected to form under chemical equilibrium are indicated as shaded regions in (A) (7).

NH_3 above the ~ 4 -bar level (2). The advance in our understanding is due to the upgrade in VLA sensitivity (15), higher spatial resolution in longitude-averaged images than obtained previously (2, 6), and full coverage over the entire 4- to 18-GHz frequency range.

The radio-hot belt contains numerous hot spots that contribute to the average NEB value. Spectra of these (at $\sim 10^\circ\text{N}$; Fig. 3C) were extracted from 1-GHz-wide longitude-resolved maps, where maxima in T_b were recorded. We determined values for four different hot spots on each day and averaged these. The true T_b may be slightly higher, because our maps do not resolve structure within the hot spots. A comparison with models shows that hot spots are characterized by a low NH_3 concentration, less than $\sim 10^{-4}$ over the 1- to 8-bar pressure level (profile e). A reasonable match to the data is given by profile f, with a concentration $\sim 10^{-5}$ at the highest altitudes ($P < 1$ bar), gradually increasing at deeper levels.

Just south of the radio-hot belt, striking oval-shaped dark regions are visible at 4 to 8 GHz (Fig. 2D); these are also quite prominent at 8 to 12 GHz (Fig. 2C) and only barely visible at higher frequencies (Fig. 2, A and B). Spectra of these regions ($\sim 4^\circ\text{N}$), referred to as plumes, are shown in Fig. 3D. A comparison with models shows that the plumes bring NH_3 gas from deep ($P > 8$ bar) atmospheric levels where the ammonia concentration is 5.7×10^{-4} , up to high altitudes ($P \sim 1.5$ bar), contrary to previous findings that there are no locations where the full deep NH_3 concentration is brought up to the 2-bar level (4). A two-layer circulation pattern with thunderstorm-dominated upwelling (4) is therefore inconsistent with NH_3 concentrations in equatorial regions.

These plumes (Fig. 2, C and D) display a regular wave pattern with wavelength 30° and are most pronounced over a 180° range in longitude.

Table 1. VLA data and products. Column 1: Observations were conducted: A configuration: 2014/05/04; B configuration: 2013/12/23 and 2014/01/09; C configuration: 2014/12/27; D configuration: 2014/08/16. Column 2: VLA frequency band. Column 3: Center frequency of each 1-GHz-wide map. Column 4: Jupiter's effective equatorial radius (R_{eff}) for the data from the combined arrays. The C-band longitude-resolved map was constructed from only A-configuration data, with $R_{\text{eff}} = 17487''$. Column 5: Disk-averaged T_b (final value) (5). Columns 6 and 7: Resolution or beam size (HPBW, full width at half power) in the final longitude-smeared images. Column 8: HPBW near the center of the disk in the final longitude-resolved images. $1''$ in latitude or longitude at Jupiter's disk center corresponds to ~ 1200 km.

VLA array configuration	Band	Frequency (GHz)	R_{eff} (")	T_b (K)	HPBW (")	HPBW (km)	HPBW (km)
B+D	Ku	13.18	15.80	159.5 ± 4.8	0.25	1130	~ 1550
B+D	Ku	14.21	15.80	154.5 ± 4.6	0.25	1130	~ 1450
B+D	Ku	15.18	15.80	150.6 ± 4.5	0.25	1130	~ 1300
B+D	Ku	16.21	15.80	146.4 ± 4.4	0.25	1130	~ 1250
B+D	Ku	17.38	15.80	143.5 ± 4.3	0.25	1130	~ 1180
B+C	X	8.50	21.46	187.7 ± 5.7	0.35	1166	~ 2300
B+C	X	9.52	21.46	177.5 ± 5.4	0.35	1166	~ 2100
B+C	X	10.46	21.46	172.4 ± 5.2	0.35	1166	~ 2000
B+C	X	11.46	21.46	165.8 ± 5.0	0.35	1166	~ 1750
A+C	C	4.52	21.46	247.5 ± 7.4	0.25	833	~ 1275
A+C	C	5.49	21.46	223.3 ± 6.7	0.25	833	~ 1100
A+C	C	6.50	21.46	207.6 ± 6.2	0.25	833	~ 980
A+C	C	7.50	21.46	192.9 ± 5.8	0.25	833	~ 900

A comparison of the location of five plumes on the 8- to 12-GHz map on 23 December 2013 (indicated by red arrows in Fig. 2C) with that on 9 January 2014 (5) reveals an eastward phase velocity of 102.2 ± 1.4 m/s relative to the System III coordinate system, which is ~ 20 to 25% slower than the 7.8°N eastward jet at 130 m/s (16). These characteristics are very similar to those displayed by $5\text{-}\mu\text{m}$ hot spots (17). These plumes could be the deep signature of the equatorially trapped Rossby wave thought to be responsible for forming the

$5\text{-}\mu\text{m}$ hot spots. Numerical simulations of such Rossby waves showed regions with a high NH_3 concentration in between (and slightly south of) the simulated hot spots (10, 11). At higher altitudes, the ammonia gas in these plumes will condense out, and as such could be responsible for the spectroscopically identified fresh ammonia ice clouds detected by the Galileo spacecraft at these latitudes (18).

Other prominent features in the radio maps are anticyclones, in particular the Great Red Spot (GRS)

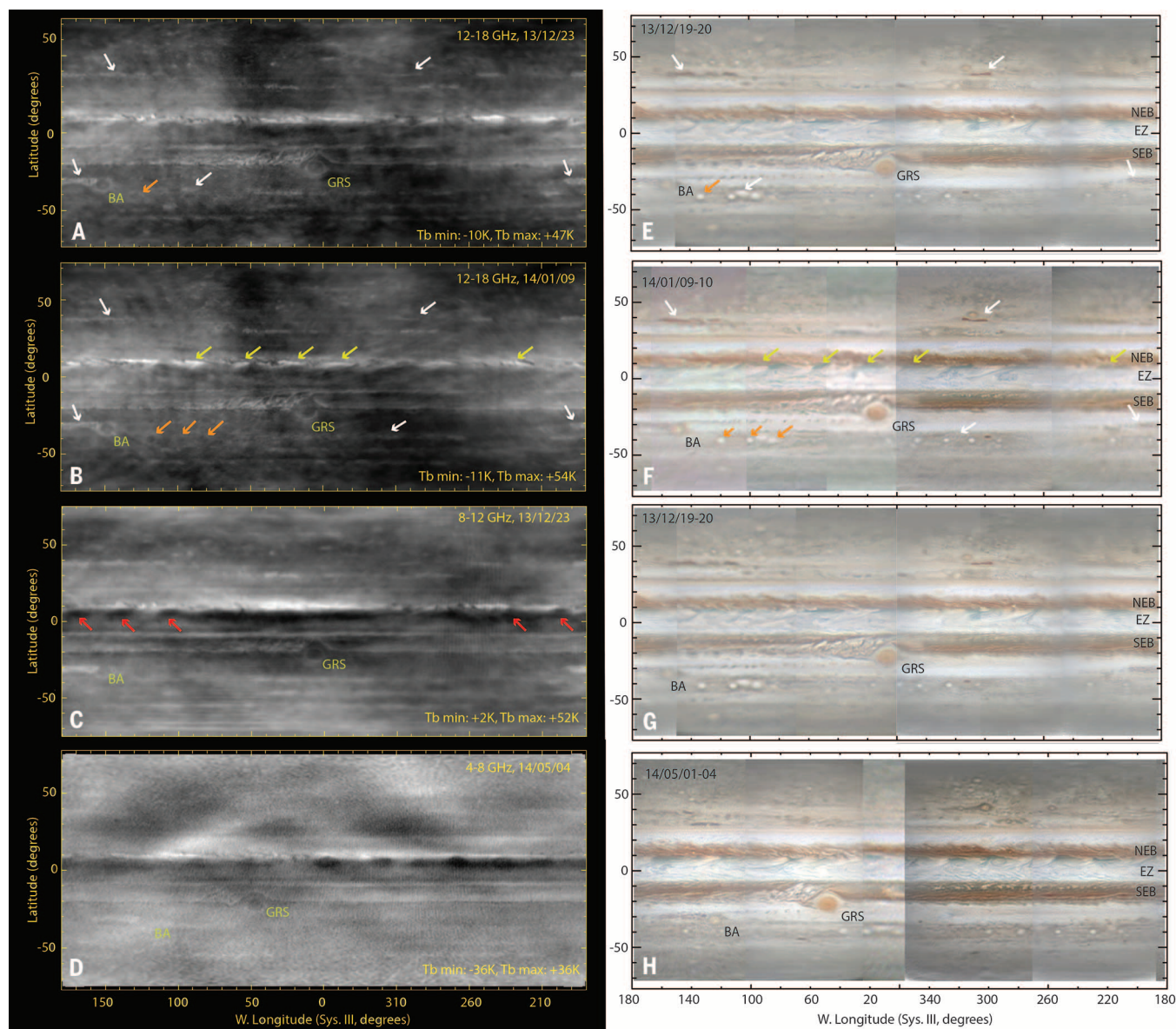


Fig. 2. Longitude-resolved VLA maps of Jupiter. (A to D) Longitude-resolved radio maps of Jupiter, after subtraction of a uniform limb-darkened disk (5). Each map has been integrated over the full ~4- to 6-GHz bandwidth. (E to H) Visible-light maps taken close in time with the VLA maps, as compiled by the amateur community (8). The axes indicate west longitude (in System III, prime meridian rotation angle of the magnetic field) and planetographic latitude. In addition to the GRS and Oval BA, several fea-

tures discussed in the text are highlighted by arrows on both a 12- to 18-GHz and visible wavelength map. The red arrows in Fig. 2C indicate the plumes used to derive their phase velocity through comparison with the 8- to 12-GHz map from 9 January 2014 (5). T_b min and T_b max give the differences in temperature for the minimum and maximum observed deviations from zero (i.e., with respect to the uniform limb-darkened disk that was subtracted).

and Oval BA but also the series of white ovals at 40°S (orange arrows) and numerous other small ovals. Anticyclones look relatively dark, often surrounded by a radio-bright ring, in contrast to cyclonic features, which are radio-bright (white arrows). These features are most apparent in the 8- to 12- and 12- to 18-GHz maps (i.e., at pressure levels <2 to 3 bar) (Fig. 1). The GRS is partially embedded in the SEB, which is relatively quiescent east of the GRS and extremely turbulent to the northwest. This turbulence produces the same fine-scale inhomogeneity in the radio maps

as well as the visible clouds. Oval BA is also characterized by a turbulent, relatively radio-bright, region to the west (resembling a cyclonic feature) and a quiescent region to the east. Figure 3, E to F, shows spectra of the GRS and Oval BA. The NH_3 concentration over the GRS itself looks similar to that of the EZ, except that it is depleted by a factor of ~2 down to ~1.5 bar (profile b) as compared to the EZ. The NH_3 concentration in the bright ring is depleted twice as much, down to ~2 to 2.5 bar (profile d). Although one would expect Oval BA and the GRS to have

similar NH_3 profiles, given their similar secondary circulation and sensitivity to environmental stratification (19), the VLA spectra reveal differences that might be related to entrainment from surrounding belts and zones with different NH_3 concentrations.

Our VLA maps at 8 to 18 GHz reveal structure at every resolvable length scale, tracing dynamical flows primarily at pressures <2 to 3 bar, where ammonia is strongly modulated by cloud condensation. At all observed frequencies, we find a radio-hot belt near the 7.8°N eastward jet, which

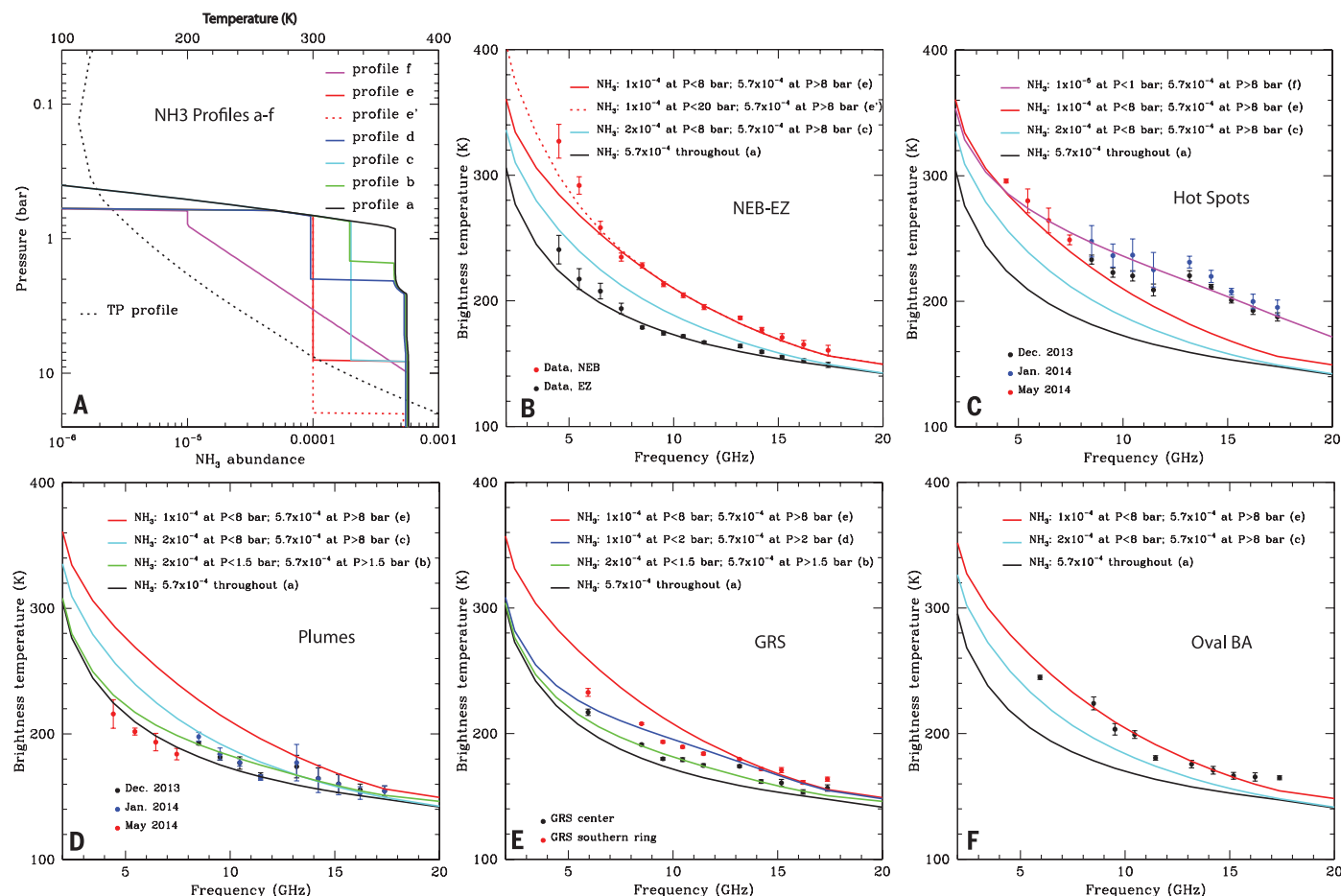


Fig. 3. Frequency dependence of specific features. (A) Altitude profiles of the NH_3 concentration used in the various models. The black-dotted line shows the temperature-pressure curve for NH_3 within and above the NH_3 ice cloud ($\text{RH} = 100\%$), whereas for the horizontal lines at a pressure of 0.6 bar, $\text{RH} = 1\%$. (B) Longitude-averaged brightness temperature as a function of frequency for the NEB and EZ, with RT models superimposed; T_b maxima (NEB) and

minima (EZ) from fig. S3 are plotted (5). Error bars are the standard deviation along the constant-latitude line. (C to F) T_b versus frequency for the GRS, Oval BA, hot spots, and plumes. Models are superimposed. The T_b for the GRS, Oval BA, and four plumes are averaged over the central regions; the values for the four plumes were averaged. The error bars give the standard deviation. The T_b for hot spots are local maxima; the error bars indicate the spread in the measured T_b .

contains the radio counterpart of the $5\text{-}\mu\text{m}$ hot spots, characterized by a low NH_3 concentration down to ~ 8 bar. The ascending branch of the equatorially trapped Rossby wave that produces the $5\text{-}\mu\text{m}$ hot spots carries the deep atmospheric NH_3 concentration up to the visible cloud layers, producing dark plumes in the VLA maps.

REFERENCES AND NOTES

- M. H. Wong, P. R. Mahaffy, S. K. Atreya, H. B. Niemann, T. C. Owen, *Icarus* **171**, 153–170 (2004).
- I. de Pater, D. Dunn, K. Zahnle, P. N. Romani, *Icarus* **149**, 66–78 (2001).
- R. J. Sault, C. Engel, I. de Pater, *Icarus* **168**, 336–343 (2004).
- A. P. Showman, I. de Pater, *Icarus* **174**, 192–204 (2005).
- See the supplementary materials.
- I. de Pater, D. DeBoer, M. Marley, R. Freedman, R. Young, *Icarus* **173**, 425–438 (2005).
- M. H. Wong, S. K. Atreya, W. R. Kuhn, P. N. Romani, K. M. Mihalka, *Icarus* **245**, 273–281 (2015).
- Marco Vedovato constructed groundbased optical Jupiter maps (from images taken by Christopher Go, Tadashi Horiuchi, Michel Jacquesson, Manos Kardasis, John Rozakis, Ian Sharp, Joost Verheyden, and Sean Walker) using Grisch Hahn's WinJupos software, available from <http://jupos.org>.
- J. J. Lissauer, I. de Pater, *Fundamental Planetary Science* (Cambridge Univ. Press) (2013).
- A. J. Friedson, *Icarus* **177**, 1–17 (2005).
- A. P. Showman, T. E. Dowling, *Science* **289**, 1737–1740 (2000).
- I. de Pater et al., *Icarus* **237**, 211–238 (2014).
- M. Asplund, N. Grevesse, A. J. Sauval, P. Scott, *Annu. Rev. Astron. Astrophys.* **47**, 481–522 (2009).
- G. F. Lindal, *Astron. J.* **103**, 967–982 (1992).
- R. A. Perley, C. J. Chandler, B. J. Butler, J. M. Wrobel, *Astrophys. J.* **739**, L1 (2011).
- X. S. Asay-Davis, P. S. Marcus, M. H. Wong, I. de Pater, *Icarus* **211**, 1215–1232 (2011).
- J. L. Ortiz et al., *J. Geophys. Res.* **103**, 23051–23069 (1998).
- K. H. Baines, R. W. Carlson, L. W. Kamp, *Icarus* **159**, 74–94 (2002).
- M. H. Wong, I. de Pater, X. Asay-Davis, P. S. Marcus, C. Y. Go, *Icarus* **215**, 211–225 (2011).

ACKNOWLEDGMENTS

This research was supported by NASA Planetary Astronomy (PAST) award NNX14AJ43G and NASA Outer Planets Research Program award NNX11AM55G. The National Radio Astronomy Observatory (NRAO) is a facility of NSF operated under cooperative agreement by Associated Universities, Inc. VLA data used in this report, associated with project code 13B-064, are available from the NRAO Science Data Archive at <https://archive.nrao.edu/archive/advquery.jsp>. Ground-based optical Jupiter maps (8) are available from the Planetary Virtual Observatory & Laboratory (PVOL) website at <http://www.pvol.ehu.es/pvol/index.jsp?action=iopw>. We thank three anonymous reviewers for their thoughtful comments on this paper.

SUPPLEMENTARY MATERIALS

www.sciencemag.org/content/352/6290/1198/suppl/DC1
Materials and Methods
Figs. S1 to S5
Tables S1 and S2
References (20–26)

8 January 2016; accepted 29 April 2016
10.1126/science.aaf2210

APPLIED OPTICS

Photonic spin-controlled multifunctional shared-aperture antenna array

Elhanan Maguid,^{1*} Igor Yulevich,^{1*} Dekel Veksler,^{1*} Vladimir Kleiner,¹
Mark L. Brongersma,² Erez Hasman^{1†}

The shared-aperture phased antenna array developed in the field of radar applications is a promising approach for increased functionality in photonics. The alliance between the shared-aperture concepts and the geometric phase phenomenon arising from spin-orbit interaction provides a route to implement photonic spin-control multifunctional metasurfaces. We adopted a thinning technique within the shared-aperture synthesis and investigated interleaved sparse nanoantenna matrices and the spin-enabled asymmetric harmonic response to achieve helicity-controlled multiple structured wavefronts such as vortex beams carrying orbital angular momentum. We used multiplexed geometric phase profiles to simultaneously measure spectrum characteristics and the polarization state of light, enabling integrated on-chip spectropolarimetric analysis. The shared-aperture metasurface platform opens a pathway to novel types of nanophotonic functionality.

Multifunctional planar systems that can perform a number of concurrent tasks in a shared aperture were recently introduced in the field of phased-array antennas for radar applications. In particular, modern radio frequency sensing, communication, and imaging systems based on sparse phased-array antennas are able to operate at different

frequency bands, polarizations, scanning directions, etc. These capabilities are ascribed to subarrays of elementary radiators, sharing a common physical area that constitutes the complete aperture of the phased array (1–4). The shared-aperture concept can be adopted to realize multifunctional photonic antenna arrays. The recent implementation of metasurfaces, or metamaterials of reduced

dimensionality, is of particular relevance, as it opens up new opportunities to acquire virtually flat optics. Metasurfaces consist of a dense arrangement of resonant optical antennas on a scale smaller than the wavelength of external stimuli (5–10). The resonant nature of the light-matter interaction of an individual nanoantenna affords substantial control over the local light scattering properties. Specifically, the local phase pick-up can be manipulated by tailoring the antenna material, size, and shape, as well as environment-antenna resonance shaping (11–15), or through the geometric phase concept (10, 16–20). The latter concept is an efficient approach for achieving spin-controlled phase modulation, whereas the photon spin is associated with the intrinsic angular momentum of light (21). Such a geometric phase metasurface (GPM) transforms an incident circularly polarized light into a beam of opposite helicity, imprinted with a geometric phase $\phi_g(x, y) = 2\sigma_\pm \theta(x, y)$, where $\sigma_\pm = \pm 1$ denotes the polarization helicity [photon spin in \hbar units (\hbar is Planck's constant h divided by 2π)] of the incident light, and $\theta(x, y)$ is the nanoantenna orientation (22). Here we incorporate the shared-aperture phased antenna array concept and spin-controlled two-dimensional (2D) optics based on nanoantennas. By use of the geometric phase mechanism, the

¹Micro and Nanooptics Laboratory, Faculty of Mechanical Engineering, and Russell Berrie Nanotechnology Institute, Technion – Israel Institute of Technology, Haifa 32000, Israel. ²Geballe Laboratory for Advanced Materials, Stanford University, 476 Lomita Mall, Stanford, CA 94305, USA.

*These authors contributed equally to this work. †Corresponding author. Email: mehasman@technion.ac.il

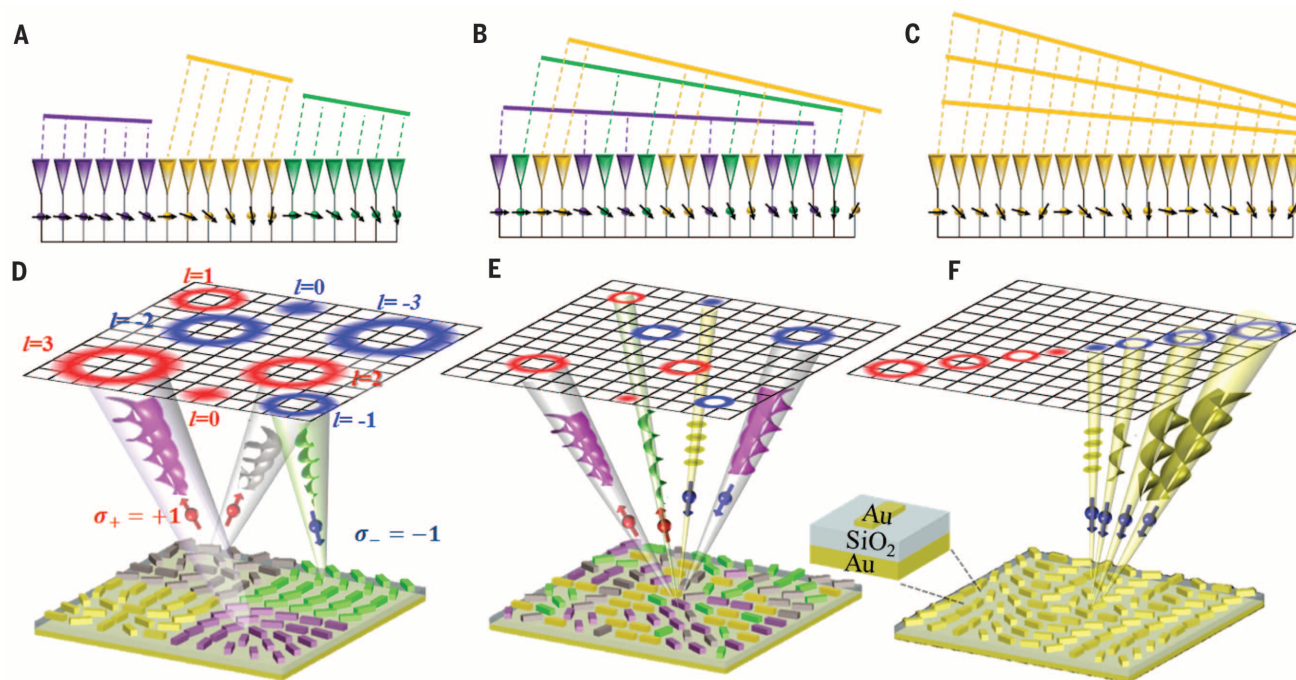


Fig. 1. Schematic of shared-aperture concepts. (A to C) Segmented (A), interleaved (B), and HR (C) 1D phased arrays. (D to F) Schematic far-field intensity distribution of wavefronts with positive (red) and negative (blue) helicities emerging from segmented (D), interleaved (E), and HR (F) GPMs composed of gap-plasmon nanoantennas (inset). Here, l denotes the topological charge of the spin-dependent OAM wavefronts [for more details, see (22)].

spin-orbit interaction phenomenon, a multifunctional GPM, is implemented (Fig. 1).

Photonic GPMs with spatially interleaved phase profiles are designed by the random mixing of optical nanoantenna subarrays, where each subarray provides a different phase function in a spin-dependent manner. This approach makes use of the peculiar ability of random patterns to yield extraordinary information capacity and polarization helicity control via the geometric phase concept. We realized a high-efficiency multifunctional GPM in which the phase and polarization distributions of each wavefront are

independently controlled. These GPMs are based on gap-plasmon resonator (GPR) nanoantennas that consist of metal-insulator-metal layers that enable high reflectivity by increasing the coupling between the free wave and the fundamental resonator mode. Moreover, adjustment of the GPR nanoantenna's dimensions enables the design of a high-efficiency half-wave plate (22, 23). For the reflection mode of a single wavefront, we found a diffraction efficiency of $\sim 79\%$, which is in good agreement with the theory (10, 18, 19) and the finite-difference time-domain (FDTD) simulation (fig. S1, D to F) (22). Then, to design a metasurface

generating multiple spin-dependent wavefronts carrying orbital angular momentum (OAM), the GPR nanoantennas were randomly distributed into equal interleaved subarrays. The nanoantennas of each j th subarray were oriented according to the relation $2\theta_j(x, y) = k_j x + l_j \varphi$, to obtain momentum redirection $\sigma_z k_j$ and topological charge (winding number) $\sigma_z l_j$; φ is the azimuthal angle (Fig. 2A). We measured the far-field intensity distribution by illuminating the metasurface with circularly polarized light at a wavelength of 760 nm, and we observed three-by-two spin-dependent OAM wavefronts with the desired topological

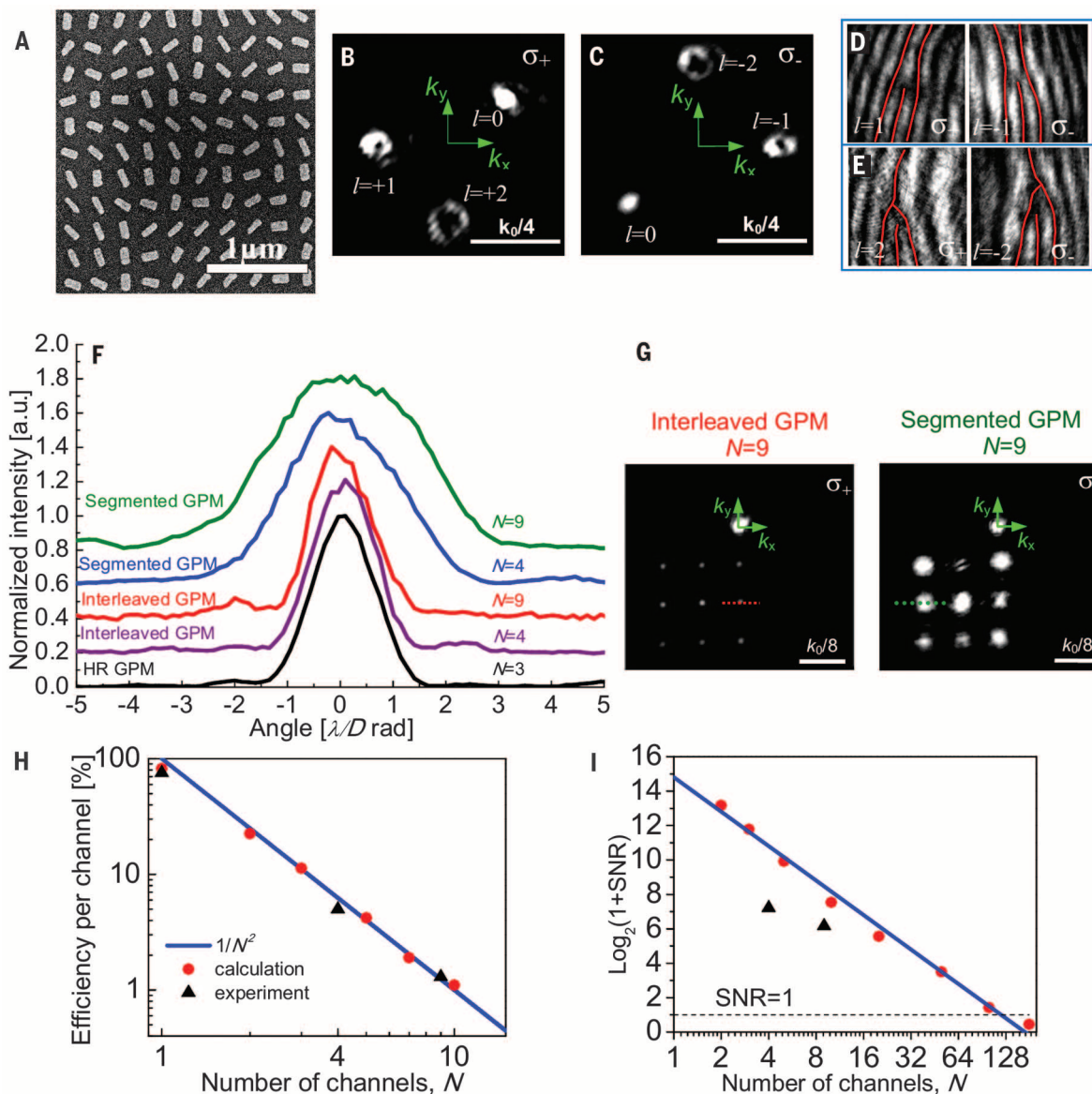
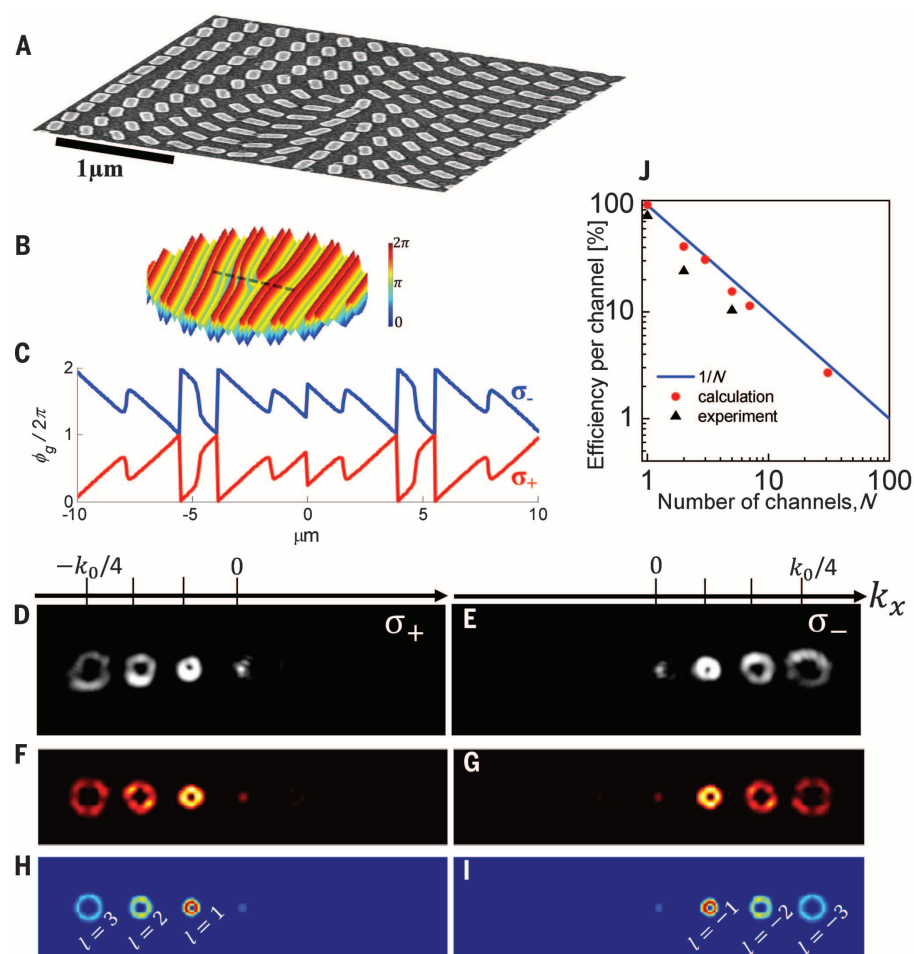


Fig. 2. Multiple wavefront shaping via interleaved GPMs. (A) Scanning electron microscope image of a gap-plasmon GPM of aperture $D = 50 \mu\text{m}$. (B and C) Measured spin-flip momentum deviation of three wavefronts with different OAMs. σ_+ denotes the incident spin. k_0 is the wave number of the incident beam. (D and E) Interference pattern of the spin-flipped components with a plane wave, observed from different GPMs generating OAM wavefronts of $l = \pm 1$ (D) and $l = \pm 2$ (E), for σ_- and σ_+ illumination. (F) Observed angular width of plane waves emerging

from shared-aperture GPMs of different types and numbers of generated channels, corresponding to different colors. a.u., arbitrary units; rad, radians. (G) Measured momentum deviations for the interleaved and segmented GPMs, wherein the intensity distributions of nine channels in (F) are presented along the dashed colored lines. (H and I) Efficiency per channel (H) and number of bits per channel (I). Red dots and black triangles denote the calculation and experiment results, respectively. The blue lines correspond to $\sim 1/N^2$.

Fig. 3. Spin-dependent asymmetric HR. (A) Scanning electron microscope image of the fabricated gap-plasmon HR GPM. (B) Geometric phase distribution of the entire HR GPM for σ_{\pm} . (C) Calculated phase distributions along the 20- μm dashed line in (B) for σ_{-} (blue) and σ_{+} (red). (D to I) Measured [(D) and (E)], FDTD-simulated [(F) and (G)], and calculated Fourier amplitude [(H) and (I)] spin-dependent HR diffractions of OAM orders, for right (σ_{+}) and left (σ_{-}) circular polarization illuminations at a wavelength of $\lambda = 760$ nm. The dim zero-order spot arises from an additional harmonic of the “triplicator” phase function and is of negligible efficiency (2%). (J) Efficiency per channel. Red dots and black triangles denote the calculation and experiment results, respectively. The blue line corresponds to $1/N$.



charges of 0, ± 1 , and ± 2 (Fig. 2, B and C), in agreement with FDTD simulation (fig. S2). The corresponding OAMs were verified by measuring the dislocation strength by the interference of the vortex beams with a plane wave (Fig. 2, D and E). An additional peculiar twist in the field of metasurfaces relies on space-variant polarization manipulation, which may encompass a broader class of wavefront shaping. An interleaved GPM enables us to obtain multiple vectorial vortices by coherent superposition of wavefronts with opposite helicities (fig. S6 and movies S1 and S2) (22).

We used far-field measurements to experimentally examine the angular resolution characteristics of the interleaved and segmented GPMs. In the segmentation approach, increasing the number of wavefronts (N) results in an angular width of $\Delta\theta \sim \sqrt{N} \cdot \lambda/D$, whereas for the interleaved GPM it is approximately λ/D for an arbitrary N , matching the diffraction-limited angular resolution of the shared aperture of size D at a wavelength λ (Fig. 2, F and G, and figs. S4 and S5). However, the above analysis does not hold the promise to obtain high information capacity for the interleaved approach, as it is also strongly influenced by the noise originated from channels mixing. The signal-to-noise ratio (SNR) determines the available number of bits per channel as

$\log_2(1 + \text{SNR})$ and sets the limit N_c for the channel capacity when $\text{SNR} = 1$. To estimate the effect of an incrementally growing number of wavefronts on SNR, the far-field intensity distributions were calculated via Fourier transform (22). The calculation shows that the SNR scales as $1/N^2$, leading to a channel capacity limit of $N_c \approx 130$ for the interleaved GPM of $D = 50$ μm (Fig. 2I). Moreover, both the calculations and experiments show that the intensity per channel decreases according to $1/N^2$ (Fig. 2H).

Unlike the interleaved GPM, the harmonic response (HR) metasurface is not limited by the intensity scaling of $1/N^2$. The HR concept relies on different optimization methods, iterative and analytic, and has been implemented in a variety of realms such as holography, communication, and radar (24–26). To obtain spin-dependent asymmetric harmonic diffraction orders, we incorporated the HR and geometric phase concepts. The geometric phase function can be expanded to spin-dependent OAM harmonic orders $A_m \exp[i m \sigma_{\pm} (kx + \varphi)]$ (where A_m is the amplitude of m th order and i is the square root of -1), where $\sigma_{\pm} m k$ is the momentum redirection of m th order. The phase function can be optimized to achieve identical intensities $|A_m|^2 \approx 1/(b-a+1)$ for selected asymmetric orders $a < m < b$ with maximal optical efficiency. We adopted an op-

timized analytic solution [the “triplicator” (25)] to realize a GPM (Fig. 3, A to C) providing three spin-dependent asymmetric OAM harmonic orders (22). The GPM was illuminated with right and left circularly polarized light, and the spin-dependent diffraction pattern consisting of multiple OAM harmonic orders of $l_{\pm} = \sigma_{\pm}, 2\sigma_{\pm}, 3\sigma_{\pm}$ corresponding to $m = 1, 2, 3$ was observed (Fig. 3, D and E). The diffraction patterns were verified by the spin-dependent FDTD simulation (Fig. 3, F and G) and by calculating Fourier amplitudes (Fig. 3, H and I). The efficiencies of each order were measured to be $|A_m|^2 \approx 0.21$ with uniformity of ± 0.01 , leading to a total efficiency of $\sim 63\%$, in accordance with the intensity scaling of $1/N$ (Fig. 3J) (22). Furthermore, we experimentally confirmed that the HR approach is manifested by diffraction-limited angular resolution of the shared aperture (Fig. 2F, and fig. S7, B and F). In light of the above, the HR concept constitutes a suitable platform to realize a well-angular resolved multibeam possessing negligible noise and thus able to provide high information capacity, whereas the interleaving approach suffers from the speckle noise and is hindered by capacity reduction. On the other hand, the latter approach offers high flexibility in multifunctional wavefront generation, whereas with the HR concept, harmonic sequence restricts this flexibility. Moreover, the

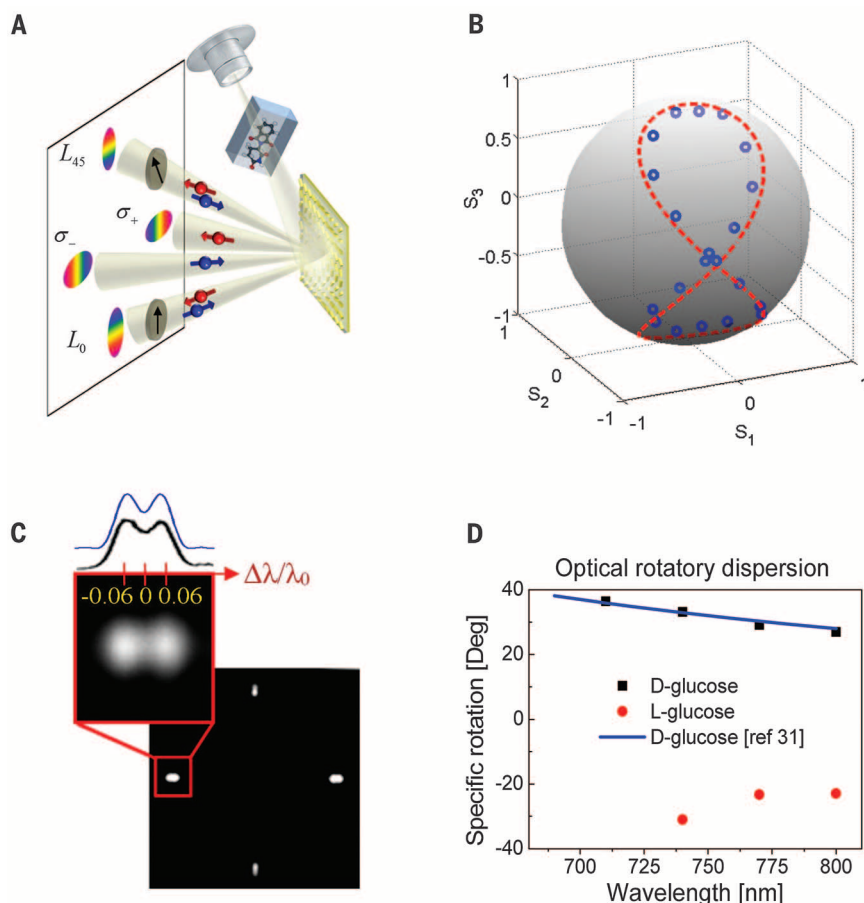


Fig. 4. Spectropolarimeter metasurface. (A) Schematic setup of the spectropolarimeter. The SPM is illuminated by a continuum light passing through a cuvette with chemical solvent, then four beams of intensities I_{σ_+} , I_{σ_-} , I_{L45} , and I_{L0} are reflected toward a charge-coupled device camera. (B) Predicted (red dashed curve) and measured (blue circles) polarization states, obtained by a polarization-state generator (a linear polarizer followed by a rotated quarter-wave plate), depicted on a Poincaré sphere. (C) Measured far-field intensities for elliptical polarization at two spectral lines (with wavelengths of 740 and 780 nm) and (inset) the corresponding resolving power (black line) and calculation (blue line) of the 50- μm diameter SPM. (D) ORD for the specific rotations of D- and L-glucose. Black squares and red circles represent the measured ORD of D- and L-glucose, respectively. The blue line depicts the dispersion acquired from (31).

reported spin-controlled multifunctional metasurfaces based on shared-aperture approaches are studied in terms of information capacity by means of Wigner phase-space distribution to establish a link between the Shannon entropy and the capacity of photonic system (fig. S8) (22).

Spectropolarimetry is an application for the simultaneous measurement of the spectrum and polarization state of light and is widely used to characterize chemical compounds. Implementing spectropolarimetric devices with metasurfaces opens new avenues for on-chip detection. Recently, on-chip chiroptical spectroscopy (27) was presented, measuring the differential absorption between left- and right-circular polarizations. The device used in this experiment is unable to provide full polarization analysis. Furthermore, it has been shown that a metasurface allows for the simultaneous determination of the Stokes parameters (i.e., the polarization state of light) (28, 29) without consideration of the spectral analysis. Here we propose a simple, fast, and compact technique, based on an interleaved GPM, that can simultaneously characterize the polarization state and spectrum of a wave transmitted through a semitransparent object. The spectropolarimeter metasurface (SPM) is composed of three interleaved linear phase profiles ($\phi_g^{(1)} = \sigma_x k_x x$; $\phi_g^{(2)} = \sigma_x k_y y$; $\phi_g^{(3)} = \sigma_y k_y y$) associated with different nanoantenna subarrays. When a probe beam with an arbitrary polariza-

tion state impinges on the SPM, two beams of intensities $I_{\sigma_{\pm}}$, consisting of opposite helicity states, and two additional beams emerge. The latter have identical polarizations, conjugate with respect to the incident beam, and being projected onto linear polarizers at 0° and 45° determines the linearly polarized components I_{L0} and I_{L45} , respectively (Fig. 4A). The Stokes parameters of the probed beam are then calculated by the expressions (28) $S_0 = 2(I_{\sigma_+} + I_{\sigma_-})/\eta$, $S_1 = 2(I_{L0}/\eta - S_0)$, $S_2 = 2(I_{L45}/\eta - S_0)$, and $S_3 = 2(I_{\sigma_+} - I_{\sigma_-})/\eta$, where the coefficient (η) is determined by a calibration experiment (fig. S9). The SPM of 50- μm diameter was normally illuminated by a supercontinuum light source, passing through the acousto-optic modulator, which enables the tunability of various wavelengths. Figure 4B shows the measured and calculated Stokes parameters on a Poincaré sphere for an analyzed beam impinging the SPM at a wavelength of 760 nm with different polarizations, obtained by a polarization-state generator (linear polarizer followed by a rotated quarter-wave plate). The spectral resolving power is defined according to the Rayleigh criterion as $\lambda/\Delta\lambda = q/M_{x,y}^2$, where $M_{x,y}^2$ is the beam quality parameter in each direction (x, y) and q is the number of phase-modulation periods (30). The resolving power of the SPM was measured and found to be $\lambda/\Delta\lambda \approx 13$ (Fig. 4C). The obtained value is in good agreement with the calculated

resolving power for SPM with $q \approx 17$ periods and a laser beam quality of $M_{x,y}^2 = 1.3$. We measured the optical rotatory dispersion (ORD) for the specific rotations of D-glucose (chiral molecule) and its enantiomer L-glucose that were dissolved in water with predetermined concentrations (Fig. 4D) (22). The ORD of D-glucose shows a good agreement with the values found in the literature (31), whereas the L-glucose ORD is manifested by the opposite behavior as expected. We achieved real-time on-chip spectropolarimetry by exploiting the interleaved GPM. The reported alliance of the spin-enabled geometric phase and shared-aperture concepts sheds light on the multifunctional wavefront manipulation in a spin-dependent manner. The introduced asymmetric HR and interleaved GPMs constitute suitable candidates to realize on-demand multifunctional on-chip photonics.

REFERENCES AND NOTES

1. D. M. Pozar, S. D. Targonski, *IEEE Trans. Antenn. Propag.* **49**, 150–157 (2001).
2. R. L. Haupt, *IEEE Trans. Antenn. Propag.* **53**, 2858–2864 (2005).
3. A. M. Sayeed, V. Raghavan, *IEEE J. Sel. Top. Signal Process.* **1**, 156–166 (2007).
4. I. E. Lager, C. Trampuz, M. Simeoni, L. P. Ligthart, *IEEE Trans. Antenn. Propag.* **57**, 2486–2490 (2009).
5. A. Papakostas et al., *Phys. Rev. Lett.* **90**, 107404 (2003).
6. X. Yin, Z. Ye, J. Rho, Y. Wang, X. Zhang, *Science* **339**, 1405–1407 (2013).

7. A. Pors, O. Albrektsen, I. P. Radko, S. I. Bozhevolnyi, *Sci. Rep.* **3**, 2155 (2013).
8. A. V. Kildishev, A. Boltasseva, V. M. Shalaev, *Science* **339**, 1232009 (2013).
9. N. Yu, F. Capasso, *Nat. Mater.* **13**, 139–150 (2014).
10. D. Lin, P. Fan, E. Hasman, M. L. Brongersma, *Science* **345**, 298–302 (2014).
11. M. G. Nielsen, D. K. Gramotnev, A. Pors, O. Albrektsen, S. I. Bozhevolnyi, *Opt. Express* **19**, 19310–19322 (2011).
12. D. Gregely *et al.*, *Nat. Commun.* **5**, 4354 (2014).
13. J. Sun *et al.*, *Nano Lett.* **14**, 2726–2729 (2014).
14. H.-S. Ee, J.-H. Kang, M. L. Brongersma, M.-K. Seo, *Nano Lett.* **15**, 1759–1765 (2015).
15. K. E. Chong *et al.*, *Nano Lett.* **15**, 5369–5374 (2015).
16. Z. Bomzon, V. Kleiner, E. Hasman, *Opt. Lett.* **26**, 1424–1426 (2001).
17. Z. Bomzon, G. Biener, V. Kleiner, E. Hasman, *Opt. Lett.* **27**, 1141–1143 (2002).
18. G. Biener, A. Niv, V. Kleiner, E. Hasman, *Opt. Lett.* **27**, 1875–1877 (2002).
19. A. Niv, G. Biener, V. Kleiner, E. Hasman, *Opt. Express* **14**, 4208–4220 (2006).
20. N. Dahan, Y. Gorodetski, K. Frischwasser, V. Kleiner, E. Hasman, *Phys. Rev. Lett.* **105**, 136402 (2010).
21. K. Y. Bliokh, F. J. Rodríguez-Fortuño, F. Nori, A. V. Zayats, *Nat. Photonics* **9**, 796–808 (2015).
22. Full details can be found in the supplementary materials on Science Online.
23. A. Pors, M. G. Nielsen, S. I. Bozhevolnyi, *Opt. Lett.* **38**, 513–515 (2013).
24. H. Dammann, K. Görtler, *Opt. Commun.* **3**, 312–315 (1971).
25. F. Gori *et al.*, *Opt. Commun.* **157**, 13–16 (1998).
26. J. Albero *et al.*, *Appl. Opt.* **52**, 3637–3644 (2013).
27. A. Shaltout, J. Liu, A. Kildishev, V. Shalaev, *Optica* **2**, 860–863 (2015).
28. Y. Gorodetski, G. Biener, A. Niv, V. Kleiner, E. Hasman, *Opt. Lett.* **30**, 2245–2247 (2005).
29. A. Pors, M. G. Nielsen, S. I. Bozhevolnyi, *Optica* **2**, 716–723 (2015).
30. N. Davidson, L. Khaykovich, E. Hasman, *Opt. Lett.* **24**, 1835–1837 (1999).
31. A. Penzkofer, *J. Anal. Sci. Methods Instrum.* **3**, 234–239 (2013).

ACKNOWLEDGMENTS

This research was supported by the United States–Israel Binational Science Foundation, the Israel Science Foundation, the Israel Nanotechnology Focal Technology Area on Nanophotonics for Detection, and KLA-Tencor.

SUPPLEMENTARY MATERIALS

www.sciencemag.org/content/352/6290/1202/suppl/DC1
Supplementary Text
Figs. S1 to S9
References (32–44)
Movies S1 and S2

28 January 2016; accepted 8 April 2016
Published online 21 April 2016
10.1126/science.aaf3417

MAGNETISM

Orbital-exchange and fractional quantum number excitations in an f-electron metal, Yb₂Pt₂Pb

L. S. Wu,^{1,2,3} W. J. Gannon,^{1,2,4} I. A. Zaliznyak,^{2*} A. M. Tselvik,² M. Brockmann,^{5,6} J.-S. Caux,⁶ M. S. Kim,² Y. Qiu,⁷ J. R. D. Copley,⁷ G. Ehlers,³ A. Podlesnyak,³ M. C. Aronson^{1,2,4}

Exotic quantum states and fractionalized magnetic excitations, such as spinons in one-dimensional chains, are generally expected to occur in 3d transition metal systems with spin 1/2. Our neutron-scattering experiments on the 4f-electron metal Yb₂Pt₂Pb overturn this conventional wisdom. We observe broad magnetic continuum dispersing in only one direction, which indicates that the underlying elementary excitations are spinons carrying fractional spin-1/2. These spinons are the emergent quantum dynamics of the anisotropic, orbital-dominated Yb moments. Owing to their unusual origin, only longitudinal spin fluctuations are measurable, whereas the transverse excitations such as spin waves are virtually invisible to magnetic neutron scattering. The proliferation of these orbital spinons strips the electrons of their orbital identity, resulting in charge-orbital separation.

It is generally believed that fractional quantum excitations such as spinons in one-dimensional (1D) spin chains proliferate and govern magnetism only in systems with small and isotropic atomic magnetic moments, such as spin-1/2 Cu²⁺. In contrast, large and anisotropic orbital-dominated moments, such as those produced by strong spin-orbit coupling in the rare

earths, are considered to be classical, becoming static as temperature $T \rightarrow 0$ because the conventional Heisenberg-Dirac exchange interaction (I , 2) cannot reverse their directions. Here we present the results of neutron-scattering measurements on the 3D compound Yb₂Pt₂Pb that profoundly challenge this conventional wisdom.

The unusual properties of Yb₂Pt₂Pb derive in part from its crystal structure (Fig. 1, A and B), where the Yb³⁺ ions form ladders along the c axis, separated by Pt and Pb; the rungs of the ladders (dashed lines in Fig. 1A) lie on the orthogonal bonds of the Shastry-Sutherland lattice (SSL) (3) in the ab planes. Equally important is the strong spin-orbit coupling, which combines spin and orbital degrees of freedom into a large, $J = 7/2$ Yb moment. The absence of a Kondo effect indicates minimal coupling of Yb to the conduction electrons of this excellent metal (4, 5). A point-charge model (6) indicates that the crystal electric field (CEF) lifts the eightfold degeneracy of

the Yb³⁺ moments, producing a Kramers doublet ground state that is a nearly pure state of the total angular momentum, $J, |J, m_J\rangle = |7/2, \pm 7/2\rangle$. The estimated anisotropy of the Landé g factor is in good agreement with that of the measured magnetization, $g_{||}/g_{\perp} = 7.5(4)$ (4–7), implying strong Ising anisotropy in Yb₂Pt₂Pb, which confines the individual Yb moments to two orthogonal sublattices in the ab plane.

The quantum states of the $|\pm 7/2\rangle$ Ising doublet are the superpositions of its “up” and “down” components, $\alpha_1|7/2\rangle + \alpha_1|-7/2\rangle$, and therefore the doublet can be viewed as an effective quantum spin-1/2. However, familiar interactions like the Zeeman, Heisenberg-Dirac exchange, and dipole interactions that are bilinear in J can only change the total angular momentum quantum number by $\Delta m_J = \pm 1$; they have no matrix elements that would allow transitions between the moment-reversed states of the ground state wave function. Only multiple virtual processes involving excited states could reverse individual Yb moments, but these processes are expected to be very weak because the ground and first excited states are separated by as much as 25 meV, according to specific heat (4) and inelastic neutron-scattering measurements (6). This would suggest that Yb₂Pt₂Pb would display only static, classical Ising behavior, but our data are not consistent with this picture.

Here we report neutron-scattering experiments on Yb₂Pt₂Pb that reveal a continuum of low-energy quantum excitations that display the distinctive spinon dispersion along the c axis (Fig. 2A), typical of the $S = 1/2$ Heisenberg-Ising XXZ spin Hamiltonian (8),

$$H = J \sum_n (S_n^x S_{n+1}^x + S_n^y S_{n+1}^y + \Delta S_n^z S_{n+1}^z) \quad (1)$$

where J is the Heisenberg spin-exchange coupling and Δ is its anisotropy. This observation provides definitive evidence that the Yb moments in Yb₂Pt₂Pb behave as quantum-mechanical spins-1/2 (9). The spinon spectrum $M(\mathbf{Q}, E)$ is fully gapped, but the gap is much smaller than the excitation bandwidth, indicating only moderate Ising anisotropy, $\Delta \gtrsim 1$. The lack of any wave

¹Department of Physics and Astronomy, Stony Brook University, Stony Brook, NY 11794, USA. ²Condensed Matter Physics and Materials Science Division, Brookhaven National Laboratory, Upton, NY 11973, USA. ³Quantum Condensed Matter Division, Oak Ridge National Laboratory, Oak Ridge, TN 37831, USA. ⁴Department of Physics and Astronomy, Texas A&M University, College Station, TX 77843, USA. ⁵Max Planck Institute for the Physics of Complex Systems, Nöthnitzer Strasse 38, 01187 Dresden, Germany. ⁶Institute for Theoretical Physics, University of Amsterdam, Science Park 904, 1098 XH Amsterdam, Netherlands. ⁷NIST Center for Neutron Research, National Institute of Standards and Technology, Gaithersburg, MD 20899, USA. *Corresponding author. Email: zaliznyak@bnl.gov

vector Q_{HH} dispersion for this gap (Fig. 2B), or for the scattering intensity in the ab plane (Fig. 2C), indicates that the dispersing excitations are confined to the ladder rails, which form an array of weakly coupled spin-1/2 chains.

The overall wave vector dependence of the energy-integrated intensity $M(Q)$ (Fig. 2, C and D) reveals that the excitations in each of the two orthogonal sublattices of Yb moments in $\text{Yb}_2\text{Pt}_2\text{Pb}$ are longitudinally polarized. This is clearly dem-

onstrated in Fig. 2D, where the $M(Q)$ dependence on H in the (H, H, L) scattering plane is very accurately described by the projections of Yb moments on the wave vector, consistent with the polarization factor in the neutron-scattering cross-section, which is only sensitive to magnetic fluctuations perpendicular to Q . The longitudinal character of magnetic excitations in $\text{Yb}_2\text{Pt}_2\text{Pb}$ is a direct consequence of the strong orbital anisotropy imposed by the crystal field and the resulting strongly anisotropic Landé g -factor. Even if the effective spin Hamiltonian that describes the low-energy dynamics in $\text{Yb}_2\text{Pt}_2\text{Pb}$ has modes involving transverse spin fluctuations, such as spin waves, they virtually do not couple to physical fields at our disposal and are de facto invisible in experiments. In particular, the measured longitudinal spectrum, which is typical of a spin-1/2 XXZ chain (Fig. 2), indicates the presence of transverse spinon excitations (8, 10–12), but these are not seen in experiments. That the XY-part of the effective spin Hamiltonian Eq. 1 is unobservable results from the well-understood effect of quantum selection rules. The direct consequence for our measurements is that we do not observe a (transverse) magnon, which is expected (13) when a magnetic field $B = 4$ T applied along (1-10) crystal direction saturates Yb moments that are parallel to the field (4–7), bringing this sublattice to the ferromagnetic (FM) state (Fig. 1B). Instead, FM chains do not contribute to magnetic scattering, and this allows us to use the 4 T data as a background that can isolate their contribution at $B = 0$ (Fig. 2D).

To establish the hierarchy of energy scales in the effective $S = 1/2$ XXZ Hamiltonian, we fit the energy cuts at different values of Q_L to a phenomenological half-Lorentzian line shape (14), which accounts both for the sharp continuum onset and its broad, asymmetric extent to higher energies (Fig. 3, A and B). We can thus very accurately determine the lower boundary, $E_L(Q_L)$, of the spinon continuum (points in Fig. 2A), which we fit to the exact Bethe-Ansatz expression for the XXZ Hamiltonian (Eq. 1) (8, 10, 11),

$$E_L(Q_L) = \min\{\Delta_s + \varepsilon_s(Q_L), 2\varepsilon_s(Q_L/2)\},$$

$$\varepsilon_s(Q_L) = \sqrt{I^2 \sin^2(\pi Q_L) + \Delta_s^2 \cos^2(\pi Q_L)} \quad (2)$$

Here Δ_s is the gap and I the bandwidth of the spinon dispersion, $\varepsilon_s(Q_L)$, both of which are functions of the J and Δ parameters of the Hamiltonian Eq. 1 (6). The fit yields values $I = 0.322(20)$ meV and $\Delta_s = 0.095(10)$ meV for the spinon dispersion parameters, which correspond to $\Delta \approx 3.46$, and $J = 0.116(10)$ meV in the effective spin-1/2 XXZ Hamiltonian, and the excitation gap at $Q_L = 1$, $E_g = 2\Delta_s = 0.19(2)$ meV. Despite the strong anisotropy of the individual Yb moments, their inferred coupling in the spin chain is surprisingly close to the isotropic Heisenberg limit $\Delta = 1$, as evidenced by the smallness of the excitation gap E_g compared to their observed bandwidth $\gtrsim 1$ meV (Fig. 2A).

Computations carried out on the XXZ Hamiltonian Eq. 1 closely reproduce key aspects of

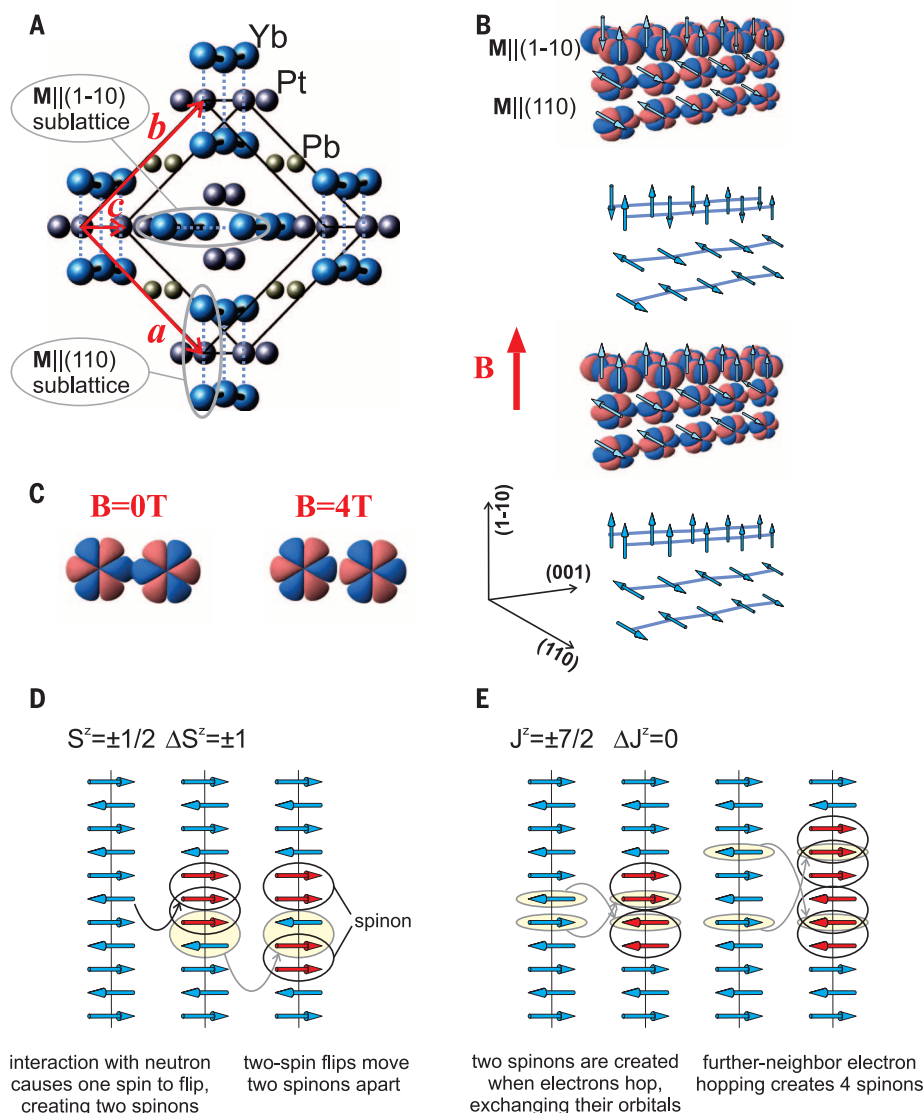


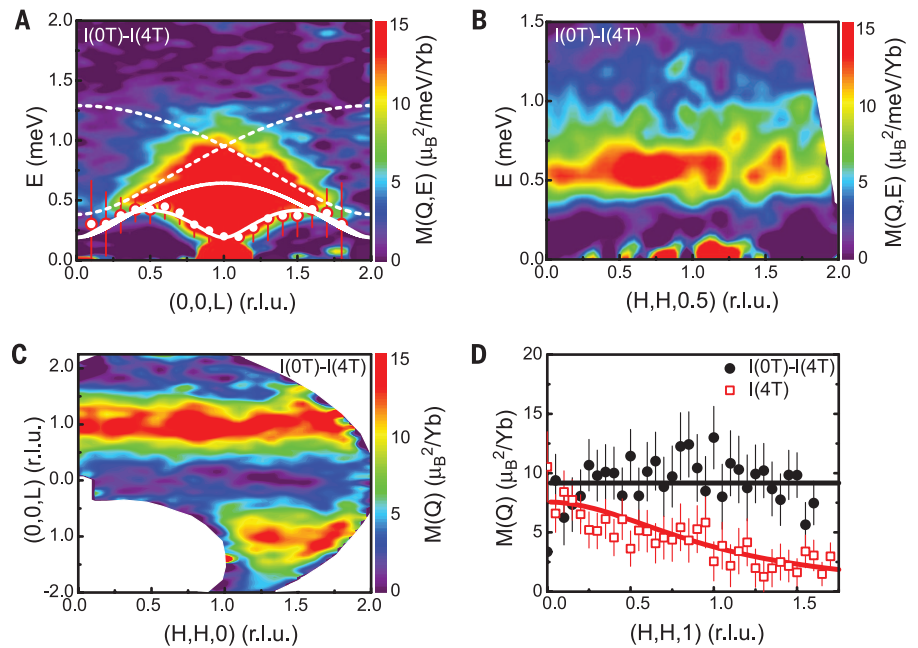
Fig. 1. Quantum orbital-spin chains in $\text{Yb}_2\text{Pt}_2\text{Pb}$. (A) Crystal structure of $\text{Yb}_2\text{Pt}_2\text{Pb}$; red arrows show the lattice axes. (B) The double chain magnetic structure for $T < T_N = 2.07$ K without magnetic field (top) and in a 4 T field applied along the (1-10) direction (bottom). The Yb orbitals are depicted as the isosurfaces, at 1 part per million electronic density, of the $4f |m_L| = 3$ hydrogenic wave functions for an effective Slater nuclear charge of ^{70}Yb (29). Blue arrows indicate the ordered magnetic moment directions, which are parallel to the local Ising easy axes, horizontal for the (110) and vertical for the (1-10) sublattice. Crystal axes are shown by black arrows. Thick red arrow shows magnetic-field direction. (C) Orbital overlaps for antiferromagnetic ($B = 0$) and fully saturated ($B = 4$ T) state. (D) Illustration of the two-spinon excitation process via spin flip (magnon) creation in $S = 1/2$ antiferromagnetic chain. Such processes correspond to the change of angular momentum, $\Delta m_S = \Delta S^z = \pm 1$, and are allowed by selection rules that govern interaction with a physical field, such as magnetic field of a neutron, or a photon. (E) For $m_J = J^z = \pm 7/2$, angular momenta in $\text{Yb}_2\text{Pt}_2\text{Pb}$, flipping magnetic moment requires $\Delta m_J = \pm 7$ and therefore cannot be induced via single-particle processes. The only processes allowed by the selection rules are those with $\Delta m_J = 0$, such as when two electrons hop, exchanging their orbitals, i.e., pairwise permutations of electrons. Permutation of two nearest-neighbor electrons creates two spinons, while further-neighbor hopping, such as the permutation of the next-nearest-neighbor electrons in opposite-polarity orbitals illustrated in the figure, results in a four-spinon state.

Fig. 2. Fractional spinon excitations in Yb₂Pt₂Pb.

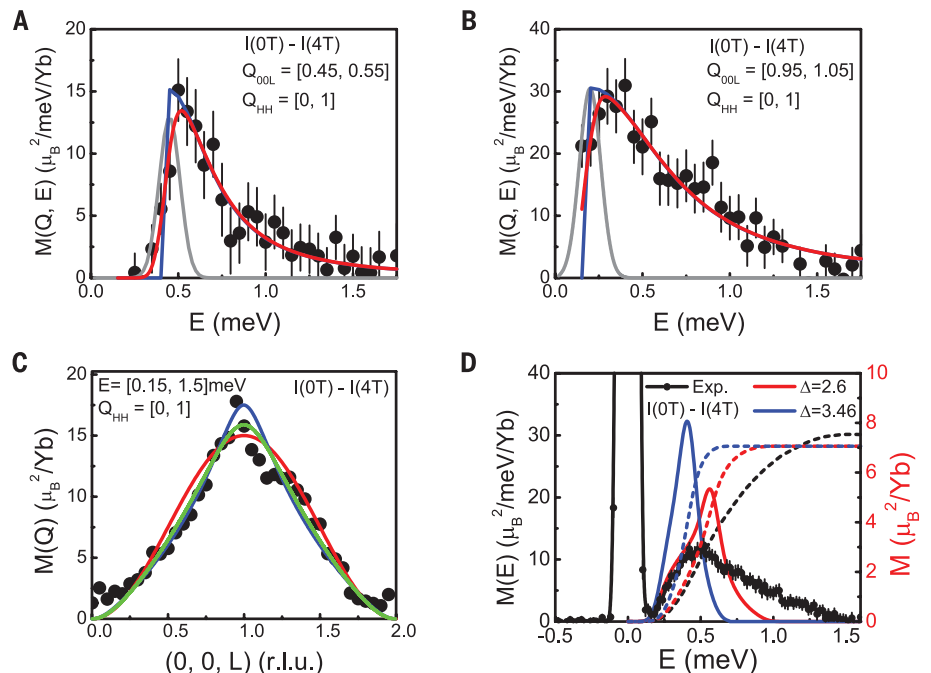
(A) The dispersion of the spectrum of magnetic excitations along the Q_L direction in reciprocal space of Yb₂Pt₂Pb at $T = 0.1$ K, obtained by averaging the scattered neutron intensity over the first Brillouin zone in Q_{HH} , along the perpendicular, $(H, H, 0)$ direction. Circles: onset of the excitation continuum determined by fitting the constant- Q_L data. Solid white lines: lower and upper boundaries of the two-spinon continua. Dashed lines: upper boundaries of the four-spinon continua (6). (B) The dispersion of the scattered neutron intensity along the Q_{HH} direction for $Q_L = 0.5 \pm 0.1$. (C) The partial static structure factor, $M(\mathbf{Q})$, obtained by integrating the scattered intensity from 0.15 to 1.5 meV. $M(\mathbf{Q})$ depends on the relative orientation of the scattering vector $\mathbf{Q} = (H, H, L)$ and the direction of magnetic moment fluctuations (30). (D) At 4 T, $M(\mathbf{Q})$ (red squares) follows the projection of the (110) sublattice moments on the scattering wave

$$\text{vector (polarization factor } P(4\text{ T}) = \frac{(Lc^*)^2}{2(Ha^*)^2 + (Lc^*)^2}.$$

red line), indicating that only magnetic fluctuations along the (110) moments contribute to magnetic scattering. Both polarizations are present when $B = 0$ T, consistent with equal longitudinal spinon spectral weight in both (110) and (1-10) sublattices. By subtracting the 4 T data from the 0 T data (black dots), we can isolate the scattering from fluctuations along the field direction, (1-10), which are always perpendicular to the scattering vector \mathbf{Q} and whose polarization factor is constant (black line). The agreement between the polarization factors and our data confirms that only fluctuations of the Yb moments that lie along the respective (110) or (1-10) direction are seen in our experiment and that there is no measurable transverse component of magnetic moment or excitations. Error bars in all figures represent 1 SD.

**Fig. 3. Spinon line shapes and the onset of the continuum in Yb₂Pt₂Pb.**

The spectrum of the dynamical structure factor of magnetization fluctuations, $M(\mathbf{Q}, E)$, in Yb₂Pt₂Pb for (A) $Q_L = 0.50(5)$ ($q_{\text{chain}} = \pi/2$) and (B) $Q_L = 1.00(5)$ ($q_{\text{chain}} = \pi$), both integrated within 1 Brillouin zone in Q_{HH} . The red lines show fits to the “half-Lorentzian” line shape (blue) convoluted with the Gaussian of 0.1 meV full width at half-maximum representing the resolution of the DCS spectrometer (light gray), (14). (C) The energy-integrated scattering function $M(\mathbf{Q})$ obtained by summing the normalized data over the first Brillouin zone in Q_{HH} compares favorably with that calculated for the effective $S = 1/2$ Heisenberg-Ising Hamiltonian with $\Delta = 2.6$ and $J = 0.205$ meV and with the effective g -factor $g^{\text{eff}} \approx 10$ (blue line), and with $\Delta = 3.46$, $J = 0.116$ meV, and $g^{\text{eff}} \approx 13$ (green line). A fit to the leading Ising-limit ($\Delta \gg 1$) expression, $M(\mathbf{Q}) = \frac{(g^{\text{eff}}\mu_B)^2}{2\Delta^2} \sin^2(\frac{\pi Q_L}{2})$, (red line) is less satisfactory, emphasizing that effective spin-1/2 Hamiltonian in Yb₂Pt₂Pb is not extremely Ising-like. This is consistent with the observation that the gap in the spinon spectrum, $E_g \approx 0.19$ meV (B), is markedly smaller than the bandwidth, ≥ 1 meV, Fig. 2A. (D) The energy dependence of the \mathbf{Q} -integrated intensity, which represents the local dynamical structure factor, $M(E)$, of magnetization fluctuations in Yb₂Pt₂Pb. The energy-integral of the $M(E)$ inelastic intensity (black dashed line, right scale) gives the square of the total fluctuating magnetic moment of $\approx 7.6\mu_B^2$ per Yb. Computational results for $M(E)$ and its energy integral are compared for $\Delta = 2.6$ (red solid and dashed lines) and $\Delta = 3.46$ (blue solid and dashed lines).



our experimental results. The mixed Heisenberg-Ising character of Yb₂Pt₂Pb is evident in the broad peak at $Q_L = 1$ in the structure factor $M(\mathbf{Q})$ found by integrating the experimental and computed spectra in energy (Fig. 3C). $M(\mathbf{Q})$ is inter-

mediate between the near divergence expected for isotropic interactions ($\Delta = 1$) and the leading-order Ising expression (15) $M(\mathbf{Q}) = 2M_0^2 \frac{1}{\Delta^2} \sin^2(\frac{\pi Q_L}{2})$, where $M_0 = \frac{1}{2}g^{\text{eff}}\mu_B$ is Yb magnetic moment, g^{eff} being the effective spin-1/2 g -factor for the local

Ising direction. Crystal electric field calculations for the Yb ground state doublet in Yb₂Pt₂Pb indicate $g_{\parallel}^{\text{eff}} = 7.9$ and $g_{\perp}^{\text{eff}} \leq 0.8$ (6), so that magnetic neutron-scattering intensity, which is proportional to $(g_{\parallel}^{\text{eff}})^2$, is at least a factor of 100 weaker

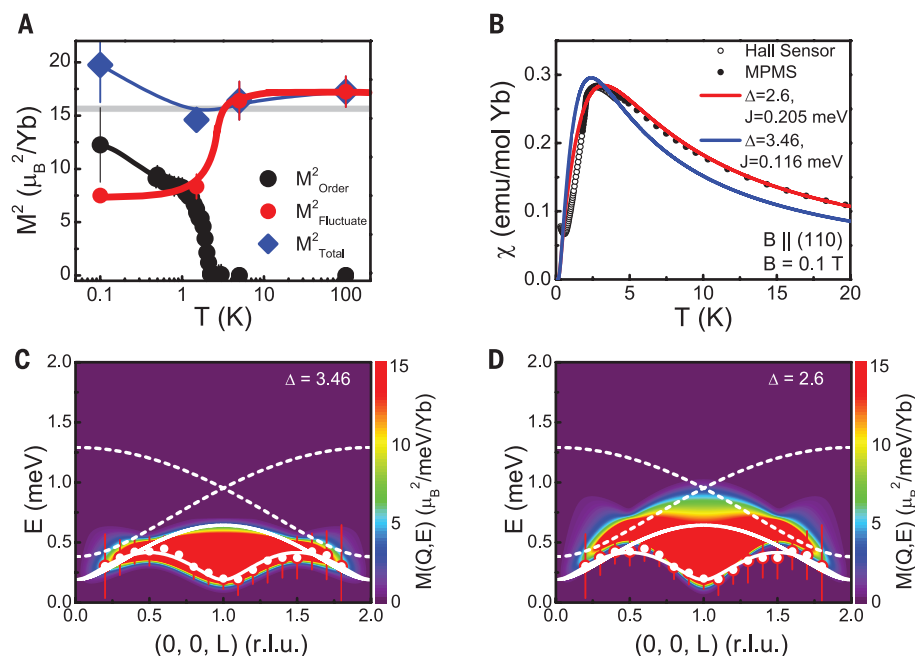


Fig. 4. Spinons in $\text{Yb}_2\text{Pt}_2\text{Pb}$: theory and experiment. (A) Temperature dependencies of the ordered Yb moment from neutron-diffraction measurements (black circles), the fluctuating moment from the energy and wave-vector integrated normalized $M(Q, E)$ (red points), and the total (blue points). (B) The temperature dependence of the static, uniform magnetic susceptibility $\chi(T)$ for $\text{Yb}_2\text{Pt}_2\text{Pb}$ (black circles), measured with a magnetic properties measurement system ($T \geq 1.8$ K) and a Hall sensor magnetometer ($0.2 \text{ K} \leq T \leq 4 \text{ K}$), shows good agreement with $\chi(T)$ calculated for the XXZ chain, for $\Delta = 2.6$ and $J = 0.205 \text{ meV}$ (red line, $g^{\text{eff}} \approx 7.4$). Agreement is less good for $\Delta = 3.46$ and $J = 0.116 \text{ meV}$ (blue line, $g^{\text{eff}} \approx 6.5$). (C and D) The longitudinal structure factor, $M(Q, E)$, of the XXZ spin-1/2 chain Eq. 1 calculated using the algebraic Bethe ansatz (11, 12, 20) (C) for $\Delta = 3.46$ and $J = 0.116 \text{ meV}$ and (D) for $\Delta = 2.6$ and $J = 0.205 \text{ meV}$. The experimentally determined lower boundary $E_L(Q_L)$ is shown (circles) along with the calculated lower and upper two-spinon (solid lines) and the upper four-spinon (broken lines) boundaries, as described in the text. The calculation is normalized to the total experimental intensity by using the sum rule for a single component of the dynamical structure factor, which holds for spin-1/2, $\iint S^Z(Q, E) \frac{dQ}{2\pi} dE = \frac{1}{4}$.

for the transverse, XY-polarized fluctuations, in agreement with what we observe.

The Q -integrated scattering in Fig. 3C yields a fluctuating moment $M_{\text{fluct}}^2 \approx 7.1 \mu_B^2/\text{Yb}$ at 0.1 K, about half as large as the ordered moment M_{order}^2 determined in previous work (16). The energy integral of the local autocorrelation function $M(E)$, which is obtained by integrating the measured intensity in Q , yields a similar result, $\approx 7.6 \mu_B^2/\text{Yb}$ (Fig. 3D), with the difference indicating a systematic error resulting from different data binning. The sum rule for the effective spin-1/2 dictates that the integral intensity in each polarization channel is $(S^a)^2 = 1/4$ ($a = x, y, z$). Therefore, the sum $M_{\text{fluct}}^2 + M_{\text{order}}^2$ gives a total Yb moment, $M_{\text{total}}^2 = (\frac{1}{2} g^{\text{eff}} \mu_B)^2$. Combining the inelastic spectrum and the elastic order parameter measurements in $\text{Yb}_2\text{Pt}_2\text{Pb}$ (6), we find M_{total} that is between 3.8 and 4.4 μ_B/Yb [$g^{\text{eff}} = 8.2(5)$] for temperatures from 0.1 to 100 K (Fig. 4A), fully consistent with the predictions of the point charge model. The spinons provide virtually all of the magnetic dynamics in $\text{Yb}_2\text{Pt}_2\text{Pb}$, and they are completely captured by our experiments. This result immediately rules out a naïve explanation that the observed longitudinal magnetic response

could originate from the two-magnon continuum, as in conventional magnets, because in that case the continuum would comprise only a small part of the dynamical spectral weight (17, 18). Moreover, stable magnons do not exist in an antiferromagnetic spin-1/2 chain, where the elementary excitations are spinons, and the system's one-dimensionality is clearly established by the measured dispersion (Fig. 2, A to C). Finally, the static spin susceptibility $\chi_s(T)$ computed for spin-1/2 XXZ chain with $g^{\text{eff}} \approx 7$ closely reproduces direct measurements of $\chi(T)$ (Fig. 4B).

Further comparison with the exact result (19) for the XXZ model (Eq. 1), however, indicates that the fluctuations measured in $\text{Yb}_2\text{Pt}_2\text{Pb}$ at 0.1 K are stronger than the predicted spinon contribution to the dynamical spin structure factor, which for $\Delta = 3.46$ is only $\approx 20\%$ of the ordered spin contribution S_{order}^2 . Figure 3D makes it clear that the calculated $M(E)$ underestimates the contribution of the high-energy states in $\text{Yb}_2\text{Pt}_2\text{Pb}$. Direct comparison of the detailed energy dependencies of the measured (Fig. 2A) and computed (broadened by the instrumental resolution of 0.1 meV) (Fig. 4C) spectra of longitudinal excitations reveals that there is considerable spectral weight

present in the experimental data above the upper boundary of the two-spinon continuum, $E_U(Q_L) = \max\{\Delta_s + \epsilon_s(Q_L), 2\epsilon_s(Q_L/2)\}$, that is absent in the computed spectrum (10, 11). A somewhat better agreement can be obtained by fitting the measured intensity to the calculated longitudinal structure factor $M(Q, E)$ and adjusting Δ and J as fit parameters instead of adopting the values determined from the lower boundary of the continuum. This results in $\Delta = 2.6$ and $J = 0.205 \text{ meV}$ (Fig. 4D), shifting the two-spinon spectral weight to higher energy and also providing better agreement with the measured susceptibility (Fig. 4B) and $M(Q)$ (Fig. 3C). However, this improvement is achieved at the cost of the excellent experimental and theoretical agreement for the lower spinon boundary, which, in fact, is determined very precisely from the line fits (Fig. 3, A and B). This dilemma is resolved by noting that the observed high-energy magnetic spectral weight in $\text{Yb}_2\text{Pt}_2\text{Pb}$ is consistent with a substantial contribution of four-spinon states, whose upper boundaries (12) are shown by the broken lines in Fig. 2A. This result is quite unexpected, given that two-spinon excitations account for all but a few percent of the total spectral weight (12, 13, 20) in the nearest-neighbor Heisenberg-Ising chain.

We now show that these seemingly perplexing experimental results can be understood in terms of the interplay of 4f-electron exchange, strong spin-orbit coupling, and a crystal field that lifts the large orbital degeneracy of the $J = 7/2$ multiplet. The intersite electron hopping in the f -electron Hamiltonian for $\text{Yb}_2\text{Pt}_2\text{Pb}$, which we adopt in the form of a 1D Hubbard model (6), leads to an electronic interaction (21) whose physical nature is not a Heisenberg-Dirac spin exchange (1, 2), but rather an orbital exchange (Fig. 1), a realization that has been appreciated in the physics of Kondo effect (22, 23) and more recently in certain cold-atom systems (24).

The orbital-exchange interaction in $\text{Yb}_2\text{Pt}_2\text{Pb}$ is a natural generalization of the Heisenberg-Dirac spin exchange between the two electrons, and has the same physical origin in the electronic Coulomb repulsion (1, 2). The magnetism in $\text{Yb}_2\text{Pt}_2\text{Pb}$ is tied to the wave function of a single 4f hole with orbital momentum $L = 3$, $|m_L| = 3$, having sixfold symmetry around the J quantization axis, given by the magnetic structure as perpendicular to the rails of Yb ladders in $\text{Yb}_2\text{Pt}_2\text{Pb}$ crystal. The energy cost for hopping between sites, which in $\text{Yb}_2\text{Pt}_2\text{Pb}$ is synonymous with orbital exchange, is reduced when neighboring Yb ions are in alternating states of $m_L = \pm 3$, because in that case, the exchange of electrons between the two sites required for hopping involves the overlap of two identical orbital lobes along the ladder rails (Fig. 1, B and C). The sixfold symmetry of the f -orbital breaks the rail-rung equivalence and ensures that this energy advantage is not accrued for hopping in a transverse direction, decoupling the ladder rails. Combined with the weak interactions between orthogonal ladders mandated by the SSL geometry (4), this leads to the spin-chain nature of the emergent effective Hamiltonian.

The leading-order Coulomb contribution for the low-energy manifold of electronic states (6, 25) is given by the two-electron permutation operator, P_{12} , which in the cases where only electronic spins are at play, reduces to the usual Heisenberg spin exchange, $\sim S_1 S_2$. For the case of a J -manifold, which in the absence of crystal fields is highly degenerate, it has the form of a permutation operator acting on a $(2J + 1) \times (2J + 1)$ -dimensional space of two neighboring Yb ions. The permutation operator interchanges states $|m_{j1}, m_{j2}\rangle$ and $|m_{j2}, m_{j1}\rangle$ with equal weights, thus including the process $|7/2, -7/2\rangle$ to $|-7/2, 7/2\rangle$ where both moments simultaneously reverse, which cannot be achieved through conventional Heisenberg-Dirac spin exchange (Fig. 1, D and E). The crystal field lifts the degeneracy of the Yb moments, and although the effective interaction that emerges after the projection on the manifold of the lowest Kramers doublets $m_j = \pm 7/2$ has the form of the antiferromagnetic $S = 1/2$ XXZ Hamiltonian, it retains the birthmark of its unusual origin in exchange processes that are distinct from those having the conventional Heisenberg $J_1 J_2$ form.

The effective spin-1/2 physics emerges in $\text{Yb}_2\text{Pt}_2\text{Pb}$ from the combination of high-energy (Coulomb, spin-orbit, hopping) interactions. The spin-orbit coupling virtually quenches the electronic spin degree of freedom, forcing its alignment with the large orbital moment, and in this way the effective spin-1/2 XXZ model effectively describes the quantum dynamics of the electronic orbital degree of freedom. This is directly evidenced in our experiments by the large, $\approx 4\mu_B$ magnetic moment carried by spinons. The orbital exchange sets the scale for these emergent quantum dynamics, which we find by comparing the measured spinon dispersion with computed spectra (Fig. 4).

Because the orbital angular momentum dominates the total Yb moment, magnetic order in $\text{Yb}_2\text{Pt}_2\text{Pb}$ is synonymous with orbital order, and the configuration depicted in Fig. 1, D and E, is a natural way to understand how permutation of two neighboring electrons generates two spinons in the antiferromagnetic background. This is a process that entails charge-orbital separation, because the electron count per site is unchanged by correlated hopping, but the phases of the orbital wave function on both sites are reversed. Further-neighbor orbital exchange leads to states with four spinons (Fig. 1E). Hence, long-range hopping, either by virtue of the in-chain itinerancy of the 4f electrons or via coupling to the conduction electrons in metallic $\text{Yb}_2\text{Pt}_2\text{Pb}$, provides a natural mechanism for the spectral weight of the excitations that we observe above the two-spinon but within the four-spinon continuum boundaries.

Our results provide a specific mechanism for charge-orbital separation in $\text{Yb}_2\text{Pt}_2\text{Pb}$, where the proliferation of spinons implies that electrons lose their orbital-phase identity. When united with the previous demonstrations of spin-charge and spin-orbital separation, this finding completes the triad of electron fractionalization phenomena in one dimension (26–28).

REFERENCES AND NOTES

- W. Heisenberg, *Z. Phys.* **49**, 619–636 (1928).
- P. A. M. Dirac, *Proc. R. Soc. London, A Contain. Pap. Math. Phys. Character* **123**, 714–733 (1929).
- B. S. Shastri, B. Sutherland, *Physica B+C* **108**, 1069–1070 (1981).
- M. S. Kim, M. C. Bennett, M. C. Aronson, *Phys. Rev. B* **77**, 144425 (2008).
- M. S. Kim, M. C. Aronson, *Phys. Rev. Lett.* **110**, 017201 (2013).
- See supplementary materials on Science Online for details.
- A. Ochiai et al., *J. Phys. Soc. Jpn.* **80**, 123705 (2011).
- H. A. Bethe, *Z. Phys.* **71**, 205–226 (1931).
- L. Faddeev, L. Takhtajan, *Phys. Lett. A* **85**, 375–377 (1981).
- A. H. Bougourzi, M. Karbach, G. Müller, *Phys. Rev. B* **57**, 11429–11438 (1998).
- J.-S. Caux, J. Mossel, I. P. Castillo, *J. Stat. Mech.* **2008**, P08006 (2008).
- J.-S. Caux, R. Hagemans, *J. Stat. Mech.* **2006**, P12013 (2006).
- M. Mourigal et al., *Nat. Phys.* **9**, 435–441 (2013).
- I. A. Zaliznyak, S.-H. Lee, S. V. Petrov, *Phys. Rev. Lett.* **87**, 017202 (2001).
- N. Ishimura, H. Shiba, *Prog. Theor. Phys.* **63**, 743–758 (1980).
- W. Müller et al., *Phys. Rev. B* **93**, 104419 (2016).
- D. A. Tennant et al., *Phys. Rev. B* **67**, 054414 (2003).
- T. Huberman et al., *Phys. Rev. B* **72**, 014413 (2005).
- R. Baxter, *J. Stat. Phys.* **9**, 145–182 (1973).
- A. C. Walters et al., *Nat. Phys.* **5**, 867–872 (2009).
- K. I. Kugel, D. I. Khomskii, *Sov. Phys. JETP* **37**, 725 (1973).
- B. Coqblin, J. R. Schrieffer, *Phys. Rev.* **185**, 847–853 (1969).
- P. Coleman, *Phys. Rev. B* **28**, 5255–5262 (1983).
- A. V. Gorshkov et al., *Nat. Phys.* **6**, 289–295 (2010).
- G. Uimin, Y. Kudasov, P. Fulde, A. Ovchinnikov, *Eur. Phys. J. B* **16**, 241–244 (2000).
- B. J. Kim et al., *Nat. Phys.* **2**, 397–401 (2006).
- J. Schlappa et al., *Nature* **485**, 82–85 (2012).
- P. W. Anderson, *Phys. Today* **50**, 42 (1997).
- J. C. Slater, *Phys. Rev.* **36**, 57–64 (1930).
- G. L. Squires, *Introduction to the Theory of Neutron Scattering* (Cambridge Univ. Press, UK, ed. 3, 2012).

ACKNOWLEDGMENTS

Work at Brookhaven National Laboratory (I.A.Z., A.M.T., M.S.K.) was supported by the Office of Basic Energy Sciences (BES), Division of Materials Sciences and Engineering, U.S. Department of Energy (DOE), under contract DE-SC00112704. Work at Stony Brook (L.S.W., W.J.G., M.C.A.) was supported by NSF-DMR-131008. L.S.W. was also supported by the Laboratory Directed Research and Development Program of Oak Ridge National Laboratory (ORNL). This research at ORNL's Spallation Neutron Source was sponsored by the Scientific User Facilities Division, Office of Basic Energy Sciences, U.S. DOE. Work at NIST Center for Neutron Research (NCNR) is supported in part by the NSF under Agreement no. DMR-1508249. J.-S.C. and M.B. acknowledge support from the Netherlands Organization for Scientific Research (NWO) and the Foundation for Fundamental Research on Matter (FOM) of the Netherlands.

SUPPLEMENTARY MATERIALS

www.sciencemag.org/content/352/6290/1206/suppl/DC1
Materials and Methods
Supplementary Text
Figs. S1 to S10
Tables S1 to S3
References (31–53)

17 December 2015; accepted 29 April 2016
10.1126/science.aaf0981

BIOENERGY

Water splitting–biosynthetic system with CO₂ reduction efficiencies exceeding photosynthesis

Chong Liu,^{1,2*} Brendan C. Colón,^{3*} Marika Ziesack,³ Pamela A. Silver,^{3†} Daniel G. Nocera^{1†}

Artificial photosynthetic systems can store solar energy and chemically reduce CO₂. We developed a hybrid water splitting–biosynthetic system based on a biocompatible Earth-abundant inorganic catalyst system to split water into molecular hydrogen and oxygen (H₂ and O₂) at low driving voltages. When grown in contact with these catalysts, *Ralstonia eutropha* consumed the produced H₂ to synthesize biomass and fuels or chemical products from low CO₂ concentration in the presence of O₂. This scalable system has a CO₂ reduction energy efficiency of ~50% when producing bacterial biomass and liquid fusel alcohols, scrubbing 180 grams of CO₂ per kilowatt-hour of electricity. Coupling this hybrid device to existing photovoltaic systems would yield a CO₂ reduction energy efficiency of ~10%, exceeding that of natural photosynthetic systems.

Sunlight and its renewable counterparts are abundant energy sources for a sustainable society (1, 2). Photosynthetic organisms harness solar radiation to build energy-rich organic molecules from water and CO₂.

¹Department of Chemistry and Chemical Biology, Harvard University, Cambridge, MA 02138, USA. ²Division of Chemistry and Biological Chemistry, School of Physical and Mathematical Sciences, Nanyang Technological University, 637371 Singapore. ³Department of Systems Biology, Harvard Medical School, Boston, MA 02115, USA.

*These authors contributed equally to this work. †Corresponding author. Email: dnocera@fas.harvard.edu (D.G.N.); pamela_silver@hms.harvard.edu (P.A.S.)

Numerous energy conversion bottlenecks in natural systems limit the overall efficiency of photosynthesis (3). Most plants do not exceed 1%, and microalgae grown in bioreactors do not exceed 3%; however, efficiencies of 4% for plants and 5 to 7% for microalgae in bubble bioreactors may be achieved in the rapid (short-term) growth phase (3). Artificial photosynthetic solar-to-fuels cycles may occur at higher intrinsic efficiencies (4–7), but they typically terminate at hydrogen (8), with no process installed to complete the cycle via carbon fixation. This limitation may be overcome by interfacing H₂-oxidizing autotrophic

microorganisms to electrodes that generate hydrogen or reducing equivalents directly (9–14).

We recently developed a hybrid inorganic-biological system that uses the catalysts of the artificial leaf (15, 16) in combination with the bacterium *Ralstonia eutropha* (17) to drive an artificial photosynthetic process for carbon fixation into biomass and liquid fuels (18). In this system, water is split to oxygen by a cobalt phosphate (CoP_i) catalyst and hydrogen is produced by a NiMoZn alloy at applied voltages of $E_{\text{appl}} = 3.0$ V. Because the maximum energy efficiency is limited by the value of E_{appl} relative to the thermodynamic potential for water splitting ($= E_{\text{appl}}/1.23$ V), a reduction in E_{appl} leads to biomass and liquid fuel efficiencies that surpass those of previous integrated bioelectrochemical systems and are commensurate with natural photosynthetic yields (18). However, reactive oxygen species (ROS) produced at the cathode were detrimental to cell growth. Because hydrogen peroxide (H₂O₂), as well as short-lived superoxide (O₂^{•−}) and hydroxyl radical (HO[•]) species, are thermodynamically favored against H₂ production at pH = 7, ROS production dominated at or below the potential to generate H₂. When E_{appl} reached a sufficient overpotential to drive water splitting, H₂ production to support cell growth outweighed the toxic effects of ROS (18). In addition, leaching of Ni from the NiMoZn alloy into solution inhibited microbial growth.

To develop a biocompatible catalyst system that is not toxic to the bacterium and lowers the overpotential for water splitting, we used a ROS-resistant cobalt-phosphorus (Co-P) alloy cathode (Fig. 1A, pathway 1). This alloy drives the hydrogen evolution reaction (HER) while the self-healing CoP_i anode (19, 20) drives the oxygen evolution reaction (OER). The electrode pair works in concert to maintain extraneous cobalt ions at low concentration and to deliver low E_{appl} that splits water to generate H₂ for *R. eutropha*, which

supports CO₂ reduction into complex organic molecules at high efficiency. The Co-P alloy, which is known to promote HER under alkaline solutions (21), exhibits high HER activity in water at neutral pH with minimal ROS production. X-ray photoelectron spectroscopy of Co-P thin films supports the elemental nature of the alloy (fig. S1), and energy-dispersive x-ray spectroscopy (fig. S2) establishes a phosphorus composition of 6 weight percent, which we have found to exhibit optimal HER activity in water at neutral pH with a fara-

daic efficiency of $99 \pm 2\%$ (fig. S3). Moreover, the activity of this Co-P alloy surpasses the activity of the Earth-abundant NiMoZn and stainless steel (SS) cathodes used previously (18) (Fig. 1B). At constant voltage, a stable HER current is maintained for at least 16 days (Fig. 1C). Negligible H₂O₂ is produced during HER (Fig. 1D), in contrast to that of simple metallic cathodes of Pt and SS.

The Co-P HER and CoP_i OER catalysts work in synergy to form a biocompatible water-splitting system that salvages Co²⁺ cations leached from the

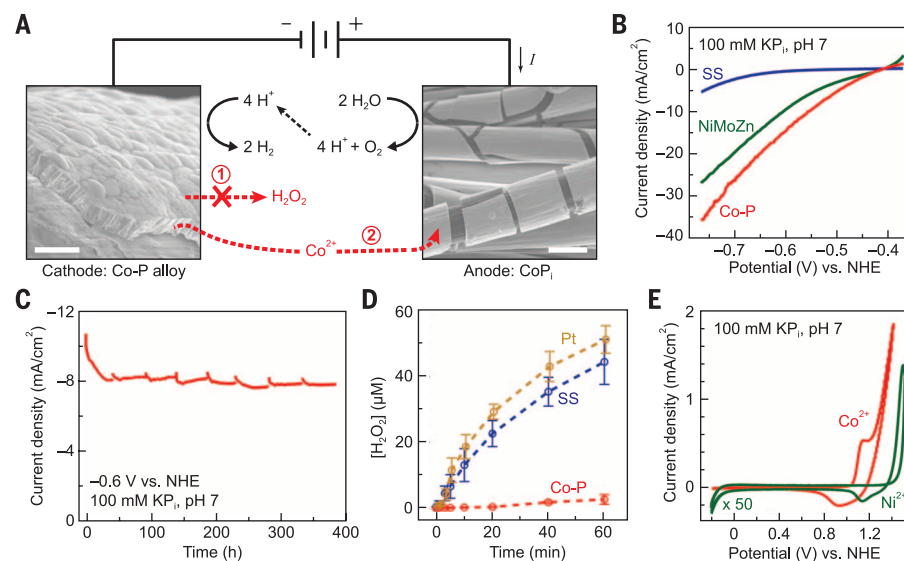


Fig. 1. Active water-splitting catalyst pair with minimal biological toxicity. (A) Reaction diagram and scanning electron microscopy images for Co-P alloy cathode and CoP_i anode. The main water-splitting reaction is shown in black; the side reactions that yield toxicants are in red. Scale bars, 10 μm. (B) Current-voltage (I - V) characteristics of different HER catalysts (10 mV/s). (C) Stability of Co-P cathode, as demonstrated by 16-day chronoamperometry. (D) Assay of H₂O₂ accumulation for various cathodes combining with CoP_i anode: yellow, Pt; blue, stainless steel (SS); red, Co-P alloy. $E_{\text{appl}} = 2.2$ V. Error bars denote SEM; $n = 3$. (E) Cyclic voltammetry of Co²⁺ and Ni²⁺ in the presence of phosphate (P_i). Metal concentrations are both 0.5 mM; 50 mV/s. The current for Ni²⁺ is magnified by a factor of 50.

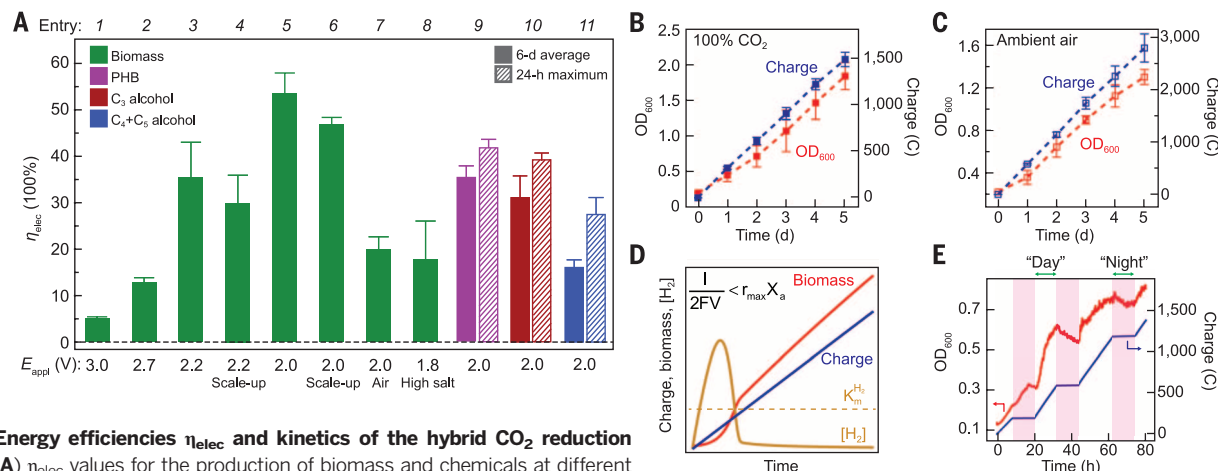
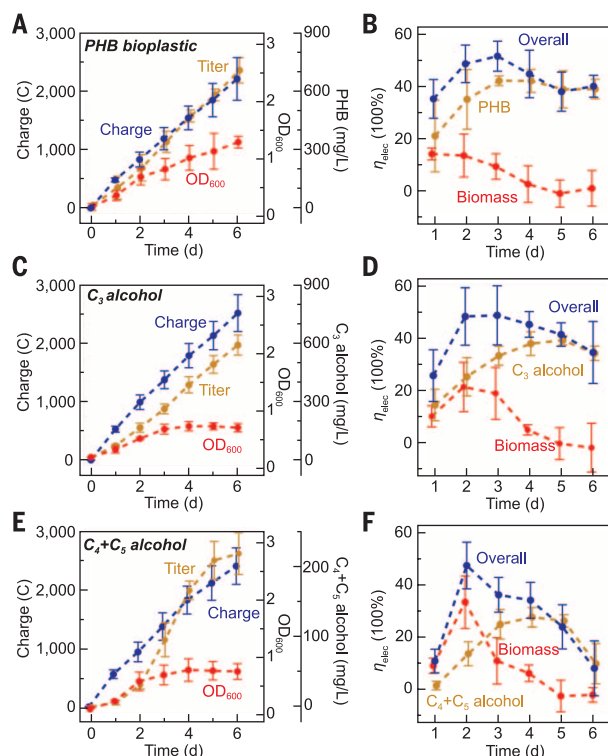


Fig. 2. Energy efficiencies η_{elec} and kinetics of the hybrid CO₂ reduction device. (A) η_{elec} values for the production of biomass and chemicals at different values of E_{appl} and various configurations (table S1). Solid bars are 5- to 6-day averages; hatched bars are 24-hour maxima. Error bars denote SEM; $n \geq 3$. (B and C) Optical density at 600 nm (OD₆₀₀; indicator of biomass accumulation) and amounts of electric charges that were passed, plotted versus the duration of experiments with 100% CO₂ (B) and air (C) in the headspace at 1 atm pressure. $E_{\text{appl}} = 2.0$ V. Error bars denote SEM; $n = 4$ for (B) and $n = 3$ for (C). (D) A microbial growth model predicts linear correlation between electric charges and biomass accumulation, when the H₂ generation rate by water splitting ($I/2FV$) is smaller than the maximum rate of H₂ consumption by active biomass ($r_{\text{max}}X_a$) (23) (fig. S12). Dashed line indicates Michaelis constant of hydrogenase for H₂. (E) Real-time monitor of biomass accumulation under "day"/"night" cycle test.

Fig. 3. Efficient synthesis of selectively produced chemicals from CO₂ and water. (A to F) PHB [(A) and (B)], isopropanol (C₃) [(C) and (D)], and C₄ and C₅ alcohols [(E) and (F)] were selectively produced from the hybrid device. In (A), (C), and (E), the OD₆₀₀ values, concentrations of selective chemicals, and charges passed through the electrodes are plotted versus the duration of experiments. Shown in (B), (D), and (F) are averaged η_{elec} values for different products, measured at 24-hour intervals. Also shown are overall η_{elec} values combining biomass and chemical formation. The η_{elec} values for biomass, defined as intracellular organics excluding PHB, have been corrected to exclude the PHB interference in (B) (23) (see fig. S13 for values before correction). Error bars denote SEM; $n = 3$.



electrodes (Fig. 1A, pathway 2). In the cyclic voltammogram of Co²⁺ in the phosphate buffer (pH = 7) (Fig. 1E), a pre-wave to the catalytic water-splitting current corresponds to the oxidation of Co²⁺ to Co³⁺, which drives deposition of the catalyst. The CoP_i catalyst is also known to exhibit a deposition rate that is linearly proportional to Co²⁺ concentration (22). The self-healing property of CoP_i is derived from this interplay of the potential at which OER occurs versus the potential at which the catalyst deposits (20). In concert, the Co-P and CoP_i catalysts preserve extremely low concentrations of Co²⁺ in solution through activity derived from the self-healing process. Inductively coupled plasma mass spectrometry (ICP-MS) analysis of a Co-P/CoP_i catalyst system ($E_{\text{appl}} = 2.2$ V) (23) reveals submicromolar levels of Co²⁺ in solution after 24 hours. This concentration of Co²⁺ (0.32 ± 0.06 μM) is well below the concentration of Co²⁺ (half-maximal inhibitory concentration $\text{IC}_{50} \approx 25$ μM) that is toxic to *R. eutropha* (fig. S4). When diffusion between the two electrodes is impeded by a porous glass frit, Co²⁺ concentrations rise to ~ 50 μM . We note that for the NiMoZn cathode, Ni²⁺ concentrations are not regulated by self-healing, as NiP_i cannot form from P_i (24), and the deposition of NiO_x occurs at >1.5 V versus normal hydrogen electrode (NHE) (Fig. 1E; see fig. S5 for comparison with potentials of relevant redox processes).

Interfacing the biocompatible Co-P/CoP_i water-splitting catalysts with *R. eutropha* results in a system capable of CO₂ fixation. The CoP_i catalyst was deposited on a high-surface area carbon cloth as the electrode support (Fig. 1A and fig. S6), resulting in high currents (fig. S7) and a faradaic efficiency of $96 \pm 4\%$ (fig. S8). CO₂ reduction pro-

ceeded under a constant voltage within a batch reactor (fig. S9), which was half-filled with a solution containing only inorganic salts (mostly phosphate) and trace metal supplements (23).

The CoP_i/Co-P/*R. eutropha* hybrid system can store more than half its input energy as products of CO₂ fixation at low E_{appl} (Fig. 2A and table S1). Entries 1, 2, 3, and 5 show that η_{elec} increases with decreasing E_{appl} under 100% CO₂ until $E_{\text{appl}} < 2.0$ V. Below $E_{\text{appl}} = 2.0$ V (entry 8), a higher salt concentration (108 mM phosphate buffer) is required to facilitate mass transport and attendant current (fig. S10). However, high salt concentrations are undesirable for *R. eutropha* metabolism. Thus, a concentration of 36 mM phosphate and $E_{\text{appl}} = 2.0$ V resulted in optimal η_{elec} : the highest η_{elec} achieved for biomass production was $54 \pm 4\%$ (entry 5, $n = 4$) over a duration of 6 days. Our CO₂ reduction efficiency from H₂ is comparable to the highest demonstrated by *R. eutropha* during H₂ fermentation (25). This biomass yield is equivalent to assimilating ~ 4.1 mol (180 g) of CO₂ captured at the cost of 1 kWh of electricity. The amount of captured CO₂ is 10% of the amount caught by amine-based carbon capture and storage (~ 2000 g at the cost of 1 kWh) (26), whose processed product cannot be used as fuel. Enlarging the batch reactor volume by a factor of 10 did not perturb the efficiency (entries 4 and 6), indicating that the system is scalable and the reactor volume does not pose immediate limits. Note that η_{elec} under air (400 ppm CO₂) is $20 \pm 3\%$ (entry 7, $n = 3$), which is lower than for pure CO₂ by a factor of only 2.7, although the partial pressure of CO₂ is reduced by a factor of 2500. This indicates that CO₂ is not a limiting reagent (see below). The $\sim 20\%$ of η_{elec} for biomass is equivalent to as-

similating ~ 1.5 mol of CO₂ captured from about 85,200 liters of air at ambient condition with the cost of 1 kWh of electricity.

We also isolated a ROS-resistant variant of *R. eutropha* from one SS/CoP_i water-splitting reactor after 11 consecutive days of operation ($E_{\text{appl}} = 2.3$ V) with a H₂O₂ generation rate of ~ 0.6 $\mu\text{M}/\text{min}$. Genome sequencing found several mutations between the strain (BC4) and the wild type (H16) (table S2). In the presence of paraquat as a ROS inducer (27), the IC_{50} of paraquat for BC4 is almost one order of magnitude higher than that of the wild type (fig. S11). There is no obvious benefit of the BC4 strain with regard to η_{elec} (table S1), further confirming the absence of ROS in our system (see above). Nonetheless, BC4 should find great utility for achieving high η_{elec} in systems where ROS is problematic.

We found that biomass accumulation scales linearly with the amount of charge passed under pure CO₂ (Fig. 2B) or ambient CO₂ levels (Fig. 2C). The linear growth is accounted for by a model that combines governing equations for H₂ generation from water splitting and biomass accumulation from carbon fixation (23). The model predicts a linear correlation between biomass and charge passed after an induction period of low population density of bacteria and high H₂ concentration (Fig. 2D and fig. S12), which is consistent with the data shown in Fig. 2, B and C, where the induction period is too short to be observed. Gas chromatography measurements revealed a H₂ concentration in the reactor headspace of $0.19 \pm 0.04\%$ ($n = 3$) in 100% CO₂ and $0.10 \pm 0.05\%$ ($n = 3$) in air, corresponding to 1.5 ± 0.3 μM and 0.8 ± 0.4 μM , respectively, in water. These concentrations of H₂ are well below the Michaelis constant of ~ 6 μM for membrane-bound hydrogenases in *R. eutropha* (28), which suggests that H₂ is readily consumed by *R. eutropha*. Moreover, similar linear growth conditions for both pure and ambient CO₂ atmospheres provide evidence that H₂ oxidation rather than CO₂ reduction is rate-limiting for biosynthesis. Lastly, *R. eutropha* halted growth during “night” cycles and continued CO₂ reduction 12 hours later upon resumption of the water-splitting reaction (Fig. 2E), confirming the intrinsic dependence of *R. eutropha* on H₂ generation. These data also reveal that the CoP_i/Co-P/*R. eutropha* hybrid system is compatible with the intermittent nature of a solar energy source. Direct CO₂ reduction from air highlights the relatively high affinity of *R. eutropha* for CO₂ at low pressures and at high O₂ concentrations, in contrast to results reported for synthetic catalysts (29), individual enzymes (30, 31), and strictly anaerobic organisms such as acetogens and methanogens (11–14) (table S3).

Metabolic engineering of *R. eutropha* enables the renewable production of an array of fuels and chemical products (17). When *R. eutropha* confronts nutrient constraints coupled with carbon excess, the biosynthesis of poly(3-hydroxybutyrate) (PHB) is triggered in the wild-type H16 strain as an internal carbon storage pathway (17). As such, digestion is necessary for PHB collection (23). Under a constant rate of water splitting, PHB synthesis was not manifest until nitrogen became

limiting (~2 days), as indicated by the cessation of biomass accumulation (Fig. 3A) as well as the η_{elec} measured every 24 hours (Fig. 3B and fig. S13). With a titer of ~700 mg/liter, the 6-day average for PHB synthesis was $\eta_{\text{elec}} = 36 \pm 3\%$ (Fig. 2A, entry 9) with a 24-hour maximum of $\eta_{\text{elec}} = 42 \pm 2\%$ ($n = 3$) (Fig. 3B). In engineered strains (32, 33), this PHB pathway could be modified to excrete the fusel alcohols isopropanol (C_3), isobutanol (C_4), and 3-methyl-1-butanol (C_5), which possess energy densities of 24, 28, and 31 MJ/liter, respectively. The culture supernatant was then analyzed to quantify the secreted alcohols (23). The accumulation of these liquid fuels followed trends similar to those observed for PHB synthesis. As shown in Fig. 3, C and E, biomass production reached a plateau while isopropanol titers grew to ~600 mg/liter and $C_4 + C_5$ alcohol titers grew to ~220 mg/liter. An engineered *R. eutropha* strain produced isopropanol with a 6-day average $\eta_{\text{elec}} = 31 \pm 4\%$ (Fig. 2A, entry 10) and a 24-hour maximum of $\eta_{\text{elec}} = 39 \pm 2\%$ ($n = 4$) (Fig. 3D); a strain engineered to produce $C_4 + C_5$ alcohols averaged a 6-day $\eta_{\text{elec}} = 16 \pm 2\%$ (Fig. 2A, entry 11) with a 24-hour maximum of $\eta_{\text{elec}} = 27 \pm 4\%$ ($n = 3$) (Fig. 3F). The achieved titers are higher than previous reported values, and η_{elec} values have increased by a factor of at least 20 to 50 (10, 18). *R. eutropha* has demonstrated tolerance toward isopropanol (fig. S14), allowing for enriched product concentrations under extended operation.

Our combined catalyst design mitigates biotoxicity at a systems level, allowing water-splitting catalysis to be interfaced with engineered organisms to realize high CO_2 reduction efficiencies that exceed natural photosynthetic systems. Because E_{appl} required for water splitting is low (1.8 to 2.0 V), high η_{elec} values are achieved that translate directly to high solar-to-chemical efficiencies (η_{SCE}) when coupled to a typical solar-to-electricity device ($\eta_{\text{SCE}} = \eta_{\text{solar}} \times \eta_{\text{elec}}$). For a photovoltaic device of $\eta_{\text{solar}} = 18\%$, the Co-P[CoP]*R. eutropha* hybrid system can achieve $\eta_{\text{SCE}} = 9.7\%$ for biomass, 7.6% for bioplastic, and 7.1% for fusel alcohols. This approach allows for the development of artificial photosynthesis with efficiencies well beyond that of natural photosynthesis, thus providing a platform for the distributed solar production of chemicals.

REFERENCES AND NOTES

- N. S. Lewis, D. G. Nocera, *Proc. Natl. Acad. Sci. U.S.A.* **103**, 15729–15735 (2006).
- N. S. Lewis, D. G. Nocera, *The Bridge* **46**, 41–47 (2015); www.nae.edu/Publications/Bridge/140630/140646.aspx.
- R. E. Blankenship et al., *Science* **332**, 805–809 (2011).
- S. Licht et al., *Int. J. Hydrogen Energy* **26**, 653–659 (2001).
- F. F. Abdi et al., *Nat. Commun.* **4**, 2195 (2013).
- C. R. Cox, J. Z. Lee, D. G. Nocera, T. Buonassisi, *Proc. Natl. Acad. Sci. U.S.A.* **111**, 14057–14061 (2014).
- J. Luo et al., *Science* **345**, 1593–1596 (2014).
- T. R. Cook et al., *Chem. Rev.* **110**, 6474–6502 (2010).
- T. Zhang, *Science* **350**, 738–739 (2015).
- H. Li et al., *Science* **335**, 1596 (2012).
- K. P. Nevin, T. L. Woodard, A. E. Franks, Z. M. Summers, D. R. Lovley, *mBio* **1**, e00103–10 (2010).
- S. Cheng, D. Xing, D. F. Call, B. E. Logan, *Environ. Sci. Technol.* **43**, 3953–3958 (2009).
- C. Liu et al., *Nano Lett.* **15**, 3634–3639 (2015).
- E. M. Nichols et al., *Proc. Natl. Acad. Sci. U.S.A.* **112**, 11461–11466 (2015).
- M. W. Kanan, D. G. Nocera, *Science* **321**, 1072–1075 (2008).
- S. Y. Reece et al., *Science* **334**, 645–648 (2011).
- A. Pohlmann et al., *Nat. Biotechnol.* **24**, 1257–1262 (2006).
- J. P. Torella et al., *Proc. Natl. Acad. Sci. U.S.A.* **112**, 2337–2342 (2015).
- D. A. Lutterman, Y. Surendranath, D. G. Nocera, *J. Am. Chem. Soc.* **131**, 3838–3839 (2009).
- D. K. Bediako, A. M. Ullman, D. G. Nocera, *Top. Curr. Chem.* **371**, 173–213 (2016).
- I. Paseka, J. Velicka, *Electrochim. Acta* **42**, 237–242 (1997).
- Y. Surendranath, D. A. Lutterman, Y. Liu, D. G. Nocera, *J. Am. Chem. Soc.* **134**, 6326–6336 (2012).
- See supplementary materials on Science Online.
- M. Dincă, Y. Surendranath, D. G. Nocera, *Proc. Natl. Acad. Sci. U.S.A.* **107**, 10337–10341 (2010).
- J. Yu, A. Dow, S. Pingali, *Int. J. Hydrogen Energy* **38**, 8683–8690 (2013).
- G. T. Rochelle, *Science* **325**, 1652–1654 (2009).
- J. R. Roede, G. W. Miller, in *Encyclopedia of Toxicology*, P. Wexler, Ed. (Academic Press, ed. 3, 1984), pp. 756–758.
- M. Ludwig, J. A. Cracknell, K. A. Vincent, F. A. Armstrong, O. Lenz, *J. Biol. Chem.* **284**, 465–477 (2009).
- A. M. Appel et al., *Chem. Rev.* **113**, 6621–6658 (2013).
- A. Parkin, J. Seravalli, K. A. Vincent, S. W. Ragsdale, F. A. Armstrong, *J. Am. Chem. Soc.* **129**, 10328–10329 (2007).
- T. Reda, C. M. Plugge, N. J. Abram, J. Hirst, *Proc. Natl. Acad. Sci. U.S.A.* **105**, 10654–10658 (2008).
- E. Grousseau, J. Lu, N. Gorret, S. E. Guillouet, A. J. Sinskey, *Appl. Microbiol. Biotechnol.* **98**, 4277–4290 (2014).
- J. Lu, C. J. Brigham, C. S. Gai, A. J. Sinskey, *Appl. Microbiol. Biotechnol.* **96**, 283–297 (2012).

ACKNOWLEDGMENTS

We thank N. Li for ICP-MS measurement and reagents, and J. Torella, C. Myhrvold, C. Lemon, and M. Huynh for helpful discussions. C.L. acknowledges X. Ling at Nanyang Technological University. Supported by a Lee Kuan Yew Postdoctoral Fellowship (C.L.), a predoctoral fellowship from the NSF Graduate Research Fellowships Program (B.C.C.), Office of Naval Research Multidisciplinary University Research Initiative award N00014-11-1-0725 (P.A.S.), Air Force Office of Scientific Research grant FA9550-09-1-0689 (D.G.N.), the Wyss Institute for Biologically Inspired Engineering (P.A.S.), and the Harvard University Climate Change Solutions Fund. This work was performed under the First 100 W Program at Harvard University. C.L., B.C.C., M.Z., P.A.S., and D.G.N. are inventors on patent applications (62/218,131) filed by Harvard University and Harvard Medical School related to the technology described in this paper. The genome sequences are accessible in the NCBI SRA database under accession number SRP073266.

SUPPLEMENTARY MATERIALS

www.sciencemag.org/content/352/6290/1210/suppl/DC1

Methods

Tables S1 to S3

Figs. S1 to S14

References (34–49)

18 February 2016; accepted 22 April 2016

10.1126/science.aaf5039

ECOTOXICOLOGY

Environmentally relevant concentrations of microplastic particles influence larval fish ecology

Oona M. Lönnstedt* and Peter Eklöv

The widespread occurrence and accumulation of plastic waste in the environment have become a growing global concern over the past decade. Although some marine organisms have been shown to ingest plastic, few studies have investigated the ecological effects of plastic waste on animals. Here we show that exposure to environmentally relevant concentrations of microplastic polystyrene particles (90 micrometers) inhibits hatching, decreases growth rates, and alters feeding preferences and innate behaviors of European perch (*Perca fluviatilis*) larvae. Furthermore, individuals exposed to microplastics do not respond to olfactory threat cues, which greatly increases predator-induced mortality rates. Our results demonstrate that microplastic particles operate both chemically and physically on larval fish performance and development.

Global plastic production is estimated to be about 300 million metric tons (MMT) annually and is increasing by 20 MMT per year (1). As a direct consequence of the massive use of plastics in modern society, plastic waste is accumulating, especially in and around urbanized areas, where it often ends up in waterways and is ultimately transported into the ocean (2, 3). Because plastic polymers show minimal biological degradation, they remain in the environment for hundreds to thousands of

years, where they break down into smaller pieces owing to ultraviolet radiation, physical forces, and hydrolysis (4). Hence, plastic particles continue to accumulate as small fragments (hereafter termed microplastics, and defined as <5 mm in size) throughout the world's oceans (4, 5). Plastic debris can affect marine biota both physically (e.g., by blocking the alimentary tract when ingested) (6) and chemically (e.g., by leaching toxic pollutants that are part of the plastics or that have been absorbed by the plastic) (7).

To date, passive ingestion of plastic microdebris by filter feeders is known to occur, but the ecological significance of ingestion is poorly understood (3, 4, 8). There is increasing concern that

Department of Ecology and Genetics, Limnology, Uppsala University, Uppsala, Sweden

*Corresponding author. Email: oona.lonnstedt@ebc.uu.se

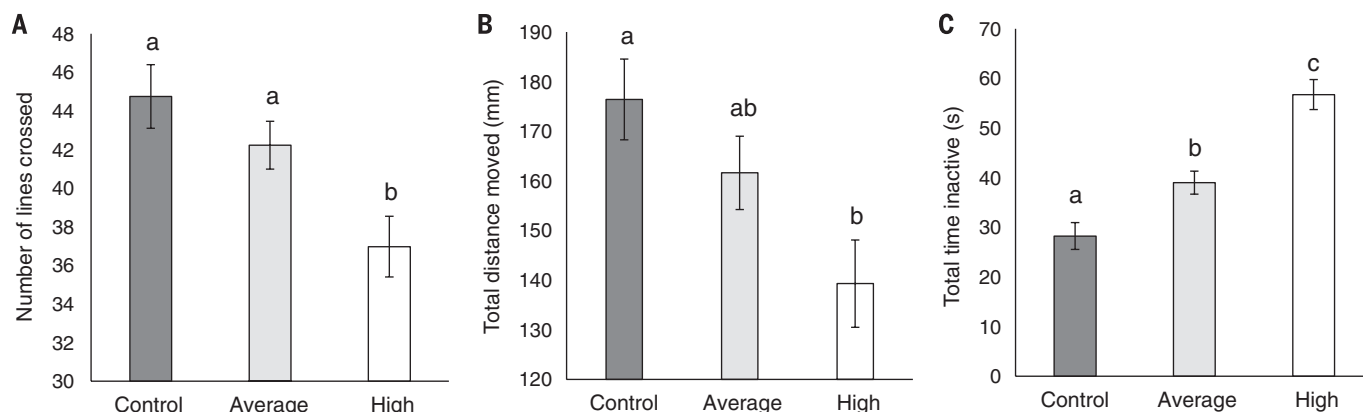


Fig. 1. Fish behavior when exposed to polystyrene microplastic particles. Mean (\pm SE) number of (A) lines crossed (a measure of activity), (B) total distance moved (mm), and (C) total time spent inactive (s) for 10-day-old *P. fluviatilis* were affected by microplastic concentration (control, average, or high).

the accumulation of microplastic waste could affect the functioning of marine ecosystems; however, the mechanisms by which effects will manifest have not been identified. This is especially true for eggs, embryos, and larvae of aquatic organisms, which are particularly vulnerable to water-borne pollutants owing to their limited ability to regulate their internal environment (9). In particular, early life stages of fishes are under strong selection, driven by high rates of predator-induced mortality (10, 11). Hence, selection is often mediated by antipredator behaviors and proximate factors (e.g., feeding history and growth) (12). To better understand potential effects of microplastic waste on the vulnerable younger life stages of fish, we examined how natural levels of microplastic particles affected the development, behavior, and survival of Eurasian perch (*Perca fluviatilis*).

The abundance of microplastic particles on the Swedish coast is in the range of 150 to 2400 particles/ m^3 to 68,000 to 102,000 particles/ m^3 , with average values being 7000 to 10,000 plastic particles/ m^3 , based on zooplankton sampling (net mesh size 10 to 300 μm) (13, 14). Many juvenile fish are likely to encounter high concentrations of microplastic debris in their nursery habitats, as microplastic pollutants often accumulate in shallow coastal habitats (13–15). Polystyrene is one of the five major types of microplastic debris found in the marine environment (3, 16), and ingestion of polystyrene particles has been found to alter behaviors (17) and disturb the fat metabolism in freshwater fishes (18). Hence, in the current study, we used three different concentrations of polystyrene micro-

plastic particles (90 μm): (i) no microplastics (0 particles/ m^3), (ii) average microplastic concentration (10,000 particles/ m^3), and (iii) high microplastic concentration (80,000 particles/ m^3).

Fish across all treatments were fed the same concentrations of newly hatched *Artemia* sp. nauplii twice daily (ad libitum, 75,000 nauplii/ m^3).

To assess direct chemical effects of polystyrene microplastics on fish, we collected fertilized egg strands of *P. fluviatilis* from natural populations in the Baltic Sea and placed them in 1000-ml glass aquaria that contained one of the three microplastic concentrations and filtered estuarine water (19). We then monitored the number of successful hatching events over a 3-week period ($N = 5$ with 58 to 60 eggs per replicate aquaria). Overall, successful hatching rates of fish were significantly related to microplastic concentration [analysis of variance (ANOVA): $F_{2,12} = 19.4$, $P = 0.0002$]. Fish that were not exposed to microplastics during egg development had high hatching rates typical of most teleosts [e.g., (20)], with 96% successfully hatching compared to eggs that were exposed to polystyrene particles. Fish in the high-concentration treatment had the lowest hatching rates, at 81%, whereas fish exposed to average microplastic concentrations displayed hatching rates of 89%. This suggests that polystyrene particles may be chemically affecting larvae in both average and high concentrations, as exposure potentially reduces hatching rates of fertilized *P. fluviatilis* eggs.

Behavior is a crucial determinant for essential fitness correlates (e.g., overall health), such as growth, reproduction, and survival (21). To investigate if exposure to microplastic particles during the first weeks of development altered fish behavior, we measured activity rates [defined as the number of lines crossed on a grid (5 mm by 5 mm) present on the

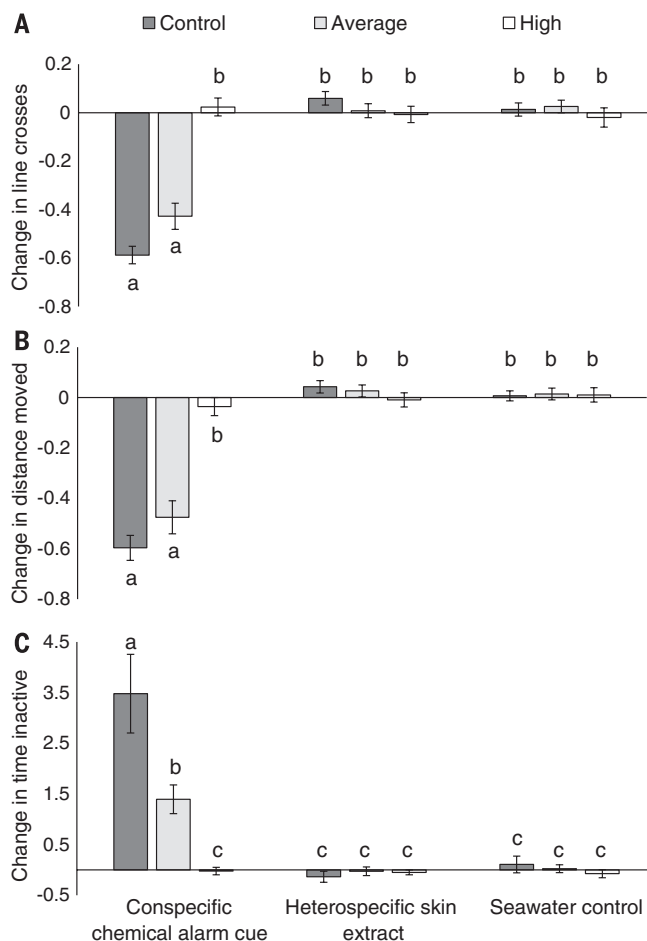


Fig. 2. Innate responses to olfactory threat cues are affected by exposure to microplastic particles. Fish exposed to high concentrations of microplastic particles did not significantly alter their proportional change in (A) activity, (B) area use (mm), or (C) freezing behavior after being exposed to a conspecific chemical alarm cue compared to the two controls [alarm cue from a heterospecific fish (flounder, *Platichthys flesus*) or water controls].

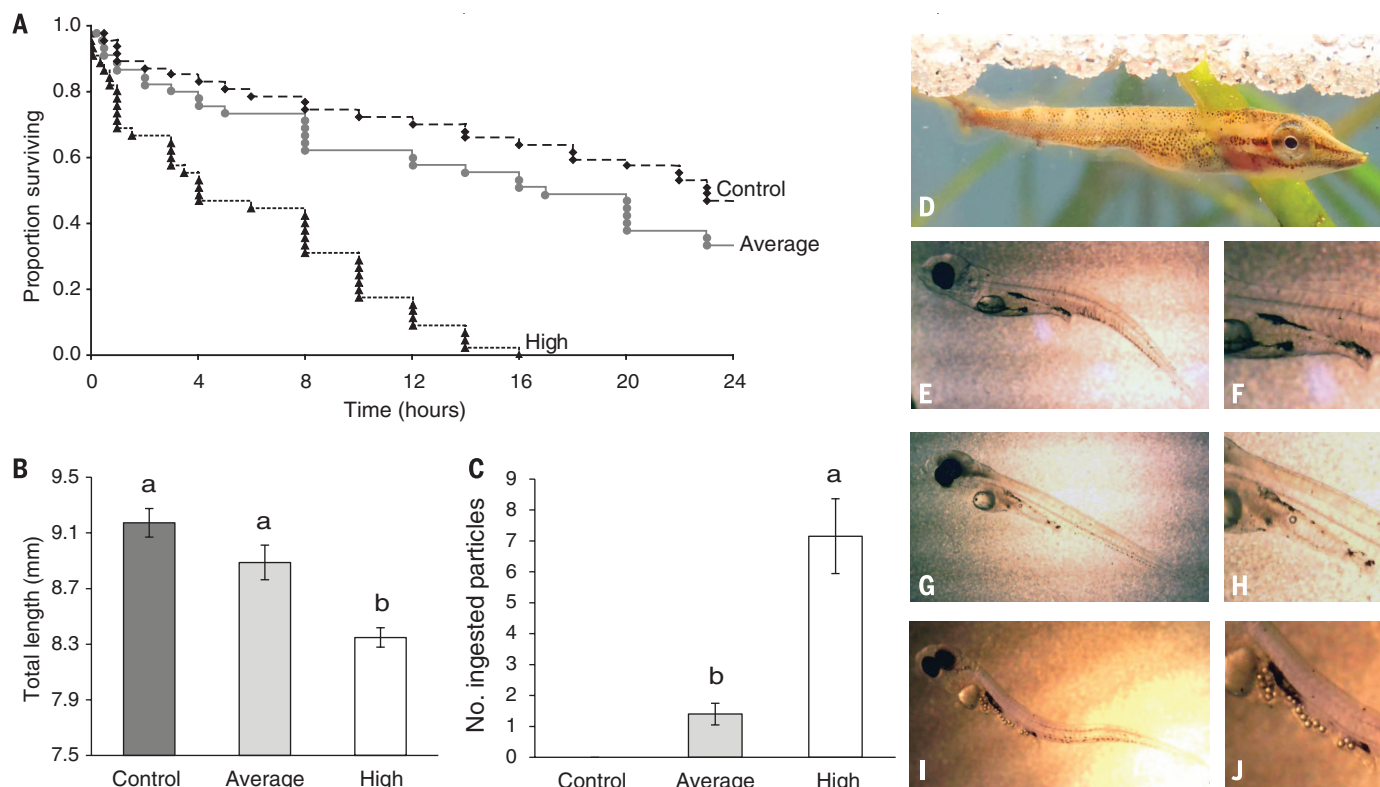


Fig. 3. Exposure to microplastic particles affects survival, growth, and mean number (\pm SE) of ingested microplastic particles. (A) Survival curves (Kaplan-Meier plot) of 10-day-old *P. fluviatilis* larvae from the three different microplastic treatments. **(B)** Standard length and **(C)** number of microplastic particles found in stomach contents were also affected by treatment. Juvenile pike [*Esox lucius* (**D**)] are a common and natural piscivore that preys on larval perch. Larvae exposed to the different treatments had consumed varying amounts of microplastic particles: no microplastics (**E** and **F**); average amounts of microplastics (**G** and **H**); or high amounts of microplastics (**I** and **J**).

bottom of the aquarium], total distance moved (total distance fish swam over the 3-min observation period), and the amount of time fish were immobile (s) using standardized protocols ($N = 36$) (12, 22). We found clear effects of exposure to polystyrene microplastics (average and high concentrations) on behavior of 10-day-old fish larvae [2-factor multivariate analysis of variance (MANOVA): $F_{6,180} = 8.47$, $P < 0.00001$; Fig. 1, A to C]. There was a nonsignificant effect of exposure tank on behaviors of individual fish (2-factor MANOVA: $F_{39,267} = 0.99$, $P = 0.49$). Hatched larvae that were reared under control conditions had higher activity rates (2-factor ANOVA: $F_{2,92} = 7.24$, $P = 0.0012$; Fig. 1A), swam greater distances (2-factor ANOVA: $F_{2,92} = 5.14$, $P = 0.0076$; Fig. 1B), and spent less time motionless (2-factor ANOVA: $F_{2,92} = 28.98$, $P < 0.00001$; Fig. 1C) compared to fish that were reared under microplastic treatment conditions.

Early life-history stages of many aquatic organisms are inherently vulnerable to predators, and an innate ability to detect predators is critical for survival (10–12). One way naïve prey avoid predators is through an innate response to damage-released chemical alarm cues, and although the olfactory sense in larval fish is sensitive to changes in habitat composition (22) and ocean chemistry (23), it is unknown if olfactory threat responses are affected by exposure to

microplastic pollutants. By recording behaviors of fish from the three different microplastic treatments before and after the injection of an alarm cue, we could determine innate fear responses of naïve 10-day-old *P. fluviatilis* ($N = 12$). We found a strong influence of microplastic exposure and concentration on the response of fish to olfactory threat cues (2-factor MANOVA: $F_{12,291} = 6.59$, $P < 0.00001$; Fig. 2, A to C). Fish reared under control conditions displayed lowered activity rates (2-factor ANOVA: $F_{4,97} = 29.72$, $P < 0.0001$; Fig. 2A), decreases in distance moved (2-factor ANOVA: $F_{4,97} = 23.44$, $P < 0.0001$; Fig. 2B), and a greater incidence of freezing behavior (e.g., time immobile: 2-factor ANOVA: $F_{4,97} = 12.94$, $P < 0.0001$; Fig. 2C) in response to conspecific alarm cues. Although there was a tendency of fish reared in the average microplastic concentrations to display weaker threat responses compared to control fish, they still displayed significantly stronger threat responses to chemical alarm cues compared to the two control cue treatments (heterospecific skin extract and water controls; Tukey's HSD (honest significant difference) test $P < 0.02$; Fig. 2, A to C). In contrast, *P. fluviatilis* larvae reared in high microplastic concentrations did not exhibit an antipredator response when exposed to threat cues compared to controls (Fig. 2, A to C).

To assess more direct ecological effects of microplastic exposure on fish, we measured indi-

vidual survival rates of 2-week-old larvae from the different treatments when exposed to a natural and common predator on larval perch, juvenile pike (*Esox lucius*, 31 ± 1.5 mm total length). Survival of fish was monitored every 2 to 6 hours over a 24-hour period in mesocosms simulating natural conditions ($N = 45$ to 47) (19). We found that microplastic exposure during development influenced survival rates of *P. fluviatilis* ($\chi^2_{2,0.05} = 34.02$, $P < 0.0001$). Survival of fish larvae was highest and most similar to natural survival rates at this life stage [e.g., (20)] when reared under control conditions, with 46% still alive after 24 hours (Fig. 3A). Fish reared in average microplastic concentrations had a lower survival rate, with 66% consumed after 24 hours. Larvae reared in high microplastic concentrations had the lowest survival rates, with 100% consumed by pike within 24 hours. Observed survival patterns in the current study emphasize the importance of behavioral responses to threat cues, as larval fish failing to respond to conspecific alarm cues had threefold (high microplastics = 37 out of 45) higher mortality rates compared to control larvae (no microplastics = 12 out of 47) in the first 10 hours after exposure to a predator (Fig. 3A) ($P < 0.001$).

Two weeks after hatching, total length (mm) differed significantly between fish exposed to the different microplastic concentrations (2-factor ANOVA: $F_{2,45} = 17.16$, $P < 0.0001$; Fig. 3B; $N = 20$).

Fish reared in the highest microplastic concentrations were significantly smaller (8.35 ± 0.07 mm) than fish reared in average concentrations (8.89 ± 0.12 mm) or than those without exposure to microplastics (9.17 ± 0.1 mm). There was also a significant difference in the number of ingested microplastic particles between the three treatments (2-factor ANOVA: $F_{2,45} = 79.24$, $P < 0.0001$; Fig. 3C; $N = 20$). Larvae from the high microplastics treatment had consumed an average of 7.15 ± 1.2 polystyrene particles, with stomachs containing solely plastic particles. In contrast, fish from the average microplastics treatment consumed 1.4 ± 0.35 plastic particles but also consumed the food source (*Artemia* sp. nauplii) that was available at similar concentrations across all three treatments. Fish that were reared in water that contained no microplastics only had *Artemia* sp. nauplii in their stomachs (Fig. 3, E to J). These results suggest that newly hatched larvae favor microplastic particles over the more natural food source of free-swimming zooplankton. Other aquatic organisms have been found to both passively and actively ingest plastic waste (8, 24). Here it appears that larvae preferentially feed on plastic particles.

Our results suggest that environmentally relevant concentrations of microplastic particles operate both chemically and physically on the early life stages of perch. Not only are crucial behaviors such as activity and feeding affected, but innate responses to olfactory threat cues are impaired. Such loss of predator-avoidance behaviors greatly increased predator-induced mortality rates of larvae.

Increases in microplastic pollution in the Baltic Sea and marked recruitment declines of the coastal keystone species (e.g., perch and pike) have recently been observed (25). It has been suggested that population decline is related to feeding in the juvenile stage, where resource deficits may have led to increased mortality (26). Our study suggests a potential driver for the observed decreased recruitment rate and increased mortality. If early life-history stages of other species are similarly affected by microplastics, and this translates to increased mortality rates, the effects on aquatic ecosystems could be profound. Our findings highlight ecologically important and previously underappreciated effects of microplastic particles that enter marine ecosystems and emphasize the need for new management strategies to control the release of microplastic waste products.

REFERENCES AND NOTES

- "Plastics—the Facts 2013," Plastics Europe, Belgium (2013).
- R. C. Thompson et al., *Science* **304**, 838 (2004).
- M. A. Browne et al., *Proc. Biol. Sci.* **282**, 20142929 (2015).
- C. J. Moore, *Environ. Res.* **108**, 131–139 (2008).
- A. L. Andrady, *Mar. Pollut. Bull.* **62**, 1596–1605 (2011).
- M. Cole et al., *Environ. Sci. Technol.* **47**, 6646–6655 (2013).
- C. M. Rochman, E. Hoh, B. T. Hentschel, S. Kaye, *Environ. Sci. Technol.* **47**, 1646–1654 (2013).
- S. L. Wright, R. C. Thompson, T. S. Galloway, *Environ. Pollut.* **178**, 483–492 (2013).
- R. Sussarellu et al., *Proc. Natl. Acad. Sci. U.S.A.* **113**, 2430–2435 (2016).
- W. C. Leggett, E. Deblois, *Neth. J. Sea Res.* **32**, 119–134 (1994).
- K. M. Bailey, E. D. Houde, *Adv. Mar. Biol.* **25**, 1–83 (1989).
- O. M. Lönnstedt, M. I. McCormick, M. G. Meekan, M. C. O. Ferrari, D. P. Chivers, *Proc. Biol. Sci.* **279**, 2091–2098 (2012).
- F. Norén, *KIMO Sweden* (2007).
- F. Norén, K. Norén, K. Magnusson, *Läns. Västra Götaland Rapp.* **52** (2014).
- D.-H. Chae, I.-S. Kim, S.-K. Kim, Y. K. Song, W. J. Shim, *Arch. Environ. Contam. Toxicol.* **69**, 269–278 (2015).
- A. L. Andrady, M. A. Neal, *Philos. Trans. R. Soc. London B Biol. Sci.* **364**, 1977–1984 (2009).
- K. Mattsson et al., *Environ. Sci. Technol.* **49**, 553–561 (2015).
- T. Cedervall, L.-A. Hansson, M. Lard, B. Frohm, S. Linse, *PLOS ONE* **7**, e32254 (2012).
- Materials and methods are available as supplementary materials on Science online.
- J. W. Treasurer, *Environ. Biol. Fishes* **8**, 3–16 (1983).
- B. R. Smith, D. T. Blumstein, *Behav. Ecol.* **19**, 448–455 (2008).
- O. M. Lönnstedt, M. I. McCormick, D. P. Chivers, M. C. O. Ferrari, *J. Anim. Ecol.* **83**, 1178–1185 (2014).
- D. L. Dixon, P. L. Munday, G. P. Jones, *Ecol. Lett.* **13**, 68–75 (2010).
- C. M. Rochman et al., *Sci. Rep.* **5**, 14340 (2015).
- G. Sundblad, U. Bergström, A. Sandström, P. Eklöv, *ICES J. Mar. Sci.* **71**, 672–680 (2014).
- L. Junggren et al., *ICES J. Mar. Sci.* **67**, 1587–1595 (2010).

ACKNOWLEDGMENTS

This study was financially supported by Uppsala University–Campus Gotland and the Swedish Research Council Vetenskapsrådet. All work reported herein was conducted in accordance with the guidelines for the care and use of animals in research of the Swedish Board of Agriculture with approval by the Uppsala University Ethics Committee. We thank A. Nissling, J. Sundin, G. Rosenqvist, M. Cunha, I. Wallin, R. Gydmo, and L. Vallin for logistic support and A. Roswald, I. Lönnstedt, and M. McCormick for comments and statistical advice. The data reported in this paper are archived at the research database at Uppsala University and are also included in the online supplementary materials.

SUPPLEMENTARY MATERIALS

www.sciencemag.org/content/352/6290/1213/suppl/DC1
Materials and Methods
Figs. S1 and S2
References (27–35)

16 November 2015; accepted 21 April 2016
10.1126/science.aad8828

CELL REPROGRAMMING

Conversion of human fibroblasts into functional cardiomyocytes by small molecules

Nan Cao,^{1,2} Yu Huang,¹ Jiashun Zheng,^{4,5} C. Ian Spencer,¹ Yu Zhang,^{1,2} Ji-Dong Fu,⁶ Baoming Nie,^{1,2} Min Xie,^{1,2} Mingliang Zhang,^{1,2} Haixia Wang,^{1,2} Tianhua Ma,^{1,2} Tao Xu,^{1,2} Guilai Shi,^{1,2} Deepak Srivastava,^{1,3,4,*} Sheng Ding^{1,2,*†}

Reprogramming somatic fibroblasts into alternative lineages would provide a promising source of cells for regenerative therapy. However, transdifferentiating human cells into specific homogeneous, functional cell types is challenging. Here we show that cardiomyocyte-like cells can be generated by treating human fibroblasts with a combination of nine compounds that we term 9C. The chemically induced cardiomyocyte-like cells uniformly contracted and resembled human cardiomyocytes in their transcriptome, epigenetic, and electrophysiological properties. 9C treatment of human fibroblasts resulted in a more open-chromatin conformation at key heart developmental genes, enabling their promoters and enhancers to bind effectors of major cardiogenic signals. When transplanted into infarcted mouse hearts, 9C-treated fibroblasts were efficiently converted to chemically induced cardiomyocyte-like cells. This pharmacological approach to lineage-specific reprogramming may have many important therapeutic implications after further optimization to generate mature cardiac cells.

Advances in reprogramming enable the fate of a cell to be changed, with potential applications for regenerative therapy. Cardiomyocyte (CM)-like cells can be reprogrammed from somatic fibroblasts by overexpression of cardiac genes in vitro (1–6) and in vivo (5, 7–10). However, efficiently transdifferentiating human noncardiac cells into highly functional CMs has remained a major challenge (1, 4, 6). In contrast to conventional reprogramming by genetic methods, a chemical reprogramming approach introduces small molecules that interact with and modulate endogenous factors in the starting cell type (e.g., fibroblast) in the absence of target cell type-specific proteins. Small molecules have certain advantages

over genetic methods: They are convenient to use, can be efficiently delivered into cells, provide

¹Gladstone Institute of Cardiovascular Disease, San Francisco, CA 94158, USA. ²Department of Pharmaceutical Chemistry, University of California–San Francisco, San Francisco, CA 94158, USA. ³Department of Pediatrics, University of California–San Francisco, San Francisco, CA 94158, USA. ⁴Department of Biochemistry and Biophysics, University of California–San Francisco, San Francisco, CA 94158, USA. ⁵California Institute for Quantitative Biosciences, University of California–San Francisco, San Francisco, CA 94158, USA. ⁶Department of Medicine, Heart and Vascular Research Center, Case Western Reserve University, Cleveland, OH 44106, USA.

*These authors contributed equally to this work. †Corresponding author. Email: sheng.ding@gladstone.ucsf.edu

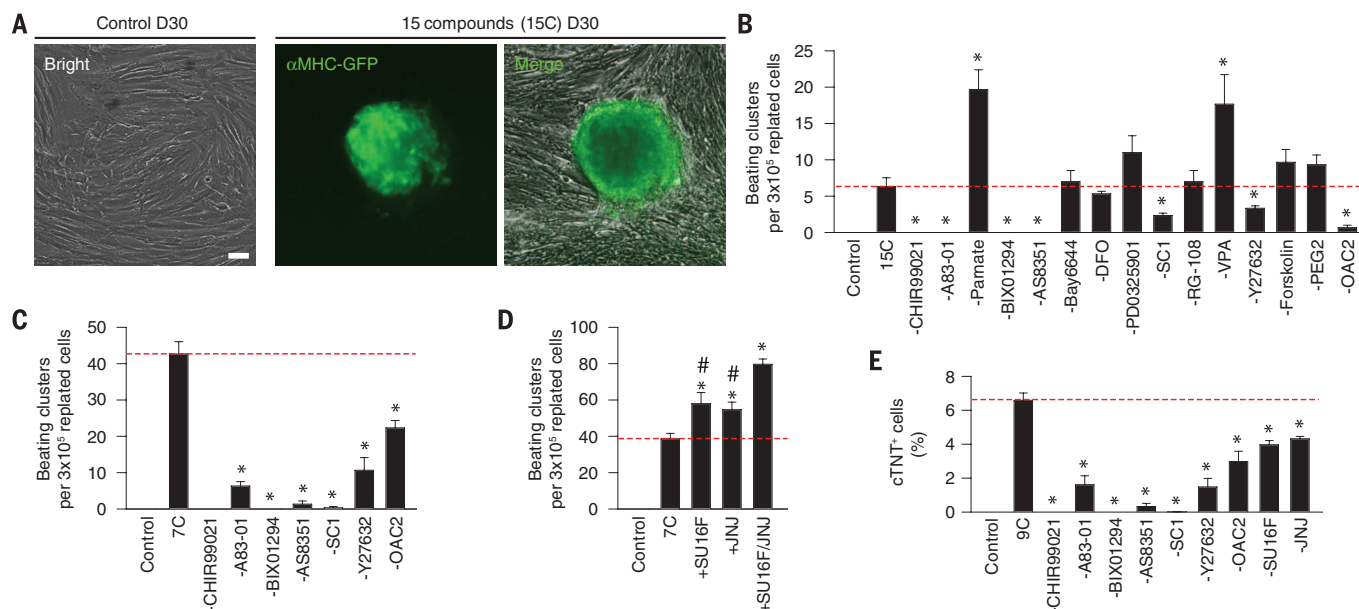


Fig. 1. ciCMs from HFFs. (A) A representative contracting cluster induced by 15C at reprogramming day 30 (D30). Scale bars, 100 μ m. (B to E) Number of contracting clusters (B to D) and flow cytometry analyses of cTNT (E) under the indicated conditions ($n = 3$). A minus (plus) sign indicates removal from (addition to) the small-molecule combination. The red dashed line indicates values of 15C (B), 7C (C and D), and 9C (E). Plotted are means with standard errors. * $P < 0.05$ versus 15C (B), 7C (C and D), or 9C (E). # $P < 0.05$ versus +SU16F/JNJ.

greater temporal control, and are nonimmunogenic and more cost-effective. Moreover, their effects can be fine-tuned by varying their concentrations and combinations. Here we report the identification of a combination of small molecules that enables reprogramming of human fibroblasts into chemically induced functional CMs (ciCMs) that uniformly display contractile properties.

To induce cardiac reprogramming of human fibroblasts, we used an established human foreskin fibroblast (HFF) line that contains no cardiac cells, as assayed by quantitative reverse transcriptase polymerase chain reaction (qRT-PCR), flow cytometry, and immunofluorescence analyses (fig. S1). HFFs were virally transduced with an alpha myosin heavy chain (α MHC)-green fluorescent protein (GFP) reporter (11) to specifically label CMs. Based on the cell activation and signaling-directed (CASD) reprogramming paradigm (12, 13), we treated cells with compounds that induce or enhance cellular reprogramming to alternative fates (cell activation) in conjunction with cardiogenic molecules (signaling-directed) to induce cardiogenesis. We initially screened a collection of 89 small molecules that are known to facilitate reprogramming (table S1). Each compound was added to a baseline cocktail containing SB431542, CHIR99021, parnate, and forskolin, which enabled cardiac reprogramming in an earlier study when combined with a single gene, *Oct4* (13). Cells were treated with the various small-molecule cocktails for 6 days and then cultured for 5 days in an optimized cardiac induction medium (CIM) containing the cardiogenic molecules activin A, bone morphogenetic protein 4 (BMP4), vascular endothelial growth factor, and CHIR99021 (fig. S2A). Positive hits

that enhanced cardiogenic gene expression (as assayed by qRT-PCR) after CIM treatment were identified and further tested in different combinations. Cells were then re-plated in human CM-conditioned medium, which may provide cardiac paracrine signals that mimic the in vivo environment for further maturation (14). After iterative rounds of testing, we found that a combination of 15 compounds (termed 15C) generated about five α MHC-GFP-positive clusters that beat spontaneously from 3×10^5 re-plated cells at day 30 (Fig. 1A), indicating reprogramming toward the cardiac fate.

To identify indispensable factors in 15C, we removed compounds one by one and treated cells with the remaining compounds. The number of beating clusters was significantly reduced by removal of CHIR99021, A83-01, BIX01294, AS8351, SC1, Y27632, or OAC2 (Fig. 1B). Together, these seven compounds (7C) were sufficient and necessary to efficiently induce cardiac reprogramming (Fig. 1C). We then screened a larger in-house-generated library containing ~300 modulators of signaling pathways, including known inhibitors of kinases, phosphatases, and other signaling receptors, with 7C as the baseline. Two inhibitors of the platelet-derived growth factor pathway, SU16F and JNJ10198409 (JNJ), accelerated the down-regulation of fibroblast genes (fig. S3) and increased the yield of beating clusters (Fig. 1D). These two inhibitors were added to 7C (9C) for subsequent assays after optimization of dosage and treatment duration (table S2 and fig. S4). At day 30, $6.6 \pm 0.4\%$ of the 9C-treated cells expressed the CM marker cardiac troponin T (cTNT), with a yield of up to 1.2 cTNT⁺ CMs per input HFF. Removal of any of the nine compounds markedly reduced the induction efficiency (Fig.

1E and fig. S2B). 9C reprogrammed human fetal lung fibroblasts (HLFs) into ciCMs with comparable efficiency (fig. S5).

Cardiogenesis involves sequential induction of mesoderm, cardiac progenitor cells (CPCs), and CMs (15). This developmental sequence, which is apparent in the differentiation of human pluripotent stem cells (hPSCs) (16–18), was observed during 9C-induced conversion of HFFs into ciCMs. After exposure to CIM, up to $27.9 \pm 4.0\%$ of the 9C-treated cells started to express a key mesoderm marker, KDR (fig. S6). These cells initiated a cardiogenic program by sequentially expressing mesoderm, CPC, and CM genes (figs. S7 and S8) and ultimately became beating ciCMs (fig. S6). Expression of CPC genes, particularly markers of second but not first heart field progenitors, was further confirmed by qRT-PCR and immunofluorescence analysis in 9C-treated cells (figs. S8A and S9). Small contracting clusters of ciCMs began to appear around day 20, continued to beat in culture (movies S1 and S2), and expressed specific CM markers (figs. S5 and S8B). Thus, they closely resembled CMs derived from hPSCs (hPSC-CMs) (fig. S1G).

Although new reprogramming protocols are improving cell yield, cardiac cells generated by genetic methods are heterogeneous, with only about 0.1% of genetically reprogrammed human iCMs achieving a high degree of reprogramming, as characterized by beating spontaneously, displaying cardiac action potentials, and expressing multiple cardiac genes uniformly in vitro (10). In contrast, we found that more than 97% of the ciCMs spontaneously beat and uniformly expressed multiple cardiac structural proteins, similar to hPSC-CMs (fig. S10). The homogeneity of ciCMs was further confirmed by single-cell

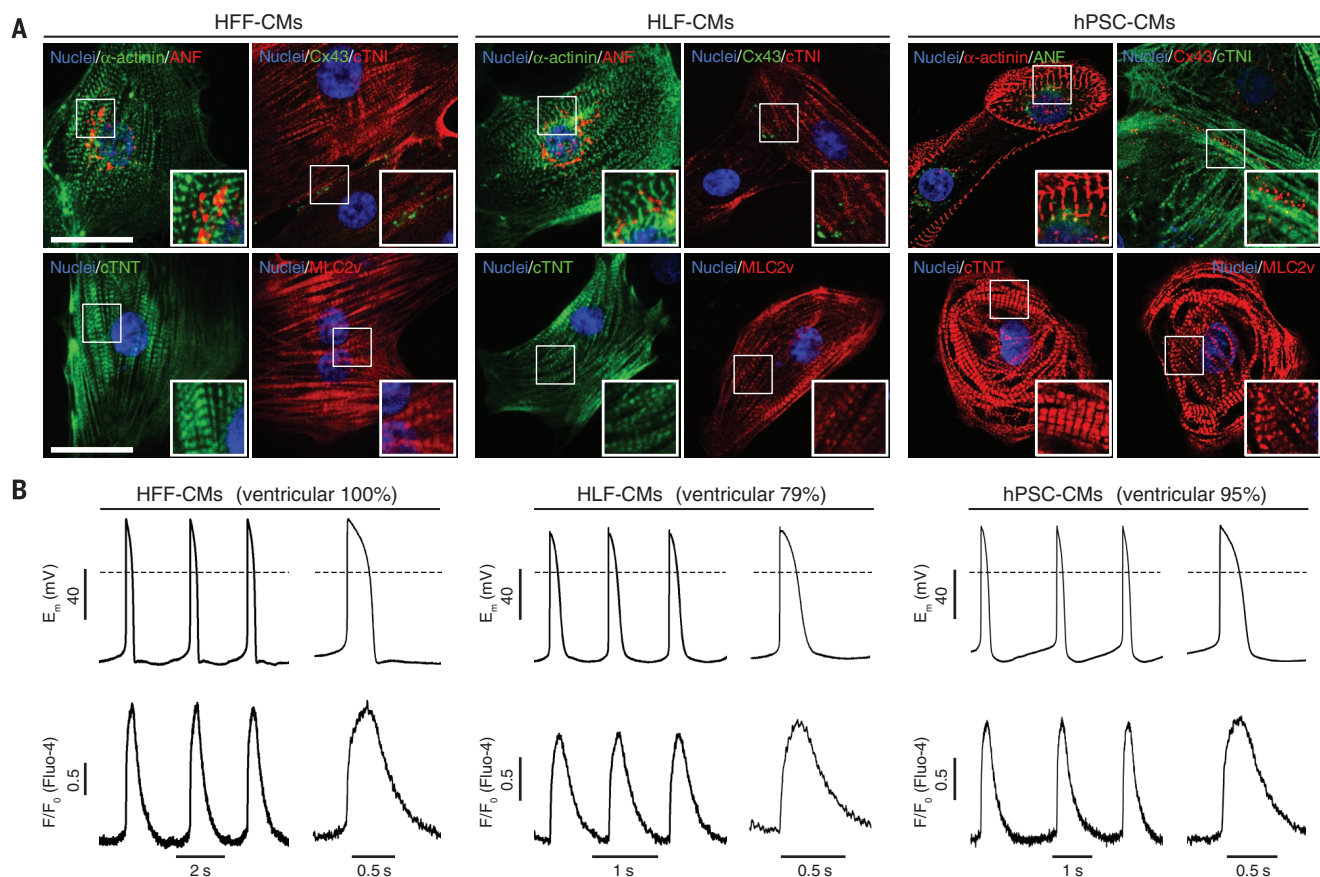


Fig. 2. Structural and functional characterization of ciCMs. (A) Immunofluorescence analyses of CM markers. Insets show boxed areas at higher magnification. Scale bars, 25 μm . (B) Representative traces of ventricular-like action potentials and Ca^{2+} transients. E_m , membrane potential. Dashed lines indicate 0 mV. F/F_0 , fluorescence relative to the baseline.

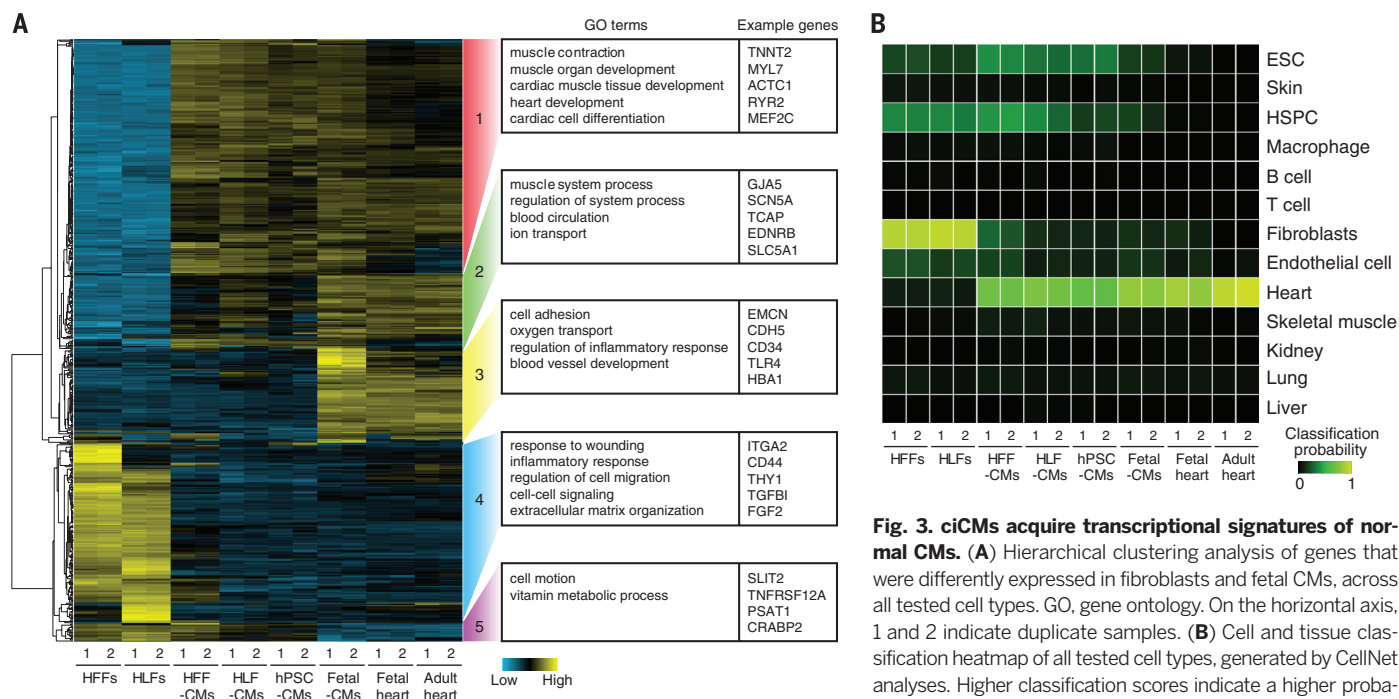


Fig. 3. ciCMs acquire transcriptional signatures of normal CMs. (A) Hierarchical clustering analysis of genes that were differentially expressed in fibroblasts and fetal CMs, across all tested cell types. GO, gene ontology. On the horizontal axis, 1 and 2 indicate duplicate samples. (B) Cell and tissue classification heatmap of all tested cell types, generated by CellNet analyses. Higher classification scores indicate a higher probability that a query sample (vertical axis) resembles the training sample (horizontal axis).

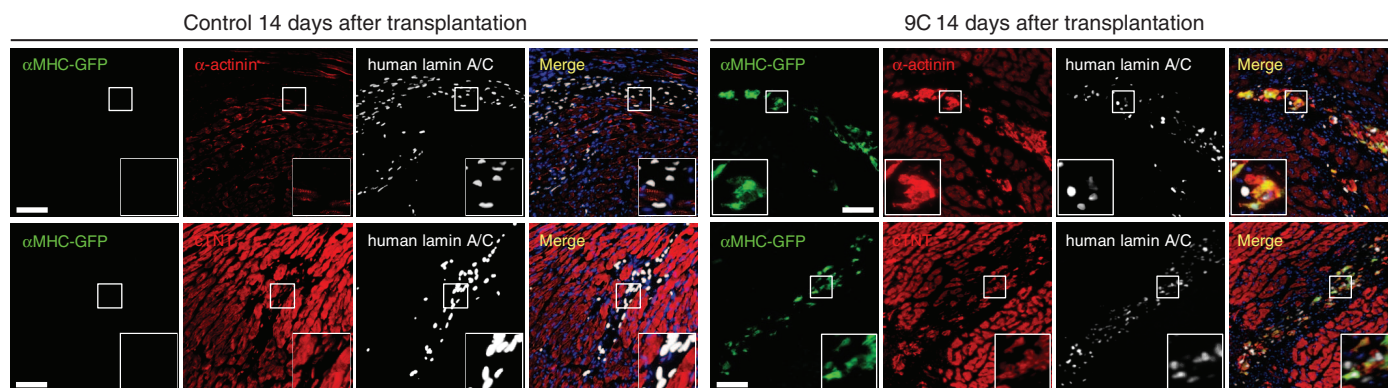


Fig. 4. 9C-treated fibroblasts convert into CMs in vivo. Immunofluorescence analyses of heart sections after transplantation of control (left) or 9C-treated (right) HFFs. Insets show boxed areas at higher magnification. Scale bars, 100 μ m.

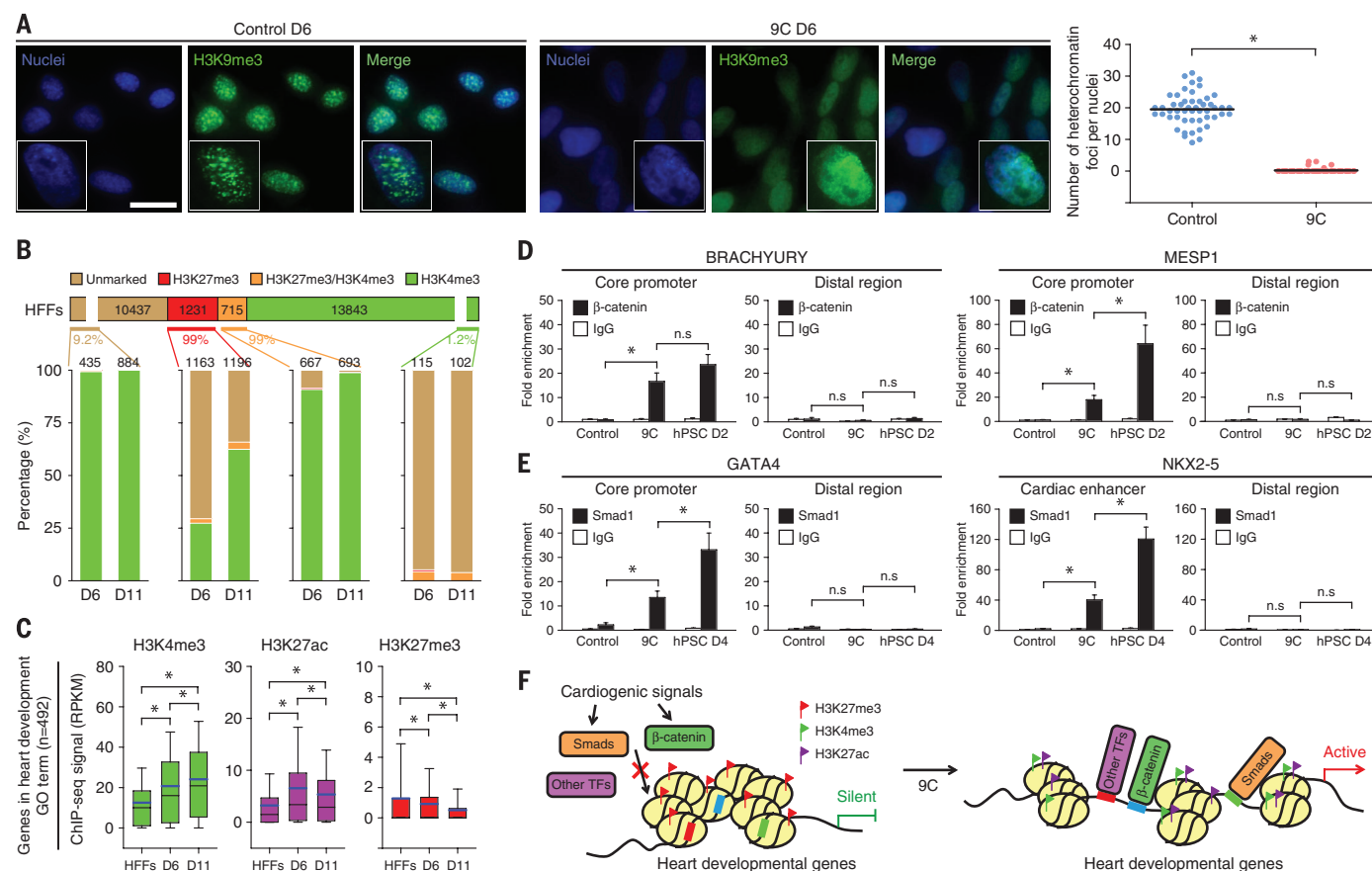


Fig. 5. 9C-treated fibroblasts have a globally more open chromatin structure and higher chromosome accessibility on core cardiogenesis genes.

(A) Heterochromatin foci shown by immunostaining for H3K9me3. Insets show a single cell nucleus at higher magnification. Scale bars, 100 μ m. On the right, the graph shows the number of heterochromatin foci per nuclei. (B) Tracing of gene status at days 6 and 11, relative to HFFs. Percentages of genes that showed dynamic changes are indicated in color-coded text. The number of genes is indicated for each bar. (C) Levels of H3K4me3, H3K27ac, and H3K27me3 en-

richment in genes in the GO "heart development" category. Black and blue bands inside the boxes represent median and mean values, respectively. Boxes represent the interquartile ranges, and whiskers represent the minimum and maximum values. RPKM, reads per kilobase of peak per million reads. (D and E) ChIP analyses of β -catenin (D) or Smad1 (E) binding on promoters and enhancers of cardiogenic genes ($n = 3$). IgG, immunoglobulin G. (F) A model for 9C-induced cardiac reprogramming. Red, blue, and green rectangles on the genes are transcription factor (TF) binding sites. * $P < 0.05$; n.s., not significant ($P > 0.05$).

qRT-PCR analyses, which revealed little, if any, difference in the expression levels of cardiac genes among individual ciCMs (fig. S11). Collectively, these results confirm that ciCMs are highly reprogrammed and largely homogeneous.

Next, we further characterized ciCMs that were reprogrammed from HFFs (HFF-CMs) and HLFs (HLF-CMs). Immunofluorescence and transmission electron microscopy revealed that ciCMs exhibited well-organized sarcomeres, closely resembling

those of hPSC-CMs (Fig. 2A and fig. S12). ciCMs also highly expressed genes involved in CM function, including those that encode atrial natriuretic factor, connexin 43, Cav3.2, HCN4, and Kir2.1 (Fig. 2A and fig. S13). Intracellular electrical

recordings from ciCMs at reprogramming days 45 to 50 revealed robust action potentials that were synchronized (1:1) with rhythmic Ca^{2+} transients (Fig. 2B and fig. S14, A and B), similar to hPSC-CMs (19); this suggests that ciCMs, in addition to being highly reprogrammed, are comparable in maturity to hPSC-CMs. Most ciCMs exhibited ventricular-like action potentials and expressed ventricular but not atrial CM markers (Fig. 2B and fig. S14). Moreover, ciCMs responded to caffeine (a ryanodine receptor agonist), isoproterenol (a β -adrenergic agonist), and carbachol (a muscarinic agonist) (fig. S15). Thus, ciCMs are functional in vitro and possess electrophysiological features that are similar to those of hPSC-CMs.

We next compared the transcriptomes of ciCMs, their parental fibroblasts, hPSC-CMs, purified human fetal CMs (1), and primary human heart tissue (20) by microarray analyses. ciCMs, hPSC-CMs, human fetal CMs, and primary heart tissue displayed transcriptional profiles that differed from those of the fibroblasts (Fig. 3 and fig. S16, A and B). The genes that were most significantly up-regulated in ciCMs were related to CM function and heart development; genes for fibroblast function, such as cell proliferation and motility, were down-regulated in ciCMs (fig. S16, C and D, and fig. S17).

We examined the expression of several maturation-related genes that are distinctly expressed during cardiogenesis (20). ciCMs closely resembled hPSC-CMs in a hierarchical clustering analysis (fig. S18A), and both CM types had a similar expression pattern of α -smooth muscle actin and ventricular myosin light chain 2v, two maturation-related markers (21) (fig. S14, C and D, and fig. S18B), indicating that ciCMs acquire maturity similar to that of hPSC-CMs. To determine whether the ciCMs had an established CM-like chromatin state, we analyzed histone and DNA methylation status in the promoter regions of several fibroblast and cardiac genes and found that ciCMs gained key epigenetic features similar to those of hPSC-CMs (fig. S19). Furthermore, ciCMs were directly reprogrammed without going through a PSC-like state (fig. S20) and maintained genomic stability relative to their parental fibroblasts (fig. S21).

Next, we investigated whether the diseased-heart niche would support the generation of ciCMs. HFFs harboring the α MHC-GFP reporter were treated with 9C for 6 days and then with CIM for 5 days and transplanted into the infarcted hearts of immunodeficient mice. HFFs not treated with 9C served as the negative control. Two weeks after transplantation, 9C-treated HFFs (identified by human-specific lamin A/C staining) robustly expressed CM markers, exhibited well-organized sarcomeres, and partially remuscularized the infarcted area (Fig. 4). These results suggest that 9C-treated cells are compatible with the diseased-heart environment and can further mature into CMs in vivo under these conditions.

We hypothesized that 9C promotes an epigenetic state characterized by open chromatin, which renders cells responsive to extrinsic cardiogenic

signals. We observed a decrease in the number of heterochromatin foci (densely stained for H3K9me3 and HP1 γ) in 9C-treated HFFs (Fig. 5A and fig. S22). Thus, 9C treatment appears to decondense closed chromatin regions in HFFs, possibly creating a more euchromatic structure at loci that are important for cardiogenesis. To assess this mechanism further, we analyzed the genome-wide epigenetic changes by chromatin immunoprecipitation-sequencing (ChIP-seq) analysis of H3K4me3 and H3K27ac (active chromatin marks) and H3K27me3 (inactive chromatin mark) at reprogramming days 6 and 11. We observed a dynamic loss of most of the H3K27me3 and specific gain of H3K4me3 among a subset of genomic loci during reprogramming (Fig. 5B). These genes were frequently related to developmental processes and cell differentiation (fig. S23). More specifically, we observed a significantly increased enrichment of H3K4me3 and H3K27ac on a cohort of heart developmental genes during reprogramming, whereas the deposition of H3K27me3 was down-regulated (Fig. 5C and fig. S24). Consistently, 9C enabled the binding of β -catenin and Smad1 (effectors of the major cardiogenic signals Wnt and BMP, respectively) to core promoters and enhancers of key heart development genes (Fig. 5, D and E). Thus, 9C appeared to convert the passive chromatin state of fibroblasts into a more euchromatic state, increasing chromatin accessibility on core cardiogenesis gene loci and thereby facilitating cardiac reprogramming (Fig. 5F).

We next investigated the role of the reprogramming compound AS8351. AS8351 and its functional analogs affect epigenetic modifications (22, 23) by competing with α -ketoglutarate (α -KG) for chelating iron [Fe(II)] in certain epigenetic enzymes, such as the JmjC domain-containing histone demethylases (JmjC-KDMs) that require α -KG and iron as co-factors (24). We hypothesized that AS8351's effects on cardiac reprogramming might in part be mediated through modulation of a specific JmjC-KDM. To test this hypothesis, we abrogated each of the 22 genes in the JmjC-KDM family by small hairpin RNAs and found that only knocking down KDM5B or using a KDM5B inhibitor (PBIT) could phenocopy AS8351 in generating ciCMs (fig. S25), suggesting that KDM5B might be a target of AS8351. KDM5B catalyzes the demethylation of tri-, di-, and mono-methylation states of H3K4 and facilitates heterochromatin formation (24). Consistent with the overall effect of 9C on reopening the closed chromatin structure, inhibition of KDM5B may facilitate this process and sustain the active chromatin marks (i.e., H3K4 methylation) at specific genomic loci.

Our study shows that reprogrammed and functional lineage-specific cells can be generated from human fibroblasts by defined small molecules and growth factors. This study not only achieved considerably higher-quality human iCMs than those previously reported but also provides a chemical approach, free of foreign genetic material, that may be adapted to generate multiple cell types. ciCMs are functionally comparable to PSC-CMs,

although generating fully mature CMs remains a critical challenge for cardiac regenerative therapies. An important feature of ciCM induction is that, in response to signals mimicking the paracrine environment in the in vivo heart, 9C-treated cells are induced to become CMs. This finding may ultimately provide a foundation for in situ repair of the heart by targeting endogenous cardiac fibroblasts with small molecules. However, many challenges (e.g., reprogramming efficiency and tissue-specific delivery of multiple drugs in an efficient and controllable manner) need to be resolved before this strategy can be considered for in vivo therapeutic applications. Additional studies are needed to determine whether unintended genomic changes occur in ciCM subpopulations and to investigate how to increase the maturity of ciCMs. Furthermore, a better understanding is needed of the underlying mechanisms for this reprogramming.

REFERENCES AND NOTES

1. J. D. Fu et al., *Stem Cell Rev.* **1**, 235–247 (2013).
2. M. Ieda et al., *Cell* **142**, 375–386 (2010).
3. T. M. Jayawardena et al., *Circ. Res.* **110**, 1465–1473 (2012).
4. Y. J. Nam et al., *Proc. Natl. Acad. Sci. U.S.A.* **110**, 5588–5593 (2013).
5. K. Song et al., *Nature* **485**, 599–604 (2012).
6. R. Wada et al., *Proc. Natl. Acad. Sci. U.S.A.* **110**, 12667–12672 (2013).
7. L. Qian et al., *Nature* **485**, 593–598 (2012).
8. K. Inagawa et al., *Circ. Res.* **111**, 1147–1156 (2012).
9. T. M. Jayawardena et al., *Circ. Res.* **116**, 418–424 (2015).
10. D. Srivastava, P. Yu, *Curr. Opin. Genet. Dev.* **34**, 77–81 (2015).
11. H. Kita-Matsuo et al., *PLOS ONE* **4**, e5046 (2009).
12. J. A. Efe et al., *Nat. Cell Biol.* **13**, 215–222 (2011).
13. H. Wang et al., *Cell Rep.* **6**, 951–960 (2014).
14. G. Blin et al., *J. Clin. Invest.* **120**, 1125–1139 (2010).
15. P. W. Burridge, G. Keller, J. D. Gold, J. C. Wu, *Cell Stem Cell* **10**, 16–28 (2012).
16. M. J. Birket et al., *Nat. Biotechnol.* **33**, 970–979 (2015).
17. L. Bu et al., *Nature* **460**, 113–117 (2009).
18. S. J. Kattman et al., *Cell Stem Cell* **8**, 228–240 (2011).
19. J. Zhang et al., *Circ. Res.* **104**, e30–e41 (2009).
20. J. Synnnergren, C. Améen, A. Jansson, P. Sartipy, *Physiol. Genomics* **44**, 245–258 (2012).
21. J. Zhang et al., *Circ. Res.* **111**, 1125–1136 (2012).
22. G. K. Azad, V. Singh, U. Golla, R. S. Tomar, *PLOS ONE* **8**, e59003 (2013).
23. I. P. Pogribny et al., *Int. J. Oncol.* **42**, 1822–1832 (2013).
24. N. Mosammaparast, Y. Shi, *Annu. Rev. Biochem.* **79**, 155–179 (2010).

ACKNOWLEDGMENTS

N.C. is supported by the California Institute for Regenerative Medicine (CIRM). J.-D.F. is supported by the American Heart Association. S.D. and D.S. are supported by the CIRM, the National Heart, Lung, and Blood Institute, the National Institutes of Health, and the Roddenberry Foundation. D.S. is supported by the Younger Family Foundation and the Whittier Foundation. Data associated with this manuscript are available in the Gene Expression Omnibus (accession numbers GSE55820 and GSE78096). N.C. and S.D. are inventors on patent applications filed by the Gladstone Institute of Cardiovascular Disease that are related to the chemical reprogramming method reported in this paper.

SUPPLEMENTARY MATERIALS

www.sciencemag.org/content/352/6290/1216/suppl/DC1
Materials and Methods
Figs. S1 to S25
Tables S1 to S6
References (25, 26)
Movies S1 and S2

23 December 2015; accepted 15 April 2016
Published online 28 April 2016
10.1126/science.aaf1502

BIOCHEMISTRY

ADP-ribose-derived nuclear ATP synthesis by NUDIX5 is required for chromatin remodeling

Roni H. G. Wright,^{1,2} Antonios Lioutas,^{1,2} Francois Le Dily,^{1,2} Daniel Soronellas,^{1,2} Andy Pohl,^{1,2} Jaume Bonet,^{2,3} A. S. Nacht,^{1,2} Sara Samino,^{4,5} Jofre Font-Mateu,^{1,2} Guillermo P. Vicent,^{1,2} Michael Wierer,^{1,2*} Miriam A. Trabado,⁶ Constanze Schelhorn,⁷ Carlo Carolis,⁶ Maria J. Macias,^{7,8} Oscar Yanes,^{4,5} Baldo Oliva,^{2,3} Miguel Beato^{1,2,†}

Key nuclear processes in eukaryotes, including DNA replication, repair, and gene regulation, require extensive chromatin remodeling catalyzed by energy-consuming enzymes. It remains unclear how the ATP demands of such processes are met in response to rapid stimuli. We analyzed this question in the context of the massive gene regulation changes induced by progestins in breast cancer cells and found that ATP is generated in the cell nucleus via the hydrolysis of poly(ADP-ribose) to ADP-ribose. In the presence of pyrophosphate, ADP-ribose is used by the pyrophosphatase NUDIX5 to generate nuclear ATP. The nuclear source of ATP is essential for hormone-induced chromatin remodeling, transcriptional regulation, and cell proliferation.

The nucleus of human cells requires a substantial amount of energy to replicate or to repair the genome and to reprogram gene expression in response to external cues, ensuring genome accessibility to mediate the extensive changes in chromatin and nucleosome organization (1). The assumption is that nuclear energetic demands are met by adenosine triphosphate (ATP) from the mitochondria. Although this may be the case in steady-state situations, it may not be sufficient for sudden extensive changes in chromatin, and nearly 60 years ago it was proposed that ATP could be generated in isolated nuclei (2, 3).

To address this issue, we measured ATP levels in living breast cancer cells by means of ATP/ADP ratio detectors targeted to the cell nucleus, mitochondria, or cytosol (4) (fig. S1, A to D). Progestin (R5020) exposure induced an increase of this ratio in some cell nuclei (Fig. 1A and fig. S1, E and F), a behavior that was not observed in cells exposed to solvent (EtOH) (Fig. 1B, right panel, and fig. S1G). Cells showing increased nuclear ATP also exhibited activated progesterone receptor (phospho-PR), whereas those with unchanged nuclear ATP levels were not hormone-responsive (Fig. 1C).

Increased nuclear ATP was confirmed in the cell population by means of luciferase constructs (5) (fig. S1, H to J) and was compromised by inhibiting mitochondrial ATP production (Fig. 1D and fig. S1K), but not by inhibiting glycolysis with 2-deoxy-D-glucose (2DG) or 3-(3-pyridinyl)-1-(4-pyridinyl)-2-propen-1-one (3PO) (fig. S1, L to O). In response to glucose, diffusion of mitochondrial ATP led to an increase in nuclear ATP (fig. S1P). This increase could be inhibited by oligomycin (fig. S1Q), leading to rapid depletion of nuclear ATP; such a result indicates that the nucleus contains a finite pool of ATP. However, in cells exposed to hormone, nuclear ATP continued to increase even when mitochondrial ATP production was inhibited by oligomycin 10 min after hormone addition (fig. S1R). Thus, mitochondrial ATP is required only during the initial minutes of hormone response.

Progestin leads to global changes in gene expression and chromatin remodeling in T47D breast cancer cells, a process that is dependent on a transient increase of PARP1-mediated poly(ADP-ribose) (PAR) (6–10) (Fig. 2A). PARP1 inhibition prevented the accumulation of PAR, whereas inhibition of PAR glycohydrolase (PARG) resulted in its persistence (Fig. 2, A and B, and fig. S2, A and B). The concomitant transient decrease in cellular nicotinamide adenine dinucleotide (NAD⁺) could be blocked by PARP inhibition (Fig. 2C). Both PAR and NAD⁺ levels eventually returned to the basal state in a PARG-dependent process (Fig. 2, B and C). Hormone-induced nuclear ATP increase was dependent on PARP1 and PARG (Fig. 2, D and E, and fig. S2, C to F); no significant changes in mitochondrial or cytoplasmic ATP levels were observed (fig. S2, C to E). Specific siRNA (small interfering RNA) knockdown showed that this nuclear ATP is dependent on PARP1 and not on other PARP family members (fig. S2G). Thus,

both the formation of PAR and its degradation to ADP-ribose (ADPR) are required for the increase in nuclear ATP levels.

PARP1 activity depends on the nuclear NAD synthase NMNAT1, which uses ATP from mitochondria (11). NMNAT1 depletion blocked the increase in nuclear ATP (Fig. 2, E and F, and fig. S2, H and I), explaining the inhibitory effect of oligomycin before but not after hormone exposure (Fig. 1D and fig. S1N). We hypothesize that after ~10 min of hormone exposure, sufficient NAD⁺ has been accumulated (Fig. 2B) to sustain the generation of ADPR and nuclear ATP.

Proteomic analysis of material immunoprecipitated with a PAR antibody in control cells and cells exposed to hormone (Fig. 3A and fig. S3A) revealed 1091 poly-ADP-ribosylated or PAR-binding proteins (table S2). We focused on hormone-induced proteins involved in ADP and ADPR metabolism and identified the ADP-sugar pyrophosphatase NUDIX5 (also known as NUDT5) (12). Because NUDIX5 interacts with both PAR and PARG (fig. S3B), is overexpressed in breast cancer (fig. S3, C to F), and is the most abundant NUDIX family member in T47D cells (fig. S3G), we explored its involvement in nuclear ATP generation. NUDIX5 depletion (Fig. 3B) did not affect the mRNA levels of other NUDIX family members (fig. S3H) but markedly reduced the hormonal increase in nuclear ATP without affecting mitochondrial or cytoplasmic ATP (Fig. 3B and fig. S3I).

After incubation of recombinant NUDIX5 (fig. S4A) with ADPR and pyrophosphate (PPi), we detected the production of AMP and ATP both directly by mass spectrometry (Fig. 3C) and indirectly (fig. S4, B and C). In the absence of PPi, ATP generation with wild-type NUDIX5 and the catalytically inactive NUDIX5 mutant (EQ112) was comparable (fig. S4C). PPi partially decreased the efficiency of the canonical hydrolytic reaction generating AMP (fig. S4D). We observed ATP generation by NUDIX5 starting from labeled PAR in vitro, a reaction dependent on PARG and PPi (Fig. 3D and fig. S4, E and F). ATP synthesis is endergonic under standard conditions ($\Delta G_m = 12.3 \pm 7.3$ kJ/mol) (fig. S4G), and synthesis of AMP ($\Delta G_m = -22.2 \pm 7.3$ kJ/mol) is prevailing. Therefore, we hypothesize that ATP synthesis may result from increased concentrations of ADPR and PPi and possibly from posttranslational modifications of NUDIX5.

NUDIX5 is a homodimer (13). Phosphoproteomic analysis showed that NUDIX5 is phosphorylated at Thr⁴⁵ (T45) before hormone treatment (fig. S5A). A NUDIX5 phospho-T45-specific antibody showed a decrease in phosphoNUDIX5 after hormone treatment (Fig. 3E). T45 phosphorylation is important for homodimer stability, and dephosphorylation resulted in its destabilization (Fig. 3, E and G, and movies S1 and S2), eventually facilitating ATP synthesis. Overexpressed NUDIX5 T45 phosphomimetic mutant (T45D) behaved as dominant negative for hormone-induced cell proliferation and gene regulation (Fig. 3H and fig. S5B). Relative to both wild-type NUDIX5 and the phospho-null mutant

¹Centre de Regulació Genòmica (CRG), Barcelona Institute for Science and Technology, Barcelona E-08003, Spain.

²Universitat Pompeu Fabra, Barcelona E-08003, Spain.

³Structural Bioinformatics Laboratory, Universitat Pompeu Fabra, Barcelona E-08003, Spain. ⁴Metabolomics Platform, Spanish Biomedical Research Centre in Diabetes and Associated Metabolic Disorders (CIBERDEM), 28029 Madrid, Spain. ⁵Center for Omic Sciences and Department of Electronic Engineering, Rovira i Virgili University, 43007 Tarragona, Spain. ⁶Biomolecular Screening and Protein Technologies Unit, Centre de Regulació Genòmica, Barcelona E-08003, Spain. ⁷Institute for Research in Biomedicine (IRB Barcelona), Barcelona Institute of Science and Technology, Barcelona 08028, Spain. ⁸Catalan Institution for Research and Advanced Studies (ICREA), Barcelona, Spain.

*Present address: Max-Planck-Institut für Biochemie, Munich, Germany. †Corresponding author. Email: miguel.beato@crg.eu

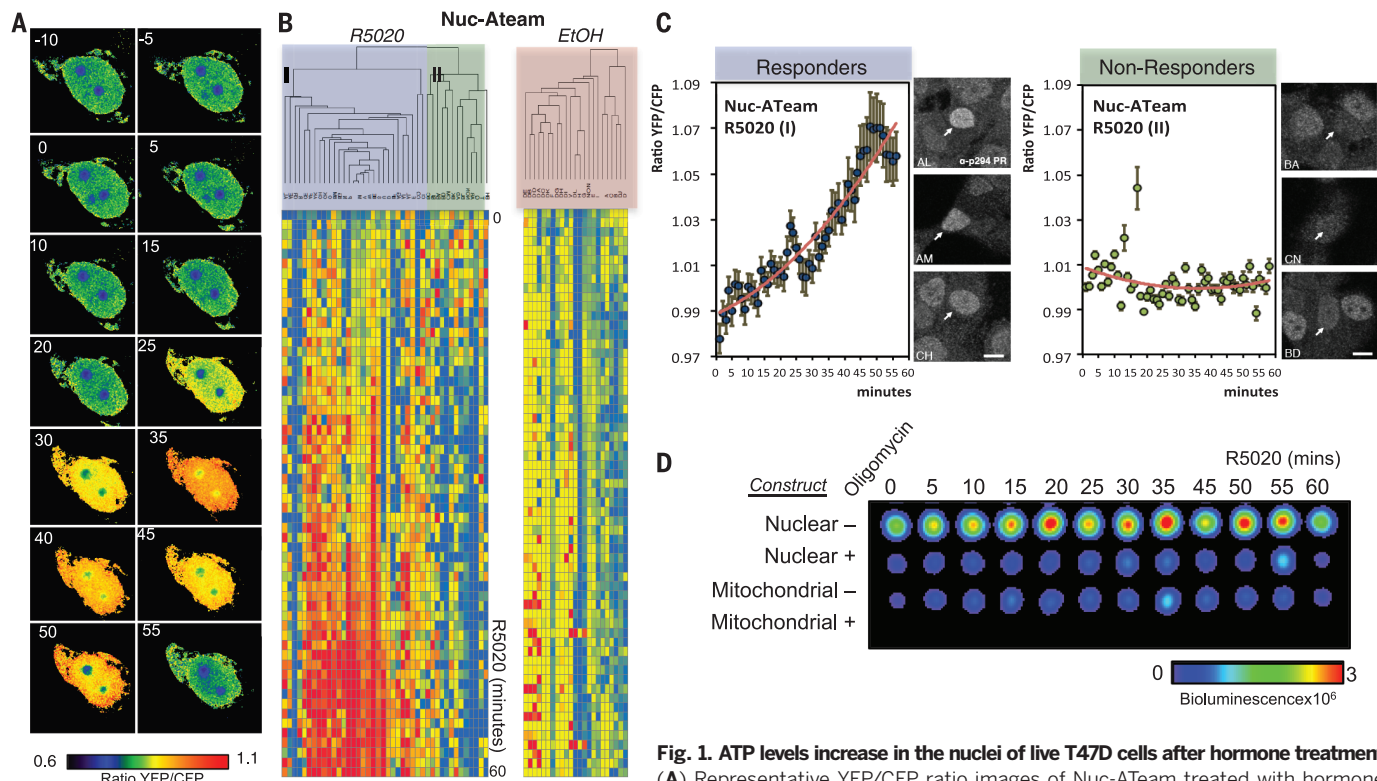


Fig. 1. ATP levels increase in the nuclei of live T47D cells after hormone treatment. (A) Representative YFP/CFP ratio images of Nuc-ATeam treated with hormone. (B) Hierarchical clustering of YFP/CFP average ratio from nuclei treated with hormone (left) or solvent (EtOH) (right). (C) Quantification of data presented in (B). Cluster I “responders” show increases in both nuclear ATP and phospho-PR S294; cluster II “nonresponders” show no increase in nuclear ATP or phospho-PR S294. Scale bar, 10 μ m; arrows indicate the cells imaged. (D) Bioluminescence image of T47D cells treated with progestin, with (+) or without (–) prior oligomycin treatment.

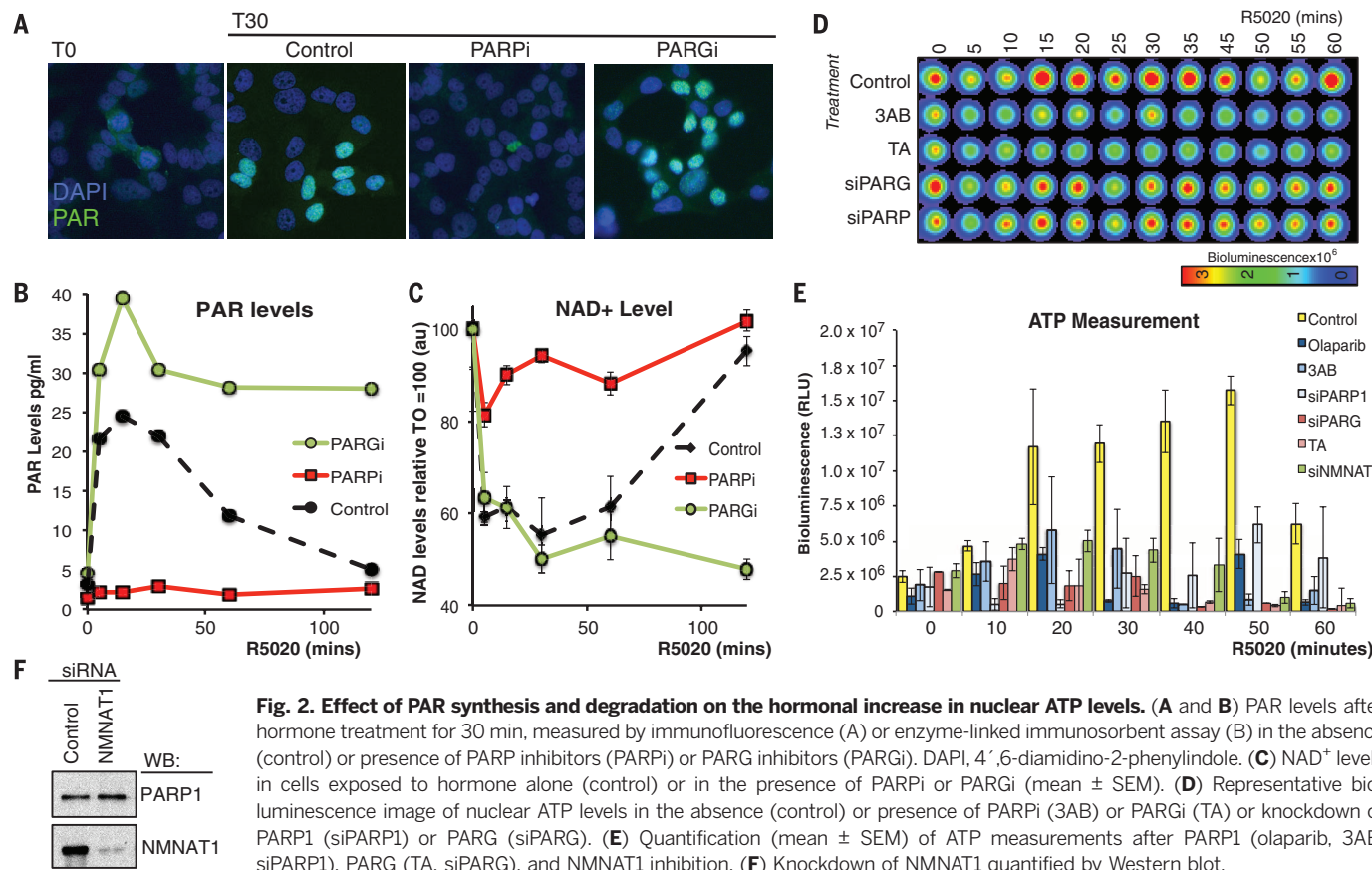


Fig. 2. Effect of PAR synthesis and degradation on the hormonal increase in nuclear ATP levels. (A and B) PAR levels after hormone treatment for 30 min, measured by immunofluorescence (A) or enzyme-linked immunosorbent assay (B) in the absence (control) or presence of PARP inhibitors (PARPi) or PARG inhibitors (PARGi). DAPI, 4',6-diamidino-2-phenylindole. (C) NAD⁺ levels in cells exposed to hormone alone (control) or in the presence of PARPi or PARGi (mean \pm SEM). (D) Representative bioluminescence image of nuclear ATP levels in the absence (control) or presence of PARPi (3AB) or PARGi (TA) or knockdown of PARP1 (siPARP1) or PARG (siPARG). (E) Quantification (mean \pm SEM) of ATP measurements after PARP1 (olaparib, 3AB, siPARP1), PARG (TA, siPARG), and NMNAT1 inhibition. (F) Knockdown of NMNAT1 quantified by Western blot.

T45A-NUDIX5, phospho-mimetic T45D-NUDIX5 strongly resisted conformational changes (fig. S5, C and D). Moreover, both wild-type and T45A-NUDIX5 (fig. S4A) generated ATP in the presence of PPI, whereas T45D-NUDIX5 did not (fig. S5E). In contrast, AMP generation by T45 mutants was only slightly affected by PPI (fig. S5, F to J; K_d values: wild type, $3.90 \pm 0.41 \mu\text{M}$; T45A, $4.44 \pm 0.53 \mu\text{M}$; T45D, $1.84 \pm 1.07 \text{mM}$).

We next explored the requirement of nuclear ATP for gene regulation. PARG inhibition or NUDIX5 depletion compromised regulation of 50% of hormone-responsive genes, with a clear overlap (Fig. 4A). The majority (70%) of NUDIX5- and PARG-dependent genes required both activities, and most of these genes also depended on poly-ADP-ribosylation (Fig. 4B). Progesterin-induced cell proliferation is abrogated by in-

hibition of PAR formation (9) and by depletion of PARG or NUDIX5 (Fig. 4C). Estrogen-induced MCF7 breast cancer cells showed increases in PAR and nuclear ATP that were dependent on the activities of ATP, PARG, and NUDIX5 (fig. S5, A to D). Gene expression changes and cell proliferation in response to estrogen were also dependent on these enzymes (Fig. 4, C and D).

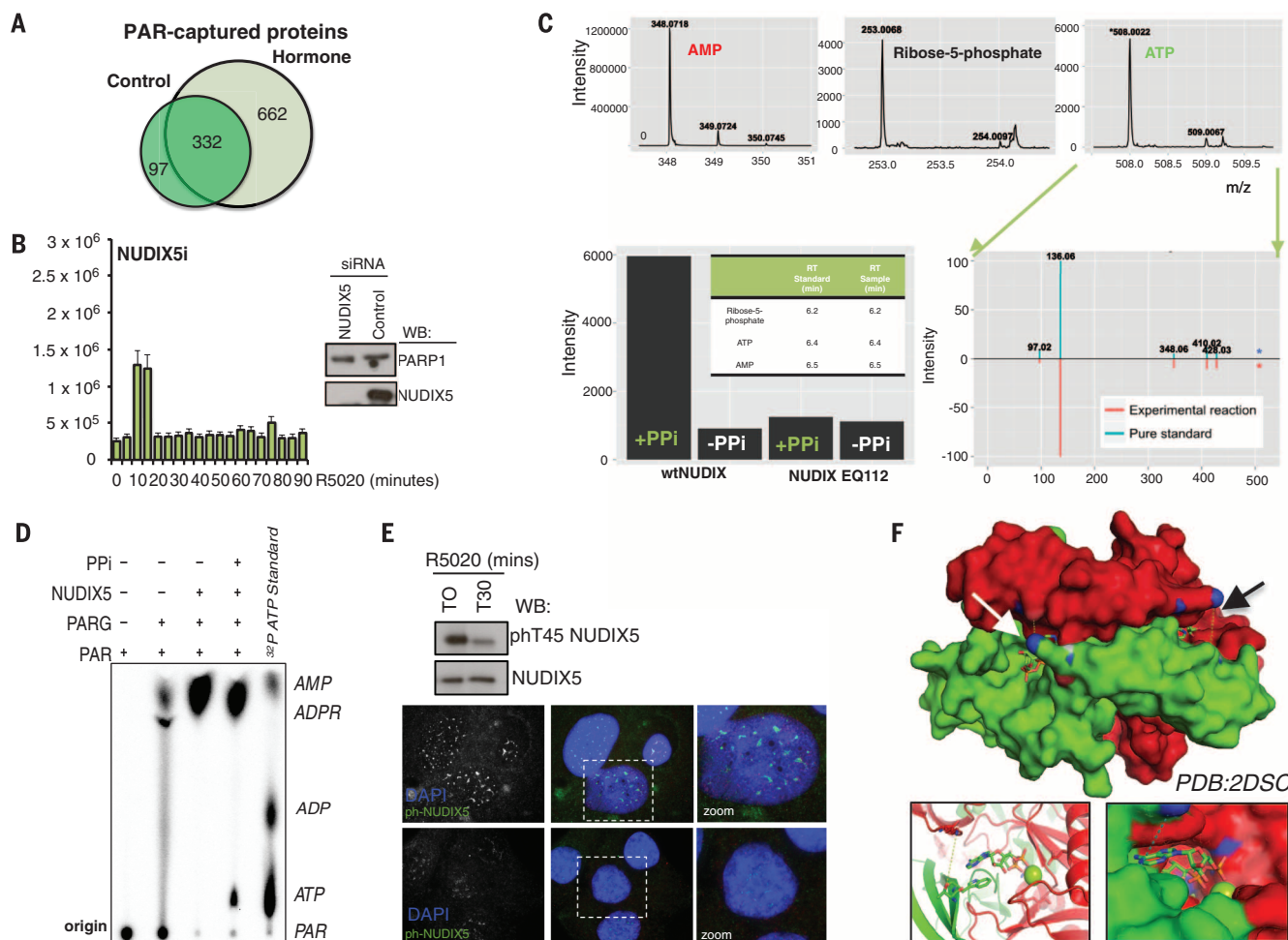


Fig. 3. Role of NUDIX5 in ATP synthesis in cell nuclei and in vitro. (A) Proteins captured by an antibody to PAR and identified by mass spectrometry.

(B) Left: Quantification (mean \pm SEM) of nuclear ATP by bioluminescence in cells depleted of NUDIX5 (NUDIX5i). Right: Protein levels measured by Western blot. (C) Relative ATP levels measured by high-resolution mass spectrometry using either wild-type or catalytically inactive NUDIX5 (EQ112) and ADPR in the presence or absence of PPI. Inset table: Retention time (RT) of AMP, ribose-5-phosphate, and ATP standards using hydrophilic interaction liquid chromatography (HILIC). (D) Production of ATP via ADPR derived from the hydrolysis of PAR by PARG, as visualized by thin-layer chromatography and autoradiography. (E) Phospho-T45 NUDIX5 in T47D^{wt} cells measured by Western blot (top) or immunofluorescence (bottom). (F) Crystal structure of NUDIX5 homodimer complex with ADPR and Mg^{2+} (PDB: 2DSC). Top: Two symmetrical contacts between T45D (blue) and K27 from the complementary chains are indicated (arrows). Bottom: View of active site of T45D with ADPR and Mg^{2+} (green sphere). (G) Dimer stability/interface energies calculated by MODELLER between 500 decoys of NUDIX5, nonphosphorylated (left) or phosphorylated (right) Wilcoxon (2.2×10^{-4}), and t distributions (4.14×10^{-4}). (H) T45D-NUDIX5 mutant behaves as dominant negative upon progesterone-induced gene expression; values are means \pm SEM.

In response to progesterin, initial displacement of histone H1 or H2A is dependent on PARP1 activity (10) but independent of PARG or NUDIX5, whereas later displacement depends on all three activities (fig. S6, E and F). Thus, initial nucleosome remodeling uses an already existing pool of nuclear ATP (Fig. 1), whereas the subsequent remodeling steps depend on PAR-derived nuclear ATP. The extent of global chromatin remodeling (H1, H2A) and recruitment of PARP1 and the ATPase bromodomain PHD finger transcription factor (BPTF) correlates well with the need for nuclear ATP (Fig. 4, E to G), which is required for extensive ATP-dependent chromatin remodeling.

In breast cancer cells, PR interacts with PARP1 (10) and with the DNA-dependent protein kinase Ku (14), which suggests that PAR and ATP could

be involved in DNA repair (15–17). Indeed, survival of MCF7 cells after DNA damage is dependent on PARP1, PARG, and NUDIX5 (fig. S7, A and B). There is evidence that hormone-induced gene expression changes, and the torsional stress endured by the chromatin is relieved by local DNA cleavage (18). After damage, PAR could serve as a local source of ATP for the extensive chromatin remodeling associated with the repair process.

Recently it was shown that PAR acts as a “seed” during nuclear compartmentalization by liquid demixing (19); such transient molecular sieves mediated by intrinsically disordered proteins may also provide a local favorable environment for ATP generation by NUDIX5. These so-called “membraneless” organelles may serve to concentrate not only the enzymes but also the substrates required for ATP generation, leading

to a local increase and specific environment for chromatin remodeling and/or repair.

Our work describes a mechanism for energy generation in the nuclei of breast cancer cells exposed to hormone. The high energetic cost of global chromatin modification is covered via the conversion of ADPR to ATP and ribose-5-phosphate catalyzed by the dephosphorylated form of NUDIX5. The pathway is ignited by mitochondrial ATP required for NMNAT1-mediated synthesis of NAD⁺, which is converted to PAR by activated PARP1 and hydrolyzed to ADPR by PARG (fig. S7, C and D). Nuclear ATP levels increase after hormone exposure independently of ongoing mitochondrial and cytoplasmic ATP sources but dependent on nuclear ADPR and PPi. This nuclear ATP is required for chromatin remodeling, transcriptional regulation, and ultimately cell proliferation.

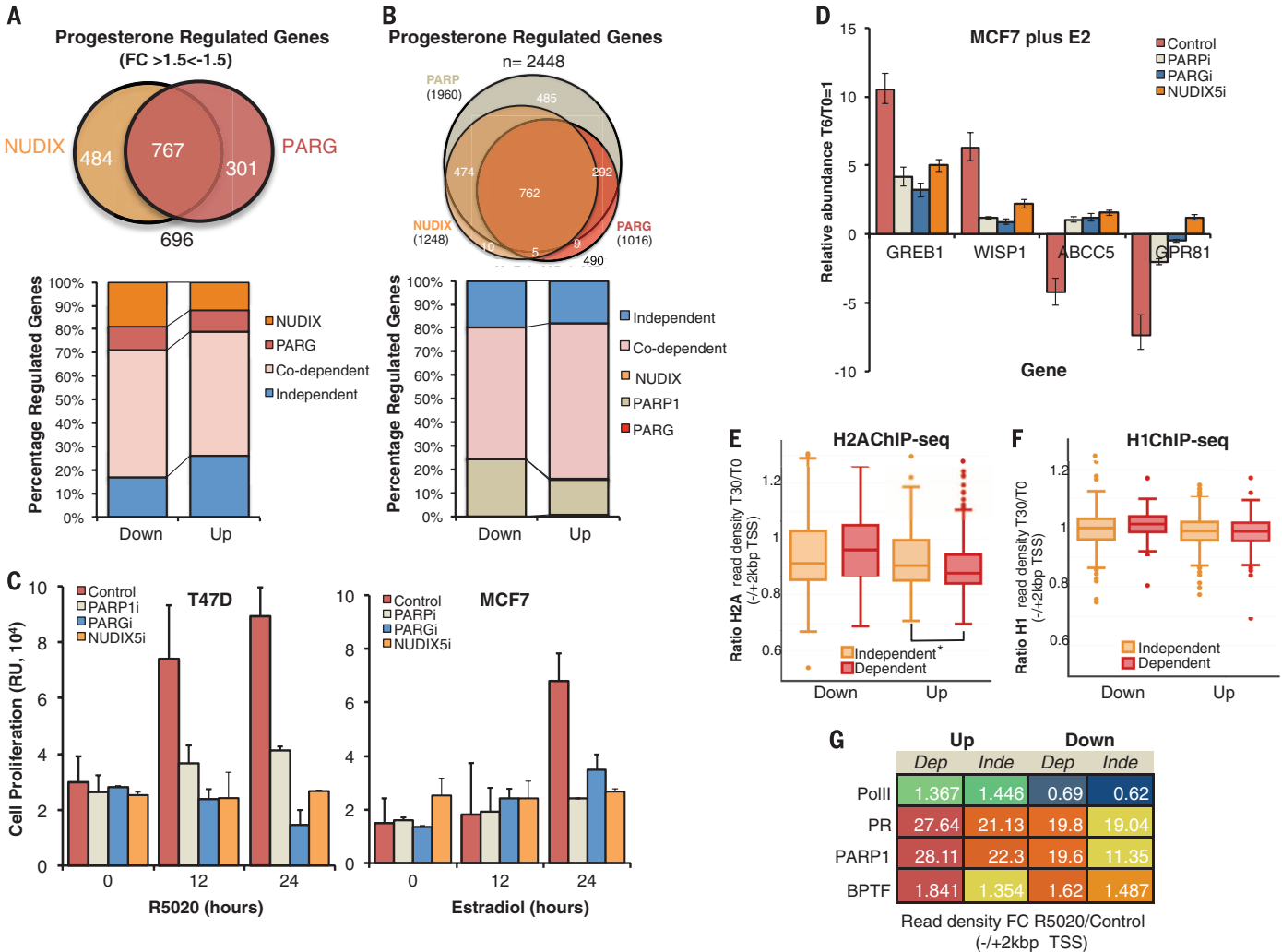


Fig. 4. ADPR-derived ATP is essential for hormone-induced gene expression and chromatin remodeling. (A and B) Top: Overlap of progesterone-regulated genes [fold change (FC) > 1.5 or FC < -1.5, $P < 0.05$]. Bottom: Quantification of up and down progesterone-regulated genes dependent on PARG and/or NUDIX (A) or PARP, PARG, and/or NUDIX (B). (C) Hormone-induced cell proliferation in T47D (left) or MCF7 (right) cells in the absence (control) or presence of PARPi or PARGi, or after knockdown of NUDIX5

(NUDIX5i); values are means \pm SEM. (D) Estrogen (E2) target gene (GREB1, WISP1, ABCC5, GPR81) expression in the absence (control) or presence of PARPi or PARGi or after NUDIX5 depletion; values are means \pm SEM. (E and F) Global analysis of H2A (E) and H1 (F) displacement as assessed by chromatin immunoprecipitation sequencing; * $P = 0.018$. (G) Recruitment of RNA polymerase II (Pol II), PR, PARP1, or BPTF to promoters of progesterone target genes, dependent (Dep) or independent (Inde) of NUDIX5 activity.

NUDIX5 overexpression in cancer patients correlates with a poor outcome in several cancer types, including breast cancer (fig. S8, A and B). The correlation with high expression of PARP1 (fig. S8C) may suggest that cancer cells depend on nuclear ATP generation. Hence, NUDIX5 is a promising target for PARP1 combinatorial drug therapy (20).

REFERENCES AND NOTES

- G. J. Narlikar, M. L. Phelan, R. E. Kingston, *Mol. Cell* **8**, 1219–1230 (2001).
- V. G. Allfrey, A. E. Mirsky, *Proc. Natl. Acad. Sci. U.S.A.* **43**, 589–598 (1957).
- I. Betel, *Arch. Biochem. Biophys.* **134**, 271–274 (1969).
- H. Imamura et al., *Proc. Natl. Acad. Sci. U.S.A.* **106**, 15651–15656 (2009).
- J. Hageman, M. J. Vos, M. A. van Waarde, H. H. Kampinga, *J. Biol. Chem.* **282**, 34334–34345 (2007).
- G. P. Vicent et al., *PLOS Genet.* **5**, e1000567 (2009).
- G. P. Vicent et al., *Genes Dev.* **25**, 845–862 (2011).
- C. Ballaré et al., *Mol. Cell* **49**, 67–79 (2013).
- F. Le Dily et al., *Genes Dev.* **28**, 2151–2162 (2014).
- R. H. G. Wright et al., *Genes Dev.* **26**, 1972–1983 (2012).
- T. Zhang et al., *J. Biol. Chem.* **287**, 12405–12416 (2012).
- A. G. McLennan, *Cell. Mol. Life Sci.* **63**, 123–143 (2006).
- M. Zha, C. Zhong, Y. Peng, H. Hu, J. Ding, *J. Mol. Biol.* **364**, 1021–1033 (2006).
- C. A. Sartorius, G. S. Takimoto, J. K. Richer, L. Tung, K. B. Horwitz, *J. Mol. Endocrinol.* **24**, 165–182 (2000).
- H. Maruta, N. Matsumura, S. Tanuma, *Biochem. Biophys. Res. Commun.* **236**, 265–269 (1997).
- S. L. Oei, M. Ziegler, *J. Biol. Chem.* **275**, 23234–23239 (2000).
- H. Maruta et al., *Biol. Pharm. Bull.* **30**, 447–450 (2007).
- B. G. Ju et al., *Science* **312**, 1798–1802 (2006).
- M. Altmeyer et al., *Nat. Commun.* **6**, 8088 (2015).
- K. M. Frizzell, W. L. Kraus, *Breast Cancer Res.* **11**, 111 (2009).

ACKNOWLEDGMENTS

We thank H. Kampinga for the luciferase plasmids, H. Imamura for the Ateam plasmids, M. Jacobson for the PARG-GST plasmid,

V. Schreiber for the PARP1-GST plasmid, S. Capdevila and J. M. Caballero for support with IVIS, and J. Valcarcel for advice with the manuscript and CRG core facilities. Supported by the Spanish MEC (CSD2006-00049; BMC 2003-02902 and 2010-15313), and Catalan government (AGAUR) grants BIO2014-57518-R (B.O.), SAF2011-30578 (O.Y.), and BFU2014-53787-P (M.J.M.). CRG and IRB Barcelona are recipients of the Severo Ochoa Award of Excellence from MINECO (Spain). Global data sets have been deposited in GEO with accession numbers GSE53855, GSE64136, GSE64161, and GSE64163.

SUPPLEMENTARY MATERIALS

www.sciencemag.org/content/352/6290/1221/suppl/DC1
Materials and Methods
Supplementary Text
Figs. S1 to S8
Tables S1 to S8
Movies S1 and S2
References (21, 22)

24 November 2015; accepted 9 May 2016
10.1126/science.1221933

RNA TRANSCRIPTION

TT-seq maps the human transient transcriptome

Björn Schwalb,^{1*} Margaux Michel,^{1*} Benedikt Zacher,^{2*} Katja Frühauf,³ Carina Demel,¹ Achim Tresch,^{4,5} Julien Gagneur,^{2,†} Patrick Cramer^{1,3,‡}

Pervasive transcription of the genome produces both stable and transient RNAs. We developed transient transcriptome sequencing (TT-seq), a protocol that uniformly maps the entire range of RNA-producing units and estimates rates of RNA synthesis and degradation. Application of TT-seq to human K562 cells recovers stable messenger RNAs and long intergenic noncoding RNAs and additionally maps transient enhancer, antisense, and promoter-associated RNAs. TT-seq analysis shows that enhancer RNAs are short-lived and lack U1 motifs and secondary structure. TT-seq also maps transient RNA downstream of polyadenylation sites and uncovers sites of transcription termination; we found, on average, four transcription termination sites, distributed in a window with a median width of ~3300 base pairs. Termination sites coincide with a DNA motif associated with pausing of RNA polymerase before its release from the genome.

Transcription of eukaryotic genomes produces protein-coding mRNAs and diverse noncoding RNAs (ncRNAs), including enhancer RNAs (eRNAs) (1, 2). Most ncRNAs are rapidly degraded, difficult to detect, and thus far have not been mappable in their full range. Mapping of transient RNAs is required, however, for analysis of RNA sequence, function, and fate.

We developed transient transcriptome sequencing (TT-seq), a protocol that maps transcriptionally active regions and enables estimation of RNA synthesis and degradation rates. TT-seq is based on 4sU-seq, which involves a brief exposure of cells to the nucleoside analog 4-thiouridine (4sU) (Fig. 1A) (3). 4sU is incorporated into RNA during transcription, and the resulting 4sU-labeled RNAs are isolated and sequenced. 4sU-seq is more sensitive than RNA-seq in detecting transient RNAs. However, 4sU-seq fails to map human transcripts uniformly, because only a short 3' region of nascent transcripts is labeled during a 5-min exposure to 4sU, and the long preexisting 5' regions dominate the sequencing data. To remove this 5' bias, TT-seq uses RNA fragmentation before isolation of labeled RNA fragments (Fig. 1A). Thus, TT-seq measures only newly transcribed RNA fragments and provides the number of polymerases transcribing a genomic position within 5 min.

When applied to human K562 cells, TT-seq samples newly transcribed regions uniformly,

whereas 4sU-seq produces a 5' bias (fig. S1A). The coverage of short-lived introns with respect to exons is estimated (4) to be 60% for TT-seq, whereas it is 23 and 8% for 4sU-seq and RNA-seq, respectively (figs. S1A and S2). TT-seq is highly reproducible (fig. S3) and enables complete mapping of transcribed regions, complementing the GRO-cap (5) and CAGE (6) protocols, which detect RNA 5' ends (Fig. 1B). TT-seq monitors RNA synthesis, whereas protocols such as PRO-seq (7), NET-seq (8), and mNET-seq (9) detect RNAs attached to polymerase. Therefore, the latter protocols yield peak signals near the promoter where polymerase pauses (Fig. 1B), whereas TT-seq does not. For paused and active genes (10), TT-seq reveals higher rates of RNA synthesis near the promoter relative to other regions (fig. S1B).

Using TT-seq data and the segmentation algorithm GenoSTAN (4, 11), we identified 21,874 genomic intervals of apparently uninterrupted transcription (transcriptional units, TUs) (Fig. 2 and fig. S4A). TT-seq is highly sensitive, recovering 65% of transcription start sites (TSSs) obtained by GRO-cap (overlapping annotations within ± 400 bp) (5). A total of 8543 TUs overlapped GENCODE annotations (12) in the sense direction of transcription (50% reciprocal overlap of annotated regions; fig. S4B). This analysis detected 7810 mRNAs, 302 long intergenic noncoding RNAs (lincRNAs), and 431 antisense RNAs (asRNA). The 2916 TUs that shared less than 50% of their length with GENCODE annotations were not classified. The remaining 10,415 TUs (48%) represented newly detected ncRNAs that we characterized further.

Transcripts arise from promoters but also from enhancers, which are regulatory elements with characteristic chromatin modifications (13, 14). To detect chromatin regions comprising putative enhancers and promoters (chromatin states), we applied GenoSTAN (11) to ENCODE ChIP-seq (chromatin immunoprecipitation–sequencing) data (15) for the coactivator p300 and a series of histone modifications (H3K27me3, H3K36me3, H4K20me1, H3K4me1, H3K4me3, H3K9ac, and

¹Department of Molecular Biology, Max Planck Institute for Biophysical Chemistry, Am Faßberg 11, 37077 Göttingen, Germany. ²Gene Center Munich, Ludwig-Maximilians-Universität München, Feodor-Lynen-Straße 25, 81377 Munich, Germany. ³Department of Biosciences and Nutrition, Center for Innovative Medicine, and Science for Life Laboratory, Karolinska Institutet, Novum, Hälsovägen 7, 141 83 Huddinge, Sweden. ⁴Department of Biology, University of Cologne, Zulpicher Straße 47, 50647 Cologne, Germany. ⁵Max Planck Institute for Plant Breeding Research, Carl-von-Linné Weg 10, 50829 Cologne, Germany. *These authors contributed equally to this work. †Present address: Department of Informatics, Technische Universität München, Boltzmannstraße 3, 85748 Garching, Germany. ‡Corresponding author. Email: gagneur@in.tum.de (J.G.); patrick.cramer@mpibpc.mpg.de (P.C.)

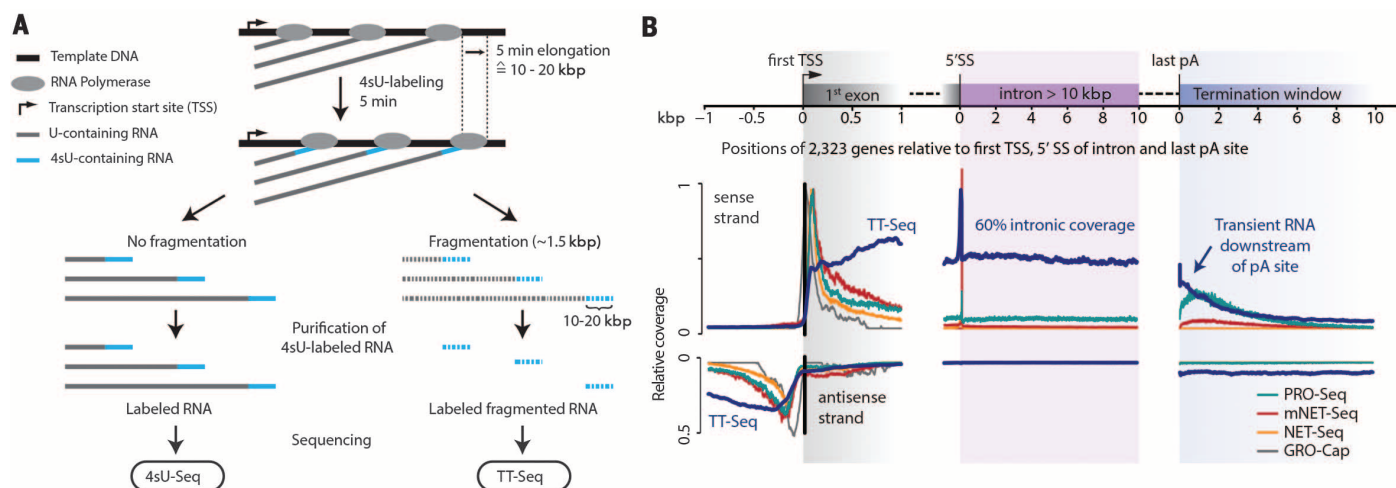


Fig. 1. TT-seq enables uniform mapping of the human transient transcriptome. (A) Workflow of 4sU-seq and TT-seq protocols. (B) Metagene coverage, comparing TT-seq with other transcriptomic methods. Shown is the average coverage for 2323 TUs lacking paused and active genes (10) around the first TSS (left), the 5' splice site of intronic sequences > 10 kbp (first intron excluded), and the last pA site. Signals are relative to the maximum signal in the first kilobase pair from the first TSS.

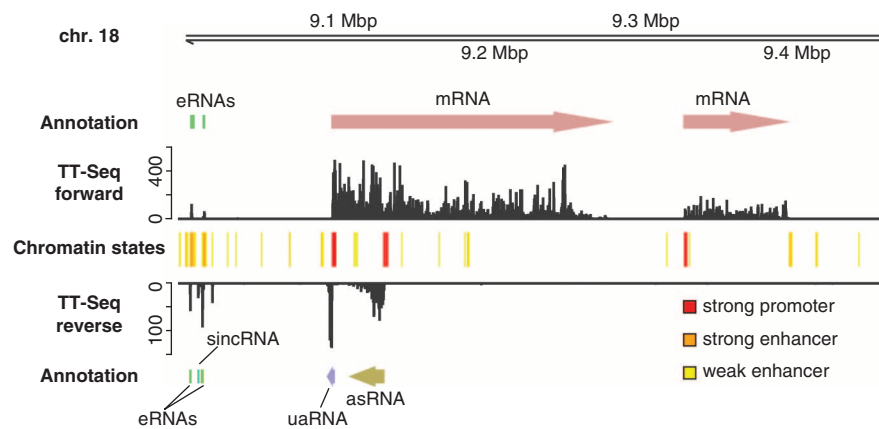


Fig. 2. Annotation of RNAs mapped by TT-seq. Example genome browser view showing RNAs from 5 of 7 transcript classes and 3 of 18 chromatin states [chromosome (chr.) 18, 9.00 to 9.54 million base pairs (Mbp)] (4). Arrows indicate the direction of transcription. Units on the y axes are read counts per 200-bp bin.

H3K27ac) and to deoxyribonuclease I hypersensitivity data (fig. S5A). Of the resulting strong enhancer state regions, 81% overlapped at least one TSS from GRO-cap (5) and 68% overlapped a polymerase II (Pol II) peak (15), compared with 52 and 37%, respectively, for ENCODE enhancer states (fig. S5, B to D).

The 10,415 nonannotated TUs were classified based on GenoSTAN-derived chromatin states and their positions relative to known GENCODE annotations (fig. S6A). TUs within 1 kilo-base pair (kbp) of a GENCODE mRNA TSS included 685 upstream antisense RNAs (uaRNAs) (16) and 778 convergent RNAs (conRNAs) (8). The 3115 TUs on the strand opposite an mRNA were classified as asRNAs when they were more than 1 kbp away from the GENCODE TSS. Remaining TUs were grouped according to their GenoSTAN chromatin state at their TSS. The 2580 TUs that originated from promoter state regions (4) were

classified as short intergenic ncRNAs (sincRNAs) (fig. S6B). Most sincRNAs (67%) were located within 10 kbp of a GENCODE mRNA TSS. The remaining 3257 TUs originated from enhancer state regions (4) and were classified as eRNAs (13, 14). The newly mapped ncRNAs are short (fig. S6C). On average, lincRNAs are five times as long as sincRNAs, and eRNAs have a median length of ~1000 nucleotides.

Kinetic modeling of TT-seq and RNA-seq data enabled us to estimate rates of RNA synthesis and degradation (Fig. 3 and fig. S7A) (4). We estimated rates of phosphodiester bond formation or breakage at each transcribed position and averaged these within TUs, thus obtaining estimates of relative transcription rates and RNA stabilities (4). We found that mRNAs and lincRNAs had the highest synthesis rates and longest half-lives. We determined a median mRNA half-life of ~50 min, compared with a previous estimate

of ~139 min (17). Other transcript classes had low synthesis rates and short half-lives, explaining why short ncRNAs are difficult to detect. eRNAs had half-lives of a few minutes, consistent with prior data (17). Short RNA half-lives correlated with a lack of secondary structure (fig. S7B). The folding energy of eRNAs was comparable to the genomic background level (fig. S7C), and only 10% of their sequence was predicted to be structured, compared with 52% in mRNAs (fig. S7D).

We further found differences in transcription from promoters versus from enhancers (2). Enhancers showed lower occupancy of initiation factors TBP and TAF1 than mRNA promoters did (12- and 3.5-fold less, respectively; $P < 10^{-16}$, Fisher's exact test), whereas TFIIB and TFIIF had similar occupancies in enhancers and promoters. Occupancies were also similar for factors involved in polymerase pausing, such as NELF-E and the P-TEFb subunit cyclin T2 (fig. S8A). Synthesis of eRNAs terminated early (fig. S6C), probably because eRNAs are not enriched in U1 small nuclear ribonucleoprotein-binding sites (U1 signals; GGUAAG, GUGAGU, or GGUGAG) that can counteract early termination and lead to RNA stabilization (18–20). eRNAs contained U1 signals at the genomic background level (47%), whereas mRNAs were enriched (69%; $P < 10^{-16}$) (fig. S8B). In all transcript classes, longer RNAs were enriched with U1 signals in the first 1000 nucleotides (fig. S8C), suggesting that evolution of stable RNAs generally involves acquisition of U1 signals.

TT-seq also enabled us to uncover transcription termination sites (TTSs). TT-seq detected transient RNA downstream of the polyadenylation (pA) site (Figs. 1B and 4 and fig. S9). Such RNA is difficult to detect because RNA cleavage at the pA site leads to an unprotected 5' end and RNA degradation by the XRN2 exonuclease (21, 22). For a total of 6977 mRNA genes, we

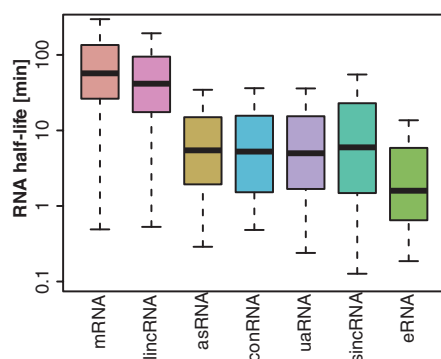


Fig. 3. Estimated RNA half-lives for different transcript classes. Black bars represent medians, boxes represent upper and lower quartiles, and whiskers represent 1.5 times the interquartile range (4).

derived, on average, four TTSs (figs. S10 and S11) (4). TTSs were located within a termination window that extended from the last pA site to an “ultimate TTS,” where RNA coverage dropped to background levels (Fig. 4, A to C). The termination window had a median width of ~3300 bp and could be up to 10 kbp wide (fig. S10D), consistent with Pol II occupancy data (Fig. 4D) (23). For the 5113 TTSs with the strongest drop in TT-seq signal (4), Pol II peaks were obtained by PRO-seq (7), NET-seq (8), and mNET-seq (9) (fig. S12), indicating that Pol II pauses at the TTS.

The derived TTSs are strongly enriched for the sequence $(C/G)_{(2-6)}A$ (window ± 5 bp; $P < 10^{-16}$, Fisher's exact test; odds ratios, 2.98 and 1.63 for C_3A and G_3A , respectively; subscript numbers denote the number of nucleotide repeats) (Fig. 4E and figs. S13 and S14) (4). This sequence can contain up to six cytosines or guanines (Fig. 4F and fig. S10E). A G_3A element has also been found in a known termination signal (24). The $C_{(2-6)}A$ and $G_{(2-6)}A$ sequences are generally followed by a T-rich $[T_{(3-6)}]$ or an A-rich $[A_{(3-6)}]$ stretch, respectively ($P < 10^{-16}$; odds ratios, 2.39 and 1.24 for T_4 and A_4 , respectively), that is located, on average, 15 bp downstream of the TTS (Fig. 4E). Such sequences were found at TTSs of all TUs (fig. S15) and can even be derived from published data (fig. S12B). In summary, the detected TTSs were highly enriched with the consensus motif $(C/G)_{(2-6)}AN_x(T/A)_{(3-6)}$, where N_x is a short stretch of nucleotides.

To test for the in vivo functionality of the derived TTS motif, we transfected expression plasmids into K562 cells that either lacked or contained four $C_3AN_8T_4$ or $C_3AN_8T_4$ motifs within 600 bp downstream of the pA site (fig. S16A and tables S1 to S4) (4). When the TTS motifs were present, significantly less RNA was detected downstream of the motifs, indicating termination of a fraction of polymerases (Wilcoxon test; fig. S16B). This experiment supports the functionality of the derived TTS motif in vivo. Termination depended on an upstream pA signal (fig. S16B), consistent with an occurrence of the motif in gene bodies, where they do not lead to transcription termination.

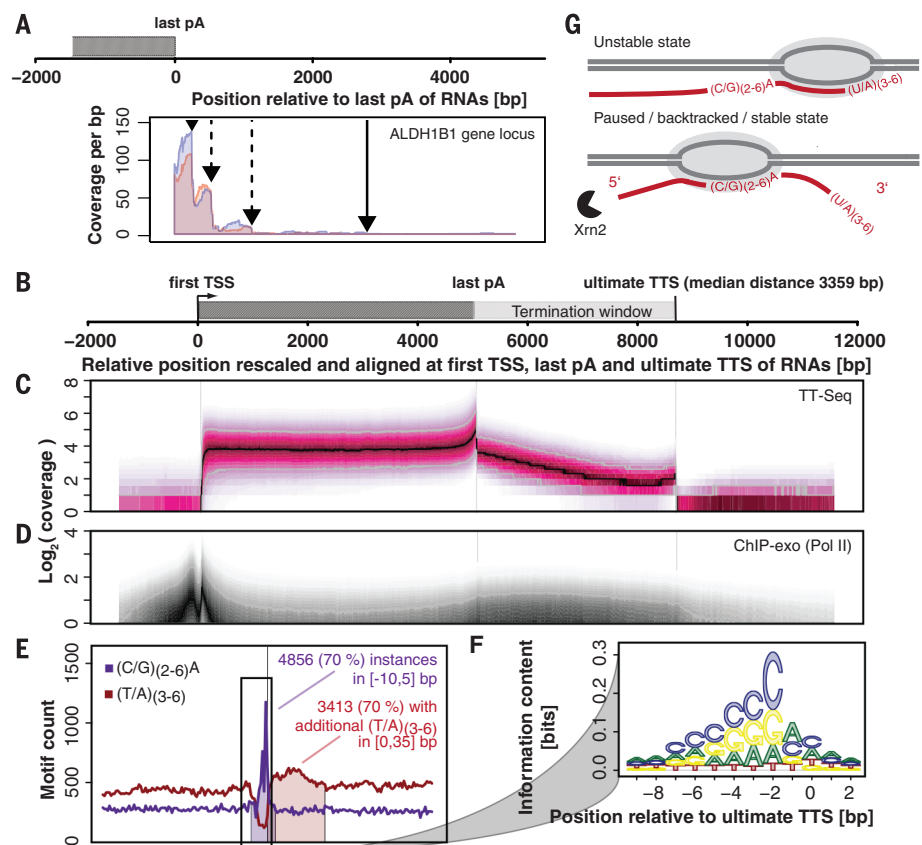


Fig. 4. Transcription termination sites. (A) TT-seq coverage for two replicates (red and blue) downstream of the pA site in the *ALDH1B1* gene locus. Arrows indicate TTSs obtained from segmentation (solid arrow, ultimate TTS). The last annotated pA site (per GENCODE) was aligned at zero. (B) Generic gene architecture. The first TSS was aligned at zero, and the last pA site was set at a rescaled distance of 5000 bp from the TSS (the real median distance is 24,079 bp for 6977 investigated genes) (4). The ultimate TTS is depicted at a median distance of 3359 bp from the last pA site (rescaled). (C) TT-seq coverage over quantiles 0.05 to 0.95 (pink area; black line, median), rescaled and aligned as in (B). (D) Pol II occupancy determined by the ChIP-exonuclease method (23), visualized as in (C) (black line, median; white line, upper quartile). (E) $(C/G)_{(2-6)}A$ and $(T/A)_{(3-6)}$ sequence count within ± 100 bp of ultimate TTSs. (F) PWM (position weight matrix) logo representation of nucleotides at positions -9 to $+2$ around the ultimate TTS (position 0). (G) Predicted polymerase states at the T-rich stretch downstream of the TTS (top) and after backtracking to the TTS (bottom) (gray, DNA; red, RNA).

Transcription over the $(C/G)_{(2-6)}AN_x(T/A)_{(3-6)}$ sequence is predicted to destabilize the polymerase complex (24, 25) because the melting temperature (4) of the DNA-RNA hybrid is low in the T/A-rich region (fig. S17). This may trigger backtracking and trap polymerase at the TTS (Fig. 4G). At the TTS, the hybrid is C/G-rich and stable, and RNA may be cleaved from its 3' end to yield a terminal A residue. Polymerase can then be released from DNA by XRN2 (21, 22). TT-seq has afforded insights into the determinants of human genome transcription and provides a complementary tool for transcriptome analysis.

REFERENCES AND NOTES

1. T. H. Jensen, A. Jacquier, D. Libri, *Mol. Cell* **52**, 473–484 (2013).
2. R. Andersson et al., *Nature* **507**, 455–461 (2014).
3. M. D. Cleary, C. D. Meiering, E. Jan, R. Guymon, J. C. Boothroyd, *Nat. Biotechnol.* **23**, 232–237 (2005).
4. Materials and methods are available as supplementary materials on Science Online.
5. L. J. Core et al., *Nat. Genet.* **46**, 1311–1320 (2014).
6. R. Kodzius et al., *Nat. Methods* **3**, 211–222 (2006).
7. H. Kwak, N. J. Fuda, L. J. Core, J. T. Lis, *Science* **339**, 950–953 (2013).
8. A. Mayer et al., *Cell* **161**, 541–554 (2015).
9. T. Nojima et al., *Cell* **161**, 526–540 (2015).
10. L. J. Core, J. J. Waterfall, J. T. Lis, *Science* **322**, 1845–1848 (2008).
11. B. Zacher et al., <http://biorxiv.org/content/early/2016/03/06/041020> (2016).
12. J. Harrow et al., *Genome Res.* **22**, 1760–1774 (2012).
13. S. Djebali et al., *Nature* **489**, 101–108 (2012).
14. T. K. Kim et al., *Nature* **465**, 182–187 (2010).
15. ENCODE Project Consortium, *Nature* **489**, 57–74 (2012).
16. R. A. Flynn, A. E. Almada, J. R. Zamudio, P. A. Sharp, *Proc. Natl. Acad. Sci. U.S.A.* **108**, 10460–10465 (2011).
17. M. Rabani et al., *Cell* **159**, 1698–1710 (2014).
18. D. Kaide et al., *Nature* **468**, 664–668 (2010).
19. M. G. Berg et al., *Cell* **150**, 53–64 (2012).
20. A. E. Almada, X. Wu, A. J. Kriz, C. B. Burge, P. A. Sharp, *Nature* **499**, 360–363 (2013).
21. S. West, N. Gromak, N. J. Proudfoot, *Nature* **432**, 522–525 (2004).

22. M. Kim *et al.*, *Nature* **432**, 517–522 (2004).
 23. B. J. Venters, B. F. Pugh, *Nature* **502**, 53–58 (2013).
 24. R. Ashfield *et al.*, *EMBO J.* **13**, 5656–5667 (1994).
 25. M. L. Kireeva, N. Komissarova, D. S. Waugh, M. Kashlev, *J. Biol. Chem.* **275**, 6530–6536 (2000).

ACKNOWLEDGMENTS

The sequencing data and the annotation file have been deposited in the Gene Expression Omnibus database under accession code GSE75792. We thank H. Blum, S. Krebs, and A. Graf (Laboratory for Functional Genome Analysis, Gene Center, Ludwig-Maximilians-Universität München) for help with

sequencing and J. A. Feuillet, J. Soeding, A. Sawicka, and C. Bernecky for help and discussions. K.F. was supported by the Center for Innovative Medicine (CIMED) at Karolinska Institutet and by the Science for Life Laboratory (SciLifeLab) in Stockholm. C.D. was supported by a Deutsche Forschungsgemeinschaft (DFG) fellowship at the Graduate School of Quantitative Biosciences Munich. A.T. was supported by a German Federal Ministry of Education and Research (BMBF) eBio grant and by DFG grant SFB 680. J.G. was supported by the Bavarian Research Center for Molecular Biosystems and the Bundesministerium für Bildung und Forschung, Juniorverbund in der Systemmedizin "mitOmics" (grant FKZ 01ZX1405A). P.C. was funded by the Advanced

Grant TRANSIT of the European Research Council, the DFG, the Volkswagen Foundation, CIMED, and SciLifeLab.

SUPPLEMENTARY MATERIALS

www.sciencemag.org/content/352/6290/1225/suppl/DC1
 Materials and Methods
 Figs. S1 to S17
 Tables S1 to S4
 References (26–39)

2 December 2015; accepted 6 May 2016
 10.1126/science.aad9841

NONHUMAN GENETICS

Genomic and archaeological evidence suggests a dual origin of domestic dogs

Laurent A. F. Frantz,^{1*} Victoria E. Mullin,^{2†} Maud Pionnier-Capitan,^{3,4} Ophélie Lebrasseur,¹ Morgane Ollivier,³ Angela Perri,⁵ Anna Linderholm,^{1,6} Valeria Mattiangeli,² Matthew D. Teasdale,² Evangelos A. Dimopoulos,^{1,7} Anne Tresset,⁴ Marilynne Duffraisse,³ Finbar McCormick,⁸ László Bartosiewicz,⁹ Erika Gál,¹⁰ Éva A. Nyerges,¹⁰ Mikhail V. Sablin,¹¹ Stéphanie Bréhard,⁴ Marjan Mashkour,⁴ Adrian Bălăşescu,¹² Benjamin Gillet,³ Sandrine Hughes,³ Olivier Chassaing,³ Christophe Hitte,¹³ Jean-Denis Vigne,⁴ Keith Dobney,^{14,15} Catherine Hänni,³ Daniel G. Bradley,^{2*} Greger Larson^{1*}

The geographic and temporal origins of dogs remain controversial. We generated genetic sequences from 59 ancient dogs and a complete (28x) genome of a late Neolithic dog (dated to ~4800 calendar years before the present) from Ireland. Our analyses revealed a deep split separating modern East Asian and Western Eurasian dogs. Surprisingly, the date of this divergence (~14,000 to 6400 years ago) occurs commensurate with, or several millennia after, the first appearance of dogs in Europe and East Asia. Additional analyses of ancient and modern mitochondrial DNA revealed a sharp discontinuity in haplotype frequencies in Europe. Combined, these results suggest that dogs may have been domesticated independently in Eastern and Western Eurasia from distinct wolf populations. East Eurasian dogs were then possibly transported to Europe with people, where they partially replaced European Paleolithic dogs.

Dogs were the first domestic animal and the only animal domesticated before the advent of settled agriculture (1). Despite their importance in human history, no consensus has emerged regarding their geographic and temporal origins, or whether dogs were domesticated just once or independently on more than one occasion. Although several claims have been made for an initial appearance of dogs in the early upper Paleolithic (~30,000 years ago; e.g. (2)), the first remains confidently assigned to dogs appear in Europe ~15,000 years ago and in Far East Asia over 12,500 years ago (3). Although archaeologists remain open to the idea that there was more than one geographic origin for dogs [e.g. (4, 5)], most genetic studies have concluded that dogs were probably domesticated just once (6), disagreeing on whether this occurred in Europe (7), Central Asia (8), or East Asia (9).

Recent paleogenetic studies have transformed our understanding of early human evolution [e.g. (10, 11)]. We applied a similar approach to reconstruct the evolutionary history of dogs. We generated 59 ancient mitochondrial DNA

(mtDNA) sequences from European dogs (from 14,000 to 3000 years ago) as well as a high-coverage nuclear genome (28x) of an ancient dog dated to ~4800 calendar years before the present (12) from the Neolithic passage grave complex of Newgrange (*Sí an Bhrú*) in Ireland. We combined our ancient sample with 80 modern publically available full genome sequences and 605 modern dogs (including village dogs and 48 breeds) genotyped on the CanineHD 170,000 (170 K) single-nucleotide polymorphism (SNP) array (12).

We first assessed characteristics of the Newgrange dog by typing SNPs associated with specific phenotypic traits and by inferring its level of inbreeding, compared to other breed and village dogs (12). Our results suggest that the degree of artificial selection and controlled breeding during the Neolithic was similar to that observed in modern free-living dogs. In addition, the Newgrange dog did not possess variants associated with modern breed-defining traits, including hair length or coat color. And although this dog was likely able to digest starch less efficiently

than modern dogs, it was able to do so more efficiently than wolves (12).

A phylogenetic analysis based on 170 K SNPs revealed a deep split separating the modern Sarloos breed from other dogs (Fig. 1A). This breed, created in the 1930s in the Netherlands, involved breeding German Shepherds with captive wolves (13), thus explaining the breed's topological placement. The second deepest split [evident on the basis of both the 170 K SNP panel (Fig. 1A) and genome-wide SNPs (fig. S4)] separates modern East Asian and Western Eurasian (Europe and the Middle East) dogs. Moreover, the Newgrange dog clusters tightly with Western Eurasian dogs. We used principal components analysis (PCA), D statistics, and the program TreeMix (12) to further test this pattern. Each of these analyses unequivocally placed the Newgrange dog with modern European dogs (figs. S5 to S7). These findings demonstrate that the node separating the East Asian and Western Eurasian clades is older than the Newgrange individual, which was directly radiocarbon dated to ~4800 years ago.

Other nodes leading to multiple dog populations and breeds [including the basal breeds (1)

¹The Palaeogenomics and Bio-Archaeology Research Network, Research Laboratory for Archaeology and History of Art, University of Oxford, Oxford, UK. ²Smurfit Institute of Genetics, Trinity College Dublin, Dublin 2, Ireland.

³CNRS/ENS de Lyon, IGFL, UMR 5242 and French National Platform of Paleogenetics, PALGENE, Ecole Normale Supérieure de Lyon, 46 Allée d'Italie, 69364 Lyon Cedex 07, France/Université Grenoble Alpes, Laboratoire d'Ecologie Alpine (LECA), F-38000 Grenoble, France. ⁴CNRS/Muséum National d'Histoire Naturelle/Sorbonne Universités, Archéozoologie, Archéobotanique: Sociétés, Pratiques et Environnement (UMR 7209), CP56, 55 rue Buffon, F-75005 Paris, France. ⁵Department of Human Evolution, Max Planck Institute for Evolutionary Anthropology, 04103 Leipzig, Germany. ⁶Department of Anthropology, Texas A&M University, College Station, TX 77843-4352, USA. ⁷School of Biology, Aristotle University of Thessaloniki, Thessaloniki, Greece. ⁸School of Geography, Archaeology and Palaeoecology, Queen's University Belfast, University Road, Belfast, Northern Ireland, UK. ⁹Osteoarchaeological Research Laboratory, University of Stockholm, Stockholm, Sweden.

¹⁰Archaeological Institute, Research Centre for the Humanities, Hungarian Academy of Sciences, Budapest, Hungary. ¹¹Zoological Institute, Russian Academy of Sciences, Universitetskaya Nab. 1, 199034 Saint-Petersburg, Russia. ¹²The National Museum of Romanian History, 12 Calea Victoriei, 030026 Bucharest, Romania. ¹³Institut de Génétique et Développement de Rennes, CNRS-UMR6290, Université de Rennes 1, Rennes, France.

¹⁴Department of Archaeology, School of Geosciences, University of Aberdeen, St. Mary's, Elphinstone Road, AB24 3UF, UK.

¹⁵Department of Archaeology, Classics and Egyptology, University of Liverpool, 12-14 Abercromby Square, Liverpool L69 7WZ, UK.

*Corresponding author. Email: laurent.frantz@arch.ox.ac.uk (L.A.F.F.); greger.larson@arch.ox.ac.uk (G.L.); dbradley@tcd.ie (D.G.B.) †These authors contributed equally to this work.

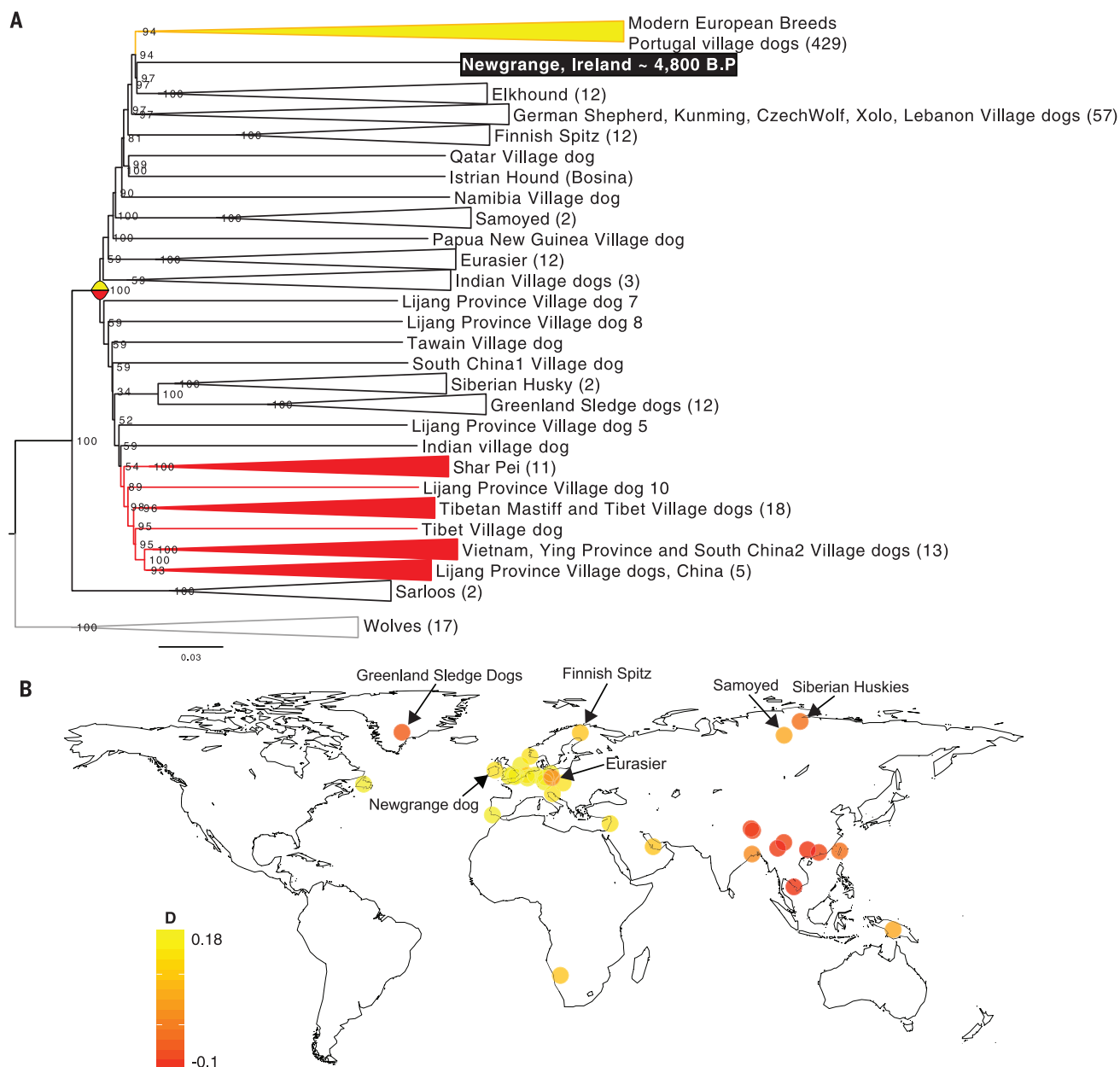


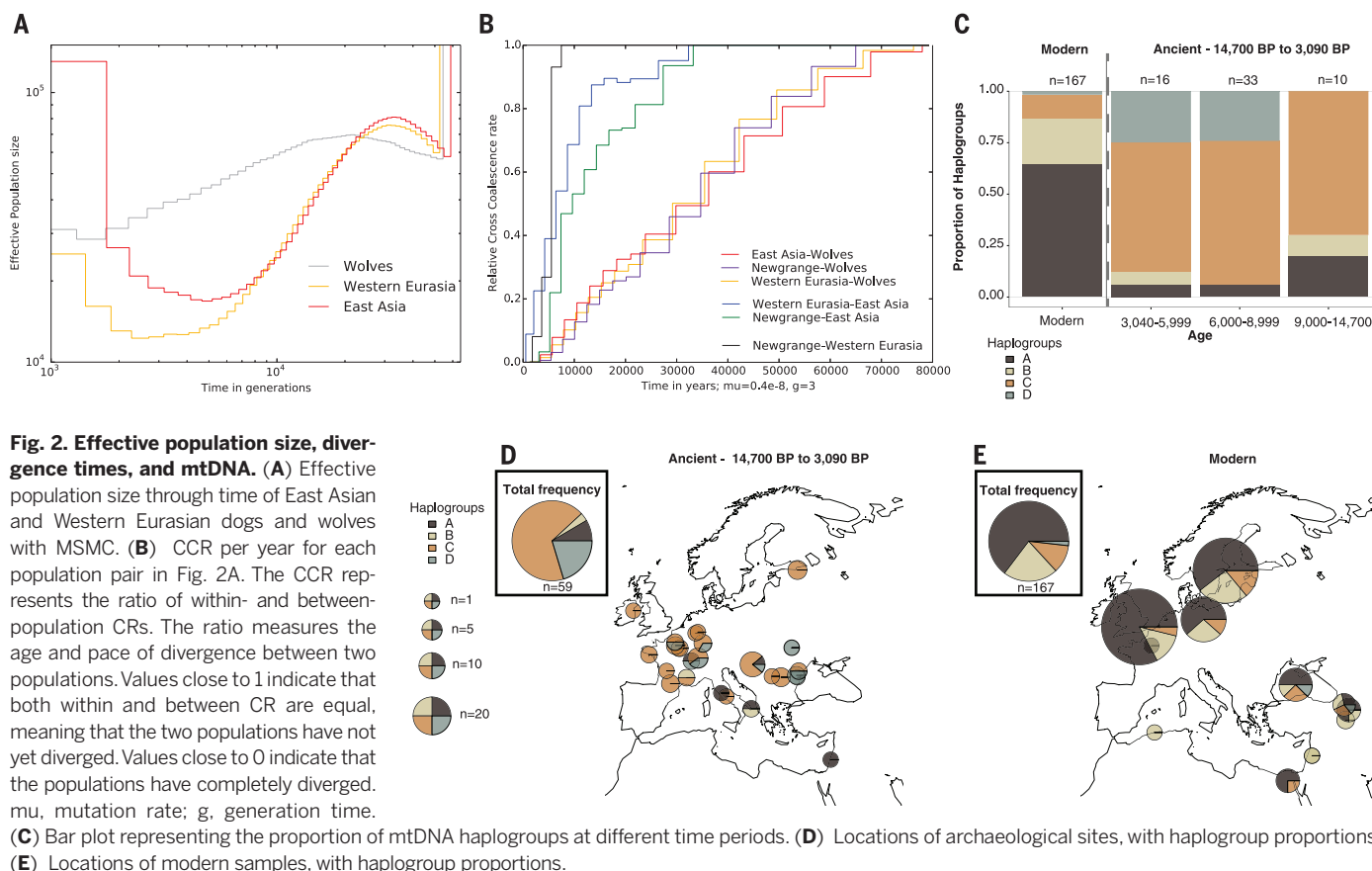
Fig. 1. Deep split between East Asian and Western Eurasian dogs. (A) A neighbor-joining tree (with bootstrap values) based on identity by state (12) of 605 dogs. Red and yellow clades represent the East Asian and Western Eurasian core groups, respectively (12). **(B)** A map showing the location and relative proportion of ancestry [mean *D* values (12)] of dogs (fig. S10). Negative values (red) indicate that the population shares more derived alleles with the East Asian core, whereas positive values (yellow) indicate a closer association with the Western Eurasian core.

such as Greenland sledge dogs or the Siberian husky (Fig. 1A)] are poorly supported, suggesting that these breeds probably possess mixed ancestry from both Western Eurasian and East Asian dog lineages. To further assess the robustness of the deep split and those nodes associated with the potentially admixed lineages, we defined Western Eurasian and East Asian “core” groups (Fig. 1A), supported by the strength of the node leading to each cluster (12). We then used *D* statistics to assess the affinity of each population to either Western Eurasian or East Asian core groups (12). The results of this analysis again revealed a clear East-West geographic pattern across Eurasia as-

sociated with the deep phylogenetic split (Fig. 1B). Breeds such as the Eurasier, Greenland sledge dogs, and Siberian huskies [all basal breeds from northern regions (1)], however, possess strong signatures of admixture with the East Asian core samples (fig. S11), as do populations sampled in East Asia that clustered alongside Western Eurasian dogs (such as a Papua New Guinean village dog; Fig. 1A).

We used the multiple sequentially Markovian coalescent (MSMC) (12, 14) to reconstruct the population history of East Asian and Western Eurasian dogs. An analysis of individual high-coverage genomes demonstrated a long shared

population history between the Newgrange dog and modern dogs from both Western Eurasia and East Asia (fig. S15). A reconstruction using two genomes per group improved the resolution for recent time periods (Fig. 2A) and revealed a bottleneck in the Western Eurasian population, after its divergence from the East Asian core. A similar bottleneck observed in non-African human populations has been interpreted as a signature of a migration out of Africa (15). We therefore speculate that the analogous bottleneck observed in our data set could be the result of a divergence and subsequent transportation of dogs from east to west, supporting suggestions



drawn from recent analyses of modern dog genomes (8, 9, 16).

We then used MSMC to compute divergence times as a means to assess the time frame of the shared population history among dogs, and between dogs and wolves. To obtain reliable time estimates, we used the radiocarbon age of the Newgrange dog to calibrate the mutation rate for dogs (12) (fig. S16). This resulted in a mutation rate estimate of between 0.3×10^{-8} and 0.45×10^{-8} per generation, which is similar to that obtained with an ancient grey wolf genome (17). Using this mutation rate, we calculated the divergence time between the two modern Russian wolves (18) used in this study and the modern dogs to be 60,000 to 20,000 years ago (fig. S17 and Fig. 2B). This date should not be interpreted as a time frame for domestication, because the wolves we examined may not have been closely related to the population(s) that gave rise to dogs (6).

These analyses also suggested that the divergence between the East Asian and Western Eurasian core groups (~14,000 to 6400 years ago) occurred commensurate with, or several millennia after, the earliest known appearance of domestic dogs in both Europe (>15,000 years) and East Asia (>12,500 years) (1) (Fig. 2B and fig. S17). In addition, admixture signatures from wolves into Western Eurasian dogs most likely pushed this estimated time of divergence deeper into the past (12), meaning that the expected time of divergence between the Eastern and Western cores is probably later than our estimate. These results

imply that indigenous populations of dogs were already present in Europe and East Asia during the Paleolithic (before this genomic divergence). Under this hypothesis, this early indigenous dog population in Europe was replaced (at least partially) by the arrival of East Eurasian dogs.

To investigate this potential replacement, we sequenced and analyzed 59 hypervariable mtDNA fragments from ancient dogs spread across Europe, and we combined those with 167 modern sequences (12). Each sequence was then assigned to one of four major well-supported haplogroups (groups A to D) (19). Although the majority of ancient European dogs belonged to either haplogroup C or D (63 and 20%, respectively) (Fig. 2, C to E). Using simulations, we showed that this finding cannot be explained by drift alone (12). Instead, this pattern arose from clear turnover in the mitochondrial ancestry of European dogs, most likely as a result of the arrival of East Asian dogs. This migration led to a partial replacement of ancient dog lineages in Europe that were present by at least 15,000 years ago (1).

Although the mtDNA turnover is obvious, the nuclear signature reveals an apparent long-term continuity. Assessments of ancestry in humans have demonstrated that major (nuclear) turnovers can be difficult to detect without samples from the admixing population (11). A genome-wide PCA analysis revealed that PC2 clearly discriminates the Newgrange dog from other modern dogs (fig.

S8), suggesting that this individual could possess ancestry from an unsampled population.

Our MSMC analysis revealed that the population split between the Newgrange dog and the East Asian core [as measured by cross coalescence rate (CCR)] is older (on average) than the split between modern Western Eurasian and East Asian lineages (Fig. 2B). Simulations suggest that this pattern could be explained by a partial replacement model in which the Newgrange dog retained a degree of ancestry from an outgroup population (fig. S20, A and B) that was different from modern wolves (12). Alternatively, this pattern could also be explained by secondary gene flow from Asian dogs into modern European dogs (fig. S20C). Nevertheless, our simulations show that secondary gene flow has a smaller effect on CCR than the partial replacement model (fig. S20, B and D). Moreover, secondary gene flow cannot explain the placement of the Newgrange dog on our genome-wide PCA (fig. S8). Overall, these observations are consistent with a scenario in which the Newgrange dog retained a degree of ancestry from an ancient canid population that falls outside of the variation of modern dogs, but that is also different from modern wolves. This pattern also suggests that the replacement of European indigenous Paleolithic dogs may not have been complete.

To assess the consistency between our results and the archaeological record, we compiled evidence for the earliest dog remains across Eurasia (Fig. 3A). We found that although dogs are present at

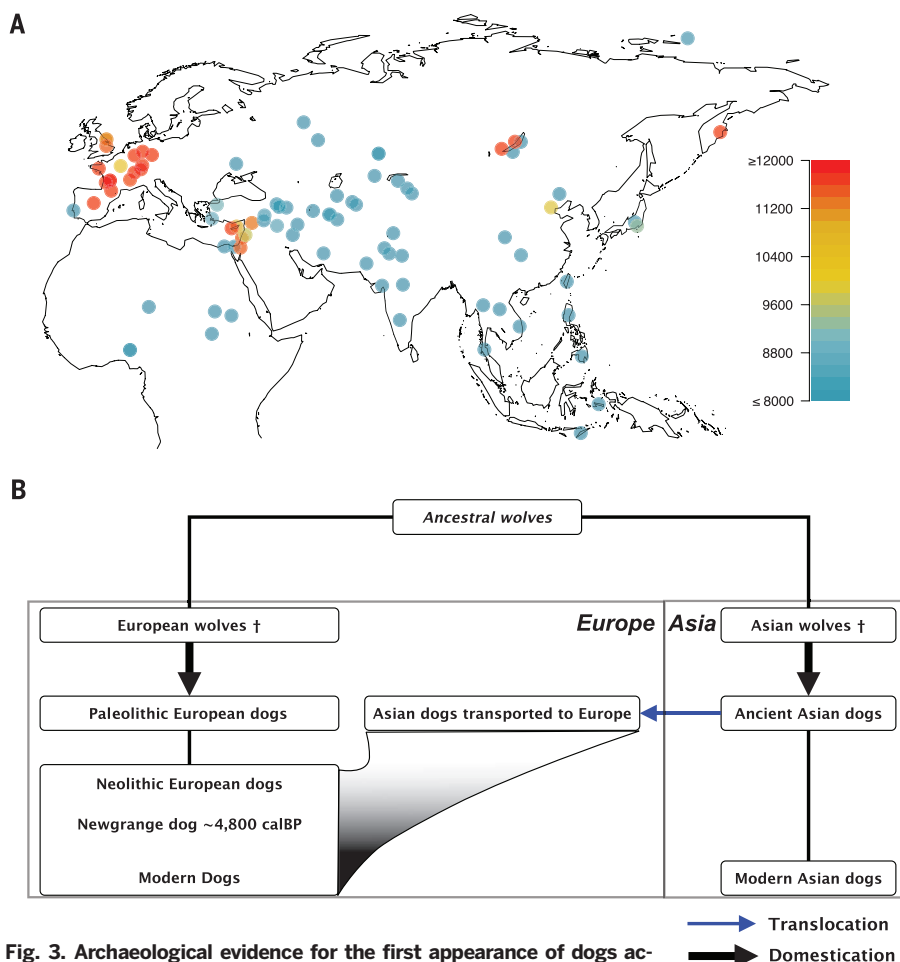


Fig. 3. Archaeological evidence for the first appearance of dogs across Eurasia and a model of dog domestication. (A) Map representing the geographic origin and age of the oldest archaeological dog remains in Eurasia (12). (B) A suggested model of dog domestication under the dual-origin hypothesis. An initial wolf population splits into East and West Eurasian wolves that were then domesticated independently before becoming extinct (as indicated by the † symbol). The Western Eurasian dog population (European) was then partially replaced by a human-mediated translocation of Asian dogs at least 6400 years ago, a process that took place gradually after the arrival of the eastern dog population.

sites as old as 12,500 years in Eastern Eurasia (China, Kamchatka, and East Siberia) and 15,000 years in Western Eurasia (Europe and the Near East), dog remains older than 8000 years have yet to be recovered in Central Eurasia (Fig. 3A and table S7). Combined with our DNA analyses, this observation suggests that two distinct populations of dogs were present in Eastern and Western Eurasia during the Paleolithic.

The establishment of these populations is consistent with two scenarios: a single origin of Eurasian dogs, followed by early transportation, founder effects, isolation, and drift; or two independent domestication processes on either side of Eurasia. In the first scenario, the archaeological record should reveal a temporal cline of the first appearance of dogs across Eurasia stemming from a single source. Given the current lack of dog remains prior to 8000 years ago in Central Eurasia, a scenario involving a single origin followed by an early dispersal seems less likely.

Given our combined results, we suggest the following hypothesis: Two genetically differenti-

ated and potentially extinct wolf populations in Eastern (8, 9) and Western (7) Eurasia may have been independently domesticated before the advent of settled agriculture (Fig. 3A). The eastern dog population then dispersed westward alongside humans at some point between 6400 and 14,000 years ago, into Western Europe (10, 11, 20), where they partially replaced an indigenous Paleolithic dog population. Our hypothesis reconciles previous studies that have suggested that domestic dogs originated either in East Asia (9, 19) or in Europe (7). For numerous reasons, the null hypothesis should be that individual animal species were domesticated just once (21). The combined genetic and archaeological results presented here, however, suggest that dogs, like pigs (22), may have been independently domesticated twice. Nevertheless, given the complexity of the evolutionary history of dogs and uncertainties related to mutation rates, generation times, and the incomplete nature of the archaeological record, our scenario remains hypothetical. Genome sequences derived from ancient Eurasian dogs and

wolves, combined with detailed morphological and contextual studies of the archaeological remains, will provide the necessary means to assess whether dog domestication occurred more than once.

REFERENCES AND NOTES

- G. Larson et al., *Proc. Natl. Acad. Sci. U.S.A.* **109**, 8878–8883 (2012).
- M. Germonpré, M. Lázničková-Galetová, M. V. Sablin, *J. Archaeol. Sci.* **39**, 184–202 (2012).
- M. Pionnier-Capitan et al., *J. Archaeol. Sci.* **38**, 2123–2140 (2011).
- T. Dayan, *J. Archaeol. Sci.* **21**, 633–640 (1994).
- M. Ollivier et al., *PLOS One* **8**, e75110 (2013).
- A. H. Freedman et al., *PLOS Genet.* **10**, e1004016 (2014).
- O. Thalmann et al., *Science* **342**, 871–874 (2013).
- L. M. Shannon et al., *Proc. Natl. Acad. Sci. U.S.A.* **112**, 13639–13644 (2015).
- G.-D. Wang et al., *Cell Res.* **26**, 21–33 (2016).
- M. E. Allentoft et al., *Nature* **522**, 167–172 (2015).
- W. Haak et al., *Nature* **522**, 207–211 (2015).
- See the supplementary materials.
- D. Morris, *Dogs: The Ultimate Dictionary of Over 1,000 Dog Breeds* (Trafalgar Square, North Pomfret, VT, 2008).
- S. Schiffels, R. Durbin, *Nat. Genet.* **46**, 919–925 (2014).
- H. Li, R. Durbin, *Nature* **475**, 493–496 (2011).
- M. Pilot et al., *Proc. R. Soc. B Biol. Sci.* **282**, 20152189 (2015).
- P. Skoglund, E. Ersmark, E. Palkopoulou, L. Dalén, *Curr. Biol.* **25**, 1515–1519 (2015).
- G. D. Wang et al., *Nat. Commun.* **4**, 1860 (2013).
- P. Savolainen, Y. P. Zhang, J. Luo, J. Lundberg, T. Leitner, *Science* **298**, 1610–1613 (2002).
- L. M. Cassidy et al., *Proc. Natl. Acad. Sci. U.S.A.* **113**, 368–373 (2016).
- G. Larson, J. Burger, *Trends Genet.* **29**, 197–205 (2013).
- L. A. F. Frantz et al., *Nat. Genet.* **47**, 1141–1148 (2015).

ACKNOWLEDGMENTS

Raw reads of the Newgrange dog have been deposited at the European Nucleotide Archive (ENA) with project number PRJEB13070. Mitochondrial sequences as well as genotype files (in plink format) were deposited on Dryad (doi:10.5061/dryad.8gp06). We thank G. Wang, J. Schraiber, L. Orlando, L. Dalén, R. E. Green, P. Savolainen, and E. Loftus for their valuable input; and A. Oszás, I. Zalai-Gaál, R.-M. Arbogast, A. Beeching, A. Boroneant, O. Lecomte, S. Madeleine, C. and D. Mordant, M. Patou-Mathis, P. Pétrequin, L. Salanova, J. Schibler, A. Tsuneki, and F. Valla for providing archaeological material. L.A.F.F., O.L., A.L., and G.L. were supported by a European Research Council grant (ERC-2013-StG-337574-UNDEAD) and Natural Environmental Research Council grants (NE/K005243/1 and NE/K003259/1). L.A.F.F. was supported by a Junior Research Fellowship (Wolfson College, University of Oxford). M.P.-C. was supported by a BDI CNRS grant. V.E.M., V.M., M.D.T., and the sequencing of the Newgrange dog genome were funded by ERC Investigator grant 295729-CodeX awarded to D.G.B. We also acknowledge the National Museum of Ireland for providing the petrous bone of the Newgrange dog and the Science Foundation Ireland Award 12/ERC/B2227 and Trinseq. A.B. was supported by a Romanian National Authority for Scientific Research (PN-II-ID-PCE-2011-3-1015). The work at ENS Lyon and at Muséum National d'Histoire Naturelle Paris was also supported by Nestlé Purina. The authors declare no conflict of interest.

SUPPLEMENTARY MATERIALS

www.sciencemag.org/content/352/6290/1228/suppl/DC1
Materials and Methods
Figs. S1 to S29
Tables S1 to S7
References (23–119)

2 February 2016; accepted 25 April 2016
10.1126/science.123161

INNATE IMMUNITY

An endogenous caspase-11 ligand elicits interleukin-1 release from living dendritic cells

Ivan Zanoni,^{1,2,3} Yunhao Tan,¹ Marco Di Gioia,¹ Achille Broggi,¹ Jianbin Ruan,⁶ Jianjin Shi,⁵ Carlos A. Donado,¹ Feng Shao,⁵ Hao Wu,^{6,7} James R. Springstead,⁴ Jonathan C. Kagan^{1*}

Dendritic cells (DCs) use pattern recognition receptors to detect microorganisms and activate protective immunity. These cells and receptors are thought to operate in an all-or-nothing manner, existing in an immunologically active or inactive state. Here, we report that encounters with microbial products and self-encoded oxidized phospholipids (oxPAPC) induce an enhanced DC activation state, which we call “hyperactive.” Hyperactive DCs induce potent adaptive immune responses and are elicited by caspase-11, an enzyme that binds oxPAPC and bacterial lipopolysaccharide (LPS). oxPAPC and LPS bind caspase-11 via distinct domains and elicit different inflammasome-dependent activities. Both lipids induce caspase-11-dependent interleukin-1 release, but only LPS induces pyroptosis. The cells and receptors of the innate immune system can therefore achieve different activation states, which may permit context-dependent responses to infection.

Pattern recognition receptors (PRRs) promote immune defenses upon encountering lipopolysaccharide (LPS) and other microbial products, which are collectively known as pathogen-associated molecular patterns (PAMPs). PRRs also recognize self-encoded molecules called damage-associated molecular patterns (DAMPs) (1, 2). The existence of self-derived PRR ligands complicates our current understanding of PRRs as determinants of self/nonself discrimination.

Oxidized phospholipids derived from 1-palmitoyl-2-arachidonoyl-*sn*-glycero-3-phosphorylcholine (PAPC), known as oxPAPC, represent one class of DAMPs. oxPAPC is found in dying cells (3) and can reach concentrations of 10 to 100 μ M in damaged tissues (4, 5). oxPAPC is an LPS mimic that, depending on context, promotes or inhibits Toll-like receptor 4 (TLR4)-dependent inflammation (6–8). The existence of LPS and a self-derived LPS mimic provides a model to dissect the activities of PAMPs and DAMPs in innate immunity.

If oxPAPC is truly an LPS mimic, then LPS and oxPAPC should exhibit similar activities. We therefore determined whether oxPAPC activates TLR4 in murine bone marrow-derived macrophages (M Φ) and dendritic cells (DCs). LPS, but not oxPAPC, induced TLR4 dimerization and endocytosis, MyD88-IRAK4 interactions (i.e., myddosome formation), and expression of the cytokines interleukin (IL)-6, tumor necrosis factor- α (TNF α), IL-1 β , and interferon- β (IFN- β) (Fig. 1, A to C, and fig. S1, A to C). Furthermore, oxPAPC-treated cells contained undetectable viperin or phosphorylated STAT1, both of which were abundant upon LPS treatment (Fig. 1D and fig. S1D). These data indicate that oxPAPC cannot activate TLR4.

Some DAMPs only induce cytokine release from cells previously exposed to microbial products. For example, adenosine triphosphate (ATP) activates IL-1 β release from cells primed with TLR ligands (9). We therefore examined IL-1 β release from LPS-primed DCs. Interestingly, oxPAPC, similar to ATP, induced the release of cleaved IL-1 β from LPS-primed DCs (Fig. 2, A and B, and fig. S2, A and B). oxPAPC also elicited IL-1 β release from primed DCs isolated from the spleens of mice (fig. S2D).

¹Harvard Medical School and Division of Gastroenterology, Boston Children's Hospital, Boston, MA, USA. ²Department of Biotechnology and Biosciences, University of Milano-Bicocca, Milan, Italy. ³Unit of Cell Signalling and Innate Immunity, Humanitas Clinical and Research Center, Rozzano, Milan, Italy. ⁴Department of Chemical and Paper Engineering, Western Michigan University, Kalamazoo, MI, USA. ⁵National Institute of Biological Sciences, Beijing 102206, China. ⁶Department of Biological Chemistry and Molecular Pharmacology, Harvard Medical School, Boston, MA, USA. ⁷Program in Cellular and Molecular Medicine, Boston Children's Hospital, Boston, MA, USA. *Corresponding author. Email: jonathan.kagan@childrens.harvard.edu

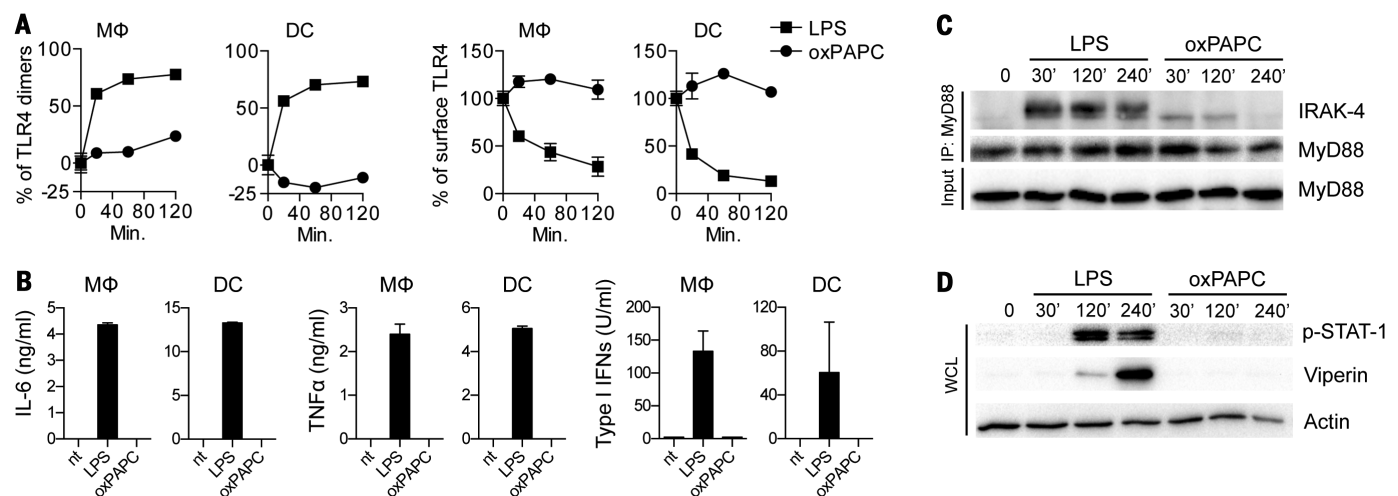


Fig. 1. oxPAPC does not induce TLR4 signaling. (A) M Φ s or DCs were treated with LPS or oxPAPC for the indicated time points. TLR4 dimerization and endocytosis were measured by flow cytometry. The line graphs represent means and standard deviations (SDs) of four replicates. (B) M Φ s or DCs were treated with LPS or oxPAPC. Cytokine production was analyzed 18 hours later. Means and SDs of four replicates are shown. (C) Myddosome formation in

M Φ s was assessed at the indicated time points after treatment with LPS or oxPAPC by coimmunoprecipitation (IP) of IRAK4 with MyD88 followed by Western analysis of the proteins indicated. (D) Whole-cell lysates (WCL) were collected and DCs were monitored for STAT-1 phosphorylation and viperin expression after treatment with LPS or oxPAPC. [(C) and (D)] One experiment representative of three is shown.

Oxidation of PAPC to oxPAPC generates a heterogeneous mixture of lipids (fig. S4, A and B). To determine whether alternative sources of oxPAPC have similar activities, we generated oxPAPC enriched in PEIPC [1-palmitoyl-2-(5,6 epoxisoprostanoil)-sn-glycero-3-phosphocholine] (fig. S4C), an active component of oxPAPC (10). Like oxPAPC, PEIPC induced IL-1 β release from LPS-primed DCs (Fig. 2B).

In contrast to the effects on IL-1 β release, neither ATP nor oxPAPC influenced the abundance of cell-associated IL-1 β (Fig. 2B and fig. S2C) or the secretion of TNF α (fig. S2, D and E). Additionally, when DCs were treated simultaneously with LPS/ATP or LPS/oxPAPC (i.e., no priming), IL-1 β release was only induced by LPS/oxPAPC (fig. S3B), suggesting differences in how these DAMPs promote IL-1 β release. When the phosphocholine variant 1,2-dimyristoyl-sn-glycero-3-phosphocholine (DMPC) was used, it could not elicit IL-1 β release (fig. S3C). In contrast, purified components of oxPAPC (KODIA-PC, POVPC, or PGPC) elicited IL-1 β release (fig. S3C). In all cases, LPS-induced TNF α secretion was unaffected (fig. S3C). Individual lipids within oxPAPC therefore promote IL-1 β release.

Inflammasomes are cytoplasmic protein complexes that trigger IL-1 β release (9). To determine

whether IL-1 β release is inflammasome-dependent, we examined DCs from apoptosis-associated speck-like protein containing a CARD (ASC) knockout (KO), caspase-1 KO, caspase-1/caspase-11 double (d)KO, or NOD-like receptor family, pyrin domain-containing 3 (NLRP3) KO mice, each of which are defective for inflammasome functions (11, 12). All of these factors were required for oxPAPC-induced IL-1 β release (Fig. 2C), whereas no inflammasome regulator was required for LPS-induced TNF α secretion (fig. S2F).

Interestingly, oxPAPC could not elicit IL-1 β release from M Φ s (fig. S3A). To explain this finding, we considered that DCs are better “primed” than M Φ s because they produce more TNF α than M Φ s in response to LPS (fig. S2E). However, IFN- γ -treated M Φ s were primed as well as DCs, yet they could not respond to oxPAPC (fig. S3D). Transfection of oxPAPC elicited IL-1 β release from DCs primed with the TLR2 ligand Pam3CSK, but not M Φ s, whereas LPS transfection of M Φ s elicited IL-1 β release (Fig. 2D). ATP treatments also revealed differences between M Φ s and DCs. DCs and M Φ s die upon LPS/ATP with similar kinetics but release different amounts of IL-1 β (Fig. 2E and fig. S2A) and express different levels of ASC (fig. S3, E and F) but not other inflammasome components (fig. S3F). oxPAPC therefore

revealed differences in inflammasome-related activities in bone marrow-derived M Φ s and DCs (fig. S5). We do note, however, that populations of DCs and M Φ s may exist that exhibit different responses to oxPAPC than those described above.

Further analysis of the mechanisms of inflammasome activation revealed that potassium efflux promoted ATP-induced, but not oxPAPC-induced, IL-1 β release (fig. S6, A to C). Additionally, oxPAPC did not alter mitochondrial functions (fig. S6D).

Caspase-11 is an LPS receptor that promotes IL-1 β release by noncanonical inflammasomes (13). Interestingly, oxPAPC-mediated IL-1 β release was largely abolished in caspase-11 KO DCs (Fig. 3A), whereas ATP-mediated IL-1 β release remained intact. TNF α secretion was unaffected by caspase-11 deficiency (fig. S6E). Microscopic analysis revealed that oxPAPC and ATP induced the formation of ASC and caspase-1 containing “specks” in LPS-pretreated DCs (Fig. 3B), albeit with different kinetics (fig. S6F). These structures are recognized as individual inflammasomes (14), and in the specific case of oxPAPC stimulations, speck formation was caspase-11 dependent (Fig. 3B and fig. S6G). Caspase-11 is therefore likely required for oxPAPC-induced IL-1 β release because it promotes inflammasome assembly in DCs.

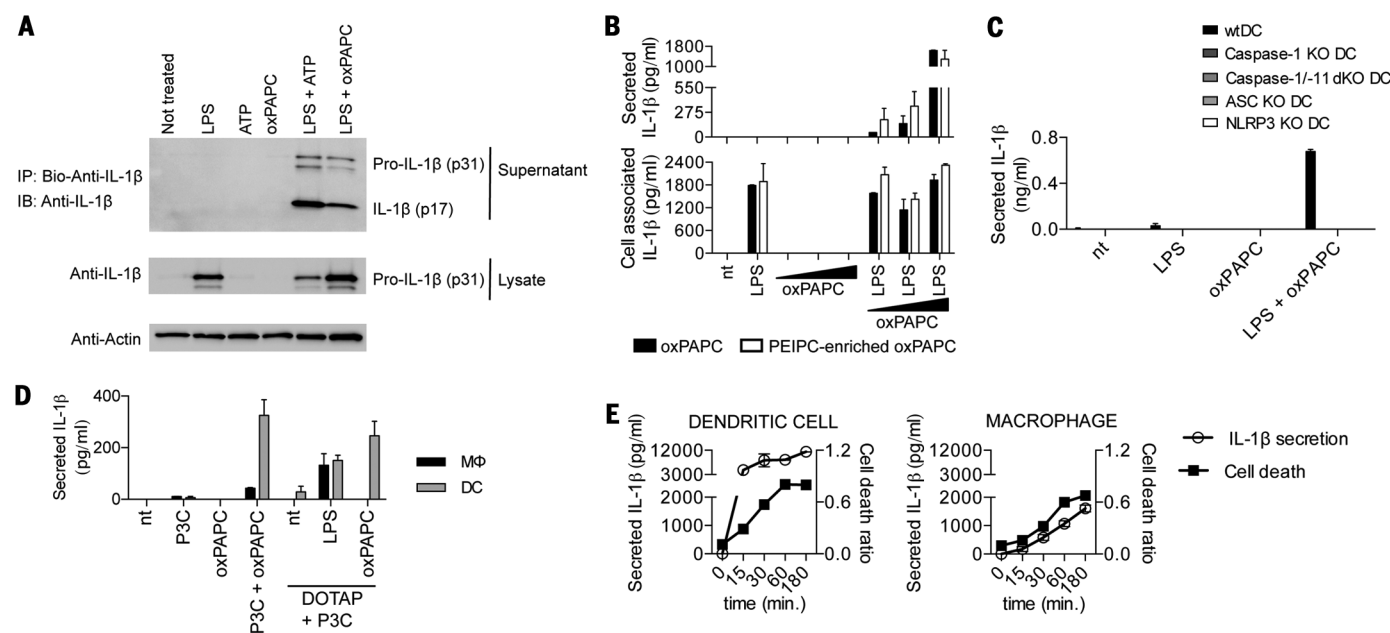


Fig. 2. oxPAPC induces the activation of the NLRP3 inflammasome in DCs. (A) DCs primed with LPS, followed by ATP or oxPAPC treatment. Cell culture supernatant from DCs subjected to indicated treatments was collected, and processed IL-1 β (p17) production was assessed. One experiment representative of three is shown. (B) DCs were treated with LPS alone; were treated with 10, 50, or 120 μ M of oxPAPC; or were primed with LPS for 3 hours and then treated with oxPAPC. For this experiment, commercially available oxPAPC and an oxPAPC enriched in PEIPC were used. Eighteen hours after LPS administration, secreted (left panel) and cell-associated (right panel) IL-1 β was measured by enzyme-linked immunosorbent assay (ELISA). Means and SDs of four replicates are shown. (C) DCs of the genotypes indicated were treated with LPS alone, were treated with oxPAPC alone, or were primed with

LPS for 3 hours and then treated with oxPAPC. Eighteen hours after LPS administration, IL-1 β secretion was measured by ELISA. Means and SDs of four replicates are shown. (D) M Φ s and DCs were treated with Pam3CSK (P3C) alone, were treated with oxPAPC alone, or were primed with Pam3CSK for 3 hours and then treated with oxPAPC, DOTAP alone, and LPS or oxPAPC encapsulated in DOTAP (N-[1-(2,3-Dioleoyloxy)propyl]-N,N,N-trimethylammonium methyl-sulfate). Eighteen hours after P3C administration, IL-1 β was measured by ELISA. Means and SDs of four replicates are shown. (E) DCs (left panel) or M Φ s (right panel) were primed with LPS for 3 hours and treated with ATP. At indicated time points, IL-1 β was measured by ELISA, and cell death was measured by propidium iodide permeabilization assay. Means and SDs of four replicates are shown.

Interestingly, multiple TLR ligands primed DCs for oxPAPC responsiveness, as Pam3CSK-primed DCs induced IL-1 β release in response to oxPAPC (fig. S6H) by an NLRP3-, ASC-, and caspase-11-dependent process (fig. S6H). The TLR9 ligand CpG-DNA also primed DCs for oxPAPC responsiveness (fig. S6I). Similarly, oxPAPC, but not DMPC, elicited IL-1 β release from an LPS- or CpG-DNA-primed splenic DC line called D1 (I5) (fig. S6J). oxPAPC therefore activates multiple DCs upon encounters with diverse TLR ligands. The finding that multiple TLR

ligands prime DCs for oxPAPC responsiveness eliminates the possibility that oxPAPC acts as an LPS carrier to caspase-11.

We considered that oxPAPC interacts with caspase-11, like LPS (I3). Endogenous caspase-11 (but not caspase-3) was captured from DC or immortal bone marrow-derived M Φ (iM Φ) lysates through interactions with biotin-LPS or biotin-oxPAPC (figs. S4D and S7A and Fig. 3C). Caspase-11 was not captured by the biotinylated NOD2 ligand muramyl dipeptide (MDP) (Fig. 3C). oxPAPC displayed a dose-dependent signal with immobilized

catalytically inactive caspase-11(C254A) using surface plasmon resonance (SPR), as did LPS (Fig. 3D). In contrast, DMPC did not bind caspase-11, and oxPAPC did not bind immunoglobulin G (fig. S7B). The dissociation constant (K_d) between caspase-11 and oxPAPC was calculated as 1.3×10^{-6} M, whereas the K_d for interactions with LPS is 3.78×10^{-6} M (I3). Gel filtration chromatography revealed that oxPAPC also promoted caspase-11 oligomerization (Fig. 3E), with monomers eluting at 15.03 ml, dimers at 13.82 ml, and higher-order oligomers earlier.

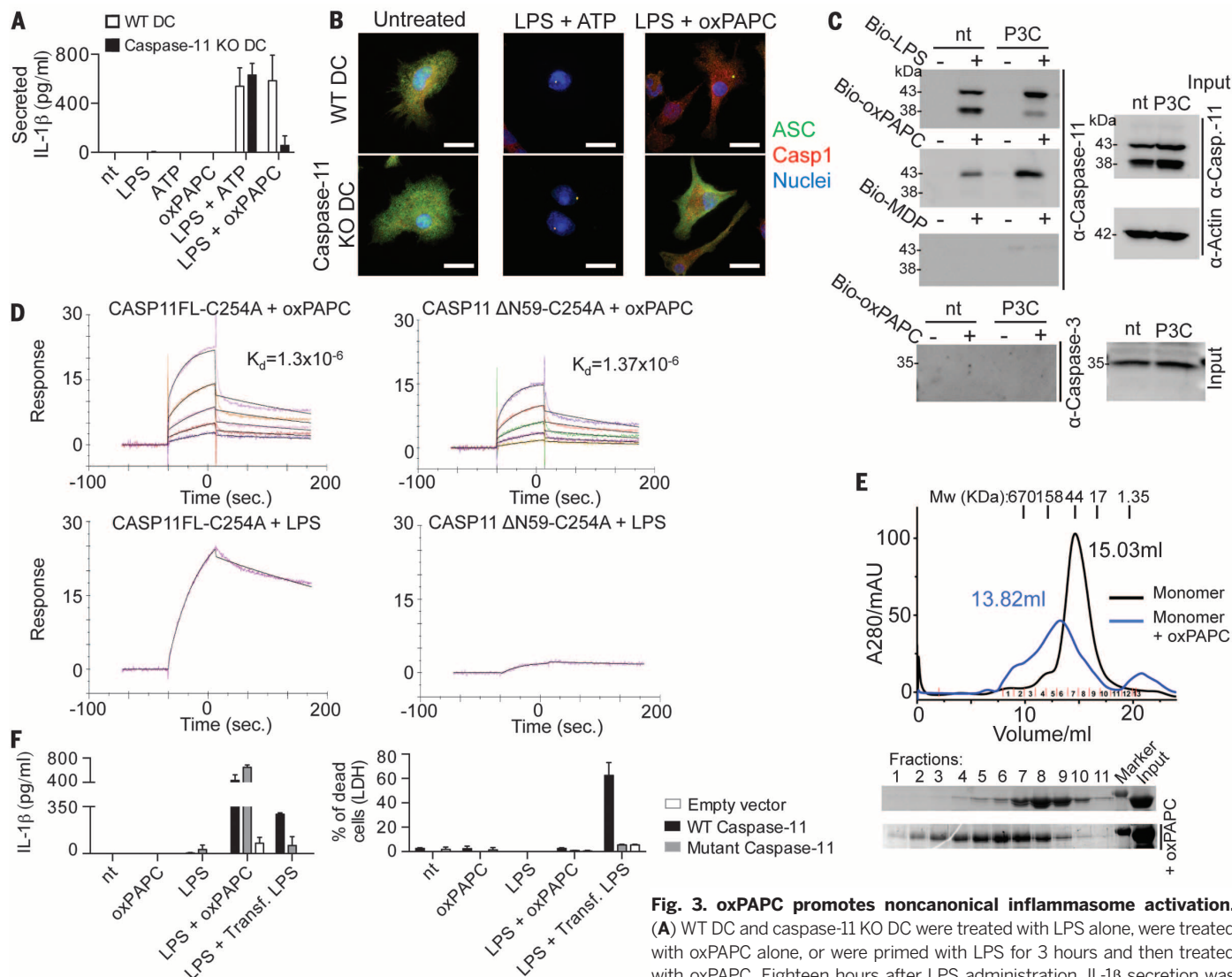


Fig. 3. oxPAPC promotes noncanonical inflammasome activation.

(A) WT DC and caspase-11 KO DC were treated with LPS alone, were treated with oxPAPC alone, or were primed with LPS for 3 hours and then treated with oxPAPC. Eighteen hours after LPS administration, IL-1 β secretion was measured by ELISA. Means and SDs of four replicates are shown. (B) DCs

were left untreated or primed with LPS and then stimulated with ATP or oxPAPC. Specks containing ASC (green) and caspase-1 (Casp1, red) were analyzed 18 hours after LPS stimulation. Nuclei are shown in blue. Panels are representative of four independent experiments. Scale bar, 10 μ m. (C) S100 fractions of nontreated (nt) or P3C-primed (P3C) M Φ s were incubated with biotin-LPS (Bio-LPS), biotin-oxPAPC (Bio-oxPAPC), or biotin-MDP (Bio-MDP). Endogenous proteins associated with biotinylated ligands were captured by streptavidin beads and revealed by Western analysis. Shown is a representative blot out of three independent experiments. (D) SPR analysis of the interactions between the proteins and lipids indicated. (E) Gel filtration analysis of the size of caspase-11 complexes before and after exposure to oxPAPC. Complex size was monitored by A280 or Western analysis, as indicated. Shown is a representative blot out of three independent experiments. (F) Bone marrow cells were infected with the pMSCV2.2-IRES-GFP (internal ribosomal entry site–green fluorescent protein) vector (empty), the pMSCV2.2-IRES-GFP vector encoding WT caspase-11 (WT caspase-11), or the same vector containing a catalytic mutant caspase-11 (C254A). DCs were primed or not with LPS and then stimulated with oxPAPC, or transfected with LPS-containing FuGENE (Trans.LPS). Eighteen hours after LPS priming, supernatants were collected and IL-1 β was measured by ELISA. Cell viability was assessed by measuring LDH release. Means and SDs of four replicates are shown.

Mutation of lysine residues within the caspase-11 CARD (caspase activation and recruitment domain) prevents interactions with LPS (13), as assessed by the ability of biotin-LPS to capture caspase-11 produced in 293T cells (fig. S7C). Interestingly, these mutations did not prevent interactions with biotin-oxPAPC (fig. S7C). Moreover, the isolated caspase-11 catalytic domain (but not the CARD) retained the ability to bind biotin-oxPAPC (fig. S7D). SPR analysis verified these results, because nearly identical affinities of oxPAPC for caspase-11 or the catalytic domain (noted as Δ N59) were calculated (Fig. 3D). LPS could not bind the caspase-11 catalytic domain (Fig. 3D), as expected (13). These data establish that distinct domains within caspase-11 bind LPS and oxPAPC.

The interaction of oxPAPC with the catalytic domain prompted us to examine caspase-11 enzymatic activity. Whereas LPS strongly increased activity of caspase-11 monomers, oxPAPC displayed minimal activity (fig. S7E). We also examined preexisting caspase-11 oligomers, where intrinsic activity is high (fig. S7E). Interestingly, whereas LPS stimulated this activity further, oxPAPC suppressed intrinsic activity (fig. S7E). Moreover,

oxPAPC blocked LPS-induced caspase-11 activity in a dose-dependent manner (fig. S7F). These data indicate that LPS promotes, but oxPAPC prevents, caspase-11 activity.

To determine whether caspase-11 activity is required for oxPAPC-induced IL-1 β release, we reconstituted caspase-11 KO DCs with wild-type (WT) or catalytic mutant (C254A) caspase-11 or empty vector. LPS elicited IL-1 β release from cells expressing WT caspase-11 but not empty vector or mutant caspase-11 (Fig. 3F). These data confirm that caspase-11 activity promotes LPS-induced IL-1 β release (16, 17). Interestingly, WT and mutant-reconstituted DCs released IL-1 β in response to oxPAPC (Fig. 3F). TNF α release was unaffected under all conditions (fig. S7G). Two modes of caspase-11-mediated IL-1 β release therefore exist, with catalytic activity only being necessary for LPS responses.

In addition to caspase-11, oxPAPC-induced IL-1 β release requires caspase-1 (Figs. 2C and 3A). Interestingly, independent of caspase-11, biotin-oxPAPC captured endogenous caspase-1 from cell lysates, whereas biotin-LPS could not (fig. S7, H and I). These data support a model whereby

oxPAPC and LPS promote inflammasome formation via distinct mechanisms, with oxPAPC specifically forming a caspase-1/11 heterocomplex that may promote IL-1 β release. The precise mechanisms that govern oxPAPC-caspase interactions, and how these interactions promote inflammasome activities, await further investigation.

Pyroptosis, another inflammasome-dependent activity (18), is characterized by the loss of plasma membrane integrity and the release of cytoplasmic proteins and organelles. Caspase-11 activity was necessary for transfected LPS to induce pyroptosis, as assessed by lactate dehydrogenase (LDH) release from the cytosol (Fig. 3F). Surprisingly, oxPAPC did not elicit pyroptosis (Fig. 3F). We explored this observation further in WT DCs, where LPS/ATP or transfected LPS induced pyroptosis with differing kinetics (Fig. 4A). Interestingly, although LPS transfection or oxPAPC treatment induced similar amounts of IL-1 β release (Fig. 4B), only LPS transfection caused pyroptosis (Fig. 4A and fig. S8A).

To corroborate these observations, we examined plasma membrane integrity of individual cells containing ASC specks. Cells treated with

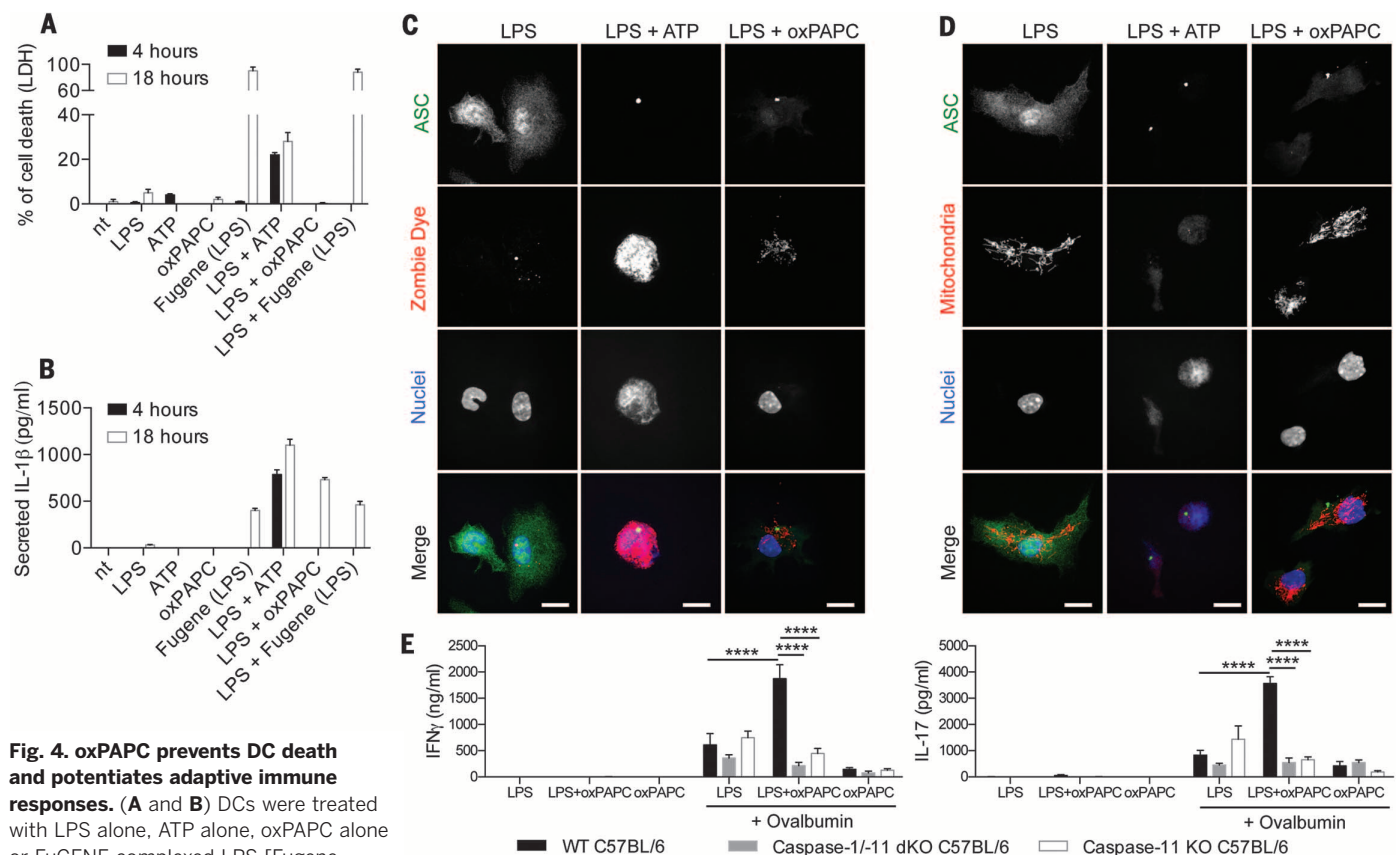


Fig. 4. oxPAPC prevents DC death and potentiates adaptive immune responses. (A and B) DCs were treated with LPS alone, ATP alone, oxPAPC alone or FuGENE-complexed LPS [Fugene (LPS)], or were primed for 3 hours with LPS and then treated with the indicated stimuli. Cell death was measured by LDH release (A), or IL-1 β secretion was measured by ELISA (B). Means and SDs of four replicates are shown. (C and D) DCs were pretreated with LPS for 3 hours and then activated with ATP or oxPAPC. Eighteen hours later, cells were stained for ASC (green), nuclei (blue), (C) Zombie dye (red), or (D) active mitochondria (red). Scale bars, 10 μ m. Panels are representative of three independent experiments. (E) CD4 $^{+}$ T cells were isolated from the

draining lymph nodes 40 days after immunization with OVA + LPS in IFA (LPS), OVA + LPS + oxPAPC in IFA (LPS + oxPAPC), or OVA + oxPAPC in IFA (oxPAPC) of WT, caspase-1/11 dKO, or caspase-11 KO mice. CD4 $^{+}$ T cells were restimulated or not with OVA in the presence of DCs. IFN- γ (left panel) and IL-17 (right panel) secretion was measured 5 days later by ELISA. Bar graphs represent means and standard errors of two experiments with five mice per group. * P < 0.05; ** P < 0.01; *** P < 0.005.

LPS/ATP contained specks, and these cells lost mitochondria and stained positive for Zombie dye, a cytoplasmic stain (Fig. 4, C and D). In contrast, cells treated with LPS/oxPAPC contained specks but retained functional mitochondria and displayed minimal Zombie staining (Fig. 4, C and D). These data indicate that oxPAPC-induced inflammasomes do not promote pyroptosis and suggest that oxPAPC promotes IL-1 β release from living cells. Moreover, not only does oxPAPC not induce pyroptosis, this lipid counteracted the slow-acting death pathways activated by LPS (19) (fig. S8B).

Because oxPAPC promotes DC viability and IL-1 β promotes T cell activation (20, 21), we examined whether oxPAPC displayed adjuvant activity. WT, caspase-11, and caspase-1/-11 dKO mice were injected subcutaneously with LPS, ovalbumin (OVA), and/or oxPAPC that was emulsified in incomplete Freund's adjuvant (IFA). After 40 days, CD4⁺ T cells were isolated from draining lymph nodes and exposed to DCs that were pulsed (or not) with OVA. T cell activation was examined by measuring IL-2, IL-17, and IFN- γ secretion. Interestingly, LPS/oxPAPC immunizations yielded substantially higher levels of all cytokines examined, as compared with immunizations with LPS alone (Fig. 4E and fig. S8C). The ability of oxPAPC to enhance T cell activation was lost in caspase-11 or caspase-1/-11 dKO mice (Fig. 4E and fig. S8C). Similar results were obtained measuring T cell responses 7 days after immunization (fig. S8D). oxPAPC therefore potentiates LPS-mediated T cell activation in a caspase-11-dependent manner.

In this study, we report two states of DC activation. The first state results from encounters with PAMPs, which induce TLRs to up-regulate several factors that promote T cell activation (22). The second state of DCs is "hyperactive" and

results from coincident encounters with PAMPs and oxPAPC, an abundant lipid at sites of tissue damage. The codetection of PAMPs and oxPAPC promotes activities elicited by the classical DC activation state but also promotes DC survival and IL-1 β release. As such, hyperactive DCs are superb inducers of T cell-mediated immunity. We speculate that promoting DC hyperactivation may benefit vaccination regimens and may naturally be important during highly infectious encounters, where tissue damage and microbial products are abundant.

Our analysis also revealed caspase-11 to be an unusual PRR, which binds PAMPs and DAMPs via distinct domains and has distinct modes of activation. We consider CARD engagement by LPS to be an antimicrobial mode of caspase-11 activation, designed to expose intracellular bacteria to infiltrating neutrophils after pyroptosis (23). In contrast, catalytic domain engagement by oxPAPC may be an immunoregulatory mode of caspase-11 activation, designed to promote T cell activation, specifically in DCs (fig. S5). This study therefore provides a mandate to examine whether other PRRs have multiple states of activation.

REFERENCES AND NOTES

1. T. Pradeu, E. L. Cooper, *Front. Immunol.* **3**, 287 (2012).
2. H. Kono, K. L. Rock, *Nat. Rev. Immunol.* **8**, 279–289 (2008).
3. M. K. Chang *et al.*, *J. Exp. Med.* **200**, 1359–1370 (2004).
4. J. A. Berliner, A. D. Watson, *N. Engl. J. Med.* **353**, 9–11 (2005).
5. N. Leitinger, *Curr. Opin. Lipidol.* **14**, 421–430 (2003).
6. Y. Imai *et al.*, *Cell* **133**, 235–249 (2008).
7. K. A. Shirey *et al.*, *Nature* **497**, 498–502 (2013).
8. V. N. Bochkov *et al.*, *Nature* **419**, 77–81 (2002).
9. V. Pétrilli, C. Costert, D. A. Muruve, J. Tschopp, *Curr. Opin. Immunol.* **19**, 615–622 (2007).
10. J. R. Springstead *et al.*, *J. Lipid Res.* **53**, 1304–1315 (2012).
11. F. Martinon, K. Burns, J. Tschopp, *Mol. Cell* **10**, 417–426 (2002).
12. Z. Ye, J. P. Ting, *Curr. Opin. Immunol.* **20**, 3–9 (2008).
13. J. Shi *et al.*, *Nature* **514**, 187–192 (2014).
14. A. Stutz, G. L. Horvath, B. G. Monks, E. Latz, *Methods Mol. Biol.* **1040**, 91–101 (2013).
15. C. Winzler *et al.*, *J. Exp. Med.* **185**, 317–328 (1997).
16. N. Kayagaki *et al.*, *Nature* **526**, 666–671 (2015).
17. J. Shi *et al.*, *Nature* **526**, 660–665 (2015).
18. Y. Aachoui *et al.*, *Science* **339**, 975–978 (2013).
19. I. Zanoni *et al.*, *Nature* **460**, 264–268 (2009).
20. J. E. Sims, D. E. Smith, *Nat. Rev. Immunol.* **10**, 89–102 (2010).
21. D. Schenten *et al.*, *Immunity* **40**, 78–90 (2014).
22. A. Iwasaki, R. Medzhitov, *Nat. Immunol.* **16**, 343–353 (2015).
23. I. Jorgensen, E. A. Miao, *Immunol. Rev.* **265**, 130–142 (2015).


ACKNOWLEDGMENTS

We thank members of the Kagan laboratory for helpful discussions. The results reported in this manuscript are tabulated in the main paper and in the supplementary materials. J.C.K. and Boston Children's Hospital have filed an international patent application (PCT/US2016/012994) that relates to the adjuvant activity of oxPAPC. J.C.K. is supported by NIH grants AI093589, AI072955, and P30 DK34854 and a gift from Mead Johnson & Company. J.C.K. holds an Investigators in the Pathogenesis of Infectious Disease Award from the Burroughs Wellcome Fund. I.Z. is supported by NIH grant 1R01AI121066-01A1, Harvard Digestive Diseases Center grant P30 DK34854, and the Cariplo Foundation. Y.T. is supported by a fellowship of the Jane Coffin Childs Fund (Merck Fellow). J.S. is supported by NIH grant 1R15HL121770-01A1. J.S. and F.S. performed the experiments in Fig. 3D but were not involved in the experimental design or interpretation of data.

SUPPLEMENTARY MATERIALS

www.sciencemag.org/content/352/6290/1232/suppl/DC1
Materials and Methods
Figs. S1 to S8
References (24–26)

22 January 2016; accepted 13 April 2016
Published online 21 April 2016
10.1126/science.aaf3036



Too young to win a prize
in Stockholm this December?
We don't think so.



Get published in *Science* and win \$30,000 USD. Enter today: www.sciencemag.org/scilifelabprize
Cell and Molecular Biology | Ecology and Environment | Genomics and Proteomics | Translational Medicine

Science
AAAS

Knut och Alice
Wallenbergs
Stiftelse

SciLifeLab

Don't miss the debut of ***Science Immunology***.

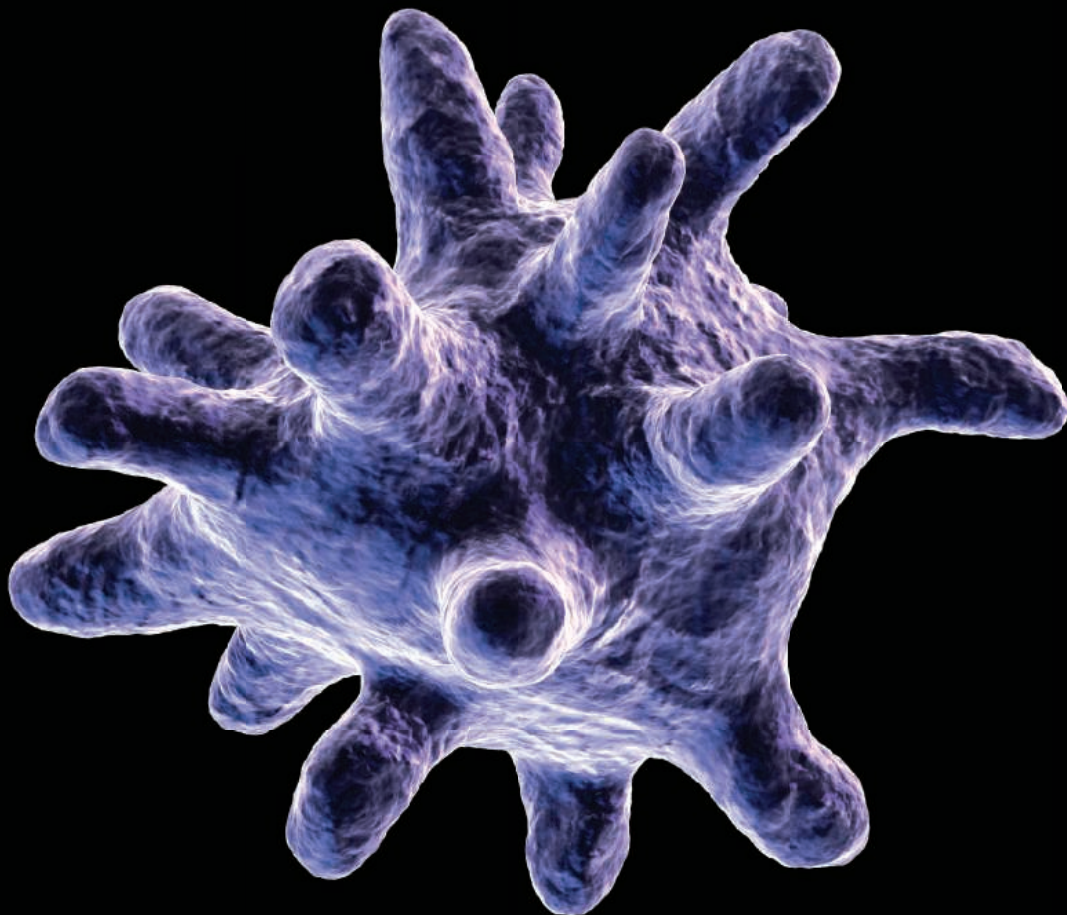


Image: Eraxion / iStockPhoto

————— NOW ACCEPTING PAPERS —————

Science is expanding its reach into immunology—now offering the newest online-only, weekly journal in the *Science* family of publications. *Science Immunology* will provide original, peer-reviewed research articles that report critical advances in all areas of immunological research, including studies that provide insight into the human immune response in health and disease.

Be a part of the *Science Immunology* debut issue publishing Summer 2016!

Submit your manuscript today at
ScienceImmunology.org.

ScienceImmunology

AAAS



2015 Winner
Shigeki Watanabe, Ph.D.
Johns Hopkins University
For research on synaptic
vesicle endocytosis

Call for Entries

**Application Deadline
June 15, 2016**

Eppendorf & Science Prize for Neurobiology

The annual Eppendorf & Science Prize for Neurobiology is an international award which honors young scientists for their outstanding contributions to neurobiological research based on methods of molecular and cell biology. The winner and finalists are selected by a committee of independent scientists, chaired by Science's Senior Editor, Dr. Peter Stern. Researchers who are not older than 35 years are invited to apply.

You could be next to win this prize and to receive

- > Prize money of US\$25,000
- > Publication of your work in Science
- > Full support to attend the Prize Ceremony held in conjunction with the Annual Meeting of the Society for Neuroscience in the USA
- > An invitation to visit Eppendorf in Hamburg, Germany

It's easy to apply!

Learn more about the Prize and its past winners at:

www.eppendorf.com/prize



At this very moment
Markus Hengstschläger
is giving a lecture on
human DNA in Vienna.
Change the DNA of your
meetings now!

ACV.AT
MESSECONGRESS.AT
VIENNA.CONVENTION.AT

VIENNA

Prof. Markus Hengstschläger, Director of the Institute of Medical Genetics, Medical University of Vienna © Andreas Hofer

IPA™ Integrated Patch Clamp Amplifier and Data Acquisition System

NEW



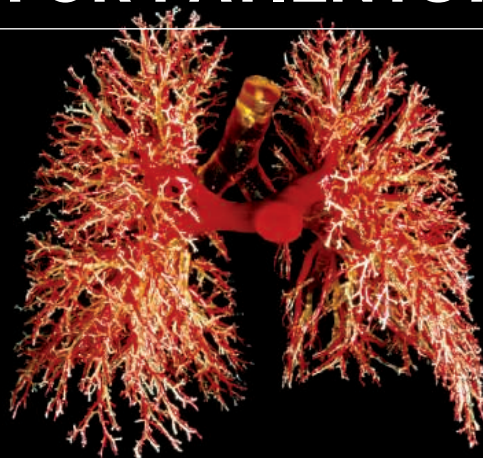
BENEFITS

- Single controller and ROE will run two stepper motor drive manipulators.
- Self-detecting, daisy-chain capability allows control of four manipulators from the ROE-200.
- User-friendly interface: single button access to all major functions.
- New accelerated mode for fast, manual manipulator movement.
- Easy toggle selection of mode.

SUTTER INSTRUMENT

PHONE: 415.883.0128 | FAX: 415.883.0572
EMAIL: INFO@SUTTER.COM | WWW.SUTTER.COM

WILL YOUR RESEARCH LEAD TO BETTER LIVES FOR PATIENTS?



Gopinath Sutendra and Evangelos D. Michelakis, "Pulmonary Arterial Hypertension: Challenges in Translational Research and a Vision for Change", *Sci. Transl. Med.* 5, 208sr5 (2013) Credit: Science Source

Science Translational Medicine | **AAAS**
INTEGRATING SCIENCE, ENGINEERING, AND MEDICINE

Find out more about the scope of the journal and submit your research today. **ScienceTranslationalMedicine.org**

myIDP: A career plan customized for you, by you.



For your career in science, there's only one **Science**



**Recommended by
leading professional
societies and the NIH**

Features in myIDP include:

- Exercises to help you examine your skills, interests, and values.
- A list of 20 scientific career paths with a prediction of which ones best fit your skills and interests.
- A tool for setting strategic goals for the coming year, with optional reminders to keep you on track.
- Articles and resources to guide you through the process.
- Options to save materials online and print them for further review and discussion.
- Ability to select which portion of your IDP you wish to share with advisors, mentors, or others.
- A certificate of completion for users that finish myIDP.

Visit the website and start planning today!

myIDP.sciencecareers.org

ScienceCareers In partnership with:



Be Among the First to Publish in ***Science Robotics***

Image: jim / AdobeStock



NOW ACCEPTING
MANUSCRIPTS

ScienceRobotics.org

Science Robotics is a unique journal created to help advance the research and development of robotics for all environments. *Science Robotics* will provide a much-needed central forum to share the latest technological discoveries and to discuss the field's critical issues.

Join in the excitement for the Fall 2016 debut!

ScienceRobotics
AAAS

Next-Generation Sequencing Control

The Archer SureShot Triple (ALK, RET, ROS1) Fusion-Positive Control has recently been launched to benchmark greater confidence in gene fusion detection using Archer FusionPlex Panels. The reference control is comprised of formalin-fixed paraffin-embedded (FFPE) curls of homogeneously mixed, precisely defined cell lines that contain EML4-ALK, CCDC6-RET, and SLC34A2-ROS1 fusions. When used alongside FusionPlex Panels that contain ALK, RET, or ROS1 fusions, the SureShot controls are a powerful measure of extraction, library preparation, sequencing, and panel performance. SureShot Negative Controls are also available, containing 100% wild-type cells that carry no target-gene fusion.

ArcherDX

For info: 877-771-1093
www.archerdx.com

Genotyping Solution

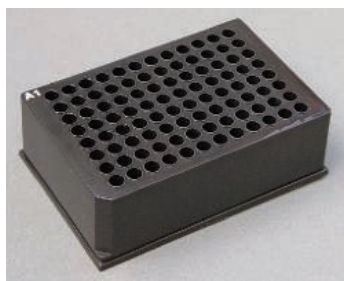
The Eureka Genotyping Solution is a new, targeted genotyping-by-sequencing (GBS) solution that delivers high-throughput sample processing with low cost per sample. This result is enabled by an innovative, multiplexed combination of allele- and sample-specific barcodes that support high sample plexing on a sequencer while delivering high-quality single nucleotide polymorphism (SNP) analysis. The Eureka genotyping assay overcomes the challenges associated with current GBS technologies, which are susceptible to variability in genomic reads and missing SNP information, high cost, and complex informatics analysis. Customers can access the Eureka genotyping assay as a service provided by Affymetrix Research Services Laboratory or as a kit-based product to run in their own facility. Complementing the Eureka genotyping offerings, the new 24-sample configuration on the high-density Axiom 96 platform can interrogate upward of 800,000 markers, while the new 96-sample configuration on the Axiom 384 HT platform can assay about 50,000 genetic variants.

Affymetrix

For info: 888-362-2447
www.affymetrix.com/agrigenotyping

Vascular Contrast Agent

BriteVu offers the latest in terminal vascular contrast agents for use with advanced imaging such as micro-computed tomography (micro-CT). BriteVu fills the vascular system down to the capillary level, creating a detailed and highly visible cast. Important features



Black Deep Well Plate

Porvair's new 96-well black deep well plate offers a working volume of 1 mL per well, which in conjunction with black sealing films, ensures that light sensitive assays and samples are not degraded by exposure to light, even over long-term storage periods. Manufactured from polypropylene, Porvair's black deep well microplate has excellent heat- and solvent-resistant qualities. Using only ultrapure grade polymers means that the black deep well plate has near-zero leachates, ensuring long-term sample integrity. The black plate is fully validated to be ribonuclease and deoxyribonuclease free, allowing it to be used with even the most sensitive biological samples. Benefiting from a cylindrical well design with round bottoms, the plate allows optimal mixing and easy sample recovery. Precisely manufactured to ANSI/SLAS dimensions, it is fully compatible with all commercially available microplate readers and automated liquid-handling equipment.

Porvair Sciences

For info: +44-(0)-1978-666222
www.porvair-sciences.com

include ease of use, low cost, high radiodensity, and safe ingredients. BriteVu has been successfully used in numerous mammal, reptile, and bird species—even human cadavers—to visualize the entire vascular system and specific organs or regions with incredible detail. Given its complete blood vessel filling, researchers can generate accurate 3D vascular maps for cancer, trauma, stroke, diabetes, malformations, and normal and other disease tissue states using CT. BriteVu can also be used in angiogenesis, drug development, and other studies.

Scarlet Imaging

For Info: 800-341-9024
www.scarletimaging.com

GF-1 Viral Nucleic Acid Extraction Kit

The GF-1 Viral Nucleic Acid Extraction Kit is designed for rapid and efficient purification of viral DNA/RNA from samples such as serum, plasma, body fluid, or virus-infected cell culture supernatant. The purification is based on the usage of denaturing agents to provide efficient cell lysis, denaturation of proteins, and subsequent release of DNA or RNA. Special buffers provided in the kit are optimized to enhance the binding of DNA or RNA onto a specially treated glass filter membrane for efficient recovery of highly pure DNA or RNA. The kits require no organic-based extraction. They are highly pure DNA or RNA, ready to use for routine molecular biology applications such as PCR and reverse transcription PCR.

Vivantis

For info: +603-8025-1603
www.vivanttechnologies.com

Gel Analysis Software

The new version of UltraQuant is a further step forward for this very user-friendly gel analysis software. Version 8.31.15 has a number of new and improved functions, making it one of the most convenient

gel analysis packages available. UltraQuant is included with all Omega Lum systems, where it works seamlessly alongside the SmartCapture Technology imaging platform. Once an image is captured, UltraQuant can quickly and easily provide a full analysis of the gel or blot using a minimum of steps. Naturally, UltraQuant has a fully automatic mode for the detection of lanes and bands across the gel or blot. Detection sensitivity can be set to an optimum position to achieve the best result. A very effective and easy-to-use edit function gives the user complete control over any lane or band that needs to be added or subtracted.

Gel Company

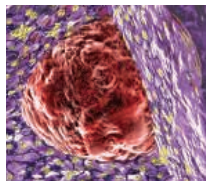
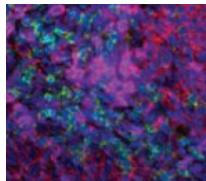
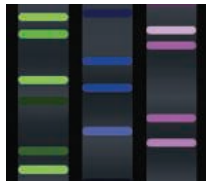
For info: +44-(0)-1223-515440
www.gelcompany.com

Electronically submit your new product description or product literature information! Go to www.sciencemag.org/about/new-products-section for more information.

Newly offered instrumentation, apparatus, and laboratory materials of interest to researchers in all disciplines in academic, industrial, and governmental organizations are featured in this space. Emphasis is given to purpose, chief characteristics, and availability of products and materials. Endorsement by *Science* or AAAS of any products or materials mentioned is not implied. Additional information may be obtained from the manufacturer or supplier.

want new technologies?

antibodies
apoptosis
biomarkers
cancer
cytometry
data
diseases
DNA
epigenetics
genomics
immunotherapies
medicine
microbiomics
microfluidics
microscopy
neuroscience
proteomics
sequencing
toxicology
transcriptomics



watch our **webinars**

Learn about the latest breakthroughs, new technologies, and ground-breaking research in a variety of fields. Our expert speakers explain their quality research to you and answer questions submitted by live viewers.

VIEW NOW!

webinar.sciencemag.org

Science
AAAS

Brought to you by the *Science*/AAAS
Custom Publishing Office



@SciMagWebinars

WHO WILL WIN THE PRIZE

**The result will be unveiled in June.
The winners will receive:**

- ★ A Grand Prize of \$25,000 and a Runner-Up Prize of \$5,000 will be awarded.
- ★ The Grand Prize Winning Essay will be published in *Science*;
a brief abstract of the Runner-Up Essay will be published in *Science*.

**The 2016 award ceremony will be held in
San Francisco, on 23rd June, 2016.**

Stem cells and regenerative medicine is
the new frontier in life sciences.

Boyalife, *Science*, and *Science Translational Medicine*
jointly establish a global award to recognize and
reward scientists in the fields of stem cells and
regenerative medicine with a focus on developing cell-based
treatments for cancer, degenerative disorders,
immunotherapy and stem cells transplantation.



Learn more about the Prize, visit :
<http://www.sciencemag.org/prizes/boyalife>



BOYALIFE
For Better Health

Science
AAAS

**Science
Translational
Medicine**
AAAS



There's only one **Science**

Science Careers Advertising

For full advertising details, go to ScienceCareers.org and click For Employers, or call one of our representatives.

Tracy Holmes

Worldwide Associate Director
Science Careers
Phone: +44 (0) 1223 326525

THE AMERICAS

E-mail: advertise@sciencecareers.org
Fax: +1 (202) 289 6742

Tina Burks

Phone: +1 (202) 326 6577

Nancy Toema

Phone: +1 (202) 326 6578

Online Job Posting Questions

Phone: +1 (202) 312 6375

EUROPE / INDIA / AUSTRALIA / NEW ZEALAND / REST OF WORLD

E-mail: ads@science-int.co.uk
Fax: +44 (0) 1223 326532

Sarah Lelarge

Phone: +44 (0) 1223 326527

Kelly Grace

Phone: +44 (0) 1223 326528

Online Job Posting Questions

Phone: +44 (0) 1223 326528

JAPAN

Katsuyoshi Fukamizu (Tokyo)

E-mail: kfukamizu@aaas.org
Phone: +81 3 3219 5777

Hirofumi Mashiki (Kyoto)

E-mail: hmashiki@aaas.org
Phone: +81 75 823 1109

CHINA / KOREA / SINGAPORE / TAIWAN / THAILAND

Ruolei Wu

E-mail: rwu@aaas.org
Phone: +86 186 0082 9345

Danny Zhao

E-mail: dzhao@aaas.org
Phone: +86 131 4114 0012

All ads submitted for publication must comply with applicable U.S. and non-U.S. laws. Science reserves the right to refuse any advertisement at its sole discretion for any reason, including without limitation for offensive language or inappropriate content, and all advertising is subject to publisher approval. Science encourages our readers to alert us to any ads that they feel may be discriminatory or offensive.

ScienceCareers

FROM THE JOURNAL SCIENCE 

ScienceCareers.org



EMBL offers a highly collaborative, uniquely international culture. It fosters top quality, interdisciplinary research by promoting a vibrant environment consisting of young, independent researchers with access to outstanding graduate students and postdoctoral fellows. EMBL is an inclusive, equal opportunity employer offering attractive conditions and benefits appropriate to an international research organisation.

Group Leader Mechanisms in Infection Biology

at EMBL/CSSB Hamburg, Germany

State-of-the-art infrastructures for applications in life sciences on DESY Campus, Hamburg, Germany, provide a world-class environment for most challenging experiments in structural biology with high scientific significance. The Hamburg Unit of EMBL has built an integrated facility in structural biology with three synchrotron radiation beamlines for applications in macromolecular X-ray crystallography and small angle X-ray scattering of biological samples at the new PETRA III ring. Access to state-of-the-art cryo-electron microscopy will be established within the Center for Structural Systems Biology (CSSB) on DESY Campus. EMBL is a partner of CSSB, which fosters highly interdisciplinary research across its members in infection biology with a main emphasis on structural and systems biology approaches. Laboratory and office space of the EMBL group leader position will be in the new CSSB building.

The successful candidate is expected to have his/her research focus in the following:

- Research interests in viral, bacterial or parasitic infection biology
- Possible topics are: translocation, secretion, host/pathogen interactions, pathogen metabolism
- Links to potential clinical applications are desirable

The candidate should have a record and future interest in the following techniques:

- Experience and research projects using integrative structural biology approaches
- Innovative use of X-ray radiation in structural biology, including Free Electron Laser applications (optional)
- Experience on complementary techniques, e.g. mass spectrometry, proteomics, metabolomics, and computational modeling approaches are advantageous
- Plans for complementary functional experiments

The candidate will take a leading role both at CSSB and the EMBL Hamburg Unit, and is expected to be interested in a high level of collaborations with other EMBL and CSSB faculty. She/he should have a PhD or similar degree in a relevant research area, at least three years of postdoctoral experience and an excellent research record.

Please apply online through www.embl.org/jobs and include a cover letter, CV and a concise description of research interests and future research plans. Please also arrange for 3 letters of recommendation to be emailed directly by your referees to references@embl.de at the latest by 28 June 2016.

Interviews are planned for the last week of August 2016.

Further details on Group Leader appointments can be found under www.embl.org/gl_faq.

For further information about research at EMBL please visit ...

www.embl.org



廣州醫科大學
GuangZhou Medical University

State Key Lab of Respiratory Disease, China: seeking talents to lead respiratory research

Employer

State Key Lab of Respiratory Disease, Guangzhou Medical University, Guangzhou, China

Location

Guangzhou, China

Research Discipline

Focus on respiratory Diseases, including but not limited to: respiratory infections and immunology, lung stem cell and regeneration, lung injury, COPD, asthma, lung cancer, bioinformatics with a focus on respiratory diseases.

Job Type

Professor, Associate Professor, Assistant Professor.

Salary

Highly competitive salary and benefits that is comparable to the best packages (including housing subsidy) in Guangzhou and Pearl Delta region will be provided depending on the candidate's qualifications.

Further information

The State Key Laboratory of Respiratory Disease (SKLRD), led by Director and Academician Prof. Nanshan ZHONG, and Executive Director Prof. Ling CHEN, is a leading research Centre for Respiratory Diseases in China. SKLRD was jointly established by Guangzhou Institute of Respiratory Disease (GIRD)/Guangzhou Medical University, and Guangzhou Institute of Biomedicine and Health (GIBH)/Chinese Academy of Sciences. SKLRD aims to improve the quality of life by advancing the medical sciences in prevention and treatment of respiratory diseases. Current research areas include studying epidemiology and influencing factors, identifying disease mechanisms, exploring new treatment and prevention modalities of respiratory diseases. SKLRD is committed to focus on translational research with a focus on unmet medical needs and to take the discovery in basic research into more effective treatment and prevention of respiratory diseases. SKLRD published 175 SCI papers in 2015. Some of the research work represented the leading advancement in the field of respiratory diseases, such as the new etiology and management of COPD, the new mechanism and treatment for asthma, the visualization of influenza virus infection in living mice, the new diagnostics for respiratory diseases. In 2016, SKLRD will expand its laboratory space into a newly renovated building in the center city. A new Guangzhou respiratory Center that integrated clinical research and basic research is under construction. SKLRD is striving to become a world leading research center in the field of respiratory diseases.

SKLRD is seeking highly qualified scientists to fill leading scientist positions. The candidates will be supported to apply for "1000 Talent Program" or "Young 1000 Talent Program", "NSF Distinguished Scholar" or "NSF Young Distinguished Scholar", and "Pearl River Scholar".

Successful candidates must possess a Ph.D or MD degree from top universities, have publications in internationally peer-reviewed journals in recent 5 years. Preference will be given to those with a strong background and successful experiences in both clinical and basic research.

Applicants should send curriculum vitae, one-page future research proposal, PDF reprints of 5 representative publications, and your inquiries to: sklrddirector@gird.cn and taochen@gird.cn



蘇州大學
SOOCHOW UNIVERSITY

FACULTY POSITIONS Soochow University Institutes for Translational Medicine

The Soochow University Institutes for Translational Medicine (SU-ITM) is a new research establishment with a mission to accelerate the advancement in strategies for patient care and healthy improvement through bridging strong university-wide foundation in basic research with clinicians, patients and pharmaceutical industry. SU-ITM strives for its excellence in translating discoveries from basic research in immunology, stem cells and cancer into prophylactically and therapeutically novel strategies and new products by soliciting expertise in various research enterprises across all campuses of Soochow University and affiliated hospitals. SU-ITM will focus on unmet medical needs of autoimmune, metabolic and degenerative disorders, and cancers. Excellent research platforms have been established for the SU-ITM mission in precision medicine, strategies of stem cell and regenerative medicine, immunological therapies, and novel diagnostic techniques.

SU-ITM seeks outstanding scholars to fill several academic positions at different levels to strengthen the research programs in cancer, immunology, stem cell biology, and drug discovery with strong emphasis on translational research. Qualified applicants should have a doctoral degree (Ph.D., M.D./Ph.D., or an equivalent) and received minimally 3 years of post-doctoral training. A good record of publications in top-tier journals is required.

Soochow University offers generous start-up funding, newly renovated laboratory space and state-of-the art research equipment and facilities. SU-ITM has an outstanding research environment including adjacent Suzhou Cold Spring Harbor meeting facility, excellent opportunities to collaborate with colleagues at Soochow University and affiliated hospitals as well as other institutes in nearby Shanghai metropolitan (25 min by train). Excellent recruitment package including relocation fees, competitive stipend and social benefits will be offered. Soochow University is highly experienced in assisting application for national scholar programs such as Thousand Talents Program and Young Thousand Talents Program.

Interested applicants should forward their curriculum vitae, a statement of research proposal, 3-5 exemplary publications, and 2-3 recommendation letters to Dr. Yufang Shi, the Dean of Soochow University Institutes for Translational Medicine (shiyufang2@gmail.com) or Dr. Yongjing Chen (chenyongjing@suda.edu.cn), Soochow University Institutes for Translational Medicine, Soochow University, 199 Ren Ai Road, Suzhou Industrial Park, Suzhou 215123, China.

Cyrus Tang Medical Institute

The Cyrus Tang Medical Institute is a newly established research institute at Soochow University in Suzhou, China. The Institute is jointly funded by the Cyrus Tang Foundation of the U.S. and the Jiangsu government. With the construction of a major building complex underway, the Institute is expected to recruit >100 PIs over the next 5 years. Research areas include, but are not limited to, **vascular biology, hematology, cell biology, cancer, stem cells, developmental biology, structural biology and genomic medicine**. We encourage diverse approaches to address fundamentally important questions in biology and medicine.

We are seeking Associate Professor and Professor candidates capable of leading independent research groups and competing for national talent programs. Candidates with strong training background at world top universities are encouraged to apply. Successful applicants should have a Ph.D. or M.D./Ph.D., outstanding publications in high-profile journals and the ability to develop innovative research projects.

Soochow University will provide generous start-up funds, sufficient lab space, and competitive salary and benefit packages.

Please send your CV, research plans and a list of 3 references to Ms. Qiaoqiao Chen at Cyrus Tang Hematology Center, Soochow University, 199 Ren-Ai Road, Suzhou 215123, China; Email: cqq@suda.edu.cn



暨南大學
JINAN UNIVERSITY

Recruitment of scholars (2016)

The Big Data Decision Institute (BDDI) of Jinan University (JNU) integrated institution resources from School of Finance, School of Medical, School of Life Science, School of Medicine, and more than 20 affiliated hospitals of JNU, as well as JNU's national key discipline resources of finance, clinical medicine, pharmacology and other disciplines that enter the ESI top 1%.

For better development, we invite global applications for the following posts.

Open Positions

1. BDDI: 10 full-time professors, associate professors, assistant professors, and unlimited number of post-doctors.
2. Sino-US Joint research team: 1-2 post-doctors working at University of Kansas, US.

Basic Requirements

1. Related research fields of big data-based Precision Medicine or Quantitative Investment, or mastering machine learning and data mining;
2. Doctorate degree in related areas;
3. Meeting the team value "team working, innovation, dedication, integrity and modesty".

Posts & Requirements

Job title	Requirements
The Big Data Decision Institute	
High-level Talent (referring to the payment of American colleges)	
Leading talent	<ul style="list-style-type: none"> • International well-known professors or associate professors, directors of national key projects, winners of national talent program, etc.
Outstanding talent	<ul style="list-style-type: none"> • International famous associate professors or influential assistant professors, members of Young Overseas .High-level Talents Introduction Plan, participants of national key project; • Have papers published in Nature (once having a paper published in Nature, applicants can directly apply for high professional title), Science, PNAS, MS, ISR or other A+ journals.
Top-notch talent	<ul style="list-style-type: none"> • Have highly-cited papers or other influential achievements, e.g., have papers published in journal with impactor over 20 or articles individually cited by others more than 50 times in ISI.
Excellent young doctor	<ul style="list-style-type: none"> • Have numbers of first/corresponding author papers published in international popular SCI / SSCI publications.
Post-doctor	<ul style="list-style-type: none"> • Have solid research foundation or unpublished papers. <p>Note: Post-doctor can obtain an up to 280,000 RMB annual salary. Excellent Post-doctor can be sent to Sino-US Joint research team and get a 120,000 RMB subsidy</p>
Sino-US Joint research team	
Post-doctor	<ul style="list-style-type: none"> • Fields related to Medical Information, being familiar with data mining algorithms. • Working at Medical Information center, University of Kansas, US. <p>Note: Payment according to the remuneration of post-doctors in U.S. government.</p>

Materials Required

1. Detailed resume and 2-5 representative papers;
2. After the preliminary examination, applicants need to provide documentary evidence such as academic and degree certificate, copies of ID card, etc.

Contact Us

Prof. Hu and Assistant Chen
E-mail: bddi.jnu@qq.com
TEL : 13632313877 (Chen)
020-85227283 (Talent Office)



第三軍醫大學

Faculty Positions Available in the Third Military Medical University, Chongqing, China

The Third Military Medical University (TMMU), with a history of over 70 years, is located in the mountain city of Chongqing, one of the four municipalities directly under the jurisdiction of the Central Government of China. This university is a national key university, one of the military "2110 Project" key universities, and one of the first universities allowed to grant doctor's degree and to offer eight-year medical education program in China. Currently, the university has 3 academicians of Chinese Academy of Sciences and Chinese Academy of Engineering and over 200 high-level talents including distinguished professors entitled "Changjiang Scholar" and winners of "National Outstanding Youth Foundation." The TMMU has 25 national key disciplines, key state laboratories and national engineering centers, and three grade-A affiliated hospitals. Now, the TMMU is seeking high-level medical talents from home and abroad. Applicants must have a nationality of China and a Ph.D. and/or M.D. degree.

Positions and Remuneration Packages

1. **Members of the national "One Thousand Talents Long term Program"**: A settling-down allowance of 3 million yuan and 8-million-yuan research fund with an annual salary of 1 million yuan.
2. **Members of the national "One Thousand Young Talents Program"**: A settling-down allowance of 1 million and 500 thousand yuan and 5-million-yuan research fund with an annual salary of 400 thousand yuan.

Further information is available at www.edu.cn/tmmu.

Contact Person: Ms. Fan

Tel: +86-23-68752105 13883596876

Email: sydrceb@sina.com

Address: Cadre Office of Politics Department, Third Military Medical University, Gaotanyan No.30 Center Street, Shapingba District, Chongqing 400038, P.R.China.



西南交通大學
Southwest Jiaotong University

Southwest Jiaotong University, Chengdu, China Invites Applications for the Academic Positions

Southwest Jiaotong University (SWJTU), founded in 1896 and located in Chengdu, the capital of Sichuan province--China's dynamically growing West, SWJTU is an elite university with national key multidisciplinary "211" and "985 Feature" projects directly managed by the Ministry of Education. SWJTU is currently on the strategic "Developing and Strengthening the University by Introducing and Cultivating talents" campaign.

Thus, you are cordially invited to apply for the following academic positions. More information is available at <http://www.swjtu.edu.cn/>

Positions and Requirements

- A. High-level Talented Leaders**: Candidates should be qualified to be listed in national top talents programs such as Program of Global Experts, Top Talents of National Special Support Program, "Chang Jiang Scholars", China National Funds for Distinguished Young Scientists and National Award for Distinguished Teacher.
- B. Young Leading Scholars**: Candidates are preferable to be listed or qualified for the following programs: National Thousand Young Talents Program, The Top Young Talents of National Special Support Program (Program for Supporting Top Young Talents), Science Foundation for the Excellent Youth Scholars.
- C. Excellent Young Academic Backbones**
- D. Excellent Doctors and Post Doctoral Fellows**

Please contact Mr. Yu Wang, Ms. Ye Zeng, Ms. Qing Ya Wang

Telephone number: +86-28-66367238/ 66366202

Email: talent@swjtu.edu.cn

Address: Human Resources Department, SWJTU, Western Park of High-Tech Zone, Chengdu, Sichuan, China, 611756



Diversity in Aging Research Pipeline Program

Post-doctoral Positions:

The National Institute on Aging (NIA), a research component of the National Institutes of Health (NIH) and the Department of Health and Human Services (DHHS) is the lead federal agency for aging, age-related disease, and Alzheimer's disease research. The NIA Intramural Research Program through its **Diversity in Aging Research Pipeline Program (DARPP)** is advertising a postdoctoral fellowship position. The goal of DARPP is to enhance diversity within the workforce of aging researchers and to provide training opportunities in aging research for underrepresented minorities and students from socioeconomically disadvantaged backgrounds. Successful candidates will be exceptionally qualified scientists-in-training who are interested in joining the NIA research community.

Candidates must have a Ph.D. (or M.D.) degree in molecular biology, biochemistry, bioinformatics, genomics, epidemiology, neuroscience or a related biomedical science field. Prior experience in aging research is not required. All applicants must be from a population underrepresented in the biomedical sciences, and have less than 5 years of postdoctoral experience. Candidates may be U.S. citizens or permanent-residents. Salary will be commensurate with research experience, according to the NIH intramural pay scale.

Interested applicants should e-mail curriculum vitae, a brief description of their research interests, and 3 letters of reference to: The DARPP Selection Committee c/o Mrs. Taya Dunn Johnson, E-mail: dunnt@grc.nia.nih.gov. The application deadline is **July 17, 2016**. Interviews will be conducted in August 2016. For more information about the NIA intramural program please visit: <http://www.grc.nia.nih.gov/>.

HHS and NIH are Equal Opportunity Employers.

The NIH is dedicated to building a diverse community in its training and employment programs.



Postdoc Positions

The Center for Systems Biology Dresden calls for applications for several open postdoc positions in within the prestigious

ELBE Postdoctoral Fellowship Program

in the following areas

- **Computer Science, Computational Science, and Applied Mathematics**
- **Bioinformatics and Computational Biology**
- **Biological Physics, Biophysics and Theoretical Biology**

We seek outstanding candidates with a degree in the listed areas and a strong interest in working in a multi-disciplinary environment towards developing and using computational and physical methods to address **key questions in biology** and to transform data into knowledge.

The Center for Systems Biology Dresden is a joint activity by the Max Planck Institute of Molecular Cell Biology and Genetics (MPI-CBG) and the Max Planck Institute of the Physics of Complex Systems (MPI-PKS). The center is a highly interactive and collaborative workplace with an international atmosphere where English is the working language, and has a strong commitment to interdisciplinary training and career development. The center provides access to cutting-edge computer infrastructure, genome sequencing technology and wet lab facilities. The MPI-CBG has been awarded one of the "Best Places To Work for Postdocs" in 2011.

ELBE Fellowships are awarded on a competitive basis to outstanding young researchers with a doctoral degree. To foster collaboration, fellows are usually affiliated with two hosting groups working in different disciplines.

Dresden was awarded "City of Science" in 2006 and is one of the leading scientific centers in Europe with 3 Max Planck and 13 other research institutes, and the Dresden University of Technology as one of eleven Universities of Excellence in Germany. Dresden has half a million inhabitants and is considered one of the most beautiful cities of Germany, located 2 hours from Berlin and Prague.

The Max Planck Society is an equal opportunity employer: handicapped individuals are strongly encouraged to apply. The Center for Systems Biology, the MPI-CBG and the MPI-PKS aim to increase the number of women in scientific positions. Female candidates are therefore particularly welcome.

Deadline for applications is **September 14, 2016**. For details about the application procedure, please visit our website <http://mpg-sysbio.de/index.php?id=jobs>



Advance your career
with expert advice from
Science Careers.



Download Free Career
Advice Booklets!

ScienceCareers.org/booklets

Featured Topics:

- Networking
- Industry or Academia
- Job Searching
- Non-Bench Careers
- And More



ScienceCareers

FROM THE JOURNAL SCIENCE AAAS

VILLUM INVESTIGATOR

– a new opportunity in Denmark for the
curiosity-driven scientist.



The aim of VILLUM Investigator Programme is to support researchers who have the potential to make significant contributions to technical and natural sciences.

It is expected that the VILLUM Investigators identify and pursue significant research questions and that they push their chosen research fields and / or methods into new areas of investigations.

Applicants to the VILLUM Investigator Programme are expected to be active researchers who have a track record of significant and excellent research achievements in the last 10 years.

Conditions

A VILLUM Investigator is appointed for a six-year renewable period, at a Danish university or another Danish research institution. Applicants may apply for up to DKK 40m (USD 6m), including start-up costs.

APPLICATION DEADLINE 28 SEPTEMBER 2016.

We expect to be able to award grants to approximately 10 VILLUM Investigators. Research projects are expected to commence in spring 2017.

Read more on www.veluxfoundations.dk

THE VELUX FOUNDATIONS

VILLUM FONDEN X VELUX FONDEN

THE VELUX FOUNDATIONS are non-profit, private charitable foundations supporting technical and natural sciences, environmental, social and cultural projects. In 2015, they granted a total of over DKK 800m.

Karolinska Institutet seeks a new Vice-Chancellor

Karolinska Institutet (KI) is a medical university with the mission to conduct research and education of the highest quality. KI's vision is to make a significant contribution to the improvement of human health. Achieving this vision will require groundbreaking research, the translation of medical advances into societal applications, and the successful provision of highly-skilled professionals to the workforce.

Last day of application is **15th of August 2016.**

For more information and expressions of interest, please visit ki.se/newvicechancellor



Karolinska
Institutet



Three Faculty Positions in Ecology

The Department of Ecology and Evolutionary Biology (EEB) at the University of Michigan seeks applicants for three assistant professor (tenure-track) positions in ecology. These are university-year appointments with an expected start date of September 1, 2017.

(1) Ecosystem Ecologist. We welcome applicants who study ecosystem processes in any of the planet's major ecosystems, including aquatic, terrestrial, wild-land, managed, and urban ecosystems. We are especially interested in individuals who include field and experimental approaches in their research. Areas of interest include, amongst others, biogeochemistry, carbon sequestration, and the effects of environmental change on ecosystem pools and fluxes.

(2) Population/Community Ecologist. We welcome applicants who study processes in any ecosystem or habitat type, including managed and urban systems. We also encourage individuals interested in interdisciplinary research. Areas of interest include, amongst others, mechanisms of population regulation; causes of species extinctions; and maintenance of biodiversity, community structure and ecosystem function under environmental change. Ideally, candidates will have an empirical research program that bridges to ecological theory.

(3) Theoretical Ecologist. We seek applicants who bring cutting-edge theoretical, mathematical, and computational tools to the study of ecological systems of any kind, including traditional fields such as population dynamics and community assembly as well as emerging subdisciplines such as urban ecology, macroecology, microbial ecology, disease ecology, and eco-immunology. Applicants with inter- and trans-disciplinary interests and who integrate theoretical development with empirical tests, whether alone or in collaboration, are especially encouraged to apply. This position will be a joint appointment with the University of Michigan Center for the Study of Complex Systems.

For all three positions, we are especially interested in individuals who will leverage the facilities available at the University of Michigan, including world class biodiversity collections, a local field research facility (the Edwin S. George Reserve), and a large educational and research facility in northern Michigan (the University of Michigan Biological Station).

Applications should include a cover letter, CV, a concise statement describing their current and future plans for research, a statement of their teaching philosophy and experience and evidence of teaching excellence (if any), and a statement of activities contributing to diversity, equity and inclusion in Academia. Applicants should also include the names and email addresses of three references.

EEB is committed to fostering ethnic and gender diversity throughout the department, and is especially interested in candidates contributing to the diversity and excellence of our academic community through their teaching, research, and/or service. To apply, please see <http://www.resources-eeb.lsa.umich.edu/search16/index.php>. Review of applications will begin on **September 1, 2016** (Ecosystem Ecologist), **September 15, 2016** (Population/Community Ecologist), and **October 1, 2016** (Theoretical Ecologist) and will continue until the positions are filled.

Women and minorities are encouraged to apply and the University is supportive of the needs of dual career couples. The University of Michigan is an Equal Opportunity/Affirmative Action Employer.

10 ways that *Science* Careers can help advance your career

1. Register for a free online account on ScienceCareers.org.
2. Search thousands of job postings and find your perfect job.
3. Sign up to receive e-mail alerts about job postings that match your criteria.
4. Upload your resume into our database and connect with employers.
5. Watch one of our many webinars on different career topics such as job searching, networking, and more.
6. Download our career booklets, including Career Basics, Careers Beyond the Bench, and Developing Your Skills.
7. Complete an interactive, personalized career plan at “my IDP.”
8. Visit our Career Forum and get advice from career experts and your peers.
9. Research graduate program information and find a program right for you.
10. Read relevant career advice articles from our library of thousands.

Visit ScienceCareers.org
today — all resources are free



ScienceCareers

FROM THE JOURNAL SCIENCE  AAAS

SCIENCECAREERS.ORG

VANDERBILT UNIVERSITY
MEDICAL CENTER

Director for Operations, Vanderbilt Vaccine Center

Vanderbilt University Medical Center (VUMC) is a premier teaching and research hospital located in Nashville, Tennessee, consistently ranked in the top 20 for NIH funding that supports a broad array of biomedical research endeavor. Vanderbilt University Medical Center is world renowned because of the innovation, work ethic and collegiality of its employees. From our health care advances to our compassionate care, Vanderbilt owes its accomplishments and reputation to staff and faculty who bring skill and drive and innovation to the medical center day after day. World-leading academic departments and comprehensive centers of excellence pursue scientific discoveries and transformational educational and clinical advances across the entire spectrum of health and disease. The Vanderbilt Vaccine Center at VUMC manages a portfolio of about \$60M of research funded by the NIH, DoD, and other sources, publishes regularly in top-tier academic journals, generates frequent intellectual property disclosures and patent applications, and licenses antibodies for clinical development in partnership with clinical research and pharmaceutical partners. The Center conducts basic and translational research in human immunology, with a focus on human monoclonal antibodies. The facility uses diverse sophisticated technical methods including high throughput screening/ expression, next generation deep sequencing, EM and crystallography techniques. The work involves human subjects, animals, biohazards, intellectual property, export-import, and other complex logistical areas.

We are seeking a Director for Operations who will provide leadership in coordinating the dynamic, extramurally-funded and productive research program within the Vanderbilt Vaccine Center. The Director for Operations will work closely with the Center Director to oversee a growing team committed to discovery of novel antibody therapeutics for infectious diseases and development of novel methods for antibody discovery. The Director for Operations will have experience in the conduct of all aspects of translational science research, including: implementing large-scale multi-site investigations and programs; managing large scale research operations and business; and regulatory and compliance procedures. Experience in immunology, entrepreneurship and familiarity with Lean principles are desirable. Preferred candidates will have an advanced degree (PhD and/or MD, and MBA) in a related field, and a record of scientific productivity.

As the largest employer in middle Tennessee, Vanderbilt University Medical Center welcomes those who are interested in ongoing development as part of a caring, culturally sensitive and professional atmosphere. Vanderbilt University Medical Center is located a little more than a mile from downtown Nashville "Music City, U.S.A.", and our students, trainees, faculty and staff benefit from increased opportunity for professional growth and access to many other benefits enabled by Vanderbilt, including public events and discussions, athletic opportunities, a beautiful setting and, above all, sense of community and purpose.

Interested individuals should submit an application for the **Director/Operations, Vanderbilt Vaccine Center - VUMC-1602710** position via the Vanderbilt University Medical Center Careers portal: https://vanderbilt.taleo.net/careersection/vu_cs/jobdetail.ft?job=1602710

For other inquiries, contact **Susan Meyn** in the Vanderbilt University Medical Center Office of Research: s.meyn@vanderbilt.edu

FDA
Principal Investigator Positions
at the
U.S. Food and Drug Administration

The mission of the Office of Biotechnology Products (OBP, Center for Drug Evaluation and Research, U.S. Food and Drug Administration) is to protect public health by assuring the quality, safety, efficacy, availability, and security of therapeutic protein and monoclonal antibody products. OBP's laboratory research programs investigate the structure, manufacture, and molecular actions of protein-based drugs to inform science-based regulatory standards and review activities.

OBP is seeking to recruit three qualified and motivated individuals, with Ph.D. and/or M.D. degrees, for career-conditional principal investigator positions in the areas of **metabolism (including cancer)** (1 position), **bioprocessing** (1 position), and **glycobiology** (1 position). The successful candidates will actively develop independent, OBP mission-relevant research programs, review product applications, and participate in formulating FDA policy. Several years of post-doctoral experience and a record of scientific accomplishment in the relevant area of scientific specialty are required. Positions are located on the FDA main campus in White Oak, MD, and are supported with intramural funding. Salary is commensurate with experience.

To apply, send curriculum vitae, 1-2 page statement of your proposed research program within the above stated research and review mission of the Office of Biotechnology Products, and names of three references to **Dr. David Frucht (Chair), OBP PI Search Committee (c/o Dr. Daniel Harris), 10903 New Hampshire Ave., WO71-2205, Silver Spring, MD 20993-0002, or email Daniel Harris (daniel.harris@fda.hhs.gov)**. Please indicate to which of the positions you are applying and clearly describe how you will develop your proposed research program to address the overall regulatory mission of OBP. Applications must be received by **July 10th, 2016**. E-mail applications are preferred. *U.S. citizens or permanent residents only.*

The Food and Drug Administration is an Equal Opportunity Employer.



The brand new "Oncopole" campus, based in Toulouse (South West of France), gathers academic, scientific, medical, clinical, technological and pharmaceutical research on cancer. Its missions are to improve fundamental knowledge on all aspects of cancer biology and to provide patients with rapid access to innovative and individualized treatments.

Fondation Toulouse Cancer Santé, jointly with Pierre-Fabre Research Institute, is recruiting an outstanding young immuno-oncologist for a team leader position within the Cancer Research Center of Toulouse (CRCT).

Candidates will be required to detail information about their previous work and submit a competitive project proposal.

Applications: CV, research project (4 pages), publications & patents list, grants, references in English - 10 pages max

Applications must be sent to: join.crct@inserm.fr with reference: **"TCS IRPF Immuno-Onco"**

Only applications received before **July 31st 2016** will be considered.

For more information, please visit:
www.toulousecancer.fr

By Antoni Margalida

Flying free before building my nest

I spent the first 17 years of my scientific life as a freelance naturalist, with no more academic credentials than a bachelor's degree in library and information science. It was challenging, but I found it intellectually rewarding, and I enjoyed exploring my scientific passion without facing the pressure and uncertainty typically endured by trainees pursuing academic careers. I was able to simply let my creativity develop. Then, 7 years ago, my career took a turn when I attended a conference about bearded vultures, which led me to earn my Ph.D. at the age of 38. Now, as a postdoc pursuing an academic research career, I am taking advantage of all that I learned during my years as an independent scientist.

I took this unconventional path because of the poor employment prospects for biologists in Spain in the 1980s, which deterred me from studying science. But I had become fascinated by bearded vultures as a teenager, and my emotional attachment to these birds of prey and to conservation never faded. So, after finishing my bachelor's degree, I signed a 6-month contract with the regional government to monitor bearded vulture breeding sites, and my scientific career began.

Not long after, the Catalan government was seeking a naturalist to do similar work. Someone told the government officials about a passionate young naturalist who spent all his time watching vultures, and they contacted me. I worked on regional projects as a self-employed naturalist, gradually getting involved in international conservation research efforts, and finally found myself as a freelance wildlife technician for the Spanish government.

As my research progressed, I published because I wanted to share my findings, not because I was hoping for an advanced degree or items for my CV. I didn't have to worry about racking up papers, the reputation of the journals I published in, or where I stood on the author list. This freedom allowed me to pursue the questions I was most interested in and to develop risky projects that might take ages to yield rewards, if any. And even though the salary of my early years did not even cover the cost of gasoline to get to the remote field sites, I felt I was the luckiest man in the world to work with the species that fascinated me most.

But at that conference in 2009, an influential conservation biologist approached me after my talk. He was interested in my field studies and publications, and we continued our discussion over dinner. He was surprised that I did not



"My emotional attachment to these birds of prey and to conservation never faded."

have a doctorate and suggested that I prepare a Ph.D. thesis under his supervision. I was astonished: He did not know me personally, although he had read the majority of my papers. I was also excited, because a doctorate would open career doors that had previously been closed to me. It would give me access to competitive research funds, which would enable me to tackle more ambitious scientific questions and conservation challenges.

So, 1 year later, I enrolled as a Ph.D. student. I worked with my adviser to select 31 of my papers, submitted them as a Ph.D. thesis, and was awarded my degree. I am now a postdoctoral researcher, with hopes of establishing my own research group.

I miss my earlier freedom to some extent, but the financial security of a full-time position is a real asset, especially now that I have a family, and the tools and collaborations that academia offers are extremely rewarding. At the same time, I'm glad I took an unconventional path. I believe that if I had gone straight into academia, where bibliometrics rule the lives of today's young researchers, I would have been less adventurous in my choice of projects. Blazing my own trail before returning to academia helped me on my road to becoming a successful, fulfilled scientist. ■

Antoni Margalida is a postdoctoral researcher in the Department of Animal Science at the University of Lleida in Spain and an associated senior scientist in the Division of Conservation Biology at the University of Bern. He thanks Tim Birkhead, Karl Schulze-Hagen, and Rhys E. Green for advice and Raphaël Arlettaz for his continuous support. Send your story to SciCareerEditor@aaas.org.